



Universidad
de Alcalá

Programa de Doctorado en Química

**INNOVATIVE ANALYTICAL DESIGNS BASED ON
NANOMATERIALS AND MICROMOTORS FOR
(BIO)-SENSING APPLICATIONS IN BIOLOGICAL
MEDIA**

PhD Thesis by

KAISONG YUAN

Supervisors:

Dra. BEATRIZ JURADO SÁNCHEZ

Prof. JESÚS ALBERTO ESCARPA MIGUEL

Prof. ZHENGJIN JIANG

Alcalá de Henares, Septiembre 2020

Resumen

El cáncer y las enfermedades infecciosas se encuentran entre las 10 principales causas de mortalidad, ocasionando 6 millones de muertes anualmente. Los métodos de diagnóstico actuales carecen de especificidad para la detección de biomarcadores específicos para estas enfermedades, lo que requiere de pruebas de diagnóstico largas e invasivas, que en última instancia suponen un retraso en el tratamiento efectivo de estas enfermedades. En este contexto, los graves efectos secundarios de la quimioterapia o la radioterapia y la creciente resistencia a los antibióticos utilizados para el tratamiento de infecciones bacterianas suponen una limitación adicional. Otro desafío importante es el hecho de que muchas empresas farmacéuticas pusieron fin a numerosas investigaciones dirigidas al descubrimiento de nuevos agentes antimicrobianos, debido a su bajo margen de beneficio. Los avances recientes en Nanociencia y Nanotecnología podrían proporcionar metodologías y medios alternativos para abordar los retos biomédicos existentes en el tratamiento y diagnóstico de infecciones bacterianas o cáncer.

La técnica de amplificación o aumento de la señal Raman por la superficie (también conocida como SERS) es una poderosa herramienta analítica basada en la mejora de la dispersión Raman de (bio) moléculas adsorbidas en superficies metálicas o en nanoestructuras plasmónicas. El uso de sustratos metálicos plasmónicos como los nanocompuestos Ag@Au es fundamental para lograr una detección ultrasensible de biomarcadores en muestras clínicas. Sin embargo, la escasa estabilidad de estos *nanocompuestos* limita su aplicación.

Los nanomateriales 2D tales como el grafeno se han utilizado como sustratos para la inmovilización de nanopartículas metálicas, evitando así su oxidación, y promoviendo su estabilidad a largo plazo. Además, la funcionalización de nanopartículas magnéticas con sondas como péptidos antimicrobianos permite llevar a cabo una etapa de pre-concentración previa del analito objeto de estudio y un posterior marcaje con nanopartículas o ligandos con actividad SERS, aumentando así la versatilidad de la técnica en el análisis clínico permitiendo llevar a cabo la determinación multiplexada y directa de bacterias patógenas.

Los micromotores se pueden definir como micro/nanopartículas que pueden convertir un *combustible químico*, o un estímulo de luz, magnético o acústico en movimiento autónomo. El tamaño, la forma y los mecanismos de propulsión de los micromotores son factores cruciales en el diseño de futuras aplicaciones. Así, los micromotores se pueden dividir en tres grupos principales de acuerdo con el mecanismo de propulsión: (a) micromotores catalíticos (tubulares y Janus); b) micromotores biocompatibles o *fuel-free* e impulsados por fuentes de energía magnética, ultrasónica, o térmica y c) micromotores biohíbridos.

Una clave para desarrollar micromotores altamente eficientes en aplicaciones biomédicas reside en la incorporación de materiales funcionales avanzados, con el objetivo de incorporar ligandos y otros componentes funcionales y/o modular el modo de propulsión. En este contexto, los micromotores también pueden beneficiarse enormemente de las propiedades sobresalientes de los nanomateriales 2D, como son la elevada relación superficie-volumen y la presencia de grupos funcionales para una posterior funcionalización selectiva, que es fundamental para el tratamiento y diagnóstico de enfermedades infecciosas y cáncer.

La combinación de nanomateriales 2D con micromotores exige un diseño y una selección adecuada de la técnica de fabricación. Los micromotores Janus son una clase de materiales cuyas superficies tienen dos o más propiedades físicas distintas, lo que permite que se produzcan dos tipos de química simultáneamente. Se han explorado una gran cantidad de técnicas de fabricación, desde la deposición física de vapor de metales en micropartículas hasta técnicas de emulsión en disolución y autoensamblado. La gran cantidad de estrategias sintéticas para la preparación de micromotores Janus permite modular sus propiedades mediante la incorporación de diversos nanomateriales (nanopartículas metálicas, 2D, entre otros) y (bio)-receptores específicos. Además, los micromotores tubulares constituidos por nanomateriales 2D pueden prepararse fácilmente mediante el método de electrodeposición asistida por membranas. La transferencia de masa mejorada causada por el movimiento cooperativo de múltiples micromotores Janus o tubulares puede conducir a nuevos tratamientos biomédicos y protocolos de detección más rápidos y eficientes.

Por todo ello, el principal objetivo de esta Tesis Doctoral es el desarrollo de estrategias analíticas de vanguardia basadas en nanomateriales y micromotores para aplicaciones de (bio)-sensado en medios biológicos. Para conseguir el objetivo principal de esta Tesis Doctoral se han establecido los siguientes objetivos específicos:

1. Sintetizar y caracterizar nanocompuestos Janus basados en grafeno y nanopartículas metálicas para la detección SERS y destrucción de bacterias patógenas.

2. Sintetizar y caracterizar micromotores Janus basados en nanomateriales 2D (grafeno, grafidino y fósforo negro) para la detección óptica y destrucción de bacterias patógenas.

3. Sintetizar y caracterizar de micromotores tubulares basados en grafidino para la detección óptica de toxinas bacterianas y la destrucción de células patógenas (cancerígenas).

4. Desarrollar dispositivos de detección ópticos portátiles integrando micromotores tubulares y Janus basados en materiales 2D para la detección in situ de biomarcadores y bacterias.

Estos objetivos, la hipótesis de trabajo y la definición de los hitos específicos de esta Tesis Doctoral, se recogen en el **Capítulo I**.

El **Capítulo II** introduce una visión general de los enfoques nanotecnológicos de vanguardia para el diagnóstico de cáncer e infecciones bacterianas, que van desde estrategias Raman basadas en el uso de nanopartículas y nanomateriales de carbono; a estrategias recientes basadas en micromotores.

Los resultados más relevantes derivados de la Tesis Doctoral se recogen en los **Capítulos III-VI**.

El **Capítulo III** recoge todos los resultados relacionados con el diseño de nuevas estrategias SERS basadas en el uso de nanocompuestos de grafeno/nanopartículas metálicas o nanopartículas magnéticas modificadas con péptidos antimicrobianos como elementos de captura en la detección y

destrucción de bacterias patógenas. En un primer enfoque, se emplean nanocompuestos de Au@Ag ensamblados en conchas de mejillón como sustratos naturales en aplicaciones SERS. Las conchas de mejillón ofrecen un sustrato ideal dado que están compuestas principalmente por CaCO_3 , lo que resulta en una gran hidrofobicidad que promueve el enriquecimiento de las bacterias objeto de estudio. Por otro lado, la estructura rugosa de este (bio)-sustrato resulta en una acumulación de las nanopartículas, generando *hot spots* que conducen a un aumento de la sensibilidad en la detección SERS. Así, se obtuvo un límite de detección de 10^{-9} M para la detección de Rodamina 6G. Posteriormente los sustratos SERS desarrollados se aplicaron satisfactoriamente para la identificación simultánea de *Escherichia Coli*, *Staphylococcus Aureus* y *Pseudomonas Aeruginosa* mediante análisis discriminante.

Inspirado por la estrategia SERS anterior, se desarrolló a continuación un nuevo biosensor basado en una estructura sándwich para el aislamiento y detección de múltiples patógenos bacterianos mediante la separación magnética y posterior detección SERS. El ensayo se basa en nanopartículas magnéticas funcionalizadas con péptidos antimicrobianos como sondas de "captura" para el aislamiento de bacterias y nanocompuestos de óxido de grafeno decorados con nanopartículas de plata-oro y modificados con ácido 4-mercaptofenilborónico (4-MPBA) como etiquetas SERS. Cuando se combinan diferentes tipos de patógenos bacterianos con las etiquetas SERS, las "huellas digitales" de 4-MPBA muestran los cambios correspondientes debido a cambios en los eventos de reconocimiento entre el ácido 4-MPBA y las distintas membranas externas de las bacterias objeto de estudio. El 4-MPBA puede utilizarse además como un estándar interno para corregir las intensidades de SERS con alta reproducibilidad, así como un indicador de señal Raman para mejorar la sensibilidad y amplificar las diferencias entre las "huellas dactilares" bacterianas. Así, se aislaron y detectaron con éxito tres patógenos bacterianos (*Escherichia Coli*, *Staphylococcus Aureus* y *Pseudomonas Aeruginosa*), a una concentración de 10^1 unidades formadoras de colonias por mililitro. Por otro lado, las nanopartículas de Fe_3O_4 modificadas con péptidos antimicrobianos presentan una alta actividad antibacteriana y pueden actuar como agentes antibacterianos en el almacenamiento a largo plazo de sangre para futuras aplicaciones de transfusión de sangre seguras. El método se aplicó de forma satisfactoria al análisis de muestras de sangre total de pacientes infectados.

El **Capítulo IV** describe la síntesis y aplicaciones de micromotores Janus basados en nanomateriales 2D para la captura selectiva, detección y destrucción de bacterias y biomarcadores relacionados. En primer lugar, se describe la síntesis de micromotores Janus basados en GO, GDY y fósforo negro (BP) que integran "tres motores" para el control del movimiento utilizando diferentes estímulos como combustible químico, radiación electromagnética y campos magnéticos. Los micromotores pueden producirse en masa recubriendo microesferas de poliestireno que actúan como molde con una capa de oro, nanomateriales 2D y nanopartículas de Pt o MnO_2 como "motores catalíticos"; nanopartículas de Fe_2O_3 como "motores magnéticos" y puntos cuánticos como "motores de luz". El diseño y la composición de los micromotores es clave para obtener una propulsión óptima y controlada en disolución. Así, la velocidad del micromotor puede ser controlada empleando distintas fuentes de energía. En los modos de propulsión catalítico-magnético o catalítico-luz, los micromotores integran un sistema de aceleración que permite aumentar su velocidad hasta 3.0 y 1.5 veces después de la aplicación del campo magnético o la irradiación de radiación electromagnética, respectivamente. En el modo catalítico-magnético-luz, dicho aumento de velocidad se puede combinar en una sola unidad para un mejor control del movimiento del micromotor en medios complejos. Así, la capacidad para un movimiento adaptativo de los micromotores desarrollados puede ser muy beneficioso en futuras aplicaciones de detección que utilicen los micromotores en muestras biológicas complejas con un alto contenido de proteínas y otros compuestos que pueden obstaculizar el movimiento de los micromotores y, por lo tanto, la eficiencia del proceso.

En un segundo enfoque, se describe una estrategia de detección OFF-ON basada en los micromotores Janus de GDY, GO y BP/ Fe_2O_3 /PtNPs para la detección de la toxina del cólera como un biomarcador bacteriano relevante. La estrategia se basa en el empleo de un péptido de afinidad fluorescente específico como receptor, que se une al nanomaterial 2D de los micromotores. En presencia de la toxina del cólera, el péptido es liberado de la superficie del micromotor, recuperando la fluorescencia del péptido de afinidad, inicialmente amortiguada por su interacción con el nanomaterial 2D. Las distintas propiedades superficiales de cada nanomaterial juegan un papel fundamental en la capacidad de captura/liberación del péptido, lo que afecta en última

instancia a las propiedades analíticas. La adsorción del péptido de afinidad obedece a un modelo cinético de segundo orden utilizando los tres nanomateriales 2D en conexión con micromotores, lo que indica una fuerte influencia de interacciones de quimisorción y una mayor capacidad de carga para los micromotores basados BP. Sin embargo, la cinética de liberación es más rápida para los nanomateriales GDYO y GO, lo que indica una contribución de interacciones π e hidrófobas en la adsorción de la sonda (péptido de afinidad) y la desorción de la misma en presencia de la toxina del cólera. La estrategia desarrollada se aplicó satisfactoriamente a la detección directa de la toxina de cólera en suero humano y cultivos bacterianos. El movimiento autónomo del micromotor integrando los materiales 2D permite un funcionamiento eficiente en entornos miniaturizados y muestras complejas, lo que es muy prometedor para el diseño de nuevos sensores basados en micromotores o para comprender la interacción entre micromotores y homólogos biológicos en aplicaciones clínicas.

Un tercer enfoque basado en detección óptica explora el uso de péptidos antimicrobianos para la inactivación de bacterias siguiendo un enfoque similar al descrito en la detección SERS, pero esta vez a bordo de micromotores. Para esta aplicación se emplearon micromotores Janus de GO/Fe₂O₃/ PtNPs modificados con el péptido antimicrobiano Nisina e impulsados por campos magnéticos y catalíticos. Los micromotores modificados se utilizan para la captura/inactivación selectiva de bacterias grampositivas y biopelículas. La interacción específica de la nisina con la unidad de lípido II de la bacteria *Staphylococcus Aureus* junto con el movimiento autónomo del micromotor mejora 2 veces la capacidad de captura/destrucción de la bacteria en comparación con el péptido libre y micromotores estáticos. La alta estabilidad de la nisina junto con el movimiento mejorado del micromotor permite el empleo de la estrategia en muestras complejas. La estrategia es además altamente selectiva para bacterias grampositivas frente a bacterias gramnegativas (*Escherichia Coli*). Estos resultados son especialmente prometedores para el diseño de micromotores modificados con antibióticos (péptidos formados por aminoácidos y polisacáridos y que poseen actividad microbiana) personalizados que puedan responder a los cambios que hacen que las bacterias sean resistentes.

El **Capítulo V** ilustra la síntesis y aplicación de micromotores tubulares de GDY para la detección de biomarcadores y la destrucción de células cancerosas. En primer lugar, se describe la síntesis de los micromotores conteniendo una capa externa de GDY y diversas capas catalíticas internas (Pt/Ni, MnO₂ o Pd /Cu) mediante un protocolo de deposición electroquímica en membrana. El GDY se electrodeposita directamente mediante voltamperometría cíclica. La capa GDY da como resultado la generación de una capa metálica interna rugosa, lo que permite el funcionamiento del micromotor a niveles muy bajos de peróxido de hidrógeno (0.5%). Además, la capa externa de GDY es rica en carbonos sp y sp² con una red π conjugada. Esto da como resultado un área superficial muy aumentada para una mayor carga de medicamentos contra el cáncer o receptores específicos. Se observa una alta biocompatibilidad con casi el 100% de viabilidad celular en ensayos de citotoxicidad con micromotores en movimiento en presencia de células HeLa. En un primer ejemplo, los micromotores GDY modificados con doxorrubicina se utilizan para la liberación controlada de este fármaco mediante cambios de pH y destrucción de las células cancerosas HeLa. En un segundo ejemplo se ilustra la modificación de los micromotores con péptidos de afinidad específicos para la detección OFF-ON fluorescente sensible y selectiva de la toxina del cólera B mediante el reconocimiento específico de la región de la subunidad B de la toxina diana y la endotoxina de *Escherichia Coli*.

Finalmente, el **Capítulo VI** describe la integración de las estrategias de detección desarrolladas en los capítulos anteriores en instrumentación portátil. El diseño se basa en el acoplamiento de una lente de gran aumento con la cámara de un teléfono inteligente. A continuación, el sistema se integra en una plataforma impresa en 3D que permite "enfocar" la muestra, la cual se coloca en un compartimento de la plataforma diseñada para tal fin. La cámara del teléfono permite visualizar directamente el movimiento del micromotor y cambios en la disolución, reemplazando así los microscopios ópticos de alta resolución empleados hasta la fecha para este tipo de estrategias. Para lograr la detección fluorescente, se puede irradiar directamente la muestra con diodos láser comerciales con diferentes longitudes de onda, colocando el filtro apropiado entre la cámara y la lente de aumento. Este enfoque universal

permite emplear las estrategias de detección basadas en micromotores para la detección *in situ* de los analitos diana descritos en esta Tesis Doctoral.

Teniendo en cuenta los resultados obtenidos, la conclusión principal y transversal de esta Tesis Doctoral es la identificación del extraordinario potencial de los nanomateriales 2D junto con nanopartículas y micromotores para el aislamiento-detección-destrucción de células patógenas y (bio) - marcadores relevantes en enfoques de diagnóstico y tratamiento avanzado de enfermedades.

Se ha demostrado que la combinación de nanocompuestos de grafeno con nanopartículas de oro recubiertas de plata como partículas marcadoras de detección SERS es muy relevante, evitando importantes inconvenientes como la oxidación de las nanopartículas y aumentando la densidad de los "*hot spots*" para un aumento de la sensibilidad final de estas estrategias. Además, la presencia de grupos funcionales permite incorporar ligandos específicos para el aislamiento de bacterias diana con capacidad para inactivar células dañinas como bacterias. El resultado principal ha sido el diseño de biosensores SERS multifuncionales para el aislamiento, discriminación y destrucción de bacterias, con alto potencial para el diagnóstico clínico.

La relevancia de los nanomateriales 2D también se ha puesto de manifiesto de forma transversal en relación con los micromotores en el campo biomédico. Las aproximaciones analíticas de autoensamblaje y electrosíntesis en membranas permiten la síntesis de micromotores tubulares y Janus, respectivamente; lo que da como resultado enfoques sinérgicos que combinan las propiedades físicas y químicas de los nanomateriales 2D con las prestaciones intrínsecas de los micromotores catalíticos (movimiento autónomo, mezcla mejorada y envío localizado de fármacos). El resultado principal ha sido el diseño de una batería de micromotores tubulares y Janus para la detección de toxinas bacterianas y la destrucción de células patógenas (cáncer y bacterias) con biorreceptores específicos. Los nanomateriales 2D mejoraron la velocidad general de los micromotores en medios biológicos complejos al tiempo que mejoraron la inmovilización de receptores específicos.

La capacidad de movimiento autónomo de los micromotores integrando nanomateriales 2D y la capacidad de moverse en entornos ultraminiaturizados han permitido desarrollar estrategias portátiles para la detección "*in situ*" de

estos biomarcadores. El resultado principal ha resultado ser el diseño de un protocolo universal integrado en un teléfono inteligente para la detección fluorescente o basada en movimiento de biomarcadores de bacterias para un rápido diagnóstico y tratamiento de enfermedades importantes.

El conjunto de los resultados obtenidos pone de manifiesto que el empleo sinérgico de nanomateriales y micromotores 2D, son enfoques nanotecnológicos muy prometedores en el panorama científico contemporáneo para el diagnóstico y tratamiento de enfermedades, que redundarán en un beneficio tangible para la sociedad en un futuro no muy lejano.

Summary

Cancer and infectious diseases are among the top 10 global causes of death, causing 6.0 million deaths worldwide. Current diagnosis methods lack specificity for related biomarker's detection, requiring invasive diagnosis tests that can delay efficient treatment. In addition, the serious side effects of chemotherapy or radiotherapy and the antibiotic resistant nature of some bacteria delay the efficient treatment of such serious illnesses. Another major challenge is the fact that many pharmaceutical companies stopped research efforts for the discovery of new antimicrobial agents due to their low profit margin. Recent advances in nanoscience and nanotechnology can provide alternative means to solve such complex biomedical challenges.

Surface-enhanced Raman spectroscopy (SERS) is powerful analytical tool based on the enhancement of the Raman scattering of (bio)-molecules adsorbed on metal surfaces or in plasmonic nanostructures. The use of SERS plasmonic substrates such as Ag@Au nanocomposites is essential to achieve ultra-sensitive detection of biomarkers in clinical samples. However, the poor stability of such nanocomposites limits their application.

2D nanomaterials such as graphene (GO) nanosheets have been used as convenient substrates for loading metal nanoparticles, preventing its oxidation, with a long-term stability without hampering SERS activity. In addition, functionalization of the magnetic beads with probes such as antimicrobial peptides offered target isolation, followed by forming sandwich structure together with SERS tags, thus confer them with multifunctional capabilities for isolation-discrimination and killing of i.e. pathogenic bacteria cells.

Micromotors can be defined as tools -with a size ranging from few nanometers to micrometers- that can convert a chemical fuel, light, magnetic or acoustic energy input into autonomous motion to perform several tasks. The size, shape and propulsion mechanisms of micromotors will exert a strong influence on a given biological application. Thus, micromotors can be divided into three main groups according to the propulsion mechanism: (a) chemically powered (catalytic) micromotors (tubular and Janus); (b) fuel free micromotors powered by biocompatible sources (magnetic, ultrasound, light or thermal energy sources) and (c) biohybrid micromotors.

Summary

A key to develop micromotors with high performance for biomedical applications is to explore the incorporation of advanced functional materials for i.e. further functionalization or to tune the propulsion mode. In this context, micromotors can also greatly benefit from the outstanding properties of 2D nanomaterials, such as the high surface-to-volume ratio and the presence of multiple functional groups for further functionalization, which is fundamental for the treatment and diagnosis of infectious diseases and cancer.

The combination of 2D nanomaterials with micromotors demands for a judicious design of the fabrication technique. Janus micromotors are a unique class of materials whose surfaces have two or more distinct physical properties, allowing thus for two types of chemistry to occur simultaneously. A plethora of fabrication routes have been explored, including the deposition of metallic thin films on microbeads, pickering emulsion or self-assembly. The myriad of synthetic strategies for the preparation of Janus micromotors allow to easily tune its properties and for the easy incorporation of 2D nanomaterials and bioreceptors. In addition, tubular micromotors composed entirely of 2D nanomaterials can be easily prepared by the so-called template assisted electrodeposition method. The enhanced mass transfer caused by the cooperative motion of a swarming of Janus or tubular micromotors can lead to novel and more efficient biomedical treatments or biomarkers sensing protocols.

Therefore, the main objective of this Doctoral Thesis is the development of innovative analytical designs based on nanomaterials and micromotors for (bio)-sensing applications in biological media. To achieve the main objective of this Doctoral Thesis, the following specific objectives have been established:

- 1.** To synthesize and characterize Janus nanosheets based on graphene and metal nanoparticles for SERS detection and killing of pathogenic bacteria.
- 2.** To synthesize and characterize Janus micromotors based on 2D nanomaterials (graphene, graphdyine and black phosphorous) for optical detection and killing of pathogenic bacteria.

3. To synthesize and characterize graphdyine based tubular micromotors for optical detection of bacteria toxins and pathogenic cell killing.
4. To develop optical portable detection devices with 2D Janus and tubular micromotors for on-site biomarker and bacteria detection.

The above-mentioned objectives, hypotheses and specific milestones of this Doctoral Thesis have been summarized in **Chapter I**.

Chapter II includes a judicious overview of cutting-edge nanotechnological approaches for the diagnosis of cancer and bacterial infections, ranging from Raman strategies based on the use of nanoparticles and carbon nanomaterials as tags; to recent micromotors based strategies.

The most relevant results derived from the Doctoral Thesis are discussed in **Chapters III-VI**.

Chapter III gathers all the results related to the design of novel SERS strategies based on the use graphene/nanoparticles composites as tags and antimicrobial peptide modified magnetic beads as capture elements in the detection and killing of pathogenic bacteria. On a first approach, size-tunable Au@Ag nanoparticles are assembled into mussel shells as natural SERS substrates. The periodic 3D microstructures which mainly consist of CaCO₃ in the mussel shell results in superior hydrophobicity for analyte enrichment, and the crossed nanoplates and nanochannels provides rich SERS hot spots, which together lead to high sensitivity. Highly sensitive SERS detection with a detection limit as low as 10⁻⁹ M for rhodamine 6G was obtained. The as-prepared SERS substrates were applied for the simultaneous identification of *Escherichia Coli*, *Staphylococcus Aureus*, and *Pseudomonas Aeruginosa* by discriminant analysis.

Inspired by the previous SERS strategy, a new biosensor based on a sandwich structure was next developed for the isolation and detection of multiple bacterial pathogens *via* magnetic separation and SERS tags. The assay relies on antimicrobial peptide (AMP) functionalized magnetic nanoparticles as

Summary

"capturing" probes for bacteria isolation and gold coated silver decorated graphene oxide (Au@Ag-GO) nanocomposites modified with 4-mercaptophenylboronic acid (4-MPBA) as SERS tags. When different types of bacterial pathogens are combined with the SERS tags, the "fingerprints" of 4-MPBA show corresponding changes due to the recognition interaction between 4-MPBA and different kinds of bacterial cell wall. Compared with the label-free SERS detection of bacteria, 4-MPBA here can be used as an internal standard (IS) to correct the SERS intensities with high reproducibility, as well as a Raman signal reporter to enhance the sensitivity and amplify the differences among the bacterial "fingerprints". Thus, three bacterial pathogens (*Escherichia Coli*, *Staphylococcus Aureus* and *Pseudomonas Aeruginosa*) were successfully isolated and detected, with the lowest concentration for each of the strains detected at just 10^1 colony forming units per milliliter. The AMP modified Fe_3O_4 NPs feature high antibacterial activities and can act as antibacterial agents with low cellular toxicology in the long-term storage of blood for future safe blood transfusion applications. The method was applied to the analysis of raw blood samples from infected patients, with excellent performance.

Chapter IV describe the synthesis and applications of 2D nanomaterials-based Janus micromotors for bacteria isolation, sensing and killing. First, GO, GDY and black-phosphorus (BP) coated micromotors integrating "three engines" for motion control using different stimuli such as chemical fuel, light and magnetic fields are described. Micromotors are mass-produced by wrapping gold-sputtered polystyrene microspheres with the 2D nanomaterials, followed by simultaneous assembly of Pt or MnO_2 NPs as "bubble (catalytic)-engines"; Fe_2O_3 NPs as "magnetic engines" and quantum dots (QDs) as "light engines". Micromotors design and composition is key to get the desired propulsion performance. In *bubble-magnetic* and *bubble-light mode*, a "built-in" acceleration system allows to increase micromotor speed up to 3.0 and 1.5 times after application of the magnetic field or light irradiation, respectively. In *bubble-magnetic-light* mode, such speed increase can be combined in a single unit for *on-demand* braking and accelerating systems. Such adaptative moving behavior can be very beneficial for future sensing applications using the micromotors in complex biological samples with high content of proteins and

other compounds that can hamper the micromotors movement and thus, overall efficiency.

On a second approach, an OFF-ON (bio)-sensing strategy based on GDY, GO and BP/Fe₂O₃/PtNPs Janus micromotors for Cholera toxin B detection as a relevant bacteria biomarker is described. A specific fluorescent labeled affinity peptide is loaded into the 2D nanomaterial part of the micromotors, which is released upon specific interaction with a target Cholera Toxin B, increasing the fluorescent of the solution in a concentration dependent manner. The distinct surface properties of each nanomaterial play a critical role in the loading/release capacity of the peptide, greatly influencing the release profiles. Peptide sorption obeys a second order-kinetic model using the three 2D nanomaterials in connection with micromotors, indicating a strong influence of chemisorption process and a higher loading capacity for BP micromotors. Yet, release kinetics are faster for GDYO and GO nanomaterials, indicating a contribution of π and hydrophobic interactions in the probe sorption (Cholera Toxin B affinity peptide) and target probe release (in presence of Cholera Toxin B). Excellent release capacity and micromotor performance is observed also in complex samples such as human serum and bacteria cultures. The unique micromotor movement in connection with 2D nanomaterials allow for efficient operation in miniaturized settings and complex samples, offering considerable promise for the design of novel micromotor based sensors or to understand the interaction between micromotor and biological counterparts in a myriad of clinical applications.

A third approach explore the use of AMP for bacteria isolation-killing, but this time on board of micromotors. Thus, catalytic and magnetic propelled GO/Fe₂O₃/PtNPs Janus micromotors modified with the antimicrobial peptide Nisin are used for highly selective capture/inactivation of gram-positive bacteria units and biofilms. Specific interaction of Nisin with the Lipid II unit of *Staphylococcus Aureus* bacteria in connection with the enhanced micromotor movement results in a 2-fold increase of the capture/killing ability, as compared with free peptide and static counterparts. The high stability of Nisin along with the high towing force of the micromotor allow for efficient micromotor operation in untreated raw media (juice, serum and tap water samples). The high selectivity of the protocol is illustrated by the dramatically lower interaction with gram-negative bacteria (*Escherichia Coli*). This hold considerable promise to

design micromotors with tailored antibiotics that can respond to the changes that make the bacteria resistant.

Chapter V illustrates the synthesis and application of GDY micromotors for biomarker sensing and cancer cell killing. First, tubular GDY micromotors containing diverse inner catalytic layers (Pt/Ni, MnO₂ or Pd/Cu) are prepared by a greatly simplified electrochemical deposition protocol. GDY is directly electrodeposited in a membrane template by cyclic voltammetry. The GDY layer results in the generation of a rough inner metallic layer, allowing for micromotor operation at low (0.5 %) peroxide levels. In addition, the outer GDY layer is rich in sp and sp² carbons with a conjugated π network. This results in a highly increased surface area for a higher loading of anticancer drugs or enhanced quenching ability over other 2D based micromotors such as GO or smooth tubular micromotors. High biocompatibility with almost 100 % cell viability is observed in cytotoxicity assays with moving micromotors in the presence of HeLa cells. On a first example, GDY micromotors loaded with doxorubicin (DOX) are used for pH responsive release and HeLa cancer cells killing. The use of affinity peptide engineered GDY micromotors is also illustrated for highly sensitive and selective fluorescent OFF-ON detection of Cholera toxin B via specific recognition of the Subunit B region of the target toxin and *Escherichia Coli* endotoxin.

Finally, **Chapter VI** describes the integration of the developed sensing approaches into portable instrumentation. The design relies on the coupling of high-magnification lens with the camera of a smartphone. The system is next integrated into a 3D-printed platform which allows to “focus” the sample, which is placed in a specifically designed compartment of the platform. The camera of the smartphone allows to take pictures and record videos of the micromotor movement for motion-based sensing approaches. To achieve fluorescent detection, commercial laser diodes with different wavelengths can be directly irradiated in the samples, positioning the appropriate filter between the camera and magnification lens. Such universal approach allows to translate the micromotor-based sensing strategies for on-site detection of the target analytes described in this PhD.

Considering the results obtained, the main and transversal conclusion of this Doctoral Thesis is the demonstration of the future and present potential of 2D nanomaterials in connection with nanoparticles and micromotors for the isolation-detection-killing of pathogenic cells and relevant (bio)-markers in diagnosis and advanced disease treatment approaches.

The combination of graphene nanosheets with silver coated gold nanoparticles modified with Raman reporter as tags commonly used in SERS detection approaches has been demonstrated to be highly relevant, avoiding important drawbacks such as the oxidation of the nanoparticles while increasing the density of "hot-spots" by increasing the density of tags. In addition, the presence of functional groups allows to incorporate specific ligands for target isolation with capabilities to inactivate harmful cells such as bacteria, going beyond sensing and discriminating among pathogenic bacteria. The main outcome was the design of multifunctional SERS biosensors for the simultaneous isolation, discrimination and killing of bacteria, with high potential for clinical diagnosis and safe blood transfusions.

The relevance of 2D nanomaterials has also been revealed transversely in connection with micromotors following the core applications of this PhD in the biomedical field. Self-assembly and template electrosynthesis approaches allow for the synthesis of Janus and tubular micromotors, resulting in synergistic approaches that combines the unique physical and chemical properties of 2D nanomaterials with the intrinsic benefits of catalytic micromotors (autonomous movement, enhanced mixing and localized delivery). The main outcome was the design of battery of Janus and tubular micromotors for bacterial toxins detection and pathogenic cells killing (cancer and bacteria) in connection with specific bioreceptors. The 2D nanomaterials enhanced both the overall micromotors speed in complex (bio)-media while improving the immobilization of specific receptors.

The unique moving nature of the 2D nanomaterials micromotors and the capability to move in ultra-miniaturized environments allowed to develop portable strategies for future "on-site" detection of such important biomarkers. The main outcome was the design of a universal protocol integrated in a smartphone for motion based or fluorescent detection of bacteria biomarkers for fast diagnosis and treatment of important illnesses.

Summary

All these indicates that 2D nanomaterials, nanoparticles and micromotors (as also illustrated in the most relevant bibliography) are very promising nanotechnological approaches in the contemporary scientific scene for the diagnosis and treatment of serious global concerns, which will result in tangible benefit for the society in the no-so distant near future.

I. Hypothesis, motivation and milestones.	1
II. Introduction.	7
II.1. Diseases: from diagnosis to treatment using nanotechnology.	9
II.2. Raman strategies for diagnosis of diseases.	9
II.3. Review article. Micromotors for diagnosis and therapy of diseases.	35
II.4. References.	63
III. Janus nanostructures based on graphene and metal nanoparticles for SERS detection and killing of pathogenic bacteria.	81
III.1. Introduction and objectives.	83
III.2. Article 1. Self-assembly of Au@Ag nanoparticles on mussel shell as natural SERS substrates for the detection of pathogenic bacteria.	87
III.3. Article 2. Antimicrobial peptide based magnetic recognition elements and Au@Ag-GO SERS tags with stable internal standards: a three in one biosensor for isolation, discrimination and killing of multiple bacteria in whole blood.	105
IV. Janus micromotors based on 2D nanomaterials for detection and killing of pathogenic bacteria.	135
IV.1. Introduction and objectives.	137
IV.2. Article 3. 2D nanomaterials wrapped Janus micromotors with built-in microengines for bubble, magnetic and light driven propulsion.	141
IV.3. Article 4. Janus micromotors coated with 2D nanomaterials as dynamic interfaces for (bio)-sensing.	157
IV.4. Article 5. Dual-propelled lanbiotic based Janus micromotors for selective inactivation of bacteria biofilms.	175
V. Graphdiyne tubular micromotors for toxin detection and pathogenic cell killing.	193
V.1. Introduction and objectives.	195
V.2. Article 6. Graphdiyne tubular micromotors: Electrosynthesis, characterization and self-propelled capabilities.	197
V.3. Article 7. Graphdiyne micromotors in living biomedica.	211
VI. Optical portable detection with 2D Janus micromotors: towards on-site screening.	223
VI.1. Introduction and objectives.	225
VI.2. Article 8. Smartphone-based Janus micromotors strategy for real-time detection of clinical biomarkers.	227
VI.3. Article 9. Integrated micromotor optical fluorescence smartphone for real-time point-of-care testing.	239
VII. Conclusions.	253
VIII. Appendices.	259

Table of contents

CHAPTER I.

Hypothesis, motivation and milestones

Despite the progress achieved so far in pharmaceutical technology and drug discovery, cancer and infectious diseases are still among the top 10 global causes of death worldwide. The major challenge of current diagnosis is the lack of specificity in the detection and the requirements to perform multiple and invasive diagnosis tests that can delay efficient treatment. In addition, some existing drawbacks hamper the efficiency of the existing treatments, *i.e.* serious side effects of chemotherapy and the antibiotic resistant nature of a myriad of microorganism responsible for infectious diseases.

Surface enhanced Raman scattering has become a subject of interest for the detection of chemicals, biological species and microorganisms. The main reason is its high sensitivity, simple preparation, non-destructive nature, low sample requirements and intrinsic selectivity due to its fingerprint. Traditional SERS substrates may include noble metals such as silver or gold nanoparticles. Recently, the combination of different types of nanomaterials into Janus-type structures have attracted the interest of the scientific community. Silver-coated gold nanoparticles (Au@Ag NPs) are an ideal substrate with higher SERS activity and more uniform particle size distribution. In addition, graphene and related 2D nanomaterials, owing to its large surface area and good biocompatibility, can increase SERS performance using low amount of sample volumes in a myriad of analytical and theragnostic applications.

Self-propelled micromotors are micro-scale devices consisting of a self-propelled structure equipped with sensing and/or actuating attachments. The broad scope of operations and applications, along with the ultra-small dimensions, accessibility and force offered by synthetic nano/micromotors, open new possibilities for diagnosis and therapy operations, overcoming some of the unmet challenges. Indeed, the movement of micromotors can create turbulent flows that impart efficient micromixing, further improving the interaction between the active surface and the targets, and consequently, reducing the sensing time even in nanoliter-scale samples. Another important feature of micromotors is their self-propulsion ability in the solution, allowing for enhanced target removal and drug delivery for future therapy. 2D nanomaterials such as graphene or black phosphorous can impart the micromotors with a rough surface area for the subsequent incorporation of a higher loading of the active nanoparticles, which are responsible for the motion control behavior, allowing thus to tune the propulsion mode. Combined with some ingenious detection

I. Hypothesis, motivation and milestones

strategies -modification with target recognition elements, or fluorescent elements- disease diagnosis can be performed in a more rapid, selective and sensitive manner. In addition, the capacity of some micromotors to self-penetrate and interact with tumor tissues and cancer cells make them excellent candidates for cells capture/removal and drug delivery.

In sum, new nanomaterials such as Janus microparticles and micromotors can add a rich dimension in analytical and theragnostic applications, improving their overall performance compared with traditional means. Given growing societal needs caused by global illness and considering the promising capabilities of the trinomial 2D nanomaterials-micromotor-microparticles, the working hypothesis here is that if such entities can be combined and used for the isolation-detection and killing of pathogenic cells and related biomarkers. This will allow the early diagnosis of related diseases, improving both health and quality of live and well-being for all individuals, holding great potential also for the development of novel treatment procedures.

Accordingly, the main objective of this Doctoral Thesis is the development of innovative analytical designs based on nanomaterials and micromotors for (bio)-sensing applications in biological media. In order to achieve the general objective, different specific objectives have been also defined as follow:

- 1.** Synthesis and characterization of Janus nanosheets based on graphene and metal nanoparticles for SERS detection and killing of pathogenic bacteria.
- 2.** Synthesis and characterization of Janus micromotors based on 2D nanomaterials (graphene, graphdyine and black phosphorous) for optical detection and killing of pathogenic bacteria.
- 3.** Synthesis and characterization of graphdyine based tubular micromotors for optical detection of bacteria toxins and pathogenic cell killing.
- 4.** Development of optical portable detection devices with 2D Janus micromotors for on-site biomarker and bacteria detection.

According to the objectives of this Doctoral Thesis, the following milestones have also been designed in order to reach the main goals proposed, running across a selected (bio)-analytical and biomedical applications:

- 1.** Development of bioinspired SERS active Janus platforms modified with Au@Ag nanoparticles for bacteria detection.
- 2.** Development of antimicrobial peptide based magnetic recognition elements and Au@Ag-GO SERS tags with stable internal standards for isolation, discrimination and killing of multiple bacteria in whole blood.
- 3.** Synthesis and characterization of 2D nanomaterials wrapped Janus micromotors with built-in microengines for bubble, magnetic and light driven propulsion.
- 4.** Development of fluorescent strategies based on 2D nanomaterials wrapped Janus micromotors for fluorescent sensing of bacteria toxins.
- 5.** Development of lanbiotics modified 2D nanomaterials wrapped Janus micromotors for isolation and killing of pathogenic bacteria.
- 6.** Synthesis and characterization of 2D graphdyine tubular micromotors.
- 7.** Development of fluorescent strategies based on tubular graphdyine micromotors for fluorescent sensing of bacteria toxins.
- 8.** Development of drug loading and delivery strategies based on tubular graphdyine micromotors for cancer cell killing.
- 9.** Development of smarphone-based Janus micromotor strategies for motion-based and fluorescent detection of bacteria and related biomarkers in clinical samples.

CHAPTER II.
Introduction

II.1. Diseases: from diagnosis to treatment using nanotechnology.

Despite the progress achieved so far in pharmaceutical technology and drug discovery, cancer and infectious diseases are still among the top 10 global causes of death (causing 6.0 million deaths worldwide). Early diagnosis can help to decrease overall costs in the treatment of such issues and most importantly, decrease the mortality rate [2]. Yet, target biomarkers are present in very low levels in early cancer stage [4]. Infectious cells can be grown *in-vitro* to obtain sufficient cells, increasing the detection sensitivity, yet such procedures are time consuming, not meeting the requirements for “fast” detection. The balancing between fast discrimination and sensitive detection of infectious cells is the key to provide effective guidance in antibiotic therapy [5, 6]. In addition, diseases diagnosis is also hampered by the inherent complexity of biological media, which prevent direct detection without sample processing [7, 8]. On the other hand, some existing drawbacks hamper the efficiency of the existing treatments, *i.e.* serious side effects of chemotherapy or radiotherapy and the antibiotic resistant nature of a myriad of microorganism responsible for infectious diseases [9]. In addition, many pharmaceutical companies stopped research efforts for the discovery of new antimicrobial agents due to their low profit margin. Consequently, it is crucial to develop efficient platforms to solve complex biomedical challenges.

Nanotechnology is the study and application of nanomaterials with dimensions ranging from 1 to 100 nm. The small size, distinct surface properties and ability for functionalization of such nanoparticles added a new dimension to overcome the existing challenges, leading to novel diagnosis and treatment therapies for detection and treatment of such diseases [10, 11]. We will focus in this PhD and in this introductory in two relevant techniques, surface enhanced Raman scattering in connection with nanoparticles for enhanced disease diagnosis and micro/nanomotors. More details will be described in the following sections.

II.2. Raman strategies for diagnosis of diseases.

Surface enhanced Raman scattering (SERS) is a very promising tool for direct detection of many biomarkers in disease diagnosis applications. The technique relies in the enhancement of inelastic light scattering molecules (or analytes)

II. Introduction

attached or combined with plasmonic metals or semiconductor materials [12-14]. Since the first discovery of SERS phenomena in 1974, researchers have proven the powerful and effectiveness of such technique in analytical science, ranging from environmental monitoring to biological/biomedical detection [15-19]. The broad scope of operations and applications, along with the high sensitivity, rich molecular "*finger-print*" information (specificity), in-situ and non-destructive detection [20-22], pave new ways for SERS application in cancer and infectious disease diagnosis [23, 24]. Indeed, cancer/infectious cells and related biomarkers are mostly composed of proteins or other organic molecules with inherent Raman signal, allowing for direct Raman detection and target discrimination based on the different Raman response (*finger-prints*) of their particular compositions. Other important features of SERS include high sensitivity and fast detection, allowing disease diagnosis even at a signal cell/molecular level [26-28]. The type, size and shape of the SERS substrate use for enhancing the Raman signal will exert a strong influence on a given biological application. Therefore, SERS substrates can be divided into two main groups according to the enhancement mechanism: (a) electromagnetic enhancement (EM) or (b) chemical enhancement (CM). EM derives its enhancing ability from electromagnetic effects on nano-structured metallic surfaces and contributes most of the signal amplification with an enhancement factor (EF) of 10^4 - 10^{10} . CM is caused by charge transfer, with a lower degree of the overall Raman enhancement (2 orders) [29, 30]. The integration of both mechanisms into hybrid SERS substrates show considerable promise for synergistic enhancement and metal protection, achieving fast and reliable disease diagnosis from biological samples [31, 32]. Using some ingenious designs such as magnetic separation or sandwich strategy, and combined with SERS tags encapsulated with specific recognition elements, Raman reporter and novel metal, disease diagnosis would be conducted with a high selectivity and in a sensitive manner [33, 34]. **Figure II.1.** illustrates a schematic summary of the previously described strategies.

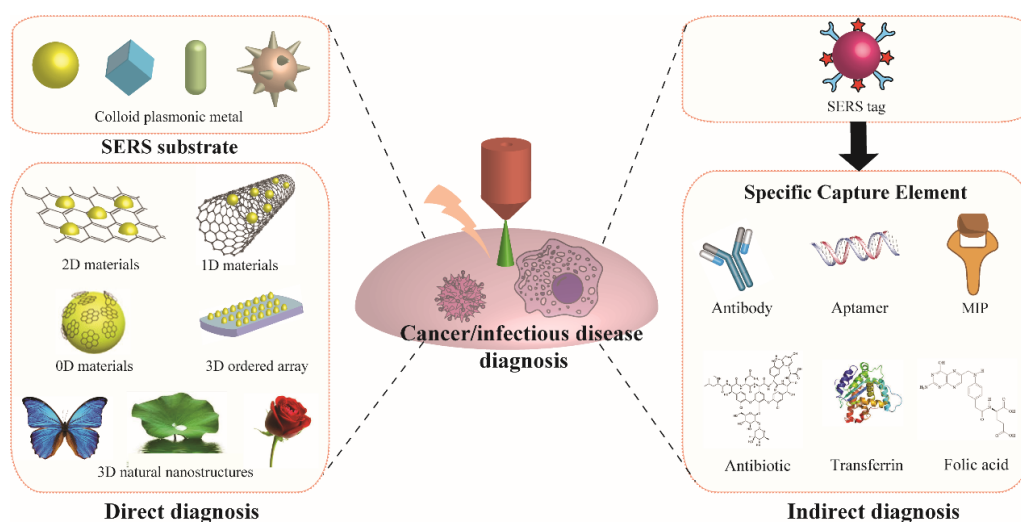


Figure II.1. Schematic illustration of SERS strategies for cancer and infectious disease diagnosis

As can be seen in **Figure II.1.**, researchers can directly detect cancer or infectious cells/biomarkers and benefit from their specific Raman finger print in discrimination, which originates from the different Raman-active molecules of the cell lines [36-39]. Indeed, disease diagnosis conducted in this way can provide a rich spectrum containing information of the analyte, giving possibilities for further in-depth studying of related diseases at the molecular level [40-42]. The major challenge of current direct detection is the low content and small Raman scattering cross-section of Raman active chemicals on the cell surface, leading to weak SERS signals and limited sensitivity in disease diagnosis [45, 46]. Therefore, different substrates for signal enhancement were explored [47]. Colloid plasmonic metals with EM effect such as gold and silver nanoparticles have been the traditional choices when it generally produced using a simply synthetic method [49, 50]. To increase the efficiency of the Raman enhancement, different shapes of nanomaterials, such as nanostar, nanorod, nanocube, etc., with abundant branches or edges, were explored [51-53]. In addition, some semiconductors with CM effect, such as graphene, MoS₂, etc., have been also introduced to further improve SERS properties [54-56], to protect the active SERS substrate labeled with the reporter from degradation or to impart surface functionality [57, 58]. Apart from sensitivity, signal stability is another challenge in direct diagnosis of cancer and infectious diseases. Most colloid plasmonic metals are obtained by chemical synthesis method, causing a heterogeneous size distribution. In addition, colloidal SERS substrates prepared by simply mixing the tag with the biological sample are prone to the generation

II. Introduction

of heterogeneous and random "hot-spots", which lead to differences of enhancement factors to the Raman active-molecules and unstable signals [17, 59, 60]. 3D ordered SERS substrates have been designed to solve this problem, using bottom-up or top-down method to build solid plasmonic metal with controlled nanogaps and fixed spatial position [61-64]. Some natural creatures are born to be with ordered nanostructures, endowing them with specific functionalities such as super-hydrophobicity, strong adhesive force, or rich color, etc [66-68]. Such natural nanostructures also are widely used in fabricating 3D solid substrates, with low-cost, environment friendly nature, easy preparation, etc [69, 70]. In addition, cancer/infectious disease diagnosis means sensing target from a biological sample, therefore, interferences from complex matrix also turn into a critical point in clinical application. A typical solution rely on the introduction of indirect SERS strategy, involving a Raman reporter, SERS active nanomaterial and specific recognition element to fabricate a "three-in-one" SERS tag, thus providing strong SERS signal and realizing specific affinity with target cells even in complex matrix [71-73].

II.2.1. Direct SERS detection of cancer and infectious diseases.

Direct SERS sensing of target analytes is achieved by the attachment to the SERS substrate directly, obtaining both qualitative ("*finger-print*" of spectra) and quantitative (signal intensity) information from the resulting SERS spectra [74]. A major superiority of direct SERS over other strategies is the obtention of a rich spectrum with "*finger-printing*" information of the target molecules without any further labeling [75-77]. In the diagnosis of cancer and infectious disease, this strategy can provide in-depth information from biomarkers, cells and/or their interactions, thus providing possibility for reveal targets compositions and disease mechanism [78-81]. Yet, the low content of Raman active molecules on cancer/infectious cell surfaces and the relatively low concentrations of related biomarkers in biological fluids, lead to the low intensity of Raman signal, thus hampering adequate sensitivity in the detection. In addition, the heterogeneous aggregation of the SERS active nanoparticles can lead to low reproducibility. The key to achieve high sensitivity and reproducibility is to select and tailor the composition of the SERS substrates. Different specific nanostructures have been designed, including plasmonic metal colloids, hybrid substrates integrating nanomaterials with different dimensions (0D, 1D, 2D) into plasmonic

nanoparticles, 3D ordered solid nanostructures as period substrate and even the incorporation of magnetic materials for target enrichment. More details will be given below.

II.2.1.1. Plasmonic metal nanoparticles as SERS substrates.

Direct SERS sensing with *i.e.* silver, gold, and copper nanocolloids involves the direct mixing with the sample to induce the generation of biomarker-nanoparticle or cell-nanoparticles aggregations. The as generated SERS “hot-spots” will greatly increase the intensity of the Raman signal. Different shapes and compositions have been explored, including nanoparticles [82, 83], nanorods (NRs) [84, 85], nanostars [86, 87], and nanocubes [88, 89], etc. For example, Wang et al [90] synthesized silver dendrites for direct SERS detection and discrimination of *Salmonella Enterica* in the presence of *Escherichia Coli*. Thus, the scanning-electron microscopy (SEM) images of **Figure II.2. A(a)** show the morphology of the silver dendrites-*Salmonella enterica* complex. Further Raman mapping of the specific peaks allows for the specific detection (Raman shift, 1332 cm^{-1}) of *Salmonella Enterica* with a limit of detection (LOD) of 10^4 CFU mL^{-1} (see **Figure II.2. A(b)**). In addition, such SERS substrate have higher enhancement activity for *Gram* negative bacteria than *Gram* positive, which helps to reduce interference from *Gram* positive bacteria in discrimination (**Figure II.2. (c)**). Such work provides a simple, fast, and sensitive strategy for the direct detection and discrimination of bacterial cells, which is a typical application of the plasmonic colloid.

II. Introduction

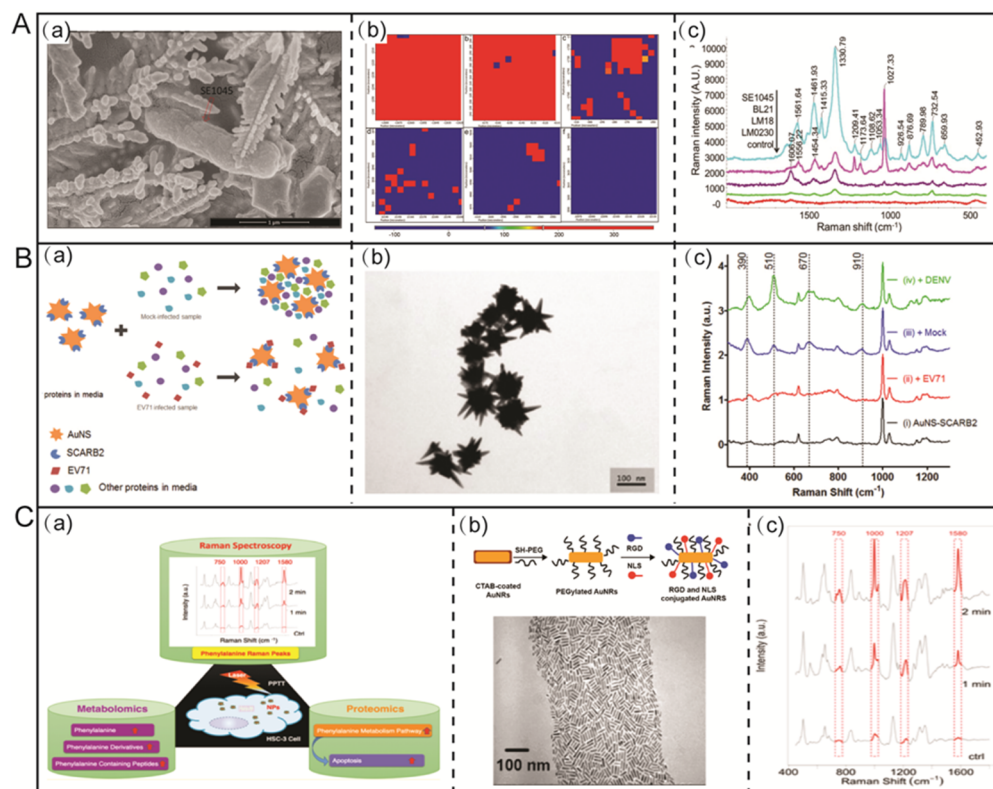


Figure II.2. Plasmonic metal nanoparticles as SERS substrates for cancer and bacteria diagnosis. (A) Direct SERS sensing of bacteria using Ag dendrites as Raman enhancement substrate (a) SEM of *Salmonella Enterica* (SE1045) mixed with Ag dendrites; (b) SERS mapping of different concentrations of bacteria at 2.1×10^8 CFU mL⁻¹, 2.1×10^7 CFU mL⁻¹, 2.1×10^6 CFU mL⁻¹, 2.1×10^5 CFU mL⁻¹, 2.1×10^4 CFU mL⁻¹, and control, (c) SERS spectra of different strains using Ag dendrites as substrate. (B) Gold nanostars as SERS substrate for direct diagnosis of hand, foot, and mouth disease causing enterovirus (EV) 71 (a) Schematic of SERS sensing of EV71 based on anti-aggregation of gold nanostars, (b) TEM image of gold nanostars, (c) Raman spectra of SCARB2 modified Au nanostars added to mock-infected cell culture in the presence and absence of EV71, and in the presence of DENV virus. (C) Gold nanorod as SERS substrate for revealing cancer cell death mechanism (a) Schematic of the gold nanorod applied in the SERS study of cancer cell death mechanism, (b) schematic showing surface modification of Au nanorod, (c) SERS spectra collected from a single HSC-3 cell under NIR laser exposure for 1 and 2 min. Reprinted with permission from ref. [90], [91] and [92].

Another example was conducted by Reyes et al [91], who developed a SERS strategy for direct and rapid determination of Enterovirus 71 (EV71) using Au nanostars colloids as plasmonic substrate. The surfaces of Au nanostars (SEM morphology is shown in **Figure II. 2. B(b)**) were modified with EV71 affinity protein, recombinant scavenger receptor class B member 2 (SCARB2) protein, for the further specific detection of target. In biological sample, nonspecific proteins from background would induce the aggregation of SCARB2 modified Au nanostars, thus producing Raman signals (peaks at 390, 510, 670, and 910 cm⁻¹

¹) of modified protein from Au nanostars surface. While EV71 virus are presented in the biological sample, SCARB2 modified Au nanostars can be combined with EV71 and followed by the anti-aggregating of Au nanostar colloids, leading thus to a diminishing of the Raman peaks (**Figure II.2 B(a)**). **Figure II.2 B(c)** revealed that peaks at 510, 670, and 910 cm^{-1} only disappear in the presence of EV71 virus while not in the presence of DENV virus or mock-infected cell culture supernatant, which proved the high specificity of the proposed method. Some plasmonic nanocolloids such as Au nanorods (AuNRs) [93, 94], multilayered Au nanoshells [95], Au nanostars [96] etc., not only show excellent SERS activity but also with high efficient photothermal conversion efficiency by converting near-infrared laser light to localized heat, thus have been used in cancer related photothermal therapy. However, the mechanism of photothermal therapy in cancer cell treatment is still unclear. The *in-situ* detection and time-dependent changes of Raman *finger-prints* of target molecules allow to explore the mechanism of some biological and chemical process [97, 98]. Ali et al [92] employed AuNRs with high photothermal conversion efficient to study the underlying photothermal effect of such nanorods (**Figure II.2. C(a)**). Using a seedless method, average sizes of AgNRs were controlled to 25 nm \times 6 nm, which can improve light/heat conversion. Further surface modification of PEG, Arg-Gly-Asp (RGD) and nuclear localization signal (NLS) improve the biocompatibility, cell uptake and targeting ability of the AuNRs (**Figure II.2 C(b)**). After cell (HSC-3 cell) uptake by AuNRs, near infrared spectroscopy (NIR) laser was used to irradiation of cells at different time intervals and lead to the increase of temperature. Simultaneously, the Raman spectra were recorded to monitor molecular changes from the AgNRs containing microenvironment. As depicted in **Figure II.2 C(c)**, peaks intensities at 750, 1000, 1207, and 1580 cm^{-1} increased after exposing to NIR laser. From the changes of SERS peaks, the authors deduced some related conclusions including "phenylalanine increases in the microenvironment (perturbation of phenylalanine metabolism) during photothermal therapy", and "apoptotic cells (*cytochrome c*-mediated apoptosis) increase during thermal heating". Combined with metabolomics and proteomics experiments, this work demonstrates the potential of AuNRs for photothermal therapy at and from the molecular level. Other plasmonic colloid metal that have been used as SERS substrate for direct sensing of cancer/infectious and related biomarkers are summarized in **Table II.1**.

Table II. 1. Plasmonic colloid metal as SERS substrate for direct sensing of cancer/infectious cells and related biomarkers.

Target analyte/cell	Interaction mode	Peaks (cm ⁻¹)	Sensitivity	Ref
Ag NPs				
<i>Staphylococcus Aureus</i>	Aptamer as capture elements	735,1337, 1458	1.5 CFU mL ⁻¹	[1]
Prostatic cancer (DNA/RNA) biomarkers	Electrostatic interaction	560, 742, 788, 913, 1035, 1180, 1247, 1334, 1457, 1539, 1632	100 copies of input RNA	[3]
<i>Mycobacterium Bovis BCG</i> , <i>Mycobacterium tuberculosis</i> , <i>Staphylococcus aureus</i> , <i>Staphylococcus Epidermis</i> , <i>Bacillus Cereus</i>	In-situ coating	731,1031,1326, 1463	10 ² CFU mL ⁻¹	[9]
Prostate cancer (RNA) biomarkers	Electrostatic interaction	742	100 synthetic RNA copies	[25]
AuNPs				
Colorectal cancer biomarkers	Simple mix	724,1263,1573	Above 90%	[35]
Au nanostars				
<i>Protein Kinase A activity for cancer screening</i>	---	725, 1395	---	[43]
Au/Ag bimetallic NPs				
<i>Escherichia Coli</i> , <i>Salmonella typhimurium</i> , <i>Bacillus subtilis</i>	Simple mix	656, 730, 958, 1082, 1324, 1581	---	[44]
Au@Ag				
<i>Escherichia Coli</i> , <i>Staphylococcus Aureus</i>	Interaction between negative (bacteria) and positive (PEI)	655, 729, 958, 1328, 1583 (<i>E.coli</i>) 733	10 ³ CFU mL ⁻¹	[48]
Exosomes as cancer biomarkers	Electrostatic attachment and <i>in situ</i> formation	668,707,786,1179,1490,1563(BI6F10) 645,1000,1211,1326,1381,1563,1592	>90%	[65]

II.2.1.2. Nanomaterials incorporated plasmonic metal nano-hybrid as SERS substrates.

2D nanomaterials. Traditional Raman signal enhancement mechanisms mainly depend on EM enhancement utilizing plasmonic noble metals as SERS substrates [99, 100]. Another important enhancement mechanisms named CM could be realized by the introduction of two-dimensional (2D) materials such as graphene [101, 102], molybdenum disulfide (MoS_2) [103, 104], boron nitride (BN) [105], and black phosphorous (BP) [106], etc. Even though EM show apparent higher enhancement factor than CM in contributing to the Raman signal enhancement, 2D nanomaterials could offer unique superiorities such as chemically inertness, a biocompatible surface for further bio-sensing [107], large surface area for high efficient targets adsorption [108], rich functional groups for surface chemical modification [109] and stabilization of the noble metals from oxidation [110]. Importantly, further surface modification of the 2D substrates also help to suppress background signals due to the stronger interaction between the 2D nanomaterials and the target molecules after modification [111]. The convenient marriage of plasmonic metal and 2D nanosheets led to novel platforms with high SERS activity, high stability, low background signal and multi-functionality with a broad scope of applications [112-114]. Meng et al. [115] developed a graphene-silver nanoparticles-silicon (G@AgNPs@Si) sandwich SERS chip, as depicted in **Figure II.3 A(a)**. AgNPs were growth in-situ on silicon substrates (Si), followed by wrapping Ag surfaces with a graphene (G) monolayer. Such G@AgNPs@Si nano-hybrids show synergistic effects including electromagnetic enhancement (Si-reflected plasmon resonance; AgNPs-scattered plasmon resonance) and chemical enhancement (graphene-based charge-transfer resonance), which results in superior SERS activity. The chip was modified with vancomycin for direct capture and sensing of *Staphylococcus Aureus* and *Escherichia Coli* (**Figure II.3 A(b)**). From **Figure II.3 A(c)**, sharp Raman peaks at 1237 cm^{-1} and 1465 cm^{-1} can only be identified in SERS spectrum of *Staphylococcus Aureus*, while peaks at 654 cm^{-1} and 1218 cm^{-1} are specifically identified in *Escherichia Coli*. In this way, different types of bacteria can be discriminated in a direct method through their specific *fingerprints*.

II. Introduction

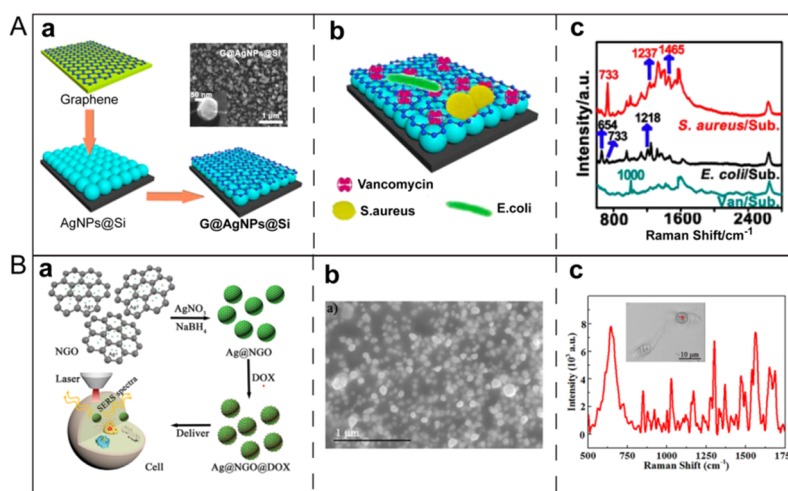
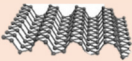
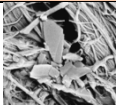
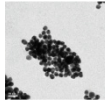
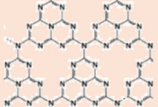
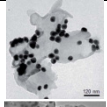
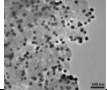
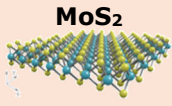
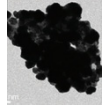
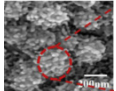
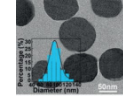
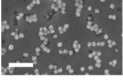

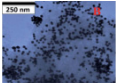


Figure II.3. 2D materials integrated SERS substrates for cancer and infectious disease sensing. **(A)** Graphene-silver nanoparticles-silicon (G@AgNPs@Si) as SERS substrate for bacteria discrimination. (a) Schematic illustration for the preparation of G@AgNPs@Si sandwich SERS substrate, inset image is the SEM of the G@AgNPs@Si nano-hybrid, (b) Schematic illustration of the developed SERS substrate modified with Vancomycin for bacteria capture, (c) SERS spectra of Vancomycin modified G@AgNPs@Si nano-hybrid incubated with *Staphylococcus Aureus* and *Escherichia Coli*. **(B)** Nanosized graphene oxide coated with silver nanoparticles (Ag@NGO) as SERS substrate for intracellular detection. (a) Schematic illustration in the synthesis of Ag@NGO nano-hybrid and corresponding intracellular SERS biosensing, (b) SEM morphology of Ag@NGO nano-hybrid, (c) SERS spectrum of HepG-2 after incubating with Ag@NGO nano-hybrid. Reprinted with permission from references [115] and [113].

Zeng et al [113] fabricated a SERS substrate using nanosized graphene oxide coated with silver nanoparticles (Ag@NGO). The NGO here showed superior chemical inertness and optical penetration, thus providing ultrathin layer to protect AgNPs from oxidation (**Figure II.3 B(a)**). Such Ag@NGO complex have uniform size with ~20 nm in diameter and round morphology, which help to intracellular uptake in the further biomedical sensing application (**Figure II.3 B(b)**). Some specific peaks such as 1651, 1564, 1302, 1030, 850 and 642 cm⁻¹ can be clearly distinguished in the SERS detection of HepG-2 cancer cell (**Figure II.3. B(c)**). Such Raman signals are only produced inside the cells, indicating the successful cell penetration of the Ag@NGO nanoparticles. An updated list of recent 2D nanomaterials such as BP, g-C₃N₄, MoS₂, h-BN and WS₂, etc. have been used in connection with plasmonic metals as SERS substrate for cancer and infectious disease diagnosis are listed in **Table II.2**.

Table II. 2. 2D materials incorporated plasmonic metal as SERS substrates for direct sensing of cancer/infectious cells and related biomarkers

2D material	Nano-hybrid	Structure	Target analyte/cell	Ref
Black phosphorus (BP) 	BP-Au filter		<i>Staphylococcus Aureus</i> <i>Escherichia Coli</i> Listeria	[116]
	BP-Au nanosheets		HepG2 cells	[117]
			Breast tumors	[118]
			Fibroblasts	[119]
g-C₃N₄ 	g-C ₃ N ₄ nanosheet Au@Ag		HeLa cell	[120]
	Mesoporous g-C ₃ N ₄		6-thioguanine	[121]
MoS₂ 	MoS ₂ -Au nanosheets		Fibroblasts	[119]
	AuNPs GO@MoS ₂ AuNPs		DNA	[122]
Boron nitride (BN)	Cu@HG@BN nanosheets		In vitro microRNA sensing	[123]
	AuNS@hBN		Quorum sensing of bacterial biofilms	[80]
WS₂ 	WS ₂ -Au nanosheets		<i>Salmonella DT104</i> <i>Salmonella Typhi</i>	[124]

1D nanomaterials. As an important member of 1D materials family, carbon nanotubes (CNTs) have broad applications ranging from analyte loading to biological sensing due to their unique structure and properties [125-127]. CNTs comprise single-wall carbon nanotubes (SWCNTs) and multi-wall carbon nanotubes (MWCNTs), which are composed of sp²-hybridized carbon atoms, exhibiting high chemical stability [128], larger surfaces area [129] and biocompatibility [130]. The inherent tubular morphology of CNTs allow for the direct growth of plasmonic metal on their surfaces without any pretreatment. In addition, the as deposited nanoparticles are restricted to the nanoscale size due to the small diameter of CNTs [131]. Researchers have also exploited the inherent stability of SWCNTs against photo-bleaching to design a myriad of ratiometric SERS nanosensors [132, 133]. Beqa et al. [134] prepared nano-

II. Introduction

hybrid composed by Au nano-popcorn/SWCNTs for theragnostic applications. **Figure II. 4.A(a)** shows the schematic of the fabrication process, in which SWCNTs were functionalized with a sulfydryl- group, followed by Au nano popcorn attachment onto the nanotube surfaces *via* "Au-S" bond. In the following step, S6 aptamer with sulfydryl- group was attached to the nano-hybrid. This nano-hybrid show superior performance in the sensing of SK-BR-3 cancer cells. After Au nano-popcorn were adsorbed onto the SWCNTs surfaces, Raman signal from SWCNTs (D band, 1300 cm^{-1} ; G band, 1590 cm^{-1}) increased approximately by an order of magnitude. Importantly, the SK-BR-3 cancer cell can induce the aggregation of the aptamer modified nano-hybrid to generate hot spots, and results in 3 orders of magnitude of SWCNTs Raman intensity (**Figure II. 4.A(b)**). The strategy is highly specific as revealed in the low Raman signal enhancements in the presence of other cells (MDA-MB or HaCaT normal skin cell) of **Figure II.4.A(c)**. Wang et al. [135] modified SWCNTs with Ag or AuNPs for cancer cell imaging. As depicted in **Figure II.4. B(a)**, the SWCNTs were first modified with DNA, followed by seed growth of the nanoparticles to generate the SWCNT-Ag or SWCNT-Au nano-hybrids. The surfaces of the as-prepared nano-hybrid were further modified with polyethylene glycol (PEG) to improve the stability in physiological conditions. Next, the authors modified the nano-hybrid with folic acid (FA) for specific attachment of human carcinoma KB cells and cell imaging. As expected, KB cells incubated with FA modified nano-hybrid showed apparent Raman signals (**Figure 4.B(b)**), while Hela cell show no obvious Raman signals (**Figure 4. B(c)**).

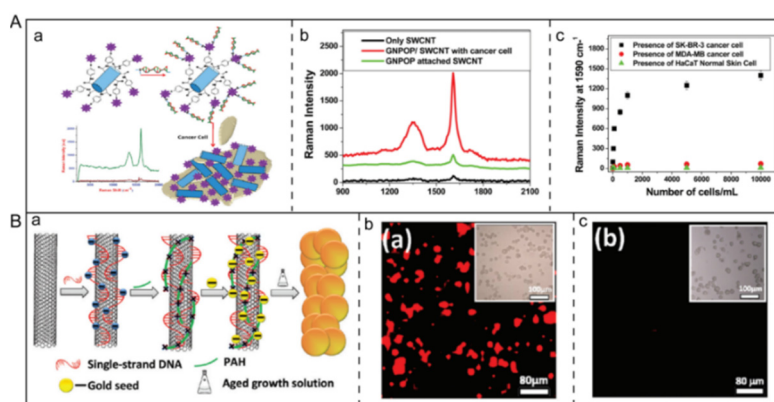


Figure II.4. (A) Au nano popcorn modified SWCNTs nano-hybrid for specific diagnosis of SK-BR-3 cancer cell. (a) Schematic illustration in the synthesis of SERS nano-hybrid and its application in cancer cell diagnosis, (b) Raman spectrum of SWCNTs, Au nano popcorn modified SWCNTs

nano-hybrid, and Au nano popcorn modified SWCNTs nanocomposites decorated with SK-BR-3 cancer cell, (c) SERS intensity changes at 1590 cm^{-1} after the addition of different amounts of SK-BR-3, MDA-MB human breast cancerous, and HaCaT normal skin cells to aptamer modified nano-hybrid; **(B)** SWNCT-Ag-PEG-FA or SWNCT-Au-PEG-FA nano-hybrids for specific Raman imaging of KB cell (a) Schematic illustration of the synthesis of nano-hybrids, Raman image of SWNCT-Au-PEG-FA incubated with KB cell (b) and Hela cell (c). Reprinted with permission from references [134] and [135].

0D nanomaterials. Compared to traditional 2D nanosheets, 0D materials show unique advantages, such as higher adsorption abilities due to the larger specific surface areas [136] or higher SERS activity derived from Van Hove singularities in electronic density of states [137]. Bhunia et al. [138] reported the development of carbon-dot/silver-nanoparticle (C-dot-Ag-NP) PDMS SERS films for bacteria sensing. For preparation, the PDMS precursors and ascorbic acid derivative are heated at 60°C to form the PDMS film. The encapsulated ascorbic acid derivative acts as carbon precursors for C-dots formation by reduction with silver acetate at 125°C (**Figure II.5. A(a, i)**). Such design results in the generation of uniform C-dots with diameters between 2 and 5 nm (**Figure II.5. A(a, iii)**), along with flexible and resilient nature (**Figure II.5. A(a, ii)**). The integration of AgNPs and C-dots played a critical role for the high SERS activity, whereas no Raman peaks were obtained using PDMS films containing only AgNPs or C-dots (**Figure II.5. A(b)**). The C-dot-Ag-NP-PDMS films were utilized for the detection of *Pseudomonas Aeruginosa*, as well as the distinguishing among *Bacillus Aureus* and *Erwinia Amylovora* 238 (**Figure II.5. A(c)**). Fei et al[139] used MoS_2 quantum dots as reducers to reduce HAuCl_4 to fabricated Au nanoparticles@ MoS_2 quantum dots (Au NP@ MoS_2 QDs) nano-hybrid as SERS substrates for cancer cell imaging (**Figure II.5. B(a)**). As indicated in the TEM observation, such nano-hybrid possess core@shell structures with ultrathin MoS_2 QDs-coating (**Figure II.5. B(b)**). Such AuNPs@ MoS_2 QDs nano-hybrids were further used for 4T1 cells imaging, which showed much higher SERS intensity compared with single MoS_2 QDs or AuNPs (**Figure II.5 B(c)**).

II. Introduction

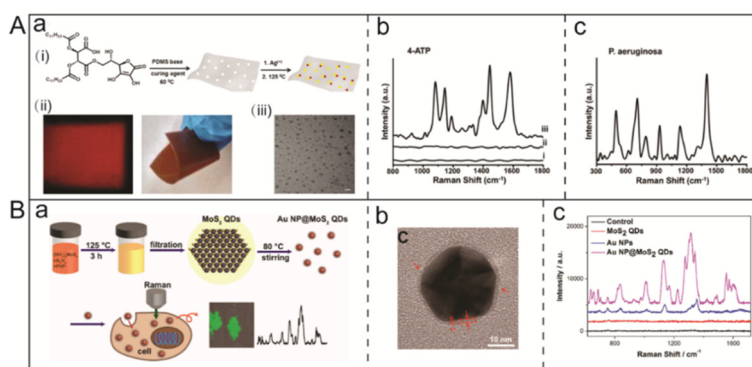


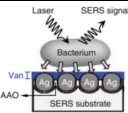
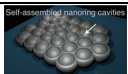
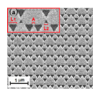
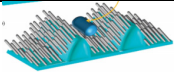
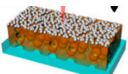
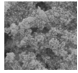
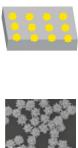
Figure II.5. (A) Combination of 0D nanomaterials and plasmonic metal nanomaterials as nano-hybrid for cancer and infectious disease diagnosis. **(A)** Carbon-Dot/Silver nano-hybrid as SERS films for bacteria detection, (a) Schematic illustration of the synthesis of C-dot-Ag-NP-PDMS films (i), fluorescence image and photograph showing the flexibility of the film (ii), TEM of nanoparticles taken from PDMS (iii), (b) SERS spectra of ATP obtained from C-dot-PDMS without AgNPs (down line), Ag-NP-PDMS without C-dots (middle line), and C-dots-Ag-NP-PDMS (top line), (c) SERS spectrum of 10⁴ CFU/mL of *Pseudomonas Aeruginosa*; **(B)** AuNP@MoS₂ quantum dots nano-hybrid for SERS sensing of cancer cell, (a) Schematic illustration of the synthesis of AuNP@MoS₂ quantum dots nano-hybrid and related biological SERS application, (b) TEM of AuNP@MoS₂ quantum dots nano-hybrid showing the core@shell nanostructure, (c) SERS spectra of 4T1 cells mixed with MoS₂ QDs (red line), AuNPs (blue line) and nano-hybrid (violet line).

II.2.1.3. 3D ordered solid nanostructures as SERS substrates.

One obstacle that traditional plasmonic nanoparticles-based SERS sensing need to overcome is the relatively low repeatability of the signal intensity. The aggregation degrees of the nanoparticles colloids are random and heterogeneous, resulting in different SERS enhancement ability to the attached target analytes even in the same sample [140, 141]. 3D solid nanostructures hold great promise to solve this drawback. Indeed, the composition of 3D nanostructures can be tailored to obtain periodic nanostructures with specific nanogaps at fixed positions, resulting in a high repeatability and sensitivity SERS sensing [17, 142, 143]. The synthesis is carried out by bottom-up self-assembly methods [144, 145] or top-down nanolithography techniques [146, 147]. One of an effective method about bottom-up fabrication of 3D solid SERS substrate is the nanosphere lithography (NSL), in which nanospheres with uniform sizes are firstly synthesis and form monolayer on a flat substrate as a mask. The mask is then deposited with noble metal film using thermal evaporation or electron beam deposition technique, followed by sonication or stripping process to remove the nanosphere mask and an array of ordered nanostructures on the surface of the substrate [148-150]. For the top-down fabrication, electron beam

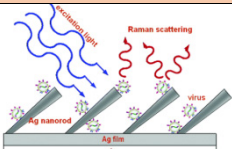
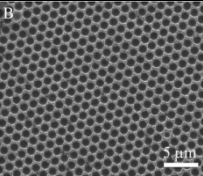
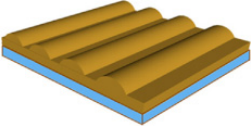
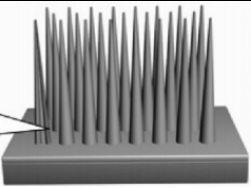
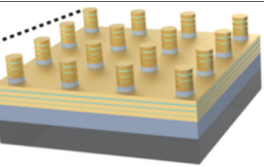
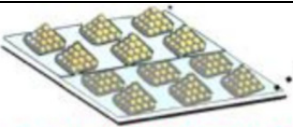
lithography (EBL) is widely used to produce periodic nanostructures with arbitrary shapes and tunable interparticle nano-gaps in a very small distance, which is key for both repeatable and high active SERS enhancement [151, 152]. Many 3D nanostructures with specific design have been used as SERS substrate for cancer and infectious disease detection (see **Table II. 3**).

Table II. 3. 3D ordered nanomaterials as SERS substrates for direct sensing of cancer/infectious cells and related biomarkers

Nanomaterial	Schematic of the SERS substrate	Target analyte/cell	Interaction mode	Ref
AgNPs arrays		<i>Lactobacillus plantarum</i> , <i>Escherichia coli</i>	Vancomycin as capture element	[153]
Ag nanoring cavities		DNA base (adenine)	Direct contact	[154]
Au octupolar metastructures		<i>Brucella</i>	Phage capture elements	as [155]
Silver nanorod (AgNR) array on PDMS substrate		<i>Pseudomonas Aeruginosa</i>	Direct contact	[156]
AgNPs on mesoporous silicon substrate		<i>Escherichia Coli</i> , <i>Staphylococcus Epidermidis</i>	Direct contact	[157]
Ag film substrate		Circulating tumor cells (CTCs)	Direct contact	[158]
Highly branched AuNPs on silicon wafer		Carcinoma cancer cells	Direct contact	[42]

II. Introduction

Table II. 3. (cont.) 3D ordered nanomaterials as SERS substrates for direct sensing of cancer/infectious cells and related biomarkers

Nanomaterial	Schematic of the SERS substrate	Target analyte/cell	Interaction mode	Ref
Ag nanorod array		Respiratory viruses (RSV) strain A2, A/Long and B1	Direct contact	[159]
Ag-Cr coated nanovoid structure		Cytochrome c	Direct contact	[160]
Au grating		DNA (discriminated DNA-DNA interaction)	Complementary between single oligonucleotide	[161]
Ag-coated nanowire arrays		<i>Bacillus Anthracis</i> spores	Direct contact	[162]
Multilayered metal-insulator metal nanostructures		Breast cancer	Grown on the substrate directly	[163]
Au ordered superlattices		Kynurenine, tryptophan, purine derivatives	Direct contact	[164]

The amazing nature has bred functional structures and materials to endow the creatures with specific features. For instance, hierarchical nanostructures impart lotus leaf and rose petal with surface superhydrophobicity [163, 164], photonic crystal structures introduce butterfly wings with vibrant colors [165], high density of nano-size tentacles in toe-pads make gecko exhibit strong adhesive force to the wall [166], etc. Such natural periodic 3D structures can act as excellent bio-templates for decoration with noble metal nanoparticles to fabricate SERS substrates [68, 167, 168]. Chen et al. [169] used cicada wings

as bio scaffold arrays and bio-templates for decoration with Ag NPs, forming thus 3D SERS substrates with hierarchical nanogaps. As depicted in **Figure II.6 A(a)**, the decoration of the bio-template is conducted by ion-sputtering techniques just in one step and the proposed SERS substrate was applied for the direct sensing of virus. SEM show top views (i)(ii) and side view (iii) of the Ag decorated nanopillar arrays (**Figure II.6 A(b)**), indicating a periodic 3D nanostructures, resulting this in a high reproducibility in target sensing (**Figure II.6 A(c, i)**), along with plenty nanogaps to generate more hot spots for highly sensitive detection (**Figure II.6 A(c, ii)**). Lateral real application has used this bio-SERS substrate for the discrimination among PCV2, PRV, and H5N1 virus due to the specific Raman spectrum of different kinds of virus, which exhibited great potential as an powerful SERS substrate for low-cost, sensitive, and reliable bio-sensing of analytes.

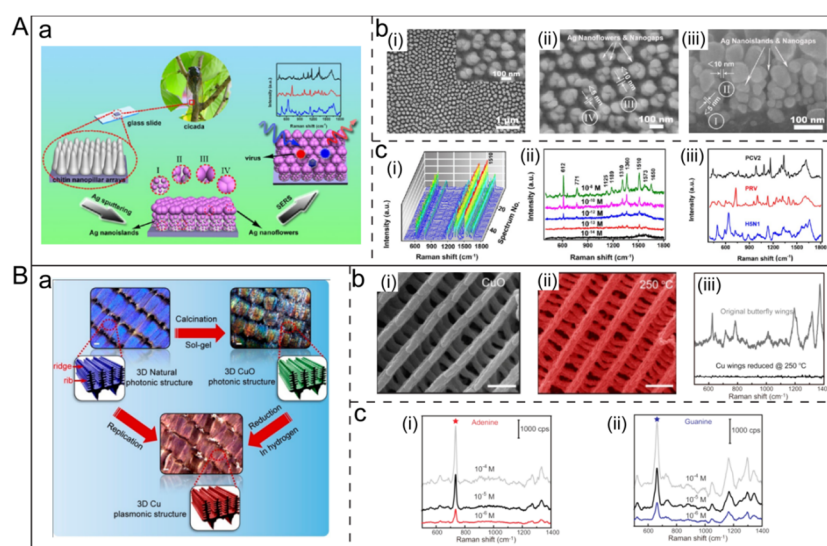


Figure II.6. Natural 3D nanostructures as template in building solid ordered SERS substrates. **(A)** Bio scaffold arrays of cicada wings as 3D template for fabrication of biomimetic SERS substrate (a) Schematic of fabrication process for Ag-decorated cicada wings as 3D biomimetic substrate and its application in virus detection, (b) SEM of 3D biomimetic Ag-decorated substrates, (c) SERS spectra of Rhodamine 6G (R6G) obtained at 50 random spots chosen from 10 Ag-decorated biomimetic substrates (i), SERS spectra of different concentrations of R6G solution using the Ag-decorated 3D biomimetic substrate for Raman enhancement (ii), SERS spectra of PCV2, PRV, and H5N1 using the Ag-decorated 3D biomimetic substrate for Raman enhancement. **(B)** Butterfly wings with photonic crystal nanostructures as 3D template for fabrication of SERS substrate (a) Schematic illustration in the fabrication of GuO photonic structures using butterfly wings and further route to pure it into 3D Cu plasmonic structures, (b) SEM of CuO decorated butterfly wings substrate (i) and Cu decorated butterfly wings substrates after reduction process (ii), comparison of Raman signals of the 3D Cu decorated butterfly wings

II. Introduction

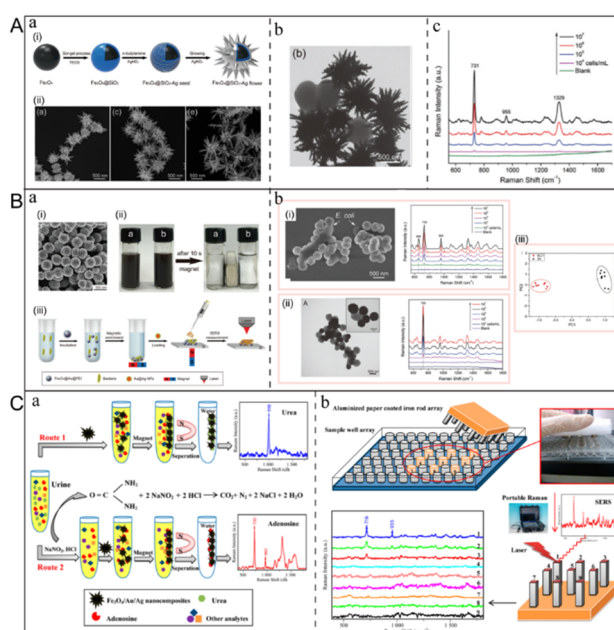
substrates and the original CuO decorated butterfly wings substrates, (c) SERS spectra of DNA base molecules, adenine (i) and guanine (ii), acquired using the Cu decorated butterfly wings substrates. Reprinted from references [169] and [170], with permission.

Another example is reported by Zhang et al. [170], who exploited replicated photonic crystals of butterfly wing as bio-templates for decoration of Cu superstructures (**Figure II. 6 B.(a)**). However, the original chitin and protein from butterfly wings caused SERS signal impurities and fluorescence interferences in the target sensing. To solve such issue, the authors employed a reduction method using H₂ to obtain Cu decorated wing SERS substrate with low background signals. SEM images of **Figure II.6 B.(b)** show the morphology of bio-template SERS substrate before (i) and after (ii) the reduction process, in which high periodic 3D structures could be easily identified and no obvious changes of the morphology occurs after reducing by H₂ in high temperature. Compared with original butterfly wing, Cu butterfly wings shows very clean SERS spectra after the reduction process (iii). In the further real application, DNA base molecular (**Figure II.6 B.(c)**) adenine (i) and guanine (ii) were detected, with excellent sensitivity at much lower cost.

II.2.1.4. Magnetic nanomaterials incorporated nano-hybrids as SERS substrates.

The incorporation of magnetic properties endows SERS substrates with extra abilities such as target capture and separation, interferences removal, and centrifugation. The most widely used structures compromise a magnetic core and a novel metal shell. Different types of magnetic materials have been used as magnetic beads, such as Fe₃O₄ [165, 166], MnFe₂O₄ [167], CoFe₂O₄ [168], Ni [169, 170], FePt [171], and CoPt [172]. The coating of the magnetic core with plasmonic nanoparticles can be performed by in-situ growth [173, 174] or ex-situ assembly [175, 176] methods. For example, Wang et al. [177] synthesized a Fe₃O₄@SiO₂@Ag nano-hybrid with a flower-like shape for capture and sensing of bacteria. As shown in **Figure II.7. A (a, i)**, SiO₂ beads are coated with magnetic nanoparticles, followed by silver grown on their surfaces. Interestingly, by adjusting the amount of AgNO₃, the structure of the nano-hybrid can be tailored into a micro-flower shape with a high degree of branches (**Figure II.7. A (a, ii)**). Such design endow the nano-hybrid with some superiorities: a) excellent dispersion for improved response to the applied

magnetic field; b) larger surface area for enhanced target capture; c) sharp tips from the branches for better hot spots in Raman signal enhancement; and d) the possibility of sample preconcentration due to the presence of a magnetic Fe_3O_4 core. The resulting $\text{Fe}_3\text{O}_4@\text{SiO}_2@\text{Ag}$ nano-hybrid was modified with an aptamer for specific capture of *Staphylococcus Aureus* (**Figure II.7. A(b)**), with a limit of detection of 10^4 cells per milliliter. On another example, $\text{Fe}_3\text{O}_4@\text{Au}$ nano-hybrids were prepared by ex-situ assembly of 3 nm of AuNPs seed into Fe_3O_4 (**Figure II.7. B(a, i)**) [48]. The as-prepared $\text{Fe}_3\text{O}_4@\text{Au}$ nano-hybrid own superior magnetic properties, allowing for the separation from the dispersion phase within 10 seconds under outside magnetic field (**Figure II.7. B(a, ii)**). By further coating the $\text{Fe}_3\text{O}_4@\text{Au}$ with positive polyethylenimine (PEI), the nano-hybrid are able to capture negative bacteria due to the electrostatic interaction (**Figure II.7. B(a, iii)**), allowing for the capture and SERS enhanced detection of *Escherichia Coli* (**Figure II.7. B(b, i)**) and *Staphylococcus Aureus* (**Figure II. 7. B (b, ii)**). Related SEM measurements showed that Au surfaces of the nano-hybrid tightly attached to bacterial wall to form $\text{Fe}_3\text{O}_4@\text{Au}@PEI$ -bacteria complex. With the enrichment effect of the magnetic core and SERS activity of the outside Au surfaces of the nano-hybrid, a concentration of bacteria as low as 10^3 cells per mL can be easily identified. A major advantage of direct detection of targets by SERS is the different of Raman finger printing among the analytes, which could be used to specific detection by principal component analysis (PCA) (**Figure II.7 B(b, iii)**).



II. Introduction

Figure II.7. Magnetic nanomaterials incorporated novel metal nanoparticles nano-hybrids. **(A)** Highly branched flower-like $\text{Fe}_3\text{O}_4@\text{SiO}_2@\text{Ag}$ nano-hybrid for bacteria detection, (a) Schematic illustration in the synthesis of $\text{Fe}_3\text{O}_4@\text{SiO}_2@\text{Ag}$ micro-flowers (i) and their SEM characterization of nanohybrids prepared using different concentrations of AgNO_3 , from left to right, 0.1 mM, 0.2 mM, 0.3 mM(ii), (b) TEM of aptamer modified $\text{Fe}_3\text{O}_4@\text{SiO}_2@\text{Ag}$ nano-hybrids after capturing *Staphylococcus Aureus* to form the complex; **(B)** Synthesis of PEI-modified Au-coated magnetic microspheres for pathogen bacteria sensing, (a) SEM of the as-synthesis $\text{Fe}_3\text{O}_4@\text{Au}$ microparticles (i) and their magnetic separation behaviors (ii), schematic illustration of the capture and enrichment process for the rapid SERS bacteria detection (iii), (b) SEM of $\text{Fe}_3\text{O}_4@\text{Au}@PEI\text{-}E.coli$ (i) and $\text{Fe}_3\text{O}_4@\text{Au}@PEI\text{-}Staphylococcus Aureus$ (ii) complexes and corresponding SERS spectra from different concentrations of bacteria after capture and enrichment procedure, differentiation between *Escherichia Coli* BL21 and *Staphylococcus Aureus* 24018 obtained from 2D-PCA plot (iii). **(C)** Direct detection of lung cancer biomaker in urine by magnetically assisted SERS method, (a) Schematic of detection of adenosine in urine by SERS through a direct method and indirect azo coupling reaction method, (b) Array setup and procedures for detection of adenosine in urine samples using a portable Raman. Reprinted from references [177], [48] and [178], with permission.

The integration of magnetic nanoparticles and noble metal nanoparticles also have been used for cancer cells detection and related biomarkers diagnosis. Related report from Yang's group [178] used $\text{Fe}_3\text{O}_4/\text{Au}/\text{Ag}$ nano-hybrids for adenosine sensing in urine sample from lung cancer patients. Without modification of the nano-hybrid surfaces, targets (adenosine) bind to the outside metal NPs by their $-\text{NH}_2$ groups, followed by magnetic separation and enrichment of the nanoparticles from the urine sample. However, the large amount of urea from the urine sample interfere in the SERS measurement, hence an azo-coupling was employed to eliminate the urea (**Figure II.7. C(a)**). In the following step, the proposed SERS method have also been applied for fast screening hundreds of samples in an array setup. The corresponding urine samples, $\text{Fe}_3\text{O}_4/\text{Au}/\text{Ag}$ nano-hybrid, and azo-coupling reaction reagents (NaNO_2 and HCl) were mixed into the sample wells. Then aluminized paper coated iron rod array was dipped into the tubes to collect $\text{Fe}_3\text{O}_4/\text{Au}/\text{Ag}$ nano-hybrid containing the targets. Such design allows for the fast determination of trace cancer biomarker (adenosine) directly from urine samples, as well as a smart and high throughput system for human healthcare (**Figure II. 7. C(b)**).

II.2.1.5. Non plasmonic nanostructures as SERS substrates.

Some semiconductor materials possess inherent Raman signals by charge-transfer mechanisms, paving a new way for SERS based on chemical mechanism

[179]. Some advantages of the use of such nanomaterials including chemical stability, resistance to degradation, high absorptivity and low cost [180-183]. Such properties endow the semiconductor-based SERS substrate with promising applications in cancer and infectious cells/biomarkers sensing. This kind of materials used for Raman signal enhancement could be mainly divided into inorganic and organic semiconductors. Normally, inorganic semiconductors are based on solid-state structures of metal oxides [184, 185], metal sulfides [186, 187], metal halides [188, 189], and single elements [190, 191]. Haldavnekar [192] fabricated ZnO-based semiconductor quantum probes for the sensing of cancer cells. After performing femtosecond laser interaction, the size of ZnO semiconductor was reduced to quantum scale (**Figure II. 8. A(a, i)**), which is key to the high SERS activity with an enhancement factor of up to $\sim 10^6$. The quantum scale semiconductors were further decorated on a 3D nano-dendrite platform to realize self-targeting, cell adherence, and proliferation (**Figure II. 8. A(a, ii)** and **Figure II. 8. A(b, i)**). The proposed platform was utilized for in-vitro sensing and discrimination among two cancer cells and a non-cancer cell line. As depicted in **Figure II. 8. A(b)**, SEM showed that Hela cells, breast cancer (MDAMB231) cells, and fibroblast (NIH3T3) cells can adhere to the nano-dendrite platform. The corresponding SERS spectra also showed distinct fingerprints for cancer cells and non-cancer cells. Keshavarz et al. [193] used multiphoton ionization growth on a Ti substrate, to fabricate TiO_x (Q-structured) nano particles restricted to quantum scale (**Figure II. 8 B(a)**). The resulting TiO_x semiconductors display high SERS activity with an enhancement factor of 3.4×10^7 . **Figure II. 8 B(b)** showed SEM morphology of fibroblast-NIH3T3 cell (i), Hela cell (ii), and breast cancer-MDAMB231 cell (iii) connected with the Q-structured TiO_x semiconductor and corresponding SERS spectra show the differences among the different types of cells.

II. Introduction

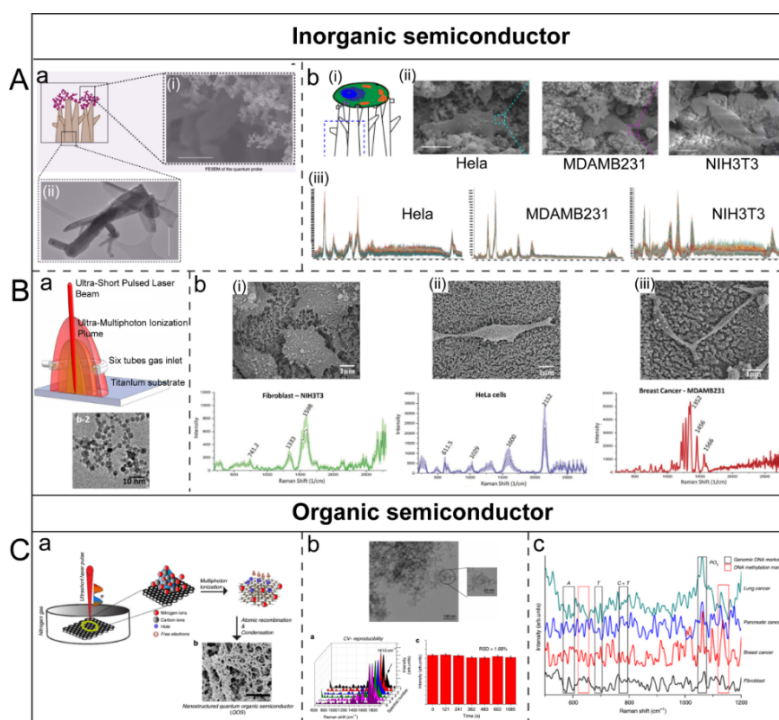


Figure II.8. Non plasmonic nanostructures as SERS substrate. **(A)** Inorganic semiconductor ZnO-based SERS substrate for in vitro cancer cells detection (a) Schematic and SEM images illustrating the quantum scale ZnO-based semiconductor decorated on the nano-dendrite platform; (b) Schematic illustration of the ZnO semiconductor decorated nano-dendrites platform for cell adhesion (i), SEM of HeLa cells, breast cancer (MDAMB231) cells, and fibroblast (NIH3T3) cells adhered to the proposed platform (ii) and corresponding SERS spectra (iii). **(B)** Inorganic semiconductor TiO_x as SERS substrates for cancer diagnostics (a) Schematic illustration in the synthesis of TiO_x semiconductor and correspond SEM show quantum scale of the as-prepared semiconductor, (b) SEM showing fibroblast-NIH3T3 cells (i), HeLa cells (ii), and breast cancer-MDAMB231 cells (iii) interacted with the TiO_x SERS substrate and SERS spectra showing differences among different cell lines. **(C)** Organic semiconductors SERS substrate for cancer stem cell makers sensing, (a) Schematic illustration in the fabrication of organic semiconductor, (b) SEM of the quantum scale organic semiconductor and reproducibility analysis of SERS signals of crystal violet, (c) SERS spectra of genomic DNA from different types of cells. Reprinted with permission from references [192], [193] and [194], with permission.

Organic semiconductors present extra properties (e.g. structural adaptability, biocompatibility) compared with the inorganic counterparts due to their π -conjugated carbon-based structures, which can generate weak interactions between the molecules by van der Waals and π - π forces. Such properties endow organic semiconductors with higher suitability for SERS sensing of biological samples [12, 195, 196]. Ganesh et al. [194] synthesized organic semiconductor as SERS substrates for investigating the epigenetic profile of cancer stem cells. As depicted in **Figure II. 8 C(a)**, the organic semiconductor is synthesized

using ultra-short pulsed laser under nitrogen gas environment, which enabled the shrinking of organic semiconductor into quantum scale. Such quantum scale endows the organic semiconductor with increased charge carrier mobility, which is necessary for efficient charge transfer in SERS. The TEM images illustrates the particle size distribution of the organic semiconductor, with a diameter of 3.4 nm, which are in the quantum scale. Importantly, such organic semiconductors own high SERS activity with 10^{12} enhancement factor. Uniform intensity with a low RSD can be obtained by this SERS substrate (**Figure II. 8 C(b)**). The authors employed the SERS substrate for epigenetic analysis of four different cell lines, including fibroblast cells (NIH3T3), breast cells (MDA-MB231), pancreatic cancer (AsPc-1), and lung cancer (H69-AR) cells. As shown in **Figure II.8 C(c)**, genomic DNA of different cell lines had different peak intensities due to the differences in base composition. Combined with multivariate statistical analysis, the genomic DNA of cancerous and non-cancerous cell can be successfully analyzed.

II.2.2. Indirect cancer and infectious disease diagnosis based on SERS tag.

The complexity of some biological samples and complex samples prevent direct SERS detection of a myriad of biomarkers, cancer cell or bacteria. To solve such problem, indirect detection is performed using Raman tags that can interact specifically with the target analyte, providing strong Raman signals. A representative SERS tag mainly includes Raman enhancement nanomaterials, Raman reporter, and specific capture elements. Even though such indirect sensing strategy may lose some optical spectrum information, they could act as a powerful analytical techniques for efficient disease diagnosis with high sensitivity and selectivity [197, 198]. In addition, some SERS tags also suffer from poor stability of Raman signal due to the random aggregation of nanomaterials or extreme sample conditions (pH, ion strength, etc). The introduction of shell structures such as silica sols [199] or polystyrene-shells [200], will solve this problem, by enhancing the stability of the SERS probe. Some shells using biomolecules such dopamine or SiO_2 also can enhance biocompatible of SERS tags, thus reduce cytotoxicity in disease diagnosis [201, 202].

II. Introduction

Raman reporters are basic elements for designing efficient SERS tags, and should possess the following characteristics: A) stable and intense Raman signal; B) clean spectral region with specific peaks that are easily to identify; C) ability to combine with Raman enhanced materials. A large number of molecules such as Rhodamine [203], crystal violet [200], malachite green [204], 5,5-dithiobis-(2-nitrobenzoic acid (DTNB) [205], methylene blue (MB) [206], p-aminothiophenol (PATP) [207], etc., have been widely employed as Raman reporters for the fabrication of SERS tags. By incorporating a Raman reporter, the SERS tag could be used to provide Raman signal with high stability and intensity. However, the delivery of SERS tags to specific targeting cancer or infectious cells/biomarkers is of great importance due to the complex matrix of biological samples. Therefore, researchers introduced the capture elements for high specificity detection. The capture element can be an antibody, an aptamer, a molecularly imprinted polymer, an antibiotic or other recognition elements such as transferrin. Some cancer and infectious disease diagnosis using different types of recognition elements and SERS detection are listed in **Table II. 4.**

Table II. 4. SERS tags with using different specific recognition elements for indirect cancer and infectious disease diagnosis


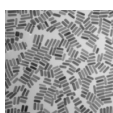
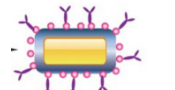
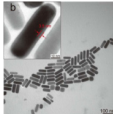
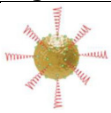
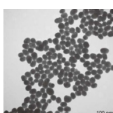
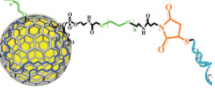
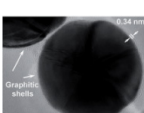
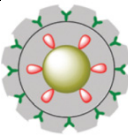
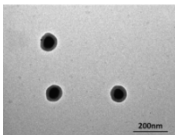
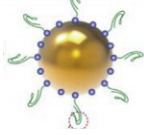
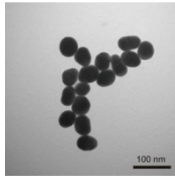

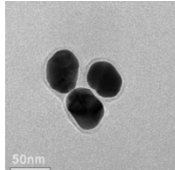
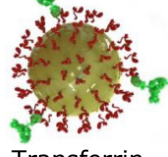
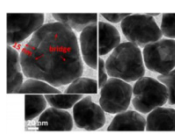
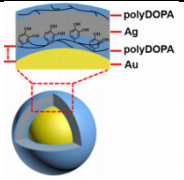
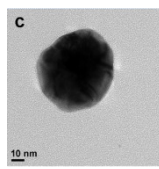
	SERS tags		Reporter	Target analyte/cells	Ref
	Structure	Morphology			
Antibody	 Antibody-DTNB-Au nanorod		DTNB	<i>Staphylococcus aureus</i>	[208]
	 Antibody-DTNB-Au@Ag nanorod		DTNB	Circulating tumor cells	[209]
Aptamer	 Aptamer-conjugated Au		DTNB, MBA	<i>Escherichia Coli</i> <i>Staphylococcus aureus</i>	[210]
	 Aptamer-DSPE-graphene isolated Au nanocrystals (GLANs)		2D graphene	HepG2, A549 cell lines	[211]

Table II. 4. (cont.) SERS tags with using different specific recognition elements for indirect cancer and infectious disease diagnosis

	SERS tags		Reporter	Target analyte/cells	Ref
	Structure	Morphology			
MIPs	 <p>MIP-PATP-Ag nanoparticles</p>		PATP	Sialic acid (cancer cells and tissues imaging)	[212]
Antibiotic	 <p>Vancomycin (Van)-MBA-Au</p>		MBA	<i>Staphylococcus aureus</i>	[213]
Luteinizing hormone releasing hormone (LHRH)	 <p>LHRH-pMBA-Au nanoparticles</p>		4-mercaptobenzoic acid (pMBA)	Circulating tumor cells	[214]
Transferrin	 <p>Transferrin-BDT-Au</p>		1,4-benzenedithiol (BDT)	Hela cell	[215]
Folic acid	 <p>FA-Au@polyPOPA@Ag</p>		Rh6G MB	Human lung adenocarcinoma cell line A549	[216]

II.2.3. Perspective on the use of SERS techniques for cancer and infectious disease diagnosis.

Cancer and infectious diseases are now the major causing of death around the world, thus the development of simple, rapid, and effective diagnosis tools for related cells or biomarkers sensing is important for clinical fast discrimination and reducing mortality. Driven by the development of optical and material science, SERS have shown great potential for some disease diagnosis, including cancer cell, microorganism, and related biomarkers sensing. In this introduction, we have discussed recent advances in SERS based strategies for cancer and infectious diseases diagnosis *via* direct and indirect way. Yet, despite

II. Introduction

such SERS based strategies have provided quick, sensitive, and specific platform for disease diagnosis, Raman signal enhancement is a very complex phenomena and depend on the nanomaterials size, aggravation degree and analyte/substrate interaction mode. Therefore, clinical application needs to focus on the reproducibility of signal output in quantification of disease targets. As signal amplification of analyte largely depends on the strength of EM field that distributed around plasmonic nanomaterials with remarkable differences, even the same molecule close to different position of the nanomaterials will lead to different signal intensity output. In addition, EM field distribution from different signal nanoparticle interact with each other when two nanoparticles are getting close to a specific distance. Hence, EM field distribution of whole aggravated nanoparticles is different from a signal nanoparticle [217-219]. Except 3D ordered solid to fabricate SERS substrate with controlled and uniformed "hot-spot" as describe above, internal standard (IS) strategy is another way to realize quantitative SERS analysis, in which unstable signal from inhomogeneous distribution of EM field will be corrected by the internal peaks. Despite such strategies is in development, recent work showed their specific superiors in quantitative sensing [220-222].

Another important challenge that still requires attention is the biocompatibility of SERS substrate for living cancer and infectious cells imaging, or in-vitro analyte monitoring. The most used plasmonic metal (Ag, Au, Cu, etc.) possess high cytotoxicity, thus may cause changes in cell structures (target protein or other organic chemicals) and influence on the mapping/sensing results. The coating of metal nanomaterials with biocompatible materials such as polyethylene glycols [223], SiO₂ [202], etc can reduce their cytotoxicity. However, the coating of biocompatible membrane may hamper the Raman enhancement ability of SERS substrate [224]. Integration of carbon materials such as graphene also can reduce cytotoxicity of metals [107], still the total size of nano-hybrid need to be taken into account due to the optimal nanomaterial radius for endocytosis is on the order of 25-30 nm [225]. Therefore, further efforts still should be focus on fabrication of SERS substrates with good biocompatible and SERS activity.

Apart from that, the development of portable and miniature SERS platforms is also important to expand the applicability of disease diagnosis with higher realistic scenarios. Current attempts such as portable Raman device [226] and

microchips [227], etc., make the disease diagnosis more flexible, still traditional SERS techniques are widely used in cancer and infectious disease diagnosis due to their superior SERS performance such as sensitivity, spectral resolution, and mapping functionality. Therefore, further efforts still need to focus on realizing disease diagnosis in a portable way to meet the clinical needs.

II.3. Review 1. Micromotors for diagnosis and therapy of diseases.

Inspired by natural proteins motors, scientist have created micromotors capable of converting energy into movement and forces. Such nano/micro-scale devices consist of a self-propelled structure equipped with sensing and/or actuating attachments. The broad scope of operations and applications, along with the ultra-small dimensions, accessibility and force offered by synthetic nano/micromotors, open new possibilities for diagnosis and therapy operations, overcoming some of the unmet challenges [228-239]. Indeed, the movement of nano/micromotors can create turbulent flows that can impart efficient micromixing and enhance mass transfer, further improving the interaction between the active surface and the targets, and consequently, reducing the reaction or sensing time [240, 241]. Another important feature of nano/micromotors is their self-propulsion ability in the solution, allowing for enhanced target removal and drug delivery for future therapy. The size, shape and propulsion mechanisms of nano/micromotors will exert a strong influence on a given biological application. Thus, micromotors can be divided into three main groups according to the propulsion mechanism: (a) chemically powered (catalytic) micromotors; (b) fuel free micromotors powered by biocompatible sources (magnetic, ultrasound, light and thermal energy sources) and (c) biohybrid micromotors. Catalytic nano/micromachines include tubular micromotors by template electrodeposition [242, 243] and rolled-up technology [234], polymer stomatocytes [244] and Janus micromotors powered either by external or natural fuels [245, 246]. Fuel free micromotors compromise magnetically actuated flexible/helical swimmers and US-powered nanowires [247, 248]. Cell-based micromotors belongs to category c [249], with the first remotely controlled cell-based micromotor demonstrated by Schimdt group [250].

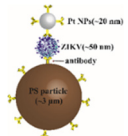
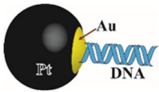
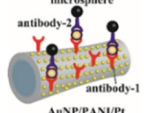
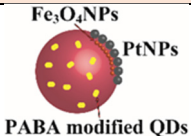
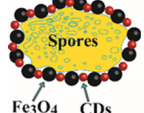
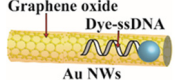
II. Introduction

Many of these nano/micromotors show considerable promise for navigation through complex biological fluids, reaching hard-to-access bodily locations for biosensing or treatment at the cellular level [251, 252]. Indeed, the enhanced mass transfer caused by the cooperative motion of a swarming of micromotors can help to shorten the treatment times or for (bio)-sensing purposes based on analyte induced changes on its motion behavior. Combined with some ingenious detection strategies (modification with target recognition elements, or fluorescent elements) disease diagnosis can be performed in a more rapid, selective and sensitive manner. In addition, the capacity of some nano/micromotors to self-penetrate and interact with tumor tissues and cancer cells make them excellent candidates for cells capture/removal and drug delivery. The unique moving nature and integrated sensing capabilities of nano/micromotors can lead to novel approaches for the prompt and early diagnosis or treatment of diseases, reducing sanitary cost but most importantly allowing for fast treatment to decrease mortality rates.

II.3.1. Nano/micromotors in diagnosis.

Nowadays, many analytical approaches have been exploited for sensing of cancer and infectious related targets, including cancer biomarkers, cancer cells and microorganisms. The most widely employed are polymerase chain reaction (PCR), enzyme-linked immunosorbent assays (ELISA), electrochemical approaches, SERS and fluorescent approaches. Early micromotor works in such fields have added a new analytical dimension for the realization of revolutionary sensing approaches with novel detection mechanisms by utilizing speed changes as output signal (the so-called motion based sensing) or by the incorporation of active sensing/capture elements in the micromotor structure for "*on-the-fly*" dynamic sensing. More details will be given in the following sections. **Table II.5.** illustrates selected recent developments for the sensing of cancer biomarkers and pathogenic cells.

Table II.5. Nano/Micromotors for sensing of cancer biomarkers and pathogenic cells

Analyte (recognition element)	Micromotor design	Propulsion	Ref.
Motion-based sensing			
Zika virus (antibody)		Catalytic (H ₂ O ₂)	[253]
HIV-1 virus (DNA)		Catalytic (H ₂ O ₂)	[254]
Carcinoembryonic antigen (Anti-CEA antibody)		Catalytic (H ₂ O ₂)	[255]
Fluorescent switching			
Bacterial endotoxins (lipopolysaccharides) (PABA modified GQDs)		Catalytic (H ₂ O ₂)	[256, 257]
<i>Clostridium difficile</i> toxins (Carbon dots)		Magnetic	[258]
miRNA in cancer cells (Dye-ssDNA)		Ultrasound	[251]

II.3.1.1. Motion-based sensing.

Motion-based sensing micromotor approaches exploit analyte induced changes on the micromotor speed. For example, Draz et al, developed a nanomotor-based strategy (integrated into a cellphone) for Zika Virus (ZIKV) detection based on analyte induced acceleration of Pt nanomotors in connection with anti-ZIKV antibody functionalized polystyrene beads. The presence of virus in a testing sample results in the accumulation of platinum nanomotors (also functionalized with the specific antibody) on the surface of the beads, causing their motion in H₂O₂ solution. Thus, overall speed of the beads was ~5 times higher in ZIKV spiked samples as compared with the Brownian motion of virus-free control samples (**Figure II.9, A**). Importantly, the presence of other viruses including herpes simplex virus, human cytomegalovirus or dengue virus types 1 and 2 do not produce any speed increase, indicating the high specificity of the procedure as a result of the use of specific antibodies [253].

II. Introduction

A most sophisticated micromotor based cell-phone approach relies on DNA-modified Pt-Au micromotors for loop-mediated isothermal amplification/molecular detection of Human immune-deficiency virus (HIV-1). The strategy is depicted in **Figure II.9, B**: a) loop-mediated isothermal amplification of the nucleic acid of HIV-1 and large-size looped amplicons; b) amplicons mixing with DNA-modified micromotors consisting of Pt-Au nanoparticles coated polystyrene beads; c) capture of amplicons on micromotor surface and subsequent generation of motile assemblies with a catalytic head of motors and large tail of DNA; d) motion and speed tracking with a mobile phone device and peroxide solutions. According to the previous strategy, the presence of HIV-1 RNA in a sample results in the formation of large-sized amplicons that hamper peroxide accessibility or block the catalytic part of the micromotors, reducing its motion in a RNA concentration dependent manner. The system allows the qualitative detection of HIV-1 ($n = 54$) at a clinically relevant threshold value of 1000 virus particles/mL with high selectivity [254].

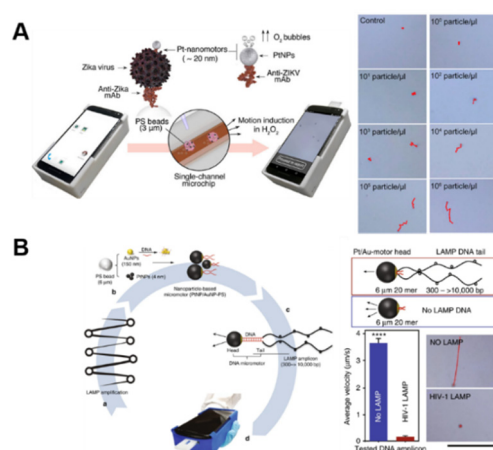


Figure II.9. Motion-based micromotor (bio) sensing strategies for virus detection. **(A)** Immunological detection of Zika virus by nanomotor-based bead-motion cellphone system. **(B)** HIV-1 molecular detection using loop-mediated isothermal amplification. a) Nucleic acid of HIV-1 and large-size looped amplicons are amplified. b) Amplicons are mixed with DNA-modified micromotors that are covered with Pt NPs and Au NPs to power the catalytic motion of motors in the fuel. c) Capture of amplicons on surface of motors results in the formation of motile assemblies with a catalytic head of motors and large tail of DNA. Hence, speed of motor will be decreased with the increase of virus. Reproduced with permission from ref. [253] and [254] with permission.

A motion-based immunoassay of cancer biomarkers (carcinoembryonic antigen) rely on gold-nanoparticle-modified self-propelled polyaniline/Pt micromotor modified with a specific capture antibody. The autonomous movement of the microsensor in the fuel-enhanced sample mixture results in the fast and selective recognition of the protein target. Following interaction with specific

secondary-antibody-modified glycidyl methacrylate microspheres, the speed of the micromotor decrease. In the system, the carcinoembryonic antigen induced changes in the speed and the number of conjugated microspheres can be used as analytical read-out, allowing to achieve excellent linear range from 1 to 1000 ng mL⁻¹. The whole procedure can be completed in 5 min without any washing and/or separation step [255].

II.3.1.2. Fluorescent switching.

Fluorescent detection *via* analyte induced fluorescent switching mechanisms is a convenient approach widely used in many field (*i.e.*, biology, pharmacology) due to the inherent advantages such as high sensitivity, selectivity, and good solubility in water which facilitates the application in biological media. The integration of fluorescence-switchable materials into micromotors has added a new dimension to fluorescent sensing of pathogens and cancer cell biomarkers with shorter detection times and localized detection for future *on-the-fly* diagnosis. Receptor functionalized quantum dots have been encapsulated into magnetic/catalytic Janus micromotors for "ON-OFF" fluorescence detection of bacterial endotoxins (see **Figure II. 10, A**). A bottom-up approach was adopted for microsensor fabrication, involving first the generation of oil-in-water emulsion containing phenylboronic acid (PABA) modified quantum dots (QDs) along with PtNPs (for catalytic propulsion) and Fe₃O₄ NPs (for magnetic guidance). The sensing strategy rely on the specific interaction of the target endotoxin or lipopolysaccharide with the PABA receptor on the GQDs, leading to a fluorescent quenching in a concentration dependant manner. As a result, endotoxins released from *Escherichia Coli* 0111:B4 or *Salmonella Enterica* bacteria can be easily detected [256, 257]. Zhang et al also have developed microrobot-based fluorescence "ON-OFF" strategy for sensing bacteria toxins (**Figure II. 10, B**). They designed a fluorescent magnetic spore-based microrobots by the deposition of magnetic NPs and encapsulation of sensing probes onto the outer native spore structure, which display high porosity. In the cooperation of natural spore, magnetic NPs, and functionalized carbon nanodots, fluorescence changes could be observed to sensing *Clostridium difficile* (*C.diff*) toxin detection within 10 min on complex samples [258].

II. Introduction

A similar approach by Wang's group describe a very interesting strategy for cancer biomarker detection (miRNAs) within cancer cells. As depicted in Fig **Figure II. 10, C**, dye-labelled single-stranded DNA (ssDNA)/graphene-oxide (GO) coated nanowires (AuNWs) motor propelled by ultrasound (US) were used for intracellular detection of target miRNA in MCF-7 and *HeLa* cancer cells. Before sensing of target miRNA-21, the fluorescence of dye-ssDNA probe is "OFF" due to the π - π interaction between GO and dye-labeled ssDNA. As soon as the nanomotor is internalized into the cell, dye-ssDNA probe is released from the GO surface to hybridize with the target miRNA-21, in which fluorescence of dye-ssDNA probe will be "ON" for further detection [251].

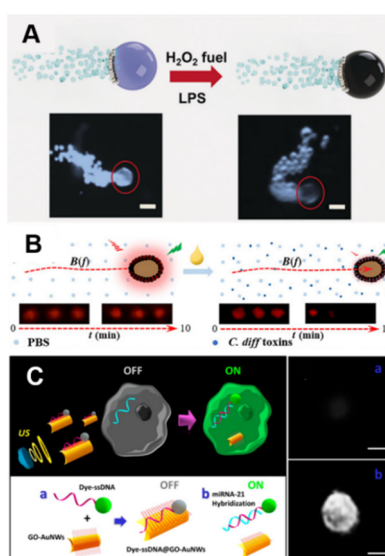


Figure II.10. Fluorescence switching micromotor (bio)-sensing strategies for bacteria toxins and cancer biomarkers detection. **(A)** Magneto-catalytic GQDs modified Janus micromotors for bacterial endotoxin detection based on fluorescence "ON-OFF" strategy. Optical microscopy images of Janus micromotors before and after the addition of the lipopolysaccharide from bacteria. **(B)** Fluorescent magnetic spore-based microrobots as a highly efficient mobile sensing platform for the detection of *Clostridium difficile* toxins using fluorescence "ON-OFF" strategy. **(C)** Intracellular detection of miRNA by US-propelled ssDNA@GO-functionalized gold nanomotors using fluorescence "OFF-ON" strategy. Reproduced with permission from ref. [256], [258] and [251], with permission.

II.3.2. Nano/micromotors for cancer and infectious diseases treatment.

Nano/micromotors have demonstrated considerable promise for cancer and infectious disease therapy, mainly by three main mechanisms: a) Micromotor modification with specific capture elements to remove the cancer or pathogenic cells, which are direct therapy methods; b) Direct micromotor contact with

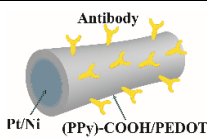
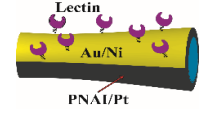
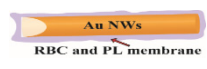
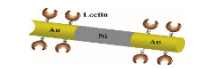
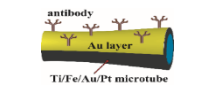
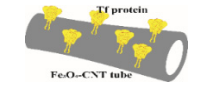
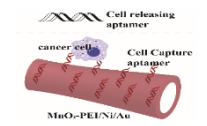
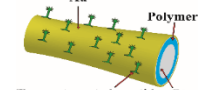
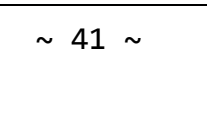
cancer or pathogenic cells for killing and c) Micromotor functionalization with smart materials (biodegradable polymers or inorganic materials, etc) for drug triggered delivery.

II.3.2.1. Receptor functionalized micromotors for specific capture and removal of pathogenic and cancer cells.

Cancer or pathogenic cells can cause a variety of illnesses to humans. To fight such diseases, a direct way is to capture and remove the cancer or pathogenic cells. A key step is to modify the micromotors with specific recognition elements (antibodies, lectins, peptides, etc) for specific interaction with the target cells.

Table II.6 shows a list of the most relevant nano/micromotors strategies for direct capture and removal of cancer and pathogenic cells.

Table II.6. Nano/Micromotors for direct capture and removal of pathogenic and cancer cells

Target (capture element)	Micromotor design	Propulsion	Ref.
<i>Bacillus globigii</i> spores (Anthrax) (antibody)		Catalytic (H ₂ O ₂)	[259]
<i>Escherichia Coli</i> (ConA lectin)		Catalytic (H ₂ O ₂)	[260]
<i>Staphylococcus Aureus</i> (RBC and PCL biomembranes)		Ultrasound	[261]
<i>Escherichia Coli</i> (ConA)		Ultrasound	[248]
<i>Staphylococcus Aureus</i> (Antibody)		Catalytic (H ₂ O ₂)	[262]
CTCs (antibody)		Catalytic (H ₂ O ₂)	[263]
HCT 116 cell from CTC suspension (Transferrin)		Catalytic (H ₂ O ₂)	[264]
Leukemia cells (HL-60) (aptamer)		Catalytic (H ₂ O ₂)	[265]
HeLa cancer cells (Peptide)		Catalytic (H ₂ O ₂)	[265]

II. Introduction

Antibody. Antibodies (IgG) are large proteins with a Y-shape that are widely used as recognition elements for the selective capture and removal of pathogenic cells. Wang's group exploited the high selectivity and performance of such recognition elements in connection with self-propelled micromotors for dynamic capture of circulating tumor cells (CTCs) [262]. Thus, **Figure II.11, A** show the *in vitro* strategy for capture and removal of CTCs based on the specific binding and transport ability of anti-carcinoembryonic antigen antibody functionalized tubular micromotors. Such early work paved the way for the use of micromotors as moving carriers for *all-in-one* selective recognition, isolation, capture and even inactivation of pathogenic cells.

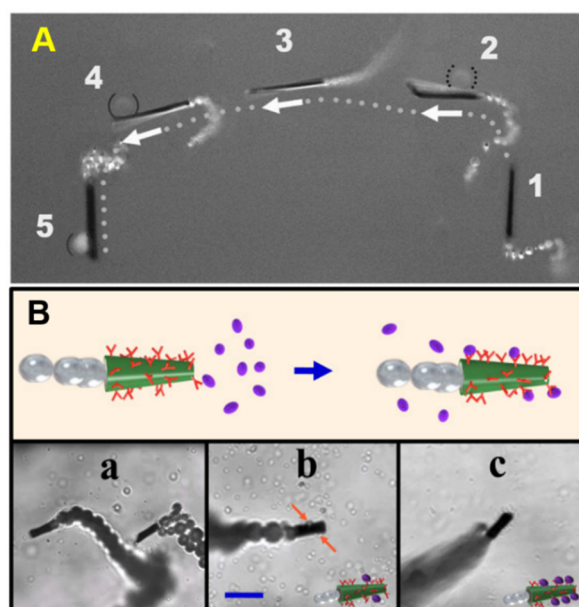


Figure II.11. Antibody functionalized micromotors for the capture and removal of pathogenic cells. (A) Antibody functionalized micromotors for cancer cell isolation: 1) approaching, 2) interaction with non-specific cell, 3) moving, 4) specific capture, 5) transporting. (B) Antibody modified polypyrrole-COOH-PEDOT/Ni/Pt for the capture, transport, and inactivation of *Bacillus globigii* spores: (a-c) microscopic images of the antibody functionalized micromotor in an aqueous solution transporting the target spore. Reprinted with permission from ref. [262] and [259].

Using the same principle, Wang's group also designed a *Bacillus globilli* antibody-functionalized micromotor to recognize, capture and transport *Bacillus globilli* spores (see **Figure II.11. B**). Thus, the microscopy images of **Figure II.11. B** (a-c) illustrates the "on-the-fly" capture of the spores using magnetically-guided functionalized micromotors in aqueous solution. The

micromotors can also swim in a spore-containing solution (real sample) for accelerating destruction of spores, including lake and tap water samples [259].

Lectins. Lectins are carbohydrate-binding glycoproteins with high specific interaction ability towards mono- and oligosaccharide present in bacterial cell-walls components. One typical example is Concavalin A (Con A), that can interact with the mannose- and glucose- protein of *Gram*-negative bacteria such as *Escherichia Coli*. Campuzano et al. used ConA modified Au/Ni/polyaniline/Pt microtubular engines for specific isolation of *Escherichia Coli* bacteria from environmental, food, and clinical samples [260]. Thus, **Figure II.12. A** shows the specific transport of *Gram*-negative *Escherichia Coli* bacteria (e-f) by the lectin-modified motors, while the *Saccharomyces cerevisiae* cells (b-d) are not captured. Later on, Gradilla et al. extended the strategy using fuel-free ultrasound-driven ConA modified nanowires to capture and transport bacteria [248]. As depicted in **Figure II.12. B** (a), three-segment Au-Ni-Au nanowires are first prepared by template method and then modified the lectin. Fig 4B shows the lectin-modified micromotors approaching (b), picking (c), and transporting (d) the bacteria. Such fuel-free acoustically driven lectin functionalized nanomotors are highly biocompatible and highly attractive for diverse in vivo biomedical applications.

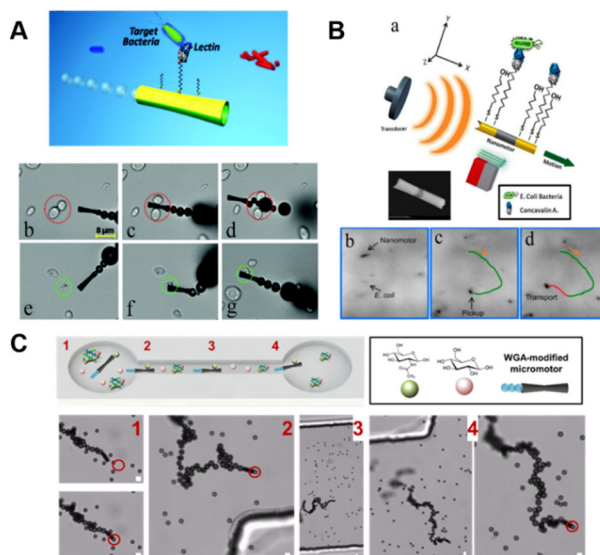


Figure II.12. Lectin-modified micromotors for bacteria capture. **(A)** ConA functionalized tubular micromotors for specific isolation of *Escherichia Coli*. Scheme of the bacteria isolation strategy; (b-d) Lectin-modified motor before, during, and after interaction of the *Saccharomyces cerevisiae* negative control, respectively; (e-g) Lectin-modified micromotors before, during, and after interaction of the *Escherichia Coli*. **(B)** Ultrasound-propelled magnetically guided ConA modified

II. Introduction

nanowires for selective capture and transport of bacteria. (a) Scheme of the bacteria capture and transport strategy; (b-d) Ultrasound-propelled ConA-modified nanomotor approaching, capturing, and transporting the *Escherichia coli*. **(C)** "On-chip" capture-transport-trapping of N-acetylglucosamine-incubated polystyrene (PS) particles (green dots) with WGA-OPD modified micromotors under the presence of an excess of glucose-incubated PS particles (red dots) in raw human serum: a micromotor capturing (1), transporting (2,3) and entering (4) the reservoirs of a PDMS chip. Reprinted with permission from ref. [260], [248] and [266].

Multiwalled carbon-nanotubes-Ni-PtNPs micromotors modified with specific lectins (ConA and wheat germ agglutinin, WGA) have been used for selective isolation and transport of bacteria within the different reservoirs of a *lab-on-a-chip* (LOC) system. The concept is illustrated in **Figure II.12. C**. WGA modified micromotors has high affinity to N-acetylglucosamine (N-Gluc) residues in the cell wall of a number of gram-negative bacteria and other cells. To demonstrate its practical applicability for *on-chip* cell capture and transport, WGA-MWCNTs-Ni-PtNPs micromotors were placed in the reservoir of a PDMS chip containing N-Gluc modified-PS particles and an excess of glucose modified PS-particles in raw human plasma. As can be seen in **Figure II.12. C**, the micromotors interact (selectively) with the N-Gluc-PS particles (1), transport them within the LOC channel (2,3) and enter a second reservoir (4) for effective sugar isolation. The selectivity of the new isolation protocol was examined by putting in contact the functionalized micromotors with PS modified particles. As expected, moving WGA microengines interact with the N-Gluc monosaccharide, but not with glucose or bare PS particles. Similarly, micromotor modified with the lectin (ConA), which have high affinity for glucose and mannose, do not interact with N-Gluc neither bare PS modified particles, whereas an interaction with glucose-PS is noted [266].

Proteins and biomimetic membranes. The use of cells (including cellular components or whole cells) and natural proteins with the dynamic movement of micromotors have led to novel and specific isolation of pathogenic cells and related toxins. Biomimetic cell coated micromotors can harness natural cell functions and possess inherent biocompatibility avoiding thus an immune response while utilizing useful secondary functions of the blood cells such as specific capture of pathogenic cells and toxins, holding considerable promise for therapeutic applications [249]. Different micromotors structures based on biofriendly propulsion mechanism such as magnetic or ultrasound fields can be

used for the assembly of red blood cell (RBC) [267] or platelets (PL) [268]. For example, RBC coated ultrasound propelled Au nanowires display enhanced removal capabilities of deadly toxins (snake venom) [269]. PL coated magnetic propelled helices can bind selectively to Shiga toxin and *Staphylococcus aureus* bacteria [270]. Esteban-Fernández de Ávila et al. have designed a dual-cell membrane-modified motor for removal of pathogenic bacteria and toxins. As depicted in Fig **Figure II.13. A**, both RBC membranes and PL were combined on the surface of ultrasound-propelled gold nanowires for the specific capture of bacteria and toxins. Right SEM images shows the specific micromotor binding with MRSA USA300 bacteria. Micromotors were further explored for the selective binding with methicillin-resistant *Staphylococcus aureus* [261].

Biological proteins represent another group of important ligands for cancer cell capture. For example, transferrin (Tf) can be used as specific bio-ligand for the specific capture of cancer cells with overexpress of Tf receptors. Such feature was exploited by Banerjee et al in connection with carbon nanotubes (CNT) micromotors as immobilization supports for specific CTCs isolation. **Figure II.13, B** show the scheme of the driving mechanism for the Tf-Fe₃O₄-CNT micromotors and efficient attachment with the cells in just 5 min [263].

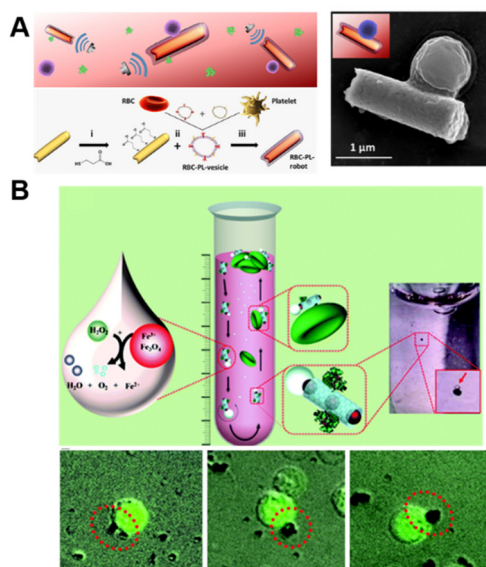


Figure II.13. Biomimetic and protein modified micromotors for CTCs and bacteria capture and removal. **(A)** Schematic of PL and RBC modified micromotors for binding and removal of bacteria. Right image shows the SEM image of a MRSA USA300 bacteria attached to an RBC-PL-micromotor. **(B)** Schematic of the driving mechanism for the Tf-Fe₃O₄-CNT micromotors (top images) and images of Tf-CNT-Fe₃O₄ micromotor attached to HCT116 (down images). Reprinted with permission from ref. [261] and [263].

Aptamers. Aptamers are single stranded nucleic acids (DNA or RNA) or proteins that can specifically bind with a target molecule, offering specific advantages over antibody-based recognition elements in pathogenic cells capture. Similar to antibodies, aptamers exhibit high binding affinity for target cancer cells or bacteria. Additionally, such recognition elements are cheap, stable, and can be mass produced. Tabrizi et al developed a nucleic acid aptamer-modified MnO₂-PEI/Ni/Au micromotors for transportation of human promyelocytic leukemia cells (HL-60) from human serum sample. **Figure II.14. A., a-e** shows the time-lapse images of HL-60 captured by the aptamer-modified micromotors in human serum sample. Despite the main aim of the strategy is to develop an electrochemical biosensor for cancer cell sensing, the strategy can be extended for future disease therapy in connection with more biofriendly propulsion mechanisms such as ultrasound or magnetic fields [264].

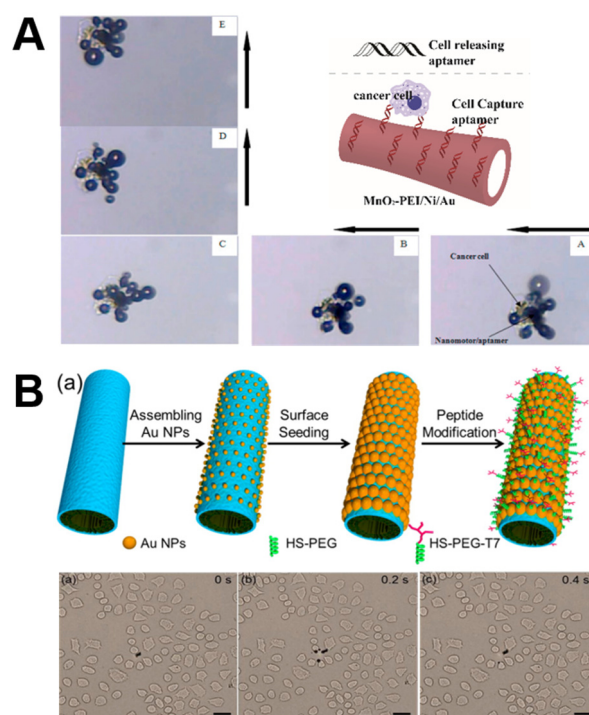


Figure II.14. Aptamers as recognition element for the capture of cancer cells. **(A)** Nucleic acid aptamer modified MnO₂-PEI/Ni/Au micromotors for isolation of cancer cells. Time-lapse images demonstrating the capture of HL-60 cancer cell by nucleic acid aptamer-functionalized micromotor in human serum sample (from A-D, capture, and transportation in the solution). **(B)** Peptide aptamer-functionalized micromotors for capture of HeLa cells. (a) Scheme of the fabrication process of the peptide modified motor; (b) Time-lapse images of the NIR-triggered motion of the peptide modified micromotor toward HeLa cells in 0.1 % H₂O₂. Reprinted with permission from ref. [264] and [265].


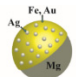

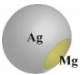

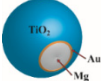
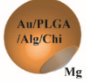
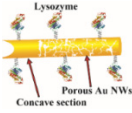
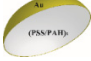
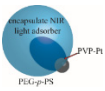
Peptide-based aptamers are artificial proteins selected or engineered to bind specific target molecules. Wu et al fabricated polymer-based micromotors by layer-by-layer assembly with an inner PtNPs layer and gold shell outer layer. The micromotor remain motionless at a low concentration of 0.1% H₂O₂, however, near-infrared (NIR) irradiation induce a photothermal effect which rapidly triggers the motion of the catalytic micromotor. The micromotors are further modified with peptide aptamer (**Figure II.14, B, a**) for specific recognition of cancer cells. **Figure II.14, B, b** shows the time-lapse images of the NIR-triggered motion of the peptide modified micromotor toward HeLa cells capture [265]. Using aptamer as capture element, researchers have gotten a cheaper method than the antibody-based strategies for the isolation of cancer cells.

II. Introduction

II.3.2.2. Direct micromotor contact and killing of pathogenic and cancer cells.

The ability of certain nanoparticles and functional materials (i.e. silver nanoparticles, photothermal agents) to disrupt the membranes of bacteria or cancer cells can be combined with the moving nature of nano/micromotors for enhanced killing of such target cells by direct contact. Some relevant examples are illustrated in **Table II.7**.

Table II.7. Nano/micromotors for direct contact and killing of pathogenic and cancer cells

Target (Killing element)	Micromotor design	Propulsion	Ref.
<i>Escherichia Coli</i> <i>Staphylococcus Aureus</i> (Silver nanoparticles)	 Pd/Ni/Ag	Magnetic	[271]
<i>Escherichia Coli</i> (Silver nanoparticles)		Catalytic (Mg/H ₂ O)	[272]
<i>Escherichia Coli</i> (Silver ions)	 AgCl	Light	[273]
<i>Escherichia Coli</i> (Silver ions)		Catalytic (Mg/H ₂ O; Mg/NaHCO ₃)	[274]
<i>Escherichia Coli</i> (Silver ions)	 Ag zeolite	Catalytic (H ₂ O ₂)	[275]
<i>Bacillus globigii</i> spores (TiO ₂)		Catalytic (Mg/H ₂ O)	[276]
<i>Escherichia Coli</i> (Chitosan)		Light Catalytic (Mg/H ₂ O)	[277]
<i>Escherichia Coli</i> <i>Micrococcus lysodeikticus</i> (Lysozyme)	 Lysozyme Porous Au NWs Concave section	Ultrasound	[278]
HeLa cancer cells (Au-NIR light)		NIR light	[279]
Human breast cancer cells (NIR light)	 PVP-Pt PEG-p-PS	Catalytic (H ₂ O ₂)	[280]

Silver and TiO₂ nanoparticles. It is well known that silver ions have excellent antibacterial activity, which has been exploited in a variety of applications such as dental wound healing or in catheters. Silver ions released in solution can interact with thiol have reported on silver-coated magnetic nanocoils to target and kill bacteria [271]. As depicted in **Figure II. 15. A**, the nanocoils are obtained by electrodeposition and selective dealloying of palladium (Pd), and subsequently coated with nickel (Ni) and silver (Ag) for the further magnetic movement and *Escherichia Coli* bacteria killing, respectively. **Figure II. 15. A** also illustrate the significant surface morphology changes on a *Escherichia Coli* bacteria before and after treatment with Pd/Ni/Ag nanocoils (see further discussion below). The bacteria killing mechanism is speculated by direct contact interaction with the silver on the outside surface of nanocoils, that cause the membrane disintegration. Similar examples were reported by Vilela et al [272], and Dong et al. [274] in which they synthesized Janus micromotors decorated with silver nanoparticles (AgNPs) for killing *Escherichia Coli* in contaminated water. Micromotors are driven by the hydrogen bubbles produce by the reaction between Mg and water and show excellent antibacterial capability in comparison with control assays in PBS and water. Silver nanostar shaped micromotors exhibit efficient motion in water by UV light irradiation while releasing Ag⁺ ions during its motion for bacteria killing [273]. Zeolite based micromotors with high surface area for improved Ag ions immobilization (which also act as catalysts for peroxide decomposition and bubble propulsion) can also target *Escherichia Coli* based on the same principle [275].

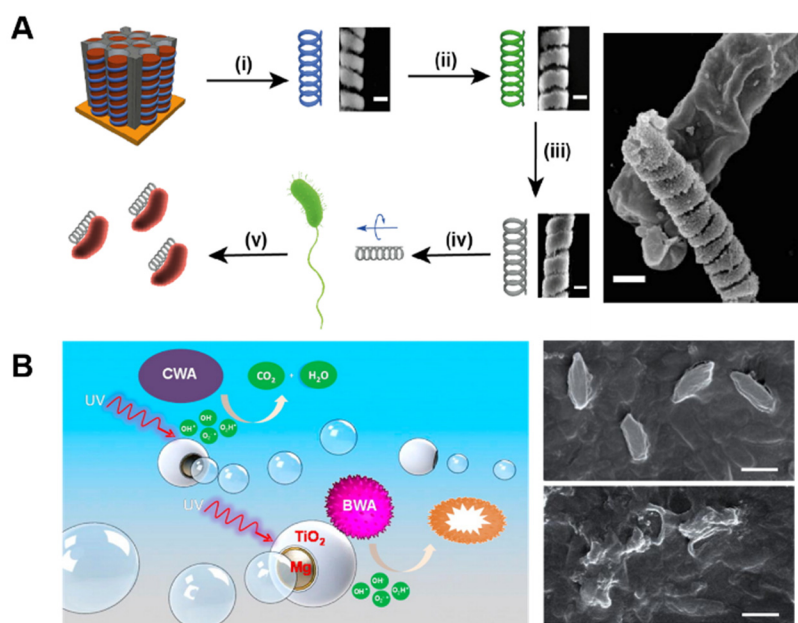


Figure II. 15. Nanoparticles modified micromotors for bacteria killing. **(A)** Schematic illustration of a Pd/Ni/Ag magnetic nanocoils for bacteria killing and corresponding SEM images of morphological changes of the *Escherichia Coli* bacteria before and after treatment. **(B)** Schematic representation of the self-propulsion and photocatalytic degradation of biological warfare agents using water-driven spherical TiO₂/Au/Mg micromotors. Right images show the SEM images of bacteria spores before and after treatment with TiO₂/Au/Mg micromotor. Reprinted with permission from ref. [275] and [276].

TiO₂ photocatalysis is widely used in a variety of applications such as photocatalytic degradation of highly resistant bacterial spores. Such degradation is one of the most efficient and environmentally friendly approaches and do not require harsh reagents or yield toxic byproducts. TiO₂ also exhibit remarkable properties (in connection with UV light) to rupture and deactivate a variety of bacillus species [281]. Inspired by this, Li et al developed an effective micromotor modified with TiO₂ for photocatalytic degradation of *Bacillus Globigii* spores. The micromotor is composed by a Mg core, AuNPs and a TiO₂ shell layer, and is driven by the hydrogen bubble thrust generated from the Mg-water reaction. During the autonomous propulsion, UV-activated TiO₂ surface of motors will generate highly oxidative species, which leads to remarkably effective photocatalytic cleaning microsystem for spore inactivation (**Figure II. 15. B**). The SEM images of Fig 7B illustrate the morphology of *Bacillus globigii*

spores before and after 10 min UV irradiation in the presence of the TiO₂/Au/Mg motors, further revealing the effectivity of the micromotors [276].

Biopolymers and enzymes. Traditional antibacterial agents such as chlorine or silver may be toxic or generate byproducts which can cause adverse side effect to human health and the environment. To overcome such drawbacks, antibacterial agents (such as biopolymers) with low toxicity and biocompatibility have been introduced. Chitosan is one of the excellent biopolymers that present good antibacterial activity and biocompatibility. Even though the antibacterial mechanism of chitosan is still not fully understood, some researches attributed it to the electrostatic interaction between chitosan and cell membrane, which cause irreversible cell membrane damage. In a representative micromotor example, Delezuk et al., modified Janus motor with chitosan for efficient bacteria killing [277]. As depicted in **Figure II. 16. A**, the Janus motors compromise a Mg core coated with an Au layer and the biodegradable polymers poly (lactic-co-glycolic acid) (PLGA), alginate (Alg) and chitosan (Chi) successively (see also corresponding SEM images). **Figure II. 16. A** show the schematic representation and corresponding SEM image of the Janus motor moving in the real sample and approaching the bacteria, contacting the bacteria, and killing bacteria. It can be clearly seen that water-driven Janus motor modified with Chi possess excellent antibacterial ability, compared with motor without Chi or static Chi micromotors.

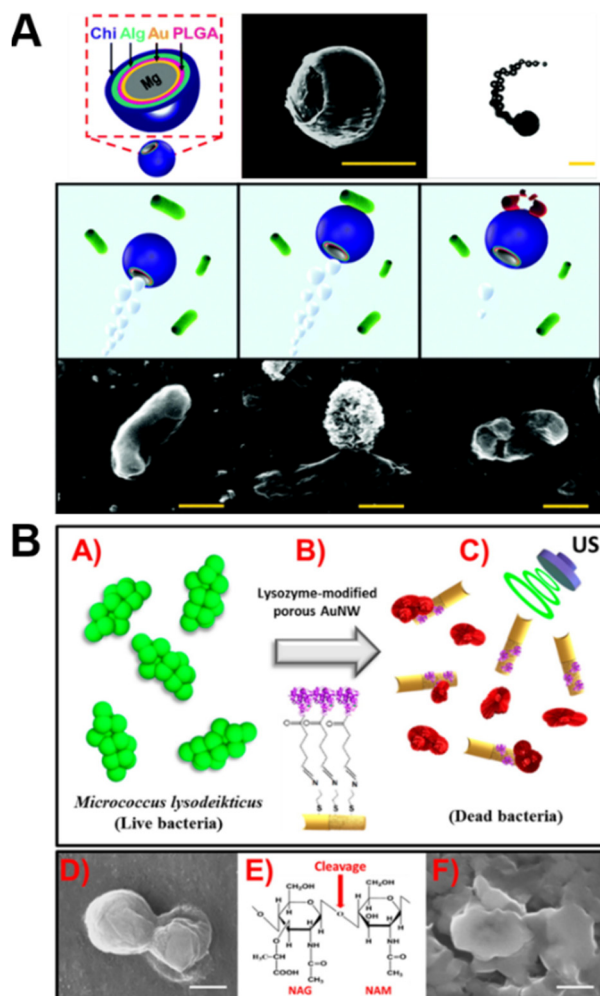
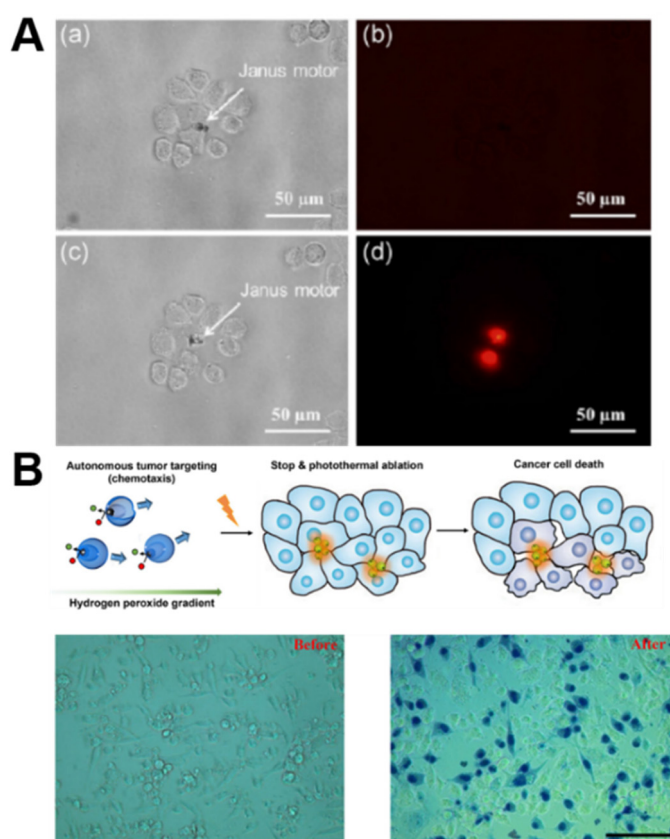


Figure II. 16. Biopolymer or enzyme modified micromotors for bacteria killing. **(A)** Schematic illustration of the structure of Mg/Au/PLGA/Alg/Chi Janus micromotor, SEM images of the as-prepared Janus micromotors and time-lapse image of the micromotor moving in drinking water. Down part shows the schematic representation and SEM images of chitosan modified Janus micromotors moving through the sample and approaching the *Escherichia Coli* bacteria (left image), contacting (middle image), and killing (right image). **(B)** Schematic illustration of the lysozyme-modified ultrasound propelled micromotors for *Micrococcus Lysodeikticus* killing(a-c). (d, f) SEM images of the bacteria before (d) and after (f) treatment and related mechanism (e). Reprinted with permission from ref. [277] and [278].

As an alternative of biofriendly antibacterial biopolymers, lysozyme-based enzymatic degradation of bacteria is also a safe, environment-friendly, and efficient route for inactivation of pathogenic cells. Lysozyme is an antibacterial glycoside-hydrolase enzyme produced by animals that forms part of the innate immune system. It can attack the protective cell walls of bacteria by catalyzing the hydrolysis of 1,4-β-linkages between N-acetylmuramic acid and N-acetyl-D-glucosamine residues in peptidoglycan [282]. Kiristi et al have used lysozyme-

modified nanomotors for effective and rapid killing of bacteria. As depicted in **Figure II. 16. B.** gold nanowires modified with lysozyme and propelled by ultrasound fields can contact the live bacteria and kill them immediately [278]. The SEM images of *Micrococcus Lysodeikticus* bacteria before and after treatment with lysozyme-modified nanomotors, clearly illustrate the dramatic changes of the morphology and structure of the bacteria cell wall. In the presence of the lysozyme-modified nanomotor, the bacteria become wrinkled, which may reflect leakage of cytoplasmic content outside the bacterial cell wall. Overall, such strategy represents a new antibacterial approach for effective, fast, and environmentally friendly killing of bacteria.

Nanoparticles for photothermal based killing of cancer cells. Due to their minimal invasiveness and high specificity (thermal therapy would selectively destroy cancer cell since cancer cell are more sensitive to an increase in temperature), photothermal therapy via NIR irradiation is becoming more and more popular in disease therapy. **Figure II. 17.** illustrates some selected examples.



II. Introduction

Figure II. 17. Micromotors for direct contact interaction killing of pathogen cells through photothermal effect. **(A)** Janus polymer multilayer capsule motors and photothermal effect on HeLa cell before (a-b) and after (c-d) NIR light irradiation. **(B)** Schematic illustration of the photothermal ablation of cancer cells using stomatocyte nanomotors; verification of photothermal effect of nanomotors using trypan blue exclusion assay, before and after NIR light illumination. Reprinted with permission from ref. [279] and [280].

Wu et al. combined gold-coated Janus microcapsule motors with photothermal effect under NIR laser to killing of HeLa cells. Micromotors were synthesized by template-assisted polyelectrolyte layer-by-layer assembly with a gold layer on one side. The NIR-driven Janus capsule motors moved well towards the HeLa cells in cell media upon NIR irradiation (see **Figure II. 17. A**). To better testify the photothermal effects, the author labeled the cells with the red fluorescence dye propidium iodide (PI) after laser irradiation. As clearly shows in **Figure II. 17. A**, prior NIR treatment cells are intact and do not display apparent damage (a-b), while cells in contact with the micromotors suffer apoptosis (c-d) and display the PI label (which can only permeate dead cells) after 30 s exposition with NIR light [279]. Another example is reported by Choi et al, in which NIR controlled "ON-OFF" motion of stomatocyte nanomotors powered by the conversion of H_2O_2 are used to photothermally ablate the cancer cells (Fig 9 B). Trypan blue is used to label death cells, allowing to estimate thus the extent of killing. As shown in **Figure II. 17. B**, most of the cells were alive without being stained by trypan blue before the NIR light irradiation [280].

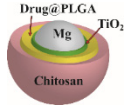

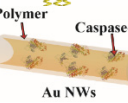
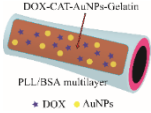
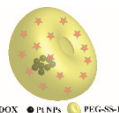
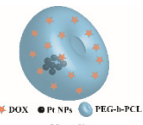
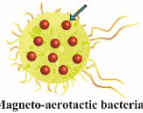
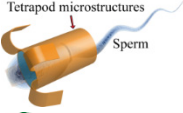
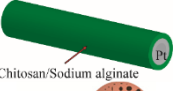
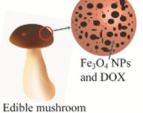
Rotating micromotors for cancer cell killing. It has been shown that tiny rotating micromotors can drill into cell material and cancer cells directly killing them. In an early work, self-propelled InGaAs/GaAs/(Cr)Pt asymmetric rolled-up micromotors propelling in hydrogen peroxide solutions move in a corkscrew-like trajectory to drill into cell material [283]. Later on, plant derived magnetic micromotors or "*medibots*" were demonstrated to kill single HeLa cells by rupturing their outer membrane [284].

II.3.2. Micromotor based drug delivery strategy for specific targeting of bacteria and cancer cells.

Main nano/micromotors based drug delivery systems for cancer and pathogenic cells killing rely on the combination of smart biomaterials with as a pH-,

thermal/light-, or redox- response behavior or cell-based structures (see **Table II.8**).

Table II.8. Nano/Micromotors based drug delivery systems for cancer and pathogenic cells killing

Target (responsive material)	Micromotor design	Propulsion	Ref.
<i>Helicobacter Pylori</i> (PLGA)		Catalytic (Mg/H ₂ O)	[285]
<i>Escherichia Coli</i> (mesoporous silica)		Bacteria driven	[286]
Gastric cancer cells (Eudragit L30 D-55)		Ultrasound	[287]
HeLa cells (Gelatin hydrogel)		Catalytic (H ₂ O ₂) Magnetic	[288]
HeLa cells (PEG and PS polymers)		Catalytic (H ₂ O ₂)	[289]
HeLa cells (PCL)		Catalytic (H ₂ O ₂)	[290]
Tumor hypoxic regions (Nanoliposomes)		Chemotactic-magnetic bacteria	[291]
HeLa spheroids (Tetrapod microstructure)		Sperm cells Magnetic	[292]
<i>Hela cells</i> (Chitosan)		Catalytic (H ₂ O ₂)	[293]
<i>Hela cells</i> (Mushroom natural membranes)		Catalytic (H ₂ O ₂ /catalase)	[294]

pH-responsive polymers. pH-sensitive polymers are a type of stimuli-responsive polymers that can respond to pH changes in the media by undergoing structural and property changes. Such unique properties make them very useful in the design of pH-responsive drug delivery system. For example, the commercial pH-responsive polymer Eudragit (copolymers derived from

II. Introduction

esters of acrylic and methacrylic acid) are usually used to release the drug in specific pH environment because they can only be dissolved at $\text{pH} > 5.5$. Li et al have used Eudragit L100-55 as pH-sensitive polymeric combined with micromotor for pH-responsive drug release. As depicted in **Figure II. 18. A. a**, the micromotor contains a Mg microsphere core coated with a thin Au layer and the drug encapsulated into the pH-sensitive polymer layer. The motors are driven by the bubbles produced from the reaction between Mg and the slightly acidic media. As the micromotor move, pH in the gastric fluid increase rapidly from 1.3 to 6.2 within 12 minutes. No release was observed using PS nanoparticles that do not contain the pH sensitive polymer [295].

Later on, Esteban-Fernández de Ávila et al used a similar pH-sensitive polymer (Eudragit L30 D-55) to coat ultrasound propelled gold nanowires for pH-sensitive drug release. The nanowires were coated with the pH-sensitive polymeric layer containing the enzyme caspase (CASP-3). As depicted in **Figure II. 18. B**, (top), due to a gradient of pH between the interior of gastric cancer cells ($\text{pH} > 5.5$) and the media ($\text{pH} < 5.5$), CASP-3 enzyme was only released from the US-propelled motors while moving inside the cancer cell. **Figure II. 18. B.** shows the images of cancer cells (left), the polymer/CASP-3@AuNWs approaching such cells under the US propulsion (middle), and after the nanomotors entering the cell, the pH-sensitive coating dissolved and released the CASP-3 enzyme which subsequently induces rapid cell apoptosis (right). Control studies performed using polymer/CASP-3@AuNWs with ultrasound propulsion, free CASP-3 with US, free CASP-3 without US, polymer/CASP-3@AuNWs without US, and US only) reveals that only the moving polymer/CASP-3@AuNWs with US can kill the cancer cell [287].

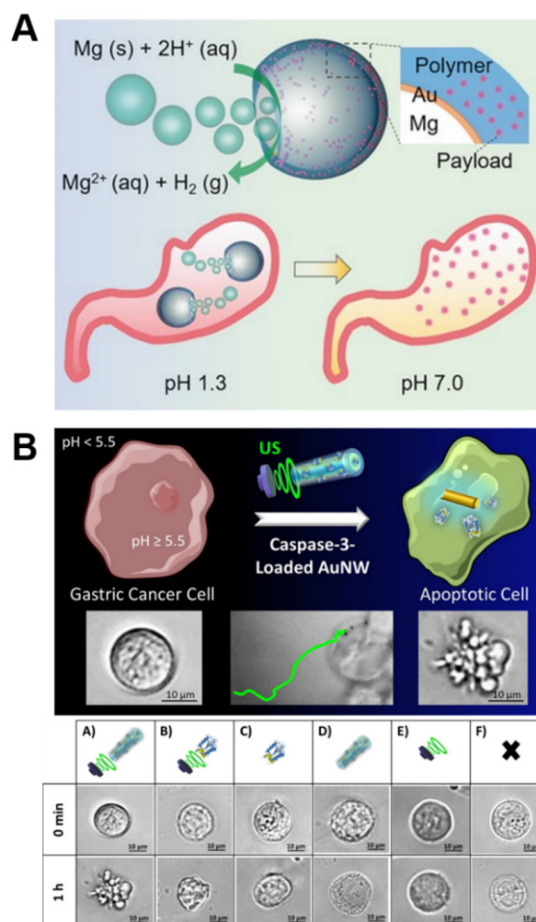


Figure II. 18. pH-sensitive polymer coated micromotors for drug delivery and release. **(A)** Schematic illustration of acid-powered Mg based micromotor coated with Eudragit L100-55 polymer for pH response drug release. **(B)** Ultrasound-propelled polymer/CASP-3@AuNWs nanomotor for intracellular delivery to induce apoptosis of gastric cancer cells and optical microscope images of the cells treated with moving polymer/CASP-3@AuNWs micromotors (a), free CASP-3 with ultrasound (b), free CASP-3 without ultrasound (c), static polymer/CASP-3@AuNWs (d), ultrasound and (e), and untreated cells. Reprinted with permission from ref. [295] and [287].

Thermal/Light-responsive biodegradable materials. Some biodegradable materials (such as gelatin or agar hydrogels) exhibit rapidly responsive ability and phase transitions in response to the surrounding temperature or light fields, along with improved capacity for drug encapsulation. Liang et al used gelatin/agar (GltAg) hydrogel as thermal-responsive material to coat graphene nanosheet. The resulting hydrogel micromotor possess light-responsive and thermal-responsive dissolving ability that can be controlled by the temperature off the media and the ratio of agar used in the synthesis (see **Figure II. 19. A**). For the GltAg hydrogel motors, when the temperature increased from 28°C to 31°C, the dissolution of GltAg0 is promoted. When the temperature increased

II. Introduction

to 34 °C micromotor start to dissolve. Apart from the thermal-response ability, light-response ability also has been studied in this paper. Graphene nanosheets (GNS) are known for their photothermal properties, thus the NIR adsorption by the atomic and molecular vibrations of GNS can generate a local gradient temperature to dissolve the GNS-GItAg hydrogel motor [296].

Wu et al also used a thermal-sensitive gelatin hydrogel in connection with template-assisted layer-by-layer assembly bovine serum albumin/poly-L-lysine micromotors. The doxorubicin (DOX) can be easily loaded in the hydrogel during synthesis for subsequent NIR light triggered release. **Figure II. 19. B** illustrates the DOX release (in brown color) from the gelatin motor and the rapid diffusion into the surrounding media after NIR irradiation [288].

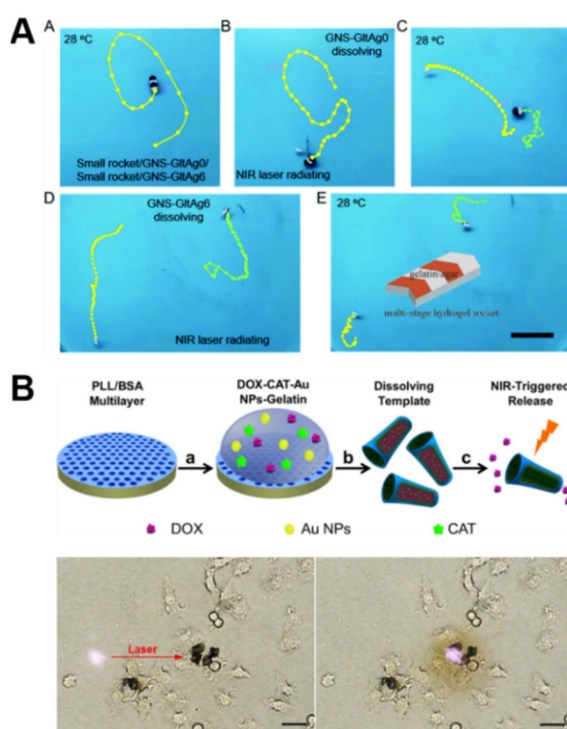


Figure II. 19. Thermal-sensitive materials based micromotors for drug delivery and release. **(A)** Thermal and light responsive gelatin/agar (GItAg) hydrogel micromotors incorporating graphene nanosheet. (a) Self-propulsion of the GItAg hydrogel motor; (b) GItAg0 on the GItAg hydrogel motor begin to dissolve when temperature increase; (c) GItAg6 on the GItAg hydrogel motor begin to dissolve when temperature further increase; (d, e) GNS-GItAg0 on the GNS-GItAg hydrogel motor begin to dissolve after NIR irradiation. **(B)** Schematic of the fabrication and light-triggered drug release process of (PLL/BSA)₁₀-DOX-CAT-AuNPs-gelation motors. Down images show the time-lapse images of DOX triggered release from the (PLL/BSA)₁₀-DOX-CAT-AuNPs-gelation motors under NIR irradiation. Reprinted with permission from ref. [296] and [288].

Redox-responsive polymers and sustained-release biodegradable polymers. Some polymers containing disulfide linkages can be reduced to thiol

groups by reductants such as glutathione (GSH). Hence, these materials can be exploited as redox-responsive release systems. Tu et al have developed redox-responsive stomatocyte nanomotor system for drug release. As depicted in **Figure II. 20. A**, the hydrophilic poly(ethylene glycol) block and the hydrophobic polystyrene block were incorporated by a disulfide bridge. Thus, incubation with GSH lead to polymer dissolution, leading to drug release. Transmission electron microscopy (TEM) characterization (in **Figure II. 20. A**) illustrates the morphology changes of the redox-responsive nanomotor structures before (left) and after (right) incubation with GSH. It can be observed that after the addition of GSH, the nanomotors tend to aggregate without a clear bilayer membrane, in contrast with the regular morphology and defined small openings before GSH addition. HeLa cells were fully treated to study the intracellular release behavior of the redox-responsive nanomotors. When the cells were incubated with DOX-loaded redox sensitive nanomotors, the fluorescence signal from DOX diffused over the HeLa cells, indicating the release of DOX due to the higher intracellular GSH level. On the contrary, only dot-like fluorescence signals were observed when cells were incubated with DOX-loaded nanomotors not containing the redox polymer [289]. Biodegradable polymers have also been designed for controlled drug release drug at a predetermined rate. For example, poly(ϵ -caprolactone) (PCL) is a polymer well known for its slow biodegradability, high biocompatibility, and good drug permeability. PCL and its copolymers have been combined with micromotors for the delivery and sustained-release of drugs. Tu et al fabricated a biodegradable PtNPs-loaded stomatocyte nanomotor containing PEG-*b*-PCL for drug delivery and release. A mixture of poly(ethylene glycol)-*b*-poly(ϵ -caprolactone) (PEG-*b*-PCL) and poly(ethylene glycol)-*b*-polystyrene (PEG-*b*-PS) was used to synthesize nanomotor. The stomatocyte bowl-shape morphology of the micromotor was obtained under osmotic folding of polymersomes. DOX was further loaded into the lumen of the structure, as well as PtNPs were encapsulated in the cavity of stomatocyte as the catalyst. The micromotors can easily internalize into HeLa cells for further drug release [290].

II. Introduction

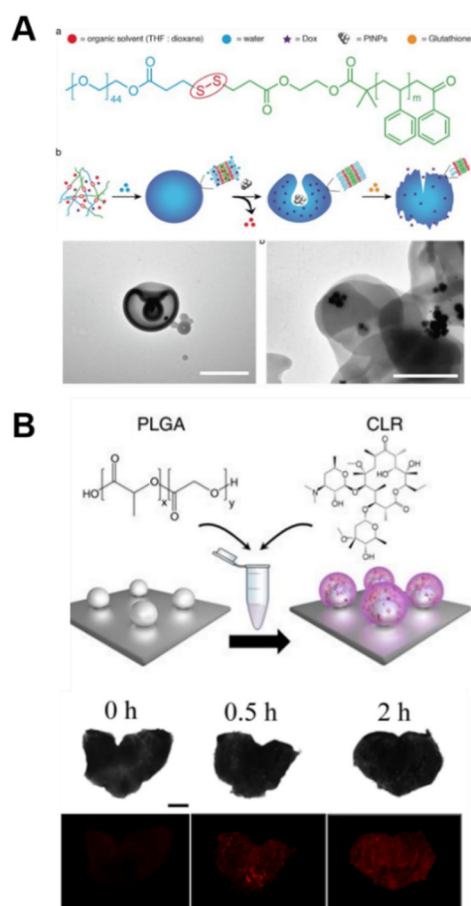


Figure II. 20. Redox-responsive polymers and sustained-release based micromotors for drug delivery and release. **(A)** Schematic of the fabrication of redox-response stomatocyte micromotors for drug delivery and release and TEM images of nanomotor before (left) and after (right) the addition of GSH. **(B)** Schematic illustration showing the loading of CLR onto Mg-based micromotors. PLGA polymer was mixed with CLR to coat the motors, bright-field of the luminal lining of freshly excised mouse stomachs at 0 h, 0.5 h and 2 h after oral dosage of Mg-based micromotors, and corresponding fluorescence images. Reprinted with permission from ref. [289] and [291].

Poly(lactic-co-glycolic acid) (PLGA) is another biodegradable polymer used for encapsulation of a broad range of therapeutic agents. For example, PLGA coated Mg-based micromotors has been used for clarithromycin (CLR) encapsulation as a model antibiotic for further *Helicobacter pylori* infection treatment in the stomach (see in **Figure II. 20. B**). Later, the CLR-loaded Mg-based micromotors prepared with DID-labeled PLGA were administered to a group of mice to study the release of the drug. **Figure II. 20. B** (bottom) shows bright-field images of freshly excised mouse stomach at 0 h, 0.5 h, and 2h after oral administration of Mg-based micromotors respectively, with the corresponding fluorescence images. Such results indicate the prolonged retention of the

micromotors in the stomach wall for controlled release of CLR, allowing for efficient treatment. Additionally, nanoliposomes also have been used in the sustained release of drugs [285]. Related report from Martel's group, report the use of magneto coccus marinus strain MC-1 to transport drug-loaded nanoliposomes into hypoxic regions of tumors [291].

Other biocompatible materials. There are also some materials without triggered-response abilities, designed for the nano/micromotor-based drug delivery and release systems. For example, mesoporous silica has been combined with micromotor for drug storage and delivery due to its biocompatibility and high surface area. Stanton et al designed drug-loaded mesoporous silica microtubes for the release of antibiotics. Interestingly, such microtubes are driven by bacteria *Magnetospirillum gryphiswalense* (MSR-1) to target an infectious biofilm. Such platform can target and dismantle harmful biofilms, as well as great potential for antibiofouling applications [292]. Similarly, Shao et al also used mesoporous silica nanoparticles for dramatical enhanced drug loading capability, which show good performance in the further drug delivery and release [297].

Another interesting design is the development of cell-based structure for carrying drugs in an effective and biocompatible way. Motile sperms are promising candidates for the therapy of cervical cancer and other gynecologic diseases. Such cells can be used for the loading of hydrophilic drugs, and sperm membrane can also protect drugs from the metabolism of body before the drugs work. Xu et al have used sperm-hybrid micromotor for the transportation of DOX. Drugs release is based on the sperm-cancer cell membrane fusion, after sperm micromotors hit the tumor walls and swim into the tumor [292]. RBCs have been also exploited for drug delivery due to their long bloodstream circulation, safety and versatile cargo-carrying abilities. Wu et al have co-encapsulated QDs, DOX, and magnetic nanoparticles inside the RBC motors for both diseases diagnose and therapy [298]. *Agaricus bisporus* mushroom microcapsules coated with magnetite nanoparticles have been used as catalase propelled micromotors with chemotactic ability for retaining and transporting drugs in alkaline medium such as human blood and releasing them in acidic medium such as the cancerous tissues for cell apoptosis [294].

II.3.3. Perspectives nano/micromotors for cancer and infectious disease diagnosis.

Driven by the advances in nanotechnology and material science, nano/micromotors have shown great potential for disease diagnosis and therapy, including pathogenic cells sensing, related cells removal, cell killing, and drug delivery applications. In this introduction, we have discussed recent advances in micromotor-based strategies for cancer and infectious diagnosis via analyte induced speed changes in the micromotors and fluorescent switching. Yet, despite such speed changes have formed the basis for new methods for sensing of targets, speed changes are very complex and depend on the size/amount of the catalyst (Pt, Mg, etc.) and the concentration of the fuel. Hence, methods for the fabrication of nano/micromotors should possess a high reproducibility. As the motors move, fuel concentration around the nano/micromotors would change, which lead to the inhomogeneity of the fuel in the solution, and as a result, speed of nano/micromotors will be influenced. Fluorescence ON-OFF strategies show high selectivity and sensitivity toward the disease diagnose, although yet fluorescence reagents may respond to interference substances, in the further targets sensing. Despite some of such strategies are still early proof of concept applications, recent works show its integration into portable devices such as mobile phone for not so far point-of-care micromotor based devices.

Another important challenge that still requires attention is most of these nano/micromotors for cancer and infectious therapy was demonstrated only *in vitro*. The opportunities and challenges of chemical, physical and biohybrid micromotors have been extensively dwelled upon previously. Thus, traditional nano/micromotors rely on hydrogen peroxide fuel, which is toxicity and might be harmful for the human health. To deal with such issue, many fuel-free or biocompatible fuel micromotors (such as magnetic-, ultrasound-, light-, Mg/H₂O, etc.) have been developed. Yet limitations still exist, a) Magnetic-, ultrasound nano/micromotors, and light- can provide fuel-free propulsion, but may hinder autonomous therapeutic interventions; b) Mg can propelled in water (or acid solution) instead of the hydrogen peroxide fuel, but such material has short lifetimes due to the rapid consumption of Mg during the propulsion. On the other hand, the drug delivery systems need to overcome the complex environment inside the human body. For example, a) the immune system of the

host organism may eliminate the nano/micromotors due to they are extraneous matter in some ways; b) the nano/micromotors need to overcome the high interstitial pressure in late stage tumors; c) some extreme conditions such as highly acidic gastric or enzyme. At last, for *in vivo* applications, the drug delivery systems should be able to be degraded into non-toxic compounds, as well as the use of surfactants should be avoided. Even though they are efficient in the target cells killing or drug delivery, potential difficulties might be the *in vivo* applications of such approaches. As already discussed by Schmidt and Medina-Sánchez, micromotors should find their way into in-vivo applications, thus is vital to detect and track them in real-time in 3D with high resolution during their journey through the body. Early recent efforts in this direction have demonstrated the real tracking of micromotors with common medical imaging techniques. Magnesium based micromotors have been successfully tracked in-vivo in mouse models by photoacoustic computed tomography. Helical and rolled-up micromotors have been tracked in real-time in phantom tissue and ex vivo chicken breast, using multispectral optoacoustic tomography. Such pioneers works indicate considerable promise for the use of micromotor in real clinical use, yet more biocompatibility studies in mammals should be performed in a similar way to that performed when authorizing the use of a new pharmaceutical drug.

Apart from that, the development of low-cost and scalable techniques for the fabrication of nano/micromotors is also important to expand the applicability of micromotors with higher realistic scenarios. Current fabrication methods including electrochemical deposition, chemical synthesis and metal sputtering, etc, require some expensive equipment and are hard to realize large-scale preparation. Even though some cheap catalyst (MnO_2 , Ag, Fe_2O_3 , etc) have been developed, traditional catalysts (expensive trace element: Pt, Pd, etc) are still widely used in the synthesis of nano/micromotors due to their superior catalytic performance. Therefore, further efforts still should be focus on the fabrication of nano/micromotors in a large-scale and economic way.

II.4 References.

1. Gao, W., et al., *Intuitive label-free SERS detection of bacteria using aptamer-based in situ silver nanoparticles synthesis*. Analytical Chemistry, 2017. **89**(18): p. 9836-9842.

II. Introduction

2. Yuan, K., et al., *Nano/Micromotors for Diagnosis and Therapy of Cancer and Infectious Diseases*. Chemistry – A European Journal, 2020. **26**(11): p. 2309-2326.
3. Wang, J., et al., *A nanoplasmonic label-free surface-enhanced Raman scattering strategy for non-invasive cancer genetic subtyping in patient samples*. Nanoscale, 2017. **9**(10): p. 3496-3503.
4. Schiffman, J.D., P.G. Fisher, and P. Gibbs, *Early Detection of Cancer: Past, Present, and Future*. American Society of Clinical Oncology Educational Book, 2015(35): p. 57-65.
5. Delgado-Viscogliosi, P., L. Solignac, and J.-M. Delattre, *Viability PCR, a Culture-Independent Method for Rapid and Selective Quantification of Viable Legionella pneumophila Cells in Environmental Water Samples*. Applied and Environmental Microbiology, 2009. **75**(11): p. 3502.
6. Davenport, M., et al., *New and developing diagnostic technologies for urinary tract infections*. Nature Reviews Urology, 2017. **14**(5): p. 296-310.
7. Cialla-May, D., et al., *Recent progress in surface-enhanced Raman spectroscopy for biological and biomedical applications: from cells to clinics*. Chemical Society Reviews, 2017. **46**(13): p. 3945-3961.
8. Li, X., S. Ye, and X. Luo, *Sensitive SERS detection of miRNA via enzyme-free DNA machine signal amplification*. Chemical Communications, 2016. **52**(67): p. 10269-10272.
9. Alula, M.T., et al., *Identification and quantitation of pathogenic bacteria via in-situ formation of silver nanoparticles on cell walls, and their detection via SERS*. Microchimica Acta, 2017. **184**(1): p. 219-227.
10. Mitchell, S.L. and E.E. Carlson, *Tiny Things with Enormous Impact: Nanotechnology in the Fight Against Infectious Disease*. ACS Infectious Diseases, 2018. **4**(10): p. 1432-1435.
11. Hartshorn, C.M., et al., *Nanotechnology Strategies To Advance Outcomes in Clinical Cancer Care*. ACS Nano, 2018. **12**(1): p. 24-43.
12. Demirel, G., et al., *Surface-enhanced Raman spectroscopy (SERS): an adventure from plasmonic metals to organic semiconductors as SERS platforms*. Journal of Materials Chemistry C, 2018. **6**(20): p. 5314-5335.
13. *Recent Developments in Plasmon-Supported Raman Spectroscopy*. 2017, WORLD SCIENTIFIC (EUROPE). 512.
14. Fateixa, S., H.I.S. Nogueira, and T. Trindade, *Hybrid nanostructures for SERS: materials development and chemical detection*. Physical Chemistry Chemical Physics, 2015. **17**(33): p. 21046-21071.
15. Guo, H., L. He, and B. Xing, *Applications of surface-enhanced Raman spectroscopy in the analysis of nanoparticles in the environment*. Environmental Science: Nano, 2017. **4**(11): p. 2093-2107.
16. Ren, X., et al., *Silver microspheres coated with a molecularly imprinted polymer as a SERS substrate for sensitive detection of bisphenol A*. Microchimica Acta, 2018. **185**(4): p. 242.
17. Bi, L., et al., *Highly sensitive and reproducible SERS sensor for biological pH detection based on a uniform gold nanorod array platform*. ACS Applied Materials & Interfaces, 2018. **10**(18): p. 15381-15387.
18. Joseph, M.M., et al., *Exploring the margins of SERS in practical domain: An emerging diagnostic modality for modern biomedical applications*. Biomaterials, 2018. **181**: p. 140-181.
19. Hong, Y., et al., *Optoplasmonic hybrid Materials for trace detection of methamphetamine in biological fluids through SERS*. ACS Applied Materials & Interfaces, 2020: p. doi.org/10.1021/acsami.0c00853.

20. Shen, J., et al., *In-situ SERS monitoring of reaction catalyzed by multifunctional Fe₃O₄@TiO₂@Ag-Au microspheres*. Applied Catalysis B: Environmental, 2017. **205**: p. 11-18.
21. Wang, X., et al., *Fast enrichment and ultrasensitive in-situ detection of pesticide residues on oranges with surface-enhanced Raman spectroscopy based on Au nanoparticles decorated glycidyl methacrylate-ethylene dimethacrylate material*. Food Control, 2014. **46**: p. 108-114.
22. Smith, W.E., *Practical understanding and use of surface enhanced Raman scattering/surface enhanced resonance Raman scattering in chemical and biological analysis*. Chemical Society Reviews, 2008. **37**(5): p. 955-964.
23. Moore, T.A.-O., et al., *In Vitro and In Vivo SERS Biosensing for Disease Diagnosis*. Biosensors, 2018. **8**(2): p. 2079-6374.
24. Sinha, S.S., et al., *Nanoarchitecture based SERS for biomolecular fingerprinting and label-free disease markers diagnosis*. Accounts of Chemical Research, 2016. **49**(12): p. 2725-2735.
25. Koo, K.M., et al., *Design and clinical verification of surface-enhanced Raman spectroscopy diagnostic technology for individual cancer risk prediction*. ACS Nano, 2018. **12**(8): p. 8362-8371.
26. Maiti, K.K., et al., *Development of biocompatible SERS nanotag with increased stability by chemisorption of reporter molecule for in vivo cancer detection*. Biosensors and Bioelectronics, 2010. **26**(2): p. 398-403.
27. Vendrell, M., et al., *Surface-enhanced Raman scattering in cancer detection and imaging*. Trends in Biotechnology, 2013. **31**(4): p. 249-257.
28. Wu, X., et al., *Improved SERS nanoparticles for direct detection of circulating tumor cells in the blood*. ACS Applied Materials & Interfaces, 2015. **7**(18): p. 9965-9971.
29. Ding, S.-Y., et al., *Electromagnetic theories of surface-enhanced Raman spectroscopy*. Chemical Society Reviews, 2017. **46**(13): p. 4042-4076.
30. Liu, B., et al., *Quantifying the contribution of chemical enhancement to SERS: A model based on the analysis of light-induced degradation processes*. The Journal of Physical Chemistry C, 2019. **123**(31): p. 19119-19124.
31. Fan, W., et al., *Free-standing silver nanocube/graphene oxide hybrid paper for surface-enhanced Raman scattering*. Chinese Journal of Chemistry, 2016. **34**(1): p. 73-81.
32. Li, X., et al., *Silver nanoparticles protected by monolayer graphene as a stabilized substrate for surface enhanced Raman spectroscopy*. Carbon, 2014. **66**: p. 713-719.
33. Chen, J., et al., *Integrating recognition elements with nanomaterials for bacteria sensing*. Chemical Society Reviews, 2017. **46**(5): p. 1272-1283.
34. Qiu, Y., et al., *Synthesis of magnetic Fe₃O₄-Au hybrids for sensitive SERS detection of cancer cells at low abundance*. Journal of Materials Chemistry B, 2015. **3**(22): p. 4487-4495.
35. Hong, Y., et al., *Label-free diagnosis for colorectal cancer through coffee ring-assisted surface-enhanced Raman spectroscopy on blood serum*. Journal of Biophotonics, 2020. **13**(4): p. e201960176.
36. Auner, G.W., et al., *Applications of Raman spectroscopy in cancer diagnosis*. Cancer and Metastasis Reviews, 2018. **37**(4): p. 691-717.
37. Geen, et al., *Raman Fingerprints in Detection of Breast Cancer*. Journal of Biosensors, Biomarkers and Diagnostics, 2016. **1**(1): p. 1-11.

II. Introduction

38. Han, X.X., Y. Ozaki, and B. Zhao, *Label-free detection in biological applications of surface-enhanced Raman scattering*. *TrAC Trends in Analytical Chemistry*, 2012. **38**: p. 67-78.
39. Gahlaut, S.K., et al., *SERS platform for dengue diagnosis from clinical samples employing a hand held Raman spectrometer*. *Analytical Chemistry*, 2020. **92**(3): p. 2527-2534.
40. Wu, L., et al., *In situ probing of cell-cell communications with surface-enhanced Raman scattering (SERS) nanoprobe and microfluidic networks for screening of immunotherapeutic drugs*. *Nano Research*, 2017. **10**(2): p. 584-594.
41. Bodelón, G., et al., *Detection and imaging of quorum sensing in Pseudomonas aeruginosa biofilm communities by surface-enhanced resonance Raman scattering*. *Nature Materials*, 2016. **15**(11): p. 1203-1211.
42. Cao, X., et al., *Label-free detection of human serum using surface-enhanced Raman spectroscopy based on highly branched gold nanoparticle substrates for discrimination of non-small cell lung cancer*. *Journal of Chemistry*, 2018. **2018**: p. 9012645.
43. He, S., et al., *Quantitative and label-free detection of protein kinase A activity based on surface-enhanced Raman spectroscopy with gold nanostars*. *Analytical Chemistry*, 2018. **90**(10): p. 6071-6080.
44. Prakash, O., et al., *Direct detection of bacteria using positively charged Ag/Au bimetallic nanoparticles: A label-free surface-enhanced Raman scattering study coupled with multivariate analysis*. *The Journal of Physical Chemistry C*, 2020. **124**(1): p. 861-869.
45. González-Solís, J., G. Luévano Colmenero, and J. Vargas-Mancilla, *Surface enhanced Raman spectroscopy in breast cancer cells*. *Laser therapy*, 2013. **22**: p. 37-42.
46. Cui, S., S. Zhang, and S. Yue, *Raman spectroscopy and imaging for cancer diagnosis*. *Journal of Healthcare Engineering*, 2018. **2018**: p. 8619342.
47. Nguyen, B.H., V.H. Nguyen, and H.N. Tran, *Rich variety of substrates for surface enhanced Raman spectroscopy*. *Advances in Natural Sciences: Nanoscience and Nanotechnology*, 2016. **7**(3): p. 033001.
48. Esteban-Fernández de Ávila, B., et al., *Aptamer-Modified Graphene-Based Catalytic Micromotors: Off-On Fluorescent Detection of Ricin*. *ACS Sensors*, 2016. **1**(3): p. 217-221.
49. Li, X., et al., *Mercaptoacetic acid-capped silver nanoparticles colloid: Formation, morphology, and SERS activity*. *Langmuir*, 2003. **19**(10): p. 4285-4290.
50. dos Santos, J.D.S., et al., *Controlling the size and shape of gold nanoparticles in fulvic acid colloidal solutions and their optical characterization using SERS*. *Journal of Materials Chemistry*, 2005. **15**(29): p. 3045-3049.
51. Tian, F., et al., *Gold nanostars for efficient in vitro and in vivo real-time SERS detection and drug delivery via plasmonic-tunable Raman/FTIR imaging*. *Biomaterials*, 2016. **106**: p. 87-97.
52. Song, C., et al., *Ultrasensitive silver nanorods array SERS sensor for mercury ions*. *Biosensors and Bioelectronics*, 2017. **87**: p. 59-65.
53. Kim, D.J., et al., *Uniform microgels containing agglomerates of silver nanocubes for molecular size-selectivity and high SERS activity*. *Small*, 2017. **13**(23): p. 1604048.

54. Yan, T., et al., *Controllable SERS performance for the flexible paper-like films of reduced graphene oxide*. Applied Surface Science, 2017. **419**: p. 373-381.
55. Shen, Y., et al., *SERS-based plasmon-driven reaction and molecule detection on a single Ag@MoS₂ microsphere: Effect of thickness and crystallinity of MoS₂*. ChemCatChem, 2018. **10**(16): p. 3520-3525.
56. Jiang, R., et al., *Metal/semiconductor hybrid nanostructures for plasmon-enhanced applications*. Advanced Materials, 2014. **26**(31): p. 5274-5309.
57. He, L., et al., *Hydrophobic ligand-mediated hierarchical Cu nanoparticles on reduced graphene oxides for SERS platform*. CrystEngComm, 2016. **18**(40): p. 7764-7771.
58. Liang, X., et al., *Tuning plasmonic and chemical enhancement for SERS detection on graphene-based Au hybrids*. Nanoscale, 2015. **7**(47): p. 20188-20196.
59. Wei, H., et al., *Improved quantitative SERS enabled by surface plasmon enhanced elastic light scattering*. Analytical Chemistry, 2018. **90**(5): p. 3227-3237.
60. Fu, H.-Y., et al., *Nanoporous Au/SnO/Ag heterogeneous films for ultrahigh and uniform surface-enhanced Raman scattering*. Journal of Materials Chemistry C, 2014. **2**(35): p. 7216-7222.
61. Wu, L.-A., et al., *Three-dimensional SERS substrates formed with plasmonic core-satellite nanostructures*. Scientific Reports, 2017. **7**(1): p. 13066.
62. Shi, R., X. Liu, and Y. Ying, *Facing challenges in real-life application of surface-enhanced Raman scattering: Design and nanofabrication of surface-enhanced Raman scattering substrates for rapid field test of food contaminants*. Journal of Agricultural and Food Chemistry, 2018. **66**(26): p. 6525-6543.
63. Lee, H.K., et al., *Designing surface-enhanced Raman scattering (SERS) platforms beyond hotspot engineering: emerging opportunities in analyte manipulations and hybrid materials*. Chemical Society Reviews, 2019. **48**(3): p. 731-756.
64. Wu, L., et al., *Highly sensitive, reproducible and uniform SERS substrates with a high density of three-dimensionally distributed hotspots: gyroid-structured Au periodic metallic materials*. NPG Asia Materials, 2018. **10**(1): p. e462-e462.
65. Fraire, J.C., et al., *Improved label-free identification of individual exosome-like vesicles with Au@Ag nanoparticles as SERS substrate*. ACS Applied Materials & Interfaces, 2019. **11**(43): p. 39424-39435.
66. Feng, L., et al., *Super-hydrophobic surfaces: From natural to artificial*. Advanced Materials, 2002. **14**(24): p. 1857-1860.
67. Bhushan, B., *Adhesion of multi-level hierarchical attachment systems in gecko feet*. Journal of Adhesion Science and Technology, 2007. **21**(12-13): p. 1213-1258.
68. Biró, L.P., et al., *Living photonic crystals: Butterfly scales - nanostructure and optical properties*. Materials Science and Engineering: C, 2007. **27**(5): p. 941-946.
69. Garrett, N.L., et al., *Bio-sensing with butterfly wings: naturally occurring nano-structures for SERS-based malaria parasite detection*. Physical Chemistry Chemical Physics, 2015. **17**(33): p. 21164-21168.
70. Zhang, M., et al., *Biomimetic synthesis of hierarchical 3D Ag butterfly wing scale arrays/graphene composites as ultrasensitive SERS substrates*

II. Introduction

- for efficient trace chemical detection. *Journal of Materials Chemistry C*, 2018. **6**(8): p. 1933-1943.
71. Fabris, L., *SERS Tags: The next promising tool for personalized cancer detection?* *ChemNanoMat*, 2016. **2**(4): p. 249-258.
 72. Guo, M., et al., *SERS tags-based novel monodispersed hollow gold nanospheres for highly sensitive immunoassay of CEA.* *Journal of Materials Science*, 2015. **50**(9): p. 3329-3336.
 73. Chen, M., et al., *High-sensitive bioorthogonal SERS tag for live cancer cell imaging by self-assembling core-satellites structure gold-silver nanocomposite.* *Talanta*, 2017. **172**: p. 176-181.
 74. Pérez-Jiménez, A.I., et al., *Surface-enhanced Raman spectroscopy: benefits, trade-offs and future developments.* *Chemical Science*, 2020. **11**: p. 4563-4577
 75. Scatena, E., S. Baiguera, and C. Del Gaudio, *Raman spectroscopy and aptamers for a label-free approach: Diagnostic and application tools.* *Journal of Healthcare Engineering*, 2019. **2019**: p. 2815789.
 76. Pahlow, S., et al., *Isolation and identification of bacteria by means of Raman spectroscopy.* *Advanced Drug Delivery Reviews*, 2015. **89**: p. 105-120.
 77. Rinken, T. and K. Kivirand, *Biosensing technologies for the detection of pathogens: A prospective way for rapid analysis.* 2018: IntechOpen.
 78. Zhang, J., X. Ma, and Z. Wang, *Real-time and in-situ monitoring of Abrin induced cell apoptosis by using SERS spectroscopy.* *Talanta*, 2019. **195**: p. 8-16.
 79. Zheng, X.-S., et al., *Label-free SERS in biological and biomedical applications: Recent progress, current challenges and opportunities.* *Spectrochimica Acta Part A: Molecular and Biomolecular Spectroscopy*, 2018. **197**: p. 56-77.
 80. Guo, J., et al., *A multifunctional SERS sticky note for real-time quorum sensing tracing and inactivation of bacterial biofilms.* *Chemical Science*, 2018. **9**(27): p. 5906-5911.
 81. Lussier, F., et al., *Dynamic-SERS optophysiology: A nanosensor for monitoring cell secretion events.* *Nano Letters*, 2016. **16**(6): p. 3866-3871.
 82. Cabello, G., et al., *Cu@Au self-assembled nanoparticles as SERS-active substrates for (bio)molecular sensing.* *Journal of Alloys and Compounds*, 2019. **791**: p. 184-192.
 83. Majumdar, D., et al., *DNA-mediated wirelike clusters of silver nanoparticles: An ultrasensitive SERS substrate.* *ACS Applied Materials & Interfaces*, 2013. **5**(16): p. 7798-7807.
 84. Khlebtsov, B., V. Khanadeev, and N. Khlebtsov, *Surface-enhanced Raman scattering inside Au@Ag core/shell nanorods.* *Nano Research*, 2016. **9**(8): p. 2303-2318.
 85. Gao, Z., et al., *In solution SERS sensing using mesoporous silica-coated gold nanorods.* *Analyst*, 2016. **141**(17): p. 5088-5095.
 86. Garcia-Leis, A., J.V. Garcia-Ramos, and S. Sanchez-Cortes, *Silver nanostars with high SERS performance.* *The Journal of Physical Chemistry C*, 2013. **117**(15): p. 7791-7795.
 87. Niu, W., et al., *Highly symmetric gold nanostars: Crystallographic control and surface-enhanced Raman scattering property.* *Journal of the American Chemical Society*, 2015. **137**(33): p. 10460-10463.

88. Jiang, B., et al., *Ag⁺-assisted heterogeneous growth of concave Pd@Au nanocubes for surface enhanced Raman scattering (SERS)*. Nano Research, 2017. **10**(10): p. 3509-3521.
89. Ben-Jaber, S., et al., *Sensitive and specific detection of explosives in solution and vapour by surface-enhanced Raman spectroscopy on silver nanocubes*. Nanoscale, 2017. **9**(42): p. 16459-16466.
90. Wang, P., et al., *Label-free mapping of single bacterial cells using surface-enhanced Raman spectroscopy*. Analyst, 2016. **141**(4): p. 1356-1362.
91. Reyes, M., et al., *Exploiting the anti-aggregation of gold nanostars for rapid detection of hand, foot, and mouth disease causing enterovirus 71 using surface-enhanced Raman spectroscopy*. Analytical Chemistry, 2017. **89**(10): p. 5373-5381.
92. Ali, M.R.K., et al., *Simultaneous time-dependent surface-enhanced Raman spectroscopy, metabolomics, and proteomics reveal cancer cell death mechanisms associated with gold nanorod photothermal therapy*. Journal of the American Chemical Society, 2016. **138**(47): p. 15434-15442.
93. von Maltzahn, G., et al., *SERS-coded gold nanorods as a multifunctional platform for densely multiplexed near-infrared imaging and photothermal heating*. Advanced Materials, 2009. **21**(31): p. 3175-3180.
94. Seo, S.-H., et al., *NIR-light-induced surface-enhanced Raman scattering for detection and photothermal/photodynamic therapy of cancer cells using methylene blue-embedded gold nanorod@SiO₂ nanocomposites*. Biomaterials, 2014. **35**(10): p. 3309-3318.
95. Gao, Y., et al., *Controlled synthesis of multilayered gold nanoshells for enhanced photothermal therapy and SERS detection*. Small, 2015. **11**(1): p. 77-83.
96. Chen, J., et al., *Indocyanine green-loaded gold nanostars for sensitive SERS imaging and subcellular monitoring of photothermal therapy*. Nanoscale, 2017. **9**(33): p. 11888-11901.
97. Qi, G., et al., *Nucleus and mitochondria targeting theranostic plasmonic surface-enhanced Raman spectroscopy nanoprobe as a means for revealing molecular stress response differences in hyperthermia cell death between cancerous and normal cells*. Analytical Chemistry, 2018. **90**(22): p. 13356-13364.
98. Xing, Y., et al., *Raman observation of a molecular signaling pathway of apoptotic cells induced by photothermal therapy*. Chemical Science, 2019. **10**(47): p. 10900-10910.
99. Zhang, J., et al., *Ultrasonic-assisted synthesis of highly defined silver nanodimers by self-assembly for improved surface-enhanced Raman spectroscopy*. Chemistry – A European Journal, 2020. **26**(6): p. 1243-1248.
100. Purbia, R., P.D. Nayak, and S. Paria, *Visible light-induced Ag nanoparticle deposited urchin-like structures for enhanced SERS application*. Nanoscale, 2018. **10**(27): p. 12970-12974.
101. Zhang, N., L. Tong, and J. Zhang, *Graphene-based enhanced Raman scattering toward analytical applications*. Chemistry of Materials, 2016. **28**(18): p. 6426-6435.
102. Liu, Z., et al., *Fe₃O₄@graphene oxide@Ag particles for surface magnet solid-phase extraction surface-enhanced Raman scattering (SMSPE-SERS): From sample pretreatment to detection all-in-one*. ACS Applied Materials & Interfaces, 2016. **8**(22): p. 14160-14168.

II. Introduction

103. Muehlethaler, C., et al., *Ultra-high Raman enhancement on monolayer MoS₂*. ACS Photonics, 2016. **3**(7): p. 1164-1169.
104. Li, J., et al., *Ag nanowire/nanoparticle-decorated MoS₂ monolayers for surface-enhanced Raman scattering applications*. Nano Research, 2018. **11**(4): p. 2181-2189.
105. Cai, Q., et al., *Boron nitride nanosheets improve sensitivity and reusability of surface-enhanced Raman spectroscopy*. Angewandte Chemie International Edition, 2016. **55**(29): p. 8405-8409.
106. Liu, Z., et al., *A two-dimensional fingerprint nanoprobe based on black phosphorus for bio-SERS analysis and chemo-photothermal therapy*. Nanoscale, 2018. **10**(39): p. 18795-18804.
107. Martín, C., et al., *Biocompatibility and biodegradability of 2D materials: graphene and beyond*. Chemical Communications, 2019. **55**(39): p. 5540-5546.
108. Anichini, C., et al., *Chemical sensing with 2D materials*. Chemical Society Reviews, 2018. **47**(13): p. 4860-4908.
109. Daukiya, L., J. Seibel, and S. De Feyter, *Chemical modification of 2D materials using molecules and assemblies of molecules*. Advances in Physics: X, 2019. **4**(1): p. 1625723.
110. Chen, S., et al., *Oxidation resistance of graphene-coated Cu and Cu/Ni alloy*. ACS Nano, 2011. **5**(2): p. 1321-1327.
111. Karthick Kannan, P., et al., *Recent advances in 2D inorganic nanomaterials for SERS sensing*. Advanced Materials, 2019. **31**(34): p. 1803432.
112. Kim, Y.-K., et al., *Facile one-pot photosynthesis of stable Ag@graphene oxide nanocolloid core@shell nanoparticles with sustainable localized surface plasmon resonance properties*. Journal of Materials Chemistry C, 2017. **5**(38): p. 10016-10022.
113. Zeng, F., et al., *Surfactant-free synthesis of graphene oxide coated silver nanoparticles for SERS biosensing and intracellular drug delivery*. ACS Applied Nano Materials, 2018. **1**(6): p. 2748-2753.
114. Zhou, Y., et al., *Ecofriendly and environment-friendly synthesis of size-controlled silver nanoparticles/graphene composites for antimicrobial and SERS actions*. Applied Surface Science, 2018. **457**: p. 1000-1008.
115. Meng, X., et al., *A graphene-silver nanoparticle-silicon sandwich SERS chip for quantitative detection of molecules and capture, discrimination, and inactivation of bacteria*. Analytical Chemistry, 2018. **90**(9): p. 5646-5653.
116. Huang, D., et al., *Black phosphorus-Au filter paper-based three-dimensional SERS substrate for rapid detection of foodborne bacteria*. Applied Surface Science, 2019. **497**: p. 143825.
117. Henan, Z., et al., *Insights into the intracellular behaviors of black-phosphorus-based nanocomposites via surface-enhanced Raman spectroscopy*. Nanophotonics, 2018. **7**(10): p. 1651-1662.
118. Yang, G., et al., *Facile synthesis of black phosphorus-Au nanocomposites for enhanced photothermal cancer therapy and surface-enhanced Raman scattering analysis*. Biomaterials Science, 2017. **5**(10): p. 2048-2055.
119. Li, D., et al., *SERS analysis of carcinoma-associated fibroblasts in a tumor microenvironment based on targeted 2D nanosheets*. Nanoscale, 2020. **12**(3): p. 2133-2141.
120. Wang, J., et al., *Synthesis of g-C₃N₄ nanosheet/Au@Ag nanoparticle hybrids as SERS probes for cancer cell diagnostics*. RSC Advances, 2015. **5**(105): p. 86803-86810.

121. Karshalev, E., et al., *Multistimuli-Responsive Camouflage Swimmers*. Chemistry of Materials, 2018.
122. Zhang, H., et al., *Formation of the AuNPs/GO@MoS₂/AuNPs nanostructures for the SERS application*. Sensors and Actuators B: Chemical, 2019. **282**: p. 809-817.
123. Liu, J., T. Zheng, and Y. Tian, *Functionalized h-BN nanosheets as a theranostic platform for SERS real-time monitoring of microRNA and photodynamic therapy*. Angewandte Chemie International Edition, 2019. **58**(23): p. 7757-7761.
124. Pramanik, A., et al., *A WS₂-gold nanoparticle heterostructure-based novel SERS platform for the rapid identification of antibiotic-resistant pathogens*. Nanoscale Advances, 2020: p. doi.org/10.1039/D0NA00141D.
125. Kavyani, S., et al., *Molecular perspective mechanism for drug loading on carbon nanotube-dendrimer: A coarse-grained molecular dynamics study*. The Journal of Physical Chemistry B, 2018. **122**(33): p. 7956-7969.
126. Dinda, S., et al., *Self-assembled vesicle-carbon nanotube conjugate formation through a boronate-diol covalent linkage*. Chemistry – A European Journal, 2017. **23**(60): p. 15194-15202.
127. Liu, H., et al., *Manipulating the functionalization surface of graphene-encapsulated gold nanoparticles with single-walled carbon nanotubes for SERS sensing*. Carbon, 2018. **140**: p. 306-313.
128. Yang, Z., et al., *Carbon nanotube- and graphene-based nanomaterials and applications in high-voltage supercapacitor: A review*. Carbon, 2019. **141**: p. 467-480.
129. Gupta, S., C.N. Murthy, and C.R. Prabha, *Recent advances in carbon nanotube based electrochemical biosensors*. International Journal of Biological Macromolecules, 2018. **108**: p. 687-703.
130. Rong, G., S.R. Corrie, and H.A. Clark, *In vivo biosensing: Progress and perspectives*. ACS Sensors, 2017. **2**(3): p. 327-338.
131. Chen, Y.-C., et al., *Silver-decorated carbon nanotube networks as SERS substrates*. Journal of Raman Spectroscopy, 2011. **42**(6): p. 1255-1262.
132. Qin, X., et al., *Nanoconjugates of Ag/Au/carbon nanotube for alkyne-mediated ratiometric SERS imaging of hypoxia in hepatic ischemia*. Analytical Chemistry, 2019. **91**(7): p. 4529-4536.
133. Jie, Z., et al., *Quantitative SERS by electromagnetic enhancement normalization with carbon nanotube as an internal standard*. Optics Express, 2018. **26**(18): p. 23534-23539.
134. Beqa, L., et al., *Gold nano-popcorn attached SWCNT hybrid nanomaterial for targeted diagnosis and photothermal therapy of human breast cancer cells*. ACS Applied Materials & Interfaces, 2011. **3**(9): p. 3316-3324.
135. Wang, X., et al., *Noble Metal Coated Single-Walled Carbon Nanotubes for Applications in Surface Enhanced Raman Scattering Imaging and Photothermal Therapy*. Journal of the American Chemical Society, 2012. **134**(17): p. 7414-7422.
136. Cheng, H., et al., *Graphene-quantum-dot assembled nanotubes: A new platform for efficient Raman enhancement*. ACS Nano, 2012. **6**(3): p. 2237-2244.
137. Liu, D., et al., *Raman enhancement on ultra-clean graphene quantum dots produced by quasi-equilibrium plasma-enhanced chemical vapor deposition*. Nature Communications, 2018. **9**(1): p. 193.

II. Introduction

138. Bhunia, S.K., et al., *Carbon-dot/silver-nanoparticle flexible SERS-active films*. ACS Applied Materials & Interfaces, 2016. **8**(38): p. 25637-25643.
139. Fei, X., et al., *Synthesis of Au NP@MoS₂ quantum dots core@shell nanocomposites for SERS bio-analysis and label-free bio-imaging*. Materials, 2017. **10**(6): p. 650.
140. Pilot, R., et al., *A review on surface-enhanced Raman scattering*. Biosensors, 2019. **9**(2): p. 57.
141. Zhao, X., M. Li, and Z. Xu, *Detection of foodborne pathogens by surface enhanced Raman spectroscopy*. Frontiers in Microbiology, 2018. **9**: p. 1236.
142. Li, J., et al., *3D ordered silver nanoshells silica photonic crystal beads for multiplex encoded SERS bioassay*. Chemical Communications, 2016. **52**(2): p. 284-287.
143. Cho, W.J., Y. Kim, and J.K. Kim, *Ultrahigh-density array of silver nanoclusters for SERS substrate with high sensitivity and excellent reproducibility*. ACS Nano, 2012. **6**(1): p. 249-255.
144. Lee, S.Y., et al., *Freestanding and arrayed nanoporous microcylinders for highly active 3D SERS substrate*. Chemistry of Materials, 2013. **25**(12): p. 2421-2426.
145. Xie, X., H. Pu, and D.-W. Sun, *Recent advances in nanofabrication techniques for SERS substrates and their applications in food safety analysis*. Critical Reviews in Food Science and Nutrition, 2018. **58**(16): p. 2800-2813.
146. Lao, Z., Y. Hu, and D. Wu. *Fabricating nanogap for SERS by combing laser printing with capillary-force self-assembly on soft base*. in *Nonlinear Optics (NLO)*. 2019. Waikoloa Beach, Hawaii: Optical Society of America.
147. Fan, M., G.F.S. Andrade, and A.G. Brolo, *A review on the fabrication of substrates for surface enhanced Raman spectroscopy and their applications in analytical chemistry*. Analytica Chimica Acta, 2011. **693**(1): p. 7-25.
148. Jiao, T., et al., *Chemical functionalization, self-assembly, and applications of nanomaterials and nanocomposites*. Journal of Nanomaterials, 2014. **2014**: p. 291013.
149. Zhao, X., et al., *Design of hybrid nanostructural arrays to manipulate SERS-active substrates by nanosphere lithography*. ACS Applied Materials & Interfaces, 2017. **9**(8): p. 7710-7716.
150. Fang, X., et al., *Hierarchically ordered silicon metastructures from improved self-assembly-based nanosphere lithography*. ACS Applied Materials & Interfaces, 2020. **12**(10): p. 12345-12352.
151. Petti, L., et al., *A plasmonic nanostructure fabricated by electron beam lithography as a sensitive and highly homogeneous SERS substrate for bio-sensing applications*. Vibrational Spectroscopy, 2016. **82**: p. 22-30.
152. Hasna, K., et al., *Fabrication of cost-effective, highly reproducible large area arrays of nanotriangular pillars for surface enhanced Raman scattering substrates*. Nano Research, 2016. **9**(10): p. 3075-3083.
153. Liu, T.-Y., et al., *Functionalized arrays of Raman-enhancing nanoparticles for capture and culture-free analysis of bacteria in human blood*. Nature Communications, 2011. **2**(1): p. 538.
154. Im, H., et al., *Self-assembled plasmonic nanoring cavity arrays for SERS and LSPR biosensing*. Advanced Materials, 2013. **25**(19): p. 2678-2685.
155. Rippa, M., et al., *Octupolar metastructures for a highly sensitive, rapid, and reproducible phage-based detection of bacterial pathogens by*

- surface-enhanced Raman scattering*. ACS Sensors, 2017. **2**(7): p. 947-954.
156. Kumar, S., et al., *A facile method for fabrication of buckled PDMS silver nanorod arrays as active 3D SERS cages for bacterial sensing*. Chemical Communications, 2015. **51**(62): p. 12411-12414.
 157. Paccotti, N., et al., *Label-free SERS discrimination and in situ analysis of life cycle in Escherichia coli and Staphylococcus epidermidis*. Biosensors, 2018. **8**(4): p. 131.
 158. Zhang, Y., et al., *Characterization and identification of lung cancer cells from blood cells with label-free surface-enhanced Raman scattering*. Laser Physics, 2019. **29**(4): p. 045602.
 159. Shanmukh, S., et al., *Rapid and sensitive detection of respiratory virus molecular signatures using a silver nanorod array SERS substrate*. Nano Letters, 2006. **6**(11): p. 2630-2636.
 160. Kahraman, M. and S. Wachsmann-Hogiu, *Label-free and direct protein detection on 3D plasmonic nanovoid structures using surface-enhanced Raman scattering*. Analytica Chimica Acta, 2015. **856**: p. 74-81.
 161. Guselnikova, O., et al., *Express and portable label-free DNA detection and recognition with SERS platform based on functional Au grating*. Applied Surface Science, 2019. **470**: p. 219-227.
 162. Zhang, B., et al., *Large-area silver-coated silicon nanowire arrays for molecular sensing using surface-enhanced Raman spectroscopy*. Advanced Functional Materials, 2008. **18**(16): p. 2348-2355.
 163. Nam, W., et al., *Refractive-index-insensitive nanolaminated SERS substrates for label-free Raman profiling and classification of living cancer cells*. Nano Letters, 2019. **19**(10): p. 7273-7281.
 164. Plou, J., et al., *Multiplex SERS detection of metabolic alterations in tumor extracellular media*. Advanced Functional Materials, 2020. **30**(17): p. 1910335.
 165. Du, J., J. Cui, and C. Jing, *Rapid in situ identification of arsenic species using a portable Fe₃O₄@Ag SERS sensor*. Chemical Communications, 2014. **50**(3): p. 347-349.
 166. Jiang, X., et al., *Metal-free SERS substrate based on rGO-TiO₂-Fe₃O₄ nanohybrid: contribution from interfacial charge transfer and magnetic controllability*. Physical Chemistry Chemical Physics, 2019. **21**(24): p. 12850-12858.
 167. Huy, L.T., et al., *Photochemical decoration of silver nanocrystals on magnetic MnFe₂O₄ nanoparticles and their applications in antibacterial agents and SERS-based detection*. Journal of Electronic Materials, 2017. **46**(6): p. 3412-3421.
 168. Yang, X., et al., *A SERS biosensor with magnetic substrate CoFe₂O₄@Ag for sensitive detection of Hg²⁺*. Applied Surface Science, 2017. **416**: p. 581-586.
 169. Ding, Q., et al., *A simple method to prepare the magnetic Ni@Au core-shell nanostructure for the cycle surface enhanced Raman scattering substrates*. Journal of Raman Spectroscopy, 2013. **44**(7): p. 987-993.
 170. Xu, X., et al., *Near-field enhanced plasmonic-magnetic bifunctional nanotubes for single cell bioanalysis*. Advanced Functional Materials, 2013. **23**(35): p. 4332-4338.
 171. Hardiansyah, A., et al., *Core-shell of FePt@SiO₂-Au magnetic nanoparticles for rapid SERS detection*. Nanoscale Research Letters, 2015. **10**(1): p. 412.

II. Introduction

172. Wang, Y., et al., *Magnetic field modulated SERS enhancement of CoPt hollow nanoparticles with sizes below 10 nm*. *Nanoscale*, 2018. **10**(26): p. 12650-12656.
173. Choi, J.-Y., K. Kim, and K.S. Shin, *Surface-enhanced Raman scattering inducible by recyclable Ag-coated magnetic particles*. *Vibrational Spectroscopy*, 2010. **53**(1): p. 117-120.
174. Fan, Z., et al., *Popcorn-shaped magnetic core-plasmonic shell multifunctional nanoparticles for the targeted magnetic separation and enrichment, label-free SERS imaging, and photothermal destruction of multidrug-resistant bacteria*. *Chemistry – A European Journal*, 2013. **19**(8): p. 2839-2847.
175. Wang, C., et al., *Polyethylenimine-interlayered core-shell-satellite 3D magnetic microspheres as versatile SERS substrates*. *Nanoscale*, 2015. **7**(44): p. 18694-18707.
176. Han, B., et al., *Application of silver-coated magnetic microspheres to a SERS-based optofluidic sensor*. *The Journal of Physical Chemistry C*, 2011. **115**(14): p. 6290-6296.
177. Wang, C., et al., *Sonochemical synthesis of highly branched flower-like Fe₃O₄@SiO₂@Ag microcomposites and their application as versatile SERS substrates*. *Nanoscale*, 2016. **8**(47): p. 19816-19828.
178. Yang, T., et al., *Facile and label-free detection of lung cancer biomarker in urine by magnetically assisted surface-enhanced Raman scattering*. *ACS Applied Materials & Interfaces*, 2014. **6**(23): p. 20985-20993.
179. Han, X.X., et al., *Semiconductor-enhanced Raman scattering: active nanomaterials and applications*. *Nanoscale*, 2017. **9**(15): p. 4847-4861.
180. Keshavarz, M., B. Tan, and K. Venkatakrisnan, *Label-free SERS quantum semiconductor probe for molecular-level and in vitro cellular detection: A noble-metal-free methodology*. *ACS Applied Materials & Interfaces*, 2018. **10**(41): p. 34886-34904.
181. Kang, T., et al., *In vitro toxicity of different-sized ZnO nanoparticles in Caco-2 cells*. *Nanoscale Research Letters*, 2013. **8**(1): p. 496.
182. Han, X.X., et al., *Potential-dependent surface-enhanced resonance Raman spectroscopy at nanostructured TiO₂: A case study on cytochrome b5*. *Small*, 2013. **9**(24): p. 4175-4181.
183. Lee, S., et al., *Rapid and sensitive phenotypic marker detection on breast cancer cells using surface-enhanced Raman scattering (SERS) imaging*. *Biosensors and Bioelectronics*, 2014. **51**: p. 238-243.
184. Yang, L., et al., *Green and sensitive flexible semiconductor SERS substrates: Hydrogenated black TiO₂ nanowires*. *ACS Applied Nano Materials*, 2018. **1**(9): p. 4516-4527.
185. Wu, H., H. Wang, and G. Li, *Metal oxide semiconductor SERS-active substrates by defect engineering*. *Analyst*, 2017. **142**(2): p. 326-335.
186. Chen, M., et al., *Improved SERS activity of non-stoichiometric copper sulfide nanostructures related to charge-transfer resonance*. *Physical Chemistry Chemical Physics*, 2020. **22**(9): p. 5145-5153.
187. Zheng, Z., et al., *Semiconductor SERS enhancement enabled by oxygen incorporation*. *Nature Communications*, 2017. **8**(1): p. 1993.
188. Cheng, Y.-F., et al., *Efficient photodegradation of dye pollutants using a novel plasmonic AgCl microrods array and photo-optimized surface-enhanced Raman scattering*. *Applied Catalysis B: Environmental*, 2017. **217**: p. 37-47.
189. Prasad, M.D., M.G. Krishna, and S.K. Batabyal, *Facet-engineered surfaces of two-dimensional layered BiOI and Au-BiOI substrates for tuning the*

- surface-enhanced Raman scattering and visible light photodetector response.* ACS Applied Nano Materials, 2019. **2**(6): p. 3906-3915.
190. Wang, X., et al., *Using Si and Ge nanostructures as substrates for surface-enhanced Raman scattering based on photoinduced charge transfer mechanism.* Journal of the American Chemical Society, 2011. **133**(41): p. 16518-16523.
 191. Cui, H., et al., *Flexible, transparent, and free-standing silicon nanowire SERS platform for in situ food inspection.* ACS Sensors, 2017. **2**(3): p. 386-393.
 192. Haldavnekar, R., K. Venkatakrishnan, and B. Tan, *Non plasmonic semiconductor quantum SERS probe as a pathway for in vitro cancer detection.* Nature Communications, 2018. **9**(1): p. 3065.
 193. Keshavarz, M., et al., *Metal-oxide surface-enhanced Raman biosensor template towards point-of-care EGFR detection and cancer diagnostics.* Nanoscale Horizons, 2020. **5**(2): p. 294-307.
 194. Ganesh, S., K. Venkatakrishnan, and B. Tan, *Quantum scale organic semiconductors for SERS detection of DNA methylation and gene expression.* Nature Communications, 2020. **11**(1): p. 1135.
 195. Yilmaz, M., et al., *Nanostructured organic semiconductor films for molecular detection with surface-enhanced Raman spectroscopy.* Nature Materials, 2017. **16**(9): p. 918-924.
 196. Demirel, G., et al., *Molecular engineering of organic semiconductors enables noble metal-comparable SERS enhancement and sensitivity.* Nature Communications, 2019. **10**(1): p. 5502.
 197. Li, Y., et al., *Raman tags: Novel optical probes for intracellular sensing and imaging.* Biotechnology Advances, 2017. **35**(2): p. 168-177.
 198. Kho, K.W., et al., *Clinical SERS: are we there yet?* Journal of Biophotonics, 2011. **4**(10): p. 667-684.
 199. Liu, X., et al., *Synthesis of core-shell surface-enhanced Raman tags for bioimaging.* Analytical Chemistry, 2010. **82**(1): p. 441-446.
 200. Yu, Q., et al., *Polystyrene encapsulated SERS tags as promising standard tools: Simple and universal in synthesis; highly sensitive and ultrastable for bioimaging.* Analytical Chemistry, 2019. **91**(8): p. 5270-5277.
 201. Zhang, L., et al., *Facile synthesis of thiol and alkynyl contained SERS reporter molecular and its usage in assembly of polydopamine protected bioorthogonal SERS tag for live cell imaging.* Talanta, 2016. **158**: p. 315-321.
 202. Wen, S., et al., *Aptamer-conjugated Au nanocage/SiO₂ core-shell bifunctional nanoprobe with high stability and biocompatibility for cellular SERS imaging and near-infrared photothermal therapy.* ACS Sensors, 2019. **4**(2): p. 301-308.
 203. Jaworska, A., et al., *Rhodamine 6G conjugated to gold nanoparticles as labels for both SERS and fluorescence studies on live endothelial cells.* Microchimica Acta, 2015. **182**(1): p. 119-127.
 204. Neng, J., et al., *A versatile SERS-based immunoassay for immunoglobulin detection using antigen-coated gold nanoparticles and malachite green-conjugated protein A/G.* Biosensors and Bioelectronics, 2010. **26**(3): p. 1009-1015.
 205. Song, D., et al., *SERS based aptasensor for ochratoxin A by combining Fe₃O₄@Au magnetic nanoparticles and Au-DTNB@Ag nanoprobe with multiple signal enhancement.* Microchimica Acta, 2018. **185**(10): p. 491.
 206. Simon, T., et al., *Designing theranostic agents based on pluronic stabilized gold nanoaggregates loaded with methylene blue for*

II. Introduction

- multimodal cell imaging and enhanced photodynamic therapy*. ACS Applied Materials & Interfaces, 2015. **7**(30): p. 16191-16201.
207. Luo, Z., et al., *Synthesis of p-aminothiophenol-embedded gold/silver core-shell nanostructures as novel SERS tags for biosensing applications*. Microchimica Acta, 2011. **173**(1): p. 149-156.
208. Wang, J., et al., *Facile synthesis of Au-coated magnetic nanoparticles and their application in bacteria detection via a SERS method*. ACS Applied Materials & Interfaces, 2016. **8**(31): p. 19958-19967.
209. Pang, Y., et al., *Dual-selective and dual-enhanced SERS nanoprobe strategy for circulating hepatocellular carcinoma cells detection*. Chemistry – A European Journal, 2018. **24**(27): p. 7060-7067.
210. Zhang, C., et al., *Sensitive and specific detection of clinical bacteria via vancomycin-modified Fe₃O₄@Au nanoparticles and aptamer-functionalized SERS tags*. Journal of Materials Chemistry B, 2018. **6**(22): p. 3751-3761.
211. Zou, Y., et al., *Isotopic graphene-isolated-Au-nanocrystals with cellular Raman-silent signals for cancer cell pattern recognition*. Chemical Science, 2018. **9**(10): p. 2842-2849.
212. Yin, D., et al., *Surface-enhanced Raman scattering imaging of cancer cells and tissues via sialic acid-imprinted nanotags*. Chemical Communications, 2015. **51**(100): p. 17696-17699.
213. Pang, Y., et al., *Dual-recognition surface-enhanced Raman scattering(SERS) biosensor for pathogenic bacteria detection by using vancomycin-SERS tags and aptamer-Fe₃O₄@Au*. Analytica Chimica Acta, 2019. **1077**: p. 288-296.
214. Tang, R., et al., *LHRH-targeting surface-enhanced Raman scattering tags for the rapid detection of circulating tumor cells*. Sensors and Actuators B: Chemical, 2019. **284**: p. 468-474.
215. Zhang, Q., et al., *Dynamic imaging of transferrin receptor molecules on single live cell with bridge gaps-enhanced Raman tags*. Nanomaterials, 2019. **9**(10): p. 1373.
216. Wen, H., et al., *Synthesis of Au@Ag core-shell nanostructures with a poly(3,4-dihydroxy-L-phenylalanine) interlayer for surface-enhanced Raman scattering imaging of epithelial cells*. Microchimica Acta, 2018. **185**(7): p. 353.
217. Uzayisenga, V., et al., *Synthesis, characterization, and 3D-FDTD simulation of Ag@SiO₂ nanoparticles for shell-isolated nanoparticle-enhanced Raman spectroscopy*. Langmuir, 2012. **28**(24): p. 9140-9146.
218. Yang, J.-L., et al., *FDTD simulation study of size/gap and substrate-dependent SERS activity study of Au@SiO₂ nanoparticles*. Chinese Physics B, 2016. **25**(8): p. 083301.
219. Tira, C., et al., *Finite-difference time-domain (FDTD) design of gold nanoparticle chains with specific surface plasmon resonance*. Journal of Molecular Structure, 2014. **1072**: p. 137-143.
220. Zou, Y., et al., *Stable and unique graphitic Raman internal standard nanocapsules for surface-enhanced Raman spectroscopy quantitative analysis*. Nano Research, 2016. **9**(5): p. 1418-1425.
221. Li, M., et al., *Background-free quantitative surface enhanced Raman spectroscopy analysis using core-shell nanoparticles with an inherent internal standard*. Analytical Chemistry, 2019. **91**(23): p. 15025-15031.
222. Shen, W., et al., *Reliable quantitative SERS analysis facilitated by core-shell nanoparticles with embedded internal standards*. Angewandte Chemie International Edition, 2015. **54**(25): p. 7308-7312.

223. Qian, X., et al., *In vivo tumor targeting and spectroscopic detection with surface-enhanced Raman nanoparticle tags*. Nature Biotechnology, 2008. **26**(1): p. 83-90.
224. Israelsen, N.D., C. Hanson, and E. Vargis, *Nanoparticle properties and synthesis effects on surface-enhanced Raman scattering enhancement factor: An introduction*. The Scientific World Journal, 2015. **2015**: p. 124582.
225. Zhang, S., et al., *Size-dependent endocytosis of nanoparticles*. Advanced Materials, 2009. **21**(4): p. 419-424.
226. Ishigaki, M., et al., *Diagnosis of early-stage esophageal cancer by Raman spectroscopy and chemometric techniques*. Analyst, 2016. **141**(3): p. 1027-1033.
227. Yeh, Y.-T., et al., *A rapid and label-free platform for virus capture and identification from clinical samples*. Proceedings of the National Academy of Sciences, 2020. **117**(2): p. 895.
228. Ozin, G.A., et al., *Dream Nanomachines*. Advanced Materials, 2005. **17**(24): p. 3011-3018.
229. Kagan, D., et al., *Chemical Sensing Based on Catalytic Nanomotors: Motion-Based Detection of Trace Silver*. Journal of the American Chemical Society, 2009. **131**(34): p. 12082-12083.
230. Sanchez, S. and M. Pumera, *Nanorobots: the ultimate wireless self-propelled sensing and actuating devices*. Chem Asian J, 2009. **4**(9): p. 1402-10.
231. Solovev, A.A., et al., *Catalytic microtubular jet engines self-propelled by accumulated gas bubbles*. Small, 2009. **5**(14): p. 1688-92.
232. Ebbens, S.J. and J.R. Howse, *In pursuit of propulsion at the nanoscale*. Soft Matter, 2010. **6**(4): p. 726.
233. Solovev, A.A., et al., *Magnetic Control of Tubular Catalytic Microbots for the Transport, Assembly, and Delivery of Micro-objects*. Advanced Functional Materials, 2010. **20**(15): p. 2430-2435.
234. Mei, Y., et al., *Rolled-up nanotech on polymers: from basic perception to self-propelled catalytic microengines*. Chem Soc Rev, 2011. **40**(5): p. 2109-19.
235. Wang, J., *Nanomachines: Fundamentals and Applications*. 2013.
236. Wang, W., et al., *Understanding the efficiency of autonomous nano- and microscale motors*. J Am Chem Soc, 2013. **135**(28): p. 10557-65.
237. Li, J., I. Rozen, and J. Wang, *Rocket Science at the Nanoscale*. ACS Nano, 2016. **10**(6): p. 5619-34.
238. Wang, J., *Self-propelled affinity biosensors: Moving the receptor around the sample*. Biosens Bioelectron, 2016. **76**: p. 234-42.
239. Karshalev, E., B. Esteban-Fernández de Ávila, and J. Wang, *Micromotors for "Chemistry-on-the-Fly"*. Journal of the American Chemical Society, 2018.
240. Orozco, J., et al., *Bubble-Propelled Micromotors for Enhanced Transport of Passive Tracers*. Langmuir, 2014. **30**(18): p. 5082-5087.
241. Rojas, D., B. Jurado-Sánchez, and A. Escarpa, *"Shoot and Sense" Janus Micromotors-Based Strategy for the Simultaneous Degradation and Detection of Persistent Organic Pollutants in Food and Biological Samples*. Analytical Chemistry, 2016. **88**(7): p. 4153-4160.
242. Gao, W., et al., *Polymer-based tubular microbots: role of composition and preparation*. Nanoscale, 2012. **4**(7): p. 2447-2453.

II. Introduction

243. Gao, W., et al., *Highly Efficient Catalytic Microengines: Template Electrosynthesis of Polyaniline/Platinum Microtubes*. Journal of the American Chemical Society, 2011. **133**(31): p. 11862-11864.
244. Wilson, D.A., R.J.M. Nolte, and J.C.M. van Hest, *Autonomous movement of platinum-loaded stomatocytes*. Nature Chemistry, 2012. **4**(4): p. 268-274.
245. Jurado-Sánchez, B. and A. Escarpa, *Janus Micromotors for Electrochemical Sensing and Biosensing Applications: A Review*. Electroanalysis, 2017. **29**(1): p. 14-23.
246. Jurado-Sánchez, B., et al., *Perspectives on Janus micromotors: Materials and applications*. Applied Materials Today, 2017. **9**: p. 407-418.
247. Wang, W., et al., *Autonomous Motion of Metallic Microrods Propelled by Ultrasound*. ACS Nano, 2012. **6**(7): p. 6122-6132.
248. Garcia-Gradilla, V., et al., *Functionalized Ultrasound-Propelled Magnetically Guided Nanomotors: Toward Practical Biomedical Applications*. ACS Nano, 2013. **7**(10): p. 9232-9240.
249. Esteban-Fernández de Ávila, B., et al., *Cell-Like Micromotors*. Accounts of Chemical Research, 2018.
250. Magdanz, V., S. Sanchez, and O.G. Schmidt, *Development of a Sperm-Flagella Driven Micro-Bio-Robot*. Advanced Materials, 2013. **25**(45): p. 6581-6588.
251. Esteban-Fernández de Ávila, B., et al., *Single Cell Real-Time miRNAs Sensing Based on Nanomotors*. ACS Nano, 2015. **9**(7): p. 6756-6764.
252. Esteban-Fernandez de Avila, B., et al., *Nanomotor-Enabled pH-Responsive Intracellular Delivery of Caspase-3: Toward Rapid Cell Apoptosis*. ACS Nano, 2017. **11**(6): p. 5367-5374.
253. Draz, M.S., et al., *Motion-Based Immunological Detection of Zika Virus Using Pt-Nanomotors and a Cellphone*. ACS Nano, 2018. **12**(6): p. 5709-5718.
254. Draz, M.S., et al., *DNA engineered micromotors powered by metal nanoparticles for motion based cellphone diagnostics*. Nat Commun, 2018. **9**(1): p. 4282.
255. Yu, X., et al., *Motor-Based Autonomous Microsensor for Motion and Counting Immunoassay of Cancer Biomarker*. Analytical Chemistry, 2014. **86**(9): p. 4501-4507.
256. Jurado-Sanchez, B., et al., *Magnetocatalytic Graphene Quantum Dots Janus Micromotors for Bacterial Endotoxin Detection*. Angew Chem Int Ed Engl, 2017. **56**(24): p. 6957-6961.
257. Pacheco, M., B. Jurado-Sanchez, and A. Escarpa, *Sensitive Monitoring of Enterobacterial Contamination of Food Using Self-Propelled Janus Microsensors*. Anal Chem, 2018. **90**(4): p. 2912-2917.
258. Zhang, Y., et al., *Real-time tracking of fluorescent magnetic spore-based microrobots for remote detection of *C. diff* toxins*. Science Advances, 2019. **5**(1): p. eaau9650.
259. Orozco, J., et al., *Micromotors to capture and destroy anthrax simulant spores*. Analyst, 2015. **140**(5): p. 1421-1427.
260. Campuzano, S., et al., *Bacterial isolation by lectin-modified microengines*. Nano Lett, 2012. **12**(1): p. 396-401.
261. Esteban-Fernández de Ávila, B., et al., *Hybrid biomembrane-functionalized nanorobots for concurrent removal of pathogenic bacteria and toxins*. Science Robotics, 2018. **3**(18).

262. Balasubramanian, S., et al., *Micromachine-Enabled Capture and Isolation of Cancer Cells in Complex Media*. Angewandte Chemie International Edition, 2011. **50**(18): p. 4161-4164.
263. Banerjee, S.S., et al., *Self-propelled carbon nanotube based microrockets for rapid capture and isolation of circulating tumor cells*. Nanoscale, 2015. **7**(19): p. 8684-8688.
264. Xu, Y., et al., *Aptamer-based hydrogel barcodes for the capture and detection of multiple types of pathogenic bacteria*. Biosensors and Bioelectronics, 2018. **100**: p. 404-410.
265. Wu, Z., et al., *Near-Infrared Light-Triggered "On/Off" Motion of Polymer Multilayer Rockets*. ACS Nano, 2014. **8**(6): p. 6097-6105.
266. Maria-Hormigos, R., B. Jurado-Sánchez, and A. Escarpa, *Tailored magnetic carbon allotrope catalytic micromotors for 'on-chip' operations*. Nanoscale, 2017. **9**(19): p. 6286-6290.
267. Hu, C.-M.J., et al., *A biomimetic nanosponge that absorbs pore-forming toxins*. Nature Nanotechnology, 2013. **8**(5): p. 336-340.
268. Gao, W., et al., *Surface Functionalization of Gold Nanoparticles with Red Blood Cell Membranes*. Advanced Materials, 2013. **25**(26): p. 3549-3553.
269. Wu, Z., et al., *Cell-Membrane-Coated Synthetic Nanomotors for Effective Biodetoxification*. Advanced Functional Materials, 2015. **25**(25): p. 3881-3887.
270. Li, J., et al., *Biomimetic Platelet-Camouflaged Nanorobots for Binding and Isolation of Biological Threats*. Advanced Materials, 2018. **30**(2): p. 1704800.
271. Hoop, M., et al., *Magnetically Driven Silver-Coated Nanocoils for Efficient Bacterial Contact Killing*. Advanced Functional Materials, 2016. **26**(7): p. 1063-1069.
272. Vilela, D., et al., *Microbots Decorated with Silver Nanoparticles Kill Bacteria in Aqueous Media*. ACS Applied Materials & Interfaces, 2017. **9**(27): p. 22093-22100.
273. Simmchen, J., et al., *Dynamics of Novel Photoactive AgCl Microstars and Their Environmental Applications*. ChemNanoMat, 2017. **3**(1): p. 65-71.
274. Ge, Y., et al., *Dual-Fuel-Driven Bactericidal Micromotor*. Nano-Micro Letters, 2016. **8**(2): p. 157-164.
275. Singh, V.V., et al., *Multifunctional Silver-Exchanged Zeolite Micromotors for Catalytic Detoxification of Chemical and Biological Threats*. Advanced Functional Materials, 2015. **25**(14): p. 2147-2155.
276. Li, J., et al., *Water-Driven Micromotors for Rapid Photocatalytic Degradation of Biological and Chemical Warfare Agents*. ACS Nano, 2014. **8**(11): p. 11118-11125.
277. Delezuk, J.A., et al., *Chitosan-based water-propelled micromotors with strong antibacterial activity*. Nanoscale, 2017. **9**(6): p. 2195-2200.
278. Kiristi, M., et al., *Lysozyme-Based Antibacterial Nanomotors*. ACS Nano, 2015. **9**(9): p. 9252-9259.
279. Wu, Y., et al., *Near-infrared light-driven Janus capsule motors: Fabrication, propulsion, and simulation*. Nano Research, 2016. **9**(12): p. 3747-3756.
280. Choi, H., et al., *Light-Guided Nanomotor Systems for Autonomous Photothermal Cancer Therapy*. ACS Applied Materials & Interfaces, 2018. **10**(3): p. 2338-2346.
281. Guo, W., et al., *TiO₂-x Based Nanoplatform for Bimodal Cancer Imaging and NIR-Triggered Chem/Photodynamic/Photothermal Combination Therapy*. Chemistry of Materials, 2017. **29**(21): p. 9262-9274.

II. Introduction

282. Yuan, S., et al., *Lysozyme-Coupled Poly(poly(ethylene glycol) methacrylate)–Stainless Steel Hybrids and Their Antifouling and Antibacterial Surfaces*. *Langmuir*, 2011. **27**(6): p. 2761-2774.
283. Solovev, A.A., et al., *Self-Propelled Nanotools*. *ACS Nano*, 2012. **6**(2): p. 1751-1756.
284. Srivastava, S.K., et al., *Medibots: Dual-Action Biogenic Microdaggers for Single-Cell Surgery and Drug Release*. *Advanced Materials*, 2016. **28**(5): p. 832-837.
285. de Ávila, B.E.-F., et al., *Micromotor-enabled active drug delivery for in vivo treatment of stomach infection*. *Nature Communications*, 2017. **8**(1): p. 272.
286. Stanton, M.M., et al., *Magnetotactic Bacteria Powered Biohybrids Target E. coli Biofilms*. *ACS Nano*, 2017. **11**(10): p. 9968-9978.
287. Esteban-Fernández de Ávila, B., et al., *Nanomotor-Enabled pH-Responsive Intracellular Delivery of Caspase-3: Toward Rapid Cell Apoptosis*. *ACS Nano*, 2017. **11**(6): p. 5367-5374.
288. Wu, Z., et al., *Biodegradable Protein-Based Rockets for Drug Transportation and Light-Triggered Release*. *ACS Applied Materials & Interfaces*, 2015. **7**(1): p. 250-255.
289. Tu, Y., et al., *Redox-Sensitive Stomatocyte Nanomotors: Destruction and Drug Release in the Presence of Glutathione*. *Angewandte Chemie International Edition*, 2017. **56**(26): p. 7620-7624.
290. Tu, Y., et al., *Biodegradable Hybrid Stomatocyte Nanomotors for Drug Delivery*. *ACS Nano*, 2017. **11**(2): p. 1957-1963.
291. Felfoul, O., et al., *Magneto-aerotactic bacteria deliver drug-containing nanoliposomes to tumour hypoxic regions*. *Nature Nanotechnology*, 2016. **11**(11): p. 941-947.
292. Xu, H., et al., *Sperm-Hybrid Micromotor for Targeted Drug Delivery*. *ACS Nano*, 2018. **12**(1): p. 327-337.
293. Wu, Z., et al., *Self-Propelled Polymer-Based Multilayer Nanorockets for Transportation and Drug Release*. *Angewandte Chemie International Edition*, 2013. **52**(27): p. 7000-7003.
294. Bhuyan, T., et al., *Magnetic Field Guided Chemotaxis of iMushbots for Targeted Anticancer Therapeutics*. *ACS Biomaterials Science & Engineering*, 2017. **3**(8): p. 1627-1640.
295. Li, J., et al., *Micromotors Spontaneously Neutralize Gastric Acid for pH-Responsive Payload Release*. *Angewandte Chemie International Edition*, 2017. **56**(8): p. 2156-2161.
296. Liang, Y., et al., *Multi-stage hydrogel rockets with stage dropping-off by thermal/light stimulation*. *Journal of Materials Chemistry A*, 2018. **6**(35): p. 16838-16843.
297. Shao, J., et al., *Chemotaxis-Guided Hybrid Neutrophil Micromotors for Targeted Drug Transport*. *Angewandte Chemie International Edition*, 2017. **56**(42): p. 12935-12939.
298. Wu, Z., et al., *RBC micromotors carrying multiple cargos towards potential theranostic applications*. *Nanoscale*, 2015. **7**(32): p. 13680-13686.

CHAPTER III.

**Janus nanostructures based
on graphene and metal
nanoparticles for SERS
detection and killing of
pathogenic bacteria**

III.1. Introduction and objectives.

Infections caused by bacterial diseases are a global health threat to the general public and demand the development of fast, sensitive and accurate diagnostic methods. Traditional methods such as standard plate colony counting, polymerase chain reaction and enzyme-linked immunosorbent assays involves complex and time-consuming steps or are expensive. To overcome such deficiencies, the development of miniaturized biosensors with much shorter analysis times, higher sensitivity and specificity is currently a hot research topic. Surface-enhanced Raman scattering (SERS) is a nondestructive and high ultrasensitive analytical technique that can provide “fingerprints” of molecules. It can be used as a qualitative tool in the analysis of unknown samples or to distinguish target molecules from a mixture of components. SERS relies on the enhancement of electromagnetic fields around metal nanoparticles to strongly increase Raman signals when molecules are attached to the nanoparticles. The main advantage of the SERS detection of pathogens is the ability to provide sharp, specific fingerprint spectra of the bacteria, making it easy to discriminate among different kinds of bacteria from a mixed sample matrix.

Noble metals such as silver, gold, and copper are widely used as SERS active substrates. Yet, the nanoprobles are used in solution, which results in random particle diffusion and heterogeneous distribution, ultimately leading to poor reproducibility in SERS detection. A convenient way to improve SERS performance is to assemble metallic nanoparticles into three-dimensional (3D) structures. The hierarchical structure of such 3D substrates results in the generation of ordered nanostructures “clusters” with localized and abundant nanometer-level gaps to interact with the target molecules. In this way, more “hot spots” are created in a small area, and the SERS signals of absorbed analytes are enhanced. Recently, some natural materials with both 3D structures and hydrophobicity have been employed in the preparation of active SERS substrates. Because of its inherent hierarchical nanostructure, such materials can not only provide 3D structures as template to decorate nanoparticles, but also possess unique hydrophobicity to form beaded droplets on its surface. Droplet evaporation results in localized spots containing nanoparticles or analytes, and thus contributes to further increase in the SERS detection sensitivity.

III. Janus nanostructures based on graphene and metal nanoparticles for SERS detection and killing of pathogenic bacteria

On the other hand, SERS tags with high sensitivity and stability are also an important factor in bacterial detection. Silver-coated gold nanoparticles (Au@AgNPs) are an excellent SERS substrate which shows higher SERS activity and more uniformity of particle size distribution compared with traditional pure AgNPs and AuNPs. However, the poor stability of Au@Ag NPs will limit their application. In this context, graphene oxide can stabilize the SERS signals and protect metal nanoparticles from oxidation, endowing this flexible substrate with a long-term stability without decline in SERS activity. As a result, the combination with GO will stabilize the SERS activity of Au@AgNPs, making the SERS active substrate more durable and will be beneficial for further chemical modification. Another smart strategy for improving SERS stability is to use an internal standard to eliminate the influence of uncontrollable aggregation of NPs, which is known to cause significant variations in SERS intensity. Ideally, 4-mercaptophenylboronic acid is a Raman signal reporter which shows a strong Raman signal and has intrinsic peaks of 1075 cm^{-1} or 1586 cm^{-1} . It can not only be used as a capture probe to combine with saccharides on bacterial cell walls, but also to correct the SERS intensities.

From the previous premises, in this chapter we will describe first the development of a SERS substrate through using mussel shell as a new kind of natural material for the self-assembly of size-tunable Au@AgNPs. The specific 3D hierarchical structures can be used as templates for the self-assembly of Au@Ag nanoparticles to form 3D supercrystals, which can lead to intense and controlled antenna effects, resulting in huge electromagnetic field. Such periodic grating microstructures will make the distribution of nanoparticles with high periodicity over the micrometer scale of the SERS substrate. Thus, the signal reproducibility could be significantly improved at a large scale. The as-prepared Au@AgNPs self-assembled mussel shell substrate is next applied for the detection and discrimination of three different kinds of pathogenic bacteria. As a result, the 3D supercrystals could reach an LOD (limit of detection) for Rhodamine 6G as low as $1 \times 10^{-9}\text{ M}$, and signal reproducibility could be significantly improved and measured with a variation of 6.5% at the peak of 613 cm^{-1} . The as-prepared SERS substrate also has been utilized in the discrimination of different kinds of pathogenic bacteria (*Escherichia*

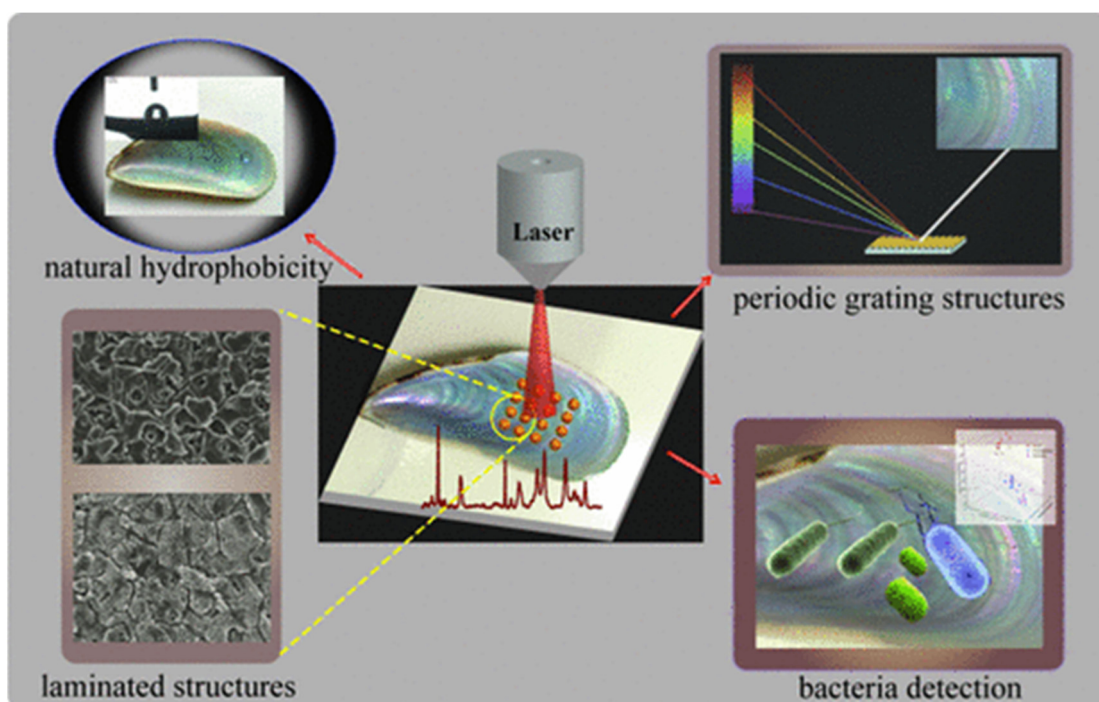
III. Janus nanostructures based on graphene and metal nanoparticles for SERS detection and killing of pathogenic bacteria

Coli, *Pseudomonas Aeruginosa*, and *Staphylococcus Aureus*) with different profiles in principal component analysis.

Inspired by the previous results, on a second work we develop a SERS sandwich strategy for the sensitive detection and discrimination of three different kinds of bacteria directly in blood samples. The assay relies on antimicrobial peptide (AMP) functionalized magnetic nanoparticles as "capturing" probes for bacteria isolation and gold coated silver decorated graphene oxide (Au@Ag-GO) nanocomposites modified with 4-mercaptophenylboronic acid (4-MPBA) as SERS tags. Thus, AMP based Fe₃O₄ NPs were first used in the selective capture and magnetic enrichment of bacteria from the mixture, and they show some superiority over ordinary 4-MPBA, antibodies, aptamers, or antibiotic based capture elements. Hence, other interference from the mixture such as cells or proteins have been effectively removed, as well as increment in sensitivity due to the magnetic enrichment. The 4-MPBA on the SERS tags not only corrected the SERS intensities, but also enhanced the sensitivity and amplified the differences in the "fingerprints". Hence, such SERS tags combine with the bacteria@Fe₃O₄ complex to form a sandwich structure following bacteria capture and providing strong Raman signals for SERS detection. When different kinds of bacteria combined with 4-MPBA, their SERS "fingerprints" showed corresponding changes. In this way, *Escherichia coli*, *Staphylococcus Aureus* and *Pseudomonas Aeruginosa* were discriminated with LOD of 10¹ CFU mL⁻¹, respectively. This novel method was further used in the detection of bacteria from clinical patients who were infected with bacteria. Additionally, we demonstrate the potential of AMP modified Fe₃O₄NPs to inactivate potential bacterial contamination in blood transfusions settings. In the validation analysis, 97.3% of the real blood samples (39 patients) could be classified effectively.

III. Janus nanostructures based on graphene and metal nanoparticles for SERS detection and killing of pathogenic bacteria

III.2. Article 1. Self-assembly of Au@Ag nanoparticles on mussel shell as natural SERS substrates for the detection of pathogenic bacteria.



III. Janus nanostructures based on graphene and metal nanoparticles for SERS detection and killing of pathogenic bacteria

Self-Assembly of Au@Ag Nanoparticles on Mussel Shell To Form Large-Scale 3D Supercrystals as Natural SERS Substrates for the Detection of Pathogenic Bacteria

Kaisong Yuan,^{†,§,°} Junxia Zheng,^{‡,°} Danting Yang,^{||} Beatriz Jurado Sánchez,^{§,#} Xiangjiang Liu,[⊥] Xinjie Guo,[†] Chusheng Liu,[†] Nicoleta Elena Dina,[¶] Jingyi Jian,[†] Zhijun Bao,[†] Ziwei Hu,[†] Zhihong Liang,[∇] Haibo Zhou,^{*,†} and Zhengjin Jiang^{*,†}

[†]Institute of Pharmaceutical Analysis, College of Pharmacy, Jinan University, Guangzhou, Guangdong 510632, China

[‡]School of Chemical Engineering and Light Industry, Guangdong University of Technology, Guangzhou 510006, China

[§]Department of Analytical Chemistry, Physical Chemistry and Chemical Engineering, University of Alcalá, Alcalá de Henares E-28871, Madrid, Spain

^{||}Department of Preventative Medicine, Zhejiang Provincial Key Laboratory of Pathological and Physiological Technology, Medical School of Ningbo University, Ningbo, Zhejiang 315211, China

[⊥]College of Biosystems Engineering and Food Science, Zhejiang University, Hangzhou 310058, China

[#]Chemical Research Institute “Andrés M. del Río”, University of Alcalá, Alcalá de Henares E-28871, Madrid, Spain

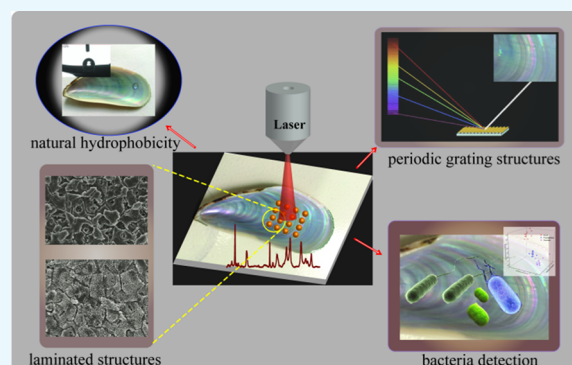
[¶]National Institute for Research and Development of Isotopic and Molecular Technologies, 67-103 Donat, 400293 Cluj-Napoca, Romania

[∇]Analysis and Test Center, Jinan University, Guangzhou, Guangdong 510632, China

Supporting Information

ABSTRACT: Herein, we developed a natural surface-enhanced Raman scattering (SERS) substrate based on size-tunable Au@Ag nanoparticle-coated mussel shell to form large-scale three-dimensional (3D) supercrystals (up to 10 cm²) that exhibit surface-laminated structures and crossed nanoplates and nanochannels. The high content of CaCO₃ in the mussel shell results in superior hydrophobicity for analyte enrichment, and the crossed nanoplates and nanochannels provided rich SERS hot spots, which together lead to high sensitivity. Finite-difference time-domain simulations showed that nanoparticles in the channels exhibit apparently a higher electromagnetic field enhancement than nanoparticles on the platelets. Thus, under optimized conditions (using Au@AgNPs with 5 nm shell thickness), highly sensitive SERS detection with a detection limit as low as 10⁻⁹ M for rhodamine 6G was obtained.

Moreover, the maximum electromagnetic field enhancement of different types of 3D supercrystals shows no apparent difference, and Au@AgNPs were uniformly distributed such that reproducible SERS measurements with a 6.5% variation (613 cm⁻¹ peak) over 20 spectra were achieved. More importantly, the as-prepared SERS substrates can be utilized for the fast discrimination of *Escherichia coli*, *Staphylococcus aureus*, and *Pseudomonas aeruginosa* by discriminant analysis. This novel Au@Ag self-assembled mussel shell template holds considerable promise as low-cost, durable, sensitive, and reproducible substrates for future SERS-based biosensors.



INTRODUCTION

The surface-enhanced Raman scattering (SERS) is a non-destructive and high ultrasensitive analytical technique that can provide “fingerprints” of molecules. It can be used as a qualitative tool in the analysis of unknown samples or to distinguish target molecules from a mixture of components. SERS relies on the enhancement of electromagnetic fields around metal nanoparticles to strongly increase Raman signals when molecules are attached to the nanoparticles.^{1,2} In general,

noble metals such as silver, gold, and copper are widely used as SERS active substrates with or without decoration.^{3–5} Yet, the nanoprobe is used in solution, which results in random particle diffusion and heterogeneous distribution, ultimately leading to poor reproducibility in SERS detection.^{6,7}

Received: January 4, 2018

Accepted: February 27, 2018

Published: March 9, 2018

A convenient way to improve SERS performance is to assemble metallic nanoparticles into three-dimensional (3D) structures. The hierarchical structure of such 3D structures results in the generation of ordered nanoparticles "clusters" with localized and abundant nanometer-level gaps to interact with the target molecules. In this way, more "hot spots" are created in a small area, and the SERS signals of absorbed analytes are enhanced.^{8–11} For the creation of varying size, shape, and precise positioning of 3D nanostructures on support materials, many strategies such as electron beam lithography,^{12,13} electrochemical deposition,^{14,15} or magnetron sputtering^{16,17} are normally employed. However, such methods are expensive, time-consuming, and require highly qualified personnel. Current trends are aimed to the use of natural 3D materials such as filter paper,¹⁸ nanoporous zeolite¹⁹ or silicon,²⁰ and cotton swab²¹ as SERS templates. Yet, the low hydrophobicity of the above-mentioned materials prevents adequate analyte and nanoparticle enrichment for highly efficient SERS detection.

Recently, some natural materials with both 3D structures and hydrophobicity have been employed in the preparation of active SERS substrates. Because of its inherent hierarchical nanostructure, such materials can not only provide 3D structures to decorate nanoparticles, but also possess unique hydrophobicity to form beaded droplets on its surface. Droplet evaporation results in localized spots containing nanoparticles or analytes, and thus contributes to further increase in the SERS detection sensitivity.^{22,23} For example, Huang et al. have demonstrated a highly efficient SERS substrate based on natural taro leaf decorated with silver nanoparticles (AgNPs). The micropapillae of the taro leaf exhibited hydrophobicity for analyte enrichment through the hydrophobic concentrating effect, and the secondary-crossed nanoplates acted as 3D templates to provide rich SERS hot spots after the decoration with AgNPs. Thereby, highly sensitive SERS detection with a detection limit as low as 10^{-8} M was achieved.²⁴ Sharma et al. employed five different types of plant leaf as the SERS substrate, in connection with gold nanoparticles (AuNPs). They found that the assembly helped by the hydrophobicity of plants surfaces helps to increase the SERS enhancement factor.²⁵ Rose petals have also been evaluated as 3D templates with natural hydrophobicity for the decoration of metal nanoparticles.^{22,26} However, such materials lack periodic structures to ensure uniform distribution of the metal nanoparticles. As an alternative, cicada and butterfly wings with the hydrophobicity nature and ordered nanostructures were evaluated as SERS substrates.^{27,28} Yet, their poor mechanical strength and short storage time hamper its practical application.

In this study, we aim to develop an SERS substrate through using the nacre from mussel shell as a new kind of natural material for the self-assembly of size-tunable Au@AgNPs. Natural mussel shells exhibit hydrophobicity because of its major inorganic composition of CaCO_3 and surface micro/nano-hierarchical structures.²⁹ Thus, nanoparticles (NPs) and analyte enrichment can be achieved to enhance the SERS sensitivity. The specific 3D hierarchical structures can be used as templates for the self-assembly of Au@Ag nanoparticles to form 3D supercrystals, which can lead to intense and controlled antenna effects, resulting in huge electromagnetic field.^{30,31} Additionally, such laminated structures give the shell a twofold increase in strength and 1000-fold increase in roughness over its constituent materials.³² Thus, the developed substrate will

show obvious higher mechanical strength compared with other natural materials such as plant leaf, petals, cicada wings, and butterfly wings. More importantly, the grating microstructures of nacre on the mussel shell, which make the iridescence color of the shell because of the interference and diffraction of the natural light, are distributed periodically.³³ Such periodic grating microstructures will make the distribution of nanoparticles with high periodicity over the micrometer scale of the SERS substrate. Thus the signal reproducibility could be significantly improved at a large scale. Interestingly, some research works have shown that the interference and diffraction surface excitation caused by the periodic grating will benefit the SERS sensitivity.³⁴ Therefore, the nacre of mussel shell can act as a new kind of natural material in the preparation of SERS 3D supercrystals to display both higher sensitivity and signal reproducibility. Another aim is to employ the as-prepared Au@AgNPs self-assembled mussel shell substrate for the detection and discrimination of three different kinds of pathogenic bacteria.

RESULTS AND DISCUSSION

Optimization of the Metal Nanoparticles. Different kinds of metal nanoparticles and different shell thicknesses of Au@AgNPs may show different Raman enhancement activities after self-assembly on the mussel shell. To optimize the most suitable metal nanoparticles in the fabrication of mussel shell substrate, the SERS activity among different thicknesses of Au@AgNPs, AgNPs, and AuNPs has been evaluated.

First, transmission electron microscopy (TEM) has been used in the characterization of AgNPs and Au@AgNPs with different thicknesses of Ag shell. Figure 1a,b has shown the low-

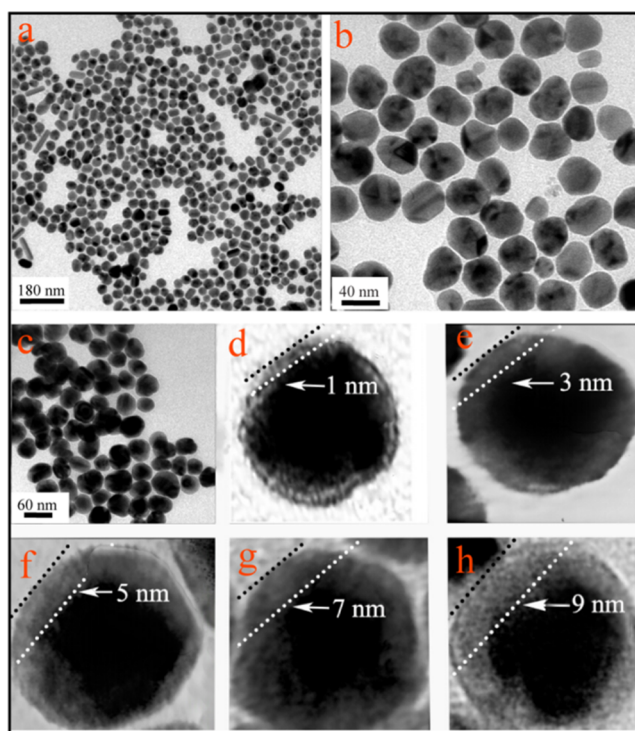


Figure 1. (a) Low-magnification TEM images of AgNPs. (b) High-magnification TEM of AgNPs. (c) Low-magnification TEM of Au@AgNPs with 5 nm thickness of Ag shell. (d–h) High-magnification TEM images of Au@AgNPs with Ag shell thicknesses of 1, 3, 5, 7, and 9 nm, respectively.

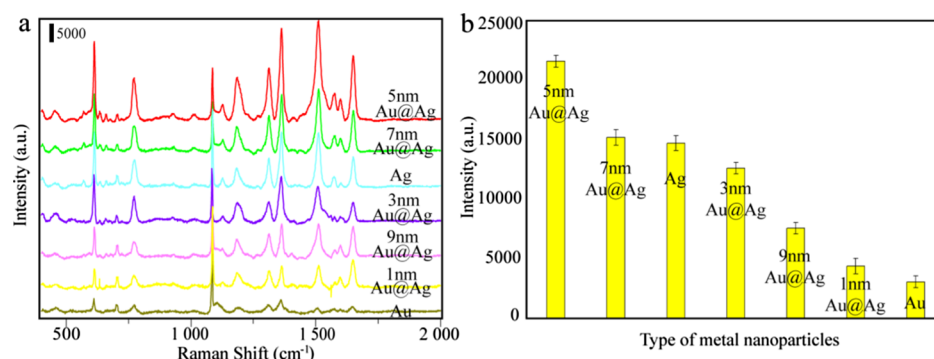


Figure 2. (a) SERS spectrum of mussel shell self-assembled with different kinds of metal nanoparticles. (b) Peaks intensity of SERS spectrum centered at 613 cm^{-1} corresponding to (a). The concentration of R6G was 10^{-3} M .

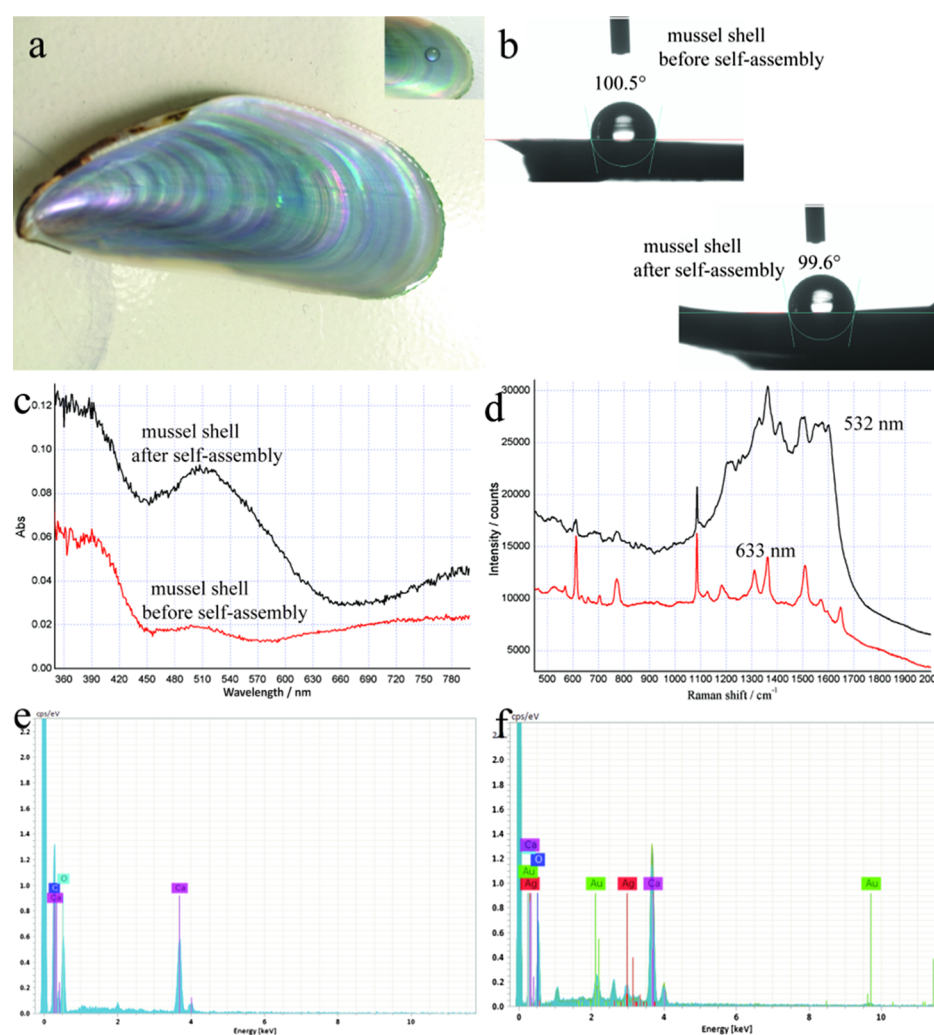


Figure 3. (a) Digital photograph of mussel shell, and the inset showing a water droplet on its surface. (b) CAs of mussel shell before and after the self-assembly of Au@AgNPs. (c) Optical absorption spectra of mussel shell before and after the self-assembly of Au@AgNPs. (d) SERS spectra of R6G solution recorded with two laser excitations. EDS spectra of mussel shell before (e) and after (f) the self-assembly of Au@AgNPs. Au@AgNPs with a 5 nm shell thickness were used in all cases.

magnification and high-magnification image of AgNPs. We can measure that the size of AgNPs is $\sim 40 \pm 12.5\text{ nm}$. Figure 1c is the low magnification of Au@AgNPs with 5 nm thickness of Ag shell, which indicated that the sizes of the Au@AgNPs are uniform. Figure 1d–h (high magnification) showed that the thickness of Ag shells increased as the amount of AgNO_3 increased, and it can be seen that the Ag shells range from 1 to

9 nm for a fixed $\sim 30 \pm 5.6\text{ nm}$ Au core. It also can be clearly observed that Au@AgNPs become larger with the increase of the Ag shell thickness. The UV–vis absorbance spectra of the as-prepared Au@AgNPs with different Ag shell thicknesses also have been measured, and the results are shown in the Figure S2. It can be observed that as the thickness of the Ag shell increased, the absorption peak shifts from 510 to 400 nm.

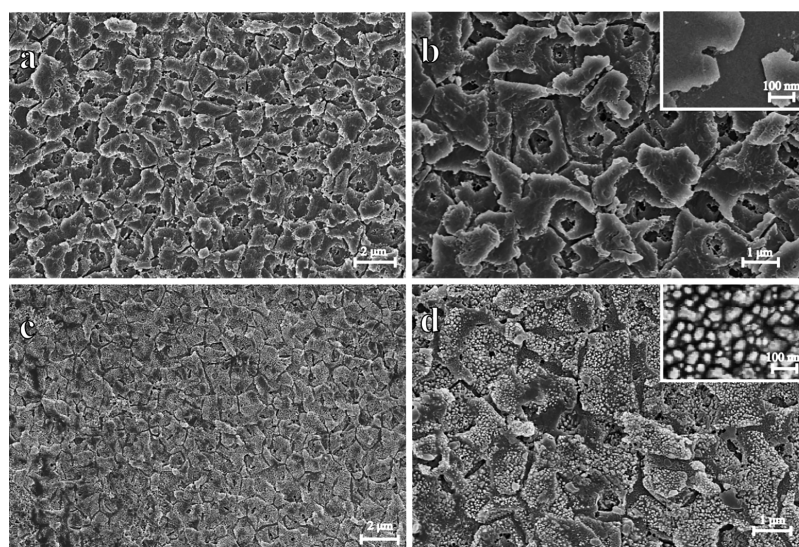


Figure 4. SEM of the blank and Au@AgNPs self-assembled mussel shell. (a,b) are both of the nanostructures of nacre on the shell before the self-assembly of Au@AgNPs. (c,d) are both of the nanostructures of nacre on the shell after the self-assembly of Au@AgNPs. The inset image on (b) is the higher magnification of the blank mussel shell, and the inset image on (d) show the higher magnification of Au@Ag self-assembled on the mussel shell substrate.

Subsequently, AuNPs, AgNPs, and Au@AgNPs with different Ag shell thicknesses have been self-assembled on the mussel shell under the same condition (20 μL of sample volume, room temperature) to evaluate their Raman enhancement activity. The concentrations of AuNPs used here is ~ 0.26 nM, whereas AgNPs is ~ 0.62 nM. The concentration of Au@AgNPs with different thicknesses of Ag shell is ~ 0.18 – 0.25 nM. The stabilizer of both AuNPs (0.5 nM) and AgNPs (1.4 nM) is sodium citrate. The stabilizer of Au@AgNPs is ascorbic acid (10 mM). R6G (10^{-3} M) was used as the probe molecule. As depicted in Figure 2a,b, it is obvious that SERS intensity of bands is enhanced as the thickness of the Ag shell increases from 1 to 5 nm, and then decreased with Ag shell above 5 nm, which may because of the unstable and easily precipitate of the Au@AgNPs when the shell thicknesses are further increased.³⁵ Thus, we conclude that the SERS enhancement effect of Au@AgNPs is related to the Ag shell thickness. We also have compared the SERS activity of Au@AgNPs to AuNPs and AgNPs. Results showed that AuNPs show weakest SERS enhancement effect among these different kinds of nanoparticles, whereas AgNPs show SERS activity between 7 and 3 nm Au@AgNPs. Thus, the Au@AgNPs with a shell thickness of 5 nm have been used for the self-assembly of mussel shell in the following research.

Characterization of the Mussel Shell-Based Substrate.

Figure 3a shows the photograph of a cleaned mussel shell. From the inset photograph, it is obvious that a water droplet can keep a sphere shape, which confirms its dewetting nature and indicates the hydrophobic property of it. As depicted in Figure 3b, the static water contact angle (CA) of the mussel shell was 100.5° before the self-assembly of nanoparticles, indicating the hydrophobic nature of the nacre mussel shell. Figure 3b also shows that the CA of the mussel shell is 99.6° after the self-assembly of Au@AgNPs with a shell thickness of 5 nm, indicating that the mussel shell still possesses hydrophobic property after the self-assembly of Au@AgNPs. Thus, these hydrophobic surfaces will accumulate the target molecule into a small size to enhance the SERS signals, even though the surfaces of the mussel shells are coated with nanoparticles.

Figure 3c shows the optical absorption spectra of Au@AgNPs (5 nm Ag shell thickness), self-assembled mussel shell, and the blank mussel shell. These two spectra all show adsorption peaks at 390 nm, attributed to the bare mussel shell. The spectra show the broad localized surface plasmon resonance (LSPR) absorption bands of Au@AgNPs at around 510 nm, which is different from its absorption spectrum in solution state (see Figure S2), indicating the formation of novel Au@AgNPs nanostructures onto the mussel shell. Previous studies have revealed that the LSPR is the major mechanism for SERS in the case of metal nanoparticles.³⁶ That is, the more wavelength match between surface plasmon band of the SERS substrate and the laser, the line may get higher SERS signals. Thus, the strongest SERS signals were obtained at 532 nm laser excitation. However, a large amount of fluorescence background signals existed in the SERS spectrum at 532 nm excitation, resulting in the loss of any useful information from Raman peaks (Figure 3d, red line). The better SERS performance was acquired with 633 nm excitation (Figure 3d, black line), which was then selected as optimal.

For the element analysis, energy-dispersive spectrometry (EDS) spectrum of elements indicates the presence of calcium, carbon, and oxygen on the mussel shell before the self-assembly of Au@AgNPs (Figure 3e). Such results are consistent with the previous reports which indicated that nacre shells are mainly composed by inorganic CaCO_3 .²⁹ Figure 3f shows silver and gold distribution after the self-assembly of Au@AgNPs with a shell thickness of 5 nm, which reveals the presence of Au@AgNPs on the substrate.

The 3D structures of nacre on mussel shells were further characterized by scanning electron microscopy (SEM). Figure 4a,b shows low- and high-magnification images of the nanostructures of nacre on the shell before the self-assembly of Au@AgNPs. A clear distribution into polygon platelets can be clearly observed. This indicated that such natural material can provide specific 3D-laminated structures when used as templates for the self-assembly of Au@Ag nanoparticles. Importantly, such laminated structures give the shell a twofold increase in strength and a 1000-fold increase in toughness over

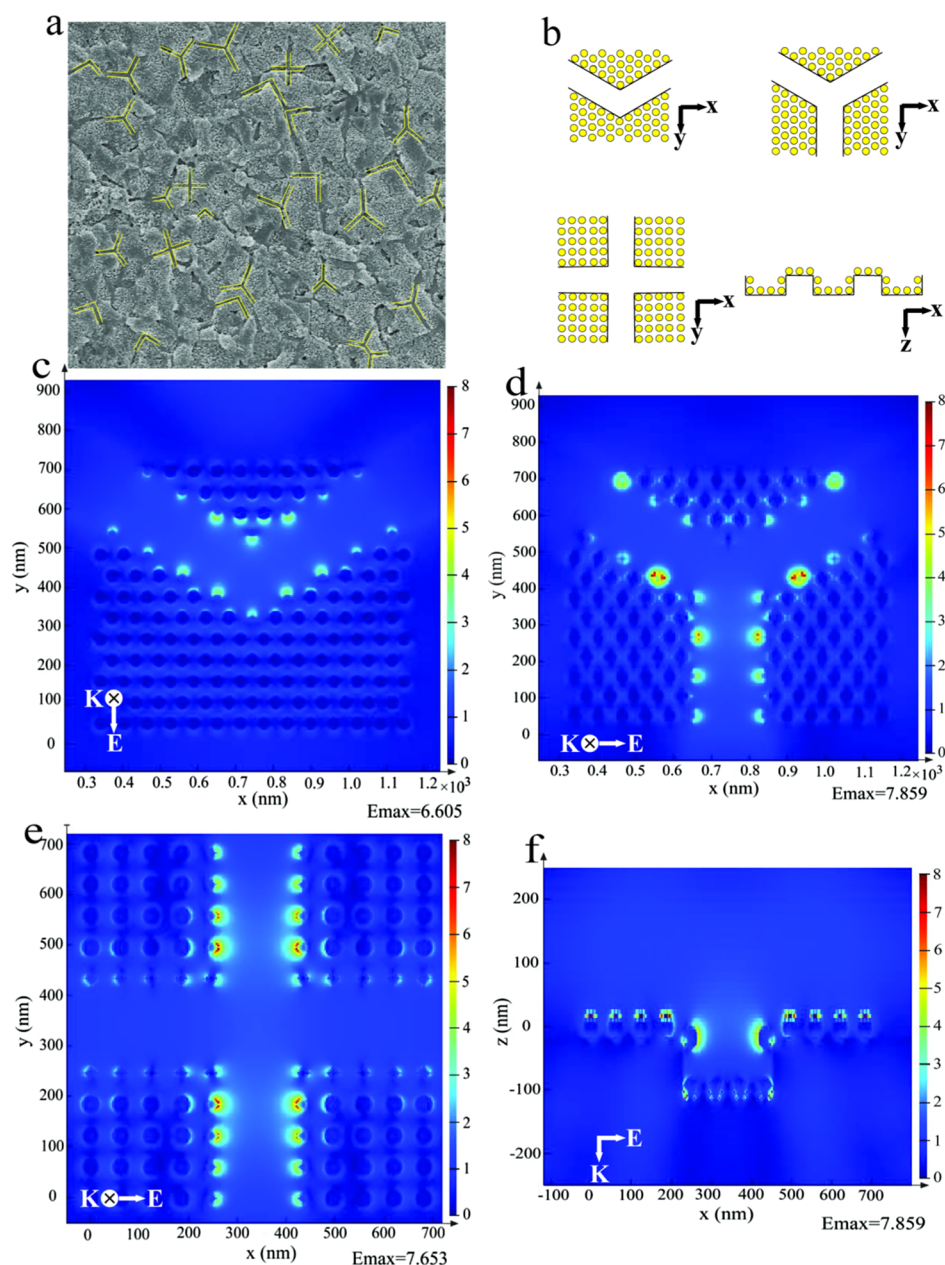


Figure 5. (a) SEM image of the mussel shell; (b) shape of the FDTD model of Au@AgNPs self-assembled mussel shell substrate; and (c–f) FDTD-simulated Ex-field enhancement of channels. The incident light with a wavelength of 633 nm enters in the z direction and is polarized in the x – y plane.

its constituent materials.³² It should be mentioned here that the nacre shell substrate displays apparent higher mechanical strength compared with the other natural materials such as plant leaf, petals, or insect wings, acting thus as a more durable SERS substrate. For example, the mussel shell was hard to be damaged even after a pulling force experiment and kept its original state under the room temperature for a long time (Figure S3). Importantly, the Au@AgNPs self-assembled the mussel shell substrate can keep its high SERS activity for a long time (up to six months) and even at high temperature (Figure S4). Also, the toughness of the surface may contribute to the hydrophobicity of the shell. Figure 4c,d shows low- and high-magnification images of the nanostructure of the nacre on the shell after the self-assembly of Au@AgNPs. As can be seen, almost all of the polygon platelets of the mussel shell are fully coated with Au@AgNPs. These NPs were orderly arranged and

homogeneously distributed along the laminated platelets of the mussel shell, the average gap between each adjacent NP which measured from 20 different random gaps is about 27 ± 5.9 nm. During the evaporation of the colloids, the spontaneous formation of the self-assembled supercrystals of Au@AgNPs takes place.^{30,31} Thus, every laminated nanoplate was formed on 3D Au@AgNPs supercrystals, and the distribution of nanoplates results in different shapes of 3D supercrystals. The gap of two adjacent 3D supercrystals is about 220 ± 49.5 nm. Such features result in a large scale of 3D supercrystals arrays (up to 10 cm^2) (Figure S5). Therefore, the obtained novel 3D supercrystals will provide a robust substrate for application as SERS spot.

Additionally, the colorful nacre on the mussel shell contributed to the reproducibility of the as-prepared substrate to some extent. Figure S6a shows the nacre of the mussel shell

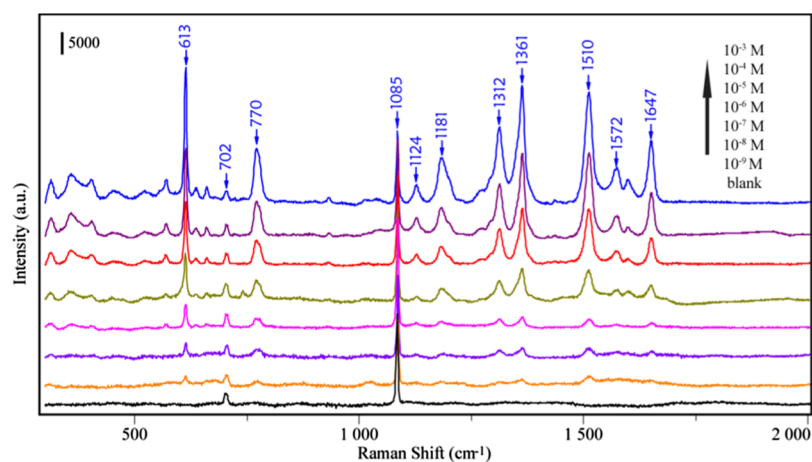


Figure 6. SERS spectra of R6G in the range of 1×10^{-3} to 1×10^{-9} M on the developed SERS substrate.

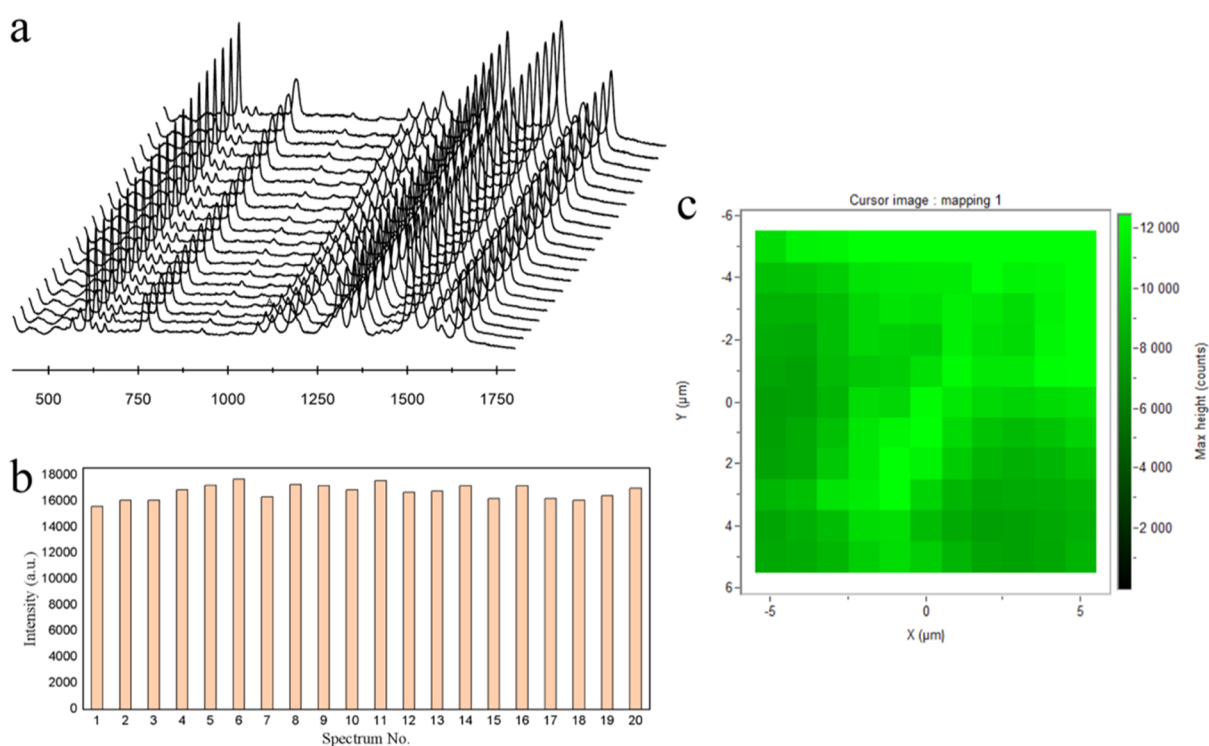


Figure 7. (a) SERS spectra of 5×10^{-4} M R6G collected from 20 random spots within an area of $100 \mu\text{m}^2$. (b) Intensity distribution of the peaks centered at 613 cm^{-1} corresponding to (a) with the RSD of 6.5%. (c) SERS mapping (step size $1 \mu\text{m}$, $10 \mu\text{m} \times 10 \mu\text{m} = 100 \mu\text{m}^2$) of one mussel shell substrate.

which was taken by a digital camera. We can see that its surface is colorful. Figure S6b shows the periodic grating microstructures of nacre on the mussel shell, which contribute to the iridescence color of the shell. Previous research works have proven that the groove density of the grating structure on the shell will exactly cause the diffraction of light.³⁷ The interference and diffraction surface excitation, caused by the periodic grating, will benefit SERS detection.³⁸ Thus, it is worth pointing out that the 3D hierarchical nanostructures, hydrophobicity, and periodic microstructures contribute to the high Raman enhancement and repeatability.

3D FDTD Simulation. We use the finite-difference time-domain (FDTD) method to study the spatial distribution of the electromagnetic fields according to the distribution of the Au@AgNPs acquired by SEM. As depicted in Figure 5a, the

distribution of 3D supercrystals is in different modes (yellow lines), and it can be divided into three shapes of the FDTD model including “V” style, “Y” style, and “cross” style (Figure 5b). In this simulation, the diameter of Au@Ag nanoparticles was set at 35 nm, the width of the channel between two platelets was set as 220 nm, and the gap between two nanoparticles was set as 27 nm. The FDTD simulation based on such 3D supercrystals with different distribution modes of “V” style, “Y” style, and “cross” style is shown in Figure 5c–e. First of all, it can be obviously observed that nanoparticles in the channels (the edge of 3D supercrystals) exhibit apparent higher electromagnetic fields than nanoparticles on the platelets (inside the 3D supercrystals) in all of these distribution modes. This can theoretically prove that nanoparticles in channels between the polygon platelets will show higher SERS activity

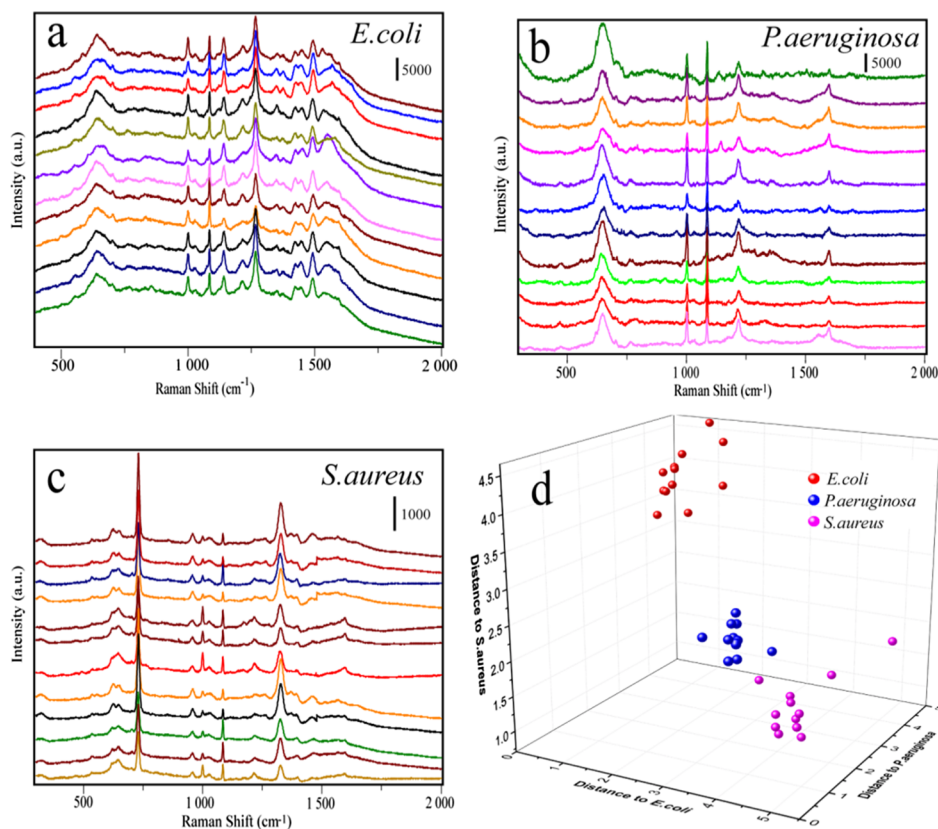


Figure 8. (a–c) SERS spectra of three different kinds of bacterium including *E. coli*, *P. aeruginosa*, and *S. aureus*. (d) DA plot showing discrimination among different kinds of bacterium.

than nanoparticles on the platelets. In other words, the mussel shell with natural platelets can serve as an excellent SERS substrate after the self-assembly of Au@AgNPs. Second, these three kinds of channels exhibit high electromagnetic field enhancement and show no apparent difference of the maximum electromagnetic field enhancement. This will make the distribution of electromagnetic field enhancement more uniform. Last, since different kinds of channel appear all over the whole mussel shell surface, the significantly enhanced electromagnetic field by the channels should dominate the enhancement of SERS signals, leading to high sensitivity and reproducibility. Figure 5f also showed the intersecting surface of these different kinds of channels on the mussel shell. We can observe that nanoparticles at the top of the channel show higher electromagnetic field enhancement than nanoparticles at the bottom of the channel, which is very useful to enhance the substrate absorption on the surface of 3D supercrystals. As the size of bacteria is larger than the channel, such target analytes thus cannot be absorbed into the channel.

SERS Performance. Figure 6 shows the SERS spectra of different concentrations of R6G droplets ($20 \mu\text{L}$) in the range of 1×10^{-3} to 1×10^{-9} M, which was detected after being evaporated naturally onto the 3D supercrystals. The Raman bands at 613 , 770 , and 1124 cm^{-1} can be assigned to C–C–C ring in-plane bending, C–H out-of-plane bending, and C–H in-plane bending, respectively. Other features at 1312 , 1361 , 1510 , 1572 , and 1647 cm^{-1} all stemmed from the aromatic C–C stretching vibrations. It can be seen that even at a concentration of 1×10^{-9} M, some peaks of R6G such as 613 and 770 cm^{-1} can be clearly identified. Additionally, the Raman bands at 702 and 1085 cm^{-1} come from the blank

mussel shell. As described above, three aspects have contributed to such Raman enhancement. First of all, the hydrophobicity of the mussel shell helps to concentrate the Au@AgNPs and analytes into a small size. Second, the specific 3D structures of the mussel shell can act as a template for the self-assembly of Au@AgNPs to form 3D supercrystals. At last, the microstructures of the nacre on the mussel shell have a periodic grating, which will enhance the Raman signal to some extent. Thus, the 3D supercrystals' substrate will bring high and stable enhancement ability. An enhancement factor (EF) of 1.02×10^7 can be obtained (please see Figure S7 in the Supporting Information).

In addition to the high SERS enhancement ability, the as-prepared mussel shell-based substrate provided reproducible SERS signals. As depicted in Figure 7a, the SERS spectra of R6G from 20 random spots within an area of $100 \mu\text{m}^2$ were recorded and the results showed that the SERS substrate provided uniform SERS enhancement upon its entire surface. Furthermore, we also compared the intensities of the 613 cm^{-1} peak of R6G, and the relative standard deviation (RSD) was calculated to be 6.5% (Figure 7b). To assess the spot-to-spot reproducibility, the mapping technique has been used by selecting $10 \mu\text{m} \times 10 \mu\text{m} = 100 \mu\text{m}^2$ area with a step size of $1 \mu\text{m}$. As depicted in Figure 7c, the intensity of the 613 cm^{-1} peak from R6G was plotted to evaluate the uniformity of the entire SERS substrate, in which every pixel represents the intensity of the Raman peak at the spatial position on the mussel shell substrates. Results have shown that the as-prepared mussel shell substrate have a good uniformity and reproducibility over its entire area.

Table 1. Comparing SERS Performance of Different Kinds of Natural Materials

samples	ref	LOD (R6G) (M)	RSD	EF	durable of the original material	analytes
mussel shell	this work	10^{-9}	6.5%	10^7	high mechanical strength; keep original state for a long time	pathogenic bacteria
rose petal	22	10^{-15}	10.0%	10^9	weak mechanical strength withered in a short time	not available
taro leaf	24	10^{-8}	9.7%	10^5	weak mechanical strength withered in a short time	not available
cicada wing	27	10^{-7}	10.1%	10^5	weak mechanical strength keep original state for a long time	thiram
rose petal	26	10^{-9}	not available	10^8	weak mechanical strength withered in a short time	not available
butterfly wing	28	10^{-10}	9.0%	10^6	weak mechanical strength withered in a short time	tumor marker

Bacteria Detection. Sensitive and simultaneous detection of pathogenic bacteria is critical for human health because of many serious and fatal diseases caused by bacterial infections. In the label-free detection of bacteria, different kinds of bacteria will show special Raman fingerprints.³⁹ In this study, three kinds of bacteria including *Escherichia coli*, *Pseudomonas aeruginosa*, and *Staphylococcus aureus* have been chosen as models to investigate the potential of the mussel shell substrate in the discrimination of bacteria. The Raman spectra of *E. coli*, *P. aeruginosa*, and *S. aureus* from 36 batches (each kind of bacteria was represented by 12 batches) were acquired and depicted in Figure 8a–c. To maximize the spectral differences resulting from the data arrays in the discrimination of bacteria, discriminant analysis (DA) has been introduced here. Figure 8d shows the 3D map of the DA results, where red balls represent *E. coli*, green balls represent *P. aeruginosa*, and blue balls represent *S. aureus*. It can be seen that they are completely independent with each other in the space, which means that our SERS method combined with DA could be used to distinguish different kinds of bacteria.

CONCLUSIONS

In summary, we have developed a low-cost, durable, sensitive, and repeatable SERS substrate based on hydrophobic and nanohierarchical structures of mussel shell. Because of the hydrophobic concentration effect, Au@AgNPs and analyte molecules both aggregate on the mussel shell. The nanohierarchical structures could act as 3D templates for the self-assembly of nanoparticles to form 3D supercrystals. FDTD results have shown that nanoparticles in the channels exhibit apparent higher electromagnetic field enhancement than nanoparticles on the platelets. The distribution of nanoplates in different modes shows no apparent difference of the maximum electromagnetic field enhancement, which makes the distribution of electromagnetic field enhancement more uniform. The periodic gratings on the mussel shell also have made the distribution of nanoparticles with high periodicity on the SERS substrate. All of these have revealed that the special structure of the nacre makes the mussel shell a good candidate for the decoration of nanoparticles to form 3D supercrystals. As a result, the 3D supercrystals could reach an LOD (limit of detection) for R6G as low as 1×10^{-9} M, and signal reproducibility could be significantly improved and measured with a variation of 6.5% at the peak of 613 cm^{-1} . The as-prepared SERS substrate also has been utilized in the discrimination of different kinds of pathogenic bacteria. As shown in Table 1, the mussel shell has demonstrated obvious advantages compared to other natural materials, and it can act as a good substrate for the detection of other practical analytes.

EXPERIMENTAL SECTION

Chemicals, Biochemicals, and Instruments. Mussel shells were purchased from the local market in China.

Rhodamine 6G (Rh6G), chloroauric acid tetrahydrate ($\text{HAuCl}_4 \cdot 4\text{H}_2\text{O}$), trisodium citrate, and ascorbic acid were supplied by Macklin (Shanghai, China). Silver nitrate (AgNO_3) was purchased from Aladdin. Ultrapure water was obtained using a Millipore water purification system. All chemicals were of the analytical grade. *E. coli* (ATCC8739), *S. aureus* (ATCC6538), and *P. aeruginosa* (PAO1) shock-frozen strains were purchased from Guangdong Microbial Culture Center (Guangdong, China).

The morphologies and microstructures of the mussel shell-based substrate were investigated by field-emission scanning electron microscopy (ZEISS ULTRA55), and the core-shell structures Au@AgNPs were characterized using a transmission electron microscope (JEM-2100F). UV–vis spectra were recorded with a Varian Cary-5000 UV–vis–NIR spectrophotometer. SERS measurements were conducted with a Raman microscope (LabRAM HR, HORIBA Scientific, Japan). The CA was measured with OCA20 machine (Data Physics, Germany).

Preparation of Au and Ag Nanoparticles (AuNPs).

Before use, all glassware were soaked in 3:1 HNO_3/HCl overnight, followed by ultrapure water and dried in the dry oven. AuNPs and AgNPs were all prepared according to the previous report with some modifications.⁴⁰ First, $125 \mu\text{L}$ of HAuCl_4 solution (0.1 M) was added to 50 mL of boiling ultrapure water under magnetic stirring. Subsequently, $750 \mu\text{L}$ of trisodium citrate (1%) was added, and the solution was agitated for 30 min to obtain a wine-red suspension. After the suspension was cooled to room temperature, the as-prepared AuNPs were filtered through a $0.22 \mu\text{m}$ Millipore membrane and stored at $4 \text{ }^\circ\text{C}$. For Ag nanoparticle preparation, 90 mg of AgNO_3 was first dissolved in 250 mL of ultrapure water and brought to boiling. Then, 10 mL trisodium citrate (1%) was added into the above solution and kept boiling for 1 h. The AgNP colloids were obtained after cooling to room temperature. The calculation of concentrations of AuNPs and AgNPs is based on the Beer's law and the extinction coefficient ($\epsilon_{\text{Au}} = 3 \times 10^9 \text{ M}^{-1} \text{ cm}^{-1}$ and $\epsilon_{\text{Ag}} = 2.3 \times 10^{10} \text{ M}^{-1} \text{ cm}^{-1}$). Thus, the concentrations of AuNPs and AgNPs are ~ 0.26 and $\sim 0.62 \text{ nM}$.³⁵

Synthesis of Au@Ag Nanoparticles with Different Ag Shell Thickness.

All glassware were treated with 3:1 HNO_3/HCl and ultrasonically with deionized water prior to use. Au@AgNPs were prepared through the reduction of silver nitrate onto the surface of as-prepared AuNPs, according to the previous report.⁴¹ In a 50 mL flask, 10 mL of the as-prepared AuNPs and 1.5 mL of ascorbic acid (0.1 M) were mixed and kept under stirring. Then, 1 mM AgNO_3 was added drop by drop and stirred for 30 min at room temperature. For different thicknesses of Ag shells from 1 to 9 nm, the volumes of 1 mM AgNO_3 solution were increased from 0.5 to 4.5 mL. The as-prepared Au@AgNPs with different Ag shell thicknesses were stored at $4 \text{ }^\circ\text{C}$ for the further self-assembly with mussel shell.

The final concentration of Au@AgNPs is $\sim 0.18\text{--}0.25$ nM, as calculated based on Au cores and the change of volume.³⁵

Fabrication of SERS Substrates. The mussels obtained commercially were first scalded with boiling water for a moment, and the meats were removed from the shell. Then, the mussel shells were washed in an ultrasound bath with ethanol and deionized water in turn for 10 min individually. As depicted in Figure S1, a 20 μL droplet of a suspension of different Ag shell thickness of Au@AgNPs was placed on the nacre of the mussel shell and allowed to dry naturally. For different experimental aims, a 20 μL droplet of rhodamine 6G with different concentrations were then placed on the SERS substrate and allowed to dry again.

Bacteria Preparation and SERS Measurements. Shock-frozen *E. coli*, *P. aeruginosa*, and *S. aureus* cells were cultivated in Luria–Bertani medium in a gyratory shaker at 100 rpm and 37 $^{\circ}\text{C}$ for 16 h. Five milliliters of bacteria were harvested and washed twice with deionized water by centrifugation at 4000 rpm and 25 $^{\circ}\text{C}$. Subsequently, the obtained bacteria were utilized for the SERS measurement.

The Raman signals of R6G and three different kinds of bacteria were obtained after the droplet evaporated naturally and measured on the Raman system with the 633 nm laser as excitation. The power density of the laser is 16.0 $\text{mW}/\mu\text{m}^2$. A 50 \times objective lens was used, and the time acquisition was 5 s.

■ ASSOCIATED CONTENT

Supporting Information

The Supporting Information is available free of charge on the ACS Publications website at DOI: 10.1021/acsomega.8b00023.

Process flow of concentrating Au@AgNPs and analytes on the nacre of mussel shell; UV–vis spectra of Au@AgNPs with different Ag shell thickness; mechanical properties among mussel shell and other different kinds of natural materials; stability of Au@AgNPs self-assembled mussel shell SERS substrate; large scale of the mussel shell substrate; colorful nacre on the mussel shell and SEM image of the periodic grating microstructures of nacre; and Raman spectrum of R6G powder and SERS spectra of R6G solution (PDF)

■ AUTHOR INFORMATION

Corresponding Authors

*E-mail: haibo.zhou@jnu.edu.cn (H.Z.).

*E-mail: jzjackson@hotmail.com (Z.J.).

ORCID

Beatriz Jurado Sánchez: 0000-0002-6584-1949

Xiangjiang Liu: 0000-0002-5419-669X

Nicoleta Elena Dina: 0000-0002-0435-2105

Haibo Zhou: 0000-0002-0098-5968

Author Contributions

*K.Y. and J.Z. contributed equally.

Notes

The authors declare no competing financial interest.

■ ACKNOWLEDGMENTS

This work was supported by the National Natural Science Foundation of China (nos. 21505053, 81773684, 21405138, and 81773593), the Pearl River S&T Nova Program of Guangzhou (201806010060 and 201610010100), the Science and Technology Planning Project of Guangdong Province,

China (nos. 2015A020211018, 2015A030401045, and 2016A030310089), the Excellent Young Teachers Program of Guangdong Provincial colleges and universities (YQ 2015061), the Science Foundation of Zhejiang Province (no. LY17H260003), and the Ningbo Natural Science Foundation (no. 2017A610226).

■ REFERENCES

- (1) Ding, S.-Y.; You, E.-M.; Tian, Z.-Q.; Moskovits, M. Electromagnetic theories of surface-enhanced Raman spectroscopy. *Chem. Soc. Rev.* **2017**, *46*, 4042–4076.
- (2) Tang, L.; Li, S.; Han, F.; Liu, L.; Xu, L.; Ma, W.; Kuang, H.; Li, A.; Wang, L.; Xu, C. SERS-active Au@Ag nanorod dimers for ultrasensitive dopamine detection. *Biosens. Bioelectron.* **2015**, *71*, 7–12.
- (3) Zhou, H.; Yang, D.; Ivleva, N. P.; Mircescu, N. E.; Niessner, R.; Haisch, C. SERS detection of bacteria in water by in situ coating with Ag nanoparticles. *Anal. Chem.* **2014**, *86*, 1525–1533.
- (4) Mei, Q.; Jing, H.; Li, Y.; Yisibashaer, W.; Chen, J.; Li, B. N.; Zhang, Y. Smartphone based visual and quantitative assays on upconversional paper sensor. *Biosens. Bioelectron.* **2016**, *75*, 427–432.
- (5) Chen, K.; Zhang, X.; MacFarlane, D. R. Ultrasensitive surface-enhanced Raman scattering detection of urea by highly ordered Au/Cu hybrid nanostructure arrays. *Chem. Commun.* **2017**, *53*, 7949–7952.
- (6) Wu, Y.; Hang, T.; Komadina, J.; Ling, H.; Li, M. High-adhesive superhydrophobic 3D nanostructured silver films applied as sensitive, long-lived, reproducible and recyclable SERS substrates. *Nanoscale* **2014**, *6*, 9720–9726.
- (7) Hasna, K.; Antony, A.; Puigdollers, J.; Kumar, K. R.; Jayaraj, M. K. Fabrication of cost-effective, highly reproducible large area arrays of nanotriangular pillars for surface enhanced Raman scattering substrates. *Nano Res.* **2016**, *9*, 3075–3083.
- (8) Chen, B.; Meng, G.; Huang, Q.; Huang, Z.; Xu, Q.; Zhu, C.; Qian, Y.; Ding, Y. Green synthesis of large-scale highly ordered core@shell nanoporous Au@Ag nanorod arrays as sensitive and reproducible 3D SERS substrates. *ACS Appl. Mater. Interfaces* **2014**, *6*, 15667–15675.
- (9) Zhang, Q.; Lee, Y. H.; Phang, I. Y.; Lee, C. K.; Ling, X. Y. Hierarchical 3D SERS substrates fabricated by integrating photolithographic microstructures and self-assembly of silver nanoparticles. *Small* **2014**, *10*, 2703–2711.
- (10) Zhang, X.; Xiao, X.; Dai, Z.; Wu, W.; Zhang, X.; Fu, L.; Jiang, C. Ultrasensitive SERS performance in 3D “sunflowerlike” nanoarrays decorated with Ag nanoparticles. *Nanoscale* **2017**, *9*, 3114.
- (11) Liu, H.; Yang, L.; Liu, J. Three-dimensional SERS hot spots for chemical sensing: Towards developing a practical analyzer. *TrAC, Trends Anal. Chem.* **2016**, *80*, 364–372.
- (12) Chirumamilla, M.; Chirumamilla, A.; Roberts, A. S.; Zaccaria, R. P.; De Angelis, F.; Kristensen, P. K.; Krahne, R.; Bozhevolnyi, S. L.; Pedersen, K.; Toma, A. Hot-spot engineering in 3D multi-branched nanostructures: Ultrasensitive substrates for surface-enhanced Raman spectroscopy. *Adv. Opt. Mater.* **2017**, *5*, 1600836.
- (13) Hatab, N. A. A.; Oran, J. M.; Sepaniak, M. J. Surface-enhanced Raman spectroscopy substrates created via electron beam lithography and nanotransfer printing. *ACS Nano* **2008**, *2*, 377–385.
- (14) Yang, S.; Lapsley, M. I.; Cao, B.; Zhao, C.; Zhao, Y.; Hao, Q.; Kiraly, B.; Scott, J.; Li, W.; Wang, L.; Lei, Y.; Huang, T. J. Large-Scale fabrication of three-dimensional surface patterns using template-defined electrochemical deposition. *Adv. Funct. Mater.* **2013**, *23*, 720–730.
- (15) Yang, S.; Slotcavage, D.; Mai, J. D.; Guo, F.; Li, S.; Zhao, Y.; Lei, Y.; Cameron, C. E.; Huang, T. J. Electrochemically created highly surface roughened Ag nanoplate arrays for SERS biosensing applications. *J. Mater. Chem. C* **2014**, *2*, 8350–8356.
- (16) Zhang, J.; Zhang, X.; Chen, S.; Gong, T.; Zhu, Y. Surface-enhanced Raman scattering properties of multi-walled carbon nanotubes arrays-Ag nanoparticles. *Carbon* **2016**, *100*, 395–407.

- (17) Cui, S.; Dai, Z.; Tian, Q.; Liu, J.; Xiao, X.; Jiang, C.; Wu, W.; Roy, V. A. L. Wetting properties and SERS applications of ZnO/Ag nanowire arrays patterned by a screen printing method. *J. Mater. Chem. C* **2016**, *4*, 6371–6379.
- (18) Lee, C. H.; Hankus, M. E.; Tian, L.; Pellegrino, P. M.; Singamaneni, S. Highly sensitive surface enhanced Raman scattering substrates based on filter paper loaded with plasmonic nanostructures. *Anal. Chem.* **2011**, *83*, 8953–8958.
- (19) Liu, N.; Gong, M.; Zhang, P.; Li, L.; Li, W.; Lee, R. Silver-embedded zeolite crystals as substrates for surface-enhanced Raman scattering. *J. Mater. Sci.* **2011**, *46*, 3162–3168.
- (20) Novara, C.; Marta, S. D.; Virga, A.; Lamberti, A.; Angelini, A.; Chiadò, A.; Rivolo, P.; Geobaldo, F.; Sergio, V.; Bonifacio, A.; Giorgis, F. SERS-active Ag nanoparticles on porous silicon and PDMS substrates: A comparative study of uniformity and Raman efficiency. *J. Phys. Chem. C* **2016**, *120*, 16946–16953.
- (21) Gong, Z.; Du, H.; Cheng, F.; Wang, C.; Wang, C.; Fan, M. Fabrication of SERS swab for direct detection of trace explosives in fingerprints. *ACS Appl. Mater. Interfaces* **2014**, *6*, 21931–21937.
- (22) Chou, S.-Y.; Yu, C.-C.; Yen, Y.-T.; Lin, K.-T.; Chen, H.-L.; Su, W.-F. Romantic story or Raman scattering? Rose petals as ecofriendly, low-cost substrates for ultrasensitive surface-enhanced Raman scattering. *Anal. Chem.* **2015**, *87*, 6017–6024.
- (23) Koch, K.; Bhushan, B.; Barthlott, W. Diversity of structure, morphology and wetting of plant surfaces. *Soft Matter* **2008**, *4*, 1943–1963.
- (24) Huang, J.-A.; Zhang, Y.-L.; Zhao, Y.-Q.; Zhang, X.-L.; Sun, M.-L.; Zhang, W. Superhydrophobic SERS chip based on Ag coated natural taro-leaf. *Nanoscale* **2016**, *8*, 11487–11493.
- (25) Sharma, V.; Kumar, S.; Jaiswal, A.; Krishnan, V. Gold deposited plant leaves for SERS: Role of surface morphology, wettability and deposition technique in determining the enhancement factor and sensitivity of detection. *ChemistrySelect* **2017**, *2*, 165–174.
- (26) Xu, B.-B.; Zhang, Y.-L.; Zhang, W.-Y.; Liu, X.-Q.; Wang, J.-N.; Zhang, X.-L.; Zhang, D.-D.; Jiang, H.-B.; Zhang, R.; Sun, H.-B. Silver-coated rose petal: Green, facile, low-cost and sustainable fabrication of a SERS substrate with unique superhydrophobicity and high efficiency. *Adv. Opt. Mater.* **2013**, *1*, 56–60.
- (27) Lv, M. Y.; Teng, H. Y.; Chen, Z. Y.; Zhao, Y. M.; Zhang, X.; Liu, L.; Wu, Z.; Liu, L. M.; Xu, H. J. Low-cost Au nanoparticle-decorated cicada wing as sensitive and recyclable substrates for surface enhanced Raman scattering. *Sens. Actuators, B* **2015**, *209*, 820–827.
- (28) Song, G.; Zhou, H.; Gu, J.; Liu, Q.; Zhang, W.; Su, H.; Su, Y.; Yao, Q.; Zhang, D. Tumor marker detection using surface enhanced Raman spectroscopy on 3D Au butterfly wings. *J. Mater. Chem. B* **2017**, *5*, 1594.
- (29) Liu, X.; Zhou, J.; Xue, Z.; Gao, J.; Meng, J.; Wang, S.; Jiang, L. Clam's shell inspired high-energy inorganic coatings with underwater low adhesive superoleophobicity. *Adv. Mater.* **2012**, *24*, 3401–3405.
- (30) Alvarez-Puebla, R. A.; Agarwal, A.; Manna, P.; Khanal, B. P.; Aldeanueva-Potel, P.; Carbo-Argibay, E.; Pazos-Perez, N.; Vigderman, L.; Zubarev, E. R.; Kotov, N. A.; Liz-Marzan, L. M. Gold nanorods 3D-supercrystals as surface enhanced Raman scattering spectroscopy substrates for the rapid detection of scrambled prions. *Proc. Natl. Acad. Sci. U. S. A.* **2011**, *108*, 8157–8161.
- (31) Gómez-Graña, S.; Pérez-Juste, J.; Alvarez-Puebla, R. A.; Guerrero-Martínez, A.; Liz-Marzán, L. M. Self-Assembly of Au@Ag nanorods mediated by gemini surfactants for highly efficient SERS-active supercrystals. *Adv. Opt. Mater.* **2013**, *1*, 477–481.
- (32) Li, X.; Chang, W.-C.; Chao, Y. J.; Wang, R.; Chang, M. Nanoscale structural and mechanical characterization of a natural nanocomposite material: The shell of red abalone. *Nano Lett.* **2004**, *4*, 613–617.
- (33) Snow, M. R.; Pring, A.; Self, P.; Losic, D.; Shapter, J. The origin of the color of pearls in iridescence from nano-composite structures of the nacre. *Am. Mineral.* **2004**, *89*, 1353–1358.
- (34) Shen, Y.; Cheng, X.; Li, G.; Zhu, Q.; Chi, Z.; Wang, J.; Jin, C. Highly sensitive and uniform surface-enhanced Raman spectroscopy from grating-integrated plasmonic nanograss. *Nanoscale Horiz.* **2016**, *1*, 290–297.
- (35) Liu, B.; Han, G.; Zhang, Z.; Liu, R.; Jiang, C.; Wang, S.; Han, M.-Y. Shell thickness-dependent Raman enhancement for rapid identification and detection of pesticide residues at fruit peels. *Anal. Chem.* **2011**, *84*, 255–261.
- (36) Tanahashi, I.; Harada, Y. Silver nanoparticles deposited on TiO₂-coated cicada and butterfly wings as naturally inspired SERS substrates. *J. Mater. Chem. C* **2015**, *3*, 5721.
- (37) Liu, Y.; Shigley, J.; Hurwit, K. Iridescence color of a shell of the mollusk *Pinctada Margaritifera* caused by diffraction. *Opt. Express* **1999**, *4*, 177–182.
- (38) Xu, S.; Xu, W.; Li, H. Method for detecting surface enhanced Raman spectrum based on interference and diffraction stimulation. E.U. Patent CN201010524200, 2010.
- (39) Zhou, H.; Yang, D.; Ivleva, N. P.; Mircescu, N. E.; Schubert, S.; Niessner, R.; Wieser, A.; Haisch, C. Label-free in situ discrimination of live and dead bacteria by surface-enhanced Raman scattering. *Anal. Chem.* **2015**, *87*, 6553–6561.
- (40) Hu, Z.; Xie, M.; Yang, D.; Chen, D.; Jian, J.; Li, H.; Yuan, K.; Jiang, Z.; Zhou, H. A simple, fast, and sensitive colorimetric assay for visual detection of berberine in human plasma by NaHSO₄-optimized gold nanoparticles. *RSC Adv.* **2017**, *7*, 34746–34754.
- (41) Olson, T. Y.; Schwartzberg, A. M.; Orme, C. A.; Talley, C. E.; O'Connell, B.; Zhang, J. Z. Hollow gold-silver double-shell nanospheres: structure, optical absorption, and surface-enhanced Raman scattering. *J. Phys. Chem. C* **2008**, *112*, 6319–6329.

Supporting Information

Self-assembly of Au@Ag nanoparticles on mussel shell to form large-scale 3D supercrystals as natural SERS substrate for detection of pathogenic bacteria

Kaisong Yuan^{a,c†}, Junxia Zheng^{b†}, Danting Yang^d, Beatriz Jurado Sánchez^{c,f}, Xiangjiang Liu^e, Xinjie Guo^a, Chusheng Liu^a, Nicoleta Elena Dina^g, Jingyi Jian^a, Zhijun Bao^a, Ziwei Hu^a, Zhihong Liang^h, Haibo Zhou^{a*}, Zhengjin Jiang^{a*}

^a Institute of Pharmaceutical Analysis, College of Pharmacy, Jinan University, Guangzhou, Guangdong 510632, China.

^b School of Chemical Engineering and Light Industry, Guangdong University of Technology, Guangzhou 510006, China.

^c Department of Analytical Chemistry, Physical Chemistry and Chemical Engineering, University of Alcalá, Alcalá de Henares E-28871, Madrid, Spain.

^d Department of Preventative Medicine, Zhejiang Provincial Key Laboratory of Pathological and Physiological Technology, Medical School of Ningbo University, Ningbo, Zhejiang 315211, China.

^e College of Biosystems Engineering and Food Science, Zhejiang University, Hangzhou 310058, China.

^f Chemical Research Institute “Andrés M. del Río”, University of Alcalá, Alcalá de Henares E-28871, Madrid, Spain.

^g National Institute for Research and Development of Isotopic and Molecular Technologies, 67-103 Donat, 400293 Cluj-Napoca, Romani

^h Analysis and test center, Jinan University, Guangzhou, Guangdong 510632, China.

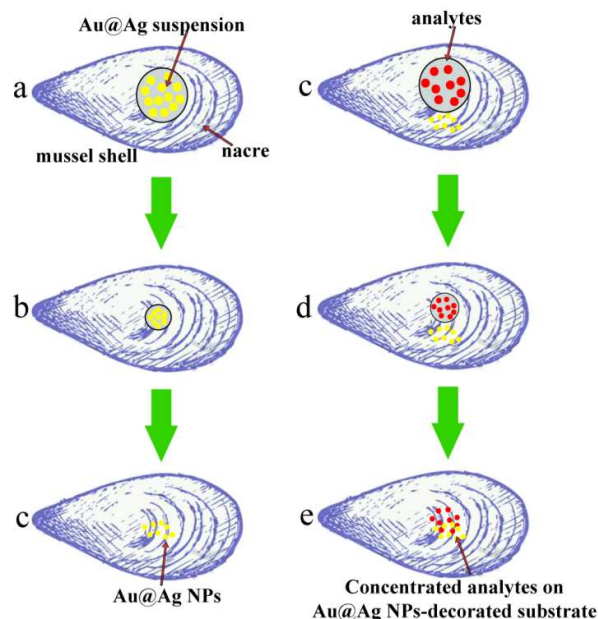


Figure S1. Schematic representation of the process flow of concentrating Au@AgNPs and analytes on the nacre of mussel shell.

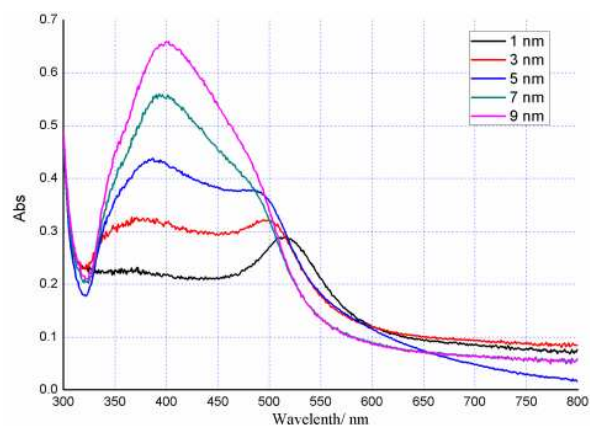


Figure S2. UV-VIS spectra of Au@Ag NPs with different Ag shell thickness.

Comparison of the durable properties. The mussel shell is of great mechanical strength compared with the other kinds of natural materials. In order to verify this conclusion, pulling force experiment was carried out among the mussel shell and other three kinds of natural materials. As depicted in Figure S2a, the rose petal, butterfly wing, lotus leaf and mussel shell were all looks perfect without any damage before the experiment. After the slight pulling force were put on all of these natural

materials respectively, the rose petal, butterfly wing and lotus leaf were all broken while the mussel shell still maintain the original state (Figure S2b). The preservation of these four kinds of natural materials also have been compared and they were placed under the room temperature for 12 hours. As depicted in Figure S2c, the rose petal and lotus leaf became withered while the butterfly wing and mussel shell keep the original state.

Additionally, Raman enhancement ability of the Au@Ag NPs self-assembled mussel shell SERS substrate can be maintained well even when they are stored at room temperature for 3 months and only a little decrease was noted after 6 months (Figure S3a). The substrate also maintains its Raman enhancement ability heating to 25, 50 and 80 °C for 1 hour (Figure S3b). Thus, our mussel shell based substrate have great mechanical strength compared with the other kinds of natural materials and can be used as a durable and wide-application SERS substrate.

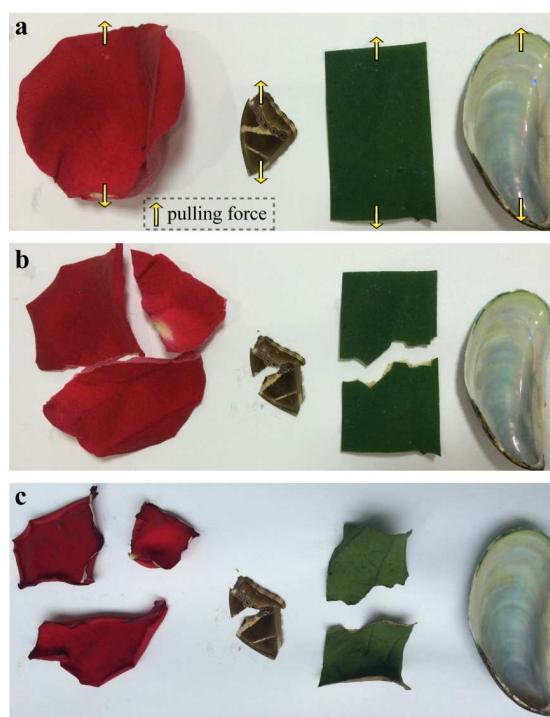


Figure S3. Comparison of the mechanical properties among mussel shell and other different kinds of natural materials. (a-b) Digital photograph of rose petal, butterfly wing, lotus leaf and mussel shell (from left to right) before (a) and after (b) the pulling force experiment. (c) Digital

photograph of the four kinds of natural materials placed under the room temperature for 12 hours

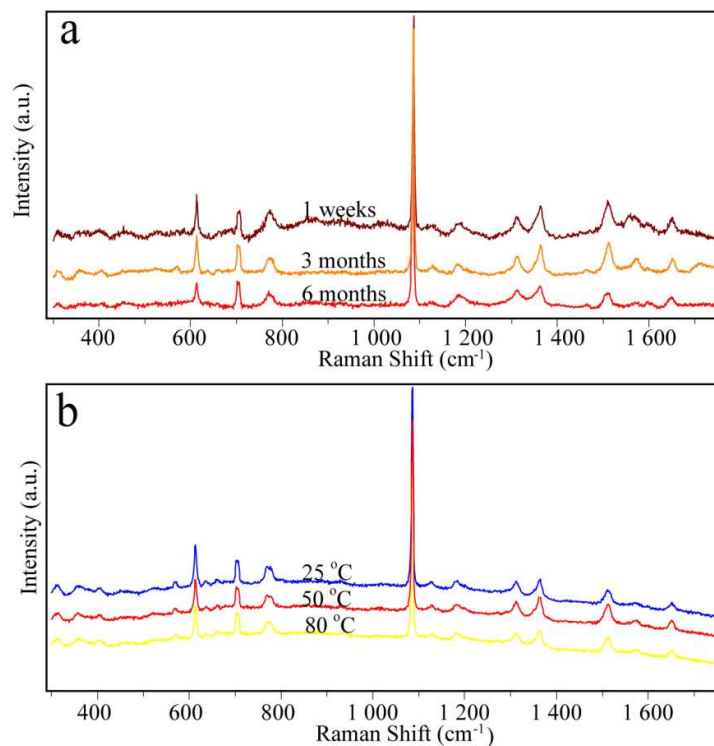


Figure S4 Stability of Au@Ag NPs self-assembled mussel shell SERS substrate. (a) SERS substrate stored for 1 week, 3 and 6 months at room temperature. (b) SERS substrate incubated at 25, 50, 80 °C.

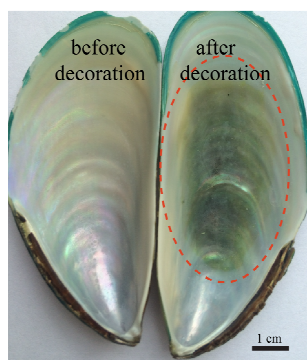


Figure S5 Large-scale of the mussel shell substrate. Before(left) and after(right) Au@AgNPs decoration.

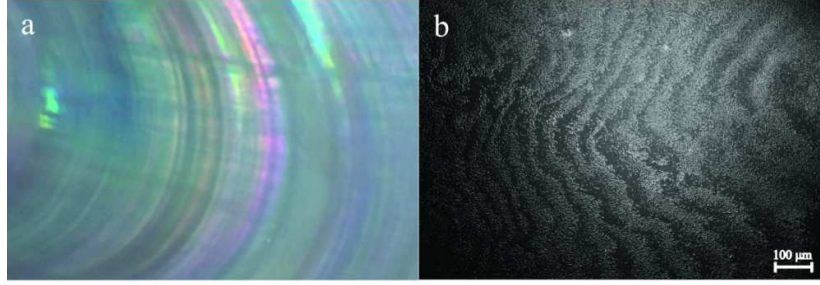


Figure S6. (a) Colorful nacre on the mussel shell taken by digital camera (b) SEM of the periodic grating microstructures of nacre from mussel shell.

Calculation of Enhancement Factor. The SERS enhancement factor (EF) for the 3D substrate was calculated as follows:¹

$$EF = \frac{I_{SERS} / N_{SERS}}{I_{RS} / N_{RS}} = \frac{I_{SERS} \times N_{RS}}{I_{RS} \times N_{SERS}} = \frac{I_{SERS}}{I_{RS}} \frac{D \times H_{\text{eff}} \times \rho_v}{D \times \rho_s} = \frac{I_{SERS}}{I_{RS}} \frac{H_{\text{eff}} \times \rho_v}{\rho_s}$$

where

a) I_{RS} is the signal-to-base Raman intensity of the analyte molecules under non-SERS conditions which in our case is R6G powder on a glass slide and I_{SERS} the intensity under SERS conditions.

b) D is the diameter of the excitation spot of the objective

c) H_{eff} [μm] is the diameter of the excitation spot of the objective, which is measured as $\sim 1.03 \mu\text{m}$ for the $50\times$ objective

d) ρ_v [$\text{mol}/\mu\text{m}^3$] is the volume density of the pure R6G powder. As the mass density of R6G powder is $1.26 \text{ g}/\text{cm}^3$ and the molecular weight of R6G is $479 \text{ g}/\text{mol}$, the ρ_v [$\text{mol}/\mu\text{m}^3$] = $(1.26/479) \times 10^{-12} = 2.63 \times 10^{-15} \text{ mol}/\mu\text{m}^3$

e) ρ_s [$\text{mol}/\mu\text{m}^2$] is the surface density of the R6G molecules adsorbed on the SERS substrate. The $20 \mu\text{L}$ droplet of 10^{-9} M R6G has $10^{-9} \times 20 \times 10^{-6} = 2 \times 10^{-14} \text{ mol}$ molecules. The droplet finally reduces to a contact area with a diameter $\sim 4190 \mu\text{m}$. Thus, ρ_s [$\text{mol}/\mu\text{m}^2$] = $2 \times 10^{-14} / (\pi \times 4190^2) = 3.628 \times 10^{-22} \text{ mol}/\mu\text{m}^2$.

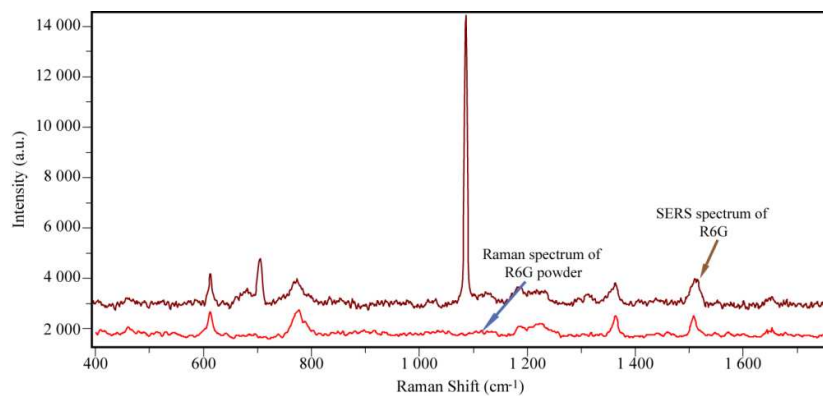


Figure S7. Raman spectrum of R6G powder on a glass slide and SERS spectra of R6G solution

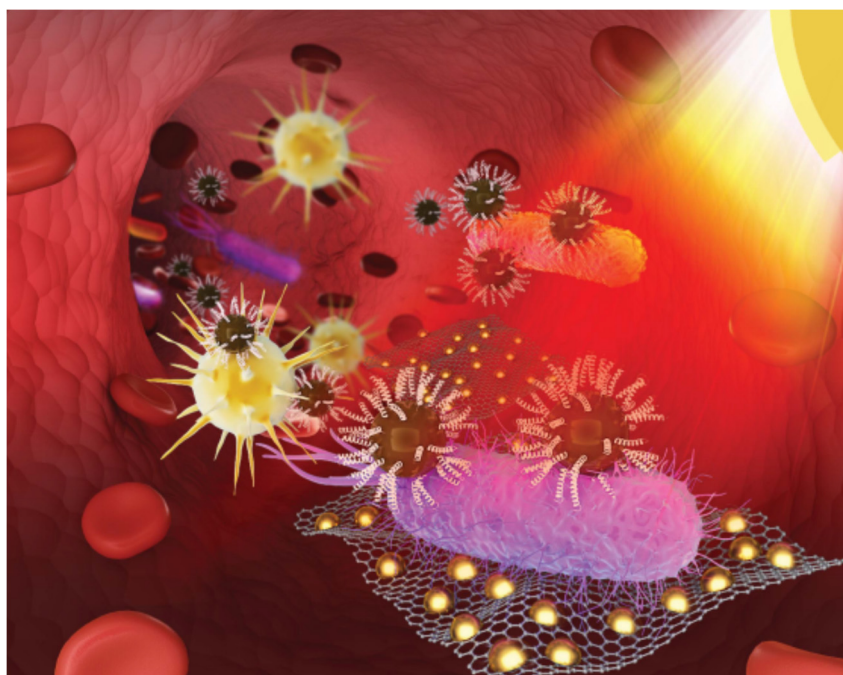
As depicted in Figure S5, Raman signals of R6G have been obviously enhanced through SERS compared with the Raman signals of R6G powder. Therefore, for the 613 cm^{-1} Raman peak, I_{RS} is ~ 1000 counts from Raman spectrum of R6G powder and I_{SERS} is ~ 3000 counts from SERS spectrum of R6G. The EF can be calculated as:

$$EF(613\text{ cm}^{-1}) = (1308/960) \times (1.03 \times 2.63 / 3.628) \times (10^{-15} / 10^{-22}) = 1.02 \times 10^7$$

References

- (1) Huang, J.A.; Zhang, Y.L.; Zhao, Y.Q.; Zhang, X.L.; Sun, M.L.; Zhang, W.J. *Nanoscale* **2016**, *8*, 11487-11493.

III.3. Article 2. Antimicrobial peptide based magnetic recognition elements and Au@Ag-GO SERS tags with stable internal standards: a three in one biosensor for isolation, discrimination and killing of multiple bacteria in whole blood.



III. Janus nanostructures based on graphene and metal nanoparticles for SERS detection and killing of pathogenic bacteria

Cite this: *Chem. Sci.*, 2018, 9, 8781

All publication charges for this article have been paid for by the Royal Society of Chemistry

Antimicrobial peptide based magnetic recognition elements and Au@Ag-GO SERS tags with stable internal standards: a three in one biosensor for isolation, discrimination and killing of multiple bacteria in whole blood†

Kaisong Yuan,^{‡,ac} Qingsong Mei,^{‡,b} Xinjie Guo,^a Youwei Xu,^d Danting Yang,^e Beatriz Jurado Sánchez,^{id c} Bingbing Sheng,^a Chusheng Liu,^a Ziwei Hu,^a Guangchao Yu,^f Hongming Ma,^f Hao Gao,^{*a} Christoph Haisch,^g Reinhard Niessner,^g Zhengjing Jiang^{*a} and Haibo Zhou^{id *a}

In this study, a new biosensor based on a sandwich structure has been developed for the isolation and detection of multiple bacterial pathogens *via* magnetic separation and SERS tags. This novel assay relies on antimicrobial peptide (AMP) functionalized magnetic nanoparticles as “capturing” probes for bacteria isolation and gold coated silver decorated graphene oxide (Au@Ag-GO) nanocomposites modified with 4-mercaptophenylboronic acid (4-MPBA) as SERS tags. When different kinds of bacterial pathogens are combined with the SERS tags, the “fingerprints” of 4-MPBA show corresponding changes due to the recognition interaction between 4-MPBA and different kinds of bacterial cell wall. Compared with the label-free SERS detection of bacteria, 4-MPBA here can be used as an internal standard (IS) to correct the SERS intensities with high reproducibility, as well as a Raman signal reporter to enhance the sensitivity and amplify the differences among the bacterial “fingerprints”. Thus, three bacterial pathogens (*Escherichia coli*, *Staphylococcus aureus* and *Pseudomonas aeruginosa*) were successfully isolated and detected, with the lowest concentration for each of the strains detected at just 10¹ colony forming units per mL (CFU mL⁻¹). According to the changes in the “fingerprints” of 4-MPBA, three bacterial strains were successfully discriminated using discriminant analysis (DA). In addition, the AMP modified Fe₃O₄NPs feature high antibacterial activities, and can act as antibacterial agents with low cellular toxicology in the long-term storage of blood for future safe blood transfusion applications. More importantly, this novel method can be applied in the detection of bacteria from clinical patients who are infected with bacteria. In the validation analysis, 97.3% of the real blood samples (39 patients) could be classified effectively (only one patient infected with *E. coli* was misclassified). The multifunctional biosensor presented here allows for the simultaneous isolation, discrimination and killing of bacteria, suggesting its high potential for clinical diagnosis and safe blood transfusions.

Received 18th October 2018
Accepted 1st November 2018

DOI: 10.1039/c8sc04637a

rsc.li/chemical-science

Introduction

Infections caused by bacterial diseases are a global health threat to the general public and demand the development of fast,

sensitive and accurate diagnostic methods.^{1,2} Traditional methods for pathogen detection fall within three categories: standard plate colony counting, polymerase chain reaction (PCR), and immunology based techniques such as enzyme-

^aInstitute of Pharmaceutical Analysis, College of Pharmacy, Jinan University, Guangzhou, Guangdong 510632, China. E-mail: haibo.zhou@jnu.edu.cn; jzjjackson@hotmail.com; tghao@jnu.edu.cn

^bSchool of Medical Engineering, Hefei University of Technology, Tunxi road 193, Hefei 230009, China

^cDepartment of Analytical Chemistry, Physical Chemistry and Chemical Engineering, University of Alcalá, Alcalá de Henares E-28871, Madrid, Spain

^dShanghai Institute for Advanced Immunochemical Studies, ShanghaiTech University, Shanghai 201210, China

^eDepartment of Preventative Medicine, Zhejiang Provincial Key Laboratory of Pathological and Physiological Technology, Medical School of Ningbo University, Ningbo, Zhejiang 315211, China

^fThe First Affiliated Hospital of Jinan University, Guangzhou, Guangdong 510632, China

^gInstitute of Hydrochemistry and Chair for Analytical Chemistry, Technical University of Munich, Marchioninstr. 17, D-81377, Munich, Germany

† Electronic supplementary information (ESI) available: Additional data and 13 supplementary figures. See DOI: 10.1039/c8sc04637a

‡ K. Y. and Q. M. contributed equally.

linked immunosorbent assays (ELISA).³ Yet, standard plate colony counting always involves separation, identification, culturing and counting, which are complex and time-consuming (typically a few days). Despite PCR and ELISA overcoming such time limitations, such methods require expensive, specialized equipment, complicated sample pretreatment, and even lack the ability to remove interference. To overcome such deficiencies, the development of miniaturized biosensors with much shorter analysis time, higher sensitivity and specificity is currently a hot research topic.^{4–6}

Surface enhanced Raman scattering (SERS) has become a subject of interest which may realize the quick, sensitive and effective detection of bacteria.⁷ The main advantage of the SERS detection of pathogens is the ability to provide sharp, specific fingerprint spectra of the bacteria, making it easy to discriminate among different kinds of bacteria from a mixed sample matrix.⁸ Recently, Wang *et al.* have modified 4-mercaptophenylboronic acid (4-MPBA) on an AgNPs@Si chip for the capture and SERS discrimination of *E. coli* and *S. aureus* in blood samples. When different kinds of bacteria are captured by the 4-MPBA modified chip, the Raman “fingerprints” of 4-MPBA will show corresponding changes; hence the bacteria can be identified. However, the capture of the bacteria is based on the interaction between boronic acid and the diol group of the saccharide. Thus, blood cells with saccharides will also be captured by the SERS chip due to the poor selectivity of 4-MPBA.⁹ Though the “fingerprints” help to discriminate bacteria from the interference, as the sample become more complex, the selectivity will be limited. To improve the detection selectively, recognition elements with higher specificity have been introduced to capture bacteria.^{10–12} They mainly include antibodies,^{13–15} aptamers,^{16,17} and antibiotics.¹⁸ Antibodies with high specificity suffer from high cost, as well as poor stability under harsh environmental conditions. Conversely, aptamers are good recognition elements with high specificity and good stability. Yet, the aptamers available for the specific capture of bacteria are limited. Antibiotics possess the advantages of low cost, high stability, and specificity for the capture of most bacteria. Nevertheless, as a small molecule, an antibiotic provides few binding sites for bacterial recognition, which may restrict their effective capture.

Antimicrobial peptides (AMPs), which are found in multiple niches in nature and typically consist of 10–40 residues, have several attractive advantages as the bacteria capture element.^{19,20} They are intrinsically stable in harsh environments, display lower costs and possess a higher density/number of recognition sites for bacteria capture due to the long chain of the peptide.²¹ Several groups have explored the viability of using AMPs as molecular recognition elements in the impedimetric^{22,23} or electrogenerated chemiluminescence²⁴ detection of bacteria. Their research has fully testified to the effective capture ability of AMP. To our knowledge, the utilization of AMP as a capture element for the SERS detection of bacteria has not yet been reported.

On the other hand, SERS tags with high sensitivity and stability are also an important factor in bacterial detection.

Silver-coated gold nanoparticles (Au@AgNPs) are an excellent SERS substrate which shows higher SERS activity and more uniformity of particle size distribution compared with traditional pure AgNPs and AuNPs.^{25,26} However, the poor stability of Au@Ag NPs will limit their application. They must be kept at low temperature or in a dark place, have a short period of viability and are unsuitable for further surface modification. Graphene-based nanocomposites will solve this problem. Graphene oxide (GO) is a type of 2-D nanomaterial with a large surface area and good biocompatibility.²⁷ It can stabilize the SERS signals and protect metal nanoparticles from oxidation, endowing this flexible substrate with a long-term stability without decline in SERS activity.^{28,29} As a result, the combination with GO will stabilize the SERS activity of Au@AgNPs, making the SERS active substrate more durable and will be beneficial for further chemical modification. Another smart strategy for improving SERS stability is to use an IS (such as 4-mercaptopyridine³⁰ or multilayered graphitic magnetic nanocapsules³¹) to eliminate the influence of uncontrollable aggregation of NPs, which is known to cause significant variations in SERS intensity. Ideally, 4-MPBA is a Raman signal reporter which shows a strong Raman signal and has intrinsic peaks of 1075 cm⁻¹ or 1586 cm⁻¹. It can not only be used as a capture probe to combine with saccharides on bacterial cell walls, as described above,⁹ but is also a desirable IS to correct the SERS intensities.

Inspired by these elegant points, we herein develop a SERS sandwich strategy for the sensitive detection and discrimination of three different kinds of bacteria directly in blood samples. AMP based Fe₃O₄NPs were first used in the selective capture and magnetic enrichment of bacteria from the mixture, and they show some superiority over ordinary 4-MPBA, antibodies, aptamers, or antibiotic based capture elements. Hence, other interference from the mixture such as cells or proteins has been effectively removed, as well as there being an increment in sensitivity due to the magnetic enrichment. Au@Ag-GO nanocomposites with high SERS activity and stability have also been fabricated, and further modified with 4-MPBA to act as SERS tags. The 4-MPBA on the SERS tags not only corrected the SERS intensities, but also enhanced the sensitivity and amplified the differences in the “fingerprints”. Hence, such SERS tags would combine with a bacteria@Fe₃O₄ complex to form a sandwich structure following bacteria capture, and provide strong Raman signals for SERS detection. When different kinds of bacteria combined with 4-MPBA, their SERS “fingerprints” showed corresponding changes. In this way, *E. coli*, *S. aureus* and *P. aeruginosa* were discriminated with LOD of 10¹ CFU mL⁻¹, respectively. This novel method was further used in the detection of bacteria from clinical patients who were infected with bacteria. Additionally, we demonstrate the potential of AMP modified Fe₃O₄NPs to inactivate potential bacterial contamination in blood transfusions settings. This biosensor holds considerable promise to act as a multifunctional platform in the simultaneous capture, discrimination and inactivation of bacteria.

Results and discussion

Pathogen detection principle *via* the SERS sandwich strategy

As illustrated in Fig. 1, the SERS sandwich strategy for the detection of bacteria is based on the formation of a sandwich structure of Fe₃O₄NPs/bacteria/SERS tags. The AMP based Fe₃O₄NPs were first cultured with a sample matrix, containing the bacteria, blood cells, and other interferences (Fig. 1A). Then AMP modified Fe₃O₄NPs will specifically bind to the bacteria, and the presence of the Fe₃O₄NPs will allow for the magnetic separation of the bacteria from the sample matrix (Fig. 1B). In this way, the blood cells or any other interference will be removed (Fig. 1C). Subsequently, SERS tags modified with 4-MPBA as bio-recognition molecules and Raman reporters are added and incubated to form the sandwich structures (Fig. 1D). In this way, the boronic acid group from 4-MPBA will bind to the peptidoglycan from the cell wall of the bacteria. Such interactions are mediated through the interaction of sugar chains or a hydrophilic peptidoglycan layer *via* a reversible cyclic *cis*-diol esterification reaction with the boronic acid group (Fig. S1†).^{32,33} The sandwich structures are then collected *via* magnetic separation and detected by a Raman spectrophotometer (Fig. 1E). In the following SERS detection, 4-MPBA will act as the Raman reporter molecule to provide a strong Raman signal. When different kinds of bacteria are combined with the SERS tags, the Raman “fingerprints” of 4-MPBA will show corresponding changes, which can be used to discriminate among different kinds of bacteria (Fig. 1F). In addition, peaks of 4-MPBA can be used to correct the SERS intensities (Fig. 1G). Hence, this novel SERS sandwich strategy enabled the highly sensitive detection and specific discrimination of pathogenic bacteria.

Fabrication and characterization of Au@Ag-GO nanocomposites

The design and fabrication of 4-MPBA modified Au@Ag-GO SERS tags are illustrated step by step in Fig. 2A, and mainly include the modification of GO with thiol groups, the adsorption of Au@AgNPs onto the GO nanosheet and further modification of Au@Ag-GO with 4-MPBA. Fig. 2A also shows that the color of the Au@AgNPs changes from orange to yellow-green after mixing with thiol modified GO (HS-GO) for 5 min and further turns black after 10 min. This is caused by the thiol induced Au@AgNPs agglomeration, which indicates the successful modification of the thiol group onto the GO surface.

Traditional AgNPs with high SERS activity lack uniformity in particle size, resulting in unstable SERS enhancement, while AuNPs with a uniform distribution are poor in SERS activity. The combination of silver and gold into the Au@AgNPs will provide both high and stable SERS activity. TEM image of Fig. S2B† displays the uniform morphology of Au@AgNPs—average diameter of 35 ± 8 nm—compared with the heterogeneous size distribution of AgNPs—average diameter of 40 ± 11 nm—(Fig. S2A†). Fig. S2C† shows the high magnification TEM images of Au@AgNPs with a gold core and a 5 nm thick silver shell. The SERS activities of AuNPs, AgNPs and Au@AgNPs are also evaluated through the Raman spectra of 10⁻⁹ M rhodamine

6G (R6G) dispersed in their colloidal solutions. The results show that SERS enhancement is higher in 5 nm Au@AgNPs than in AgNPs or AuNPs (Fig. S3A†). In our previous work, we also studied the SERS enhancement of Au@AgNPs with different shell thicknesses, and the results showed that Au@AgNPs with a 5 nm thick shell show the highest SERS enhancement.³⁴ Hence, Au@AgNPs with a 5 nm thick shell were used in the fabrication of the SERS tags.

The ratio of Au@AgNPs to GO nanosheet exerts a strong influence on the morphology of the Au@Ag-GO nanocomposites. Fig. 2C–G illustrate the TEM images of nanocomposites prepared with an increasing Au@Ag/GO ratio (mL : mg) from 0.5 : 1 to 15 : 1. We can see that as the ratio increases, more Au@AgNPs cover the GO surface. When the ratio is 0.5 : 1, few Au@AgNPs can be found on the GO nanosheet. When the ratio is 10 : 1, Au@AgNPs cover the whole GO nanosheet, forming perfect Au@Ag-GO nanocomposites with the highest SERS activities (Fig. 2B). When the ratio is 15 : 1 many aggregated Au@AgNPs can be found on the GO surface, which in turn decreases such a SERS enhancement effect. Thus, an Au@Ag/GO ratio of 10 : 1 is employed in the fabrication of Au@Ag-GO nanocomposites. The powder XRD patterns (Fig. S3B, point 1.3 in the ESI†) and FTIR (Fig. S3C, point 1.3 in the ESI†) also showed the successful fabrication of 4-MPBA modified SERS tags.

Stability and SERS activity of SERS tags

The main advantage of the Au@Ag-GO nanocomposites is the high stability of the SERS signals due to the protection of the reactive Au@AgNPs against oxidation. To confirm this, Au@AgNPs both with and without GO were stored at 4 °C for 0, 7 and 60 days. Then the SERS substrates were mixed with 10⁻⁹ R6G solutions to test their SERS activity. Fig. 3A shows that Au@AgNPs with GO still retain high SERS activity after 60 days, while the SERS activity of pure Au@AgNPs (Fig. 3B) declines seriously after only 7 days. When Au@AgNPs with GO and without GO are placed in sunlight for 0, 12, and 72 hours, the Au@Ag-GO nanocomposites (Fig. 3C) also show clearly higher stability than pure Au@AgNPs. Fig. S3D† shows that the corresponding spectra of 4-MPBA on Au@Ag-GO nanocomposites still retain high Raman intensities after lengthy storage. In addition to the high stability, Au@Ag-GO also shows high SERS activity with an enhancement factor (EF) of 1.1 × 10⁸ (please see Fig. S4, point 1.2 in ESI† for the detailed calculation process). Hence, the as-prepared Au@Ag-GO will provide stable and sensitive signals for SERS detection.

Another advantage of the combination of GO and Au@AgNPs is the higher adsorptive capacity of 4-MPBA. As a colloid solution, pure Au@AgNPs lack stability and a slight excess of 4-MPBA will lead to aggregation of the colloid. Thus, the modification of 4-MPBA onto the surface of pure Au@AgNPs must be strictly controlled, or the ability to capture bacteria will be limited. In our design, we have mixed the Au@AgNPs with different concentrations of 4-MPBA, and the results (Fig. S5A†) showed that when the concentration of 4-MPBA was in excess of 0.25 μg mL⁻¹, the colloidal solution began to change color. In

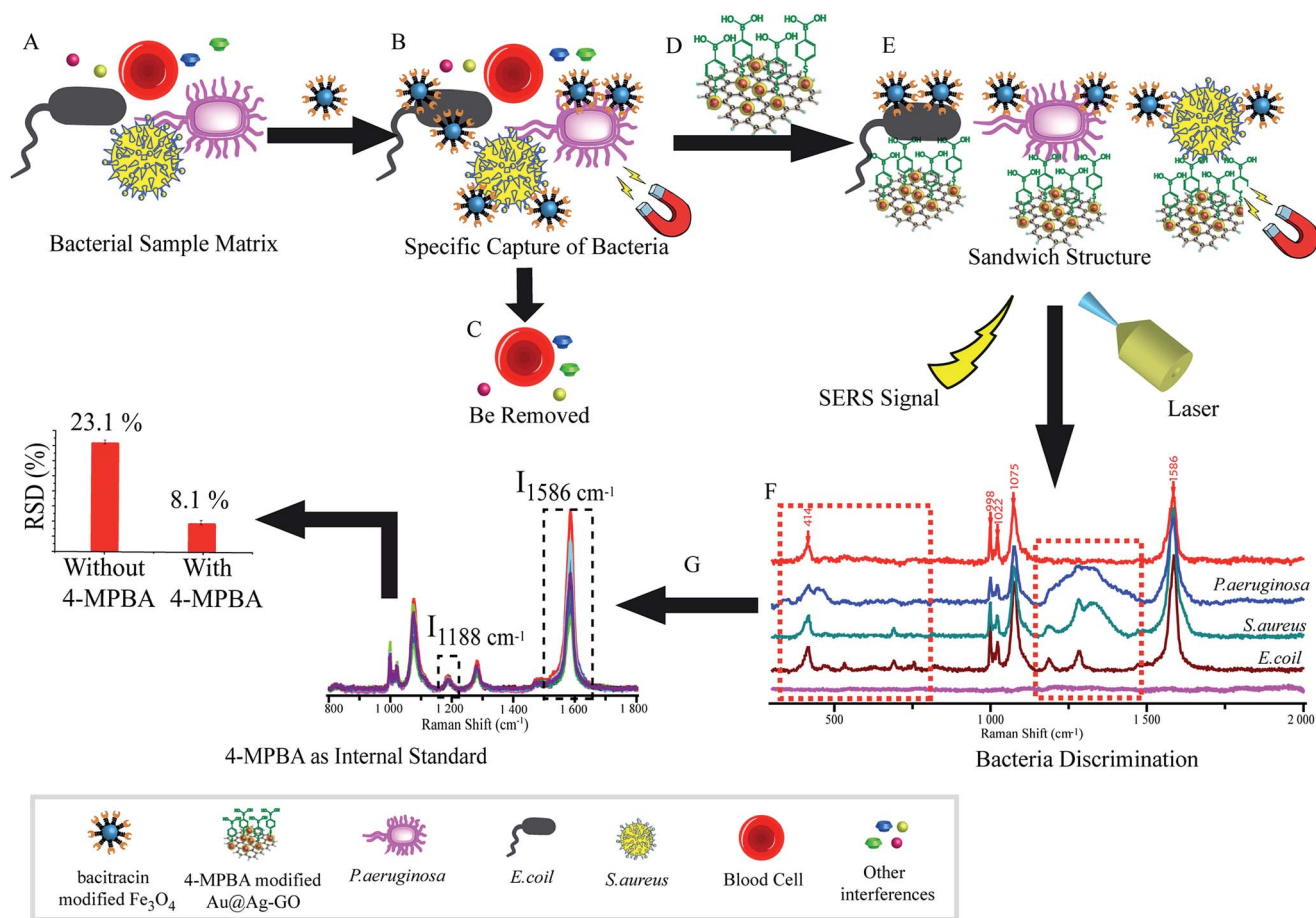


Fig. 1 Schematic illustration of the operating procedures for bacterial detection *via* a SERS sandwich strategy, in which AMP modified magnetic Fe_3O_4 NPs were utilized in the bacteria capture and 4-MPBA modified Au@Ag-GO nanocomposites were used as SERS tags. (A) AMP modified Fe_3O_4 NPs were cultured with a bacterial sample matrix, which included bacteria, blood cells or other interference; (B) the Fe_3O_4 NPs@bacteria complex was magnetically separated from the sample matrix; (C) blood cells or any other interference were removed; (D) 4-MPBA modified Au@Ag-GO nanocomposite SERS tags were cultured with the Fe_3O_4 NPs@bacteria complex to form a sandwich structure; (E) the Fe_3O_4 NPs/bacteria/SERS tags sandwich structure was magnetically separated and detected by the Raman spectrometer; (F) different kinds of bacteria were discriminated according to their Raman "fingerprints"; (G) 4-MPBA can be used as an IS to correct the SERS intensities.

contrast, the Au@Ag-GO shows high stability even in high concentrations of 4-MPBA. As plotted in Fig. S5B,[†] the UV absorption of 4-MPBA is obviously reduced after mixing with Au@Ag-GO. A comparison of the adsorbed amount of 4-MPBA between Au@Ag-GO and Au@AgNPs was conducted through measurement of their surface coverage. The calculation process is shown in the ESI[†] (point 1.1) and the results show that the adsorbed amounts of 4-MPBA on the Au@Ag-GO surface are 25 times more than on pure Au@AgNP, which indicates that the ability to capture bacteria can be greatly increased with an Au@Ag-GO nanocomposite.

Fabrication and characterization of antimicrobial peptide modified Fe_3O_4 NPs

The design and fabrication of an AMP modified Fe_3O_4 magnetic capture substrate are depicted in Fig. 4A, and mainly include the coating of SiO_2 , functionalization of the carboxyl group, and further modification of AMP. The AMP used here is bacitracin A,

with an amino sequence of L-Ile-L-thiazoline-L-Leu-D-Glu-L-Ile-L-Lys-D-Orn-L-Ile-D-Phe-L-His-D-Asp-L-Asn.³⁵

The magnetic hysteresis loops of the as-prepared Fe_3O_4 , Fe_3O_4 @ SiO_2 and Fe_3O_4 @ SiO_2 @AMP are shown in Fig. 4B. All show good ferromagnetic behavior at room temperature. The magnetic saturation (M_s) value of the Fe_3O_4 has decreased from 75.3 emu g^{-1} to 34.2 emu g^{-1} and the further modification of AMP does not apparently decrease the M_s value (31.4 emu g^{-1}). The decrease in the M_s value of Fe_3O_4 @ SiO_2 compared with Fe_3O_4 may be due to the coating with a layer of amorphous SiO_2 . The further slight decrease in the M_s value of Fe_3O_4 @ SiO_2 @AMP compared with Fe_3O_4 @ SiO_2 may be due to the coating with a layer of thin carboxyethyl silanetriol and AMP. Such an excellent magnetic property means that all of the as-prepared materials have a strong magnetic response before and after the modification and can easily separate the analytes from the mixture under an external magnetic field. Besides, the inset of Fig. 4B shows that Fe_3O_4 @ SiO_2 @AMP can be concentrated on the side of the vials within 30 s upon the placement of an

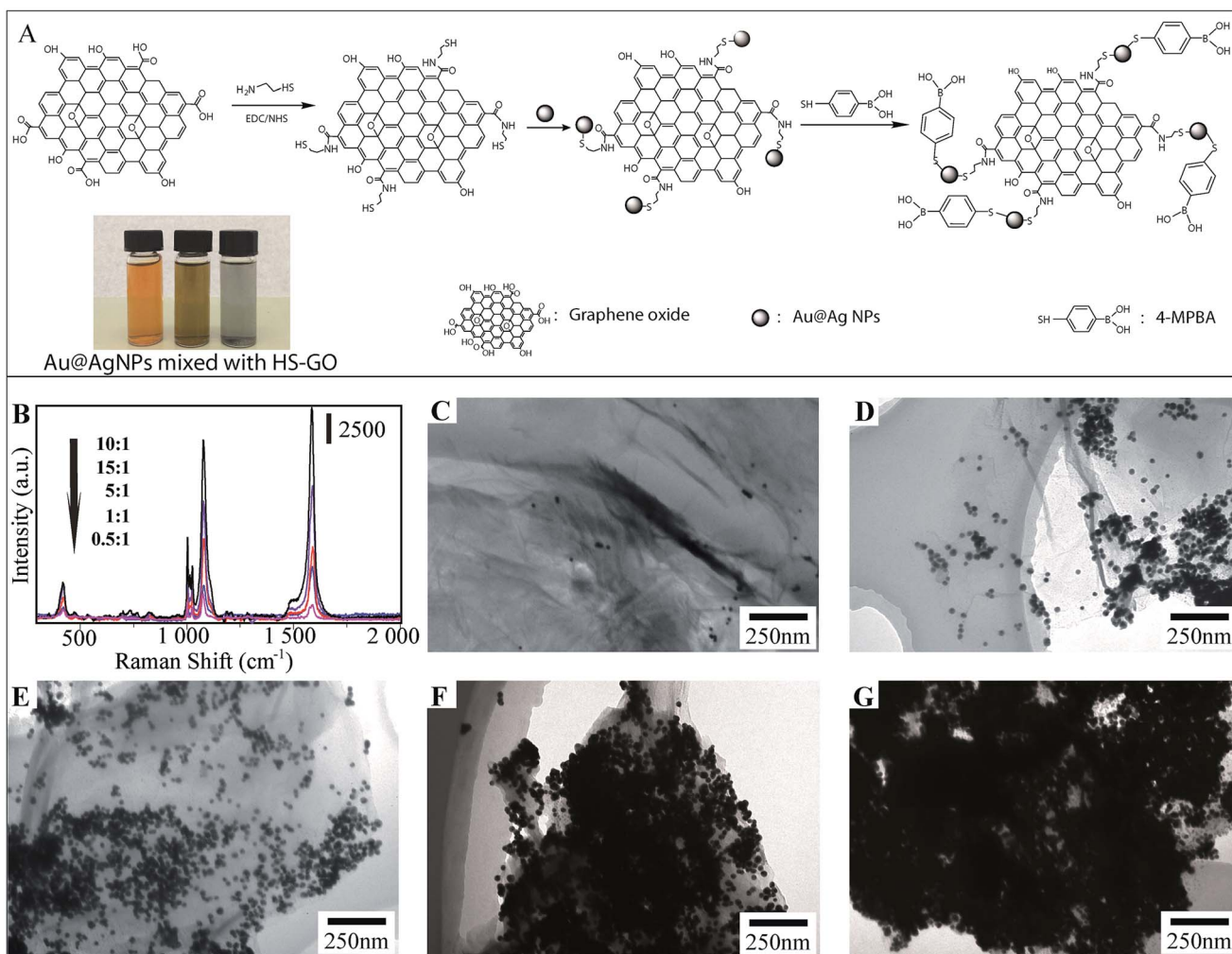


Fig. 2 (A) Schematic illustration of the fabrication of SERS tags and photographs of Ag@AuNPs (left), Au@AgNPs mixed with HS-GO for 5 min (middle) and 10 min (right); (B) SERS enhancement of Au@Ag-GO nanocomposites prepared with different Au@AgNPs/GO ratios (mL : mg): from 0.5 : 1 to 15 : 1. Raman spectra from the 4-MPBA adsorbed on the Au@Ag-GO surface; (C–G) TEM images of Au@Ag-GO nanocomposites prepared with different Au@AgNPs/GO ratios (mL : mg): 0.5 : 1 (C), 1 : 1 (D), 5 : 1 (E), 10 : 1 (F) and 15 : 1 (G).

external magnet next to the vials, which further confirmed the strong magnetic response of $\text{Fe}_3\text{O}_4@\text{SiO}_2@\text{AMP}$. For the morphology measurement, Fig. 4C shows the TEM images of the as-synthesized spherical Fe_3O_4 NPs, with average diameters of 440 ± 30 nm. The TEM image (Fig. 4D) also revealed the core-shell nanostructures of $\text{Fe}_3\text{O}_4@\text{SiO}_2$ NPs with ~ 20 nm of shell thickness. The FTIR (Fig. S6, point 1.4 in the ESI†) also showed the successful synthesis of AMP modified Fe_3O_4 NPs.

The bacteria capture ability of the as-prepared $\text{Fe}_3\text{O}_4@\text{SiO}_2@\text{AMP}$ has also been preliminarily evaluated through a microscope. Fig. 4E is the microscope photograph of the unmodified Fe_3O_4 NPs mixed with *E. coli* after magnetic separation, which shows that only a black substance (Fe_3O_4 aggregates) can be found in the images. In contrast, when we mixed the $\text{Fe}_3\text{O}_4@\text{SiO}_2@\text{AMP}$ with *E. coli* and separated them under the magnetic field, some white points appeared, as indicated with arrows in Fig. 4F. Thus, the AMP is not only successfully modified onto the surface of the Fe_3O_4 NPs, but also has good bacteria capture ability.

Molecular details of target recognition by antimicrobial peptide

In general, the antimicrobial peptide (bacitracin A, Fig. 5A) will recognize the pyrophosphate group of the lipid target on the bacteria due to the AMP-lipid interactions and indirect interactions mediated by the zinc ion and sodium ion.^{36,37} Fig. 5B shows that the interactions are augmented by interactions between the pyrophosphate and two metal ions. The zinc ion adopts an octahedral coordination geometry. Two of the interactions are with oxygen atoms from the lipid (1, 2 of the phosphate groups). The other interactions are the zinc ion interacting with the side chain of D-Glu-4, L-thiazoline-2 and L-Ile-1 from the AMP. A sixth ligand is the interaction between zinc ion and a water molecule. The sodium ion interacts with three oxygen atoms from the lipid (1, 2, 3 of the phosphate groups) and the side chain of L-Ile-5, D-Asp-11, L-Ile-8 from the AMP. Fig. S7A† also shows that AMP was wrapped tightly around the lipid pyrophosphate. As a result, the AMP forms

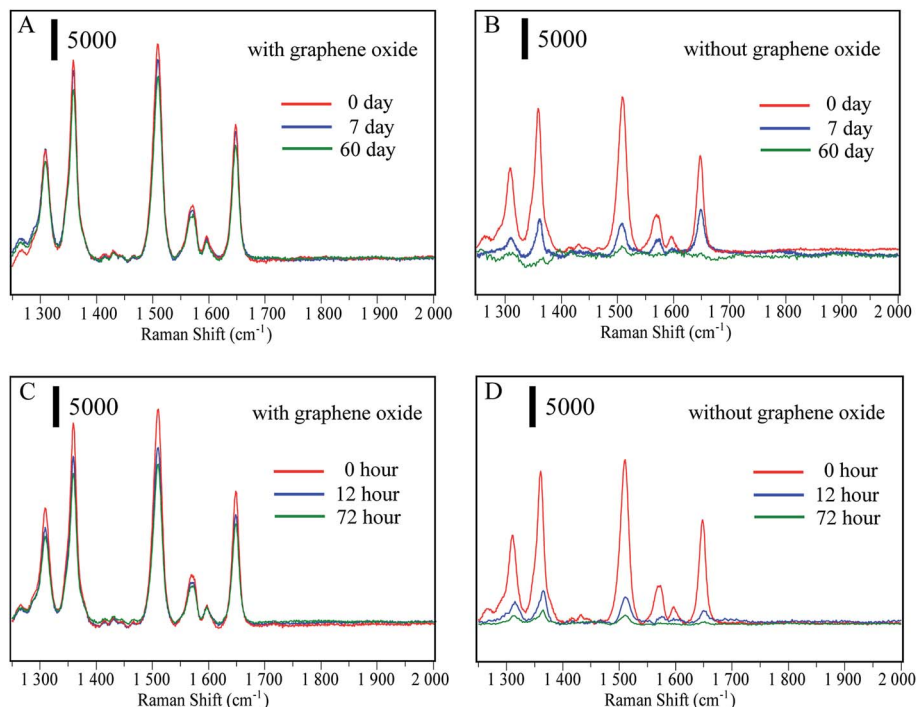


Fig. 3 (A and B) SERS spectra of 10^{-9} M R6G mixed with Au@AgNPs and Au@Ag-GO nanocomposites, both of which are stored at 4 °C for 0, 7 and 60 days; (C and D) SERS spectra of 10^{-9} M R6G mixed with Au@AgNPs and Au@Ag-GO nanocomposites, both of which are placed in sunlight for 0, 12, and 72 hours.

a compact structure that completely envelopes the ligand's pyrophosphate group, which with the co-existence of zinc and sodium ions, thus results in a strong interaction between bacteria and AMP.

Now, we turn our attention to the interaction between peptide modified Fe_3O_4 NPs and pyrophosphate. The published ternary complex of bacitracin A was used as the initial model (PDB entry: 4K7T).³⁸ Then the predicted structure was adjusted

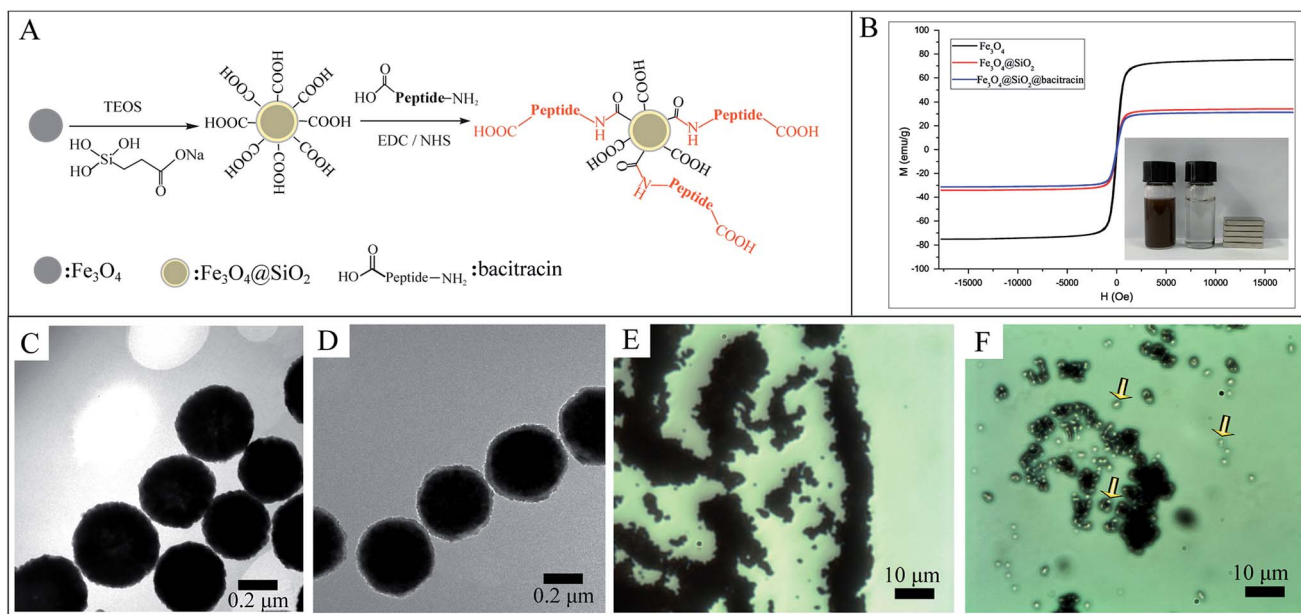


Fig. 4 (A) Schematic illustration of the fabrication of AMP based Fe_3O_4 capture substrate; (B) magnetic hysteresis curves of the synthesized Fe_3O_4 , $\text{Fe}_3\text{O}_4@SiO_2$ and $\text{Fe}_3\text{O}_4@SiO_2@AMP$; (C) TEM image of pure Fe_3O_4 NPs; (D) TEM image of $\text{Fe}_3\text{O}_4@SiO_2$ NPs with a core-shell nano-structure; (E) microscope image of unmodified Fe_3O_4 NPs after mixing with bacteria and magnetically separated; (F) microscope image of $\text{Fe}_3\text{O}_4@SiO_2@AMP$ after incubation with bacteria and magnetically separated; the captured bacteria are indicated with arrows.

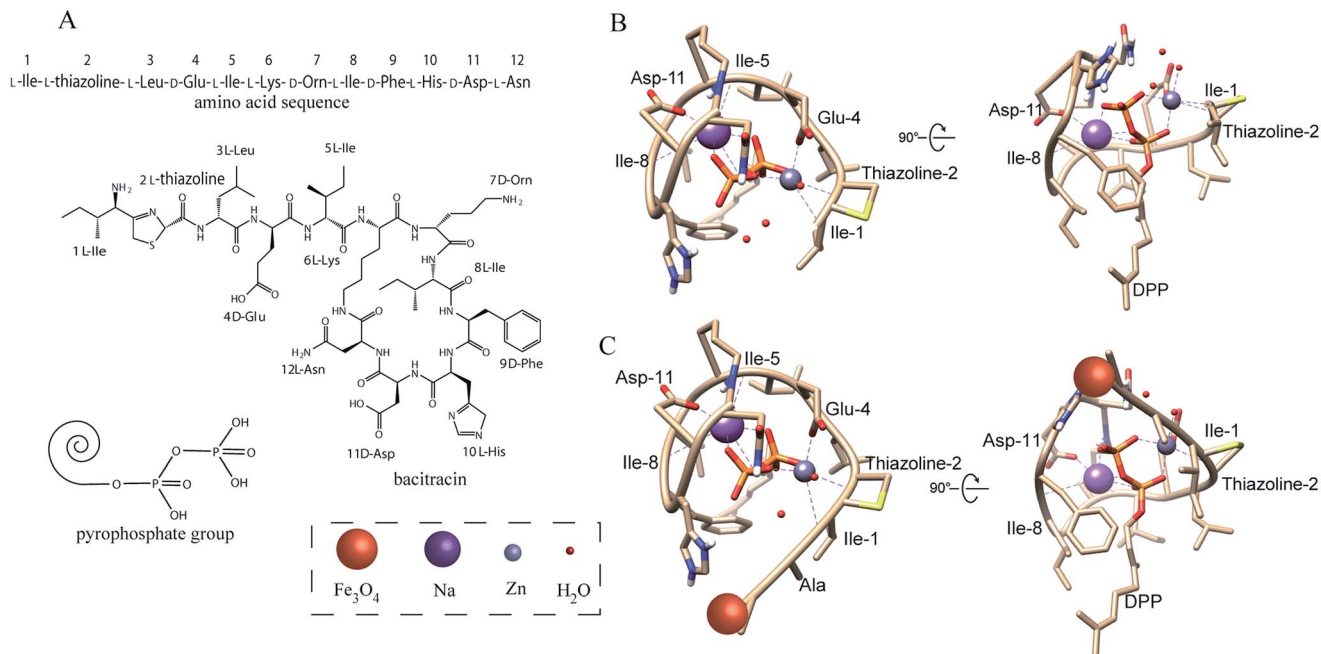


Fig. 5 (A) Amino acid sequence and chemical structure of antimicrobial peptide (bacitracin A); structure of pyrophosphate group of bacteria; (B) predicted structure of AMP bound to the pyrophosphate group of the bacteria. Some special atoms have been colored: red (oxygen), blue (nitrogen), and yellow (sulfur); (C) predicted structure of AMP modified Fe₃O₄ NPs binding to the pyrophosphate group of bacteria.

in the software COOT with minor changes at its amino-terminus.³⁹ In the peptide modification, the N-terminal amino of AMP (1 L-Ile) and the side chain of 7 D-Orn reacts with the carboxyl group on the Fe₃O₄NPs through a condensation reaction. However, the above simulation results showed that the N-terminal amino contributes to the interaction between bacteria and AMP, which may be different after modification. Thus, we simulated the interaction between the pyrophosphate group and the peptide in which the N-terminal amino has been

reacted with the carboxyl group to form an amide group. As shown in Fig. 5C, the amidation of the N-terminal amino will not change the interaction between AMP and bacteria. Fig. S7B† also shows that AMP is still wrapped tightly around the lipid pyrophosphate even after modification onto the Fe₃O₄NPs. Thus, the modification of the peptide onto the Fe₃O₄NPs will not change its recognition site. Though some AMP may react with Fe₃O₄NPs by the side chain of 7 D-Orn (less AMP reacts with the side chain of 7 D-Orn than with the N-terminal amino due to

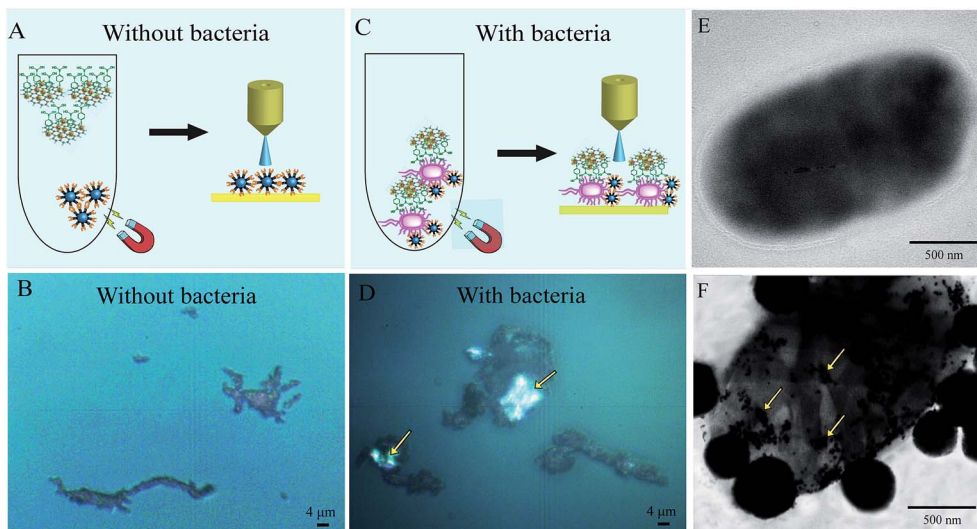


Fig. 6 Schematic illustration of SERS detection in the absence (A) and presence (C) of *E. coli* and (B and D) the corresponding Raman microscope image; (E) TEM image of *E. coli* without any treatment; (F) TEM image of SERS tags/*E. coli*/Fe₃O₄ sandwich structure; the Au@Ag-GO nano-composites are indicated by arrows.

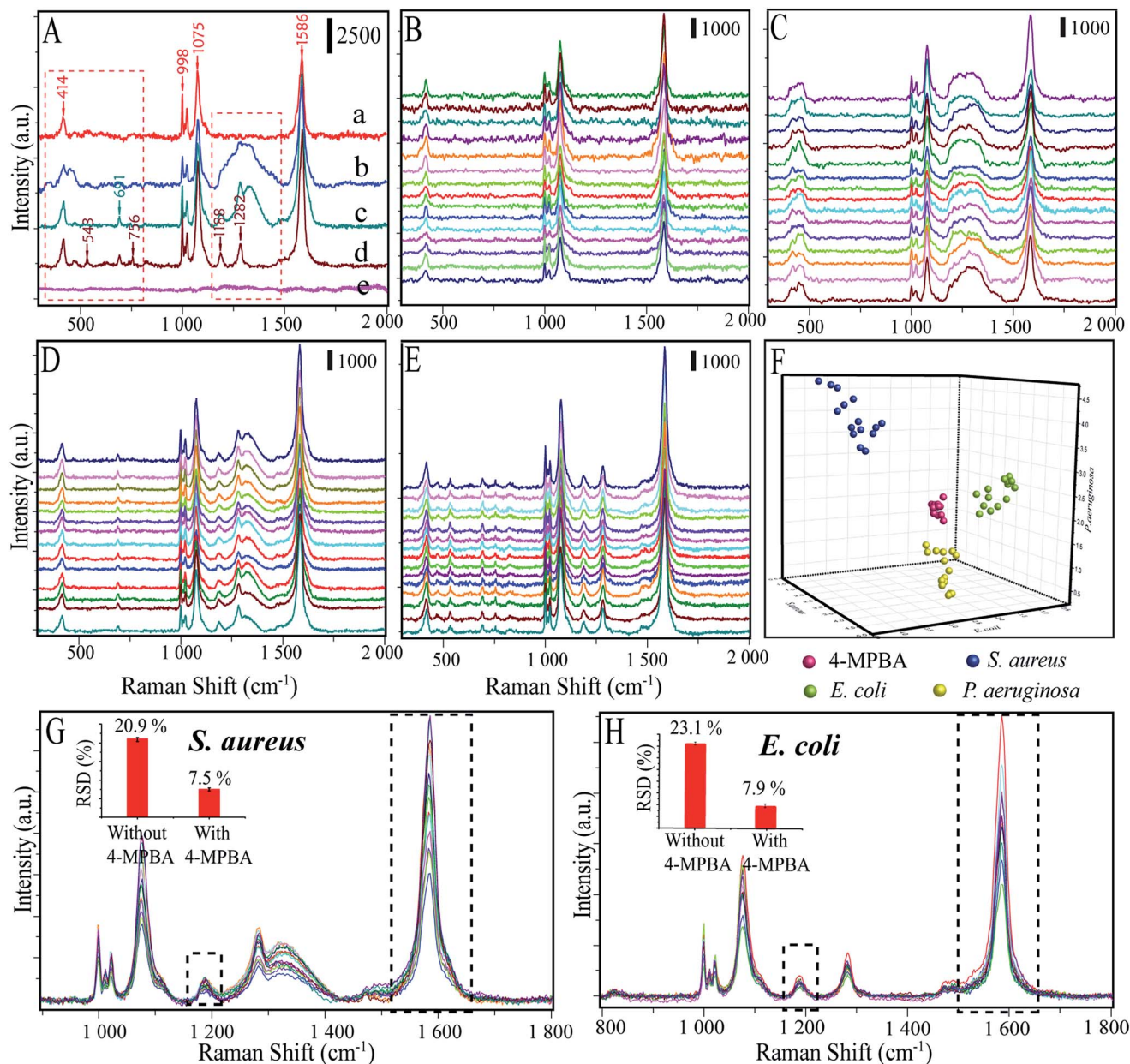


Fig. 7 (A) SERS spectra of 4-MPBA-Au@Ag-GO SERS tags (a); Raman spectra of SERS substrate incubated with *P. aeruginosa* (b), *S. aureus* (c) and *E. coli* (d) to form sandwich structures; no Raman signal was collected in the absence of bacteria (e). (B) Raman spectra of SERS tags were represented by 15 batches; (C–E) SERS spectra of *P. aeruginosa*, *S. aureus*, and *E. coli* were all represented by 15 batches with concentrations of 1×10^4 CFU mL $^{-1}$ each; (F) DA plot showing discrimination among different kinds of bacteria; (G) Raman spectra between 800 and 1800 cm $^{-1}$, where data are extracted from (D), are used for the evaluation of peak stability, the inset photographs are the RSDs (%) calculated from the peak intensity with ($I_{1586 \text{ cm}^{-1}}/I_{1188 \text{ cm}^{-1}}$) and without ($I_{1188 \text{ cm}^{-1}}$) 4-MPBA internal standard normalization; (H) Raman spectra extracted from (E), RSDs (%) are calculated from the peak intensity with ($I_{1586 \text{ cm}^{-1}}/I_{1188 \text{ cm}^{-1}}$) and without ($I_{1188 \text{ cm}^{-1}}$) 4-MPBA.

a higher steric-hinderance effect^{21,40}), this will not influence the interaction between AMP and bacteria, as the side chain of ornithine does not contribute to the interaction, according to the simulation results above.

Detection of bacteria by SERS

To prove the practicality and great potential of the sandwich strategy in application, the 4-MPBA modified Au@Ag-GO nanocomposites and AMP based Fe₃O₄NPs were all applied in

bacterial detection. As illustrated in Fig. 1, the SERS sandwich structure based on AMP recognition included the following processes. First of all, the AMP based Fe₃O₄ capture element was mixed with bacteria under shaking conditions, and then the bacteria were bound to the AMP based Fe₃O₄NPs. After magnetic separation, the bacteria-AMP-Fe₃O₄ complexes were easily separated from the complex samples and washed with PBS to remove the excess free bacteria. Subsequently, the 4-MPBA modified Au@Ag-GO nanocomposites (SERS tags) were

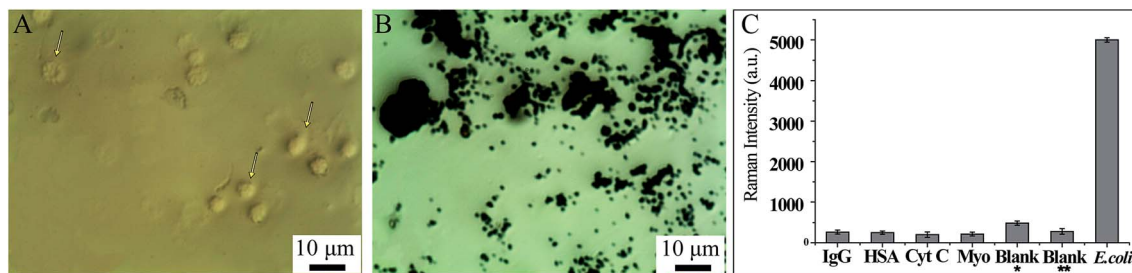


Fig. 8 (A) Microscope image of blank blood, the blood cells are indicated by arrows; (B) microscope image of AMP modified $\text{Fe}_3\text{O}_4\text{NPs}$ after mixing with blank blood and magnetically separated; (C) specificity of the detection of bacteria. *means blank whole blood without dilution, **means blank whole blood with 3 times dilution.

mixed with the above complexes to bind together with the bacteria, which was mainly caused by the interaction between the boronic acid and the diol group from the saccharides of the bacteria wall to form cyclic boronate esters.⁴¹ Hence, the SERS tags/bacteria/ $\text{Fe}_3\text{O}_4\text{NPs}$ sandwich structure was formed, creating many “hotspots” for the following SERS detection.

Fig. 6B, which corresponds to Fig. 6A, shows the substance acquired from the SERS detection process under the Raman microscope. In this situation, no bacteria were added to form the sandwich structure and only the AMP based $\text{Fe}_3\text{O}_4\text{NPs}$ were acquired. Hence, the dark substance distributed in this image can be identified as $\text{Fe}_3\text{O}_4\text{NPs}$ aggregates, and no Raman signals were collected from it (Fig. 7A(e)). Fig. 6D, which corresponds to Fig. 6C, shows the sandwich structures formed under the Raman microscope. In this situation, bacteria were added to form the sandwich structure, and thus the SERS tags could be collected. Compared with Fig. 6B, some bright areas which were caused by the SERS tags appeared, as indicated by the arrows. When we focus the laser point onto the bright area, strong Raman signals will be collected (Fig. 7A(b–d)).

Fig. 6F shows the TEM image of the SERS tags/*E. coli*/ Fe_3O_4 sandwich structure, in which the $\text{Fe}_3\text{O}_4\text{NPs}$ are surrounding the bacteria, and the Au@Ag-GO nanocomposites can be identified on the bacterial surface, as indicated by arrows. Fig. 6E also shows the TEM image of pure *E. coli*, which shows great differences from the sandwich structure.

We further investigated the applicability of this biosensor in distinguishing among different kinds of bacteria by comparing the SERS spectra of *E. coli*, *S. aureus* and *P. aeruginosa*. The Raman spectra of pure 4-MPBA-Au@Ag-GO without bacteria were measured and the results showed that five apparent peaks (*i.e.* at 414, 998, 1022, 1075, and 1586 cm^{-1}) can be identified in the SERS spectrum of 4-MPBA (Fig. 7A(a)). Such Raman bands from 4-MPBA do not interfere with the representative bacterial fingerprint bands in the range between 1100 cm^{-1} and 1400 cm^{-1} , or the peaks between 400 cm^{-1} and 800 cm^{-1} . Thus, different kinds of bacteria can be discriminated from their fingerprint recognition bands. Specifically, two sharp peaks at 1188 cm^{-1} (amide III) and 1282 cm^{-1} ($\delta(\text{CH}_2)$ amide III) were observed in the SERS spectrum of *E. coli* (Fig. 7A(d)). For *S. aureus* (Fig. 7A(c)), peaks at 1188 cm^{-1} (amide III) and 1282 cm^{-1} ($\delta(\text{CH}_2)$ amide III) still exist, and a new broad peak at 1333 cm^{-1} ($\nu(\text{COO}^-)$ and $\delta(\text{C-H})$) appeared. For the *P.*

aeruginosa, only one broad peak at 1333 cm^{-1} ($\nu(\text{COO}^-)$ and $\delta(\text{C-H})$) between 1100 cm^{-1} and 1400 cm^{-1} is observed (Fig. 7A(b)). Additionally, peaks between 400 and 800 cm^{-1} also show some differences between these three bacteria. A sharp peak appeared at 691 cm^{-1} in the detection of *S. aureus* while three sharp peaks appeared at 543 cm^{-1} , 691 cm^{-1} and 756 cm^{-1} in the detection of *E. coli*. Additionally, blank samples have also been investigated and the results show that no Raman signal can be acquired due to no bacteria being added to form the sandwich structure (Fig. 7A(e)). To make the discrimination results more reliable, Raman spectra of 4-MPBA modified Au@Ag-GO, *P. aeruginosa*, *S. aureus* and *E. coli* from 45 batches (each kind of bacteria was represented by 15 batches) were recorded and are shown in Fig. 7B–E. Discriminant analysis (DA) was used to maximize the spectral differences resulting from the data arrays in the discrimination of the bacteria. Fig. 7F shows the 3D map of the DA results, where red balls represent pure 4-MPBA modified Au@Ag-GO, green balls represent *E. coli*, blue balls represent *S. aureus* and yellow balls represent *P. aeruginosa*. It shows that these three different kinds of bacteria and pure 4-MPBA can be completely separated from each other in space, which means that this method combined with DA could be used to discriminate among different kinds of bacteria.

Furthermore, we compared our method (labeling) to the label-free detection of bacteria. In this experiment, AgNPs were simply mixed with the bacteria. As depicted in Fig. S8,† Raman signals in the label-free detection mode (without 4-MPBA) are apparently weaker than in the label detection mode (with 4-MPBA), though the bacteria were in high concentration (1×10^8 CFU mL^{-1}). Importantly, the label-free detection showed no characteristic peaks from the “fingerprints” of these three kinds of bacteria, which can hardly be discriminated with the naked eye. All these results imply that combined with 4-MPBA, our sandwich strategy can enhance detection sensitivity, as well as featuring good capability for discriminating among different kinds of bacteria.

The 4-MPBA utilized here can also act as an IS to eliminate the influence of electromagnetic heterogeneity in enhancing the substrate. As shown in Fig. 7G and H, we extracted the Raman data (800–1800 cm^{-1}) from the above raw spectra of the DA analysis (Fig. 7D and E). The band at 1188 cm^{-1} and the ratio of I_{1586}/I_{1188} were used for relative standard deviation (RSD, %) analysis. Fig. S9A† (*E. coli*) and C (*S. aureus*) showed that the

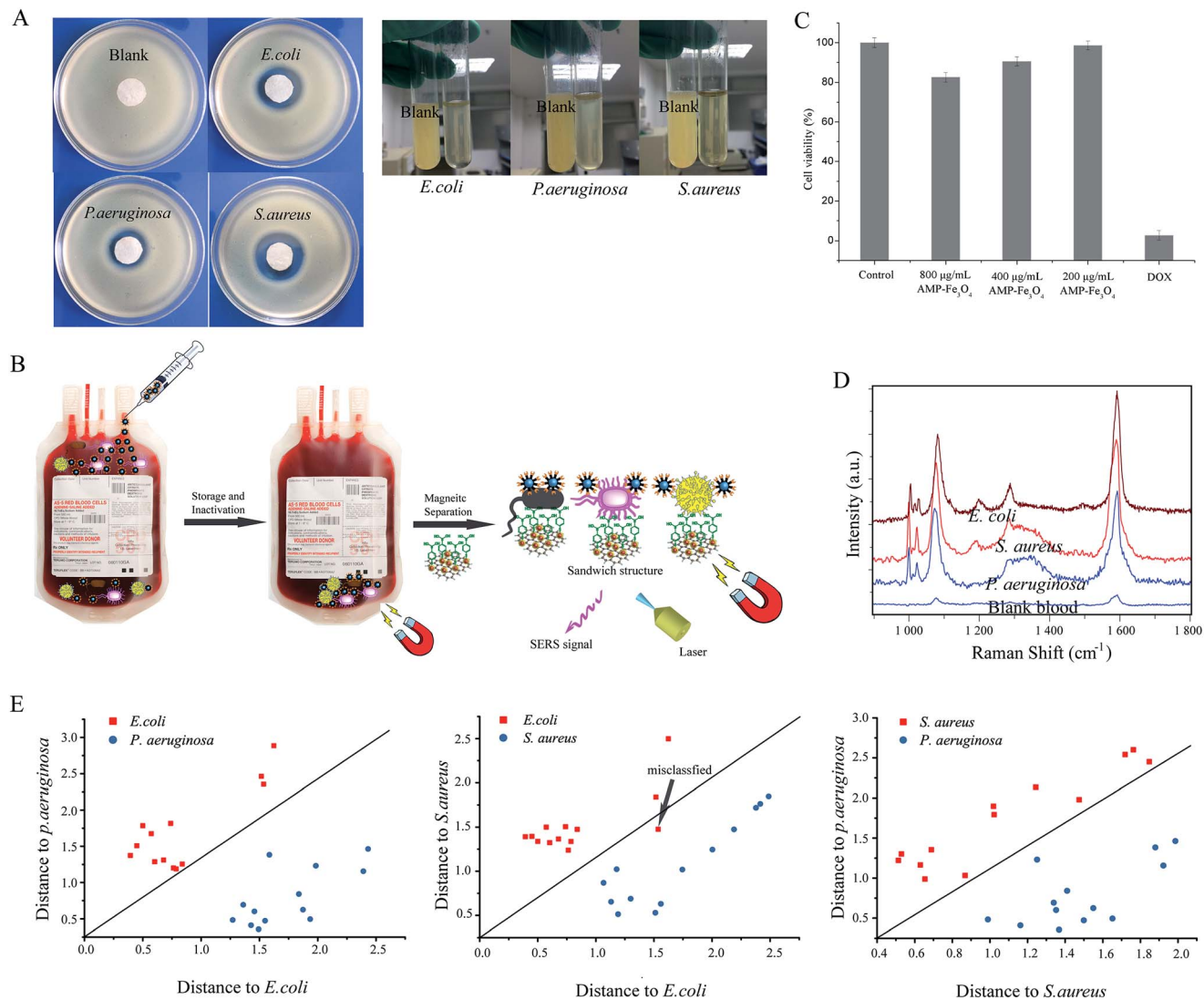


Fig. 9 (A) Antibacterial ability of AMP modified Fe₃O₄NPs in solid medium (left): the blank is *E. coli* treated with pure Fe₃O₄NPs; antibacterial ability of AMP modified Fe₃O₄NPs in whole blood (right), in which the whole blood treated with AMP modified Fe₃O₄NPs or pure Fe₃O₄NPs was cultivated with bacteria first, and then whole blood was spiked in LB medium for further cultivation; the blank is whole blood treated with pure Fe₃O₄NPs and cultivated with bacteria; (B) illustration of AMP modified Fe₃O₄NPs as an antimicrobial agent for the inactivation of bacteria in the storage of blood, and its capture of bacteria for the SERS detection of bacteria before the use of blood; (C) cytotoxicity of AMP modified Fe₃O₄NPs on cells; doxorubicin (DOX) is the positive control group; experiments were performed in triplicate; values represent the relative viability compared to untreated cells as means ± SEM of one representative experiment ($n = 3$); the error bar represents the standard error of the mean (SEM); (D) SERS spectra of whole blood from patients infected with *P. aeruginosa*, *S. aureus* or *E. coli*. Blood without any bacteria is used as the control (E) pairwise Mahalanobis distances of *E. coli*, *S. aureus* and *P. aeruginosa*. The arrow means that only one patient infected with *E. coli* was misclassified.

Raman intensities were very unstable without the 4-MPBA. In contrast (Fig. S9B and D[†]), the ratio of I_{1586}/I_{1188} apparently showed higher stability with 4-MPBA. The results are shown in the inset photographs of Fig. 7G and H. RSDs were significantly reduced from 20.9% to 7.5% (*S. aureus*), and 23.1% to 7.9% (*E. coli*) by using the 4-MPBA IS to eliminate Raman intensity variation.

This novel sandwich strategy also displays excellent enrichment and separation abilities in bacterial detection, which gives it a potential ability to detect very low concentrations of

pathogenic bacteria. The performance of the biosensor in the detection of different concentrations of bacteria was further measured through recording the changes in Raman intensity of the peaks at 1586 cm⁻¹ from the SERS mapping. As depicted in Fig. S10A–F,† the red squares in the SERS mapping results are the SERS signals acquired from different concentrations of *E. coli* (10^1 to 10^6 CFU mL⁻¹). As can be seen, the increase in numbers of red squares corresponded to an increase in bacterial concentration, and a low limit of detection (LOD) of 10^1 CFU mL⁻¹ was achieved.

Table 1 Comparison of different methods for detection of pathogenic bacteria

Method/capture element	Pathogenic bacteria	LOD	Substrate		Ref
			Capture substrate	SERS substrate	
SERS/antibody	<i>S. aureus</i>	10 ¹ CFU mL ⁻¹	MnFe ₂ O ₄ @Au	AuNR	13
SERS/antibody	<i>E. coli</i>	10 ¹ CFU mL ⁻¹	Fe ₃ O ₄	AuNPs	14
SERS/antibody	MRSA, <i>E. coli</i> , <i>S. typhimurium</i>	10 ¹ CFU mL ⁻¹	Fe ₃ O ₄ @Ag	AgNPs	15
SERS/aptamer	<i>S. aureus</i>	10 ¹ CFU mL ⁻¹	MnFe ₂ O ₄ @Au	AuNR	16
SERS/aptamer	<i>S. typhimurium</i> , <i>S. aureus</i>	~10 ¹ CFU mL ⁻¹	Fe ₃ O ₄ @Au	AuNPs	17
SERS/boric acid	<i>E. coli</i> , <i>S. aureus</i>	10 ² CFU mL ⁻¹	Silicon wafer decorated with AgNPs		9
SERS/antibiotic	<i>E. coli</i> , <i>S. aureus</i> , MRSA	10 ² CFU mL ⁻¹	Fe ₃ O ₄ @Ag		18
Electrical detection/AMP	<i>E. coli</i>	1 bacterium/μL	Microelectrode array		45
Infrared-integrated sensors/AMP	<i>L. monocytogenes</i>	1 bacterium/μL	Microfluidic channel on a biomaterial cantilever		46
SERS/AMP	<i>E. coli</i> , <i>S. aureus</i> , <i>P. aeruginosa</i>	10 ¹ CFU mL ⁻¹	Fe ₃ O ₄	Au@Ag-GO	This work

High specificity but with low stability and high cost
 High specificity but with low stability and high cost
 High specificity, simultaneous detection but with low stability, high cost and tedious modification process
 High specificity, high stability but aptamers available for specific capture of bacteria are limited
 High specificity, high stability, simultaneous detection but with tedious modification process and aptamers available for specific capture of bacteria are limited
 High stability, low cost, simultaneous detection but with poor specificity (not specific for bacteria)
 High stability, low cost, specific for bacteria but are limited in recognition sites as a small molecule
 High stability, low cost, high specificity for bacteria and more recognition sites due to the long chain of the peptide
 High stability, low cost, high specificity for bacteria and more recognition sites due to the long chain of the peptide
 High stability, low cost, high specificity for bacteria and more recognition sites due to the long chain of the peptide

Inactivation and detection of bacteria in blood

Firstly, the specificity of our SERS biosensors has been evaluated in the presence of IgG, HAS, Cyt C, Myo at the same concentrations of 4 ng mL^{-1} , as well as with blank whole blood with and without dilution. Fig. 8A shows the blood cells under a microscope: we can see that the blood cells can be easily identified (indicated by arrows). When AMP modified $\text{Fe}_3\text{O}_4\text{NPs}$ were mixed with the blank blood and magnetically separated, we can see that no blood cells can be identified under the microscope (Fig. 8B). Fig. 8C also shows that the signal intensity increased significantly in the presence of bacteria, while there were no obvious changes in SERS intensities for IgG, HAS, Cyt C, Myo or blank whole blood. This demonstrates that our SERS biosensor has good selectivity for the detection of bacteria in blood samples.

The AMP modified $\text{Fe}_3\text{O}_4\text{NPs}$ also feature good antibacterial ability. The antibacterial activity of carboxyl modified $\text{Fe}_3\text{O}_4\text{NPs}$ and AMP modified $\text{Fe}_3\text{O}_4\text{NPs}$ in a solid medium were evaluated by the disc-diffusion test, in which antibacterial ability is determined by measuring the zones of inhibition (ZOI).⁴² Fig. 9A(left) shows the ZOI of carboxyl modified $\text{Fe}_3\text{O}_4\text{NPs}$ and AMP modified $\text{Fe}_3\text{O}_4\text{NPs}$ towards *S. aureus*, *E. coli* and *P. aeruginosa*. After 24 h of incubation, carboxyl modified $\text{Fe}_3\text{O}_4\text{NPs}$ showed negligible inhibitory action against the bacteria, while AMP modified $\text{Fe}_3\text{O}_4\text{NPs}$ showed significant efficacy against the bacteria.⁴³ For the antibacterial ability in whole blood (right), we spiked the three different kinds of bacteria into the whole blood with AMP modified $\text{Fe}_3\text{O}_4\text{NPs}$ or pure $\text{Fe}_3\text{O}_4\text{NPs}$ and cultivated them. After that, a small amount of whole blood was added to the LB medium and cultivated again. Finally, the antibacterial ability was compared by the turbidity of the LB medium by the naked eye (Fig. 9A(right)). Compared with the blank, the LB medium spiked with whole blood (cultivated with bacteria and AMP modified $\text{Fe}_3\text{O}_4\text{NPs}$) is much higher in clarity. Hence, the AMP modified $\text{Fe}_3\text{O}_4\text{NPs}$ can act as a good antibacterial agent in whole blood.

Nowadays, blood transfusion safety is a serious problem that is causing general public concern. After the long-term storage of blood, bacteria will grow to some extent and the patient could suffer morbidity or mortality from a transfusion-transmitted infection. Thus, the detection of bacteria in whole blood before the blood transfusion would greatly reduce the infection. Additionally, bacterial inactivation is also an option to reduce infection risks. Hence, the development of multi-functional nanomaterials with both antibacterial and detection abilities is of great significance.⁴⁴ Our SERS tags/bacteria/ $\text{Fe}_3\text{O}_4\text{NPs}$ sandwich structure can well fulfil both the above functions. As shown in Fig. 9B, AMP modified $\text{Fe}_3\text{O}_4\text{NPs}$ can first be added to the blood to act as an antibacterial agent in the storage of blood. Before a blood transfusion, the AMP modified $\text{Fe}_3\text{O}_4\text{NPs}$ were magnetically separated from the blood, and mixed with 4-MPBA modified Au@Ag-GO nanocomposites. If bacteria exist in the blood, the sandwich structure will be formed, and will show corresponding SERS signals to indicate that the blood is not safe for transfusion. Additionally, the *in vitro* cytotoxicity of the AMP modified $\text{Fe}_3\text{O}_4\text{NPs}$ has been approved to be of low

cytotoxicity through an evaluation of murine macrophage RAW264.7 (RAW) cells. Fig. S11† shows the cell morphological changes after exposure to AMP modified $\text{Fe}_3\text{O}_4\text{NPs}$: we can observe no obvious difference between the control cells and the AMP modified $\text{Fe}_3\text{O}_4\text{NPs}$ -treated cells. Fig. 9C shows the cellular toxicology evaluation results: different concentrations of AMP modified $\text{Fe}_3\text{O}_4\text{NPs}$ (800, 400, 200 $\mu\text{g mL}^{-1}$) showed no obvious cytotoxicity, while the positive control group, doxorubicin (DOX), showed high cytotoxicity. For real applications, infected blood samples (3 times dilution) from 39 patients (provided by First Affiliated Hospital of Jinan University, Guangzhou, China; bacteria were identified by the VITEK 2 System) were immediately processed using our universal sample preparation process and detected by SERS. Fig. 9D shows one of the SERS spectra acquired from infected blood samples of patients (all the SERS spectra of infected blood samples are shown in Fig. S12†). We then analyzed the SERS results using algorithm-based DA over the whole range from 800 cm^{-1} to 1800 cm^{-1} . The DA based Mahalanobis distance plots of every sample to the centre of gravity of two classes ('*E. coli* and *P. aeruginosa* group', '*E. coli* and *S. aureus* group', and '*S. aureus* and *P. aeruginosa* group') are shown in Fig. 9E. A diagonal line was used to identify the boundary of two classes. The spectra were divided into three clusters according to the species. In the validation analysis, 97.3% of the real blood sample can be classified effectively (only one patient infected with *E. coli* was misclassified). Additionally, blood samples (3 times dilution) spiked with bacteria down to $1 \times 10^4 \text{ CFU mL}^{-1}$ were also tested. Fig. S13† shows that different kinds of bacteria are obviously detectable in the SERS. Comparatively, signals were rarely collected in the pure blood sample. Importantly, the SERS spectra of blood spiked with bacteria are similar to those of a real infected blood sample, indicating that this method is suitable for the sensitive and specific discrimination of bacteria in real applications.

Conclusions

In summary, we herein present a sandwich strategy for the rapid, sensitive detection and discrimination of three different kinds of bacteria from a matrix sample. This novel approach involves combining a sandwich strategy including modified magnetic $\text{Fe}_3\text{O}_4\text{NPs}$ for the capture and enrichment of bacteria, and a SERS tag to provide and enhance the Raman signals. For the magnetic $\text{Fe}_3\text{O}_4\text{NPs}$, AMP was first modified as a capture element in the SERS detection of bacteria. Compared with previously reported capture elements in the SERS detection of pathogenic bacteria, as shown in Table 1, this proposed method possesses the advantages of high sensitivity,^{9,18} high stability,^{13–15} low cost^{13–17} and high specificity.⁹ What is more, it is more efficient in bacteria capture due to the long chain of the peptide.¹⁷ For the SERS tags, Au@Ag-GO nanocomposites with high SERS activity and stability have been fabricated, and further modified with 4-MPBA to act as SERS tags. In SERS detection, the Raman spectrum of the bacteria will show changes in its "fingerprints" corresponding to different kinds of bacteria. In this way, *E. coli*, *S. aureus* and *P. aeruginosa* were discriminated using DA analysis with an LOD of 10^1 CFU mL^{-1} .

In applications, this novel method can be applied in the detection of bacteria from clinical patients who are infected with bacteria and the results showed that 97.3% of the real blood samples (39 patients) can be classified effectively (only one patient infected with *E. coli* was misclassified). More importantly, the AMP modified Fe₃O₄NPs also showed good antibacterial activities, which means this biosensor can act as a multifunctional platform in the simultaneous capture, discrimination and inactivation of bacteria.

Experimental section

Chemicals, biochemicals, and instruments

Antimicrobial peptide (bacitracin A), rhodamine 6G (R6G), 4-mercaptophenylboronic acid (4-MPBA), 2-aminoethanethiol (AET), iron chloride hexahydrate (FeCl₃·6H₂O), ethylene glycol, polyethylene glycol 6000, sodium acetate trihydrate (NaAc·3H₂O), ammonia solution, tetraethyl orthosilicate (TEOS) were all supplied by Macklin (Shanghai, China). 1-Ethyl-3-[3-dimethylaminopropyl] carbodiimide hydrochloride (EDC) and *N*-hydroxysuccinimide (NHS) were purchased from Energy Chemical (Shanghai, China). Carboxyethylsilanetriol sodium salt (carboxyl-silane) was purchased from J&K Scientific Ltd. Luria–Bertani (LB) medium was purchased from Qingdao Hope Bio-Technology Co., Ltd. (Qingdao, China). Fetal bovine serum (FBS), Dulbecco's Modified Media (DMEM), and penicillin-streptomycin were all obtained from Saiguo Bio-Technology Inc (Guangzhou, China). All chemicals were of the analytical grade. *E. coli* (ATCC8739), *S. aureus* (ATCC6538), and *P. aeruginosa* (PAO1) shock-frozen strains were purchased from Guangdong Microbial Culture Center (Guangdong, China).

The morphologies and microstructures of the Fe₃O₄NPs, Au@Ag-GO nanocomposites and other related nanomaterials were all investigated by field-emission transmission electron microscopy (JEM-2100F). The FTIR spectra were conducted with a Gilson 306 FT-IR Spectrometer (France). Magnetic characterization was conducted with a superconducting quantum interference device (VSM LakeShore 7404, Lakeshore, America). Powder XRD patterns of the products were investigated on a Bruker diffractometer D8 Advance (Germany).

All SERS measurements were detected with a Raman microscope (LabRAM HR, HORIBA Scientific, Japan). A 638 nm laser was used as the excitation source. A 50× microscope objective was used to focus the light from the laser and for collection of the Raman signals. The power density of the laser is 16.0 mW μm⁻². The Raman spectra were acquired within the range 400–2000 cm⁻¹ with an exposure time of 4 s and 50% of maximum laser power. For comparison purposes, the acquired Raman spectra were presented after adjusting the baselines.

Fabrication of AMP modified Fe₃O₄NPs

Fe₃O₄NPs were synthesised according to a previous report with minor modification.⁴⁷ First, 2.7 g of FeCl₃·6H₂O was added into 80 mL of ethylene glycol and stirred until completely dissolved. Subsequently, polyethylene glycol 6000 (2.0 g) and NaAc·3H₂O (7.2 g) were added and kept under stirring until fully dissolved.

Then 75 mL of the mixture was transferred into a Teflon-lined autoclave with a capacity of 100 mL and heated at 200 °C for 8 h. With magnetic separation, the as-prepared Fe₃O₄NPs were then collected and washed with deionized water and ethanol three times each.

For the synthesis of Fe₃O₄@SiO₂, 22.5 mg of Fe₃O₄NPs was added into 3 mL of ammonia solution (1.2%) and ultrasonicated for 5 min. Then 200 μL of TEOS was added and kept under ultrasonication for 90 min. After that, 10 μL of TEOS was added and kept under ultrasonication for another 90 min. The resulting products were magnetically separated and washed with deionized water for further use.

For the synthesis of carboxyl modified Fe₃O₄NPs, 80 μL of carboxyl-silane as a sodium salt was added to 1 mL of Fe₃O₄@SiO₂ suspension (10 mg mL⁻¹) in 20 mM phosphate-buffered saline (PBS, pH 7.4) and mixed for 8 h. Then the particles were magnetically separated and washed three times with 10 mM PBS. Finally, the Fe₃O₄NPs were diluted in 20 mM phosphate-buffered saline (PBS, pH 7.4).

For the synthesis of AMP modified Fe₃O₄NPs, 10 mg of carboxyl modified Fe₃O₄NPs were dispersed in 25 mL of PBS, then 16.5 mg of EDC and 10 mg of NHS were added, followed by a mixing for 4 h. Subsequently, 20 mg of bacitracin A were added and mixed for another 3 h. The as-prepared AMP modified Fe₃O₄NPs were collected by magnetic separation, washed 3 times with PBS to remove impurities, and diluted with 400 mM phosphate-buffered saline containing 150 mM zinc acetate to form a solution with a final concentration of 1 mg mL⁻¹, and stored at 4 °C for further use.⁴⁸

Fabrication of 4-MPBA modified Au@Ag-GO nanocomposites

GO was synthesized using a modified Hummer method from natural graphite,⁴⁹ while AuNPs, AgNPs, and Au@AgNPs were synthesized in the same way as in our previous report.³⁴

For the preparation of thiol functionalized graphene (HS-GO), 100 mg of GO were added to 50 mL of ethanol to produce a 2 mg mL⁻¹ solution. The mixture was then sonicated to form a homogeneous suspension. Subsequently, 1.9 g of EDC was added to the above GO suspension and mixed for 12 h to ensure the surface activation of residual carboxylated groups on the GO surface. After that, 50 mL of AET (1 mM) was added and kept under stirring for 4 h. The AET modified GO were then collected by centrifugation at 9000 rpm, and washed twice with deionized water to remove excess ATE. Thus, HS-GO were acquired.

For the preparation of Au@Ag-GO nanocomposites, 10 mL of as-prepared Au@AgNPs were added to 2 mL of HS-GO (0.1 mg mL⁻¹) and stirred for 2 h. The Au@Ag-GO nanocomposites were collected by centrifugation at 9000 rpm and washed twice with deionized water to further remove excess Au@AgNPs.

For the modification of 4-MPBA onto the Au@Ag-GO nanocomposites, 6 mL of 4-MPBA (0.01 mg mL⁻¹) were mixed with Au@Ag-GO nanocomposites for 4 h. The as-prepared 4-MPBA modified Au@Ag-GO nanocomposites were collected by centrifugation at 9000 rpm and washed twice with deionized water to remove excess 4-MPBA.

Bacteria culture

Shock-frozen *E. coli*, *P. aeruginosa*, and *S. aureus* were used as models in our experiment. Bacterial cells were cultivated in Luria–Bertani (LB) medium in a gyratory shaker at 100 rpm and 37 °C for 16 h. Afterwards, the bacterial cells at 5 mL of LB were collected through centrifugation at 4000 rpm and 4 °C, then washed twice with PBS. Finally, the bacterial cells were diluted to the desired concentrations with PBS buffer, which were measured by the optical density (OD) of media at 600 nm (OD_{600}).

Bacterial detection from PBS media and human blood

Prior to SERS analysis, the bacterial cells were diluted with PBS or human blood from healthy volunteers (3 times dilution) to the desired concentrations. In a typical experiment, 50 μ L of AMP modified Fe_3O_4 NPs and 1 mL of bacterial suspension (the concentrations differ with different experimental aims) were added to a 1.5 mL centrifuge tube. The mixture was then incubated under shaking for 1 h. After that, bacteria@ Fe_3O_4 NPs complexes were separated under a magnetic field and washed with PBS to remove unbound bacteria. Subsequently, 100 μ L of SERS tag (4-MPBA modified Au@Ag-GO nanocomposites) and 100 μ L of PBS were added to the above bacteria@ Fe_3O_4 NPs complexes. The resulting SERS tags/bacteria/ Fe_3O_4 NPs sandwich structures were magnetically separated, washed with PBS buffer 3 times, and dispersed in 50 μ L of deionized water for further SERS detection. Real infected blood samples (3 times dilution) were directly added to AMP modified Fe_3O_4 NPs, and treated by the same procedure described above.

Strain identification of real infected blood samples

The bacteria were directly identified after blood samples were cultured in blood culture bottles for 24 h. Firstly, fluids in the bottles were centrifuged (1000 rpm) to remove the blood cells. Then bacterial cells were collected by centrifugation (3000 rpm) and diluted with 0.45% saline to the equivalent of 0.5 McFarland turbidity standard. The bacterial suspensions were used for identification with the VITEK 2 system (bioMérieux, Inc). Suspensions for the comparative identification method were made according to the manufacturer's instructions, using a GN Test Kit and a GP Test Kit for the identification of Gram-negative and Gram-negative bacteria. The cards were read by kinetic fluorescence measurement and the final results were obtained automatically.

Antibacterial ability and cellular toxicity evaluation

The antibacterial ability of AMP modified Fe_3O_4 NPs on a solid medium was evaluated by a disc-diffusion test. A filter paper disk of 6 mm in diameter was dropped with 20 μ L of AMP modified Fe_3O_4 NPs (400 μ g mL^{-1}) and incubated for 36 h at 37 °C. The diameter of the clear zone around the filter disk was measured.

The antibacterial ability of AMP modified Fe_3O_4 NPs on whole blood was evaluated by the following process. Firstly, whole blood treated with AMP modified Fe_3O_4 NPs (200 μ g

mL^{-1}) or pure Fe_3O_4 NPs (200 μ g mL^{-1}) was spiked with *E. coli*, *S. aureus*, or *P. aeruginosa*, and then cultivated in a gyratory shaker at 100 rpm and 37 °C for 16 h. After cultivation, 10 μ L of whole blood with AMP modified Fe_3O_4 NPs or pure Fe_3O_4 NPs were added to LB medium, and then cultivated under the same conditions as the whole blood. After that, the turbidities of the LB medium were compared with the naked eye.

The growth inhibitory effect of AMP modified Fe_3O_4 NPs toward murine macrophage RAW264.7 cells was assessed with a classical MTT assay.⁵⁰ The cells were plated in 96-well microplates with a density of 5×10^3 per well and incubated in 100 μ L of medium (DMEM, 10% FBS, 1% penicillin-streptomycin solution) at 37 °C in a tissue culture incubator (5% CO_2) for 12 h. After that, the culture medium was replaced by fresh medium (DMEM, 10% FBS, 1% penicillin-streptomycin solution, 0.2% DMSO) containing AMP modified Fe_3O_4 NPs with concentrations of 800, 400 and 200 μ g mL^{-1} , and cultured for another 72 h. Then 20 μ L of MTT (5 mg mL^{-1}) were added into each well and incubated under the same conditions for 4 h. Finally, the culture medium was removed, 120 μ L of DMSO was added, and the 96 well microplates were shaken for 10 min. The adsorption at 570 nm was recorded using a microplate-reader (Bio-Tek).

Conflicts of interest

There are no conflicts to declare.

Acknowledgements

This work was supported by the National Natural Science Foundation of China (81773684, 21505053), Guangdong Natural Science Funds for Distinguished Young Scholars (2018B030306033), Pearl River S&T Nova Program of Guangzhou (201806010060), Science and Technology Planning Project of Guangdong Province, China (2016A030310089), Medical Scientific Research Foundation of Guangdong Province of China (A2018133), and the Fundamental Research Funds for the Central Universities (21618407). We thank Prof. Xiangjiang Liu from Zhejiang University for his help and advice.

Notes and references

- 1 R. Wu, Y. Ma, J. Pan, S.-H. Lee, J. Liu, H. Zhu, R. Gu, K.-J. Shea and G. Pan, *Biosens. Bioelectron.*, 2018, **101**, 52–59.
- 2 Q. Mei, H. Jing, Y. Li, W. Yisibashaer, J. Chen, B.-N. Li and Y. Zhang, *Biosens. Bioelectron.*, 2016, **75**, 427–432.
- 3 H. Zhou, D. Yang, N.-P. Ivleva, N.-E. Mircescu, S. Schubert, R. Niessner, A. Wieser and C. Haisch, *Anal. Chem.*, 2015, **87**, 6553–6561.
- 4 N. Reta, C.-P. Saint, A. Michelmores, B. Prieto-Simon and N.-H. Voelcker, *ACS Appl. Mater. Interfaces*, 2018, **10**, 6055–6072.
- 5 Z. Farka, T. Juřík, D. Kovář, L. Trnková and P. Skládal, *Chem. Rev.*, 2017, **117**, 9973–10042.
- 6 H. Zhou, D. Yang, N. P. Ivleva, N. E. Mircescu, R. Niessner and C. Haisch, *Anal. Chem.*, 2014, **86**, 1525–1533.

- 7 H. Liu, X. Du, Y. Zang, P. Li and S. Wang, *J. Agric. Food Chem.*, 2017, **65**, 10290–10299.
- 8 W. Gao, B. Li, R. Yao, Z. Li, X. Wang, X. Dong, H. Qu, Q. Li, N. Li, H. Chi, B. Zhou and Z. Xia, *Anal. Chem.*, 2017, **89**, 9836–9842.
- 9 H. Wang, Y. Zhou, X. Jiang, B. Sun, Y. Zhu, H. Wang, Y. Su and Y. He, *Angew. Chem., Int. Ed.*, 2015, **54**, 5132–5136.
- 10 J. H. Chen, S. M. Andler, J. M. Goddard, S. R. Nugen and V. M. Rotello, *Chem. Soc. Rev.*, 2017, **46**, 1272–1283.
- 11 X. Cao, M. Qin, P. Li, B. Zhou, X. H. Tang, M. H. Ge, L. B. Yang and J. H. Liu, *Sens. Actuators, B*, 2018, **268**, 350–358.
- 12 P. Li, B. B. Zhou, X. M. Gao, X. H. Tang, L. B. Yang, L. Hu and J. H. Liu, *Chem.–Eur. J.*, 2017, **23**, 14278–14285.
- 13 J. Wang, X. Wu, C. Wang, Z. Rong, H. Ding, H. Li, S. Li, N. Shao, P. Dong, R. Xiao and S. Wang, *ACS Appl. Mater. Interfaces*, 2016, **8**, 19958–19967.
- 14 I. H. Cho, P. Bhandari, P. Patel and J. Irudayaraj, *Biosens. Bioelectron.*, 2015, **64**, 171–176.
- 15 H. Kearns, R. Goodacre, L.-E. Jamieson, D. Graham and K. Faulds, *Anal. Chem.*, 2017, **89**, 12666–12673.
- 16 J. Wang, X. Wu, C. Wang, N. Shao, P. Dong, X. Xiao and S. Wang, *ACS Appl. Mater. Interfaces*, 2015, **7**, 20919–20929.
- 17 H. Zhang, X. Ma, Y. Liu, N. Duan, S. Wu, Z. Wang and B. Xu, *Biosens. Bioelectron.*, 2015, **74**, 872–877.
- 18 C. Wang, B. Gu, Q. Liu, Y. Pang, R. Xiao and S. Wang, *Int. J. Nanomed.*, 2018, **13**, 1159–1178.
- 19 S. Deshwal and E.-B. Mallon, *Dev. Comp. Immunol.*, 2014, **42**, 240–243.
- 20 R. Kanchanapally, B.-P.-V. Nellore, S.-S. Sinha, F. Pedraza, S.-J. Jones, A. Pramanik, S.-R. Chavva, C. Tchounwou, Y. Shi, A. Vangara, D. Sardar and P.-C. Ray, *RSC Adv.*, 2015, **24**, 18881–18887.
- 21 H. Etayash, L. Norman, T. Thundat, M. Stiles and K. Kaur, *ACS Appl. Mater. Interfaces*, 2014, **6**, 1131–1138.
- 22 H. Etayash, K. Jiang, T. Thundat and K. Kaur, *Anal. Chem.*, 2014, **86**, 1693–1700.
- 23 M. Hoyos-Nogués, S. Brosel-Oliu, N. Abramova, F.-X. Muñoz, A. Bratov, C. Mas-Moruno and F.-J. Gil, *Biosens. Bioelectron.*, 2016, **86**, 377–385.
- 24 Z. Li, H. Yang, L. Sun, H. Qi, Q. Gao and C. Zhang, *Sens. Actuators, B*, 2015, **210**, 468–474.
- 25 E. Babich, A. Redkov, I. Reduto and A. Lipovskii, *Phys. Status Solidi RRL*, 2018, **12**, 1700226.
- 26 S. Saha, M. Ghosh, B. Dutta and J. Chowdhury, *Appl. Surf. Sci.*, 2016, **362**, 364–373.
- 27 M. S. Hizir, N. M. Robertson, M. Balcioglu, E. Alp, M. Rana and M. V. Yigit, *Chem. Sci.*, 2017, **8**, 5735–5745.
- 28 X. Li, J. Li, X. Zhou, Y. Ma, Z. Zheng, X. Duan and Y. Qu, *Carbon*, 2014, **66**, 713–719.
- 29 Y. X. Zou, S. Q. Huang, Y. X. Liao, X. P. Zhu, Y. Q. Chen, L. Chen, F. Liu, X. X. Hu, H. J. Tu, L. Zhang, Z. K. Liu, Z. Chen and W. H. Tan, *Chem. Sci.*, 2018, **9**, 2742–2849.
- 30 W. Shen, X. Lin, C. Jiang, C. Li, H. Lin, J. Huang, S. Wang, G. Liu, X. Yan, Q. Zhong and B. Ren, *Angew. Chem., Int. Ed.*, 2015, **54**, 7308–7312.
- 31 Y. Zou, L. Chen, Z. Song, D. Ding, Y. Chen, Y. Xu, S. Wang, X. Lai, Y. Zhang, Y. Sun, Z. Chen and W. Tan, *Nano Res.*, 2016, **9**, 1418–1425.
- 32 S. Saito, T. L. Massie, T. Maeda, H. Nakazumi and C. L. Colyer, *Anal. Chem.*, 2012, **84**, 2452–2458.
- 33 M. Kale and M. S. Shaikh, *Int. J. Pharm. Sci.*, 2014, **6**, 27–35.
- 34 K. S. Yuan, J. X. Zheng, D. T. Yang, B. J. Sanchez, X. J. Liu, X. J. Guo, C. S. Liu, N. E. Dina, J. Y. Jian, Z. J. Bao, Z. W. Hu, Z. H. Liang, H. B. Zhou and Z. J. Jiang, *ACS Omega*, 2018, **3**, 2855–2864.
- 35 B. Wagner, D. Schumann, U. Linne, U. Koert and M. A. Marahiel, *J. Am. Chem. Soc.*, 2006, **128**, 10513–10520.
- 36 A. C. Pawlowski, W. L. Wang, K. Koteva, H. A. Barton, A. G. McArthur and G. D. Wright, *Nat. Commun.*, 2016, **7**, 13803.
- 37 K. J. Stone and J. L. Strominger, *Proc. Natl. Acad. Sci. U. S. A.*, 1971, **68**, 3223–3227.
- 38 N. J. Economou, S. Cocklin and P. J. Loll, *Proc. Natl. Acad. Sci. U. S. A.*, 2013, **110**, 14207–14212.
- 39 P. Emsley, B. Lohkamp, W. G. Scott and K. Cowtan, *Acta Crystallogr.*, 2010, **66**, 486–501.
- 40 F. Costa, I. F. Carvalho, R. C. Montelaro, P. Gomes and M. C. L. Martins, *Acta Biomater.*, 2011, **7**, 1431–1440.
- 41 X. Bi, X. Du, J. Jiang and X. Huang, *Anal. Chem.*, 2015, **87**, 2016–2021.
- 42 A. Melaiye, R. S. Simons, A. Milsted, F. Pingitore, C. Wesdemiotis, C. A. Tessier and W. J. Youngs, *J. Med. Chem.*, 2004, **47**, 973–977.
- 43 W. Zhang, X. Shi, J. Huang, Y. Zhang and Z. Wu, *ChemPhysChem*, 2012, **13**, 3388–3396.
- 44 L. Wang, J. Luo, S. Shan, E. Crew and J. Yin, *Anal. Chem.*, 2011, **83**, 8688–8695.
- 45 M. S. Mannoor, S. Y. Zhang, A. J. Link and M. C. McAlpine, *Proc. Natl. Acad. Sci. U. S. A.*, 2010, **107**, 19207–19212.
- 46 H. Etayash, M. F. Khan, K. Kaur and T. Thundat, *Nat. Commun.*, 2016, **7**, 12947.
- 47 H. Hu, Z. Wang, L. Pan, S. Zhao and S. Zhu, *J. Phys. Chem. C*, 2010, **114**, 7738–7742.
- 48 J. E. Smith, K. E. Sapsford, W. Tan and F. S. Ligler, *Anal. Biochem.*, 2011, **410**, 124–132.
- 49 P. Chettri, V. S. Vendamani, A. Tripathi, A. P. Pathak and A. Tiwari, *Appl. Surf. Sci.*, 2016, **362**, 221–229.
- 50 M. S. Zheng, Y. K. Lee, Y. Li, K. Hwangbo, C. S. Lee, J. R. Kim, S. K. S. Lee, H. W. Chang and J. K. Son, *Arch. Pharmacol. Res.*, 2010, **33**, 1307–1315.

1

Supporting Information

2 **Antimicrobial Peptide based Magnetic Recognition**
3 **Elements and Au@Ag-GO SERS Tags with Stable Internal**
4 **Standards: A Three in One Biosensor for Isolation,**
5 **Discrimination and Killing of Multiple Bacteria in Whole**
6 **Blood†**

7 **Kaisong Yuan,^{a,c,‡} Qingsong Mei,^{b,‡} Xinjie Guo,^a Youwei Xu,^d Danting Yang,^e**
8 **Beatriz Jurado Sánchez,^c Bingbing Sheng,^a Chusheng Liu,^a Ziwei Hu,^a**
9 **Guangchao Yu,^f Hongming Ma,^f Hao Gao,^{a,*} Christoph Haisch,^g Reinhard**
10 **Niessner,^g Zhengjing Jiang,^{a,*} and Haibo Zhou^{a,*}**

11 ^a Institute of Pharmaceutical Analysis, College of Pharmacy, Jinan University, Guangzhou, Guangdong
12 510632, China.

13 ^b School of Medical Engineering, Hefei University of Technology, Tunxi road 193, Hefei 230009,
14 China.

15 ^c Department of Analytical Chemistry, Physical Chemistry and Chemical Engineering, University of
16 Alcalá, Alcalá de Henares E-28871, Madrid, Spain.

17 ^d Shanghai Institute for Advanced Immunochemical Studies, ShanghaiTech University, Shanghai
18 201210, China.

19 ^e Department of Preventative Medicine, Zhejiang Provincial Key Laboratory of Pathological and
20 Physiological Technology, Medical School of Ningbo University, Ningbo, Zhejiang 315211, China.

21 ^f The First Affiliated Hospital of Jinan University, Guangzhou, Guangdong 510632, China.

22 ^g Institute of Hydrochemistry and Chair for Analytical Chemistry, Technical University of Munich,
23 Marchioninstr. 17, D-81377, Munich, Germany

24 *Institute of Pharmaceutical Analysis, College of Pharmacy, Jinan University, Guangzhou, Guangdong*
25 *510632, China. E-mail: haibo.zhou@jnu.edu.cn, jzjjackson@hotmail.com, tghao@jnu.edu.cn*

26 † Electronic supplementary information (ESI) available: Additional data and 13 supplementary figures.

1 ‡ K.Y. and Q.M. contributed equally.

2 **1. Additional data**

3 **1.1 Surface coverage of 4-MPBA on Au@AgNPs**

4 The concentration of AuNPs could be calculated based on the Beer's law and the extinction
5 coefficient ($\epsilon_{Au}=3\times 10^9 \text{ M}^{-1} \text{ cm}^{-1}$). Thus, the concentrations of AuNPs is $\sim 0.26 \text{ nM}$. As the Au@Ag
6 NPs are prepared through the coating of Au seed with Ag shell and 2.5 mL AgNO_3 was added to
7 form the 5 nm Ag shell, we can calculate that the concentration of Au@AgNPs is 0.208 nM .¹

8 The total surface coverage (θ) of 4-MPBA on the Au@AgNPs surfaces can be calculated as
9 follows according to previous report:²

$$10 \theta = \frac{0.25n}{S} = \frac{0.25nN_a}{C_{Au@Ag}V\pi d^2N_a} = \frac{0.25n}{C_{Au@Ag}V\pi d^2}$$

11 Where

12 a) S is the total surface of Au@AgNPs;

13 b) n is the total amounts of 4-MPBA;

14 c) N_a is the Avogadro's number;

15 d) $C_{Au@Ag}$ is the concentration of Au@AgNPs, which was calculated to be 0.208 nM ;

16 e) V is the volume of Au@AgNPs colloidal solution;

17 f) d is the average diameter of Au@AgNPs, which is measured $\sim 35 \text{ nm}$

18 In the calculation of surface coverage on Au@AgNPs, different amounts of MPBA were
19 added into the Au@AgNPs to measure the max adsorb amount of MPBA on the Au@AgNPs
20 surfaces. As depicted in Figure S5A, while the final concentrations of MPBA in excess of 0.25
21 $\mu\text{g/mL}$, the colloidal solution began to change its color. Thus, we set this value as the max adsorb
22 amount of MPBA. While the total amounts of 4-MPBA (average molecular area of 0.25 nm^2)
23 added were smaller than the max adsorb amount of 4-MPBA on the Au@AgNPs surfaces, it can
24 be speculated that the amounts of modified MPBA on the Au@AgNPs surfaces and the added
25 amounts of 4-MPBA were the same. In this experiment, we prepared the 4-MPBA modified
26 Au@AgNPs through the mixture of 4-MPBA (6 mL, final concentration: $10 \mu\text{g/mL}$) and
27 Au@AgNPs. As a result, the surface coverage of MPBA on the surface of Au@AgNPs was
28 calculated to be 0.51.

1 In the calculation of surface coverage on Au@Ag-GO nanocomposites, a 10 µg/mL of 4-
 2 MPBA solution (6 mL) have been used to mixed with the Au@Ag-GO nanocomposites. After the
 3 Au@AgNPs have been adhered to the GO nanosheets, the Au@Ag-GO nanocomposites will not
 4 be aggregation even in high concentration of 4-MPBA. UV-Vis results (Figure S5B) showed that
 5 large amounts of 4-MPBA have been adsorbed on the Au@Ag-GO nanocomposites and it can be
 6 calculated that 1.5 mg of 4-MPBA have been adsorbed on the Au@Ag-GO nanocomposites. Thus,
 7 the total surface coverage of 4-MPBA on Au@Ag-GO nanocomposites is calculated to be 13.11.
 8 The surface coverage is over 1.00 due to the GO nanosheets will also adsorb the 4-MPBA. After
 9 the Au@AgNPs on the GO nanosheets are full of 4-MPBA, the GO nanosheets will further adsorb
 10 the 4-MPBA.

11 In conclusion, with the combination of GO nanosheets and Au@AgNPs, the adsorb amounts
 12 of 4-MPBA on SERS substrate will be significantly enhanced compare with the simple
 13 Au@AgNPs substrate.

14 **1.2 Enhancement Calculation (EF)**

15 The EF value is calculated through the following well-established equation:³

$$16 \quad EF = \frac{I_{SERS} \times N_{bulk}}{I_{bulk} \times N_{SERS}} \quad (1)$$

17 I_{bulk} and I_{SERS} are the intensity of analyte in solution for SERS and bulk Raman spectra,
 18 respectively. N_{bulk} and N_{SERS} means the number of molecules within the laser spot excited by a
 19 laser beam in SERS and Raman scattering.

$$20 \quad N_{SERS} = N_A \times CV \frac{S_{Laser}}{S_{Sub}} \quad (2)$$

21 N_A is Avogadro constant; C means the molar concentration; V is the volume; S_{Laser} is the size
 22 of the laser spot and S_{Sub} is the size of the substrate. Hence, for SERS detection, a V_{SERS} volume
 23 of R6G is dispersed on an area of S_{SERS} at a concentration of C_{SERS} on the clean Si substrate.

$$24 \quad N_{bulk} = N_A \times \rho_v S_{Laser} \quad (3)$$

25 ρ_v [mol/µm³] means the volume density of R6G powder on a glass slide. In this experiment,
 26 mass density of R6G powder is 1.26 g/cm³, while molecular weight of R6G is 479 g/mol, thus it

1 can be calculated as $\rho_v [\text{mol}/\mu\text{m}^3] = (1.26/479) \times 10^{-12} = 2.63 \times 10^{-15} \text{ mol}/\mu\text{m}^3$

$$2 \quad EF = \frac{I_{SERS} \times \rho_v \times S_{Sub}}{I_{bulk} \times CV} \quad (4)$$

3 In our experiment, a 25 μL of R6G (10^{-9}M) was mixed with 25 μL of Au@Ag-GO
4 nanocomposites, then the mixture was drop on the glass slide and dry in the air to form a circle
5 with a diameter of 5195 μm . As depicted in Figure S4, SERS signals of R6G was obviously
6 enhanced compared with Raman signals of R6G powder. Therefore, for the 613 cm^{-1} Raman peak,
7 I_{bulk} is 2054.0 counts from Raman spectrum of R6G powder and I_{SERS} is 25410.8 counts from
8 SERS spectrum of R6G. The EF can be calculated as:

$$9 \quad EF = (25410.8 \text{ counts} \times 2.63 \times 10^{-15} \text{ mol}/\mu\text{m}^3 \times (5195 \mu\text{m})^2 \times 3.14) / (2054.0 \text{ counts} \times 10^{-9} \text{ M} \times 25 \mu\text{L} \times 10^{-6})$$

10 $= 1.1 \times 10^8$

11 **1.3 XRD and FTIR of 4-MPBA modified Au@Ag-GO SERS Tags**

12 The powder XRD patterns of GO and Au@Ag-GO are shown in Figure S2C. After the adsorbition
13 of Au@AgNPs, the presence of intense peaks of (111), (200), and (220) could be indexed to face
14 centered cubic (fcc) structure of Au@AgNPs.⁴ These confirm that Au@AgNPs have been adhered
15 to the GO nanosheets successfully.

16 The FTIR spectrum of the GO, and 4-MPBA modified Au@Ag-GO have been measured and
17 results are showed in Figure S2D. The characteristic vibrations of GO are a broad and intense
18 peak of O-H group at 3250 cm^{-1} , a C=O peak at 1723 cm^{-1} , a C-OH stretching peak at 1254 cm^{-1} , a
19 C-O stretching peak at 1060 cm^{-1} , and a peak attributed to the vibration of graphitic skeletal
20 domains at 1605 cm^{-1} . Such fact revealed that the GO surface is functionalized with different
21 kinds of oxygen-containing groups.⁵ The absorption bands of 4-MPBA modified Au@Ag-GO at
22 1594 cm^{-1} was attributed to the C=C stretching vibration of phenyl ring, while the new absorption
23 band at $\sim 1360 \text{ cm}^{-1}$ could be associated with B-O bond and confirm the presence of the boronic
24 acid derivative.⁶

25 **1.4 FTIR of AMP modified Fe₃O₄NPs**

26 The FTIR spectrum of the Fe₃O₄, SiO₂@Fe₃O₄ and AMP@SiO₂@Fe₃O₄ have been measured
27 and results are showed in Figure S6. For all the nanomaterials, the Fe-O stretching vibration can
28 be observed at 586 cm^{-1} . As well as peaks at 3367 cm^{-1} and 1635 cm^{-1} are assigned to the -OH

1 stretching vibration due to the existence of surface carboxyl. Compared with the absorption bands
2 of pure Fe_3O_4 , the characteristic absorption peaks of Si-O-Si at 1063 cm^{-1} and 1628 cm^{-1}
3 confirmed the formation of silica on the surface of Fe_3O_4 after the modification with TEOS. For
4 the $\text{AMP}@SiO_2@Fe_3O_4$, the appearance of peaks at 1087 cm^{-1} , 1043 cm^{-1} indicated C-N aliphatic
5 amines, which confirmed the successful modification of AMP.⁷

6

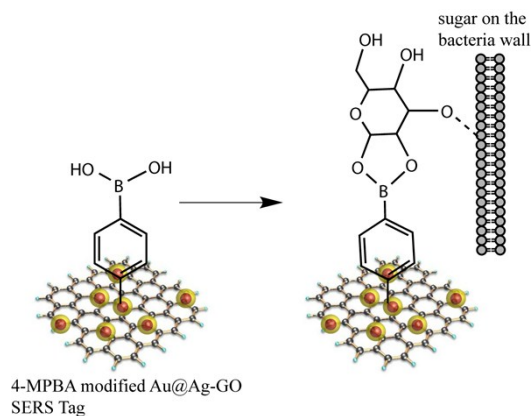


Figure S1 Recognition reactions/mechanism between 4-MPBA and bacterial wall.

10

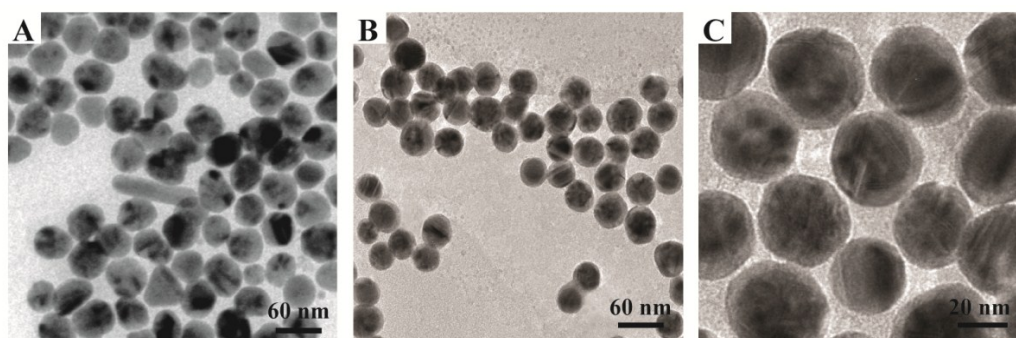
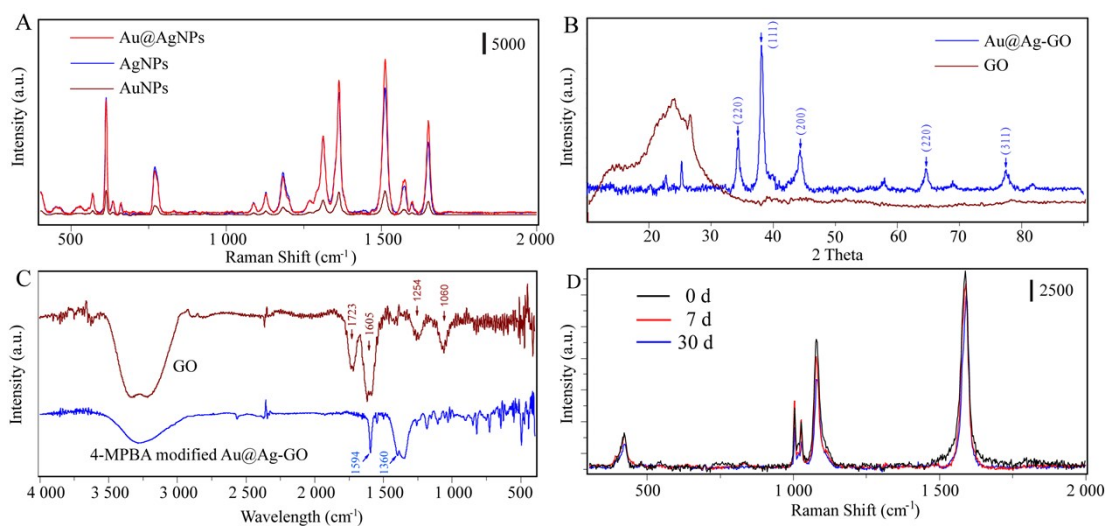
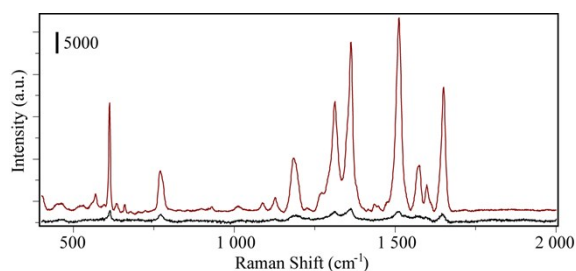


Figure S2 (A) TEM image of AgNPs; (B) TEM image of Au@AgNPs in low magnification; (C) TEM image of Au@AgNPs in high magnification.



1
 2 **Figure S3 (A)** SERS spectrum of R6G solution enhanced with Au@AgNPs (red line), AgNPs
 3 (blue line) and AuNPs (brown line); **(B)** XRD of GO nanosheets (brown line) and Au@Ag-GO
 4 nanocomposites (blue line); **(C)** FTIR of GO (brown line) and 4-MPBA modified Au@Ag-GO
 5 (blue line); **(D)** Raman spectrum of 4-MPBA adsorbed on Au@Ag-GO nanocomposites for
 6 different storage times.

7

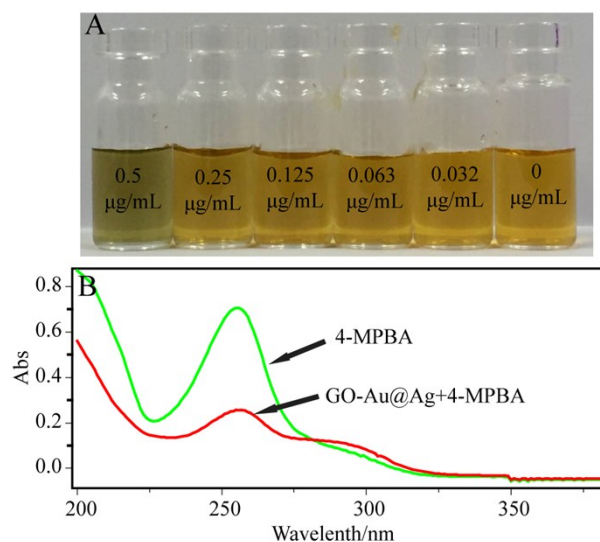


8

9

10 **Figure S4** Raman spectrum of R6G powder on a glass slide and SERS spectra of R6G solution
 11 (10^{-9} M).

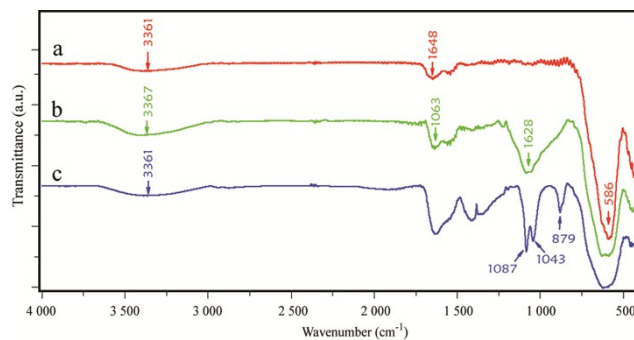
11



1

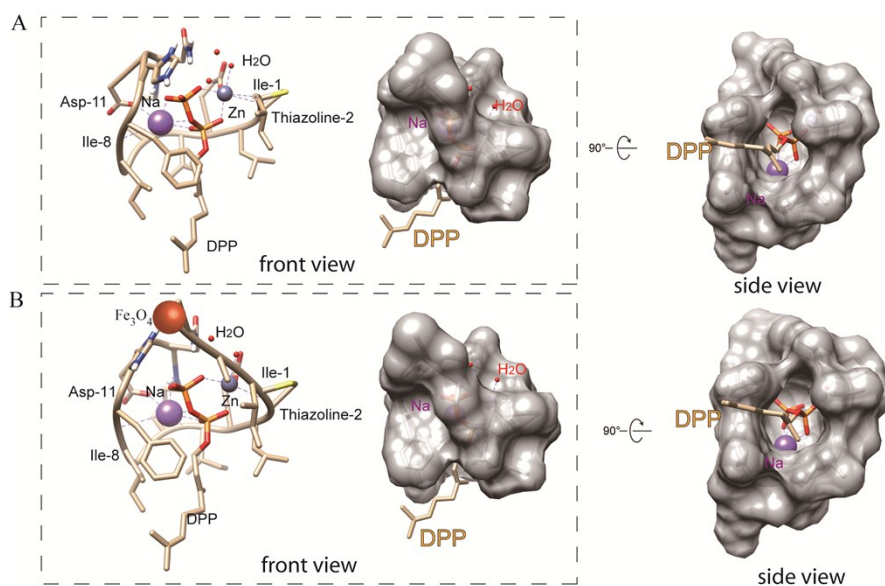
2 **Figure S5 (A)** Different amounts of MPBA mixed with Au@AgNPs, final concentrations of
 3 MPBA (from right to left) were 0, 0.032, 0.063, 0.125, 0.25, 0.5 µg/mL, respectively; **(B)** UV
 4 spectra of the 10 µg/mL MPBA solution (6 mL, green line), and the supernatant (red line) after 10
 5 µg/mL of MPBA solution were mixed with Au@Ag-GO nanocomposites. The Au@Ag-GO
 6 nanocomposites are synthesis from 6mL of Au@AgNPs (Au@AgNPs/GO ratio: 10:1), and all the
 7 Au@Ag-GO nanocomposites are collected and resolved in 6 mL of pure water.

8



9

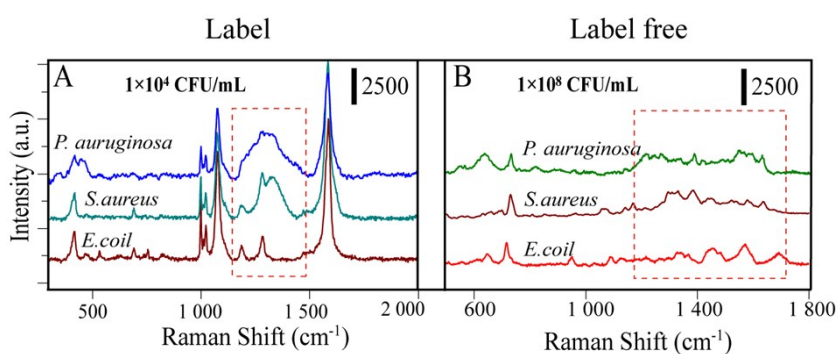
10 **Figure S6** FTIR spectra of (a) Fe₃O₄, (b) SiO₂@Fe₃O₄ and (c) AMP@SiO₂@Fe₃O₄.



1

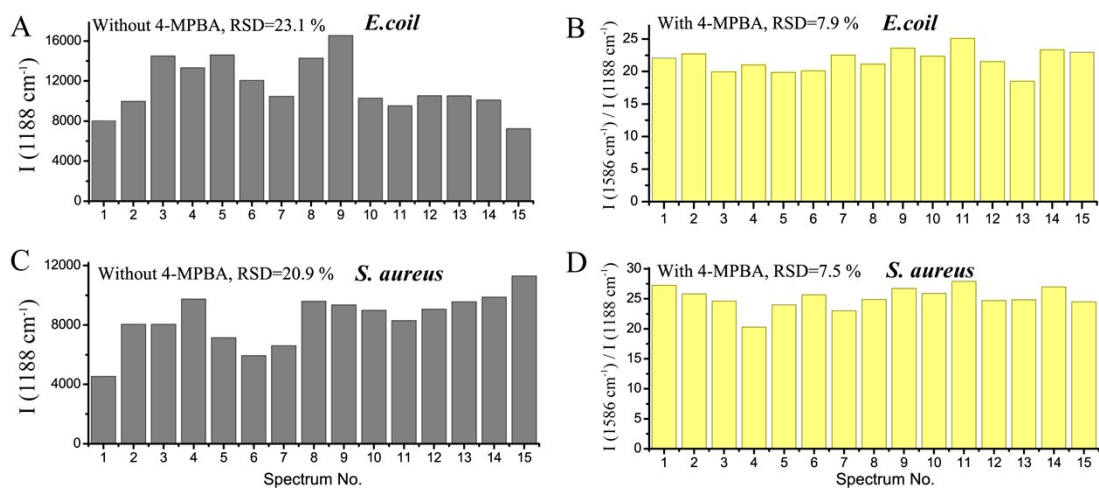
2 **Figure S7** Sequestration of the pyrophosphate group by AMP. **(A)** A semitransparent surface
 3 representation is shown to highlight the almost complete burial of the target's pyrophosphate
 4 group by AMP; **(B)** The AMP still keep burial of the target's pyrophosphate group even after
 5 peptide modification.

6



7

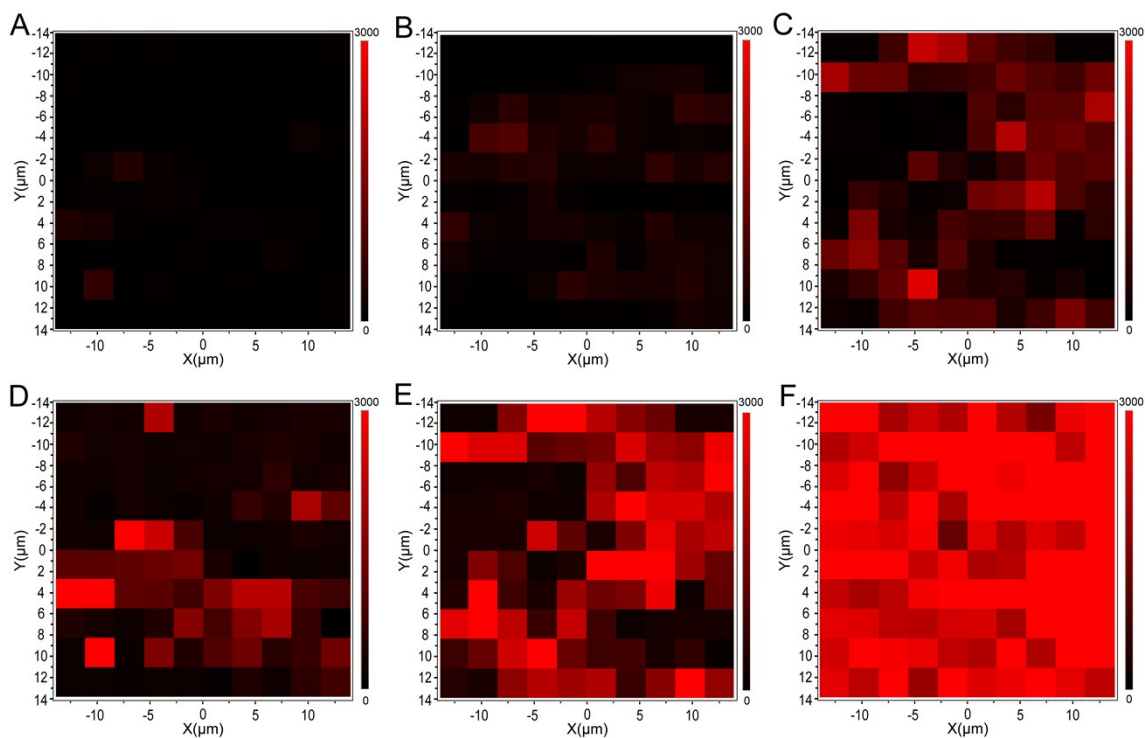
8 **Figure S8 (A)** SERS spectra of *P. auruginosa*, *S. aureus*, and *E. coli* (with 4-MPBA), with
 9 concentrations of 1×10^4 CFU/mL respectively; **(B)** Label free detection of *P. auruginosa*, *S.*
 10 *aureus*, and *E. coli* (without 4-MPBA), with concentrations of 1×10^8 CFU/mL respectively. In this
 11 situation, AgNPs were simply mixed with bacteria for SERS detection.



1

2 **Figure S9 (A)** Peak intensities of 15 batches (*E.coli*) with ($I_{1586 \text{ cm}^{-1}} / I_{1188 \text{ cm}^{-1}}$) and **(B)** without
 3 ($I_{1188 \text{ cm}^{-1}}$) 4-MPBA internal standard normalization; **(C)** Peak intensities of 15 batches (*S.aureus*)
 4 with ($I_{1586 \text{ cm}^{-1}} / I_{1188 \text{ cm}^{-1}}$) and **(D)** without ($I_{1188 \text{ cm}^{-1}}$) 4-MPBA internal standard normalization.

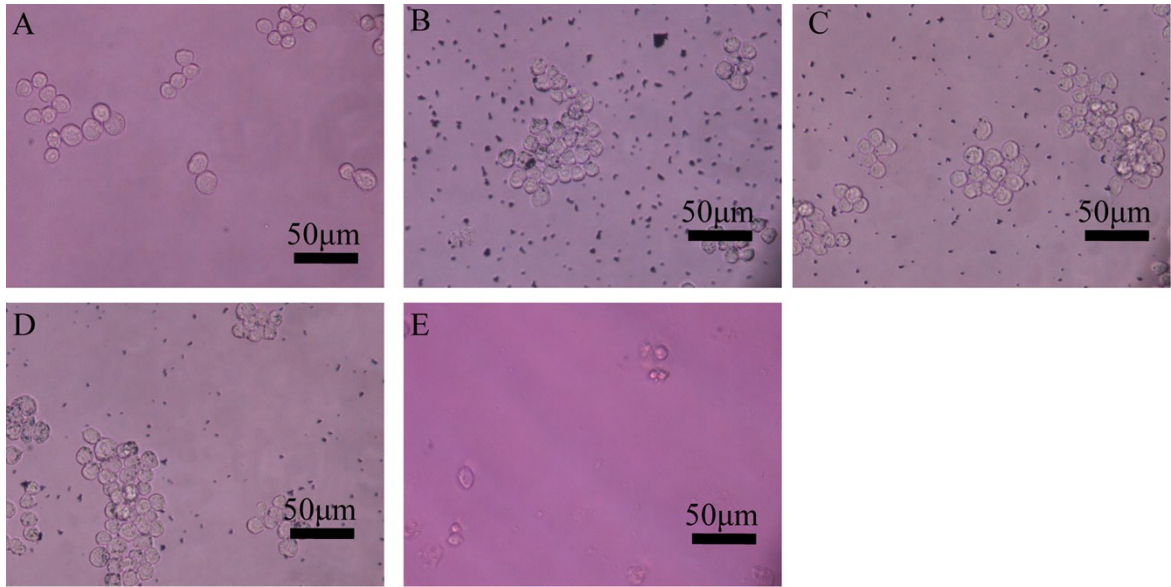
5



6

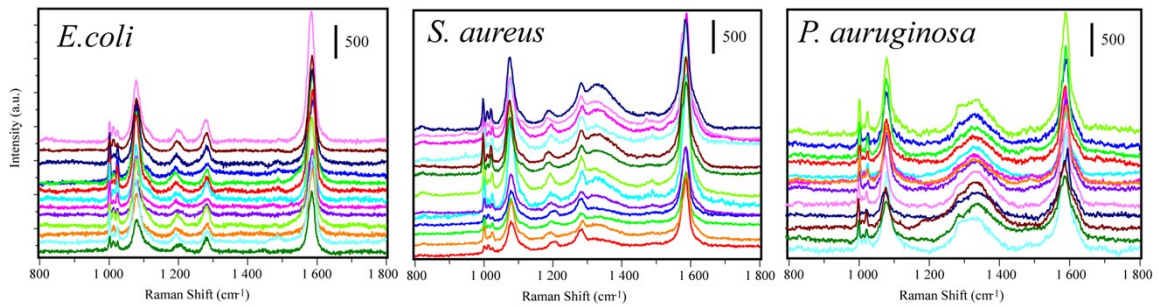
7 **Figure S10** SERS mapping in the detection of *E. coli* at different concentrations of 1×10^1 (A),
 8 1×10^2 (B), 1×10^3 (C), 1×10^4 (D), 1×10^5 (E), 1×10^6 (F) CFU/mL.

9



1
 2 **Figure S11** Cell morphology microscopic pictures showing the cytotoxicity of “AMP modified
 3 Fe₃O₄NPs” against RAW264.7 cells. **(A)** control group (untreated cell lines); **(B-D)** Treated cells
 4 with 800 μg/mL AMP-Fe₃O₄NPs (B), 400 μg/mL AMP-Fe₃O₄NPs (C), 200 μg/mL AMP-
 5 Fe₃O₄NPs (D); **(E)** Positive control group (cell lines treated with DOX).

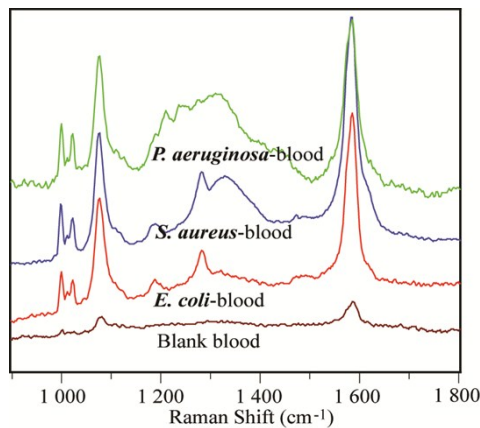
6



7

8 **Figure S12** SERS spectra of whole blood from 39 patients infected with *P. aeruginosa*, *S. aureus*
 9 and *E. coli*.

10



1 **Figure S13** SERS spectra of blood spiked with *P. aeruginosa*, *S. aureus* and *E. coli*. Blood
2 without any bacteria is used as a control.

3 **Reference**

- 4 1. B. Liu, G. Han, Z. Zhang, R. Liu, C. Jiang, S. Wang, M.-Y. Han and *Anal. Chem.*, 2011, **84**, 255–261.
- 5 2. X.S. Bi, X.Z. Du, J.J. Jiang and X. Huang, *Anal. Chem.*, 2015, **87**, 2016-2021.
- 6 3. X. Meng, H. Wang, N. Chen, P. Ding, H. Shi, X. Zhai, Y. Su and Y. He, *Anal. Chem.*, 2018, **90**, 5646-5653.
- 7 4. S. Yallappa, J. Manjanna and B.L. Dhananjaya, *Specrochim. Acta A*, 2015, **137**, 236-243.
- 8 5. J. Zhang, Y. Sun, Q. Wu, Y. Gao, H. Zhang, Y. Bai and D.Q. Song, *Colloid. Surface. B*, 2014, **116**, 211-218.
- 9 6. W. Wang, L.Y. Kong, J.M. Zhu and L. Tan, *J. Colloid. Interf. Sci.*, 2017, **498**, 1-8.
- 10 7. K. Lyappan, G. Ananthan, *Afr. J. Biotechnol.*, 2014, **13**, 4471-4475.

CHAPTER IV.

Janus micromotors based on 2D nanomaterials for detection and killing of pathogenic bacteria

IV.1. Introduction and objectives.

Bacterial infections represent a major threat in public health, causing million deaths worldwide. In hospitals, the spread of such infections can be very fast, leading to the generation of "superbugs" or multidrug resistant bacteria. Another important issue is the formation of resistant biofilms in biomedical devices, causing high-risk of concurrent infections. Prompt bacterial infection diagnosis by the detection of specific biomarkers and cells is thus essential for fast treatment. In addition, the quest for novel ways to deal with such infections and biofilms rely on the exploration of new chemical agents and nanomaterials. Indeed, the combination of different nanoparticles and nanomaterials (such as 2D nanomaterials) with multimode actions results in multifunctional entities with synergetic capabilities for enhanced bacteria inactivation and/or sensing.

Janus micromotors are a unique class of materials whose surfaces have two or more distinct physical properties, allowing thus for two types of chemistry to occur simultaneously. Current efforts in the field are aimed to impart them with adaptative moving behaviors to improve overall functionality in complex environments. Judicious design of the micromotor structure allows to incorporate different functionalities in a single unit for further control their propulsion behavior and motion direction with different energy sources (one or two stimuli) to speed-up, stop or reverse their navigation. This is extremely attractive to achieve micromotor operation in complex samples such as blood or serum, which can deactivate the part responsible for micromotor propulsion, hampering adequate operation. Several designs have been described in the literature, including magneto-catalytic hybrid micromotors (propelled by catalytic and magnetic fields); magneto-acoustic hybrid micromotors (propelled by magnetic and ultrasound fields) and catalytic-acoustic hybrid schemes. Recently, the convenient marriage between light and catalytic, magnetic or ultrasound propulsion has led to the design of micromotors with "*built-in*" braking and accelerating systems for future motion control and improved performance. In addition, carbon nanomaterials or black phosphorous impart the micromotors with a rough surface area for the subsequent incorporation of a higher loading of the active nanoparticles, which are responsible for the motion controlled behavior, allowing thus to tune the propulsion mode.

On the other hand, understanding the interaction of 2D nanomaterials based micromotors and biomolecules such as peptides, aptamers, DNA, etc, can

IV. Janus micromotors based on 2D nanomaterials for detection and killing of pathogenic bacteria

play a critical role in the biomedical field, *i.e.* to study cell interactions, developing new drugs or improving the performance of receptor based clinical sensors. Adequate micromotor functionalization with specific detection probes or therapeutic ligands in connection with autonomous movement and small size hold considerable promise for new dynamic biomedical strategies in previously inaccessible microscale environments. This is extremely useful to overcome the low detection limits and address the limitations of common biosensors or to allow penetration into cell for localized treatment.

Also, inspired by the promising capabilities of nanomaterials in the antibacterial war, the micromotor community translates the mechanisms of action of such "nanoentities" into moving schemes. Indeed, the enhanced mixing and towing force of micromotors can improve even more the efficiency in bacteria removal and inactivation processes. The antimicrobial activity of micromotors can be explained by three main mechanisms: (1) direct release of reactive oxygen species (ROS) and metal ions, (2) direct physical contact or (3) functionalization with specific antibiotics and probes. Yet, all the above mentioned configurations lacks specificity between normal cell and bacteria, which show high cytotoxicity (Ag^+ , etc), ; or towards a given type of bacteria, which can be very beneficial for improved inactivation, on particular to treat infections caused by multidrug resistance bacteria; or are prone to inactivation in biological media, hampering adequate treatment.

From the previous premises, herein we report, first, the preparation of 2D nanomaterials coated micromotors integrating "*three engines*" for motion control using different stimuli such as chemical fuel, light and magnetic fields. Micromotors are mass-produced by wrapping gold-sputtered polystyrene microspheres with already explored (graphene oxide) and novel 2D nanomaterials (black phosphorous and graphdyine oxide); followed by simultaneous assembly of Pt or MnO_2 nanoparticles as "*bubble (catalytic)-engines*"; Fe_2O_3 NPs as "*magnetic engines*" and quantum dots (QDs) as "*light engines*". In *bubble-magnetic* and *bubble-light mode*, a "*built-in*" acceleration system allows to increase micromotor speed up to 3.0 and 1.5 times after application of the magnetic field or light irradiation, respectively. In *bubble-magnetic-light mode*, such speed increase can be combined in a single unit for *on-demand* braking and accelerating systems. Fluid dynamics simulations illustrate that such adaptative behavior and improved propulsion efficiency is

IV. Janus micromotors based on 2D nanomaterials for detection and killing of pathogenic bacteria

produced by a better distribution of the fuel and thus energy propelling the micromotor by activation of the *magnetic* and/or *light* engines. The new micromotors described here -which combine multiple engines with functional nanomaterials- will be next explored for "on-the-fly" sensing and bacterial killing applications.

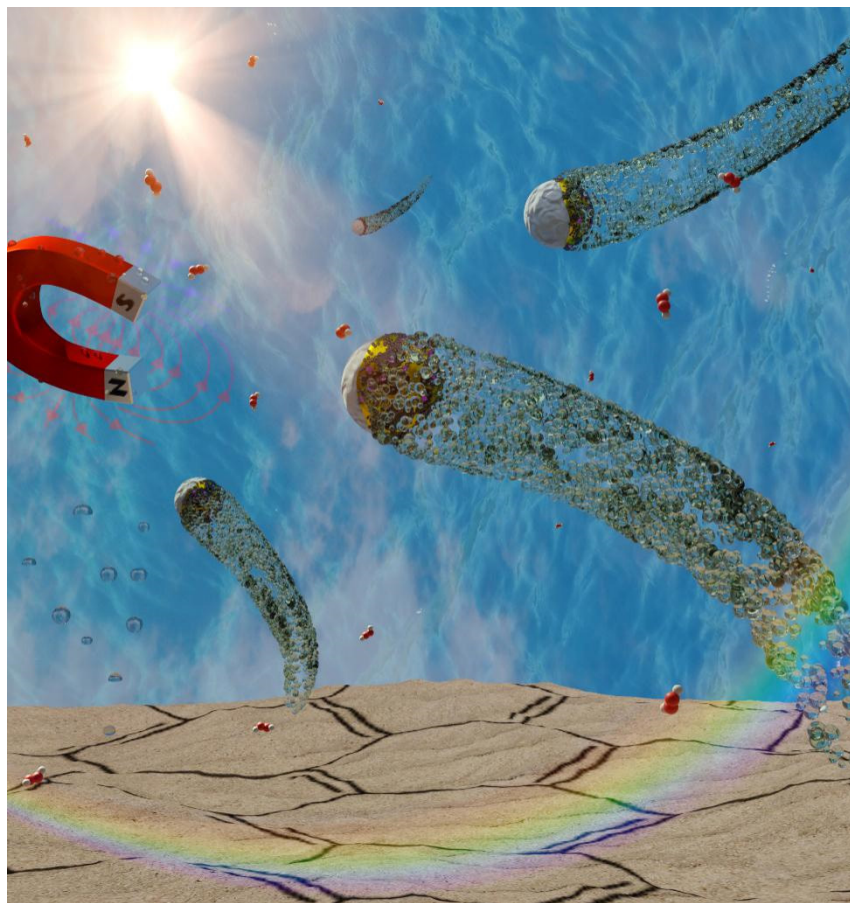
Secondly, we investigate the use of the previously developed Janus micromotors as dynamic interfaces in fluorescent assays for bacteria diagnosis applications. As a model system, we select a specific rhodamine labelled affinity peptide highly selective for Cholera Toxin B subunit. Such ON-OFF-ON system allows to mimic similar processes occurring at (bio)-interfaces and to study the related sorption and desorption kinetics. The distinct surface properties of each nanomaterial play a critical role in the loading/release capacity of the peptide, greatly influencing the release profiles. Sorption obeys a second order-kinetic model using the three 2D nanomaterials in connection with micromotors, indicating a strong influence of chemisorption process and a higher loading capacity for black phosphorous micromotors. Yet, release kinetics are faster for graphene oxide and graphdyine oxide micromotors, indicating a contribution of π and hydrophobic interactions in the probe sorption (Cholera toxin B affinity peptide) and target probe release (in presence of Cholera Toxin B). Micromotors movement also plays a critical role in such processes, allowing for efficient operation in low raw sample volumes where the high protein content can diminish probe loading/release, affecting to the overall performance. This greatly influences the final sensing performance, with a 5-fold efficient of GDYO and GO micromotors as compared with BP micromotors. Excellent release capacity and micromotor performance are observed also in complex samples such as human serum.

Thirdly, following the core of the PhD, we explore the use of the developed graphene oxide/Fe₂O₃ magnetic Janus micromotors for highly selective capture/inactivation of gram-positive bacteria units and biofilms. The strategy is based on the combination, for the first time, of a lanbiotic (Nisin) with Janus micromotors. Lanbiotics are peptides composed of methyl-lanthionine residues with a highly selective antimicrobial activity towards multidrug resistant bacteria. Nisin is a natural compound normally used for food preservation, which display specific antimicrobial activity towards gram-positive bacteria. Such peptide can bind to lipid II unit of the bacteria membranes,

IV. Janus micromotors based on 2D nanomaterials for detection and killing of pathogenic bacteria

damaging its morphology and releasing its contents. The coating of micromotors with GO impart them with a Janus structure for the subsequent asymmetric assembly of catalytic (PtNPs) and magnetic (Fe_2O_3) *engines* and results in an active rough layer for a higher loading of Nisin *via* covalent interactions. The micromotors possess adaptative propulsion mechanisms, including catalytic mode (PtNPs) in peroxide solutions or magnetic actuation (fuel free) by the action of an external magnetic field. The enhanced movement and localized delivery of the micromotors (both in catalytic and magnetic actuated mode) results in a 2-fold increase of the capture/killing ability towards *Staphylococcus Aureus* bacteria in raw media (juice, serum and tap water samples), as compared with free Nisin and static counterparts. The micromotor strategy display also high selectivity towards such bacteria, as illustrated by the dramatically lower capture/killing ability towards gram-negative *Escherichia Coli*. We will also show the ability of the micromotors to destroy bacteria and biofilms. Unlike previous micromotors based strategies, our approach displays higher selectivity towards a type of bacteria along with enhanced stability, prolonged use and adaptative propulsion modes, holding considerable promise to treat methicillin resistant antibiotic infections, for environmental remediation or food safety, among others

IV.2. Article 3. 2D nanomaterials wrapped Janus micromotors with built-in microengines for bubble, magnetic and light driven propulsion.



2D Nanomaterials Wrapped Janus Micromotors with Built-in Multiengines for Bubble, Magnetic, and Light Driven Propulsion

Kaisong Yuan, Víctor de la Asunción-Nadal, Beatriz Jurado-Sánchez,* and Alberto Escarpa*



Cite This: *Chem. Mater.* 2020, 32, 1983–1992



Read Online

ACCESS |



Metrics & More

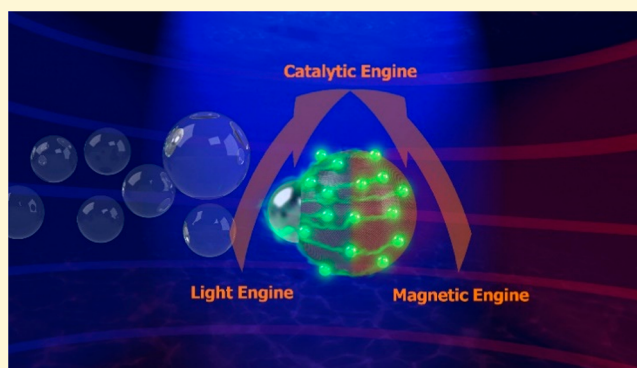


Article Recommendations



Supporting Information

ABSTRACT: Graphene oxide, graphdyne oxide, and black-phosphorus coated micromotors integrating “three engines” for motion control using different stimuli such as chemical fuel, light, and magnetic fields are described. Micromotors can be mass-produced by wrapping gold-sputtered polystyrene microspheres with the 2D nanomaterials, followed by simultaneous assembly of Pt or MnO₂ nanoparticles (NPs) as bubble (catalytic)-engines, Fe₂O₃ NPs as magnetic engines, and quantum dots (QDs) as light engines. The design and composition of micromotors are key to get the desired propulsion performance. In bubble-magnetic and bubble-light mode, a built-in acceleration system allows micromotor speed to be increased up to 3.0 and 1.5 times after application of the magnetic field or light irradiation, respectively. In the bubble-magnetic-light mode, such speed increase can be combined in a single unit for on-demand braking and accelerating systems. Fluid dynamics simulations illustrate that such adaptive behavior and improved propulsion efficiency is produced by a better distribution of the fuel and thus energy propelling the micromotor by activation of the magnetic and/or light engines. The new micromotors described here, which combine multiple engines with functional nanomaterials, hold considerable promise to develop novel nanovehicles with adaptive behavior to perform complex tasks in lab-on-a-chips or dynamic micropatterning applications.



INTRODUCTION

Nano and micromotors can be defined as tools, with a size ranging from few nanometers to micrometers, that can convert a chemical fuel, light, magnetic, or acoustic energy input into autonomous motion to perform several tasks.^{1–10} Current efforts in the field are aimed to impart them with adaptive moving behaviors to improve overall functionality in complex environments.^{11–14} Judicious design of the micromotor structure allows different functionalities to be incorporated in a single unit for further control of their propulsion behavior and motion direction with different energy sources (one or two stimuli) to speed-up, stop, or reverse their navigation. For example, a magnetocatalytic hybrid micromotor reported by Wang’s group consists of an Au–Pt nanowire (responsible for catalytic propulsion) with a Ni tail connected by an Ag segment (for magnetic propulsion). Such early design holds considerable promise to address hampering locomotion of the catalytic/phoretic mode in salt-rich complex media by the application of a magnetic field.¹⁵ Later on, our research group developed a Janus micromotors containing Pt/Fe₂O₃ nanoparticles (NPs) for dual magnetic and chemical propulsion. Such dual behavior allows bacteria endotoxin sensing to be performed in lab-on-a-chip sensors.¹⁶ Magneto-acoustic hybrid micromotors combine a ferromagnetic Ni-coated Pd helical structure with an ultrasound-active gold concave nanowire end

for dual-hybrid behavior in future biomedical applications where the magnetic behavior can assist to reach hard to access areas (i.e., hard tissues).¹⁷ Catalytic-acoustic hybrid schemes allow micromotor motion to be stop-controlled and to induce a swarming behavior for future cargo capture and transport, with designs relying on Au–Ru¹⁸ or Au–Pt nanowires¹⁹ and even PEDOT/Ni/Pt²⁰ tubular micromotors whose motion can be stopped by hindering bubble ejection under ultrasound fields. Au/Ru core–shell nanowires motors can propel by a combination of self-diffusiophoresis and electroosmosis forces in peroxide solutions by simply tailoring its length.²¹ Recently, the convenient marriage between light and catalytic, magnetic, or ultrasound propulsion has led to the design of micromotors with built-in braking and accelerating systems for future motion control and improved performance.^{22–25} Thus, the autonomous motion of light-sensitive TiO₂/Au/Pt Janus micromotors in hydrogen peroxide solutions can be reversed by ultraviolet (UV) light irradiation by changing the “active” catalyst site from Pt to TiO₂.²⁶ The different catalytic activities

Received: November 25, 2019

Revised: February 13, 2020

Published: February 14, 2020



of both metals result in such braking/acceleration behavior. Black TiO₂/Au Janus micromotors display a multiwavelength light-responsive behavior for autonomous propulsion both in H₂O₂ solutions and in water over a broad range of wavelengths (UV, blue, cyan, green, and red light).²⁷ Similarly, our group described the acceleration of multilight driven quantum dots sensitized fullerene based tubular micromotors with Pt, Pd, or MnO₂ as inner catalytic layers. Upon light irradiation (from 385 to 670 nm), electrons released from the CdS QDs are trapped in the catalytic layers, resulting in a negative net charge in the metal side, which reacts with oxygen and protons present in the media, generating additional H₂O₂ or O₂ input, which is further decomposed and increases the overall micromotor speed.²⁸ ZnO/Pt tubular micromotors display a similar on-the-fly optical acceleration nature.²⁹ Interestingly, the incorporation of a Ni layer into such ZnO based tubular micromotors introduce additional magnetic-light controlled propulsion capabilities.¹³

Apart from the inherent adaptative motion capabilities, a key to develop micromotors with high performance for future applications is to explore the incorporation of advanced functional materials for further functionalization. In addition, carbon nanomaterials,^{30–34} black phosphorus,³⁵ molybdenum disulfide (MoS₂),³⁶ or tungsten disulfide (WS₂)³⁷ impart the micromotors with a rough surface area for the subsequent incorporation of a high loading of the active nanoparticles, which are responsible for the motion control behavior, allowing the propulsion mode to be thus tuned. For example, Pumera's group illustrates that the motion of mesoporous ZnO/Pt Janus depends on the surface roughness, with a pure diffusiophoretic motion for rough micromotors and fuel-free UV light propulsion for smooth micromotors.³⁸ Yet, the incorporation of functional nanomaterials into micromotors units and the influence in the motion control behavior remains unexplored to date. In addition, only dual stimulates have been described (magnetic-catalytic, magnetic-acoustic, catalytic-acoustic, magnetic-light, and acoustic-light), without attempts to incorporate additional modes (triple or more stimulates) for forthcoming applications.

To address the above-mentioned gaps, herein we report the preparation of 2D nanomaterials coated micromotors integrating three engines for motion control using different stimuli such as chemical fuel, light and magnetic fields. Unlike previous works, here we will study the influence of the micromotor composition in the propulsion modality, which allows adapting its composition on-demand for a given application in a specific media. Micromotors can be mass-produced by wrapping gold-sputtered polystyrene (PS) microspheres with already explored (graphene oxide, GO) and novel 2D nanomaterials (black phosphorus, BP, and graphdiyne oxide, GDYO). The concept is illustrated in Figure 1. As can be seen, Pt or MnO₂ NPs were used as engines for bubble (catalytic)-propulsion, Fe₂O₃ NPs as magnetic mode handles, and QDs as light mode engines (see Figure 1A). In the following sections, we will characterize each motion modality, study the influence of the 2D nanomaterials, catalyst and peroxide, or light intensity upon the propulsion performance as well as by fluid dynamics simulations. Such knowledge will allow for additional control of the micromotor moving behavior for a given application.

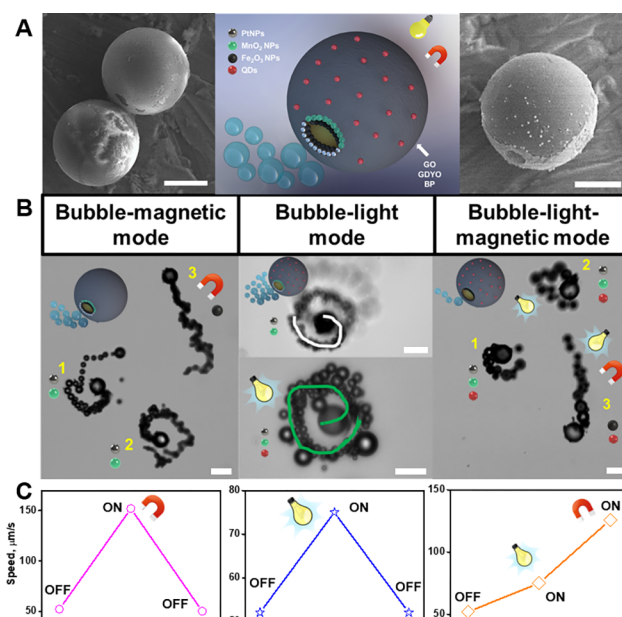


Figure 1. (A) Scanning-electron microscopy (SEM) images of the morphology of the micromotors (left and right images) and schematic of the micromotor structure (middle). Gold sputtered PS spheres (20 μm) are wrapped with GO, GDYO, or BP as nanomaterials and Pt or MnO₂ NPs as engines for bubble-propulsion, Fe₂O₃ NPs as magnetic mode engines, and CdSe@ZnS QDs as light mode engine. Scale bars, 10 μm. (B) Time-lapse images (taken from Video S1) showing the hybrid propulsion modes of a GDYO/Pt-Fe₂O₃-QDs Janus micromotors in 5% hydrogen peroxide solutions and (C) corresponding speed profiles. Scale bars, 20 μm.

EXPERIMENTAL SECTION

Reagents and Materials. Polystyrene microparticles (cat. 87896), benzyl alcohol (cat. 305197), thioglycolic acid (cat. T3758), *N*-(3-(dimethylamino)propyl)-*N*'-ethylcarbodiimide hydrochloride (cat. 03449), hydrazine solution (cat. 309400), graphene oxide (cat. 763705), black phosphorus (cat. 808970), polyethylenimine (cat. 408727), iron(III) oxide (cat. 544884), chloroplatinic acid hydrate (cat. 398322), hydrogen peroxide (cat. 216763), cysteamine (cat. M9768), potassium permanganate (cat. 223468), and CdSe@ZnS alloyed quantum dots kit (cat. 753904) were purchased from Sigma-Aldrich (Spain). Sodium dodecyl sulfate (cat. 71727) was supplied by Merck (Germany). All reagents were used without further purification. Graphdiyne was provided by Li et al. and used as received without further purification. The synthesis method has been described in a previous work.³⁹ An inverted optical microscope (Nikon Eclipse Instrument Inc. TiS/L100), coupled with 20× and 40× objectives, a Zyla CMOS digital camera and NIS Elements AR 3.2 software, was utilized for capturing movies. The speed of the micromotors was tracked using a NIS Elements tracking module. Various filters cubes were used to obtain the different light emissions: DAPI (382–393 nm), FITC (467–498 nm), and G-2A (510–560 nm).

Preparation of PS-Au Janus Microparticles. First, ordinary glass slide substrates were washed with acetone, ethanol, and pure water in an ultrasonic bath. Second, PS microparticles (aqueous suspension concentration: 2%) were dropped on the clean glass slide to form a monolayer at room temperature. The successful generation was checked by optical microscopy. Third, large-scale PS monolayers would thus be formed on the glass slide and then sputtered with a ~50 nm gold layer. At last, PS-Au monolayers were transferred to the pure water for the further modification.

Synthesis of GO Coated PS-Au Janus Microparticles. For the preparation of sulfhydryl-modified graphene oxide (HS-GO), GO (dispersion in water, 10 mL, 0.1 mg/mL) was first mixed with 0.15 g

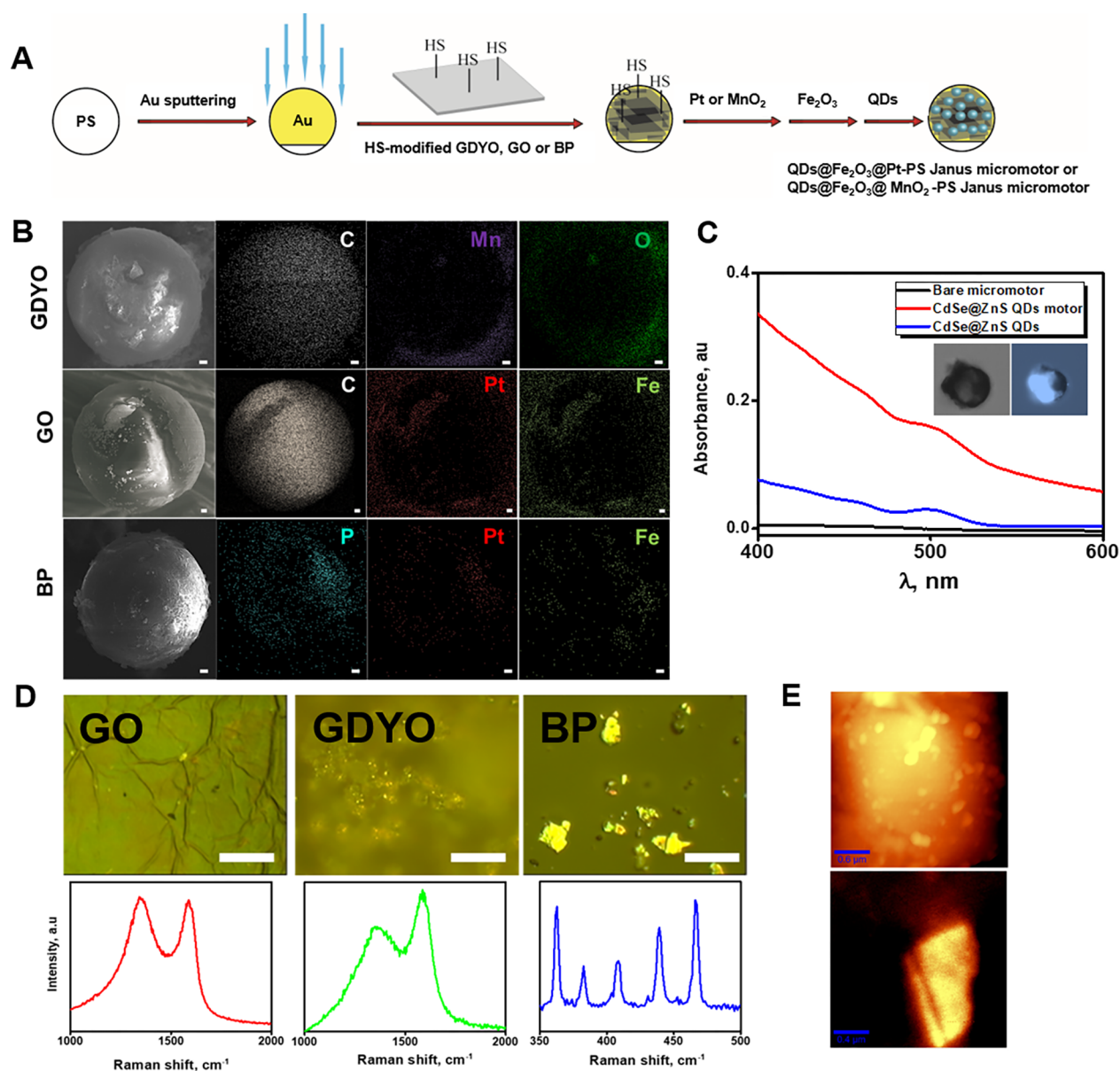


Figure 2. (A) Schematic of the Janus micromotor synthesis: 50 nm gold layer sputtered PS microparticles are incubated with thiol modified nanomaterials (GO, GDYO, or BP). After assembly to the nanoparticle surface, Pt or MnO₂ are generated in situ in the presence of the Janus microparticles, following Fe₂O₃ and QDs assembly. (B) SEM and energy-dispersive X-ray (EDX) characterization of the micromotors and element distribution. Scale bars, 1 μm. (C) UV-vis spectra of CdSe@ZnS QDs, bare, and QDs wrapped micromotors. (D) Optical microscopy images of a selected area of the micromotors and corresponding Raman spectra. Scale bars, 10 μm. (E) AFM images of GDYO and BP over the micromotor surface. Scale bars, 0.6 (top) and 0.4 μm (bottom).

of *N*-(3-(dimethylamino)propyl)-*N'*-ethylcarbodiimide hydrochloride (EDC) overnight to fully activate the carboxyl groups on the GO surfaces and then 10 mg of cysteamine (Cys) were added and mixed for another 2 h. After that, GO solution was centrifuged at 10 000 rpm for 5 min, washed with ultrapure pure water 3 times to remove the excess of Cys, and diluted to 10 mL of ultrapure water for further used. For the preparation of GO coated microparticles, 0.1 mL of the above HS-GO solution was mixed with PS-Au microparticles (0.9 mL) for 2 h to make HS-GO adhere to gold side of the PS-Au. Then the reaction solution was filtered with cyclophore track etched membrane (5 μm) to remove the free HS-GO. Herein, the GO coated PS-Au was obtained.

Synthesis of Graphdiyne Oxide (GDYO) Coated PS-Au Janus Microparticles. GDYO were made similar to an acid-oxidation method reported by Qi et al.,⁴⁰ in which 2 mg of graphdiyne (GDY) was mixed with HNO₃ (0.4 mL), H₂SO₄ (0.6 mL), and

KMnO₄ (4 mg) and stirred vigorously for 8 h at 100 °C. The reaction solution was cooled to room temperature and the pH was adjusted to 8.0 with NaOH in an ice-bath. Next, the solution was centrifuged at 10,000 rpm for 5 min and washed with ultrapure water 3 times. Herein, the GDYO was obtained. For the preparation of sulfhydryl-modified graphdiyne oxide (HS-GDYO), GDYO (dispersion in water, 10 mL, 0.1 mg/mL) was first mixed with 0.15 g of EDC overnight and then 10 mg of Cys were added and mixed for another 2 h. After that, GDYO solution was centrifuged at 10 000 rpm for 5 min, and washed with pure water for 3 times. All of the obtained HS-GDYO was diluted to 10 mL of pure water for further used. At last, same process as the synthesis of GO coated PS-Au were made to further coating the PS-Au with GDYO.

Synthesis of BP Coated PS-Au Janus Microparticles. Two-dimensional BP were made by a previous report with some modification.⁴¹ A homemade setup was prepared for ultrasonic

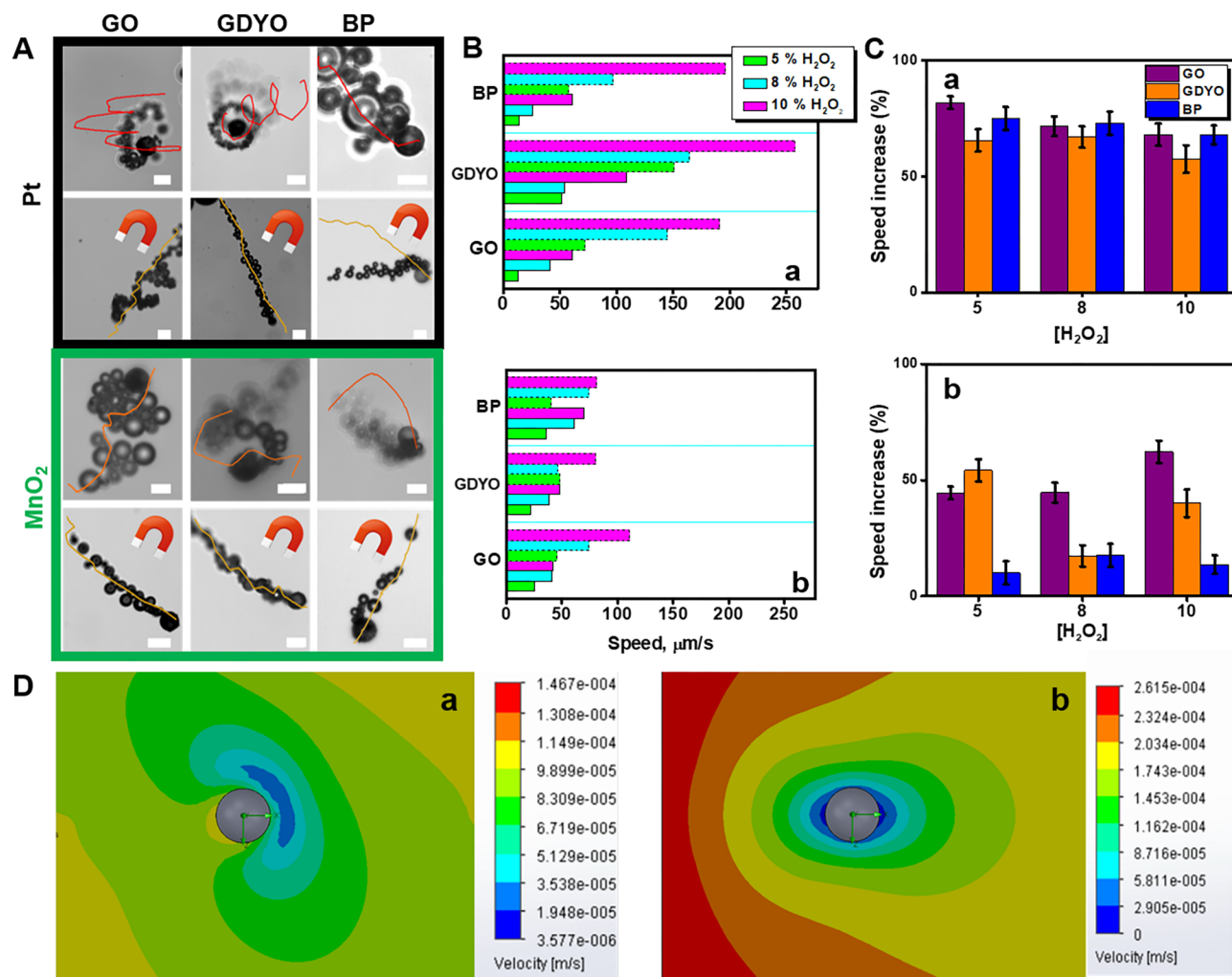


Figure 3. Bubble-magnetic hybrid Janus micromotor propulsion. (A) Time-lapse images (taken from Videos S2 and V3) showing the propulsion and corresponding tracking lines (over a 2 s period) of the micromotors in bubble and bubble-magnetic mode. (B) Influence of the nanomaterial (GO, GDYO, and BP), catalyst [(a) Pt and (b) MnO₂], and hydrogen peroxide concentration upon the micromotor speed in both bubble (continuous line in the graph bar) and bubble-magnetic (dotted line in the graph bar) modes. (C) Graph showing the speed increase (a Pt micromotors and b MnO₂ micromotors) after switching from bubble-mode to bubble-magnetic mode. (D) Simulated flow and energy mapping around the Janus micromotors structure in bubble (a) and bubble-magnetic (b) modes (see also Videos S4 and S5). Scale bar, 20 μm.

exfoliation of BP crystals. A 2% w/v SDS (20 mL) solution containing 1 mg of BP crystals inside the homemade setup was first purged with ultrahigh purity grade N₂ for 30 min to remove dissolved oxygen. Then the interface between balloon and lip, horn sonication and lip were sealed with Pattex Nural 21 several times to occlude O₂ from the outside surrounding. BP crystals inside the setup were then exfoliated by ultrasonication at 70 W for 1 h in an ice bath. After that, the solution was washed with pure water for 3 times. For the preparation of sulfhydryl-modified black phosphorus (HS-BP), BP (dispersion in water, 5 mL, 0.1 mg/mL) was first mixed with 2 mg of polyethylenimine (PEI) overnight.⁴² Then the reaction solution was centrifuged at 10 000 rpm for 5 min and washed with pure water 3 times to get the PEI@BP. The obtained PEI@BP was redispersed in 5 mL of pure water, and then 100 μL of thioglycolic acid (10 mg/mL) were added and mixed for 2 h. After that, the solution was centrifuged at 10 000 rpm for 5 min and washed with pure water 3 times to get the HS-BP. At last, the same process as the synthesis of GO and GDYO coated PS-Au were made to further coating the PS-Au with BP.

Preparation of Pt or MnO₂ Based 2D Material-PS Janus Micromotors. PtNPs were assembled into the 2D materials surfaces by an in situ synthesis method, with some modifications.⁴³ The 2D materials coated PS-Au Janus micromotors were diluted with ultrapure water (final volume: 1 mL), and then 200 μL of chloroplatinic acid hydrate (1 mg/mL) and 20 μL of hydrazine

solution (35 wt % in H₂O) were added and mixed for 2 h. After that, reaction solution was filtered with a cyclopore track etched membrane (5 μm) to remove free PtNPs. Herein, Pt-2D material-PS Janus micromotors were obtained. Fabrication of MnO₂ NPs onto the 2D materials surfaces are conducted by an in situ synthesis method, with some modifications.⁴⁴ The 2D materials coated PS-Au Janus micromotors were diluted with pure water (final volume: 1 mL), and then 200 μL of potassium permanganate (KMnO₄, 2 mg/mL) and 10 μL of benzyl alcohol (anhydrous, 99.8%) were added and mixed for 5 h. After that, the reaction solution was filtered with a cyclopore track etched membrane (5 μm) to remove the free MnO₂NPs. Herein, the MnO₂-2D material-PS Janus micromotors were obtained.

Preparation of Pt and MnO₂ Based Janus Micromotors with Magnetic Fe₂O₃ NPs and CdSe@ZnS Quantum Dots. For the fabrication of Pt or MnO₂ based Janus micromotors with magnetic Fe₂O₃ NPs, 1 mL of Pt or MnO₂ based Janus micromotors were mixed with 20 μL of Fe₂O₃ NPs (1 mg/mL) for 1 h and then filtered with a cyclopore track etched membrane (5 μm) to remove the free Fe₂O₃ NPs. Herein, the magnetic Pt based Janus micromotors were obtained. For the fabrication of Pt or MnO₂ based Janus micromotors with magnetic Fe₂O₃ NPs and CdSe@ZnS quantum dots, the above magnetic Pt based Janus micromotors were mixed with 5 μL of

CdSe@ZnS quantum dots for 1 h and then filtered with cyclopore track etched membrane (5 μm) to remove the free quantum dots.

RESULTS AND DISCUSSION

Figure 1 illustrates the concept of the multilight driven micromotor. In all cases and as reflected in the time-lapse images and corresponding tracking lines of Figure 1B, in bubble-magnetic and bubble-light mode, the built-in system allows micromotor propulsion to increase up to 3 and 1.5 times after application of the magnetic fields or light irradiation, respectively. In bubble-light-magnetic mode, such speed improvement can be combined for on-demand braking and accelerating systems (see speed profiles in Figure 1C).

As reflected in Figures 1 and 2, judicious micromotor design is key to get the desired propulsion performance. For Janus particles, the generation of a well-defined asymmetric patch in the structure is essential for the particle to experience a strong anisotropy. This will result in the accumulation of reaction products (from fuel or sample decomposition) in one side of the microparticle for directional propulsion.^{45,46} For the synthesis, we adopt a two-step protocol combining physical vapor deposition and liquid phase deposition (chemical and self-assembly) as shown in Figure 2A. First, PS nanoparticles were selected as a scaffold and coated with a thin gold layer (50 nm) which will play a dual role for nanomaterial and catalytic nanoparticles assembly (see the Experimental Section for further details). Prior to assembly, GO, GDYO, or BP were modified by the introduction of sulfhydryl (HS) group via activation of the $-\text{COOH}$ functional groups present in the materials (for GO and GDYO) or by the introduction of polyethylenimine groups, as described in the Experimental Section. Next, Pt or MnO_2 NPs were synthesized in situ in the presence of Au-2D nanomaterials coated microspheres following a seed-mediated growth type mechanism.^{47–49} To this end, we optimize the amount of nanomaterial for incubation with the Au-modified PS microspheres in order to get a small exposed gold area to promote such preferential growth. Thus, we incubate a fixed number of Au-PS microspheres with different amounts of 0.1 mg/mL solutions of sulfhydryl modified GO, GDY, and BP followed by PtNPs generation. Next, several drops (1 μL) of the as-obtained micromotors were placed on a glass slide under the microscope to check the number of motile micromotors (which was related with the successful incorporation of the PtNPs due to the presence of exposed gold). In all cases, the highest percentage of moving micromotors (80%) was obtained using 100 μL of the 2D nanomaterials solutions, whereas for higher volumes/amounts, only 5% of the micromotors were motile. Finally, Fe_2O_3 and CdSe@ZnS nanoparticles were self-assembled by incubation of the Janus microparticles with the Pt-NPs or MnO_2 -NPs, further generating thus the micromotors. The Janus structure and successful element incorporation in the micromotors are reflected in the SEM and EDX images of Figure 2B, which illustrate that the 2D nanomaterials cover the whole micromotor structure, with only a small part (the asymmetric patch) covered with Pt, MnO_2 or Fe_2O_3 NPs. UV-vis observation reveals the successful incorporation of the CdSe@ZnS QDs due to the appearance of the particular adsorption band, which cannot be observed in bare micromotor solutions (see Figure 2C). Additional Raman characterization of the micromotors indicates the presence of the nanomaterials (see Figure 2D). For GO and GDY, both D- and G-bands are clearly distinguished with minor differences

with the characteristic D and G bands of both nanomaterials,^{50,51} whereas for BP the three prominent peaks of the A_g^1 (360 cm^{-1}), B_{2g} (440 cm^{-1}), and A_g^2 (466 cm^{-1}) phonon modes are present.⁵² Simultaneously, AFM images were taken, illustrating the rough morphology of the GDY coating the micromotors (Figure 2E, top) and the characteristic morphology of a BP flake attached to the micromotor surface (Figure 2E, bottom).⁵²

We next evaluated the micromotor propulsion in bubble-magnetic mode. The time-lapse images of Figure 3A illustrate the propulsion of GO/GDY/BP-QDs-Pt- Fe_2O_3 or GO/GDY/BP-QDs- MnO_2 - Fe_2O_3 -PS Janus micromotors in 5% peroxide solutions before (top images) and after application of a magnetic field (bottom). A magnetic field was applied using a permanent neodymium magnet (N35, intensity 1.1 T). The magnet was placed at a distance of about 20 cm from the micromotor sample. At such distance, the magnetic field is parallel and does not exert a towing force on the micromotor, which orientates thus toward the applied magnetic field. Such a magnet can be easily replaced by electromagnets or permanent magnets for future applications beyond the scope of this article. A change in the trajectory from turbulent to directional can be clearly observed by the application of the magnetic field (Fe_2O_3 engine). This cause a change in the flow speed mapping around the Janus micromotors, which result in a speed increase for braking/acceleration of the micromotor, which could be very useful for future applications in complex media. Prior to further explaining the phenomena via flow simulations, we studied the effect of the type of 2D wrapping nanomaterial, catalyst, and peroxide concentration upon micromotor speed. As shown in Figure 3B, the speed increases along peroxide fuel concentrations (from 5 to 10%) from 13 ± 4 to 61 ± 30 $\mu\text{m/s}$ (GO), 52 ± 36 to 108 ± 35 $\mu\text{m/s}$ (GDYO), and 14 ± 6 to 61 ± 29 $\mu\text{m/s}$ (BP) when using Pt as catalyst. Interestingly, similar speeds were noted when using MnO_2 as a trigger for micromotor propulsion. No apparent differences among micromotors using different 2D wrapping nanomaterials or catalyst are noted, probably due to the fact that catalysts are deposited over the exposed Au layer with the same surface roughness. Yet, in bubble-magnetic mode, clear differences can be seen among micromotors propelled by Pt or MnO_2 as a catalyst. Thus, after magnetic guidance the speed of Pt micromotors increase up to 75% (in terms of speed increase, see Figure 3C,b) with a similar trend despite different 2D wrapping nanomaterials or peroxide levels are used. On the contrary, a lower speed increase percentage (40–50%) is noted in MnO_2 micromotors in magnetic mode, with the effect more pronounced at low peroxide levels. Few studies can be found in the literature about the hydrodynamics related with the motion of bubble-propelled Janus micromotors. An early model suggested that the mechanism of bubble propulsion is due to the thrust produced by bubble disengagement,⁵³ similar to tubular micromotors. Yet, a more recent study found that the previous models do not fit well with Janus micromotors (due to shape changes), attributing the fast bubble propulsion to the microbubble cavitation-induced jet flow. To further support such phenomena and observations, we selected different videos of the propulsion of the micromotors at 5% peroxide levels and performed flow simulations to study the energy mapping of the fluid around the micromotors. For this simulation we measured the speed and direction of the micromotors, decomposing the speed (velocity, v) as v_x and v_y and defining a rotation frequency as RPM. Once all of the parameters were

set, the flow speed around the motor was measured. The simulation was performed using the Flow Simulation Computational Fluid Dynamics (CFD) tool within the Solidworks 3D CAD software. Fluid velocity in the horizontal plane was depicted for clarity showing a different fluid distribution profile upon the action of the micromotor both guided and unguided. According to recent models, the bubble-growth process in Janus colloids is driven by catalytic mechanisms, and the bubble-growth process can be described by the Rayleigh–Plesset equation (physical cavitation mechanism).⁵⁴ Yet, according to recent studies related with microbubble cavitation-induced jet flow, bubble evolution and ejection is not the sole mechanism responsible for micromotor propulsion.^{55–58} Thus, another key issue needing clarification is the origin of fast, instantaneous propulsion after bubble collapse, so it is important to study the influence of the flow field to further explain the dynamics. Considering that the bubble and the micromotors usually do not locate in the same horizontal plane due to the difference of their density, the jet flow is not strictly in the horizontal plane. In other words, the main source of the fast bubble propulsion on both modes is the horizontal component of the micromotor produced by the bubble collapse rather than the impulse when the bubble leaves the surface of the Janus micromotor. As can be seen in the simulation images of Figure 3D, a higher energy (in terms of velocity) is observed around the Janus micromotors in the bubble-magnetic mode. According to the bubble cavitation-induced mechanism, this indicates a better distribution of the energy propelling the micromotor, which therefore can significantly improve the propulsion efficiency. Thus, it can be concluded that the orientation of the micromotor trajectory in bubble-magnetic mode (in comparison to bubble-mode) allow for a better distribution of the propelling energy of the micromotor, resulting in higher speeds. In other words, the increase of the directionality of the micromotor by orientation with the magnetic field can also contribute to such speed enhancement due to better fuel contact with the active nanoparticles, similar to a previous model described by our research group for tubular micromotors, which demonstrate that orienting the micromotors generates a speed increase due to the better fuel availability in the inner catalytic part.⁵⁹ The difference between the catalysts (Pt or MnO₂) can arise from its different ability to distribute such energy or to a different loading of Fe₂O₃ magnetic engines.^{54,60} Next, for future practical applications of the micromotors, we characterized its propulsion in real samples (saliva, milk, blood serum, and wine). As the magnetic effect is more pronounced for Pt micromotors, we chose them for this study. As can be seen in Figure S1 and Video S6 of the Supporting Information, despite the high viscosity and complexity of the media, micromotors propel at similar speeds to that observed in water samples in bubble mode. Yet, in bubble-magnetic mode the speed increase effect is similar for wine samples, with a slight decrease in more viscous, high-protein content saliva, milk, and blood serum samples, probably because the high viscosity of the samples disturbs somehow the improved energy distribution along the micromotors. Overall, the high towing force of the dual propelled (bubble-magnetic) microengines holds considerable promise for applications in complex samples, which are prevented by hampered locomotion.

In another conceptual step ahead, the bubble-magnetic-light three way hybrid micromotor propulsion was also explored (see Figure 4). As previously described, micromotors contain

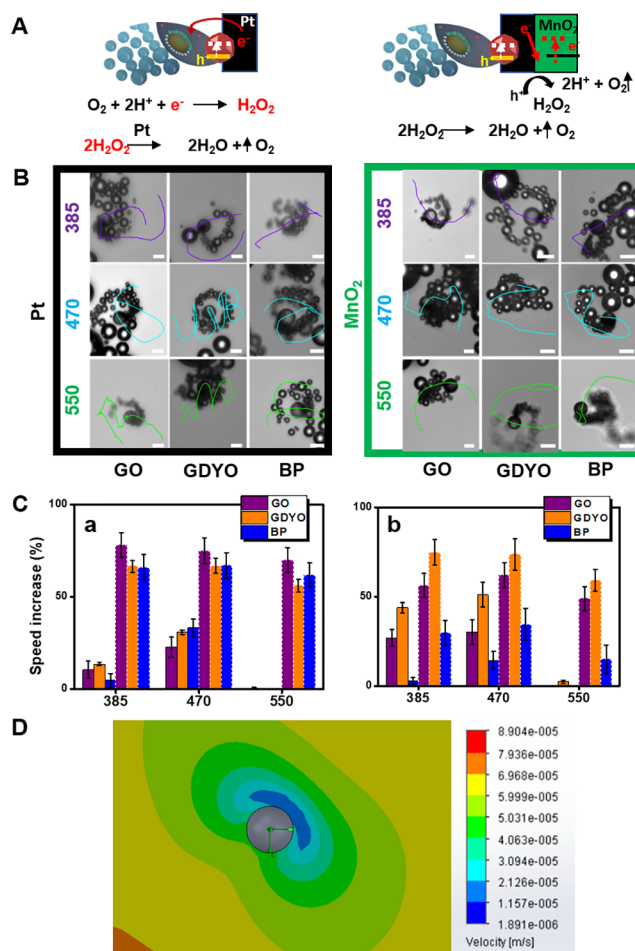


Figure 4. Bubble-light-magnetic hybrid Janus micromotor propulsion. (A) Schematic of the mechanism responsible for bubble-light-magnetic Janus micromotor propulsion. (B) Influence of the nanomaterial (GO, GDY, and BP), catalyst and light wavelength upon the micromotor speed in bubble-light mode: time-lapse images (Taken from Videos S7 and S8) showing the propulsion and corresponding tracking lines (over a 2 s period) of the micromotors in bubble and bubble-light mode. (C) Graph showing the speed increase [(a) Pt and (b) MnO₂] experience after switching from bubble-light (continuous line in the graph bar) mode to bubble-light-magnetic (dotted line in the graph bar) mode. (D) Simulated flow and turbulent energy mapping around the Janus micromotors structure in bubble-light mode (see Videos S9 and S10). Scale bars, 20 μm.

CdSe@ZnS QDs as third engine handle for acceleration-braking by light irradiation. The mechanism is depicted in Figure 4A. Upon UV or visible light irradiation, the QDs used as engine in the micromotor surface absorb photons with energies equal or higher than its bandgap energy (2.4 eV); promoting the migration of the electrons present in the valence band to the conduction band. The 2D nanomaterial layer can act as electron acceptor, promoting electron transfer toward the asymmetric Pt/Fe₂O₃ or MnO₂/Fe₂O₃ layers.⁶¹ In the case of Pt, electrons accumulate in such layer resulting in a negative net charge that reacts with oxygen and protons present in the media, generating an additional peroxide fuel input which is further decomposed to increase the micromotor speed. In the case of MnO₂, its inherent photocatalytic behavior results in the pairing of the releasing electrons with its electronic levels and subsequent promotion to the conduction band. This generates holes (h⁺) which also react with the peroxide fuel to

release additional O₂ bubbles for the micromotor acceleration.²⁸ As in the previous case, we studied the effect of the type of 2D wrapping nanomaterial and catalyst upon micromotor speed. Light intensity effect was also evaluated. The combined effect of light, wrapping nanomaterials and catalyst is shown in the time lapse-images of Figure 4B. Once the micromotors were propelling by bubble-mode at a fixed 5% peroxide level, different light illuminations were used to activate the light engine of each motor by promoting electron release from the QDs. Such light corresponds to variable photon energies: 385 (3.2 eV), 470 (2.6 eV), and 550 nm (2.3 eV). Thus, after light irradiation (see Figure S2 in the Supporting Information) the initial speed of the micromotors in bubble-mode increase from 39 ± 21 to 44 ± 15 and 75 ± 12 $\mu\text{m/s}$ after exposure to UV (385 nm) and blue (470 nm) light when using Pt. This corresponds to a speed increase of over 10–15% and 30%, respectively. A similar trend was observed regarding the wrapping 2D nanomaterials, whereas the speeds depend greatly on the light used. It should be mentioned here that at 550 nm no apparent speed increase is noted due to the band gap (2.3 eV) being lower than the band gap of the QDs (2.4 eV), thus preventing electron promotion. In the case of MnO₂ micromotors (and regarding the effect of the catalyst), the speed increases from 26 ± 12 to 42 ± 15 and 48 ± 12 $\mu\text{m/s}$ after exposure to UV (385 nm) and blue (470 nm) light. This corresponds to a speed increase of over 50% (in terms of speed increase, see Figure 4C,b), which is higher than that for Pt engines, probably due to more efficient electron promotion and products generation. As for Pt engines, no apparent acceleration is noted at 550 nm. In addition, no influence of the 2D nanomaterial is noted. Thus, it can be concluded that main variables to control the braking/acceleration system in bubble-light mode were light intensity (wavelength) and catalyst (Pt or MnO₂).

After characterizing the motion in bubble-light mode, we applied the magnetic field to activate the magnetic engine and record the resulting speed. For Pt microengines, speed increase in all cases is within the same magnitude to that noted in bubble-magnetic mode, indicating that the towing force of the magnetic activated engine surpasses the light engine (Figure 4C, a, dotted line). On the contrary, for MnO₂ microengines, a much great speed increase of up to 60% (GO), 73% (GDYO) and 34% (BP) is noted, which is from 1.4 to 3.4 times higher than bubble-magnetic mode, indicating the additive effect of both improved light induced oxygen generation and magnetic enhanced energy distribution (Figure 4C,b, dotted line). Additionally, to check a possible effect of Fe₂O₃ NPs on the light motion, we performed the light only experiments with QDs-modified micromotors without the addition of the magnetic nanoparticles. No apparent speed increase is observed, revealing the negligible contribution of such magnetic nanoparticles. Also, in the UV–vis images of micromotors containing Fe₂O₃ and PtNPs nanoparticles (bare micromotors, Figure 2C), no apparent adsorption bands are noted, as compared with micromotors containing QDs, further supporting the above-mentioned observation. Additional 3D flow numerical simulations to study the energy mapping of the fluid around the micromotors illustrate a similar trend in bubble and bubble-light modes, with a slight increase in the velocity (energy) due to the enhanced fuel or oxygen generation (see Figure 4D). For bubble-light-magnetic mode, the distribution is like that of bubble-magnetic mode. Thus, it can be concluded that main variables to control the

braking/acceleration system in bubble-light-magnetic mode were also light intensity (wavelength) and catalyst (Pt or MnO₂).

Next, for future practical applications of the micromotors, we characterized its propulsion in real samples (saliva, milk, blood serum and wine). As can be seen in Figure S3 and Video S11 of the Supporting Information, despite the high viscosity and complexity of the media, the combined effect of bubble-light and magnetic fields leads to a highly remarkable speed in all the samples tested despite the high complexity in some cases. Such speeds are higher (from 1.5 to 2 times) when compared to the similar study performed in bubble-magnetic mode, reflecting the superior capabilities of the combination of the three systems in a single engine.

CONCLUSIONS

In conclusion, we have described the preparation of multi-stimulate driven Janus micromotors with built-in engines for bubble, magnetic, and light driven propulsion and hybrid schemes. For the first time, the micromotor body also incorporates not only well-established 2D nanomaterials (GO) but novel ones (GDYO and BP) with rich outer surface chemistry to be exploited in future applications. Different variables such as type of engines (Pt or MnO₂ nanoparticles), peroxide fuel, and light can be modulated to tailor the micromotor propulsion in each mode. Thus, in bubble mode speed modulation can be achieved by changing the fuel composition, as in common catalytic micromotors. Surprisingly, in bubble-magnetic mode the main variables were peroxide level and type of catalyst used, with a speed increase of up to 75% (in terms of speed increase) for Pt based microengines and up to 50% for MnO₂ micromotors in magnetic mode, with the effect more pronounced at low peroxide levels. In bubble-light mode, the braking-acceleration system can be tailored by modulating light intensity (wavelength) and catalyst (Pt or MnO₂), with a change in the speed increase trend of 50% for MnO₂ and 30% for PtNPs, probably due to a better synergetic effect between CdSe@ZnS QDs to promote electron transfer. Finally, in the bubble-light-magnetic mode, when using PtNPs the effect of magnetic fields surpasses the light-enhanced acceleration, whereas a synergetic effect between the three engines is noted for MnO₂, with a speed increase of over 73%. Numerical simulations illustrate that such adaptive behavior and improved propulsion efficiency is produced by a better distribution of the energy propelling the micromotor by activation of the magnetic and/or light engines following the so-called bubble cavitation-induced mechanism. The new micromotors offer myriad controllable propulsion behaviors, which, along with the incorporation of functional nanomaterials such as BP or GDY, will serve as the rational and mass-scale design of hybrid microrobotics for a wide range of applications with unprecedented performance.

ASSOCIATED CONTENT

Supporting Information

The Supporting Information is available free of charge at <https://pubs.acs.org/doi/10.1021/acs.chemmater.9b04873>.

Supporting figures (PDF)

Multicatalytic, light and magnetic propulsion of GDYO-PtNPs-Fe₂O₃-QDs Janus micromotors in 5% H₂O₂ (AVI)

Bubble-magnetic propulsion of 2D nanomaterials-PtNPs-Fe₂O₃-QDs Janus micromotors in 5% H₂O₂ (AVI)

Bubble-magnetic propulsion of 2D nanomaterials-PtNPs-MnO₂-QDs Janus micromotors in 5% H₂O₂ (AVI)

Simulated flow energy mapping around the micromotor in bubble mode (AVI)

Simulated flow energy mapping around the micromotor in bubble-magnetic mode (AVI)

Janus micromotors propulsion in real samples in bubble-magnetic mode (AVI)

Bubble-light propulsion of 2D nanomaterials-PtNPs-Fe₂O₃-QDs Janus micromotors in 5% H₂O₂ (AVI)

Bubble-light propulsion of 2D nanomaterials-MnO₂-Fe₂O₃-QDs Janus micromotors in 5% H₂O₂ (AVI)

Simulated flow energy mapping around the micromotor in bubble-light mode (AVI)

Simulated flow energy mapping around the micromotor in bubble-light-magnetic mode (AVI)

Janus micromotors propulsion in real samples in bubble-magnetic-light mode (AVI)

AUTHOR INFORMATION

Corresponding Authors

Beatriz Jurado-Sánchez – Department of Analytical Chemistry, Physical Chemistry and Chemical Engineering and Chemical Research Institute “Andrés M. del Río”, University of Alcalá, Alcalá de Henares E-28871, Madrid, Spain; orcid.org/0000-0002-6584-1949; Email: beatriz.jurado@uah.es

Alberto Escarpa – Department of Analytical Chemistry, Physical Chemistry and Chemical Engineering and Chemical Research Institute “Andrés M. del Río”, University of Alcalá, Alcalá de Henares E-28871, Madrid, Spain; orcid.org/0000-0002-7302-0948; Phone: +34 91 8854995; Email: alberto.escarpa@uah.es

Authors

Kaisong Yuan – Department of Analytical Chemistry, Physical Chemistry and Chemical Engineering, University of Alcalá, Alcalá de Henares E-28871, Madrid, Spain; Institute of Pharmaceutical Analysis, College of Pharmacy, Jinan University, Guangzhou, China

Victor de la Ascunción-Nadal – Department of Analytical Chemistry, Physical Chemistry and Chemical Engineering, University of Alcalá, Alcalá de Henares E-28871, Madrid, Spain

Complete contact information is available at:

<https://pubs.acs.org/10.1021/acs.chemmater.9b04873>

Author Contributions

The manuscript was written through contributions of all authors. All authors have given approval to the final version of the manuscript.

Notes

The authors declare no competing financial interest.

ACKNOWLEDGMENTS

K.Y. acknowledges the Spanish Ministry of Science, Innovation and Universities for his predoctoral contract (RYC-2015-17558, cofinanced by EU). V..d.l.A.-N. acknowledges the FPI fellowship received from the University of Alcalá. B.J.-S.

acknowledges support from the Spanish Ministry of Science, Innovation and Universities (RYC-2015-17558, cofinanced by EU) from the University of Alcalá (CCG19/CC-029) and from the UAH/Community of Madrid (CM/JIN/2019-007). A.E. acknowledges financial support from the Spanish Ministry of Science, Innovation and Universities (CTQ2017-86441-C2-1-R) and the TRANSNANOAVANSENS program (S2018/NMT-4349) from the Community of Madrid.

REFERENCES

- (1) Paxton, W. F.; Kistler, K. C.; Olmeda, C. C.; Sen, A.; St Angelo, S. K.; Cao, Y.; Mallouk, T. E.; Lammert, P. E.; Crespi, V. H. Catalytic Nanomotors: Autonomous Movement of Striped Nanorods. *J. Am. Chem. Soc.* **2004**, *126*, 13424–13431.
- (2) Kline, T. R.; Paxton, W. F.; Mallouk, T. E.; Sen, A. Catalytic Nanomotors: Remote-Controlled Autonomous Movement of Striped Metallic Nanorods. *Angew. Chem. Int. Ed.* **2005**, *117*, 754–756.
- (3) Paxton, W. F.; Sundararajan, S.; Mallouk, T. E.; Sen, A. Chemical Locomotion. *Angew. Chem., Int. Ed.* **2006**, *45*, 5420–5429.
- (4) Gao, W.; Sattayasamitsathit, S.; Orozco, J.; Wang, J. Highly Efficient Catalytic Microengines: Template Electrosynthesis of Polyaniline/Platinum Microtubes. *J. Am. Chem. Soc.* **2011**, *133*, 11862–11864.
- (5) Gao, W.; Sattayasamitsathit, S.; Uygun, A.; Pei, A.; Ponedal, A.; Wang, J. Polymer-based tubular microbots: role of composition and preparation. *Nanoscale* **2012**, *4*, 2447–2453.
- (6) Wang, W.; Castro, L. A.; Hoyos, M.; Mallouk, T. E. Autonomous Motion of Metallic Microrods Propelled by Ultrasound. *ACS Nano* **2012**, *6*, 6122–6132.
- (7) Garcia-Gradilla, V.; Orozco, J.; Sattayasamitsathit, S.; Soto, F.; Kuralay, F.; Pourazary, A.; Katzenberg, A.; Gao, W.; Shen, Y.; Wang, J. Functionalized Ultrasound-Propelled Magnetically Guided Nanomotors: Toward Practical Biomedical Applications. *ACS Nano* **2013**, *7*, 9232–9240.
- (8) Wang, J. *Nanomachines: Fundamentals and Applications*; Wiley VCH: Weinheim, Germany, 2013.
- (9) Chen, X.-Z.; Hoop, M.; Mushtaq, F.; Siringil, E.; Hu, C.; Nelson, B. J.; Pané, S. Recent developments in magnetically driven micro- and nanorobots. *Appl. Mater. Today* **2017**, *9*, 37–48.
- (10) Karshalev, E.; Esteban-Fernández de Ávila, B.; Wang, J. Micromotors for “Chemistry-on-the-Fly”. *J. Am. Chem. Soc.* **2018**, *140*, 3810–3820.
- (11) Ren, L.; Wang, W.; Mallouk, T. E. Two Forces Are Better than One: Combining Chemical and Acoustic Propulsion for Enhanced Micromotor Functionality. *Acc. Chem. Res.* **2018**, *51*, 1948–1956.
- (12) Chen, C.; Soto, F.; Karshalev, E.; Li, J.; Wang, J. Hybrid Nanovehicles: One Machine, Two Engines. *Adv. Funct. Mater.* **2019**, *29*, 1806290.
- (13) Wang, C.; Dong, R.; Wang, Q.; Zhang, C.; She, X.; Wang, J.; Cai, Y. One Modification, Two Functions: Single Ni-modified Light-Driven Microrockets with Both Efficient Propulsion and Steerable Motion. *Chem. - Asian J.* **2019**, *14*, 2485–2490.
- (14) Wang, D.; Zhao, G.; Chen, C.; Zhang, H.; Duan, R.; Zhang, D.; Li, M.; Dong, B. One-Step Fabrication of Dual Optically/Magnetically Modulated Walnut-like Micromotor. *Langmuir* **2019**, *35*, 2801–2807.
- (15) Gao, W.; Manesh, K. M.; Hua, J.; Sattayasamitsathit, S.; Wang, J. Hybrid Nanomotor: A Catalytically/Magnetically Powered Adaptive Nanowire Swimmer. *Small* **2011**, *7*, 2047–2051.
- (16) Jurado-Sánchez, B.; Pacheco, M.; Rojo, J.; Escarpa, A. Magnetocatalytic Graphene Quantum Dots Janus Micromotors for Bacterial Endotoxin Detection. *Angew. Chem., Int. Ed.* **2017**, *56*, 6957–6961.
- (17) Li, J.; Li, T.; Xu, T.; Kiristi, M.; Liu, W.; Wu, Z.; Wang, J. Magneto-Acoustic Hybrid Nanomotor. *Nano Lett.* **2015**, *15*, 4814–4821.
- (18) Ren, L.; Zhou, D.; Mao, Z.; Xu, P.; Huang, T. J.; Mallouk, T. E. Rheotaxis of Bimetallic Micromotors Driven by Chemical-Acoustic Hybrid Power. *ACS Nano* **2017**, *11*, 10591–10598.

- (19) Xu, T.; Soto, F.; Gao, W.; Dong, R.; Garcia-Gradilla, V.; Magaña, E.; Zhang, X.; Wang, J. Reversible Swarming and Separation of Self-Propelled Chemically Powered Nanomotors under Acoustic Fields. *J. Am. Chem. Soc.* **2015**, *137*, 2163–2166.
- (20) Xu, T.; Soto, F.; Gao, W.; Garcia-Gradilla, V.; Li, J.; Zhang, X.; Wang, J. Ultrasound-Modulated Bubble Propulsion of Chemically Powered Microengines. *J. Am. Chem. Soc.* **2014**, *136*, 8552–8555.
- (21) Jang, B.; Wang, W.; Wiget, S.; Petruska, A. J.; Chen, X.; Hu, C.; Hong, A.; Folio, D.; Ferreira, A.; Pané, S.; Nelson, B. J. Catalytic Locomotion of Core–Shell Nanowire Motors. *ACS Nano* **2016**, *10*, 9983–9991.
- (22) Tang, S.; Zhang, F.; Zhao, J.; Talaat, W.; Soto, F.; Karshalev, E.; Chen, C.; Hu, Z.; Lu, X.; Li, J.; Lin, Z.; Dong, H.; Zhang, X.; Nourhani, A.; Wang, J. Structure-Dependent Optical Modulation of Propulsion and Collective Behavior of Acoustic/Light-Driven Hybrid Microbowls. *Adv. Funct. Mater.* **2019**, *29*, 1809003.
- (23) Xing, Y.; Zhou, M.; Du, X.; Li, X.; Li, J.; Xu, T.; Zhang, X. Hollow Mesoporous Carbon@Pt Janus Nanomotors with Dual Response of H₂O₂ and Near-Infrared Light for Active Cargo Delivery. *Appl. Mater. Tod.* **2019**, *17*, 85–91.
- (24) Villa, K.; Novotný, F.; Zelenka, J.; Browne, M. P.; Ruml, T.; Pumera, M. Visible-Light-Driven Single-Component BiVO₄ Micromotors with the Autonomous Ability for Capturing Microorganisms. *ACS Nano* **2019**, *13*, 8135–8145.
- (25) Villa, K.; Pumera, M. Fuel-free light-driven micro/nano-machines: artificial active matter mimicking nature. *Chem. Soc. Rev.* **2019**, *48*, 4966–4978.
- (26) Chen, C.; Tang, S.; Teymourian, H.; Karshalev, E.; Zhang, F.; Li, J.; Mou, F.; Liang, Y.; Guan, J.; Wang, J. Chemical/Light-Powered Hybrid Micromotors with “On-the-Fly” Optical Brakes. *Angew. Chem., Int. Ed.* **2018**, *57*, 8110–8114.
- (27) Jang, B.; Hong, A.; Kang, H. E.; Alcantara, C.; Charreyron, S.; Mushtaq, F.; Pellicer, E.; Büchel, R.; Sort, J.; Lee, S. S.; Nelson, B. J.; Pané, S. Multiwavelength Light-Responsive Au/B-TiO₂ Janus Micromotors. *ACS Nano* **2017**, *11*, 6146–6154.
- (28) María Hormigos, R.; Jurado-Sánchez, B.; Escarpa, A. Multi-Light-Responsive Quantum Dot Sensitized Hybrid Micromotors with Dual-Mode Propulsion. *Angew. Chem., Int. Ed.* **2019**, *58*, 3128–3132.
- (29) Dong, R.; Wang, C.; Wang, Q.; Pei, A.; She, X.; Zhang, Y.; Cai, Y. ZnO-based Microrockets with Light-enhanced Propulsion. *Nano-scale* **2017**, *9*, 15027–15032.
- (30) María-Hormigos, R.; Jurado-Sánchez, B.; Vazquez, L.; Escarpa, A. Carbon Allotrope Nanomaterials Based Catalytic Micromotors. *Chem. Mater.* **2016**, *28*, 8962–8970.
- (31) Martín, A.; Jurado-Sánchez, B.; Escarpa, A.; Wang, J. Template Electrosynthesis of High-Performance Graphene Microengines. *Small* **2015**, *11*, 3568–3574.
- (32) Ye, H.; Kang, J.; Ma, G.; Sun, H.; Wang, S. High-speed Graphene@Ag-MnO₂ Micromotors at Low Peroxide Levels. *J. Colloid Interface Sci.* **2018**, *528*, 271–280.
- (33) Vilela, D.; Parmar, J.; Zeng, Y.; Zhao, Y.; Sánchez, S. Graphene-Based Microbots for Toxic Heavy Metal Removal and Recovery from Water. *Nano Lett.* **2016**, *16*, 2860–2866.
- (34) Ma, X.; Katuri, J.; Zeng, Y.; Zhao, Y.; Sanchez, S. Surface Conductive Graphene-Wrapped Micromotors Exhibiting Enhanced Motion. *Small* **2015**, *11*, 5023–5027.
- (35) Maric, T.; Moo, J. G. S.; Khezri, B.; Sofer, Z.; Pumera, M. Black-Phosphorus-enhanced Bubble-propelled Autonomous Catalytic Microjets. *Appl. Mater. Tod.* **2017**, *9*, 289–291.
- (36) Singh, V. V.; Kaufmann, K.; de Avila, B. E.-F.; Karshalev, E.; Wang, J. Molybdenum Disulfide-Based Tubular Microengines: Toward Biomedical Applications. *Adv. Funct. Mater.* **2016**, *26*, 6270–6278.
- (37) Mayorga-Martinez, C. C.; Moo, J. G. S.; Khezri, B.; Song, P.; Fisher, A. C.; Sofer, Z.; Pumera, M. Self-Propelled Supercapacitors for On-Demand Circuit Configuration Based on WS₂ Nanoparticles Micromachines. *Adv. Funct. Mater.* **2016**, *26*, 6662–6667.
- (38) Pourrahimi, A. M.; Villa, K.; Manzanera Palenzuela, C. L.; Ying, Y.; Sofer, Z.; Pumera, M. Catalytic and Light-Driven ZnO/Pt Janus Nano/Micromotors: Switching of Motion Mechanism via Interface Roughness and Defect Tailoring at the Nanoscale. *Adv. Funct. Mater.* **2019**, *29*, 1808678.
- (39) Jia, Z.; Li, Y.; Zuo, Z.; Liu, H.; Huang, C.; Li, Y. Synthesis and Properties of 2D Carbon-Graphdiyne. *Acc. Chem. Res.* **2017**, *50*, 2470–2478.
- (40) Qi, H.; Yu, P.; Wang, Y.; Han, G.; Liu, H.; Yi, Y.; Li, Y.; Mao, L. Graphdiyne Oxides as Excellent Substrate for Electroless Deposition of Pd Clusters with High Catalytic Activity. *J. Am. Chem. Soc.* **2015**, *137*, 5260–5263.
- (41) Kang, J.; Wells, S. A.; Wood, J. D.; Lee, J.-H.; Liu, X.; Ryder, C. R.; Zhu, J.; Guest, J. R.; Husko, C. A.; Hersam, M. C. Stable Aqueous Dispersions of Optically and Electronically Active Phosphorene. *Proc. Natl. Acad. Sci. U. S. A.* **2016**, *113*, 11688–11693.
- (42) Liu, Y.; Wang, Y.; Ikram, M.; Lv, H.; Chang, J.; Li, Z.; Ma, L.; Rehman, A. U.; Lu, G.; Chen, J.; Shi, K. Facile Synthesis of Highly Dispersed Co₃O₄ Nanoparticles on Expanded, Thin Black Phosphorus for a ppb-Level NO_x Gas Sensor. *ACS Sens.* **2018**, *3*, 1576–1583.
- (43) Zhao, Y.; Zhou, Y.; O’Hayre, R.; Shao, Z. Electrocatalytic Oxidation of Methanol on Pt Catalyst Supported on Nitrogen-doped Graphene Induced by Hydrazine Reduction. *J. Phys. Chem. Solids* **2013**, *74*, 1608–1614.
- (44) Wu, S.; Chen, W.; Yan, L. Fabrication of a 3D MnO₂/graphene Hydrogel for High-Performance Asymmetric Supercapacitors. *J. Mater. Chem. A* **2014**, *2*, 2765–2772.
- (45) Pawar, A. B.; Kretzschmar, I. Fabrication, Assembly, and Application of Patchy Particles. *Macromol. Rapid Commun.* **2010**, *31*, 150–168.
- (46) Pacheco, M.; Jurado-Sánchez, B.; Escarpa, A. Lab-on-a-Micromotor: Catalytic Janus Particles as Mobile Microreactors for Tailored Synthesis of Nanoparticles. *Chem. Sci.* **2018**, *9*, 8056–8064.
- (47) Straney, P. J.; Marbella, L. E.; Andolina, C. M.; Nuhfer, N. T.; Millstone, J. E. Decoupling Mechanisms of Platinum Deposition on Colloidal Gold Nanoparticle Substrates. *J. Am. Chem. Soc.* **2014**, *136*, 7873–7876.
- (48) Fan, F.-R.; Liu, D.-Y.; Wu, Y.-F.; Duan, S.; Xie, Z.-X.; Jiang, Z.-Y.; Tian, Z.-Q. Epitaxial Growth of Heterogeneous Metal Nanocrystals: From Gold Nano-octahedra to Palladium and Silver Nanocubes. *J. Am. Chem. Soc.* **2008**, *130*, 6949–6951.
- (49) Gu, D.; Tseng, J.-C.; Weidenthaler, C.; Bongard, H.-J.; Spliethoff, B.; Schmidt, W.; Soulmani, F.; Weckhuysen, B. M.; Schüth, F. Gold on Different Manganese Oxides: Ultra-Low-Temperature CO Oxidation over Colloidal Gold Supported on Bulk-MnO₂ Nanomaterials. *J. Am. Chem. Soc.* **2016**, *138*, 9572–9580.
- (50) Zhang, M.; Wang, X.; Sun, H.; Wang, N.; Lv, Q.; Cui, W.; Long, Y.; Huang, C. Enhanced Paramagnetism of Mesoscopic Graphdiyne by Doping with Nitrogen. *Sci. Rep.* **2017**, *7*, 11535.
- (51) Wu, J.-B.; Lin, M.-L.; Cong, X.; Liu, H.-N.; Tan, P.-H. Raman Spectroscopy of Graphene-based Materials and its Applications in Related Devices. *Chem. Soc. Rev.* **2018**, *47*, 1822–1873.
- (52) Aldave, S. H.; Yogeesh, M. N.; Zhu, W.; Kim, J.; Sonde, S. S.; Nayak, A. P.; Akinwande, D. Characterization and Sonochemical Synthesis of Black phosphorus from Red Phosphorus. *2D Mater.* **2016**, *3*, 014007.
- (53) Li, L.; Wang, J.; Li, T.; Song, W.; Zhang, G. A Unified Model of Drag Force for Bubble-propelled Catalytic Micro/nano-motors with Different Geometries in Low Reynolds Number Flows. *J. Appl. Phys.* **2015**, *117*, 104308.
- (54) Zhang, J.; Zheng, X.; Cui, H.; Silber-Li, Z. The Self-Propulsion of the Spherical Pt–SiO₂ Janus Micro-Motor. *Micromachines* **2017**, *8*, 123.
- (55) Manjare, M.; Yang, B.; Zhao, Y. P. Bubble Driven Quasioscillatory Translational Motion of Catalytic Micromotors. *Phys. Rev. Lett.* **2012**, *109*, 128305.
- (56) Zwaan, E.; Le Gac, S.; Tsuji, K.; Ohl, C.-D. Controlled Cavitation in Microfluidic Systems. *Phys. Rev. Lett.* **2007**, *98*, 254501.
- (57) Michelin, S.; Lauga, E. Geometric Tuning of Self-Propulsion for Janus Catalytic Particles. *Sci. Rep.* **2017**, *7*, 42264.

(58) Yang, F.; Manjare, M.; Zhao, Y.; Qiao, R. On the Peculiar Bubble Formation, Growth, and Collapse Behaviors in Catalytic Micro-motor Systems. *Microfluid. Nanofluid.* **2017**, *21*, 6.

(59) Asuncion-Nadal, V.; Jurado-Sanchez, B.; Vazquez, L.; Escarpa, A. Magnetic Fields Enhanced the Performance of Tubular Dichalcogenide Micromotors at Low Hydrogen Peroxide Levels. *Chem. - Eur. J.* **2019**, *25*, 13157–13163.

(60) Wang, L. L.; Chen, L.; Zhang, J.; Duan, J. M.; Wang, L.; Silberli, Z. H.; Zheng, X.; Cui, H. H. Efficient Propulsion and Hovering of Bubble-Driven Hollow Micromotors underneath an Air-Liquid Interface. *Langmuir* **2018**, *34*, 10426–10433.

(61) Wang, M.; Shang, X.; Yu, X.; Liu, R.; Xie, Y.; Zhao, H.; Cao, H.; Zhang, G. Graphene–CdS Quantum Dots–Polyoxometalate Composite Films for Efficient Photoelectrochemical Water Splitting and Pollutant Degradation. *Phys. Chem. Chem. Phys.* **2014**, *16*, 26016–26023.

SUPPORTING INFORMATION

2D nanomaterials wrapped Janus micromotors with built-in multiengines for bubble, magnetic, and light driven propulsion

Kaisong Yuan,^{†§} Víctor de la Asunción-Nadal,[†] Beatriz Jurado Sánchez,^{†‡*} Alberto Escarpa^{†‡*}

[†]Department of Analytical Chemistry, Physical Chemistry and Chemical Engineering, University of Alcalá, Alcalá de Henares E-28871, Madrid, Spain. E-mail: beatriz.jurado@uah.es, alberto.escarpa@uah.es (Tel: +34 91 8854995)

[§]Institute of Pharmaceutical Analysis, College of Pharmacy, Jinan University, Guangzhou, China

[‡]Chemical Research Institute "Andrés M. del Río", University of Alcalá, Alcalá de Henares E-28871, Madrid, Spain

SUPPORTING FIGURES

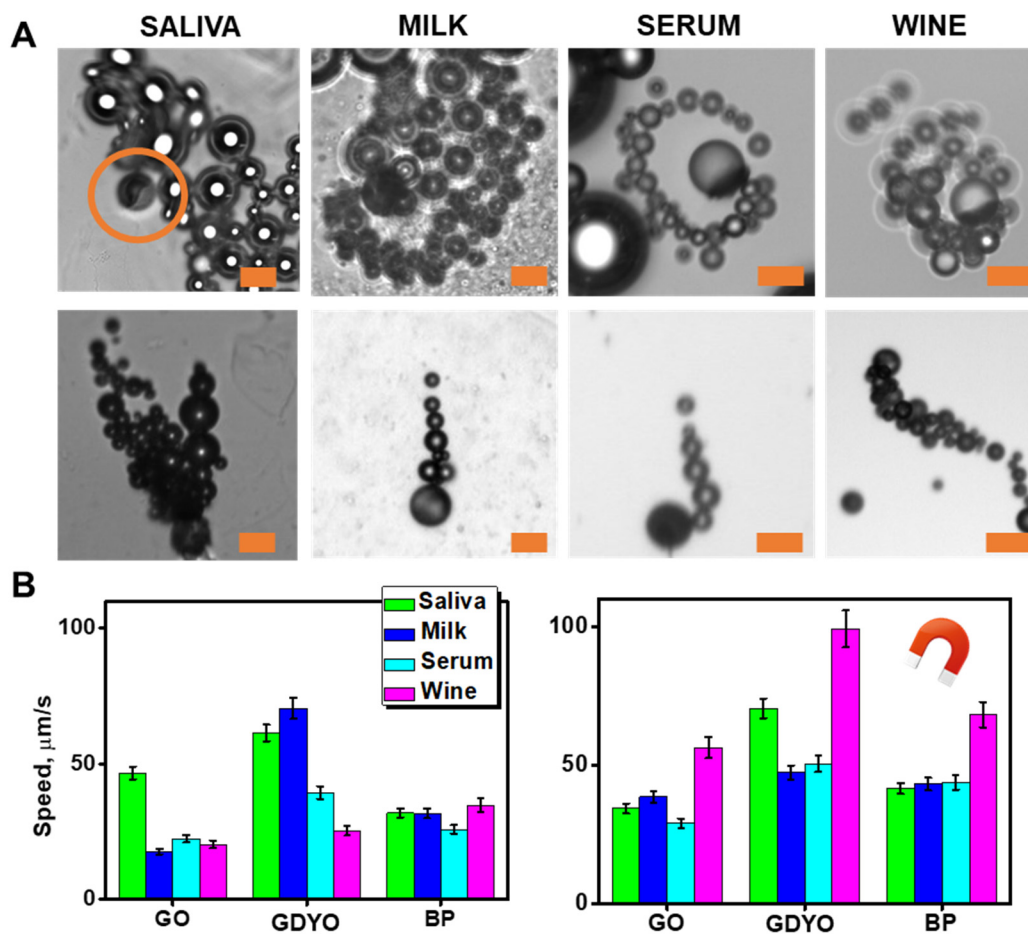


Figure S1. A) Time-lapse images (taken from Video S6) showing the efficient Janus micromotor propulsion in real samples in bubble (top) and bubble-magnetic (bottom) modes and B) Corresponding speeds in each mode for each nanomaterial at 5 % hydrogen peroxide. Scale bars, 20 μm .

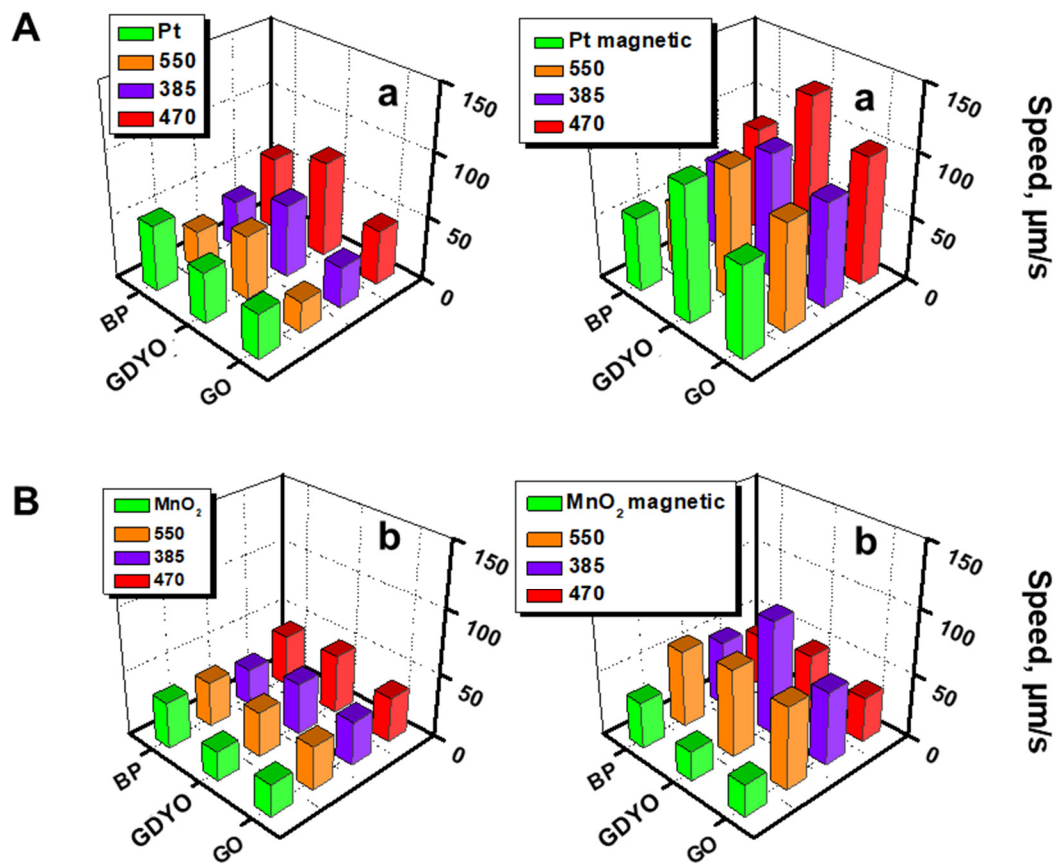


Figure S2. Speeds profiles illustrating the influence of the nanomaterial (GO, GDYO and BP), and light wavelength upon the micromotor speed in bubble-light and bubble-light magnetic modes using A) Pt and B) MnO₂ as catalysts.

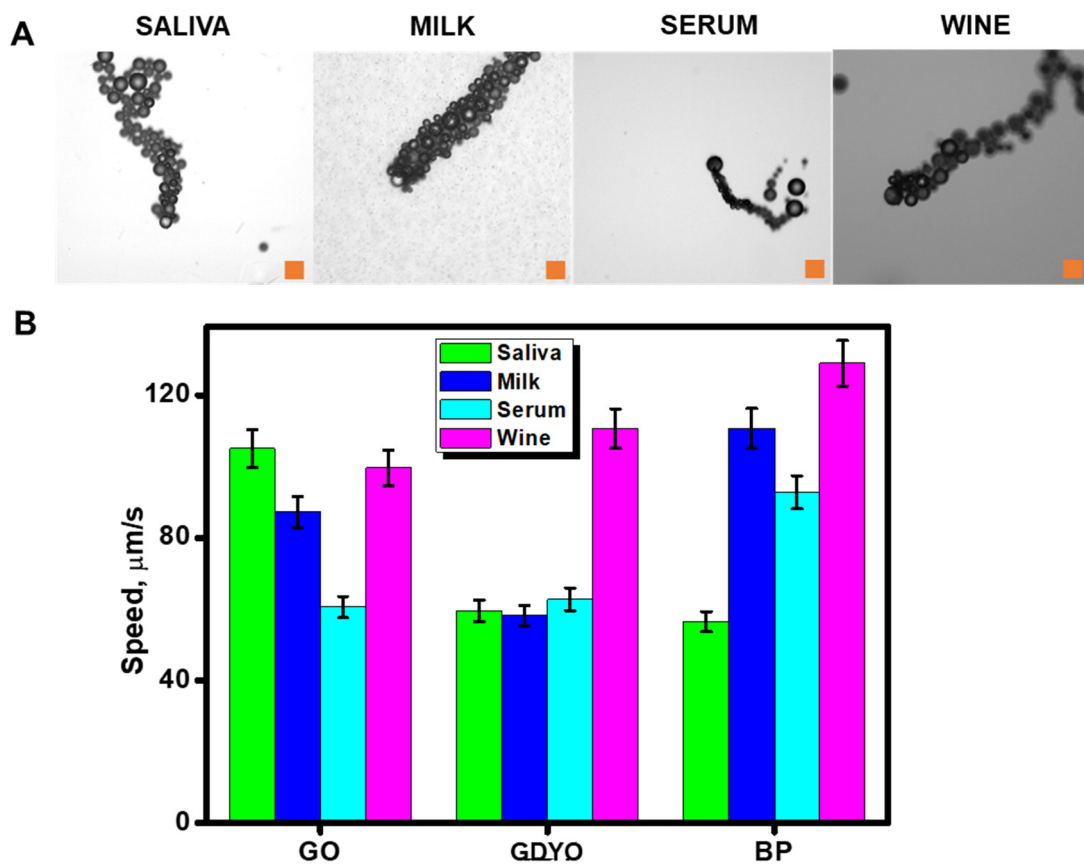
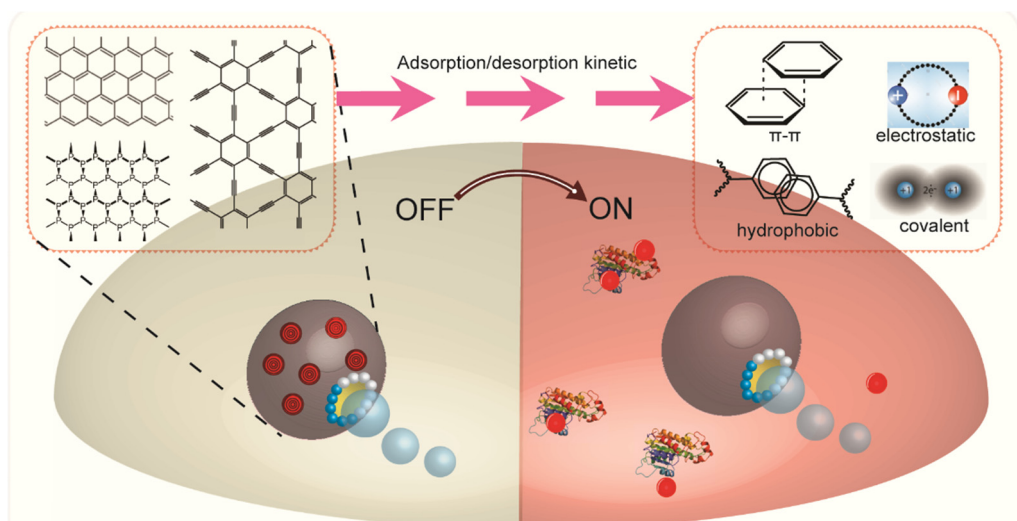


Figure S3. A) Time-lapse images (taken from Video S11) showing the efficient Janus micromotor propulsion in real biological samples in bubble-magnetic-light modes and B) Corresponding speeds in each mode for each nanomaterial at 5 % hydrogen peroxide. Scale bars, 20 μm . Light wavelength, 470 nm.

IV.3. Article 4. Janus micromotors coated with 2D nanomaterials as dynamic interfaces for (bio)-sensing (just accepted).



Janus Micromotors Coated with 2D Nanomaterials as Dynamic Interfaces for (Bio)-Sensing

Kaisong Yuan, Miguel Ángel López, Beatriz Jurado-Sánchez,* and Alberto Escarpa*

Cite This: *ACS Appl. Mater. Interfaces* 2020, 12, 46588–46597

Read Online

ACCESS |



Metrics & More

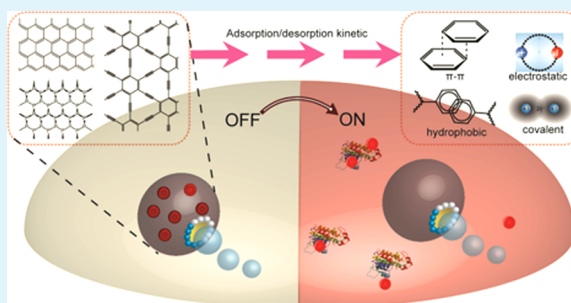


Article Recommendations



Supporting Information

ABSTRACT: In this work, we study the interaction of graphdiyne oxide (GDYO)-, graphene oxide (GO)-, or black phosphorous (BP)-wrapped Janus micromotors using a model system relying on a fluorescence-labeled affinity peptide, which is released upon specific interaction with a target Cholera Toxin B. Such ON–OFF–ON system allows mimicking similar processes occurring at (bio)-interfaces and to study the related sorption and desorption kinetics. The distinct surface properties of each nanomaterial play a critical role in the loading/release capacity of the peptide, greatly influencing the release profiles. Sorption obeys a second-order kinetic model using the two-dimensional (2D) nanomaterials in connection with micromotors, indicating a strong influence of chemisorption process for BP micromotors. Yet, release kinetics are faster for GDYO and GO nanomaterials, indicating a contribution of π and hydrophobic interactions in the probe sorption (Cholera Toxin B affinity peptide) and target probe release (in the presence of Cholera Toxin B). Micromotor movement also plays a critical role in such processes, allowing for efficient operation in low raw sample volumes, where the high protein content can diminish probe loading/release, affecting the overall performance. The loading/release capacity and feasibility of the (bio)-sensing protocol are illustrated in *Vibrio cholerae* and *Vibrio parahaemolyticus* bacteria cultures as realistic domains. The new concept described here holds considerable promise to understand the interaction of micromotor with biological counterparts in a myriad of biomedical and other practical applications, including the design of novel micromotor-based sensors.



KEYWORDS: 2D nanomaterials, micromotors, nanomotors, biosensing, peptide, toxin, Cholera B, *Vibrio cholerae*

INTRODUCTION

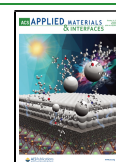
Novel diagnostic and therapeutic tools are considered as top priorities in the current scientific scenario due to the impact on human welfare. Recently, the incorporation of biological units into artificial matter has resulted in a new generation of hybrid nanomaterials with unprecedented capabilities in the biomedical field. In addition, such combination allows also for the *in vitro* study of molecular recognition mechanisms for drug development and to understand many therapeutic approaches.^{1,2} Graphene oxide (GO) is considered as the “gold standard” material for the construction of such hybrid tools, mainly in the biosensors field. Indeed, the rich outer surface of graphene, with a high density of active sites, makes it very attractive for fluorescence or electrochemical biosensing.^{3–5} In the past decade, two-dimensional (2D) materials like graphene were discovered, representing new rising stars in the field of biosensing. Indeed, transition-metal dichalcogenides, carbon and boron nitride, MXenes, black phosphorous (BP), and graphdiyne oxide (GDYO) possess remarkably new properties, such as superior mechanical strength, optoelectronic activity, high biocompatibility, etc., as transduction elements and supporting substrates in biosensing.^{6–12}

One further step in the binomial 2D nanomaterial bioreceptors was also achieved through the incorporation of such hybrid units into active matter, or micromotors.^{13–16} Such nanoscale devices are prepared by a myriad of techniques, being composed of a variety of inorganic nanomaterials and active nanoparticles.^{17–19} The unique structure offers an ideal template for the incorporation of biological receptors, in a similar way to that used in traditional biosensors. In addition, the self-propelling ability of micromotors associated with the enhanced fluid mixing adds a new dimension to biosensing application, accelerating the kinetics of reaction toward reduced time and highly efficient operations in microliter volume samples, which is of high relevance in clinical samples.^{20–22} To date, graphene oxide is the most employed 2D material for such purpose, with only one report dealing with MoS₂.²³ Most designs compromise tubular configurations

Received: August 26, 2020

Accepted: September 18, 2020

Published: October 5, 2020



and catalytic propulsion in connection with dye-labeled probes. For instance, GO/Pt and MoS₂/Pt micromotors have been loaded with aptamers for toxin detection in clinical or food samples^{23–25} and dye-labeled probes in OFF–ON DNA detection,^{26,27} respectively. In the previous examples, the material is electrodeposited from a dispersion containing the pristine material or appropriate precursors, resulting in composite materials that in most cases retain the properties of the pristine 2D units. Additional designs using appropriate dye-labeled probes compromise the self-assembly of GO into ultrasound-propelled gold nanowires for OFF–ON detection of miRNA and AIB1 oncoproteins,^{27,28} respectively.

Despite the proven potential of GO-based micromotors, little is still known about the behavior of analogous 2D nanomaterials, not to mention its interaction with the biomolecules or detection probes. Understanding the interaction of 2D nanomaterial-based micromotors and biomolecules such as peptide, aptamers, DNA, etc. can play a critical role in the biomedical field, *i.e.*, to study cell interactions, for developing new drugs or improving the performance of receptor-based clinical sensors.^{29–31} In a recent article from our research group,³² we described the preparation of 2D nanomaterial-based micromotors by combination of BP, GDYO, and GO and active nanoparticles into a Janus structure with improved propulsion behavior. In the absence of similar studies in the literature, the aim of this work is to investigate the use of micromotors as dynamic interfaces in fluorescence assays. As a model system, we select a specific Rhodamine-labeled affinity peptide highly selective for the Cholera Toxin B subunit. In the following sections, we will illustrate the role of each pristine 2D nanomaterial and the enhanced micromotor movement upon loading of the probe and subsequent release for fluorescence detection. The distinct surface properties of each nanomaterial play a critical role in the loading/release capacity of the peptide, greatly influencing the final sensing performance and release profiles. The enhanced micromotor movement also influences both loading and release kinetics, allowing for efficient operation in low sample volumes and, as will be illustrated, in complex raw samples where high protein content can diminish probe/loading release, affecting the overall performance. The feasibility of the (bio)-sensing strategy for the detection of the target toxin in *Vibrio cholerae* and *Vibrio parahaemolyticus* bacteria cultures will be also illustrated. The new concept described here holds considerable promise to understand the interaction of micromotors with biological counterparts in a myriad of biomedical and other practical applications including the design of novel micromotor-based sensors.

■ EXPERIMENTAL SECTION

Reagents and Materials. All reagents for micromotor preparation, Cholera Toxin B subunit (cat. C9972), human serum (cat. H4522), bovine serum albumin (cat. A7030), endotoxin from *Escherichia coli* O111:B4 (cat. L2630), endotoxin from *Salmonella enterica* (cat. L770), hydrogen peroxide (cat. 216763), and sodium dodecyl sulfate (cat. 71727) were supplied by Merck (Madrid, Spain) and used without further purification. The affinity peptides of Cholera Toxin B (sequence: Rhodamine B VQCRLGPPWCAK) and *Escherichia coli* endotoxin (sequence tetramethylrhodamine (TMRho)-KKNYSSSIHC) were purchased from NeoBiotec (France). The peptides were stored at –20 °C until further use. For micromotor modification, peptides were reconstituted in acetonitrile (ACN)/H₂O₂ (1:3) to a final concentration of 1000 µg/mL. Graphdiyne was provided by Li et al.³³ *Vibrio cholerae* and

Vibrio parahaemolyticus bacteria cultures were grown in LB (Luria-Bertani) in compliance with the University of Alcalá regulations. *Escherichia coli* Strain B (cat. EC11303) cells were cultivated in Luria-Bertani medium in a gyratory shaker at 100 rpm and 37 °C for 16 h. All experiments with bacteria samples were performed by “Centro de Apoyo a la Investigación en Medicina-Biología, Unidad de Cultivos Celulares” by authorized personnel and were in compliance with the University of Alcalá regulations. A Nikon Eclipse fluorescence optical microscope (TiS/L100) coupled with a Zyla cMOS digital camera and NIS Elements AR 3.2 software was utilized for capturing movies of the micromotors movement and fluorescence images of the solutions prior and after incubation with the micromotors.

Micromotor Synthesis and Characterization. Micromotor synthesis is schematically described in Figure S1A. First, a monolayer of polystyrene microparticles (20 µm, aqueous suspension concentration: 2%, cat. 87896) was sputtered with a ~50 nm gold layer. Second, the PS-Au microparticles were detached from the slide by gentle pipetting with ultrapure water and transferred to a clean eppendorf tube in a constant number. Third, 900 µL of PS-Au microparticles was coated with different nanomaterials by incubation with 100 µL of a solution containing sulphhydryl-modified BP, GO, or GDYO (prepared following a previous work)³² for 2 h, followed by filtration of such solution through a cyclopore track-etched membrane (5 µm) to remove the excess of nanomaterial. The presence of such –SH allows direct attachment to gold with a strong thiol bond, preventing thus the release of the 2D nanomaterial. As previously described in our work, the amount of nanomaterial for incubation with the PS-Au microparticles was judiciously optimized to leave a small, uncoated Au area to promote preferential growth of the PtNPs and Fe₂O₃ NPs. Briefly, a fixed number of Au-PS Janus microparticles were incubated with different amounts of 0.1 mg/mL solutions of HS-GO, HS-GDY, or HS-BP, followed by PtNPs generation. Next, the number of motile micromotors under each condition (which was related with the successful incorporation of the PtNPs due to the presence of exposed gold) was studied. The highest percentage of moving micromotors (80%) was obtained using 100 µL of the 2D nanomaterial solutions, whereas for higher or lower volumes/amounts, fewer micromotors were motile. Prolonged stability was noted after 1 week nanomaterial incorporation (not shown). Fourth, to synthesize PtNPs, the different solutions containing the 2D-coated microparticles (1 mL) were mixed with 200 µL of a solution containing 1 mg/mL of chloroplatinic acid (cat. 398322), followed by addition of 20 µL of hydrazine (cat. 309400) and 2 h of stirring. To facilitate washing and modification steps, magnetic Fe₂O₃ NPs were also incorporated in the micromotor structure by mixing 1 mL of the above-prepared solution with 20 µL of Fe₂O₃ NPs solution (1 mg/mL) for 1 h and then filtered with a cyclopore track-etched membrane (5 µm) to remove the free nanoparticles. The resulting micromotors were purified by filtration and washed with ultrapure water. Characterization was performed by scanning electron microscopy observation using a JEOL JSM 6335F microscope (JEOL USA, Massachusetts) coupled with an XFlash detector 4010 and using an acceleration voltage of 20 kV. Raman spectra were obtained with an α 300AR dual Raman/AFM microscope (WITec, Germany).

To determine the number of micromotors on a batch (both before and after modification), first, the area of 1 µL drop ($n = 10$) was measured as $A = \pi r^2$. Second, we used a higher magnification objective and counted the motors in a predefined area. This number was then extrapolated to the whole drop. The volume of micromotor solutions was adjusted (by centrifugation and supernatant removal) to have a constant number of micromotors. The number of micromotors was adjusted in the batch before modification, by removing the supernatant and using a constant volume of peptide solution for modification, adjusting the volume as well to get the desired micromotor concentration per milliliter.

Kinetics for Peptide Loading on the Micromotors Experiments. Micromotors (140 000 micromotors/mL) were mixed with 100 µL of the Cholera peptide solution (containing 10, 100, or 500 µg/mL of the affinity peptide), 150 µL of 3% sodium dodecyl sulfate, and 3% H₂O₂ for 60 min (final volume, 1 mL). Fluorescence images

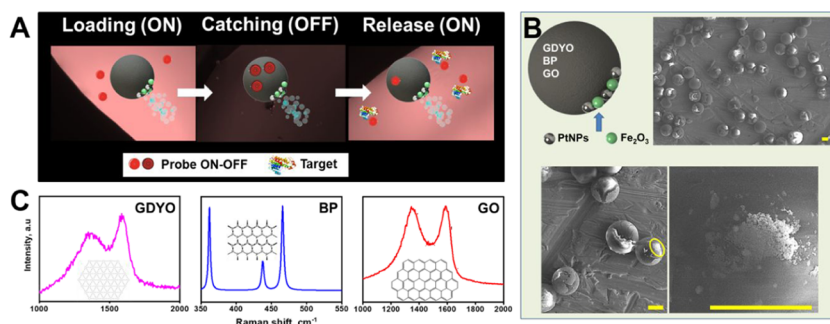


Figure 1. (A) Schematic of the use of graphdiyne oxide (GDYO)-, black phosphorous (BP)-, or graphene oxide (GO)-wrapped Janus micromotors as dynamic interfaces for biosensing in connection with fluorescence-labeled probes. Cholera Toxin B and its specific affinity peptide were used as model system for the evaluation of the micromotor performance with different nanomaterials. (B) Micromotors structure and the corresponding scanning electron microscopy (SEM) images illustrating its morphology. (C) Raman spectra of the micromotors with the wrapped 2D materials. Scale bars, 10 μm . Probe: Rhodamine B VQCRLGPPWCAK affinity peptide, Target: Cholera Toxin B.

of the solution at different times were taken with the microscope. First-order kinetics were calculated according to eq 1, where C_0 and C are the concentrations of the peptide initially and at a given time after micromotor navigation (C), respectively, k is the reaction rate constant, and t is the specific time

$$\ln \frac{C_0}{C} = kt \quad (1)$$

Second-order kinetics were studied using eq 2, where k_2 is the reaction rate constant and q_e and q_t refer to the amounts of peptides present at equilibrium and at time t , respectively

$$\frac{t}{q_t} = \frac{1}{k_2 q_e^2} + \frac{t}{q_e} \quad (2)$$

The amount of adsorption at a specific time (q_t) was calculated using eq 3, where V and m are the volume of the solution (1 mL) and mass of micromotor (1 μg), respectively

$$q_t = \frac{V(C_0 - C)}{m} \quad (3)$$

To calculate the amount of peptide loaded in the micromotors, we first recorded the fluorescence of different affinity peptide solutions (from 0 to 500 $\mu\text{g}/\text{mL}$) to construct a calibration plot. The fluorescence at each time was interpolated into the calibration curve to estimate the amount of peptide remaining in solution. Such concentration was subtracted from the initial concentration used for the loading kinetic experiments, to estimate the concentration of peptide loaded in the micromotors at each time. Also, as will be further discussed, such concentration can be also calculated by determining q_e from the kinetic plot.

Kinetics of Peptide Release and Toxin Detection. The peptide-modified micromotors were incubated with different concentrations of the Cholera Toxin B (0.1, 1, and 10 $\mu\text{g}/\text{mL}$), taking drops at different times to measure the fluorescence of the solution.

Fluorescence data were fitted to pseudo-zero-order kinetic release model following eq 4, where F is the fluorescence of the solution at time t , F_0 is the initial fluorescence at time 0, and k_0 is the zero-rate constant

$$F = F_0 k_0 t \quad (4)$$

Pseudo-first-order fitting was evaluated by eq 5, where k_1 is the first-rate constant

$$\ln F = \ln F_0 - k_1 t \quad (5)$$

Pseudo-second-order model was evaluated by eq 6, where k_2 is the second-rate constant

$$\frac{1}{F} = \frac{1}{F_0} + k_2 t \quad (6)$$

Evaluation of the Analytical Performance of the Micromotor Sensing Strategy. To evaluate the linear range, limit of detection (LOD), and limit of quantification (LOQ), the optimized peptide micromotors were mixed with different concentrations of the target toxin (from 0.001 to 10 $\mu\text{g}/\text{mL}$), 150 μL of 3% sodium dodecyl sulfate, and 3% H_2O_2 for 10 min. A drop of each solution was taken to measure the fluorescence at each concentration ($n = 10$), to plot the calibration graph. Blank samples (without Cholera Toxin B) were also measured ($n = 50$). LOD was calculated following International Council for Harmonization (ICH) guidelines as the mean blank signal plus 3 times the standard deviation of the blank. Such a signal was interpolated into the corresponding calibration plot to get the LOD. LOQ was calculated as $3.3 \times \text{LOD}$. Selectivity was evaluated in a similar manner in the absence of the target toxin and the presence of 10 $\mu\text{g}/\text{mL}$ bovine serum albumin or endotoxin from *Escherichia coli* O111:B4, which may also compete with the affinity peptide and release it. Percent recovery was estimated by fortifying raw bacteria cultures, human serum, and deionized water with 10 $\mu\text{g}/\text{mL}$ of the target toxin. *Vibrio cholerae* and *Vibrio parahaemolyticus* bacteria cultures were fortified with 0.05, 0.1, and 10 $\mu\text{g}/\text{mL}$ of the target toxin. Additional control experiments of real samples in the absence of the target toxin were also evaluated. Sensor stability was evaluated by taking aliquots of peptide-modified micromotors and using it for the detection of 10 $\mu\text{g}/\text{mL}$ of the target toxin for a week.

RESULTS AND DISCUSSION

Figure 1A illustrates the protocol followed to study the mechanism of loading/release in the micromotors. As can be seen, the initial fluorescence of the solution (imparted by the Rhodamine molecule incorporated in the peptide probe) is rapidly quenched by interaction with the 2D nanomaterial part of the micromotors, followed by specific release upon the presence of the target molecule Cholera Toxin B. Micromotors were prepared by self-assembly of the different materials in gold-sputtered microspheres (see the [Experimental Section](#) for more details). As shown in Figure 1B and Figure S1B, the 2D nanomaterial covers most of the micromotor part (a similar behavior was observed using GDYO, BP, and GO), with only an exposed area for assembly of the catalytic Pt nanoparticles for enhanced propulsion and Fe_2O_3 NPs for magnetic control. Judicious optimization of the amount of nanomaterial used for assembly into the micromotor is key to leave only a small area of the Au layer coating the micromotor for preferential assembly of the active nanoparticles and directional propulsion in peroxide solutions.³² Successful micromotor synthesis and

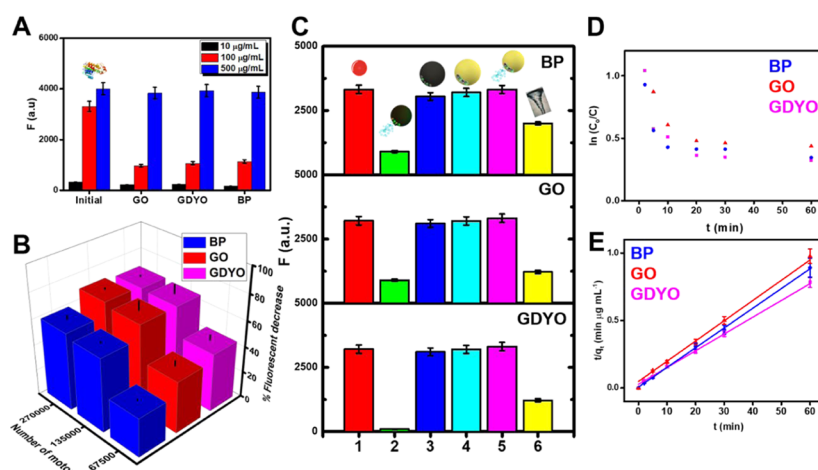


Figure 2. Probe loading capacity of the micromotors. (A) Fluorescence intensity of different concentrations of affinity peptide solutions after 60 min incubation with GO-, GDYO-, or BP-wrapped micromotors. For better understanding, see the column “initial”, which reports the value of fluorescence of peptide solutions at different concentrations before incubation with the micromotors. (B) Effect of the number of micromotors upon the fluorescence decrease (in turn, loading) of a 100 $\mu\text{g}/\text{mL}$ of affinity peptide solution. (C) Role of micromotor movement upon peptide loading: fluorescence intensity of a solution containing 100 $\mu\text{g}/\text{mL}$ of affinity peptide (1), after 20 min incubation with moving GO, GDYO, or BP micromotors (2), static micromotors (3), static Au/PtNPs/ Fe_2O_3 micromotors (4), moving Au/PtNPs/ Fe_2O_3 micromotors (5), or GO, GDYO, or BP micromotors under magnetic stirring (6). First-order (D) and second-order (E) kinetics models of peptide loading onto the micromotors.

element distribution is reflected in the energy-ray dispersing mapping images of Figure S1B in the Supporting Information. The distinct characteristics of the 2D nanomaterials will exert a strong influence on the sensing performance of the developed platforms, as will be further illustrated. To check the successful 2D nanomaterial incorporation and get more insight into the Cholera Toxin B probe interaction mechanism, Raman mapping of the micromotors was performed (Figure 1C). The typical D and G vibration bands are present in the Raman spectra (prominent band or peaks around 1350 and 1580 cm^{-1} , respectively). The D-mode is caused by the presence of disorder in sp^2 -hybridized carbon in graphene, resulting in resonance Raman spectra. The G-mode arises from the stretching of the C–C bond in graphitic materials, indicating the presence of both sp^2 and sp^3 carbons in GO micromotors. With regard to GDYO, the D and G bands correspond to sp^2 carbons as well as sp^2 and sp^3 arising from defects and some oxides, resulting from the oxidation of the material. Thus, the peptide can interact with the micromotor 2D surface via π interactions.^{5,34,35} In the case of BP, the characteristic phonon modes (A_g^1 , A_g^2 , and B_{2g}) are presented, indicating the successful incorporation into the micromotor.^{6,36} As each phosphorus atom is bonded to three adjacent phosphorus atoms, sp^3 hybridization occurs, with the “p” orbital retaining a lone pair of electrons.

Probe loading capacity in the micromotors was studied via first- and second-order kinetics. Before these studies, the amount of peptide and micromotors was studied. First, GDYO, GO, or BP micromotor solutions (containing 210 000 moving micromotors/mL) were incubated with variable amounts of the affinity peptides (see Figure 2A). For the lowest peptide concentration tested (10 $\mu\text{g}/\text{mL}$), the fluorescence is very weak, thus preventing adequate sensitivity for further detection of analytes. At a moderate concentration (100 $\mu\text{g}/\text{mL}$), a rapid fluorescence quenching of the solution (which in turn indicates loading into the micromotors) is noted. At a higher concentration, however, a saturation of the fluorescence signal is observed, as illustrated with the negligible decrease in the fluorescence signal of the solution. Thus, 100 $\mu\text{g}/\text{mL}$ was

selected as the optimal concentration. Next, we optimized the number of micromotors (see Figure 2B). The highest fluorescence quenching (which in turn can be related with a higher peptide loading) was observed using 135 000 micromotors/mL and then remained constant. After optimization of such critical variables, the role of micromotor movement and the 2D nanomaterial was evaluated (Figure 2C). While a rapid fluorescence quenching/fast loading is observed with moving micromotors, negligible loading/quenching is obtained with similar experiments using static or bare micromotors, revealing the crucial role of micromotor movement for probe loading in miniaturized environments. To check the possible role of hydrogen peroxide in the Rhodamine B fluorescence (which is used as a tag in the affinity peptide probe) and as micromotors’ movement may decrease its concentration, a control experiment using Au/PtNPs/ Fe_2O_3 micromotors (static and moving) was also performed, with a negligible fluorescence decrease, reflecting negligible influence or potential effect in the decrease of Rhodamine B fluorescence. A similar loading capacity was obtained with micromotors under magnetic stirring, which, however, requires 3 times higher volume for efficient loading.

Under the optimized conditions, kinetics of peptide loading were studied. To this end, different 2D material micromotors were incubated with 100 $\mu\text{g}/\text{mL}$ of affinity peptide solution and the decrease of fluorescence over time was recorded by taking different time-lapse fluorescence images (see Figure S2 in the Supporting Information for the raw data). The data of fluorescence decrease over time were processed using first (Figure 2D)- and second (Figure 2E)-order kinetic models, as described in the Experimental Section. Linear plots were obtained for a second-order model for BP, GO, and GDYO micromotors, indicating that affinity peptide interaction with the 2D nanomaterials occurs via chemisorption involving covalent forces and ion exchange.^{34,35} Most importantly, kinetic data can be used to compare each nanomaterial in terms of sorption rate (k_2) and the amount of peptide that can be loaded in the micromotors (q_e , amount of peptide present at equilibrium), which can be calculated from the intercept and

slope of the plot in Figure 2E, respectively. The highest loading capacity was noted for GDYO micromotors, with $78.1 \mu\text{g}/\text{mL}$ of affinity peptide loading, followed by BP ($68.5 \mu\text{g}/\text{mL}$) and GO ($66.7 \mu\text{g}/\text{mL}$) micromotors. The rate constant was higher for BP ($0.034 \mu\text{g}/\text{mL min}$), followed by GDYO and GO (0.006 and $0.005 \mu\text{g}/\text{mL min}$, respectively) (see Table 1). The

Table 1. Pseudo-Second-Order Kinetic Parameters for Affinity Peptide Loading in the Micromotors

micromotor	slope	intercept	R^2 (%)	q_e ($\mu\text{g}/\text{mL}$)	k_2 ($\mu\text{g}/(\text{mL min})$)
BP	0.0146	0.0063	99.8	68.5	0.034
GO	0.0150	0.0481	99.5	66.7	0.005
GDYO	0.0124	0.0273	99.7	78.1	0.006

adsorption mechanism in graphene-like materials can comprise a mix of several mechanisms such as π interactions, hydrophobic interactions, hydrogen bonding, and electrostatic effects.^{34,35} In the case of BP, the absence of functional active groups, along with the high loading capacity (similar to GDYO and slightly higher than GO) indicates a greater contribution to chemisorption in the adsorption mechanism, in addition to electrostatic interactions.^{6,9,36} Due to the relatively high force and stability of the interactions in chemisorption processes, molecules are not expected to be easily released, as will be further illustrated in the study of the kinetics of release.

To get further insights into the specific sorption mechanism, we studied the release kinetics of the previous micromotors in the presence of different concentrations of Cholera Toxin B subunit (see Figure 3). The mechanism of release relies on the higher affinity of Cholera Toxin B toward the labeled peptide over each 2D nanomaterial, resulting in a competitive binding that releases the probe, thus restoring the fluorescence in the solution.³⁷ The affinity peptide used contains very few charged amino acids (a single Arg and Lys), and the sequence is rich in hydrophobic amino acids such as Leu, Val, Trp, Pro, and Al, which contributes to the probe adsorption to 2D nanomaterials via π and hydrophobic interactions (GO, GDYO) or chemisorption (BP). In the presence of Cholera Toxin B, some amino acids of the peptide will “escape” from the 2D nanomaterial surfaces to combine with the toxin, forming a probe–toxin complex due to their higher affinity, changing space structures of peptide on 2D materials surfaces, and breaking the interaction balance between peptide and 2D materials. Thus, hydrophobic interactions might be involved in the interaction with Cholera Toxin B and subsequent release from the 2D nanomaterial coating the micromotor.³⁸ To check potential nonspecific binding of the toxin, we mix $10 \mu\text{g}/\text{mL}$ of the toxin with nonmodified micromotors. After 20 min navigation, the micromotors were captured with the magnet and the solution was recovered to perform the measurement. Next, we use affinity peptide micromotors to perform the detection in the $10 \mu\text{g}/\text{mL}$ solution after bare micromotor

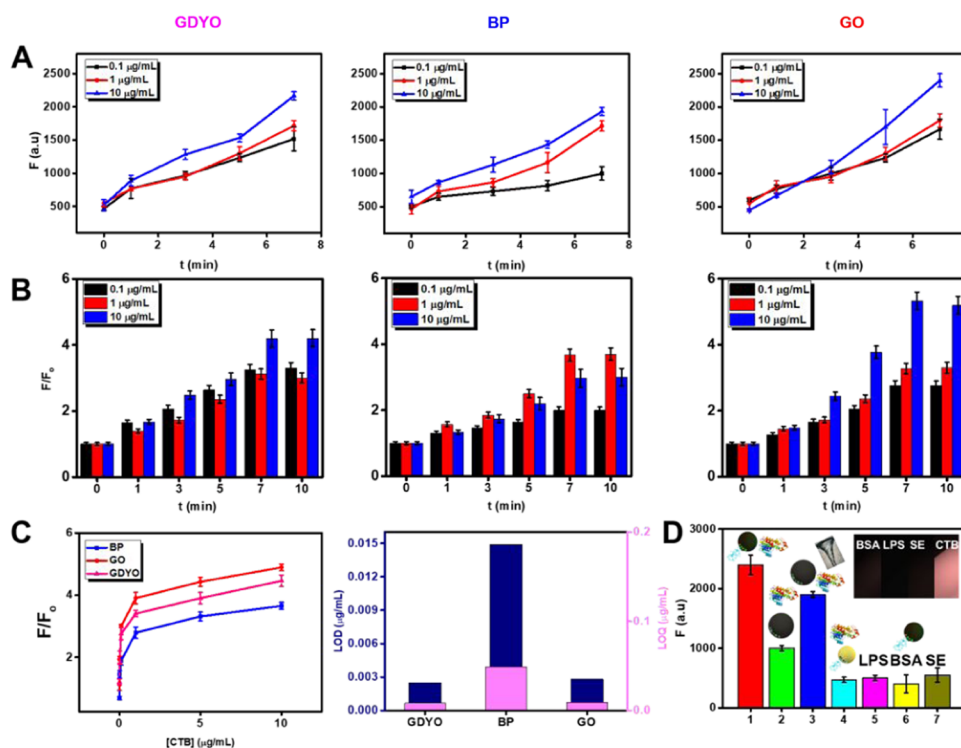


Figure 3. Release probe capacity of the micromotors in the detection of Cholera Toxin B. (A) Kinetics of release and (B) corresponding normalized fluorescence (F/F_0) plots over time after navigation of peptide-modified GO-, GDYO-, or BP-wrapped Janus micromotors in solutions containing different concentrations of the specific Cholera Toxin B subunit. (C) Relative fluorescence enhancement after 10 min navigation of the micromotors in solutions containing increasing concentration of the target toxin and corresponding limits of detection (LOD) and quantification (LOQ). Note the different scales; for LOD, refer to the left y-axis, and for LOQ, refer to the right y-axis. (D) Role of micromotor movement upon peptide release and sensitivity of the toxin sensing approach: fluorescence intensity of a solution containing $10 \mu\text{g}/\text{mL}$ of the target analyte (Cholera Toxin B, CTB) and moving (1), static (2), magnetically stirred micromotors (3), moving Au/PtNPs/ Fe_2O_3 micromotors (4), or moving micromotors in the presence of toxins for *Escherichia coli* (LPS, 5), bovine serum albumin (BSA, 6), or *Salmonella enterica* (SE, 7). The inset shows the fluorescence of the corresponding solutions.

navigation. The fluorescence signals obtained (2666 ± 58 , 2233 ± 58 , and 2367 ± 58 au for GO, BP, and GDYO micromotors, respectively) were similar to that obtained after direct detection of a solution containing the same concentration of the target toxin (2600 ± 100 , 2400 ± 170 , and 2367 ± 58 au) for GO, BP, and GDYO micromotors, respectively, indicating the absence of nonspecific interactions. To check potential nonspecific binding of the toxin–probe complex, we mix a $10 \mu\text{g/mL}$ toxin solution with $100 \mu\text{g/mL}$ of the affinity peptide. After measuring the fluorescence of the solution, we mix it with nonmodified 2D micromotors. Fluorescence of the solution remains constant after 30 min navigation, indicating the absence of nonspecific interactions. The mechanism of adsorption will also influence such a release, allowing thus to further understand the adsorption kinetics previously described. Figure 3A,B illustrates the fluorescence increase over time and corresponding normalized fluorescence (F/F_0) plots, respectively, of solutions containing 0.1, 1, and $10 \mu\text{g/mL}$ of Cholera Toxin B and GDYO, BP, or GO moving micromotors ($140\,000$ micromotors/mL) modified with $100 \mu\text{g/mL}$ of the affinity peptide (as previously described). As can be seen, toxin concentration and the type of 2D nanomaterial strongly influence the desorption efficiency. Fluorescence of the solution increases along the navigation time up to 7 min and then remained constant. Also, as expected, the normalized fluorescence (and fluorescence on the solution) increases, as the concentration of Cholera Toxin B increases, due to more analyte available to compete with the micromotors for peptide release. Thus, in terms of normalized fluorescence (F/F_0), the value is 1.3 and 1.4 higher for GO and GDYO micromotors, respectively, than the value obtained for BP micromotors. Such differences are lower at a concentration of $1 \mu\text{g/mL}$, yet at higher toxin concentrations, the differences remain, with ~ 2 times higher normalized fluorescence for GO and GDYO compared to BP. This, in turn, can influence the extent of fluorescence in the solution and further detection efficiency, as will be also explained. The relatively lower percent release in BP suggests a greater contribution of chemisorption on the interaction, whereas for GDYO and GO, as previously hypothesized, the high release percentage indicates π and hydrophobic interactions mainly. To get further insights into such a release profile, we processed the data of fluorescence with pseudo-zero-, pseudo-first-, and pseudo-second-order release kinetics models to try to understand the release behavior.^{39–41} The equations are described in the Experimental Section and were adapted from common equations used in release system models. The resulting plots, equations, and rate constants are summarized in Figure S3 and Table S1 in the Supporting Information. As can be seen, in all cases, the data fit pseudo-zero-order model indicates a continuous release of the affinity peptide over time independently from other variables such as the presence of peptide–toxin complex. Most importantly, the slope of the calibration plot (which can be an indication of k release constant) is ~ 2 times higher for GDYO and GO compared to BP micromotors, as previously described.

To further support the above-mentioned observations, and to evaluate the analytical performance of the 2D micromotor strategies, calibration plots were obtained (see Figure 3C and S4). The related data with the analytical performance are also listed in Table 2. As can be seen in Figure 3C, GO micromotors induce the highest fluorescence enhancement, followed by GDYO and BP micromotors. This influences the future sensing performance of the micromotors, as illustrated

Table 2. Analytical Performance for Cholera Toxin B Detection^a

micromotor	linear range ($\mu\text{g/mL}$)	LOD ($\mu\text{g/mL}$)	LOQ ($\mu\text{g/mL}$)
BP	0.05–10	0.015	0.05
GO	0.01–10	0.003	0.009
GDYO	0.008–10	0.002	0.008

^aMean blank signal: 509.9 ± 99.3 (au).

by the limit of detection and quantification for each micromotor, which were approximately 5–7 times lower for GO and GDYO (0.003 and $0.002 \mu\text{g/mL}$, respectively) compared to BP ($0.015 \mu\text{g/mL}$). These data can be also relevant for future applications of drug or other payload delivery from the micromotors following a similar principle. In this context, the role of micromotor movement and selectivity was further studied (see Figure 3D). The plot reveals the lower fluorescence enhancement of static (2) and magnetically stirred micromotors (3) in comparison to moving micromotors (1), in all cases in the presence of the target toxin. Low fluorescence was observed using moving Au/PtNPs/Fe₂O₃ micromotors, further revealing that no affinity peptide is nonspecifically absorbed on the micromotors. The selectivity of the sensing strategy was also assessed, and the results are plotted in this graph. We use bovine serum albumin, a common standard protein that has numerous biochemical applications. Additionally, endotoxins from *Escherichia coli* and *Salmonella enterica*, with some common features to that of Cholera Toxin B, which can potentially compete with the affinity peptide, were also tested. To this end, solutions containing $10 \mu\text{g/mL}$ of each potentially interfering toxin were mixed with the moving micromotors for 60 min. Fluorescence intensity was recorded before and after navigation, with no apparent changes (or fluorescence increase) noted in all cases, as can be also seen in the corresponding inset with the fluorescence images. Such results testify thus the high selectivity of the strategy and the potential 2D-modified micromotors for future sensing and payload delivery applications. Note that in the figure we include a mean value to simplify it. Additional tests to check the selectivity of the protocol were performed by modifying the Janus micromotors with $100 \mu\text{g/mL}$ of the affinity peptide from *Escherichia coli* (sequence TMRho-KKNYSSSISSIHIC). Next, we tested the potential release of peptide by allowing the micromotors to navigate in solutions containing $10 \mu\text{g/mL}$ of *Escherichia coli* O111:B4 endotoxin, Cholera Toxin B, *Salmonella enterica*, or BSA. Tests were performed all in water, serum, and bacteria culture samples. As can be seen in the time-lapse microscopy images and the normalized fluorescence plots (F/F_0) of Figure S5, no apparent increase in the fluorescence intensity was observed in the presence of Cholera Toxin B (which is now not the target peptide) and the other interfering compounds, with a dramatic fluorescence increase only in the presence of the target *Escherichia coli* O111:B4 endotoxin. This fact further reveals the selectivity of our strategy toward specific biomolecules. Stability of the microsensor was checked using the same micromotor solution to detect $10 \mu\text{g/mL}$ of Cholera Toxin B for a week. No apparent changes in the fluorescence intensity were noted, with a good match with the calibration plot (not shown), illustrating the sensor stability for a prolonged period.

For future practical applications, the release probe (Cholera Toxin B affinity peptide) capacity of the micromotors was

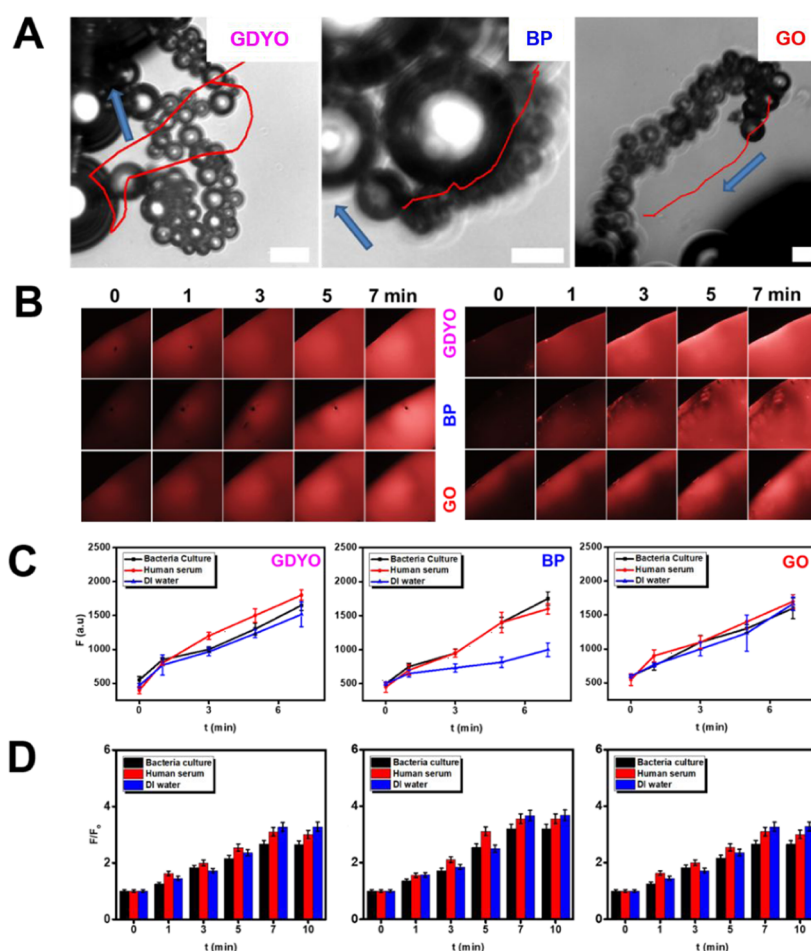


Figure 4. Release probe capacity of the micromotors in the detection of (bio)-analytes in real sample media. (A) Time-lapse images showing the propulsion of the different micromotors in human serum. (B) Time-lapse fluorescence images illustrating the peptide release using peptide-modified micromotors with different wrapping materials under the presence of $10 \mu\text{g/mL}$ of the Cholera Toxin B in bacteria culture (left) and human serum (right). (C) Kinetics of release after navigation of peptide-modified micromotors in the real sample solutions and (D) the corresponding normalized fluorescence plots (F/F_0). Scale bars, $20 \mu\text{m}$.

tested in raw bacteria cultures and human serum, compared to deionized water. Figure 4A shows the time-lapse images of GDYO, BP, and GO micromotors navigation in human serum. Efficient navigation of the modified micromotors is observed at speeds of $126 \pm 20 \mu\text{m/s}$ (GDYO), $140 \pm 30 \mu\text{m/s}$ (BP), and $120 \pm 25 \mu\text{m/s}$ (GO) in water and bacteria culture ($10\% \text{H}_2\text{O}_2$). The high complexity of human serum with a high content of proteins hampers its locomotion, resulting in diminished speeds of $63 \pm 15 \mu\text{m/s}$ (GDYO), $36 \pm 12 \mu\text{m/s}$ (BP), and $43 \pm 15 \mu\text{m/s}$ (GO), which, however, do not affect the detection efficiency. For clarity, we show only one micromotor, but note here that the cooperation of multiple micromotors is responsible here for the enhanced analyte–probe interactions and release for better detection compared to static conditions. Video S4 illustrates the cooperative motion and enhanced mixing produced during the navigation of multiple micromotors, in a similar manner to that occurring in real experiments. This is reflected in the time-lapse fluorescence images (Figure 4B) and the corresponding release plots of the micromotor navigating in human serum solutions fortified with $10 \mu\text{g/mL}$ of the toxin (Figure 4C). Such images illustrated the increase of fluorescence over time, with a strong intensity after 7 min due to successful release from the micromotors. The normalized fluorescence plots (F/F_0) of

Figure 4D further reveal that fluorescence recovery is similar in all of the samples assayed and comparable to the one obtained in DI water. Thus, the recoveries in bacteria culture sample are $80.8 \pm 3.1\%$, $95.8 \pm 4.6\%$, and $87.0 \pm 3.5\%$ for GO, GDYO, and BP micromotors, respectively. For serum samples, slightly higher recoveries are observed, $91.4 \pm 4.3\%$, $127.8 \pm 8.0\%$, and $96.4 \pm 4.9\%$ for GO, GDY, and BP, respectively. This can be due to the relatively high content of salt and charged species in the media, which can somewhat assist in the desorption of the peptide interacting with the 2D nanomaterials.^{31,42} In this context, to check possible effects of sample constituents in the generation of nonspecific signals, we performed control experiments using the peptide-modified micromotors in bacteria culture, human serum, and DI water. Drops were taken initially, and after 5 and 15 min of micromotor navigation, the fluorescence was measured. As can be seen in the plot and time-lapse images of Figure S6, no apparent increase in the fluorescence intensity was observed, as revealed by the time-lapse microscopy images and the normalized fluorescence plots (F/F_0), indicating the absence of nonspecific signals and that peptide release is highly selective in the presence of the target toxin, as also revealed by the selectivity studies performed in the presence of BSA and LPS.

To further prove the feasibility of the micromotors strategy in realistic environment, we performed the detection using our micromotors in real *Vibrio cholera* and *Vibrio parahaemolyticus* culture samples. Such study also provides a unique opportunity to perform the detection in real domains, as the target model toxin can be released by *Vibrio cholera* but not by *Vibrio parahaemolyticus*; thus, further assurance of the sensitivity of the related protocol can be also tested. The results are shown in Figure 5. As can be seen in Figure 5A, a slight fluorescence

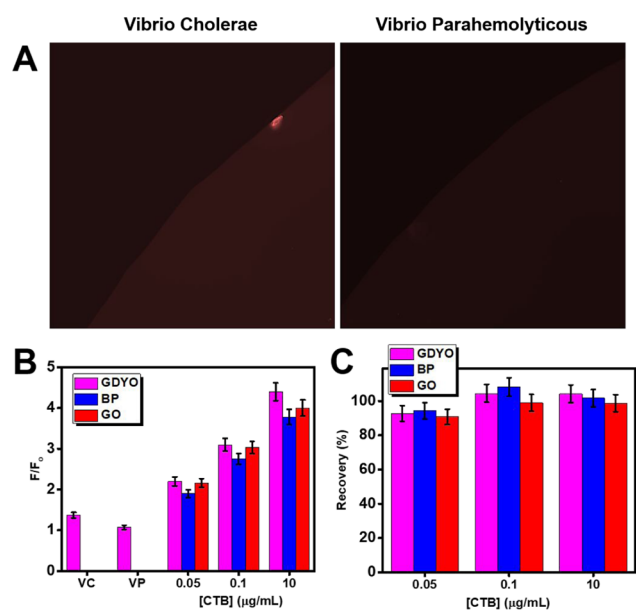


Figure 5. Cholera toxin B detection in real *Vibrio cholera* and *Vibrio parahaemolyticus* culture samples. (A) Time-lapse microscopy images showing the fluorescence of the different bacteria cultures after 10 min navigation of affinity peptide-modified GDYO micromotors and the corresponding (B) normalized fluorescence plots (F/F_0) in the bacteria cultures before and after fortifying (only *Vibrio cholera*) with different concentrations of the target toxin and (C) recovery plot. Conditions: 3 % sodium dodecyl sulfate and 3% H_2O_2 .

increase is observed after modified GDYO-based micromotors navigation (which were chosen since a lower LOD was obtained with such material) in *Vibrio cholera* cultures; thus, the micromotor strategy is able to detect Cholera toxin B in real bacteria samples, yet the determined concentration (0.0015 $\mu\text{g/mL}$) is below the LOD of the method. In the case of *Vibrio parahaemolyticus*, no apparent fluorescence increase is observed, illustrating the selectivity of the protocol. Next, the *Vibrio cholera* cultures were fortified with different concentrations of the target toxin (from 0.05 to 10 $\mu\text{g/mL}$). As can be seen in Figure 5C, excellent recoveries higher than 90% were obtained in all cases, further testifying the feasibility of the protocol in real environments.

CONCLUSIONS

Herein, we have described the use of 2D nanomaterial-wrapped Janus micromotors as dynamic interfaces in the fluorescence sensing of Cholera Toxin B using a specific labeled peptide probe as model system. This is the first study that evaluates the influence of the type of 2D nanomaterials on micromotors in fluorescence sensing approaches. The ON–OFF–ON system also allows mimicking similar processes occurring at (bio)-interfaces and to study the related sorption

and desorption kinetics. The distinct surface properties of each nanomaterial play a critical role in the loading/release capacity of the peptide, greatly influencing the release profiles. Sorption kinetics indicate a great degree of chemisorption, yet the release kinetics indicates a contribution of π and hydrophobic interactions in graphene-based Janus micromotors, with the lowest release capacity observed for BP. This greatly influences the final sensing performance, with 5-fold efficient GDYO and GO micromotors compared to BP micromotors. Excellent release capacity and micromotor performance are observed also in complex samples such as human serum. Efficient sensing operation in *V. cholerae* and *Vibrio parahaemolyticus* bacteria cultures illustrates the high micromotor operation in real environments. The unique micromotor movement in connection with 2D nanomaterials allows for efficient operation in miniaturized settings and complex samples, offering considerable promise for the design of novel micromotor-based (bio)-sensing approaches or to understand the interaction between micromotor and biological counterparts in a myriad of clinical applications.

ASSOCIATED CONTENT

Supporting Information

The Supporting Information is available free of charge at <https://pubs.acs.org/doi/10.1021/acsami.0c15389>.

Schematic of the synthesis of 2D nanomaterials-wrapped Janus micromotors (Figure S1); probe loading capacity of the micromotors (Figure S2); zero-, first-, and second-order kinetics models plots (Figure S3); calibration plots of the sensing strategy (Figure S4); selectivity of the protocol with *Escherichia coli* affinity peptide modified micromotors (Figures S5); selectivity of the protocol in real samples (Figure S6) and release kinetic parameters (Table S1) (PDF)

GDYO micromotors navigation in ultrapure water, bacteria culture, and human serum (AVI)

BP micromotors navigation in ultrapure water, bacteria culture, and human serum (AVI)

GO micromotors navigation in ultrapure water, bacteria culture, and human serum (AVI)

Movement of several 2D nanomaterials micromotors (AVI)

AUTHOR INFORMATION

Corresponding Authors

Beatriz Jurado-Sánchez – Department of Analytical Chemistry, Physical Chemistry and Chemical Engineering and Chemical Research Institute “Andrés M. del Río”, University of Alcala, Alcala de Henares E-28871 Madrid, Spain; orcid.org/0000-0002-6584-1949; Email: beatriz.jurado@uah.es

Alberto Escarpa – Department of Analytical Chemistry, Physical Chemistry and Chemical Engineering and Chemical Research Institute “Andrés M. del Río”, University of Alcala, Alcala de Henares E-28871 Madrid, Spain; orcid.org/0000-0002-7302-0948; Phone: +34 91 8854995; Email: alberto.escarpa@uah.es

Authors

Kaisong Yuan – Department of Analytical Chemistry, Physical Chemistry and Chemical Engineering, University of Alcala, Alcala de Henares E-28871 Madrid, Spain; Institute of

Pharmaceutical Analysis, College of Pharmacy, Jinan University, Guangzhou 510632, China

Miguel Angel López – Department of Analytical Chemistry, Physical Chemistry and Chemical Engineering and Chemical Research Institute “Andrés M. del Río”, University of Alcalá, Alcalá de Henares E-28871 Madrid, Spain

Complete contact information is available at:
<https://pubs.acs.org/10.1021/acsami.0c15389>

Author Contributions

The manuscript was written through contributions of all authors. All authors have given approval to the final version of the manuscript.

Notes

The authors declare no competing financial interest.

ACKNOWLEDGMENTS

B.J.-S. and K.Y. received funding for salary from the Spanish Ministry of Economy, Industry and Competitiveness for (RYC-2015-17558, co-financed by EU). B.J.-S. and M.A.L. received funding for reagents from the University of Alcalá (CCG19/CC-029). A.E., B.J.-S., and M.A.L. received funding for reagents and equipment from the Spanish Ministry of Economy, Industry and Competitiveness (CTQ2017-86441-C2-1-R) and the Community of Madrid (TRANSNANOAVANSENS program, S2018/NMT-4349, and CM/JIN/2019-007). The authors thank Cava's group for providing the *V. cholera* and *V. parahemolyticus* cultures.

REFERENCES

- (1) Taylor-Pashow, K. M. L.; Della Rocca, J.; Huxford, R. C.; Lin, W. Hybrid Nanomaterials for Biomedical Applications. *Chem. Commun.* **2010**, *46*, 5832–5849.
- (2) Johnson, B. N.; Mutharasan, R. Biosensing Using Dynamic-Mode Cantilever Sensors: A Review. *Biosens. Bioelectron.* **2012**, *32*, 1–18.
- (3) Wang, H.; Zhang, Q.; Chu, X.; Chen, T.; Ge, J.; Yu, R. Graphene Oxide-Peptide Conjugate as An Intracellular Protease Sensor for Caspase-3 Activation Imaging in Live Cells. *Angew. Chem., Int. Ed.* **2011**, *50*, 7065–7069.
- (4) Shi, H.; Zhang, B.; Liu, S.; Tan, C.; Tan, Y.; Jiang, Y. A New Strategy Involving the Use of Peptides and Graphene Oxide for Fluorescence Turn-on Detection of Proteins. *Sensors* **2018**, *18*, 385.
- (5) Joshi, S.; Sharma, P.; Siddiqui, R.; Kaushal, K.; Sharma, S.; Verma, G.; Saini, A. A Review on Peptide Functionalized Graphene Derivatives as Nanotools for Biosensing. *Microchim. Acta* **2020**, *187*, 27.
- (6) Yew, Y. T.; Sofer, Z.; Mayorga-Martinez, C. C.; Pumera, M. Black Phosphorus Nanoparticles as A Novel Fluorescent Sensing Platform for Nucleic Acid Detection. *Mater. Chem. Front.* **2017**, *1*, 1130–1136.
- (7) Anichini, C.; Czepa, W.; Pakulski, D.; Aliprandi, A.; Ciesielski, A.; Samori, P. Chemical Sensing with 2D Materials. *Chem. Soc. Rev.* **2018**, *47*, 4860–4908.
- (8) Bolotsky, A.; Butler, D.; Dong, C.; Gerace, K.; Glavin, N. R.; Muratore, C.; Robinson, J. A.; Ebrahimi, A. Two-Dimensional Materials in Biosensing and Healthcare: From In Vitro Diagnostics to Optogenetics and Beyond. *ACS Nano* **2019**, *13*, 9781–9810.
- (9) Hu, Z.; Li, Y.; Hussain, E.; Huang, X.; Zhang, Y.; Niu, N.; Shahzad, S. A.; Yu, C. Black Phosphorus Nanosheets Based Sensitive Protease Detection and Inhibitor Screening. *Talanta* **2019**, *197*, 270–276.
- (10) Neema, P. M.; Tomy, A. M.; Cyriac, J. Chemical Sensor Platforms Based on Fluorescence Resonance Energy Transfer (FRET) and 2D Materials. *TrAC, Trends Anal. Chem.* **2020**, *124*, No. 115797.

- (11) Sinha, A.; Dhanjai; Zhao, H.; Huang, Y.; Lu, X.; Chen, J.; Jain, R. MXene: An Emerging Material for Sensing and Biosensing. *TrAC, Trends Anal. Chem.* **2018**, *105*, 424–435.
- (12) Parvin, N.; Jin, Q.; Wei, Y.; Yu, R.; Zheng, B.; Huang, L.; Zhang, Y.; Wang, L.; Zhang, H.; Gao, M.; Zhao, H.; Hu, W.; Li, Y.; Wang, D. Few-Layer Graphdiyne Nanosheets Applied for Multiplexed Real-Time DNA Detection. *Adv. Mater.* **2017**, *29*, No. 1606755.
- (13) Ozin, G. A.; Manners, I.; Fournier-Bidoz, S.; Arsenault, A. Dream Nanomachines. *Adv. Mater.* **2005**, *17*, 3011–3018.
- (14) Kline, T. R.; Paxton, W. F.; Mallouk, T. E.; Sen, A. Catalytic Nanomotors: Remote-Controlled Autonomous Movement of Striped Metallic Nanorods. *Angew. Chem., Int. Ed.* **2005**, *44*, 744–746.
- (15) Gao, W.; Sattayasamitsathit, S.; Orozco, J.; Wang, J. Highly Efficient Catalytic Microengines: Template Electrosynthesis of Polyaniline/Platinum Microtubes. *J. Am. Chem. Soc.* **2011**, *133*, 11862–11864.
- (16) Mei, Y.; Solovov, A. A.; Sanchez, S.; Schmidt, O. G. Rolled-up Nanotech on Polymers: From Basic Perception to Self-Propelled Catalytic Microengines. *Chem. Soc. Rev.* **2011**, *40*, 2109–2119.
- (17) Wang, H.; Pumera, M. Emerging Materials for The Fabrication Of Micro/Nanomotors. *Nanoscale* **2017**, *9*, 2109–2116.
- (18) Wang, H.; Pumera, M. Fabrication of Micro/Nanoscale Motors. *Chem. Rev.* **2015**, *115*, 8704–8735.
- (19) Jurado-Sánchez, B.; Pacheco, M.; Maria-Hormigos, R.; Escarpa, A. Perspectives on Janus Micromotors: Materials and Applications. *Appl. Mater. Today* **2017**, *9*, 407–418.
- (20) Wang, J. Self-Propelled Affinity Biosensors: Moving the Receptor Around the Sample. *Biosens. Bioelectron.* **2016**, *76*, 234–242.
- (21) Pacheco, M.; López, M. Á.; Jurado-Sánchez, B.; Escarpa, A. Self-Propelled Micromachines for Analytical Sensing: A Critical Review. *Anal. Bioanal. Chem.* **2019**, *411*, 6561–6573.
- (22) Jurado-Sánchez, B.; Escarpa, A. Milli, Micro and Nanomotors: Novel Analytical Tools for Real-World Applications. *TrAC, Trends Anal. Chem.* **2016**, *84*, 48–59.
- (23) Singh, V. V.; Kaufmann, K.; Esteban-Fernández de Ávila, B.; Karshalev, E.; Wang, J. Molybdenum Disulfide-Based Tubular Microengines: Toward Biomedical Applications. *Adv. Funct. Mater.* **2016**, *26*, 6270–6278.
- (24) Esteban-Fernández de Ávila, B.; Lopez-Ramirez, M. A.; Báez, D. F.; Jodra, A.; Singh, V. V.; Kaufmann, K.; Wang, J. Aptamer-Modified Graphene-Based Catalytic Micromotors: Off-On Fluorescent Detection of Ricin. *ACS Sens.* **2016**, *1*, 217–221.
- (25) Molinero-Fernández, Á.; Jodra, A.; Moreno-Guzmán, M.; López, M. Á.; Escarpa, A. Magnetic Reduced Graphene Oxide/Nickel/Platinum Nanoparticles Micromotors for Mycotoxin Analysis. *Chem. - Eur. J.* **2018**, *24*, 7172–7176.
- (26) Báez, D. F.; Ramos, G.; Corvalán, A.; Cordero, M. L.; Bollo, S.; Kogan, M. J. Effects of Preparation on Catalytic, Magnetic And Hybrid Micromotors on Their Functional Features and Application In Gastric Cancer Biomarker Detection. *Sens. Actuators, B* **2020**, *310*, No. 127843.
- (27) Esteban-Fernández de Ávila, B.; Martín, A.; Soto, F.; Lopez-Ramirez, M. A.; Campuzano, S.; Vázquez-Machado, G. M.; Gao, W.; Zhang, L.; Wang, J. Single Cell Real-Time miRNAs Sensing Based on Nanomotors. *ACS Nano* **2015**, *9*, 6756–6764.
- (28) Beltrán-Gastélum, M.; Esteban-Fernández de Ávila, B.; Gong, H.; Venugopalan, P. L.; Hianik, T.; Wang, J.; Subjakova, V. Rapid Detection of AIB1 in Breast Cancer Cells Based on Aptamer-Functionalized Nanomotors. *ChemPhysChem* **2019**, *20*, 3177–3180.
- (29) Li, S.; Aphale, A. N.; Macwan, I. G.; Patra, P. K.; Gonzalez, W. G.; Miksovska, J.; Leblanc, R. M. Graphene Oxide as a Quencher for Fluorescent Assay of Amino Acids, Peptides, and Proteins. *ACS Appl. Mater. Interfaces* **2012**, *4*, 7069–7075.
- (30) Lu, C. H.; Li, J.; Zhang, X. L.; Zheng, A. X.; Yang, H. H.; Chen, X.; Chen, G. N. General Approach for Monitoring Peptide-Protein Interactions Based on Graphene-Peptide Complex. *Anal. Chem.* **2011**, *83*, 7276–82.

(31) Lu, C.; Liu, Y.; Ying, Y.; Liu, J. Comparison of MoS₂, WS₂, and Graphene Oxide for DNA Adsorption and Sensing. *Langmuir* **2017**, *33*, 630–637.

(32) Yuan, K.; de la Asunción-Nadal, V.; Jurado Sánchez, B.; Escarpa, A. 2D Nanomaterials Wrapped Janus Micromotors with Built-In Multiengines for Bubble, Magnetic, and Light Driven Propulsion. *Chem. Mater.* **2020**, *32*, 1983–1992.

(33) Jia, Z.; Li, Y.; Zuo, Z.; Liu, H.; Huang, C.; Li, Y. Synthesis and Properties of 2D Carbon-Graphdiyne. *Acc. Chem. Res.* **2017**, *50*, 2470–2478.

(34) Chen, X.; Gao, P.; Guo, L.; Wen, Y.; Fang, D.; Gong, B.; Zhang, Y.; Zhang, S. High-Efficient Physical Adsorption and Detection of Formaldehyde Using Sc- And Ti-Decorated Graphdiyne. *Phys. Lett. A* **2017**, *381*, 879–885.

(35) Chen, X.; Gao, P.; Guo, L.; Zhang, S. Graphdiyne as A Promising Material for Detecting Amino Acids. *Sci. Rep.* **2015**, *5*, No. 16720.

(36) Zhang, W.; Huynh, T.; Xiu, P.; Zhou, B.; Ye, C.; Luan, B.; Zhou, R. Revealing the Importance of Surface Morphology of Nanomaterials to Biological Responses: Adsorption of the Villin Headpiece onto Graphene and Phosphorene. *Carbon* **2015**, *94*, 895–902.

(37) Lim, S. K.; Chen, P.; Lee, F. L.; Mochhala, S.; Liedberg, B. Peptide-Assembled Graphene Oxide as A Fluorescent Turn-On Sensor for Lipopolysaccharide (Endotoxin) Detection. *Anal. Chem.* **2015**, *87*, 9408–9412.

(38) Lim, J. M.; Heo, N. S.; Oh, S. Y.; Ryu, M. Y.; Seo, J. H.; Park, T. J.; Huh, Y. S.; Park, J. P. Selection of Affinity Peptides for Interference-free Detection of Cholera Toxin. *Biosens. Bioelectron.* **2018**, *99*, 289–295.

(39) Bruschi, M. L. Mathematical models of drug release. In *Strategies to Modify the Drug Release from Pharmaceutical Systems*; Woodhead Publishing: 2015; pp 63–86.

(40) Danyuo, Y.; Ani, C. J.; Salifu, A. A.; Obayemi, J. D.; Dozie-Nwachukwu, S.; Obanawu, V. O.; Akpan, U. M.; Odusanya, O. S.; Abade-Abugre, M.; McBagonluri, F.; Soboyejo, W. O. Anomalous Release Kinetics of Prodigiosin from Poly-N-Isopropyl-Acrylamid based Hydrogels for The Treatment of Triple Negative Breast Cancer. *Sci. Rep.* **2019**, *9*, No. 3862.

(41) Jain, A.; Jain, S. K. In Vitro Release Kinetics Model Fitting of Liposomes: An Insight. *Chem. Phys. Lipids* **2016**, *201*, 28–40.

(42) Sun, X.; Fan, J.; Fu, C.; Yao, L.; Zhao, S.; Wang, J.; Xiao, J. WS₂ and MoS₂ Biosensing Platforms Using Peptides as Probe Biomolecules. *Sci. Rep.* **2017**, *7*, No. 10290.

SUPPORTING INFORMATION

Janus micromotors coated with 2D nanomaterials as dynamic interfaces for (bio)-sensing

Kaisong Yuan,^{†§} Miguel Ángel López,^{†‡} Beatriz Jurado-Sánchez,^{†*} and Alberto Escarpa^{†‡*}

[†]Department of Analytical Chemistry, Physical Chemistry and Chemical Engineering, University of Alcalá, Alcalá de Henares E-28871, Madrid, Spain. E-mail: beatriz.jurado@uah.es, alberto.escarpa@uah.es (Tel: +34 91 8854995)

[§]Institute of Pharmaceutical Analysis, College of Pharmacy, Jinan University, Guangzhou, China

[‡]Chemical Research Institute "Andrés M. del Río", University of Alcalá, Alcalá de Henares E-28871, Madrid, Spain

SUPPORTING FIGURES

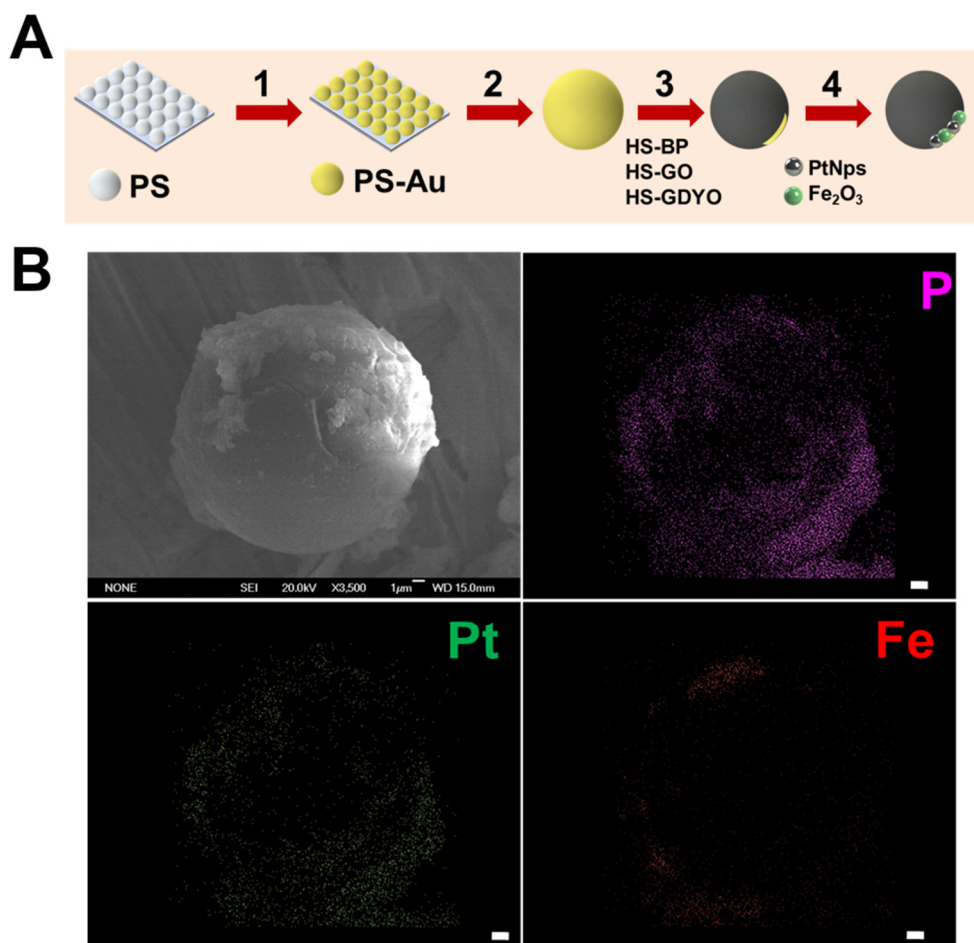


Figure S1. A) Schematic of the synthesis of 2D nanomaterials wrapped Janus micromotors: 1. Gold sputtering of 20 μm polystyrene (PS) particles; 2. Release of the PS-Au particles in solution; 3. Coating of PS-Au particles with the 2D nanomaterials, 4. Asymmetric assembly of Pt and ferrite nanoparticles. For further details please see the experimental section in the main text. B) Scanning-electron microscopy images of a black-phosphorous (BP)-PtNPs/Fe₂O₃ micromotors and corresponding energy-ray dispersing mapping showing the element distribution. Scale bar, 1 μm.

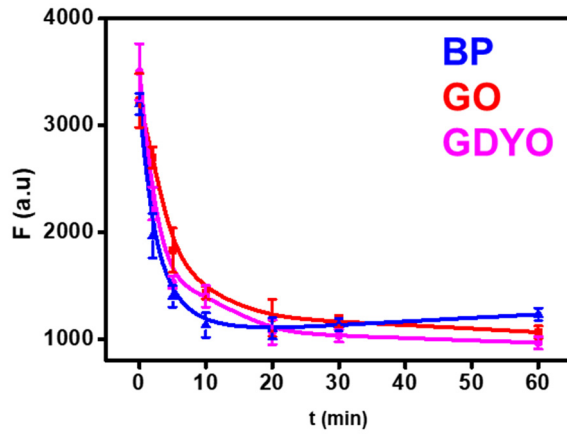


Figure S2. Probe loading capacity of the micromotors. Plot showing the decrease of fluorescent over time of solutions containing 100 $\mu\text{g/mL}$ of affinity peptide solution during navigation of BP, graphene oxide (GO) or graphdyine oxide (GDYO) micromotors (140000 micromotors/mL).

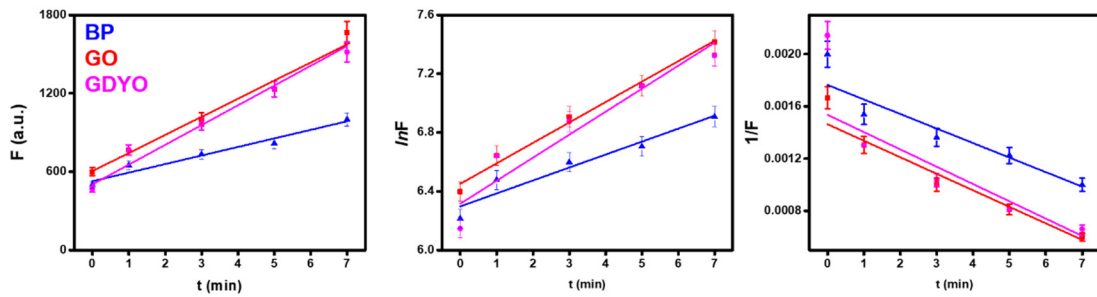


Figure S3. Zero (left), first-order (middle) and second order kinetics (right) models plot of release with the different 2D materials micromotors using the fluorescent data at different times.

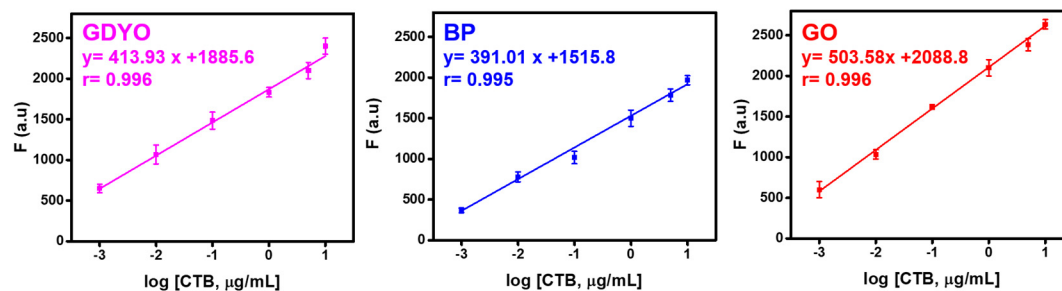


Figure S4. Calibration plots of the sensing strategy using the affinity peptide modified GDYO, BP or GO micromotors (140000 micromotors/mL) in solutions containing variable concentrations of the *Cholera Toxin B* (from 0.001 to 10 $\mu\text{g/mL}$), 150 μL of sodium dodecyl sulfate 3% and 3% H_2O_2 .

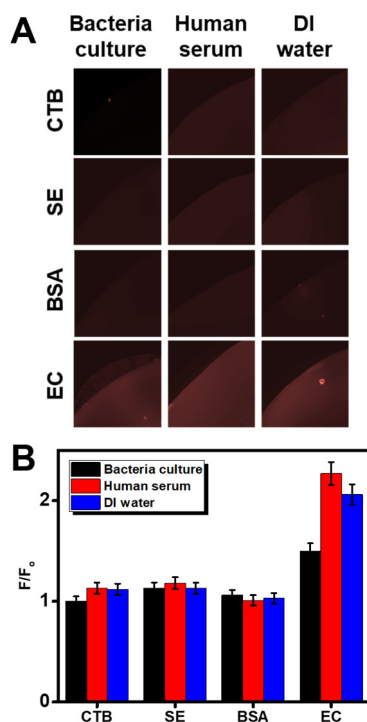


Figure S5. A) Time-lapse fluorescence images after navigation of the micromotors modified with 100 $\mu\text{g/mL}$ of the affinity peptide from *Escherichia coli* (sequence TMRho-KKNYSSSISSIHIC) in the presence of 10 $\mu\text{g/mL}$ *Escherichia coli* O111:B4 endotoxin (EC), *Cholera Toxin B* (CTB), *Salmonella Enterica* (SE) or BSA in bacteria, human serum and DI water and B) corresponding normalized fluorescence plots (F/F_0).

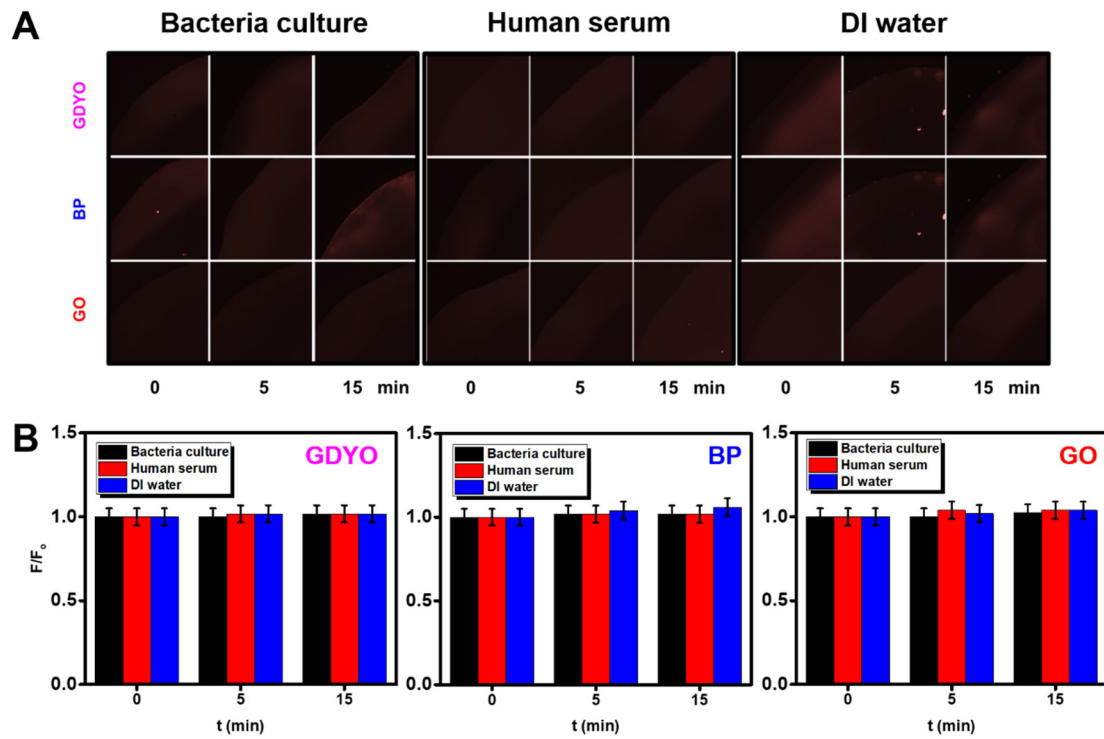


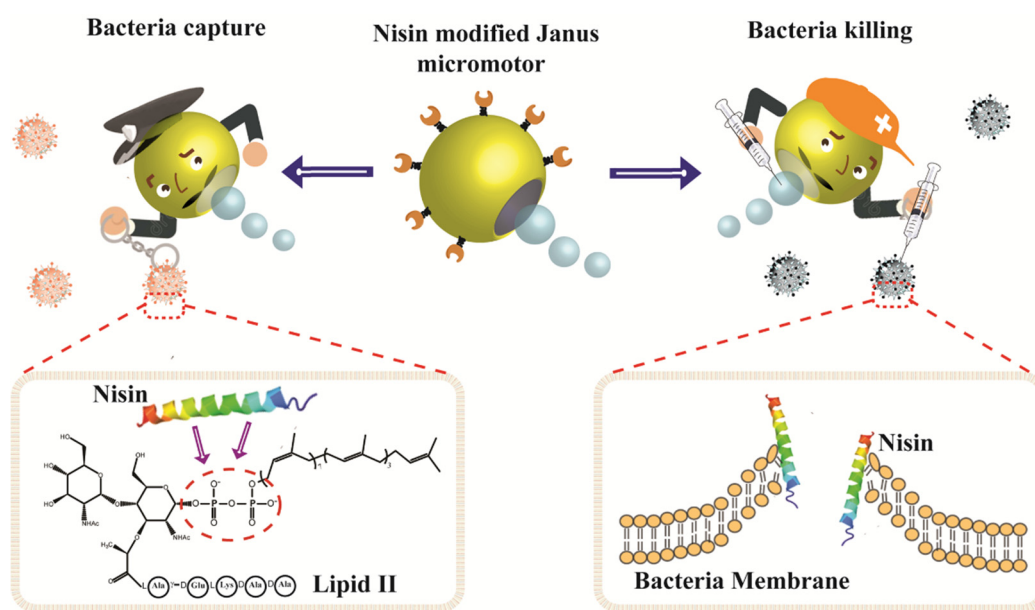
Figure S6. A) Time-lapse fluorescent images after navigation of the affinity-peptide modified micromotors in bacteria, human serum and DI water and B) corresponding normalized fluorescence plots (F/F_0).

Table S1. Pseudo zero, first and second-order kinetic parameters for affinity peptide release from the micromotors

Micromotor	Slope	Intercept	R^2 (%)
<i>Zero</i>			
BP	65.5	528	94.9
GO	140	684	98.8
GDYO	151	502	98.7
<i>First</i>			
BP	0.088	6.29	93.5
GO	0.156	6.31	95.3
GDYO	0.139	6.45	96.4
<i>Second</i>			
BP	-	-	86.8
GO	-	-	81.7
GDYO	-	-	95.6

IV. Janus micromotors based on 2D nanomaterials for detection and killing of pathogenic bacteria

IV.4. Article 5. Antimicrobial peptide modified micromotors for isolation and killing of pathogenic bacteria (under review).



Dual-propelled lanbiotic based Janus micromotors for selective inactivation of bacteria biofilms

K. Yuan,^[a,b] B. Jurado-Sánchez,^{[c]*} A. Escarpa^{[a,c]*}

[a] K. Yuan, B. Jurado-Sánchez, A. Escarpa
Department of Analytical Chemistry, Physical Chemistry, and Chemical Engineering, University of Alcalá,
Alcalá de Henares, E-28871 Madrid, Spain University of Alcalá, E-28807, Madrid, Spain
E-mail: beatriz.jurado@uah.es, alberto.escarpa@uah.es

[b] K. Yuan
Institute of Pharmaceutical Analysis, College of Pharmacy, Jinan University, Guangzhou, China

[c] B. Jurado-Sánchez, A. Escarpa
Chemical Research Institute "Andres M. del Rio", University of Alcalá, E-28807, Madrid, Spain

Supporting information for this article is given via a link at the end of the document.

Abstract: Graphene oxide/PtNPs/Fe₂O₃ "dual-propelled" catalytic and fuel-free rotary actuated magnetic Janus micromotors modified with the antimicrobial peptide Nisin are used for highly selective capture/inactivation of gram-positive bacteria units and biofilms. Specific interaction of Nisin with the Lipid II unit of *Staphylococcus Aureus* bacteria in connection with the enhanced micromotor movement and generated fluid flow results in a 2-fold increase of the capture/killing ability (both in bubble and magnetic propulsion modes) as compared with free peptide and static counterparts. The high stability of Nisin along with the high towing force of the micromotor allow for efficient micromotor operation in untreated raw media (juice, serum and tap water samples). The high selectivity of the protocol is illustrated by the dramatically lower interaction with gram-negative bacteria (*Escherichia Coli*). The double-propulsion (catalytic or fuel-free magnetic) mode of the micromotors holds considerable promise to design micromotors with tailored lanbiotics that can response to the changes that make the bacteria resistant in a myriad of clinical, environmental remediation or food safety applications.

Introduction

Bacterial infections represent a major threat in public health, causing million deaths worldwide. In hospitals, the spread of such infections can be very fast, leading to the generation of "superbugs" or multidrug resistant bacteria.^[1] Another important issue is the formation of resistant biofilms in biomedical devices, causing high-risk of concurrent infections.^[2] The quest for novel ways to deal with such infections and biofilms rely on the exploration of new chemical agents and nanomaterials. Their antimicrobial activity can be explained by three main mechanisms: (1) direct release of reactive oxygen species (ROS) and metal ions,^[2-3] (2) direct physical contact^[4] and (3) photothermal effect in connection with near-infrared (NIR) light.^[5] The combination of different nanoparticles and nanomaterials - such as 2D nanomaterials- with multimode actions results in multifunctional entities with synergetic capabilities for enhanced bacteria inactivation.^[6] Noble metal nanoparticles, liposomes,

micelles and 2D nanomaterials can be also used as "nanocarriers" for localized delivery of antibiotics, enhancing both the targeting ability and the antibacterial properties.^[2, 5b] Such strategies hold considerable promise to overcome the increasing concerns of antibiotic resistance by enhancing the overall efficiency of the processes and decreasing the levels of antibacterial agents.

Inspired by the promising capabilities of nanomaterials in the antibacterial war, the micromotor community translates the mechanisms of action of such "nanoentities" into moving schemes. Indeed, the enhanced mixing and towing force of such moving colloids can improve even more the efficiency in bacteria removal and inactivation processes.^[7] The myriad of synthetic strategies allow to tailor the micromotor composition and propulsion mechanism for a given application.^[8] For example, zeolite micromotors with a dual Ag catalytic/killing layer shows great efficiency for *Escherichia Coli* bacteria killing.^[9] Such concept was later extended to explore alternative propulsion mechanisms, leading to water propelled magnesium micromotors decorated with AgNPs^[10] or coated with Ag layers^[11] and even light propelled Ag nanostars.^[12] In a more sophisticated configuration, Wang's group encapsulated serine as chemoattractant into Mg/Ag coated micromotors. After the Mg core dissolution, *Escherichia Coli* bacteria was attracted into the micromotor shell for enhanced contact with the Ag ions and accelerated killing.^[13] Besides silver, TiO₂ have been coated in Mg spheres for light-triggered ROS generation for *Bacillus Globigii* spores deactivation.^[14] While effective, the short lifetime of Mg and Ag layers in the above mentioned configurations hampers the prolonged use of such micromotors as well as the removal after treatment. As an alternative, magnetic iron oxide nanoparticles aggregates synergistically generating ROS for enhanced but non targeted biofilm deactivation.^[15] Direct contact killing micromotors compromise alginate coated Mg spheres^[16] or Pd/Ni/Ag magnetic nanocoils^[17] that are able to bind and rupture the membrane of *Escherichia Coli* and *Staphylococcus Aureus* bacteria. Photothermal inactivation of *Klebsiella pneumoniae* has been achieved with magnetically propelled spirulina coated micromotors.^[18] Yet, all the above mentioned configurations lacks specificity towards a given type of bacteria, which can be very

beneficial for improved inactivation, on particular to treat infections caused by multidrug resistance bacteria. To address such limitations, micromotors have also been used as moving carries of antibiotic, enzymes or bioactive components for targeted isolation/killing of bacteria. Such configurations include lysozyme coated ultrasound propelled nanowires for *Micrococcus Lysodeikticus* killing,^[19] antibiotic loaded Mg spheres for *Helicobacter Pylori* treatment^[20] or silica tubes/magnetotactic bacteria hybrids for enhanced antibiotic delivery and biofilm killing.^[21] Red blood cells and platelets have been used in connection with magnetic or ultrasound propelled micromotors for direct bacteria isolation.^[22] Despite the increased specificity, the antibiotic and biological material are prone to inactivation in biological media, hampering adequate treatment. Graphene or 2D nanomaterials such as black phosphorous, chalcogenides or germanane have demonstrated their potential along with micromotor technology in a myriad of applications in environmental remediation, drug delivery or sensing.^[23] Yet, such potential in the antibacterial war remains to be demonstrated. Herein we report on a new micromotor strategy based on the combination, for the first time, of a lanbiotic (Nisin) with graphene oxide (GO) catalytic and/or magnetic rotatory actuated Janus micromotors. Lanbiotics are peptides composed of methyl-lanthionine residues with a highly selective antimicrobial activity towards multidrug resistant bacteria. Nisin is a natural compound normally used for food preservation, which display specific antimicrobial activity towards gram-positive bacteria. Such peptide can bind to lipid II unit of the bacteria membranes, damaging its morphology and releasing its contents.^[24] In this work, we report the combination of Nisin with 2D nanomaterials based micromotors for selective gram-positive bacteria killing (see **Figure 1**). The coating of micromotors with GO impart them with a Janus structure for the subsequent asymmetric assembly of catalytic (PtNPs) and magnetic (Fe_2O_3) engines and results in an active rough layer for a higher loading of Nisin via covalent interactions. The micromotors possess adaptative propulsion mechanisms, including catalytic mode (PtNPs) in peroxide solutions or magnetic actuation (fuel free) by the action of an external magnetic field. In the following sections, we will illustrate how the enhanced movement and localized fluid flow generated by the micromotors (both in catalytic and magnetic actuated mode) results in a 2-fold increase of the capture/killing ability towards *Staphylococcus Aureus* bacteria in raw media (juice, serum and tap water samples), as compared with free Nisin and static counterparts. The micromotor strategy display also high selectivity towards such bacteria, as will be illustrated by the dramatically lower capture/killing ability towards gram-negative *Escherichia Coli*. We will also show the ability of the micromotors to destroy bacteria and biofilms. Unlike previous micromotors

based strategies, our approach displays higher selectivity towards a type of bacteria along with enhanced stability, prolonged use and adaptative propulsion modes, holding considerable promise to treat methicillin resistant antibiotic infections, for environmental remediation or food safety, among others.

Results and Discussion

Figure 1 illustrates the micromotor based strategy for specific bacteria capture/killing used in this work. As shown in the schematic illustration in **Figure 1A** and the corresponding time-lapse microscopy images, the micromotors (both in bubble and magnetic modes) display high selectivity for specific binding with *Staphylococcus Aureus* bacteria. Once the bacteria contact with the Nisin moving micromotors, a hydrogen bond is formed between the amine groups in Nisin and pyrophosphate groups of the lipid II molecules in the outer bacteria membrane.^[24c] The strong bond allows Nisin molecules to penetrate the bacteria cell wall, creating pores which ultimately results in the dead of the gram-positive bacteria (see **Figure S1**). SEM images of **Figure 1C** illustrate the successful capture of *Staphylococcus Aureus* bacteria by the Nisin modified micromotors, in which all the surface is covered by the bacteria, which in some cases displays a flat morphology that can be attributed to cell rupture (see part d).

Micromotors were synthesized using a very recent approach described by our research group.^[25] Briefly, 20 μm size polystyrene spheres were coated with a thin gold layer by sputter coating. Subsequently, the micromotors were incubated with sulfhydryl modified GO for attachment to the gold layer via thiol linkages. The amount and time for GO incubation was judiciously optimized so a small Au patch was left exposed for preferential growth of Pt and iron oxide nanoparticles, imparting thus the Janus character in the micromotor for directional propulsion (for further details, see the supporting information). Next, the micromotors were modified with Nisin via covalent immobilization. To this end, the GO layer was modified with thioglycolic acid to introduce a higher loading of carboxylic acids, followed by activation with N-(3-Dimethylaminopropyl)-N'-ethyl carbodiimide hydrochloride. Such activation promotes the incorporation of Nisin by interaction with the amine group present in its structure (see **Figure S1** and **S2**). As will be further illustrated, such modification imparts the micromotors with high selectivity to interact with gram-positive bacteria. **Figure S3** illustrates the scanning-electron microscopy (SEM) of the micromotors before (A) and after modification with Nisin. No apparent changes can be clearly observed, except for a thicker layer covering the surface (see part d in the Figure). No speed changes are observed after modification, with the micromotors moving at speed of over $55 \pm 25 \mu\text{m s}^{-1}$ on both cases.

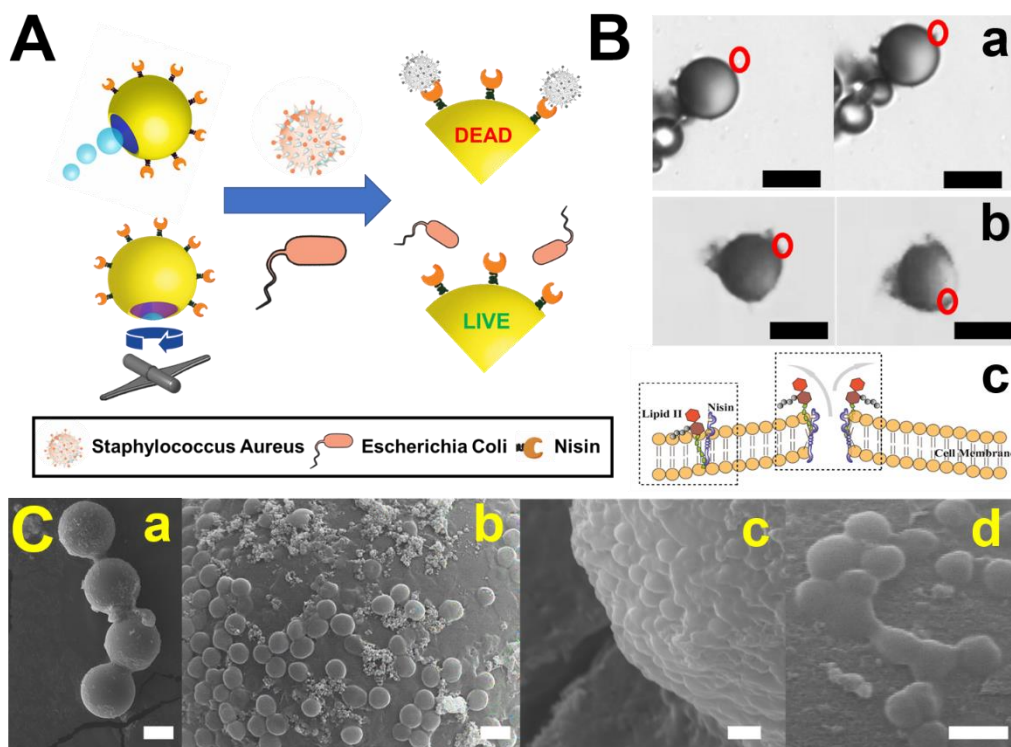


Figure 1. Antimicrobial peptide modified Janus micromotors for bacteria isolation and killing. A) Schematic of the strategy based on the modification of catalytic and magnetic driven GO/PtNPs/Fe₂O₃ Janus micromotors with Nisin and specific interaction and killing of *Staphylococcus Aureus* bacteria over *Escherichia Coli*. B) Time-lapse microscopy images (taken from **Video S1**) illustrating the “on-the-fly” capture of a *Staphylococcus Aureus* bacteria with the Janus micromotors in bubble (a) and magnetic mode (b) and schematic of killing mechanism by specific lysis after the cell membrane attached onto the Nisin modified micromotor (c). Scale bars, 20 μ m. C) SEM images of the micromotors after *Staphylococcus Aureus* bacteria capture, overall view of Nisin modified micromotors captured with *Staphylococcus Aureus* (a), detailed surfaces information taken from the local area of a Nisin modified micromotor captured with *Staphylococcus Aureus* in bubble (b) and magnetic mode (c) and some broken *Staphylococcus Aureus* on micromotor surface (d). Scale bars, 10 μ m (a) and 1 μ m (b-d).

The presence of catalytic PtNPs and iron oxide *engines* in the micromotor structure allow to adapt its motion behaviour using peroxide as fuel for catalytic propulsion and external rotating magnetic fields for fuel-free propulsion. Peroxide propulsion can be beneficial in remote setting or environmental applications for bacterial removal, exploiting the combined effect peroxide-micromotors. Yet, as will be further illustrated, the peroxide and surfactant used for catalytic propulsion exhibit moderate toxicity in a long time, which will prevent future on-body applications. Please note that our main aim here was to demonstrate the utility of antibiotics on board of micromotors for selective bacteria inactivation. The strategy, once proved and demonstrated, can be extended to any micromotor “chassis” powered by more biofriendly propulsion mechanism. To this end, inspired by rotary actuated nanomotors^[26] and by the magnetic properties of our Janus micromotors, herein we introduce a new concept of rotary actuated magnetic micromotors. As such, the use of hydrogen peroxide or surfactant is avoided since the micromotor only move/actuate by the effect of external magnetic field, holding considerable promise for in-vivo applications. Inspired by previous work and using the equipment available in our lab, we propose a dual actuated Nisin modified micromotor which can be operated by catalytic propulsion and magnetic actuation (bubble or magnetic modes, respectively). For magnetic actuation, a custom-made rotating magnetic field generating device is placed

below the micromotor solution, allowing for ON-OFF stopped rotatory motion.

As the micromotor speed and prolonged operation in solution exert a great influence on the capture/killing efficiency, the influence of peroxide fuel and frequency on the magnetic field upon micromotor speed was evaluated. As can be seen in the plot of **Figure S4**, in catalytic mode the speed increase along with peroxide concentration, with the minimum fuel concentration as low as 0.5 % to generate enhanced movement. For magnetic mode, speed increase along frequency up to 4 Hz, whereas at higher frequency highly turbulent flows disturb the micromotor movement, with an unstable pattern which results in a speed decrease. In addition, for future application, we checked the prolonged micromotor movement in 1 % peroxide solutions. Micromotor speed remains constant after 1-hour navigation in bacteria media. After 2 hours, a slight decrease in speed is noted, which further dramatically decrease after 3 hours, probably due peroxide depletion by prolonged navigation (see **Figure S4, C** and **Video S2**). This fact, however, do not hamper the efficiency of micromotors for bacteria capture and killing, as will be further illustrated. Cooperative motion of multiple micromotors, both in bubble and magnetic mode, greatly enhanced the fluid mixing for highly efficient bacteria capture and subsequent killing (see **Figure S4, C** and **Video S2**).

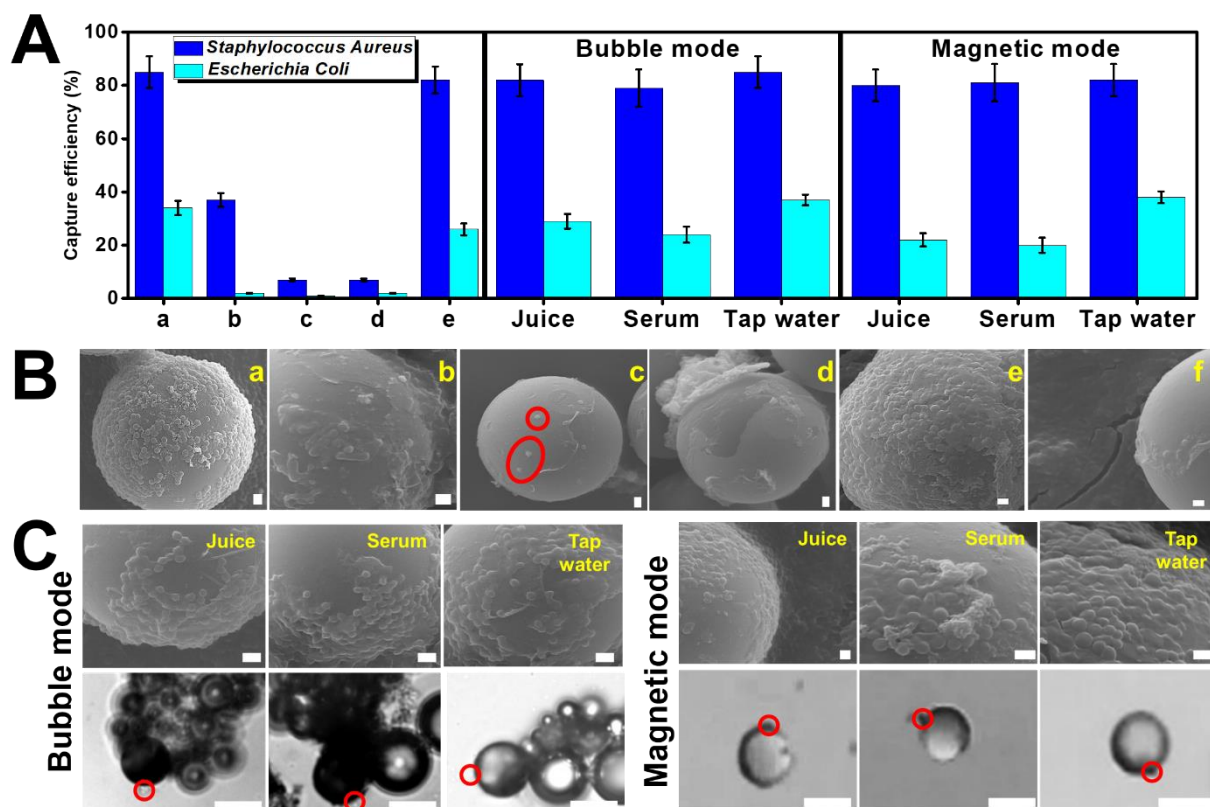


Figure 2. Selectivity and capture efficiency of the Nisin modified micromotors in bubble and magnetic mode. A) Plot showing the capture efficiency of the micromotors in control experiments and in fortified samples, where: a) moving micromotors in catalytic mode; b) static modified micromotors after 1 hour incubation; c) unmodified micromotors after 1 hour navigation in the presence of free Nisin; d) unmodified moving micromotors after 1 hour navigation and e) moving micromotors in magnetic mode. B) Corresponding SEM in control experiments and samples, where: a, b) Modified moving catalytic micromotors after 5 min navigation in *Staphylococcus Aureus* and *Escherichia Coli* cultures, respectively, c) static modified micromotors after 1 hour incubation, d) unmodified moving micromotors after 1 hour navigation, e, f) Modified magnetic moving micromotors after 5 min actuation in *Staphylococcus Aureus* and *Escherichia Coli* cultures, respectively. Scale bars, 1 μm . C) SEM and time-lapse microscopy images (taken from Video S4) illustrating the bacteria capture in the samples in catalytic and magnetic modes. Scale bars, 1 μm (SEM) and 20 μm (optical images). Conditions: 3% hydrogen peroxide, 2% SDS (catalytic mode), frequency, 4 Hz (magnetic mode), 220 micromotors mL^{-1} , 10^2 CFU mL^{-1} of *Staphylococcus Aureus* and *Escherichia Coli*. Error bars corresponds to the standard deviation of 10 measurements.

To get further insights into the efficiency and similar operation in both modes, we performed simulations on the enhanced mixing and liquid flow generated along the micromotors and study the mean squared displacement using 1 μm polystyrene particles as tracers (see **Figure S5** and **Video S3**). As can be seen in the simulations (see A and B, left part) efficient fluid flow is generated along the micromotors in both modes, which further increase the interaction micromotors-bacteria for enhanced and accelerated killing. In addition, the enhanced fluid motion in the presence of bubble and magnetic propelled micromotors is also characterized by the study of the mean-squared displacement (MSD, $\langle \Delta x^2 \rangle$) of the tracers. As illustrated in the time-lapse images of **Figure S5** and corresponding plots of **Figure S5 C**, significant movement of such passive tracers is clearly noted, with dramatically larger MSD in comparison with tracers undergoing Brownian motion. Such fact considerable promise in the dramatically enhanced bacteria inactivation as compared with static counterparts.

Figure 2 illustrates the results obtained in the capture efficiency of bacteria in bubble and magnetic modes as well as the micromotor performance in real samples. To estimate the capture efficiency and the role of enhanced mixing of the micromotors, 100 μL of Rhodamine B labelled *Staphylococcus Aureus* or *Escherichia Coli* bacteria suspensions (10^2 CFU mL^{-1}) were

incubated with the Nisin modified or control micromotors (220 micromotors mL^{-1}), 25 μL of H_2O_2 (30%) and 25 μL of SDS (3%) -in bubble mode- or at a frequency of 4 Hz -in magnetic mode- for 20 min. Fluorescent images of different drops before and after micromotor navigation or control experiments were taken using a fluorescent optical microscope and the number of bacteria was estimated via Image J program. Capture efficiency was calculated as:

$$\text{Capture efficiency (\%)} = \frac{(N_i - N_u)}{N_i} \times 100$$

where N_i and N_u correspond to the number of bacteria prior (initial) and after micromotor navigation (unbounded). For additional information, SEM images of the micromotors at the different conditions were also taken. Thus, as illustrated in the plot of **Figure 2A** and corresponding SEM images of **Figure 2B (a, e)**, the highest capture efficiency was observed after Nisin micromotor navigation in solutions containing *Staphylococcus Aureus* bacteria (85 %, both in bubble and magnetic mode), with all the surface covered with the bacteria. In contrast, low capture efficiency was noted by performing the same experiment in solutions containing *Escherichia Coli* (20-28 %, both in bubble and magnetic mode), as representative gram-negative bacteria, illustrating the selectivity and targeting ability of our protocol. From the SEM images in **Figure 2B, b and f** we can also see that only a few *Escherichia Coli* bacteria are bounded to the micromotors, probably due to non-specific electrostatic interactions.^[27] This fact further testified the selectivity of the Nisin modified micromotors towards gram-positive bacteria. The underlying reason behind such selectivity can be explained due to the Lipid II in gram-negative bacteria is protected by the membrane, preventing the interaction with Nisin.^[24c] Additional control experiments with static modified micromotors in the presence of the target bacteria

revealed the role of the enhanced micromotor movement on the capture performance, with only 35 % *Staphylococcus Aureus* bacteria capture (see also the low amount of bacteria present in the corresponding SEM images of **Figure 2B, c**). Negligible capture was observed using unmodified moving micromotors in the absence and in the presence of free Nisin, as also be testified by the absence of bacteria on micromotor surface in the images of **Figure 2B, d**. The high towing force and high stability of the Nisin probe was tested in untreated juice, serum and tap water samples. As can be seen, excellent capture efficiencies of over 80-84 % were obtained in all cases, indicating the negligible effect of sample components in the micromotor strategy, as also revealed in the SEM images of **Figure 2C (top)**, in which all the micromotors are covered by bacteria. **Figure 2C (down)** shows the corresponding time-lapse images of the bacteria capture under the microscope in real samples, with speeds of over 24 ± 19 , 23 ± 15 and $54.4 \pm 25 \mu\text{m s}^{-1}$ in juice, serum and tap water samples (bubble mode) and $41 \pm 4 \mu\text{m s}^{-1}$ (magnetic mode) respectively. The high bacteria capture efficiency allows for better contact and prolonged interaction between Nisin and bacteria membrane for enhanced destruction, as will be further illustrated for single bacteria and bacteria biofilm destruction.

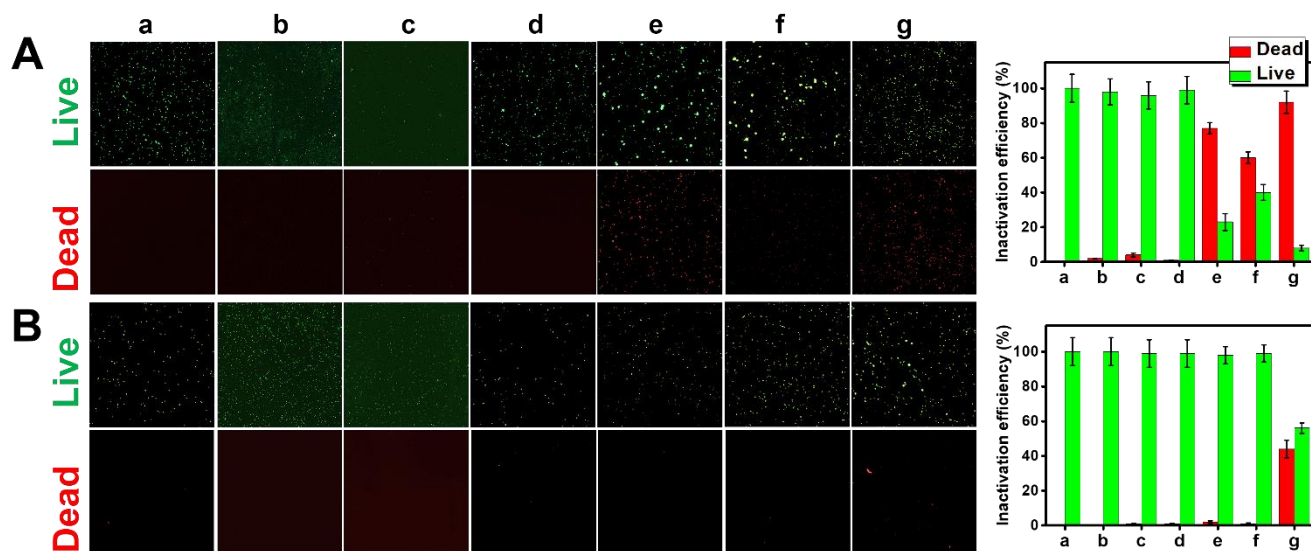


Figure 3. Killing efficiency of the Nisin modified micromotors in bubble-mode against A) *Staphylococcus Aureus* and B) *Escherichia Coli* bacteria and control experiments. Left part shows the fluorescent images of total bacteria (in green) and inactivated bacteria (in red) with the corresponding plots showing the inactivation efficiency on the right part of the image, where: a) initial conditions without contact with micromotors, b) 3% hydrogen peroxide, c) 2% SDS, d) unmodified moving micromotors, e) modified micromotors under magnetic stirring, f) static modified micromotors and g) moving modified micromotors. Conditions: 3% hydrogen peroxide, 2% SDS, 10^2 CFU mL^{-1} of bacteria, 220 micromotors mL^{-1} . Error bars corresponds to the standard deviation of 10 measurements.

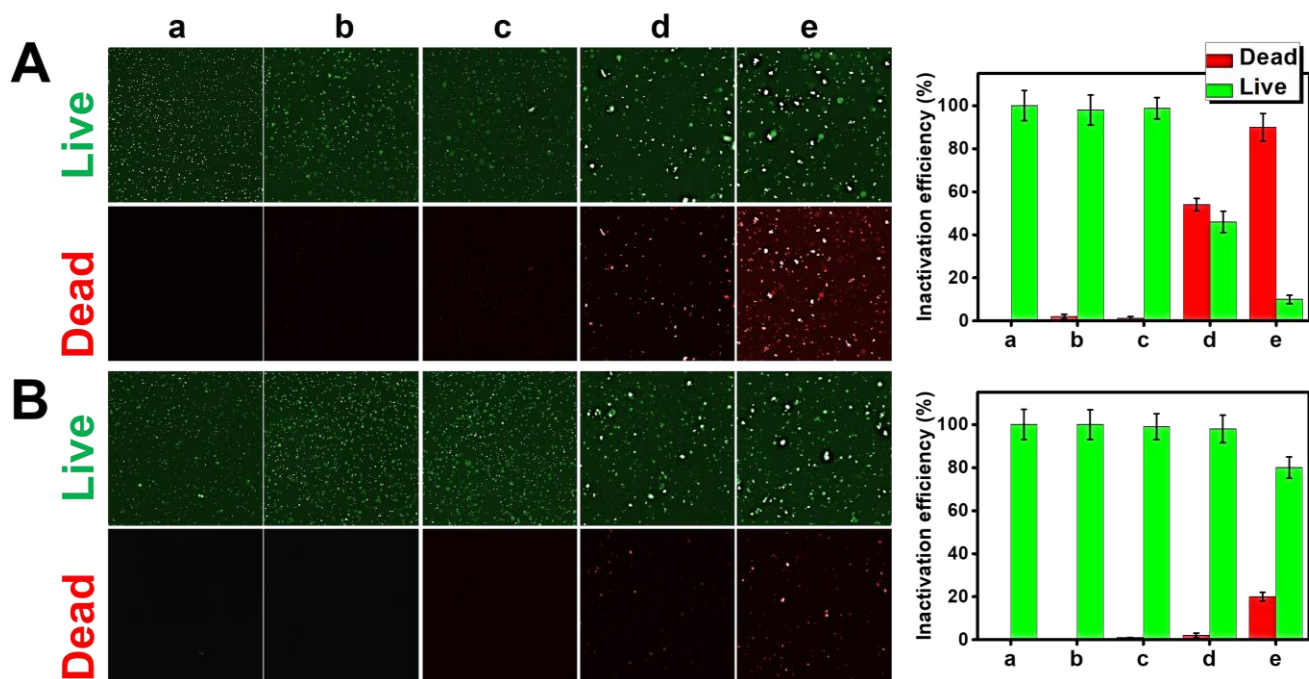


Figure 4. Killing efficiency of the Nisin modified micromotors in magnetic mode against A) *Staphylococcus Aureus* and B) *Escherichia Coli* bacteria and control experiments. Left part shows the fluorescent images of total bacteria (in green) and inactivated bacteria (in red) with the corresponding plots showing the inactivation efficiency on the right part of the image, where: a) initial conditions without contact with micromotors, b) unmodified moving micromotors, c) unmodified micromotors with free peptide under magnetic stirring, d) static modified micromotors and e) moving modified micromotors. Conditions: frequency, 4 Hz, 10^2 CFU mL⁻¹ of bacteria, 220 micromotors mL⁻¹. Error bars correspond to the standard deviation of 10 measurements.

The Nisin micromotors killing ability was first tested by evaluating the viability of both *Staphylococcus Aureus* and *Escherichia Coli* bacteria after treatment with Nisin modified micromotors and control experiments using the LIVE/DEAD assay.^[14, 19] Briefly, the assay relies on treating the bacteria with Syto-9 dye, which labels all live and dead bacteria (live in **Figure 3 and 4**) and propidium iodide dye, which only penetrated into the membrane of damage bacteria (dead in **Figure 3 and 4**). For more details on the experiments, see Experimental Procedures of Supporting Information. The results obtained in bubble-mode are listed in **Figure 3**. In the case of *Staphylococcus Aureus*, the trend of bacteria inactivation is in line of the results obtained for bacteria capture. As hydrogen peroxide and SDS can also deactivate bacteria, adequate control experiments were included. As can be seen in **Figure 3**, the LIVE/DEAD assay revealed a high compatibility with 3 % peroxide or 2 % SDS solutions, with only 1 % or 3 % *Staphylococcus Aureus* inactivation and negligible effect in *Escherichia Coli*. Also, as show in the fluorescent images and corresponding plots of **Figure 3A**, almost 100 % bacteria inactivation was obtained in experiments conducted with moving Nisin modified micromotors (g), due to prolonged contact with Nisin in connection with the enhanced micromotor movement, which results in highest inactivation percentages. Lower inactivation efficiency rates of 80% and 60% were observed in experiments using modified micromotors under magnetic stirring (e) and static conditions (f), which further reflects the enhanced peptide operation when immobilized in the micromotors. As expected, no bacteria inactivation was observed using unmodified moving micromotors (d), due to the absence of Nisin. To further evaluate the selectivity of the micromotor/capture/killing protocol, we evaluated also its ability to deactivate *Escherichia Coli* bacteria. No bacteria were inactivated in control experiments,

whereas for moving Nisin micromotors, 38 % inactivation activity is obtained (g). This data corresponds with the capture ability observed for *Escherichia Coli* bacteria and can be attributed to non-specific electrostatic interactions that can disrupt somewhat the bacteria membrane, resulting in some inactivation. This data indicates the suitability of the combination of antimicrobial-peptides with micromotors to selectively target bacteria membranes, which can help to design post-antibiotic drugs or to tailor novel agents to treat specific resistant bacteria when antibiotics are no longer effective. While bubble-propelled micromotors are used here, the concept can be easily extended to other designs relying on more biocompatible propulsion mechanism such as magnetic, ultrasound or light propelled micromotors. For example, **Figure 4** shows the experiments of LIVE/DEAD assay using magnetic actuated micromotors under the same conditions. Killing efficiencies of over 90 % are achieved with magnetic micromotors for *Staphylococcus Aureus*, whereas over 40 % is obtained with static micromotors, further revealing the role of enhanced micromotor mixing induced during actuation of rotating magnetic fields. Negligible killing efficiencies are noted with *Escherichia Coli* bacteria, as also noted in bubble-propulsion experiments. This data further reflects the utility and adaptative propulsion of our micromotors for highly efficient bacteria inactivation in connection with antimicrobial peptides.

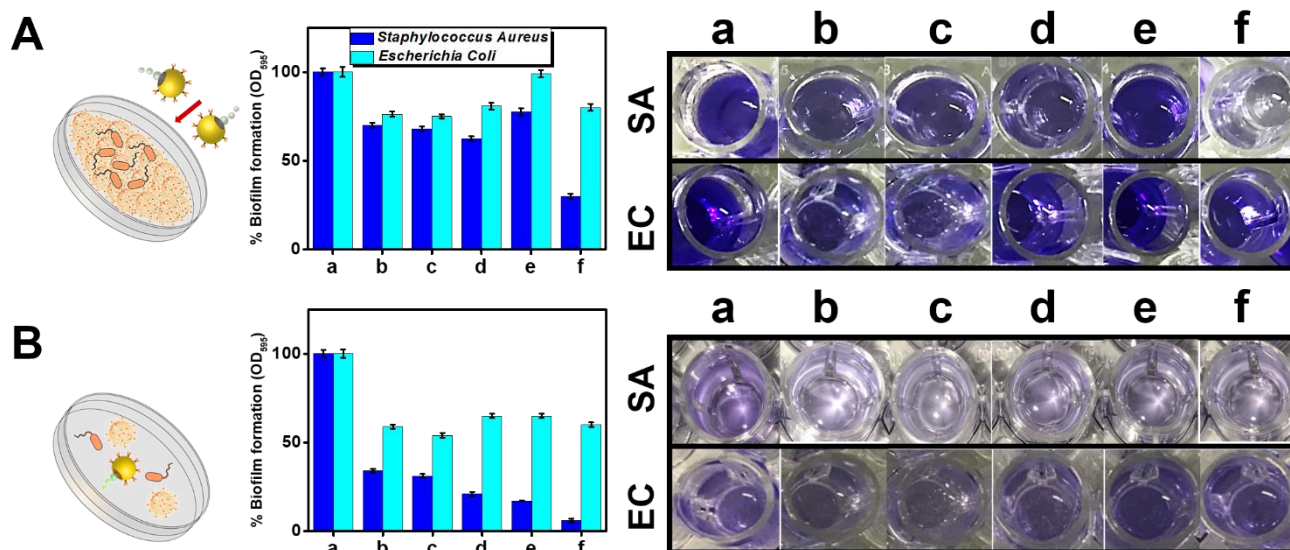


Figure 5. *Staphylococcus Aureus* (SA) and *Escherichia Coli* (EC) biofilm inhibition by Nisin modified micromotors and control experiments in bubble-mode. A) Capability of the micromotors for the fast destruction of a previously generated biofilm (1-day growth) and B) to inhibit biofilm generation by co-incubation of the micromotors and the bacteria followed by 1-day growth. The corresponding plots in each case illustrate the percentage of biofilm formation under different conditions where: a) initial conditions without micromotors, b) 1% H₂O₂, c) 2% SDS, d) unmodified moving micromotors, e) static modified micromotors, f) modified moving micromotors. Right part shows the corresponding plates (stained with crystal violet) used for OD₅₉₅ measurements at each condition. Conditions: 1 and 0.5 % hydrogen peroxide in A and B, respectively and 2% SDS. Error bars corresponds to the standard deviation of 3 measurements.

Bacteria biofilms are also a matter of great concern in biomedical devices and other settings because such contamination can cause severe side infections in short time. To address such growing concern, we also evaluated the efficiency of our micromotor for the inactivation of *Staphylococcus Aureus* or *Escherichia Coli* biofilms. The ability for both inactivates already formed biofilm and to inhibit biofilm growth was tested (see **Figures 5 and 6** for bubble and magnetic modes, respectively). For measuring the fast killing ability through rapid biofilm disruption, bacteria biofilm was growth for 24 h in 96 well-plates (see supporting information for more details) and OD₅₉₅ measurements taken to assure that the same bacteria amount was present in each plate. Next, the supernatant was removed, and each well was washed with ultrapure water to remove the free bacteria, followed by addition of 80 μ L of Nisin modified micromotor (or control micromotors), 10 μ L SDS (3%), 6.7 μ L H₂O₂ (30%) and 103.5 μ L of H₂O (in bubble mode) or treatment using the magnetic device at 4 Hz (in magnetic mode). After 40 min, the supernatant was removed, wash with ultrapure water to remove the free bacteria, and the remaining bacteria biofilm was fixed with 96% ethanol, followed by staining with 0.1% crystal violet and biofilm solubilization in methanol for further OD₅₉₅ measurements. Crystal violet labelled all adhered cells, that after Nisin micromotor treatment are detached due to membrane rupture, thus the reagent is washed away and the color in the solution disappear. Thus, the extent of color disappearance can be related to a lower biofilm generation (or higher biofilm inhibition). The data of **Figure 5A** (in terms of percent biofilm generation) illustrates the high capacity of moving Nisin micromotors to selectively inactivate *Staphylococcus Aureus*, inhibiting by 70% the biofilm formation (f). Much lower inhibition rates are noted in experiments with unmodified (d) or static (e) micromotors, revealing again the crucial role of the enhanced

micromotor movement for targeted bacteria contact and improved kinetics. As expected, *Escherichia Coli* biofilms were not inhibited due to the selectivity of our protocol, imparted by the Nisin molecule in our micromotor. The corresponding photographs at the right support this, with intense violet color in all cases except when using the moving Nisin micromotors to treat *Staphylococcus Aureus* biofilms. Yet, it should be mentioned here that control experiments with 3 % peroxide or 2 % SDS solutions, revealed more apparent effects of toxicity on bacteria cells than that observed in the LIVE/DEAD assay. For example, in fast biofilm destruction experiments, 1 % hydrogen peroxide and 2 % SDS inhibit about 20 to 30 % of the biofilms generated by both target bacteria. Such effect is more evident in experiments where both compounds were co-cultured during bacteria growth (long term bacteria inhibition). To this end, *Staphylococcus Aureus* and *Escherichia Coli* strains were growth overnight. Then 200 μ L of the bacteria culture, 20 μ L Nisin modified or control micromotors, 6.6 μ L H₂O₂ (30%), 20 μ L SDS (3%) and 153.4 μ L LB media were dispensed into a 96-well plate. The plate was incubated at 37°C 48 h to allow biofilm growth. After washing, fixing, and staining procedures as described in the Supporting Information, OD₅₉₅ measurements to estimate biofilm growth rate were performed (see **Figure 5B**). Hydrogen peroxide and SDS alone inhibit 55% of the biofilm. Yet, please note here that the combined effect peroxide-SDS-lanibiotic modified moving Janus micromotors dramatically increase the inactivation rate to over 85 and 95 % in the case of *Staphylococcus Aureus* bacteria. As such, bubble propelled lanibiotic micromotors will be ideal in water treatment or sterilization applications where peroxide and SDS or other surfactants are also used to increase its efficiency.

As an alternative, we propose to use fuel-free rotary actuated magnetic micromotors for biofilm treatment. To further

corroborate the LIVE/DEAD results and to prove the utility of the micromotors in such mode, we perform cultivation/biofilm killing experiments in a similar fashion, as also performed in bubble-mode. As can be seen in **Figure 6**, in fast and long-term biofilm destruction experiments, about 80 % of *Staphylococcus Aureus* biofilm is deactivated, whereas a low deactivation rate is noted with static modified micromotors or *Escherichia Coli* biofilms. Such results are in accordance with the one observed in bubble-mode, except that in the latter case the combined effect of modified motor-peroxide surfactant results in higher deactivation efficiencies. Yet, the biocompatible propulsion of micromotors in magnetic mode hold considerable promise for future in-vivo applications.

To get further insights into the killing mechanism of the micromotors, we performed additional LIVE/DEAD control experiments to check the potential influence of the different micromotors components upon bacteria killing efficiency as well as cultivation experiments of biofilms.

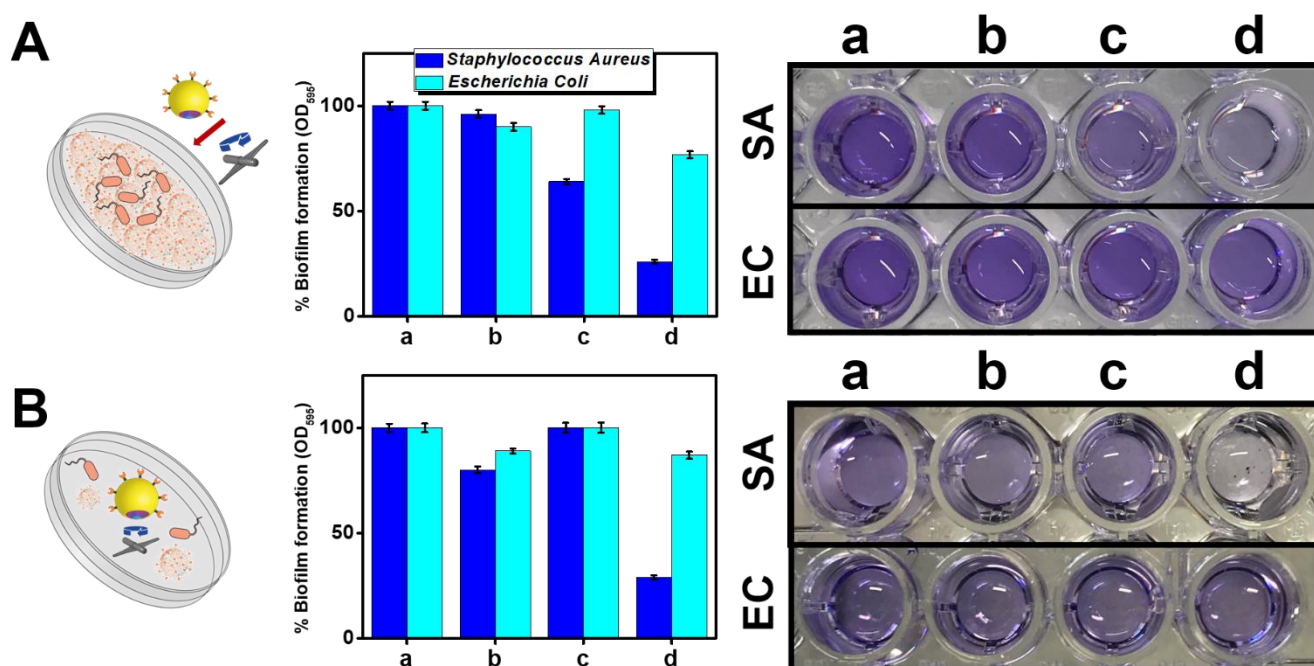


Figure 6. SA and EC biofilm inhibition by Nisin modified micromotors and control experiments in magnetic mode. A) Capability of the micromotors for the fast destruction of a previously generated biofilm (1-day growth) and B) to inhibit biofilm generation by co-incubation of the micromotors and the bacteria followed by 1-day growth. The corresponding plots in each case illustrate the percentage of biofilm formation under different conditions where: a) initial conditions without micromotors, b) unmodified moving micromotors, c) static modified micromotors, d) modified moving micromotors. Right part shows the corresponding plates (stained with crystal violet) used for OD₅₉₅ measurements at each condition. Conditions: frequency, 4 Hz. Error bars corresponds to the standard deviation of 10 measurements.

To check the role of iron oxide nanoparticles in potential generation of free radicals and bacteria killing by radical oxygen species generation (ROS), we performed control experiments using unmodified GO/PtNPs/Fe₂O₃ micromotors moving in magnetic mode (b in **Figure S6**) and moving Nisin GO-PtNPs micromotors (c in **Figure S6**). As can be seen in the microscopy images and corresponding plots of **Figure S6**, inactivation efficiencies are similar in all cases, with only 1 % variation. Most importantly, they are comparable with that obtained using micromotors containing iron oxide and platinum (both in catalytic and magnetic mode), thus it can be concluded that potential ROS generation and PtNPs do not have any effect on bacteria inactivation. In a second control experiment, potential antibacterial effect of graphene oxide was evaluated by replacing such nanomaterial with black phosphorous, for further modification with Nisin and performing the experiments in a similar manner. As can be seen in **Figure S6 d and e**,

experiments performed both under bubble and magnetic mode report similar killing efficiency to that using graphene oxide micromotors, thus such material do not exert influence on bacteria killing. Such control experiments support the proposed killing mechanism via the formation of a hydrogen bond is between the amine groups in Nisin and pyrophosphate groups of the lipid II molecules in the outer bacteria membrane. This facilitates penetration of Nisin into the bacteria cell wall, creating pores which ultimately results in the dead of the Gram-positive bacteria. Further experiment on imaging of extracellular polymeric substances (EPS) of biofilm both in *Staphylococcus Aureus* and *Escherichia Coli* were performed to further clarify the killing mechanism. Additional SEM observation was also performed. The results are illustrated in **Figure S7**. EPS are a core part in biofilms, promoting the generation of a cohesive three-dimensional framework. EPS are a complex mixture of biomolecules, mainly proteins and exopolysaccharides. Characterization of the biofilm is critical to develop and check the efficiency of chemical strategies to disrupt biofilms. To check the

effect of the moving Nisin micromotors in the EPS of the biofilm, we label *Staphylococcus Aureus* and *Escherichia Coli* biofilms with SYPRO-Ruby red dye, a dye to stain proteins. As can be seen in the confocal laser microscopy images of **Figure S7**, a high density of proteins with an interconnected network can be observed. Yet, after micromotor treatment, in the case of *Staphylococcus Aureus* the proteins can be rarely observed, indicating that the Nisin modified micromotors alter the biofilm, probably via molecular recognition of the linked peptide, which is accelerated by the rapid micromotor movement, as also illustrated by the dramatically lower effects of static modified micromotors. For *Escherichia Coli*, micromotors have low influence on EPS, as almost all proteins remain after treatment. Additionally, to get further insight into the mechanism of bacteria killing and the bond bacteria-micromotor we label the biofilm with Syto-9 and propidium iodide before and after micromotor treatment. Biofilm was growth on the surface and rapidly treated with the micromotors. After treatment, aliquots were taken, and images were focused specifically on micromotors to see bacteria attached on the surfaces. As can be seen in the corresponding microscopy images of **Figure S7**, both *Staphylococcus Aureus* and *Escherichia Coli* bacteria attach to the micromotors, but in the case of *Escherichia Coli* most bacteria remain alive whereas for *Staphylococcus Aureus* all attached bacteria are dead. Indeed, SEM observation of micromotor after long-term killing experiment reveal that biofilm can growth on the micromotor, yet, for *Staphylococcus Aureus* very few bacteria is attached to the micromotor, probably due to selective attachment and enhanced penetration of Nisin over *Escherichia Coli*, in which a well-distributed bacteria biofilm is observed on the micromotor surface. The above-mentioned data shed some lights to explain the proposed killing mechanism. Nisin has proven to be significantly more effective against gram positive bacteria such as *Staphylococcus Aureus* and corresponding biofilms. Lipid II, the docking molecule for Nisin, promote a high activity of Nisin against biofilm cells. Indeed, the EPS of the biofilm contributes to enhance such bond by hydrogen bonds, electrostatic interactions, etc that contribute to specific binding to bacteria, promoting the further permeation and generation of the pore that ultimately destroy the bacteria. In the case of *Escherichia Coli*, despite interaction with micromotors is observed via non-specific interactions, lipid II is protected by an outer membrane that hinders Nisin to interact with it and deactivate the bacteria.^[28]

Conclusion

The combination of self-propelled micromotors with a new type of antibacterial agents (lanbitotics) has been described here for the first time. Specific interaction of amine groups in Nisin molecule with the pyrophosphate groups of the lipid II molecules in the membrane of gram-positive bacteria result in the formation of pores and subsequent damage and killing. The strategy does not require additional pre-treatment of the bacteria or sample purification, allowing for its usage in raw complex samples, which is a major advantage over other micromotors strategies based on labile receptors (such as antibiotics or biological components). The presence of two engines (catalytic and magnetic) in the micromotors allow for an adaptative behavior to tailor each application. The main advantage of our micromotor strategy over free Nisin and static counterparts rely on accelerated kinetics for improved capture (as reflected by the 83% capture efficiency

percentages of moving micromotors towards *Staphylococcus Aureus*) and prolonged contact for fast inactivation. The adaptative propulsion mode imparts the strategy with a high versatility for further applications. The strategy is also very effective for selective biofilm destruction. The transport abilities of our Nisin-nanoengineered micromotor along with their capacity for intensive interactions and selectivity hold considerable promise to design post-antibiotic strategies or alternative means to treat antibiotic-resistance infections by using tailored lanbitotics. The concept can be extended to other more biocompatible designs such as ultrasound or magnetic propelled micromotors, as illustrated by the promising results obtained using the Nisin modified micromotors in magnetic mode.

Acknowledgements

K. Yuan acknowledges the Ministry of Economy, Industry and Competitiveness for his pre-doctoral contract (RYC-2015-17558, co-financed by EU). B. J-S acknowledges support from the Ministry of Economy, Industry and Competitiveness (RYC-2015-17558, co-financed by EU) from the University of Alcala (CCG19/CC-029) and from the Community of Madrid (CM/JIN/2019-007). AE acknowledges financial support from the Ministry of Economy, Industry and Competitiveness (CTQ2017-86441-C2-1-R) and the TRANSNANOAVANSENS program (S2018/NMT-4349) from the Community of Madrid. Confocal laser microscopy imaging of biofilm formation has been performed by the ICTS "NANBIOSIS", more specifically by the U-17-S01 Unit (Isabel Trabado) of the CIBER in Bioengineering at the Universidad de Alcala.

Keywords: lanbitotic • peptide • bacteria • micromotor • Janus

- [1] a) H. F. Chambers, F. R. Deleo, *Nat. Rev. Microbiol.* **2009**, *7*, 629-641; b) R. Laxminarayan, A. Duse, C. Wattal, A. K. M. Zaidi, H. F. L. Wertheim, N. Sumpradit, E. Vlieghe, G. L. Hara, I. M. Gould, H. Goossens, C. Greko, A. D. So, M. Bigdeli, G. Tomson, W. Woodhouse, E. Ombaka, A. Q. Peralta, F. N. Qamar, F. Mir, S. Kariuki, Z. A. Bhutta, A. Coates, R. Bergstrom, G. D. Wright, E. D. Brown, O. Cars, *Lancet Infect. Dis.* **2013**, *13*, 1057-1098.
- [2] G. Mi, D. Shi, M. Wang, T. J. Webster, *Adv. Healthcare Mater.* **2018**, *7*, 1800103.
- [3] S. Qayyum, A. U. Khan, *Med. Chem. Commun.* **2016**, *7*, 1479-1498.
- [4] K. L. Chen, G. D. Bothun, *Environ. Sci. Technol.* **2014**, *48*, 873-880.
- [5] a) P. C. Ray, S. A. Khan, A. K. Singh, D. Senapati, Z. Fan, *Chem. Soc. Rev.* **2012**, *41*, 3193-3209; b) L. Mei, S. Zhu, W. Yin, C. Chen, G. Nie, Z. Gu, Y. Zhao, *Theranostics* **2020**, *10*, 757-781.
- [6] a) Y. Wang, Y. Yang, Y. Shi, H. Song, C. Yu, *Adv. Mater.* **2019**, 1904106; b) X. Fan, F. Yang, J. Huang, Y. Yang, C. Nie, W. Zhao, L. Ma, C. Cheng, C. Zhao, R. Haag, *Nano Lett.* **2019**, *19*, 5885-5896.
- [7] a) G. A. Ozin, I. Manners, S. Fournier-Bidoz, A. Arsenault, *Adv. Mater.* **2005**, *17*, 3011-3018; b) S. Sanchez, M. Pumera, *Chem. Asian J.* **2009**, *4*, 1402-1410; c) S. J. Ebbens, J. R. Howse, *Soft Matter* **2010**, *6*, 726-738; d) W. Wang, T. Y. Chiang, D. Velegol, T. E. Mallouk, *J. Am. Chem. Soc.* **2013**, *135*, 10557-10565; e) J. Li, I. Rozen, J. Wang, *ACS Nano* **2016**, *10*, 5619-5634; f) E. Karshalev, B. Esteban-Fernández de Ávila, J. Wang, *J. Am. Chem. Soc.* **2018**, *140*, 3810-3820; g) Y. Mei, A. A. Solovov, S. Sanchez, O. G. Schmidt, *Chem. Soc. Rev.* **2011**, *40*, 2109-2119; h) J. Wang, *Biosens. Bioelectron.* **2016**, *76*, 234-242.
- [8] H. Wang, M. Pumera, *Chem. Rev.* **2015**, *115*, 8704-8735.
- [9] V. V. Singh, B. Jurado-Sánchez, S. Sattayasamitsathit, J. Orozco, J. Li, M. Galarnyk, Y. Fedorak, J. Wang, *Adv. Funct. Mater.* **2015**, *25*, 2147-2155.

- [10] Y. Ge, M. Liu, L. Liu, Y. Sun, H. Zhang, B. Dong, *Nano-Micro Lett.* **2016**, *8*, 157-164.
- [11] D. Vilela, M. M. Stanton, J. Parmar, S. Sánchez, *ACS Appl. Mater. Interfaces* **2017**, *9*, 22093-22100.
- [12] J. Simmchen, A. Baeza, A. Miguel-Lopez, M. M. Stanton, M. Vallet-Regi, D. Ruiz-Molina, S. Sánchez, *ChemNanoMat* **2017**, *3*, 65-71.
- [13] F. Soto, D. Kupor, M. A. Lopez-Ramirez, F. Wei, E. Karshalev, S. Tang, F. Tehrani, J. Wang, *Angew. Chem. Int. Ed.* **2020**, *59*, 3480-3485.
- [14] J. Li, V. V. Singh, S. Sattayasamitsathit, J. Orozco, K. Kaufmann, R. Dong, W. Gao, B. Jurado-Sanchez, Y. Fedorak, J. Wang, *ACS Nano* **2014**, *8*, 11118-11125.
- [15] G. Hwang, A. J. Paula, E. E. Hunter, Y. Liu, A. Babeer, B. Karabucak, K. Stebe, V. Kumar, E. Steager, H. Koo, *Sci. Robot.* **2019**, *4*, eaaw2388.
- [16] J. A. M. Delezuk, D. E. Ramírez-Herrera, B. Esteban-Fernández de Ávila, J. Wang, *Nanoscale* **2017**, *9*, 2195-2200.
- [17] M. Hoop, Y. Shen, X.-Z. Chen, F. Mushtaq, L. M. Iuliano, M. S. Sakar, A. Petruska, M. J. Loessner, B. J. Nelson, S. Pané, *Adv. Funct. Mater.* **2016**, *26*, 1063-1069.
- [18] L. Xie, X. Pang, X. Yan, Q. Dai, H. Lin, J. Ye, Y. Cheng, Q. Zhao, X. Ma, X. Zhang, G. Liu, X. Chen, *ACS Nano* **2020**, *14*, 2880-2893.
- [19] M. Kiristi, V. V. Singh, B. Esteban-Fernández de Ávila, M. Uygun, F. Soto, D. A. Uygun, J. Wang, *ACS Nano* **2015**, *9*, 9252-9259.
- [20] B. Esteban-Fernández de Ávila, P. Angsantikul, J. Li, M. A. Lopez-Ramirez, D. E. Ramirez-Herrera, S. Thamphiwatana, C. Chen, J. Delezuk, R. Samakapiruk, V. Ramez, M. Obonyo, L. Zhang, J. Wang, *Nat. Commun.* **2017**, *8*, 272.
- [21] M. M. Stanton, B. W. Park, D. Vilela, K. Bente, D. Faivre, M. Sitti, S. Sanchez, *ACS Nano* **2017**, *11*, 9968-9978.
- [22] a) B. Esteban-Fernández de Ávila, P. Angsantikul, D. E. Ramírez-Herrera, F. Soto, H. Teymourian, D. Dehaini, Y. Chen, L. Zhang, J. Wang, *Sci. Robot.* **2018**, *3*, eaat0485; b) J. Li, P. Angsantikul, W. Liu, B. Esteban-Fernandez de Avila, X. Chang, E. Sandraz, Y. Liang, S. Zhu, Y. Zhang, C. Chen, W. Gao, L. Zhang, J. Wang, *Adv. Mater.* **2018**, *30*, 1704800.
- [23] a) B. Khezri, S. M. Beladi Mousavi, Z. Sofer, M. Pumera, *Nanoscale* **2019**, *11*, 8825-8834; b) B. Khezri, S. M. Beladi Mousavi, L. Krejčová, Z. Heger, Z. Sofer, M. Pumera, *Adv. Function. Mater.* **2019**, *29*, 1806696; c) V. V. Singh, K. Kaufmann, B. Esteban Fernández de Ávila, E. Karshalev, J. Wang, *Adv. Function. Mater.* **2016**, *26*, 6270-6278; d) T. Maric, J. G. S. Moo, B. Khezri, Z. Sofer, M. Pumera, *Appl. Mater. Tod.* **2017**, *9*, 289-291. e) T. Maric, S. M. Beladi-Mousavi, B. Khezri, J. Sturala, M. Z. M. Nasir, R. D. Webster, Z. k. Sofer, M. Pumera, *Small* **2020**, *16*, 1902365.
- [24] a) J. M. Shin, J. W. Gwak, P. Kamarajan, J. C. Fenno, A. H. Rickard, Y. L. Kapila, *J. Appl. Microbiol.* **2016**, *120*, 1449-1465. b) Q. Li, M. Montalban-Lopez, O. P. Kuipers, *Appl. Environ. Microbiol.* **2018**, *84*, e0052-18; c) M. Vukomanovic, V. Zunic, S. Kunej, B. Jancar, S. Jeverica, R. Podlipec, D. Suvorov, *Sci. Rep.* **2017**, *7*, 4324; d) S. J. Lam, N. M. O'Brien-Simpson, N. Pantarat, A. Sulistio, E. H. H. Wong, Y.-Y. Chen, J. C. Lenzo, J. A. Holden, A. Blencowe, E. C. Reynolds, G. G. Qiao, *Nat. Microbiol.* **2016**, *1*, 16162.
- [25] K. Yuan, V. de la Asunción-Nadal, B. Jurado-Sánchez, A. Escarpa, *Chem. Mater.* **2020**, *32*, 1983-1992.
- [26] a) Z. Liang, D. Fan, *Sci. Adv.* **2018**, *4*, eaau0981; b) K. Kim, J. Guo, X. Xu, D. Fan, *ACS Nano* **2015**, *9*, 548-554.
- [27] Z. Li, J. Ma, J. Ruan, X. Zhuang, *Nanoscale Res. Lett.* **2019**, *14*, 195.
- [28] a) E. Breukink, I. Wiedemann, C. v. Kraaij, O. P. Kuipers, H.-G. Sahl, B. de Kruijff, *Science* **1999**, *286*, 2361-2364; b) K.-i. Okuda, T. Zendo, S. Sugimoto, T. Iwase, A. Tajima, S. Yamada, K. Sonomoto, Y. Mizunoe, *Antimicrobial Agents and Chemotherapy* **2013**, *57*, 5572-5579.

Experimental Procedures

Reagents and materials. Polystyrene microparticles (cat. 87896), thioglycolic acid (cat. T3758), hydrazine solution (cat. 309400), graphene oxide (cat. 763705), black phosphorus (cat. 808970), chloroplatinic acid hydrate (cat. 398322), iron (III) oxide (cat. 544884), hydrogen peroxide (cat. 216736), cysteamine (cat. M9768), Rhodamine 6G (Rh6G, cat. R4127), Nisin (cat. N5764), N-(3-Dimethylaminopropyl)-N'-ethylcarbodiimide hydrochloride (EDC, cat. 03449), bovine serum albumin (BSA, cat. A7906), *Staphylococcus Aureus* NCTC 6571 (cat. CRM06571M), *Escherichia Coli* NCTC 9001 (cat. CRM09001M), crystal violet (cat. C3886) and SYPRO® Ruby protein gel stain (cat. S4942) were provided by Sigma-Aldrich (Spain). Live/Dead BacLight Bacterial Viability kit (L7012) was purchased from Thermo Fisher Scientific. A microplate reader (ELX800, BIO-TEK INSTRUMENTS, INC) was used to read the OD₅₉₅ of the biofilm after crystal violet staining.

Nisin modified Janus micromotors synthesis. For the preparation of graphene oxide GO/PtNPs/Fe₂O₃ wrapped Janus microparticles, the following steps were performed: a) a monolayer of 20 µm polystyrene (PS) microparticles was sputtered with a ~50 nm gold layer and transferred to pure water; b) 100 µL of sulfhydryl-modified GO (HS-GO) dispersion were mixed with 90 µL of PS-Au, followed by filtration using 5 µm cyclopore track etched membrane to remove the unattached HS-GO; c) 1 mL of GO wrapped Janus particles were mixed with 200 µL of chloroplatinic acid (1 mg mL⁻¹) and 20 µL of hydrazine for 2 h for the in-situ synthesis of PtNPs engine. Next, micromotors were mixed with 20 µL of Fe₂O₃ NPs (1 mg/mL) for 1 h to generate the magnetic engine. Black phosphorous (BP) control micromotors were synthesized following the same procedure and using HS-BP to coat the PS-Au particles. The GO/PtNPs/Fe₂O₃ micromotors were next modified with Nisin. To this end, 10 mg of thioglycolic acid was mixed with 1 mL of the micromotor solution for 2h. Then the unbounded thioglycolic acid was removed by filtration, and the micromotors were re-diluted in 1 mL of pure water. In the following step, 20 mg EDC were added to the above thioglycolic acid modified micromotors and mixed overnight to fully activate the carboxyl group. After that, 50 mg of nisin was added and keep on mixing for another 2 h. Finally, the nisin modified micromotors were cleaned by filtration and pure water. To avoid non-specific adsorptions, BSA (1 mg mL⁻¹) was mixed (1 h) with the nisin modified micromotors to block the active site on the surface of the micromotors, which were then further cleaned by filtration and pure water.

Micromotor characterization. Scanning-electron microscopy images were taken using a JEOL JSM 6335F microscope, whereas micromotor movement was evaluated by recording videos at 25 FPS using a Zyla CMOS and DS-Qi2 camera attached to an Eclipse Ti-S inverted microscope (Nikon, Tokyo, Japan). The micromotors were tracked using the NIS Elements AR 3.2 software (Nikon, Tokyo, Japan). Confocal laser microscopy images were taken with a Leica TCS-SP5 confocal microscope (Leica Microsystems GmbH, Germany).

Capture efficiency and killing efficiency assay. To assay the capture efficient, *Staphylococcus Aureus* or *Escherichia Coli* were first labeled with 100 µg mL⁻¹ of Rh6G. Next, 100 µL of labelled bacteria, 100 µL nisin modified micromotors, 25 µL of H₂O₂ (30%) and 25 µL of SDS (3%) solutions were dropped into an Eppendorf tube and the micromotors were allowed to navigate for 20 min. In magnetic mode, solution was treated with a custom-made system that generate a rotatory magnetic field, which was set at 4 Hz. After navigation, the micromotors were filtered using a 5 µm cyclopore track etched membrane to remove the unbounded bacteria. Control experiments were performed in a similar manner. The micromotors@bacteria complex was resuspended in 1 mL of H₂O. Fluorescent images of the drops were taken using optical microscope and the number of bacteria that have been captured was estimated *via* Image J program. The fluorescence images were obtained using an Epi-fluorescence attachment with a FITC (467-498 nm) filter cube. To assay the killing efficiency, 100 µL *Staphylococcus Aureus* or *Escherichia Coli*, 50 µL Nisin modified micromotors, 25 µL of H₂O₂ (30%) and 25 µL of SDS (3%) solutions were dropped into an Eppendorf tube and the micromotors were allowed to navigate for 20 min. In magnetic mode, solution was treated with a custom-made system that generate a rotatory magnetic field, which was set at 4 Hz. After navigation, the micromotors were centrifugated at 10,000 rpm for 10 min, washed with pure water for 3 times, and resuspended in 1 mL of H₂O. Control experiments were performed in a similar fashion. We employed a fluorescence-based method to measure the amount of live and dead bacteria. 3 µL of the mixture of Syto-9 dye and propidium iodide dye were added and gently mixed for 15 min. After this, the sample was centrifuged at 10,000 rpm for 10 min and washed with ultrapure water 3 times to remove the unreacted dye, and finally resuspended in 1 mL of H₂O. Fluorescence images of the drops were taken using optical microscope and the number of live and dead bacteria was estimated *via* the program of Image J. The fluorescence images were obtained using an Epi-fluorescence attachment with a FITC (467-498 nm) or G-2A (510-560 nm) filter cubes.

Biofilm fast inhibition and long-time inhibition assay. For measuring the long-time killing ability through biofilm formation, bacteria were grown together with the corresponding micromotors for a long time. Firstly, *Staphylococcus Aureus* and *Escherichia Coli* strains were grown in LB media at 37°C overnight. Then 200 µL of the bacteria culture, 20 µL nisin modified micromotors, 6.6 µL H₂O₂ (30%), 20 µL SDS (3%) and 153.4 µL LB media were dispensed into a 96-well plate. In magnetic mode, solution was treated with a custom made system that generate a rotatory magnetic field, which was set at 4 Hz. The plate was incubated at 37°C for 24 h to allow biofilm growth. In all the cases, the final volume (400 µL) in every well was the same, including blank (only bacteria and LB media are added) and control experiments. After that, the supernatant was removed, and each well was washed with ultrapure water to get rid of the free bacteria. The remaining biofilm in each well were fixed with 96% ethanol for 15 min, followed by staining with 0.1% crystal violet for 20 min. Next, the plate was washed with ultrapure water for 3 times and the crystal violet bound to the biofilm was resolubilized with 200 µL methanol. Next, spectroscopic measurements of OD at 595 nm were taken.

For measuring the fast killing ability through rapid disruption of the biofilm, 200 µL of overnight grown bacteria and 200 µL of LB media were put into the 96-well plate and incubated at 37 °C for 24 h for biofilm formation. Then the supernatant was removed, and each well

was washed with ultrapure water to remove the free bacteria. 80 μL of nisin micromotor, 10 μL SDS (3%), 6.7 μL H_2O_2 (30%) and 103.5 μL of H_2O were added to the as-grown biofilm, followed by micromotor navigation for 40 min. In magnetic mode, solution was treated with a custom made system that generate a rotatory magnetic field, which was set at 4 Hz. Next, the same procedure used to measure the long-time killing ability experiments was used. Fluorescence images of the drops were taken using optical microscope and the number of live and dead bacteria was estimated *via* the program of Image J.

Supporting Figures

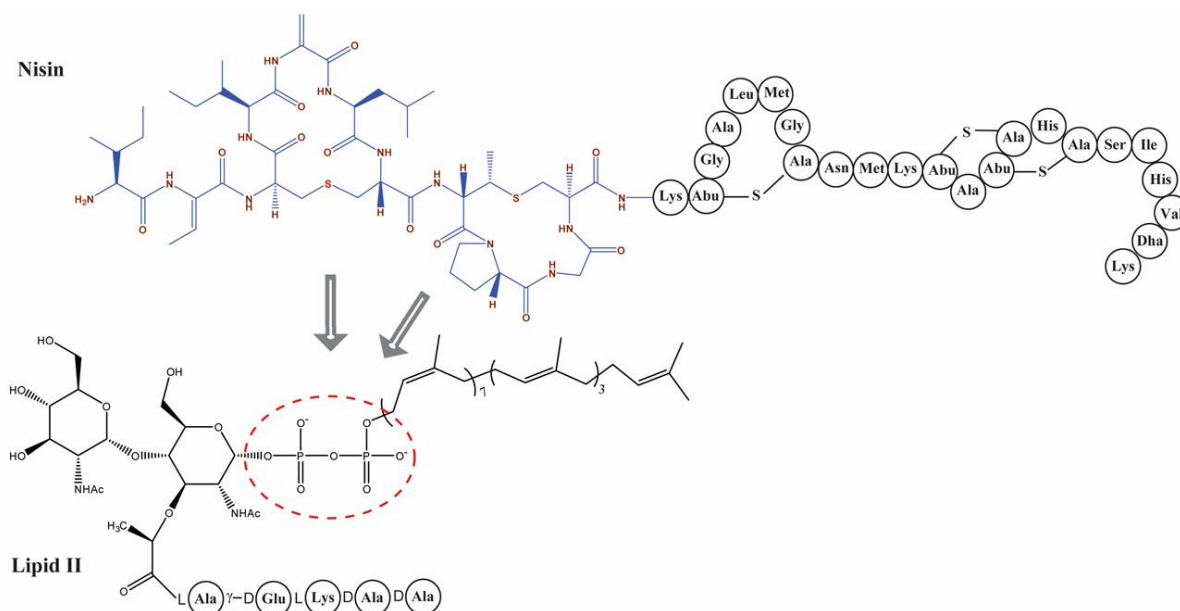


Figure S1. Nisin structure and specific interaction with the Lipid II present in the outer membrane of *Staphylococcus Aureus* for inactivation.

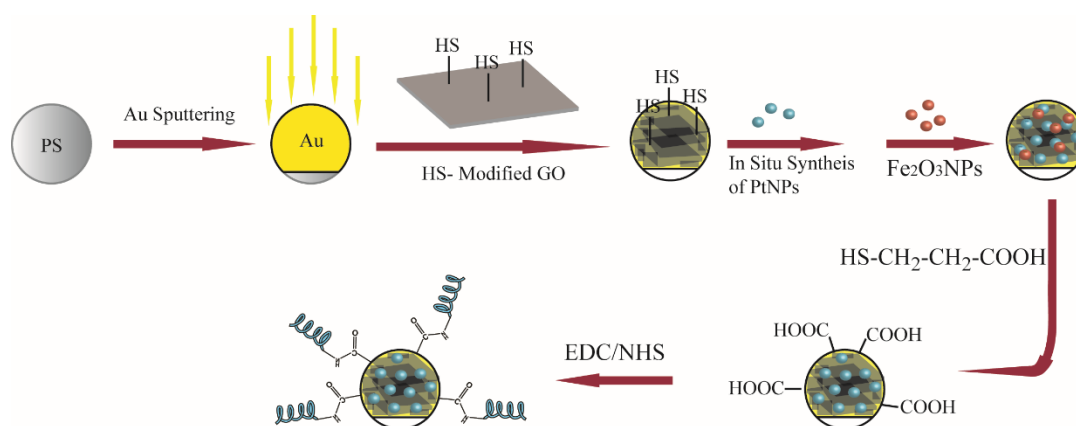


Figure S2. Schematic of the Janus micromotor preparation and modification with Nisin.

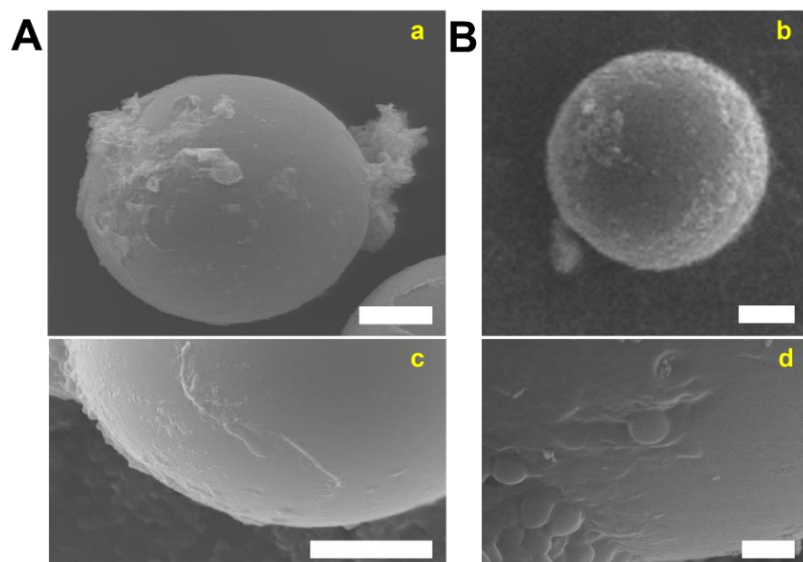


Figure S3. SEM images of GO/PtNPs/Fe₂O₃ Janus micromotors before (A) and after (B) modification with Nisin. Scale bars, 5 μm.

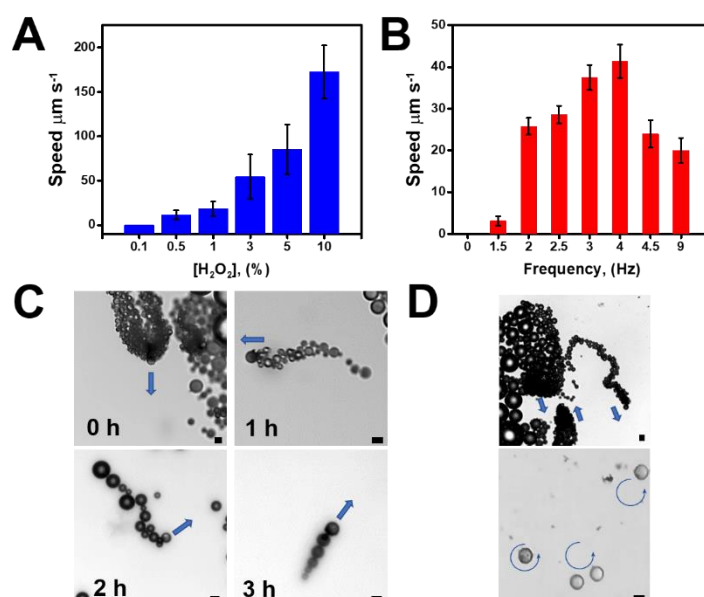


Figure S4. (A) Influence of hydrogen peroxide concentration and (B) frequency of the magnetic field, respectively, upon the speed of bubble and magnetic propelled GO/PtNPs/Fe₂O₃ Janus micromotors. (C) Time-lapse images (Taken from Video S2) of the prolonged navigation of micromotors in bubble mode at different times. (D) Time-lapse images (Taken from Video S2) of the navigation of multiple micromotors in bubble (top) and magnetic mode (bottom). Scale bars, 20 μm. Error bars corresponds to the standard deviation of 10 measurements.

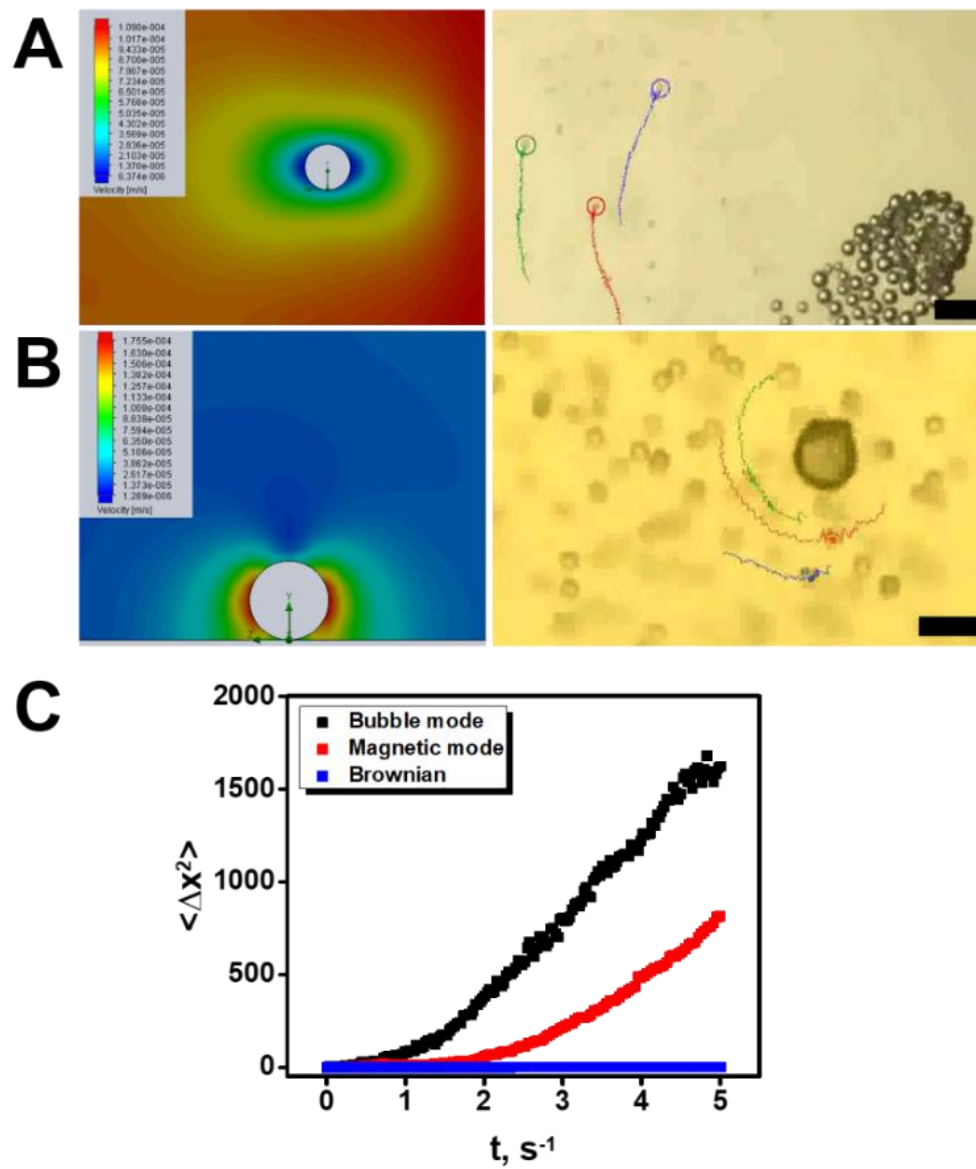


Figure S5. Characterization of the enhanced fluid mixing of Nisin modified Janus micromotors in (A) bubble and (B) magnetic mode: Simulations and time-lapse images (taken from Video S3) of the displacement of passive polystyrene particles (1 μm). C) Mean-squared displacement plot after averaging 10 passive tracers for 5 s under bubble, magnetic mode and Brownian motion. Scale bars, 20 μm .

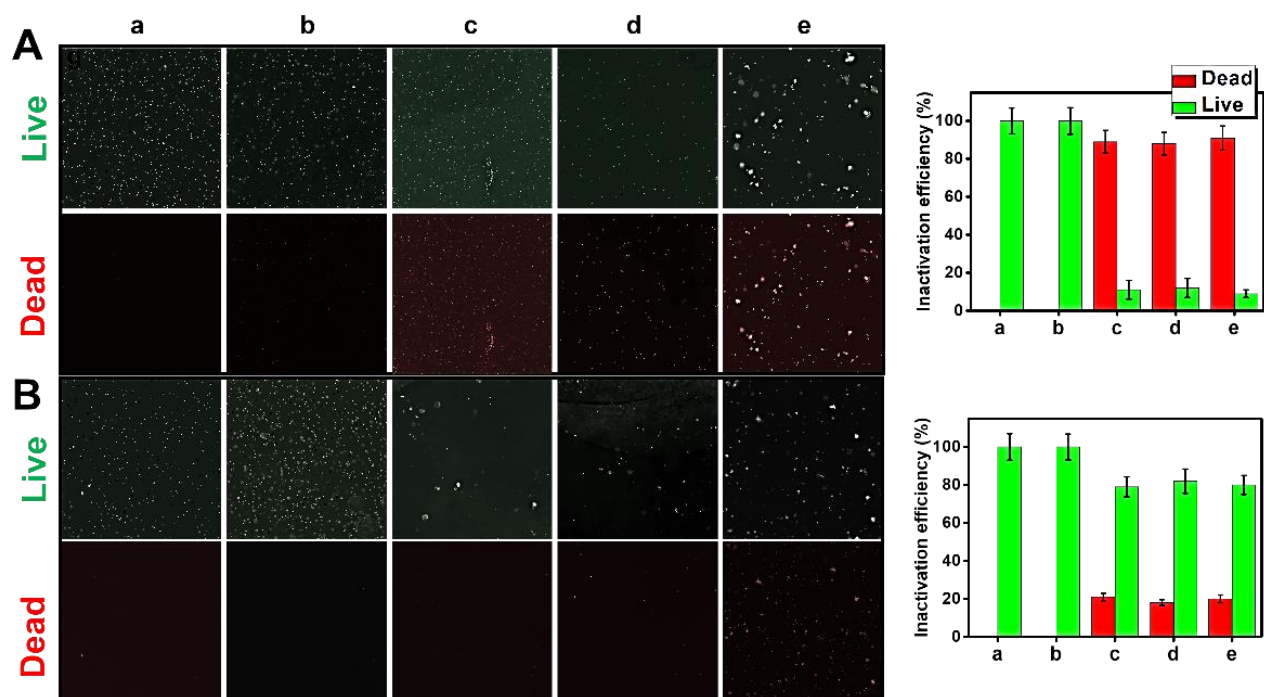


Figure S6. Control experiments using Nisin modified micromotors in against A) *Staphylococcus Aureus* and B) *Escherichia Coli* bacteria. Left part shows the fluorescent images of total bacteria (in green) and inactivated bacteria (in red) with the corresponding plots showing the inactivation efficiency on the right part of the image, where: a) initial conditions without contact with micromotors, b) unmodified GO/PtNPs/Fe₂O₃ micromotors moving in magnetic mode, c) Moving Nisin GO/PtNPs micromotors, d) Moving Nisin modified black phosphorous/PtNPs/Fe₂O₃ in bubble mode, e) Moving Nisin modified black phosphorous/Fe₂O₃ micromotors in magnetic mode. Conditions: 3% hydrogen peroxide, 2% SDS frequency (bubble mode), 4 Hz (magnetic mode), 10² CFU mL⁻¹ of bacteria, 220 micromotors mL⁻¹. Error bars corresponds to the standard deviation of 10 measurements.

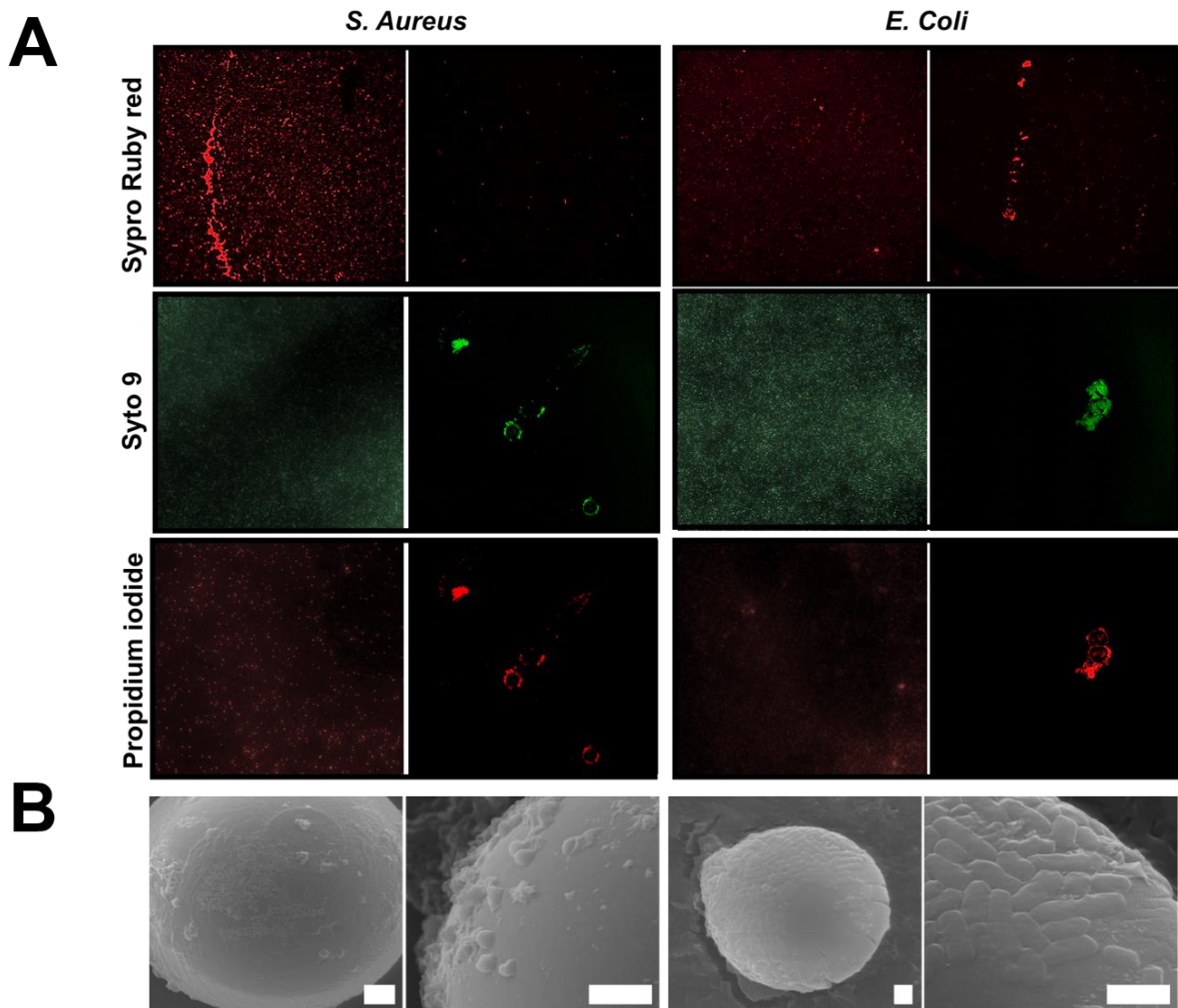


Figure S7. Study of *Staphylococcus Aureus* and *Escherichia Coli* biofilm matrix in fast and long-term killing experiments. A) Confocal laser microscopy images of each biofilm before (left) and after (right) treatment with GO/PtNPs/Fe₂O₃ micromotors. SYPRO-Ruby staining label proteins in the biofilm, Syto 9 and propidium iodide stain the DNA of all cells and dead cells in the biofilm, respectively. In this case images at the right shows the micromotors with bacteria attached collected after biofilm treatment. B) SEM images of the bacteria attached to the micromotors after long-term killing experiments in magnetic mode where the Nisin modified micromotors were added to the bacteria solution. Scale bars, 1 μ m.

CHAPTER V.

**Graphdyine tubular
micromotors for toxin
detection and pathogenic
cell killing**

V.1. Introduction and objectives.

The unique electronic structure of carbon, one of the essential elements of life, have allowed scientist to synthesize many allotropic forms with unprecedented electric, mechanical, thermal and chemical properties. A new addition to this line up of nanomaterials is 2D graphdiyne (GDY). The network of GDY consist of C₆ hexagons interconnected *via* acetylene linkages, resulting thus in a special atomic arrangement with high degree of π conjugation and tunable electronic properties even superior to those of graphene. Such excellent properties hold great potential for many applications in energy storage materials, advanced electronic components, sensing, and bioimaging applications.

GDY can be prepared with various well-defined structures such as nanotubes, nanowires and nanowalls. In the biomedical field, GDY exhibit higher adsorption/release capacity over graphene and other types of 2D nanomaterials for increased sensitivity. GDY also exhibit superior doxorubicin (DOX) loading capacity (via π stacking) and photothermal conversion ability in cancer cell treatment. A recent study has also revealed the improved biocompatibility and potential biosafety of GDY over graphene oxide related to the lack of aggregation in physiological conditions. Yet, GDY is still obtained at very low yields and is available actually at low quantities, hampering its practical applications. The combination of such material with micromotor technology is very relevant in this context, since very low amount of the material is required for the preparation of thousands of micromotors, which display an efficient performance as will be further illustrated.

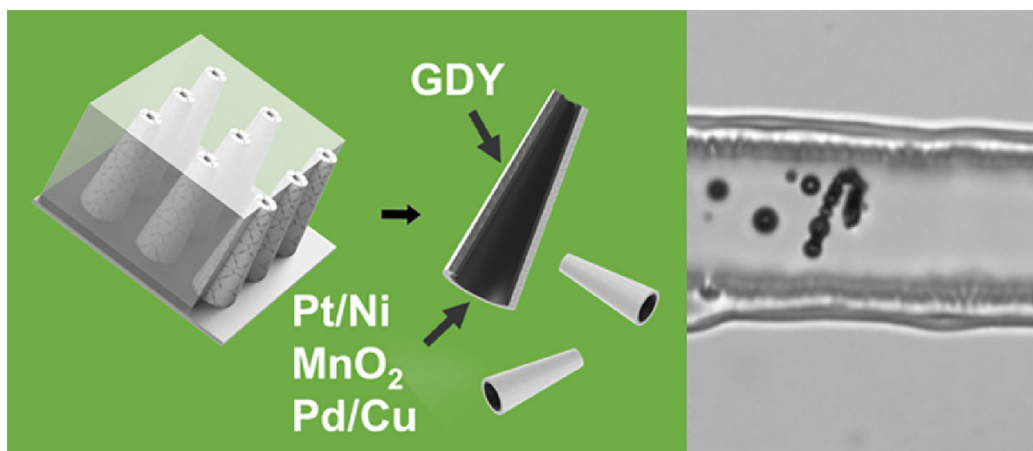
Inspired by the outstanding properties of GDY in the biomedical field, and previous works of our research group in carbon-nanomaterials based micromotors synthesis, we describe, for the first time, the preparation of tubular GDY micromotors. GDY is directly electrodeposited in a membrane template by cyclic voltammetry, followed by deposition of diverse metallic layers (Pt/Ni, MnO₂ or Pd/Cu) conferring the microtubes with structural stability to avoid microscale deformation. The GDY layer results in the generation of a rough inner metallic layer, allowing for micromotor operation at low (0.5 %) peroxide levels. The combination of the unique GDY properties with the moving capabilities of micromotors along with the efficient fluid mixing are illustrated in the micromotor operation in complex samples and navigation against fluid flows in

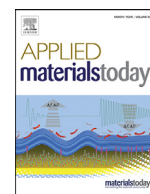
V. Graphdyine tubular micromotors for toxin detection and pathogenic cell killing

microfluidic channels. The incorporation of a Ni layer allows for efficient micromotor control for future lab-on-a-chip operations.

Secondly, we will illustrate the use of GDY/PtNPs micromotors for controlled drug delivery in cancer cell growth inhibition and sensing of bacterial toxins, taking advantage of the inherent remarkable performance and low toxicity of GDY in biomedical applications. To the best of our knowledge, this is the first time that this novel carbon allotrope is used here in connection with micromotor technology. Another novelty is the evaluation of the performance in living media such as cancer cell environment or biological fluids. We will illustrate the superior DOX loading capacity of the micromotors (in connection with the unique GDY structure) compared with graphene or polymeric micromotors and the pH-responsive drug release for HeLa cancer cells inhibition growth. Cytotoxicity assays will also demonstrate the high biocompatibility of the micromotors for future practical biomedical applications. The superior GDY loading capacity will be also proven for OFF-ON detection of Cholera toxin B in complex bio-media as representative biomarker using GDY micromotors engineered with a fluorescent labeled affinity peptide specifically designed to target a specific region (Subunit B) of the target toxin. The strategy is extended also for the detection of the endotoxin of *Escherichia Coli* with a related specific affinity peptide. The potential of GDY is finally illustrated in the removal of environmental pollutants, using Rhodamine 6G as model compound.

V.1. Article 6. Graphdiyne tubular micromotors: electrosynthesis, characterization and self-propelled capabilities.





Graphdiyne tubular micromotors: Electrosynthesis, characterization and self-propelled capabilities

Kaisong Yuan^{a,b}, Víctor de la Asunción-Nadal^a, Yuliang Li^{c,d}, Beatriz Jurado-Sánchez^{a,e,*}, Alberto Escarpa^{a,e,*}

^a Department of Analytical Chemistry, Physical Chemistry and Chemical Engineering, University of Alcalá, Alcalá de Henares E, 28871 Madrid, Spain

^b Institute of Pharmaceutical Analysis, College of Pharmacy, Jinan University, Guangzhou, PR China

^c Beijing National Laboratory for Molecular Sciences (BNLMS), CAS Key Laboratory of Organic Solids, Institute of Chemistry, CAS Research/Education Center for Excellence in Molecular Sciences, Chinese Academy of Sciences, Beijing 100190, PR China

^d School of Chemistry and Chemical Engineering, University of Chinese Academy of Sciences, Beijing 100049, PR China

^e Chemical Research Institute "Andrés M. del Río", University of Alcalá, Alcalá de Henares E, 28871 Madrid, Spain

ARTICLE INFO

Article history:

Received 23 May 2020

Revised 25 June 2020

Accepted 26 June 2020

Available online xxx

Keywords:

Graphdiyne

Micromotors

Electrosynthesis

Chip navigation

ABSTRACT

Graphdiyne (GDY) micromotors have been synthesized by direct electrochemical deposition, avoiding harsh conditions or sophisticated equipment. GDY is directly electrodeposited in a membrane template by cyclic voltammetry, followed by the deposition of diverse inner catalytic layers (Pt/Ni, MnO₂, or Pd/Cu) conferring the micromotors with structural stability to avoid nanoscale deformation. The best performance in terms of catalytic activity is observed for Pt-based micromotors, with up to 4-fold speed increase on average. In addition, compared with similarly prepared graphene oxide (GO) micromotors, a 2-fold speed enhancement is observed both in water and complex samples (saliva, blood serum, milk, and wine). The combination of the unique GDY properties with the moving capabilities of micromotors is also illustrated in the micromotor navigation against fluid flows in microfluidic channels. Practical applications are illustrated in fluorescent assay experiments for bacteria toxins detection and for the capture of a fluorescent probe, also used as model environmental pollutant. The template electrodeposition route holds great potential for the preparation of a myriad of GDY micromotors for diverse applications.

© 2020 Elsevier Ltd. All rights reserved.

1. Introduction

Micromotor technology is a continuously developing discipline with promising applications in many fields. 2D nanomaterials such as chalcogenides have been explored as emerging nanomaterials in micromotor preparation by template-electrosynthesis approaches [1]. For example, MoS₂-Pt micromotors display excellent capabilities for biosensing and drug delivery in biomedical applications [2]. WS₂ was incorporated in the surface of polyaniline/Pt microtubes as motile self-assembly elements for on-demand circuits [3]. Template-prepared WS₂/Pt micromotors show inherent IR responsive behavior for pollutant degradation [4]. The previously mentioned micromotors also show remarkable capabilities for energy generation and biosensing assays in connection with labelled affinity peptides for endotoxin detection [5]. Black phosphorous-Pt micromotors were described for the first time

by Pumera's group, showing efficient propulsion and remarkably high speeds compared with other micromotors [6]. The same group reported on a very interesting strategy by incorporating 4-fluorophenylgermanane and methylgermanane into tubular micromotors. The resulting structures exhibit different fluorescent behavior after illumination, opening new avenues for multiplexed operations such as drug delivery or biosensing [7].

A new addition to this line up of nanomaterials is two-dimensional (2D) graphdiyne (GDY) [8,9], which was proposed for the first time in 1987 by Baughman *et al.* [10] and first synthesized by Li's group [11]. The network of GDY consists of C₆ groups interconnected *via* acetylene linkages, resulting thus in a special atomic arrangement with a high degree of π conjugation and tunable electronic properties [9]. Such excellent properties hold great potential for many applications in energy storage materials [12-16], advanced electronic components [17,18], sensing [19,20], and bioimaging applications [21,22] which are now under exploration. The electronic properties along with the intrinsic bandgap and high carrier mobility of GDY have also been exploited by Zhang *et al.* for the design of heterojunction-based photodetectors [23]. In addition, GDY exhibit a strong light-matter interaction,

* Corresponding authors.

E-mail addresses: beatriz.jurado@uah.es (B. Jurado-Sánchez), alberto.escarpa@uah.es (A. Escarpa).

allowing for unique broadband Kerr nonlinear optical response for future use in passive photonic diodes [24,25].

GDY can be prepared with various well-defined structures such as nanotubes, nanowires, and nanowalls, which led to significant developments in related applications. Synthetic routes involve relatively complex procedures such as annealing, vapor-liquid-solid methods, and the use of harsh reagents [26–28]. Inspired by the remarkable capabilities of such nanostructures, herein we will illustrate the template-electrosynthesis of GDY microtubular structures with inner catalytic layers towards the development of micromotors using such exciting new material. Indeed, the field of micromotors can greatly benefit from the outstanding properties of GDY, leading to a myriad of “on-the-fly” applications to solve complex challenges. Carbon allotropes have been already used along with micromotor technology [29,30] for advanced applications such as active biocatalysis [31], analytical sensing [32–34], water purification [35–38], microfluidics operations [39] or drug delivery [40]. These catalytic microjets take advantage of the hydrogen peroxide decomposition reaction by different metals and metallic compounds (Pt, MnO₂) to eject oxygen bubbles and achieve efficient self-propulsion [41–47].

Inspired by the template electrosynthesis route for carbon allotrope and 2D micromotors preparation and from the research experience of our research group [29,30], herein we will illustrate the preparation of GDY tubular micromotors following a similar principle. The electrochemical route involves the direct electrodeposition of GDY in the inner wall of a polycarbonate membrane template by cyclic voltammetry. The subsequent electrodeposition of inner metallic layers (Pt/Ni, MnO₂, or Pd/Cu alloy) will confer the micromotors with structural stability to avoid nanoscale deformation, along with their motility for “on-the-fly” chemistry operations. The morphology and surface roughness of the micromotors, which play an important role in the improved catalytic behavior, will also be illustrated. The unique GDY properties impart the micromotors with an inner rough surface area with high electronic conductivity, resulting in the deposition of nanoparticulate-like highly conductive inner catalytic layers. This results in an extremely high catalytic activity and, in turn, towing force, as will be demonstrated by efficient operation in complex samples and improved navigation in confined microfluidic channels, even against high flow speeds. Potential applications in connection with the GDY layer are illustrated in the detection of a bacterial endotoxins using affinity peptide modified micromotors or dynamic isolation processes using Rhodamine 6G as model compound. The protocol holds great promise for the preparation of highly ordered GDY micromotors with autonomous capabilities for future applications in many fields such as drug delivery, biosensing [48], or energy generation, which are just starting to be explored.

2. Materials and methods

2.1. Reagents and materials

All reagents were purchased from Sigma-Aldrich (Spain) and used without further purification. Graphdiyne was provided by Li's group. The complete list of the chemicals and materials used are described in Table 1.

2.2. GDY and GO tubular micromotors synthesis

A polycarbonate membrane with 5 μm diameter conical pores (Catalog No. 7060–2513; Whatman, New Jersey, USA) was sputtered with a thin gold layer and used as a working electrode in a three electrodes setup. A commercial Ag/AgCl (3 M) electrode was used as a reference electrode and a Pt wire was used as the counter electrode. For each layer, different plating solutions and

Table 1
Conditions for micromotors electrodeposition.

Layer	Plating solution	Deposition technique
Graphdiyne	GDY 0.1 mg mL ⁻¹ Na ₂ SO ₄ 0.5 mol L ⁻¹	Cyclic voltammetry 0.3 V to -1.5 V at 50 mV s ⁻¹
Graphene oxide	GO 0.1 mg mL ⁻¹ Na ₂ SO ₄ 0.5 mol L ⁻¹	Cyclic voltammetry 0.3 V to -1.5 V at 50 mV s ⁻¹
PEDOT	3,4-ethylenedioxythiophene 10 mM Poly(sodium 4-styrenesulfonate) 125 mM	Amperometry 0.8 V for 2 C
Nickel (Ni)	Ni(SO ₃ NH ₂) ₂ 1.2 mol L ⁻¹ NiCl ₂ 82 mmol L ⁻¹ H ₃ BO ₃ 464 mmol L ⁻¹	Galvanostatic potentiometry -20 mA for 100 ms (10 cycles) -6 mA 360 s
Platinum (Pt)	H ₂ PtCl ₆ 4 mmol L ⁻¹ H ₃ BO ₃ 0.5 mol L ⁻¹	Amperometry -0.4 V for 750 s
Copper/Palladium (Cu/Pd)	PdCl ₂ 30 mmol L ⁻¹ CuSO ₄ 250 mmol L ⁻¹ HCl 100 mmol L ⁻¹	Amperometry -0.1 V for 7 C
Manganese oxide (MnO ₂)	Mn(CH ₃ CO ₂) ₂	Amperometry 0.75 V for 1.2 C

electrochemical methods were used. The plating solutions composition and the specific electrodeposition conditions are listed in Table 1.

2.3. Micromotor speed tracking

To measure the micromotor speed, 1 μL of micromotor dispersion was placed on a glass slide and mixed with 1 μL of 15% SDS (final concentration, 5%) and 1 μL of different fuel solutions to get the desired concentration. In the case of real media, 1 μL of the medium was also added. Videos were recorded after the addition of the fuel at a frame rate of 25 FPS using a Zyla CMOS camera attached to an Eclipse Ti-S inverted microscope (Nikon, Tokyo, Japan). The micromotors were tracked using the NIS Elements AR 3.2 software (Nikon, Tokyo, Japan) the speed per frame data was averaged in order to calculate the mean speed for each motor ($n=50$).

2.4. On-chip experiments

For on-chip experiments, a perforated PDMS microfluidic chip was placed on top of a glass slide. Firstly, the chip was filled with a 5% SDS solution to check the water tightness, next the micromotors were injected until they arrived in the desired reservoir or channel. Finally, a 3% H₂O₂ was injected until micromotor bubbling was observed. Movies were recorded using the same setup as the previous section. The micromotors were guided inside the microfluidic using a permanent neodymium magnet placed approximately 20 cm away from the microfluidic chip.

2.5. Fluorescent assay experiments

For the detection of the *Escherichia coli* 0111:B4 endotoxin, a tailored-synthesized tetramethyl rhodamine-labelled affinity peptide (sequence TMRho-KKNYSSSISSIHIC) was obtained from Neo-Biotech (Nanterre, France). GDY micromotors were modified with the peptide (1000 μg mL⁻¹) by incubation with a dry batch (approx. 500,000 motors) for 60 min under vigorous shaking. For detection, 1 μL of modified motors, 1 μL of H₂O₂ 3%, 1 μL of 5% SDS solution and 1 μL of sample (or standard solutions) were mixed on the surface of a glass slide. The fluorescence images were recorded

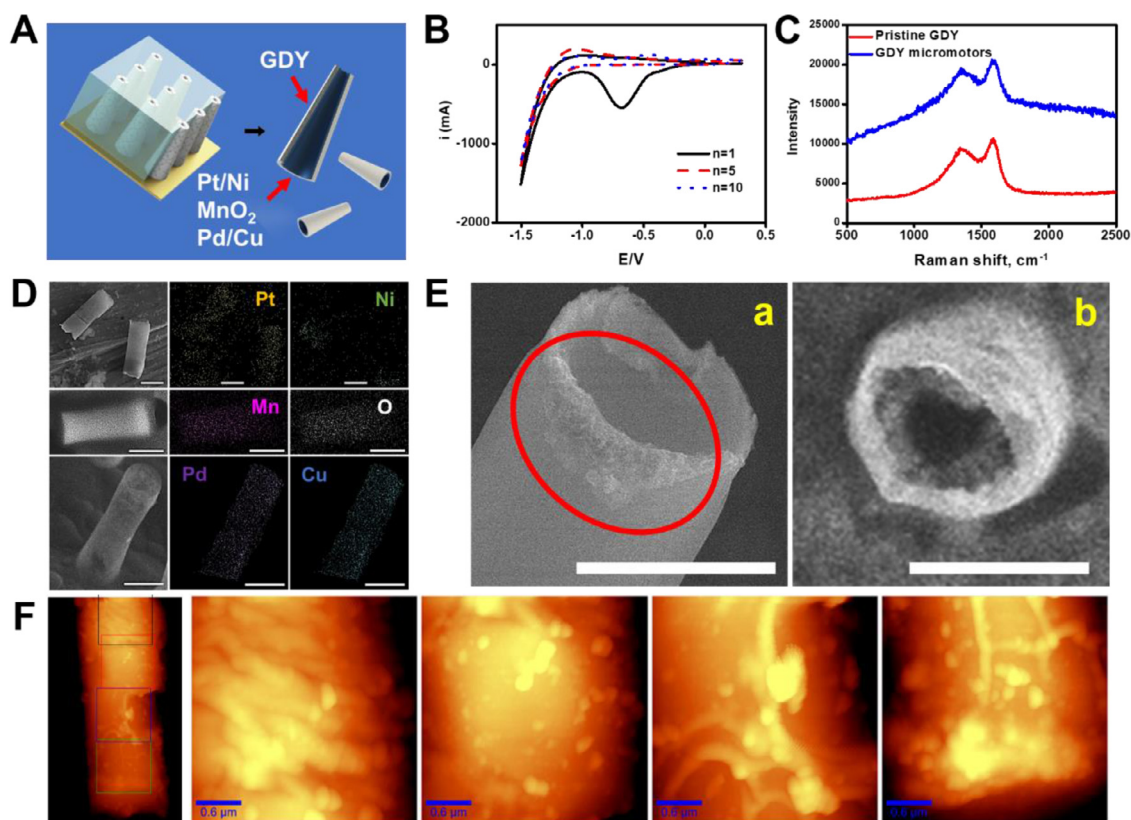


Fig. 1. Electrodeposition and characterization of GDY tubular micromotors. (A) Schematic of the synthesis of GDY micromotors based on different catalysts. (B) CV corresponding to the electrodeposition at different cycles. (C) Raman spectra of pristine GDY and GDY micromotors. (D) SEM and EDX images showing the morphology and element distribution of GDY micromotors based on Pt/Ni, MnO₂, and Pd/Cu catalysts. (E) SEM images of the rough inner metallic layer morphology of GDY-Ni/Pt (a) and Pd/Cu (b) microtubes. (F) AFM mapping of the whole micromotor and different magnified sections. Scale bars, 5 μm (D, E), and 0.6 μm (F).

by the camera of the microscope and the fluorescent measured using the NIS Elements software.

2.6. Rhodamine 6G experiments

1 mL of Rhodamine 6G solutions (4 g L^{-1}) were treated with micromotors (approx. 500,000 motors), H₂O₂ 3%, and 5% of SDS solution. Static micromotor and magnetic stirring experiments were performed in the absence of peroxide. After 1 h treatment, micromotors were captured with a magnet at the bottom of the Eppendorf and the supernatant collected for UV–Vis measurements using a PerkinElmer Lambda 20 spectrophotometer.

3. Results and discussion

Fig. 1A shows the schematic illustration of the GDY micromotors developed in this work. Prior electrodeposition, pristine GDY was characterized by transmission electron microscopy and Raman observation. Please see Figure S1 for the related images and characterization. GDY outer layer was deposited from a plating solution containing 0.1 mg mL^{-1} of GDY and $0.5 \text{ M Na}_2\text{SO}_4$ as supporting electrolyte. A cyclic voltammetry (CV) was performed to deposit this layer inside the pores ($\varnothing = 5 \mu\text{m}$) of a gold-sputtered polycarbonate membrane. As can be seen in the voltammogram, the deposition starts with an anodic current at -0.6 V , followed by a cathodic current at -1.1 V (Fig. 1B). The cyclic voltammetry profile indicates a graphene-like electrodeposition [29,30], with a decrease in the reduction peak while the potential cycling increase, indicating a reduction in the structure. Indeed, GDY structure comprises a hybrid structure of graphene (with sp^2 carbons) and

diacetylenic linkages (with sp carbons). Such a special carbon network contains a high degree of π -conjugations and carbon-carbon triple bonds whilst the defects generate active oxygen functional groups [9,49]. The application of the electric potential results in the reduction of the oxygen moieties in the GDY structure, increasing the hydrophobicity of the material, which tend to aggregate via π - π interactions, resulting in an ordered film which ultimately deposits within the walls of the template membrane via hydrophobic interactions [50]. Please note here that as previously described in several works, this “stacked” layer contains a high density of intragrain and grain-boundary defects and edges that results in a high rough layer [29,30,51]. The thickness of the GDY layer can be tailored by varying the number of scans during the CV step. For 2–5 scans, the layer is very thin, and the structures tend to collapse, preventing micromotor formation. The best performance was obtained for 10 scans. Higher scans will lead to thicker layers. In addition, thicker layers can block the opening of the pore, preventing subsequent deposition of inner Pt layers and hindering the overall performance, as previously reported in a related work from our research group [29,30]. Next, different inner layers were electrodeposited (see experimental section for further details).

To study the properties of the resulting GDY micromotors, we performed Raman spectroscopy characterization. Taking into consideration both the pristine and electrodeposited GDY spectra, we can assume the material was electrodeposited without suffering major structural changes, as the D/G ratio and the Raman shifts remain constant (Fig. 1C), thus the micromotors retain the properties of GDY. Further scanning electron microscopy (SEM) and energy-dispersive X-ray spectroscopy (EDX) characterization revealed the well-defined morphology of the micromotors, with a homogenous

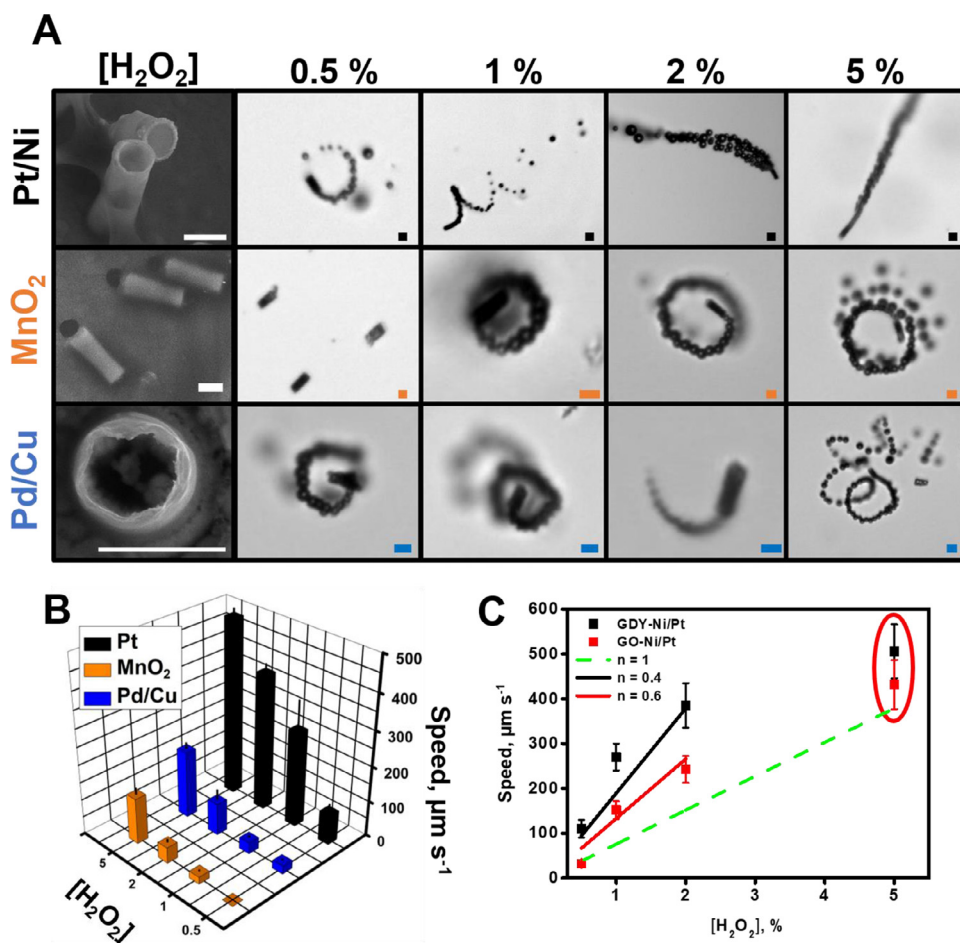


Fig. 2. Characterization of the propulsion of GDY micromotors. (A) SEM and time-lapse images (taken from Video S1) showing the propulsion of GDY micromotors based on different catalysts and peroxide levels and (B) Corresponding speed plot. (C) Theoretical (solid lines) and experimental speeds of GDY-Ni/Pt (black squares) and GO-Ni/Pt (red squares) micromotors at different peroxide levels. Scale bars, 5 μm . (For interpretation of the references to color in this figure legend, the reader is referred to the web version of this article.)

distribution of different catalysts (Pt, MnO₂, Pd/Cu alloy) and magnetic materials (Ni) in the structure (Fig. 1D). The rough morphology of the outer GDY layer results in the electrodeposition of nanoparticulate catalytic layer, as illustrated in the SEM images of Fig. 1E, a. The flipped area illustrates a nanoparticulate structure of the inner Pt layer, reflecting the increased catalytic surface for subsequent propulsion, as will be further illustrated. Indeed, the presence of the grain-boundary defects in the GDY layer implies the presence of edges and defects in the film. Pt tends to nucleate and grow in such defects, resulting in a nanoporous structure as suggested by previous reports. Such a nanoparticulate structure increases the available catalytic area for hydrogen peroxide decomposition. In addition, enhanced electron transfer has been observed in GDY/PtNPs composites due to the easier chemical interaction between Pt and the triple bond of GDY [52,53]. A similar observation is noted when using Cu/Pd as the inner layer (see Fig. 1E, b). Further proof is obtained in the atomic force microscopy (AFM) characterization of the outer layer morphology, showing a coarse layered arrangement (Fig. 1F), with crest and valleys as shown in the spots of the AFM along with all the micromotor structure (mean roughness value= 6 nm) indicating a rough morphology, which further testified the subsequent deposition of nanoparticulated inner catalytic layers.

Micromotor performance was tested using different hydrogen peroxide concentrations ranging from 0.5% to 5%. Micromotor movement was recorded and traced showing different patterns

such as circular, flower-like, and linear motion traces (see Fig. 2A). The highest speed was recorded for Pt catalyst being 2.7 times higher than Pd/Cu and 3.9 times higher than MnO₂ on average using a peroxide concentration of 5% and 5% sodium dodecyl sulfate (SDS).

To further characterize the catalytic properties of the GDY micromotors, our experimental results were cross-matched with a previously reported theoretical models for catalytic tubular micromotors [54–56]. The data can be indirectly related to the number of catalytic active sites and catalytic mass, *via* estimation of the catalytic activity through bubble generation. Thus, according to these models, for a tubular cavity with a radius R_j and a length L , the generated oxygen rate is linearly proportional to the catalytic surface area and the H₂O₂ concentration. Additionally, an equivalent available surface coefficient (n) was added. If this coefficient equals one, the available catalyst surface is equal to the geometrical inner surface, thus bigger available surfaces correspond to higher inner roughness due to the growth of catalyst nanoparticles inside the tube and the enhanced scaffolding effect of rougher outer layers. In turn, lower surfaces indicate hindered catalyst deposition or deficient fuel availability. Therefore, bubble-exPELLing frequency (f) is described as follows (Eq. 1) [54,55]:

$$f = \frac{k[\text{H}_2\text{O}_2] 2\pi LR_j/n}{V_{\text{bubble}}} = \frac{3k[\text{H}_2\text{O}_2] LR_j/n}{2R_b^3}$$

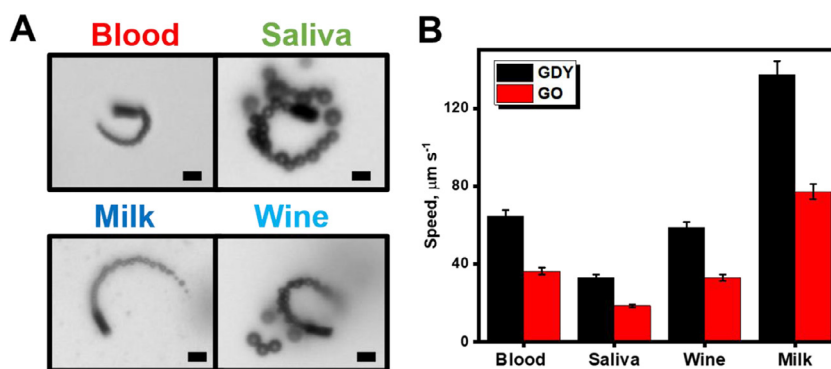


Fig. 3. GDY-Ni/Pt and GO-Ni/Pt micromotor propulsion in complex media. (A) Time-lapse images (taken from Video S2) showing the propulsion of GDY-Ni/Pt micromotors in real samples at 1 % peroxide levels. (B) Corresponding speed plot. Scale bars, 5 μm.

According to Mei's model, the displacement (l) of a micromotor by a single bubble thrust can be defined as (Eq. 2):

$$l = \frac{6R_b^2}{3R_b + \frac{L}{\ln \frac{2L}{R_b} - 0.72}}$$

Finally, the average speed can be expressed as the step length times the frequency, depending on peroxide concentration and geometrical features such as length, and radius of the studied micromotors and average bubble radius (R_b) (Eq. 3) [54-56]:

$$v_j^{ave} = f \cdot l = \frac{9k[H_2O_2] LR_j/n}{3R_b^2 + \frac{LR_b}{\ln \frac{2L}{R_b} - 0.72}}$$

Fig. 2C shows the correlation between the theoretical values, represented as solid lines, and the plotted experimental measured speeds for GDY-Ni/Pt and GO-Ni/Pt micromotors prepared in a similar manner. For GDY and GO micromotors, despite both sets micromotors have the same size and were prepared under the same conditions, at low hydrogen peroxide concentration, GDY micromotors have an available surface coefficient of 0.4, whereas GO micromotors show a coefficient of 0.6. This translates into a higher available catalytic surface of $S_{cat,GDY} = 432 \mu m^2$, and $S_{cat,GO} = 288 \mu m^2$ when compared to a perfectly smooth microtube ($S_{cat,geom} = 173 \mu m^2$) [48]. Roughly, the increase in the catalytic activity can indicate a relatively higher bubble expelling frequency, resulting in a 2-fold speed increase as compared with similarly prepared GO micromotors. In addition, compared with previous graphene-based micromotors, the speed of GDY-Pt/Ni micromotors ($110 \mu m s^{-1}$, 0.5 % H_2O_2) is similar than that reported for rGO/Pt micromotors without inner Ni layers ($170 \mu m s^{-1}$, 0.5 % H_2O_2) [30] or lower than nanographene/Ni/Pt micromotors ($340 \mu m s^{-1}$, 0.5 % H_2O_2) [36], which reflects the influence of the different graphene structures in the micromotor propulsion for a given application. Yet, the micromotor speed is higher than those observed for carbon black ($90 \mu m s^{-1}$) micromotors (also containing a Ni layer) propelling in 1 % peroxide solutions [29]. In the case of Pd/Cu and MnO_2 micromotors, we can observe a 62% and a 38% decrease in average speed respectively when compared to the Pt catalyst. Since the highest speed was noted for Pt-based micromotors, they were selected for further experiments and characterization in real domains.

The performance of GDY-Ni/Pt micromotors was also tested in raw complex media, where the high content of proteins and other constituents can deactivate the inner catalytic layer and hamper or stop the operation for "on-the-fly" applications. For comparison, GO-Ni/Pt micromotors were also tested. In every case, hydrogen peroxide and SDS were added to a final concentration of 1% and

5%. Fig. 3, A and corresponding supporting video illustrate the micromotor propulsion in blood, saliva, wine, and milk samples. The different speeds reflect the viscosity of the media and other constituents that can interfere with the catalytic layer. Low speed of $39 \pm 5 \mu m s^{-1}$, $62 \pm 6 \mu m s^{-1}$, and $59 \pm 7 \mu m s^{-1}$ were recorded for saliva, blood serum, and wine, respectively. Such a trend reflects the increased viscosity in the media (1 cP in water as compared with 1.3 cP in saliva, 1.5 cP in plasma, and 1.4 cP in wine) and the complexity of the samples tested with a high content of proteins, carbohydrates, etc. In the case of milk, no apparent speed decrease is noted as compared with water, due to the viscosity of both media is similar. It should be mentioned here that despite such sample complexity, efficient micromotor propulsion is observed. For comparison, GO-Ni/Pt micromotors were also tested (see Fig. 3B), reflecting, even more, the difference in the catalytic activity compared with GDY, with a 2-fold speed decrease for GO in all the samples assayed. As such, GDY micromotors represent a good and even complementary alternative to graphene micromotors. Even more, both materials can be combined in the future, resulting in a single micromotor benefiting from their $sp^3/sp^2/sp$ chemistry.

Micromotors have been proved to be a powerful tool in microfluidics owing to their micromanipulation and cargo towing abilities [57,58]. In this sense, the most important features to take into account are maneuverability and propulsion in the miniaturized environment, especially against fluid flows. The high towing force of GDY micromotors associated with the rough inner catalytic area (imparted by the unique rough outer GDY layer) was tested for complex operations (controlled maneuverability and navigation against flows). Fig. 4A and corresponding video (Video S3) show the navigation and controlled motion of the micromotors containing an inner Ni layer, which allows to control and tune the motion in a confined environment. More interestingly, Fig. 4B shows the performance of a micromotor inside a microfluidic channel moving against the fluid flow. Flow speed was measured by tracking small tracer particles, the maximum flow speed was 4.8 times higher than the micromotor speed. Nonetheless, the apparent micromotor speed relative to the channel walls was only 22% lower than that of the motors swimming in a still drop. Regarding the maneuverability, Ni-containing motors were used for this application. Applied magnetic fields were used in order to orient the motors along the long axis of the channel. As can be seen in Fig. 4C, the micromotor is able to follow the path avoiding bubbles without stopping its motion. After crossing the main channel, the micromotor gets to a three-way junction, where the chosen path can be switched by changing the direction of the magnetic field. The GDY micromotor is also able to enter the right channel and dock on the wall.

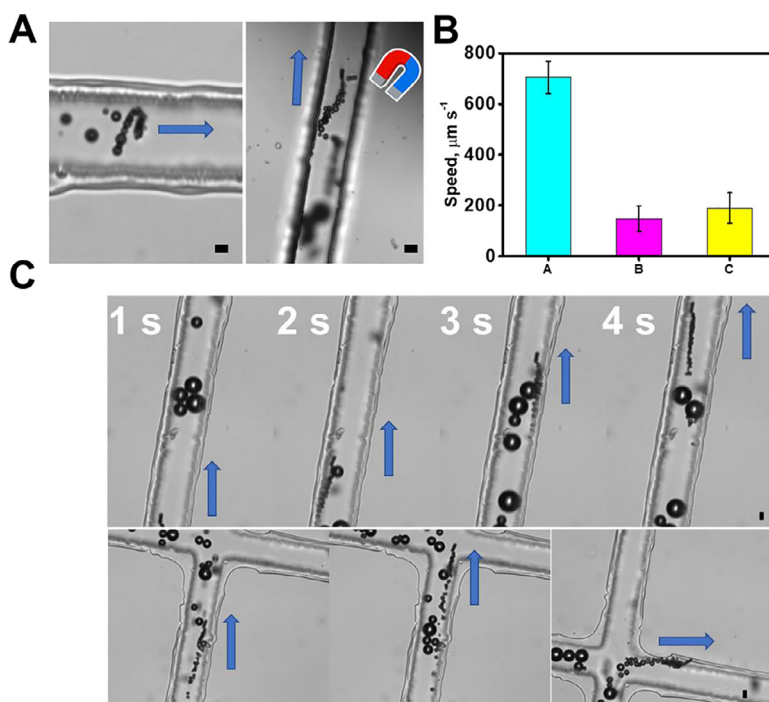


Fig. 4. GDY-Ni/Pt micromotors navigation in microchip channels with controlled motion. (A) Time lapse-images (taken from Video S3) showing the controlled navigation and high-towing force of the micromotors. (B) Graph bar showing the speed of the flow in the microchannel (A, blue) and the micromotor speed navigating against the flow (B, pink) and in drop/static solution (C, yellow). (C) Time-lapse images showing the micromotor navigation against the flow and controlled motion with a magnetic field. Scale bars, 5 μm . (For interpretation of the references to color in this figure legend, the reader is referred to the web version of this article.)

Such moving capabilities, in connection with the rich outer surface chemistry of GDY, hold great potential for the development of future applications using functionalized GDY micromotors for simplified “lab-on-a-chip” bioassays, environmental remediation with recyclable capabilities, moving supercapacitors, etc.

Next, potential applications using functionalized GDY micromotors will be demonstrated. Thus, Fig. 5 illustrates the use of affinity-peptide modified GDY micromotors for OFF-ON detection of *Escherichia Coli* endotoxin, an important biomarker for sepsis diagnosis and to assure the quality of pharmaceutical formulations [59,60].

GDY micromotors offer an ideal platform for modification with different receptors due to the presence of π groups, hydroxyl groups, etc. In this case, the affinity peptide can attach to the GDY micromotors via physical adsorption through electrostatic and π -stacking with the different aromatic, non-polar and aromatic aminoacids present in the peptide, (Cys, Leu, Gly, Pro, Ala, etc) and the π orbitals overlapping with the aromatic Rhodamine tag. As can be seen in Fig. 5A, the fluorescent of the solution is recovered after 5 min micromotor navigation (3% H_2O_2) in solutions containing the target endotoxin. Competitive binding between the peptide (with a higher affinity for the endotoxin) and the GDY surface, results in the release of the dye-labelled peptide. The normalized fluorescent plot of Fig. 5B illustrates the increase of the fluorescent on the solution along with the increase of the endotoxin concentration. Data were processed to obtain the calibration plot (see Fig. S2 in the supporting information) and evaluate the analytical performance of the strategy. The limit of detection (LOD) calculated using the standard deviation of the blank corresponds to a concentration of 1.1 ng mL^{-1} and the linear range spans from 3.6 to 100,000 ng mL^{-1} . Such LOD is comparable with the gold standard *Limulus ameobocyte lysate* (0.05 to 5 ng mL) [61], which illustrate the applicability of our micromotor protocol for practical use. We finally evaluate the recovery and selectivity of the sensing platform (see Fig. 5C). As can be seen in the normalized fluorescent plot, the

values obtained for blood and saliva samples fortified with 1 $\mu\text{g mL}^{-1}$ were similar to that observed in the calibration plots, with recoveries higher than 95% in all cases. The high selectivity of the protocol is illustrated in the negligible fluorescent recovery under the presence of the endotoxin from *Salmonella Enterica*, with a similar structure with our target endotoxin. All this data further reveals the applicability of GDY micromotor in analytical sensing.

On a second application, we evaluated the applicability of GDY micromotors for Rhodamine 6 G removal experiments. Such compound can interact via π stacking for removal of such model pollutant (see Fig. 6A).

Fig. 6B, C illustrate the experiments for the isolation of 4 g L^{-1} of Rhodamine 6 G. To this end, we mix the solutions with the moving GDY micromotors (3% H_2O_2). Control experiments were also included and for comparison GO and PEDOT micromotors were also tested. In all cases, the micromotors or static controls were left in contact with the Rh6G solution for 1 h. After that time, the motion was stopped by trapping with a magnet and the supernatant collected to perform the UV-VIS measurements (see Fig. 6B). The data was processed to obtain the percent removal/capture at each condition and the results are plotted in Fig. 6C. As can be seen, the higher removal rates were obtained with the moving GDY micromotors, followed by moving GO micromotors. Dramatically lower removal/capture was obtained with PEDOT micromotors with a smoother surface and less functional groups. The role of efficient GDY micromotor movement is further supported by the low removal/capture obtained in experiments performed at static conditions and under magnetic stirring. The data is fully supported by the pictures of Fig. 6D, in which the decrease is visually observed by the reduction of the colour of the contaminated solution. Future efforts should be aimed at improving the efficiency of the strategy to obtain higher removal percentages by increasing the number of micromotors or combining with additional treatment strategies such as light assisted degradation. Yet, the above-mentioned data also shows the better performance of GDY micromotors.

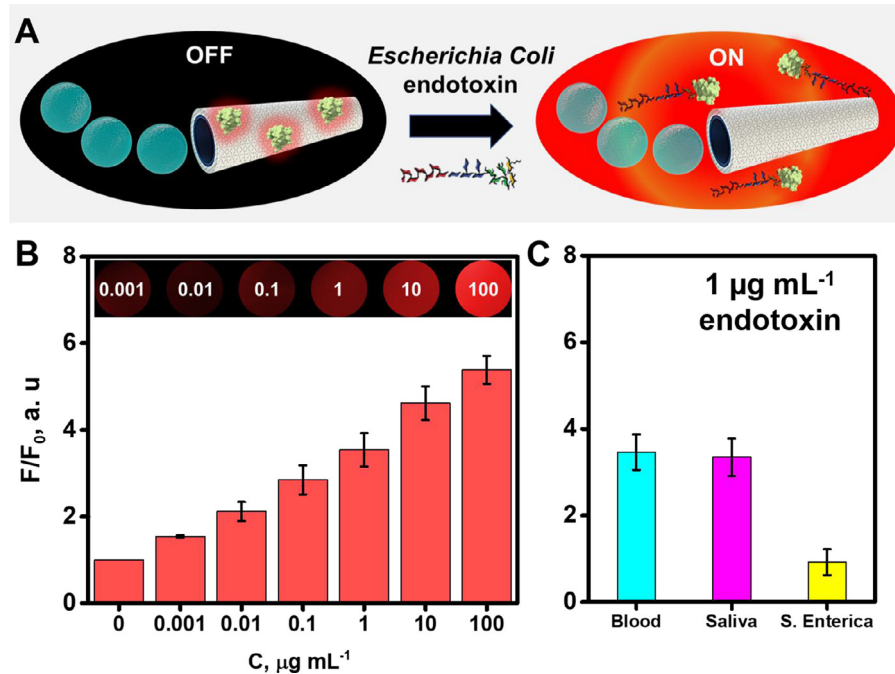


Fig. 5. GDY-Ni/Pt micromotors in fluorescent assays. (A) Schematic of the OFF-ON detection strategy using GDY micromotors modified with TMRho labelled affinity peptide (TMR-KKNYSSSISSIHIC). Under the presence of the target endotoxin (*Escherichia coli* 0111:B4), the affinity peptide attaches to the endotoxin and is released from the micromotors, resulting in the recovery of the fluorescent of the solution. (B) Normalized fluorescent plot (F/F_0) corresponding to solutions containing increasing concentrations of the target endotoxin. Inset shows time-lapse fluorescent images at each concentration. (C) Normalized fluorescent plot (F/F_0) of the recovery and selectivity of the sensing protocol.

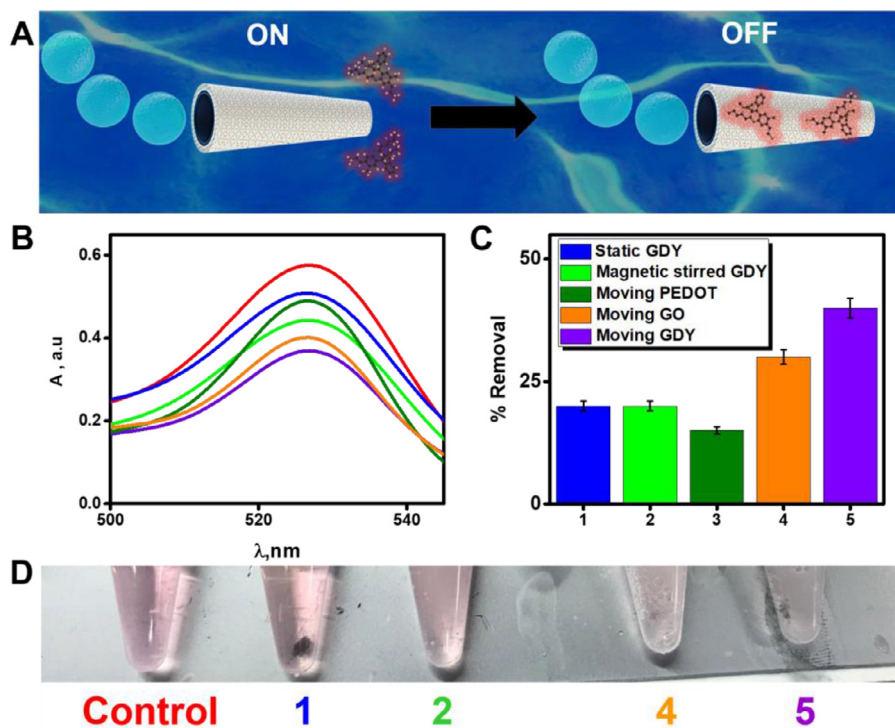


Fig. 6. GDY-Ni/Pt micromotors for environmental remediation and fluorescent dye loading. (A) Schematic of the removal/capture of Rhodamine 6 G. (B) UV-VIS plot and (C) corresponding percent removal of Rhodamine 6 G solutions (4 g L^{-1}) treated with GDY micromotors and control experiments. Please check the color of each bar for the corresponding condition. Red line in B) correspond to the absorbance of the contaminated solution prior treatment. (D) Pictures of the solutions under the different conditions. (For interpretation of the references to color in this figure legend, the reader is referred to the web version of this article.)

4. Conclusions

We have developed a greatly simplified protocol for the preparation of highly efficient GDY micromotors. Unlike previous procedures used for the synthesis of ordered GDY nanostructures, no harsh conditions or sophisticated equipment is needed, simplifying the cost for future full-scale applications. Such enhanced capabilities of GDY micromotors have been illustrated in the excellent operation in complex samples or navigation against fluid flows in microfluidic channels. The incorporation of a Ni layer allows for efficient micromotor control for future “lab-on-a-chip” operations. The rich outer GDY surface in connection with the high catalytic activity of Pt makes these GDY-based micromotors ideal for bioassays operations in miniaturized settings such as endotoxin sensing and Rhodamine removal as it was demonstrated here.

As future GDY micromotors-based applications, manganese dioxide-based GDY micromotors can be applied in environmental degradation applications due to its capacity to release OH⁻ ions, which are very useful to degrade organic pollutants. Pd-based micromotors can also be explored for future “energy-generation” applications, synergetic with the GDY properties.

Therefore, GDY micromotors are reported as a good and complementary alternative to graphene micromotors. Even more, both materials can be combined in the future, resulting in a single micromotor benefiting from their sp³/sp²/sp chemistry.

Funding

This work was supported by the Spanish Ministry of Economy, Industry and Competitiveness [grant numbers [RYC-2015-17558](#), co-financed by EU (B.J.S), [CTQ2017-86441-C2-1-R](#) (A.E)]; the [Community of Madrid](#) [grant numbers [CM/JIN/2019-007](#) (B.J.S), [TRANSNANOAVANSENS](#), [S2018/NMT-4349](#) (A.E)] and the [Universidad de Alcalá](#) [grant numbers [CCG19/CC-029](#) (B.J.S), FPI fellowship (V.A.N)].

Credit author statement

Kaisong Yuan: Conceptualization; Data Curation; Formal analysis; Investigation; Visualization; Writing - review & editing. **Víctor de la Asunción-Nadal:** Conceptualization; Data Curation; Formal analysis; Investigation; Visualization; Writing - review & editing. **Yuliang Li:** Resources. **Beatriz Jurado Sánchez:** Conceptualization; Formal analysis; Funding acquisition; Supervision; Writing - original draft; Writing - review & editing. **Alberto Escarpa:** Conceptualization; Resources; Funding acquisition; Supervision; Writing - review & editing. **Kaisong Yuan and Víctor de la Asunción Nadal contribute equally to this work.**

Data availability

The raw/processed data required to reproduce these findings cannot be shared at this time as the data also forms part of an ongoing study.

Declaration of Competing Interest

The authors declare that they have no known competing financial interests or personal relationships that could have appeared to influence the work reported in this paper.

Supplementary materials

Supplementary material associated with this article can be found, in the online version, at doi:[10.1016/j.apmt.2020.100743](#).

References

- [1] H. Wang, M. Pumera, Emerging materials for the fabrication of micro/nanomotors, *Nanoscale* 9 (2017) 2109–2116.
- [2] V.V. Singh, K. Kaufmann, B. Esteban Fernández de ávila, E. Karshalev, J. Wang, Molybdenum disulfide-based tubular microengines: toward biomedical applications, *Adv. Function. Mater.* 26 (2016) 6270–6278.
- [3] C.C. Mayorga-Martinez, J.G.S. Moo, B. Khezri, P. Song, A.C. Fisher, Z. Sofer, M. Pumera, Self-propelled supercapacitors for on-demand circuit configuration based on WS₂ nanoparticles micromachines, *Adv. Function. Mater.* 26 (2016) 6662–6667.
- [4] V. de la Asunción-Nadal, B. Jurado-Sánchez, L. Vázquez, A. Escarpa, Near infrared-light responsive WS₂ microengines with high-performance electro- and photo-catalytic activities, *Chem. Sci.* 11 (2020) 132–140.
- [5] V. de la Asunción-Nadal, M. Pacheco, B. Jurado Sánchez, A. Escarpa, Chalcogenides-based tubular micromotors in fluorescent assays, *Anal. Chem.* 92 (13) (2020) 9188–9193.
- [6] T. Maric, J.G.S. Moo, B. Khezri, Z. Sofer, M. Pumera, Black-phosphorus-enhanced bubble-propelled autonomous catalytic microjets, *Appl. Mater. Tod.* 9 (2017) 289–291.
- [7] T. Maric, S.M. Beladi-Mousavi, B. Khezri, J. Sturala, M.Z.M. Nasir, R.D. Webster, Z. Sofer, M. Pumera, Functional 2D germanene fluorescent coating of microrobots for micromachines multiplexing, *Small* (2020), doi:10.1002/smll.201902365.
- [8] M.M. Haley, Synthesis and properties of annulenic subunits of graphyne and graphdiyne nanoarchitectures, *Pure Appl. Chem.* 80 (2008) 519–532.
- [9] C. Huang, Y. Li, N. Wang, Y. Xue, Z. Zuo, H. Liu, Y. Li, Progress in research into 2D graphdiyne-based materials, *Chem. Rev.* 118 (2018) 7744–7803.
- [10] R.H. Baughman, H. Eckhardt, M. Kertesz, Structure-property predictions for new planar forms of carbon: layered phases containing sp² and sp atoms, *J. Chem. Phys.* 87 (1987) 6687–6699.
- [11] Z. Jia, Y. Li, Z. Zuo, H. Liu, C. Huang, Y. Li, Synthesis and properties of 2D carbon-graphdiyne, *Acc. Chem. Res.* 50 (2017) 2470–2478.
- [12] G. Li, Y. Li, H. Liu, Y. Guo, Y. Li, D. Zhu, Architecture of graphdiyne nanoscale films, *Chem. Commun.* 46 (2010) 3256–3258.
- [13] M. Kivala, F. Diederich, Conjugation and optoelectronic properties of acetylenic scaffolds and charge-transfer chromophores, *Pure Appl. Chem.* 80 (2008) 411–427.
- [14] A. Mohajeri, A. Shahsavari, Tailoring the optoelectronic properties of graphyne and graphdiyne: nitrogen/sulfur dual doping versus oxygen containing functional groups, *J. Mater. Sci.* 52 (2017) 5366–5379.
- [15] L. Hui, Y. Xue, H. Yu, Y. Liu, Y. Fang, C. Xing, B. Huang, Y. Li, Highly efficient and selective generation of ammonia and hydrogen on a graphdiyne-based catalyst, *J. Am. Chem. Soc.* 141 (2019) 10677–10683.
- [16] N. Wang, J. He, K. Wang, Y. Zhao, T. Jiu, C. Huang, Y. Li, Graphdiyne-based materials: preparation and application for electrochemical energy storage, *Adv. Mater.* 31 (2019) 1803202.
- [17] Y. Pan, Y. Wang, L. Wang, H. Zhong, R. Quhe, Z. Ni, M. Ye, W.-N. Mei, J. Shi, W. Guo, J. Yang, J. Lu, Graphdiyne-metal contacts and graphdiyne transistors, *Nanoscale* 7 (2015) 2116–2127.
- [18] K. Krishnamoorthy, S. Thangavel, J.C. Veetil, N. Raju, G. Venugopal, S.J. Kim, Graphdiyne nanostructures as a new electrode material for electrochemical supercapacitors, *Int. J. Hyd. Energy* 41 (2016) 1672–1678.
- [19] C. Wang, P. Yu, S. Guo, L. Mao, H. Liu, Y. Li, Graphdiyne oxide as a platform for fluorescence sensing, *Chem. Commun.* 52 (2016) 5629–5632.
- [20] J. Liu, X. Shen, D. Baimanov, L. Wang, Y. Xiao, H. Liu, Y. Li, X. Gao, Y. Zhao, C. Chen, Immobilized ferrous ion and glucose oxidase on graphdiyne and its application on one-step glucose detection, *ACS Appl. Mater. Interfaces* 11 (2019) 2647–2654.
- [21] H. Min, Y. Qi, Y. Chen, Y. Zhang, X. Han, Y. Xu, Y. Liu, J. Hu, H. Liu, Y. Li, G. Nie, Synthesis and imaging of biocompatible graphdiyne quantum dots, *ACS Appl. Mater. Interfaces* 11 (2019) 32798–32807.
- [22] S. Li, Y. Chen, H. Liu, Y. Wang, L. Liu, F. Lv, Y. Li, S. Wang, Graphdiyne materials as nanotransducer for in vivo photoacoustic imaging and photothermal therapy of tumor, *Chem. Mater.* 29 (2017) 6087–6094.
- [23] Y. Zhang, P. Huang, J. Guo, R. Shi, W. Huang, Z. Shi, L. Wu, F. Zhang, L. Gao, C. Li, X. Zhang, J. Xu, Zhang H, Graphdiyne-based flexible photodetectors with high responsivity and detectivity, *Adv. Mater.* 32 (2020) 2001082.
- [24] L. Wu, Y. Dong, J. Zhao, D. Ma, W. Huang, Y. Zhang, Y. Wang, X. Jiang, Y. Xiang, J. Li, Y. Feng, J. Xu, H. Zhang, Kerr nonlinearity in 2D graphdiyne for passive photonic diodes, *Adv. Mater.* 31 (2019) 1807981.
- [25] J. Guo, R. Shi, R. Wang, Y. Wang, F. Zhang, C. Wang, H. Chen, C. Ma, Z. Wang, Y. Ge, Y. Song, Z. Luo, D. Fan, X. Jiang, J. Xu, H. Zhang, Graphdiyne-polymer nanocomposite as a broadband and robust saturable absorber for ultrafast photonics, *Laser Photonics Rev.* 14 (2020) 1900367.
- [26] G. Li, Y. Li, X. Qian, H. Liu, H. Lin, N. Chen, Y. Li, Construction of tubular molecule aggregations of graphdiyne for highly efficient field emission, *J. Phys. Chem. C* 115 (2011) 2611–2615.
- [27] X. Qian, Z. Ning, Y. Li, H. Liu, C. Ouyang, Q. Chen, Y. Li, Construction of graphdiyne nanowires with high-conductivity and mobility, *Dalton Trans.* 41 (2012) 730–733.
- [28] J. Zhou, X. Gao, R. Liu, Z. Xie, J. Yang, S. Zhang, G. Zhang, H. Liu, Y. Li, J. Zhang, Z. Liu, Synthesis of graphdiyne nanowalls using acetylenic coupling reaction, *J. Am. Chem. Soc.* 137 (2015) 7596–7599.

- [29] R. Maria-Hormigos, B. Jurado-Sanchez, L. Vazquez, A. Escarpa, Carbon allotrope nanomaterials based catalytic micromotors, *Chem. Mater.* 28 (2016) 8962–8970.
- [30] A. Martín, B. Jurado-Sánchez, A. Escarpa, J. Wang, Template electrosynthesis of high-performance graphene microengines, *Small* 11 (2015) 3568–3574.
- [31] R. Maria-Hormigos, B. Jurado-Sánchez, A. Escarpa, Surfactant-free β -galactosidase micromotors for “On-The-Move” lactose hydrolysis, *Adv. Funct. Mater.* 28 (2018) 1704256.
- [32] R. Mariá-Hormigos, B. Jurado-Sánchez, A. Escarpa, Self-propelled micromotors for naked-eye detection of phenylenediamines isomers, *Anal. Chem.* 90 (2018) 9830–9837.
- [33] A. Molinero-Fernández, M. Moreno-Guzmán, M.A. López, A. Escarpa, Biosensing strategy for simultaneous and accurate quantitative analysis of mycotoxins in food samples using unmodified graphene micromotors, *Anal. Chem.* 89 (2017) 10850–10857.
- [34] B. Esteban-Fernández de Ávila, M.A. Lopez-Ramirez, D.F. Báez, A. Jodra, V.V. Singh, K. Kaufmann, J. Wang, Aptamer-modified graphene-based catalytic micromotors: off-on fluorescent detection of Ricin, *ACS Sens.* 1 (2016) 217–221.
- [35] B. Jurado-Sánchez, S. Sattayasamitsathit, W. Gao, L. Santos, Y. Fedorak, V.V. Singh, J. Orozco, M. Galarnyk, J. Wang, Self-propelled activated carbon Janus micromotors for efficient water purification, *Small* 11 (2015) 499–506.
- [36] B. Khezri, S.M. Beladi Mousavi, Z. Sofer, M. Pumera, Recyclable nanographene-based micromachines for the on-the-fly capture of nitroaromatic explosives, *Nanoscale* 11 (2019) 8825–8834.
- [37] D. Vilela, J. Parmar, Y. Zeng, Y. Zhao, S. Sánchez, Graphene-based microbots for toxic heavy metal removal and recovery from water, *Nano Lett.* 16 (2016) 2860–2866.
- [38] V.V. Singh, A. Martin, K. Kaufmann, S.D.S. de Oliveira, J. Wang, Zirconia/Graphene oxide hybrid micromotors for selective capture of nerve agents, *Chem. Mater.* 27 (2015) 8162–8169.
- [39] R. Maria-Hormigos, B. Jurado-Sanchez, A. Escarpa, Labs-on-a-chip meet self-propelled micromotors, *Lab Chip* 16 (2016) 2397–2407.
- [40] B. Khezri, S.M. Beladi Mousavi, L. Krejčová, Z. Heger, Z. Sofer, M. Pumera, Ultrafast electrochemical trigger drug delivery mechanism for nanographene micromachines, *Adv. Funct. Mater.* 29 (2019) 1806696.
- [41] K.M. Manesh, M. Cardona, R. Yuan, M. Clark, D. Kagan, S. Balasubramanian, J. Wang, Template-assisted fabrication of salt-independent catalytic tubular microengines, *ACS nano* 4 (2010) 1799–1804.
- [42] G.A. Ozin, I. Manners, S. Fournier-Bidoz, A. Arsenault, Dream nanomachines, *Adv. Mater.* 17 (2005) 3011–3018.
- [43] S. Sanchez, M. Pumera, Nanorobots: the ultimate wireless self-propelled sensing and actuating devices, *Chem. Asian J.* 4 (2009) 1402–1410.
- [44] A.A. Solovev, Y. Mei, E. Bermúdez Ureña, G. Huang, O.G. Schmidt, Catalytic microtubular jet engines self-propelled by accumulated gas bubbles, *Small* 5 (2009) 1688–1692.
- [45] S. Sengupta, M.E. Ibele, A. Sen, Fantastic voyage: designing self-powered nanorobots, *Angew. Chem. Int. Ed.* 51 (2012) 8434–8445.
- [46] J. Wang, *Nanomachines: Fundamentals and Applications*, Wiley VCH, 2013.
- [47] W. Wang, T.-Y. Chiang, D. Velegol, T.E. Mallouk, Understanding the efficiency of autonomous nano- and microscale motors, *J. Am. Chem. Soc.* 135 (2013) 10557–10565.
- [48] K. Yuan, V. de la Asunción-Nadal, Y. Li, B. Jurado-Sánchez, A. Escarpa, Graphdiyne micromotors in living biomedicine, *Chem. Eur. J.* 26 (38) (2020) 8471–8477.
- [49] Y.-P. Zheng, Q. Feng, N.-J. Tang, Y.-W. Du, Synthesis and photoluminescence of graphdiyne, *New Carbon Mater.* 33 (2018) 516–521.
- [50] Y. Shao, J. Wang, M. Engelhard, C. Wang, Y. Lin, Facile and controllable electrochemical reduction of graphene oxide and its applications, *J. Mater. Chem.* 20 (2010) 743–748.
- [51] Y. Xue, Z. Zuo, Y. Li, H. Liu, Y. Li, Graphdiyne-supported NiCoS nanowires: a highly active and stable 3D bifunctional electrode material, *Small* 13 (2017) 1700936.
- [52] G. Tian, Z. Qi, W. Ma, Y. Wang, On the catalytic activity of Pt supported by graphyne in the oxidation of ethanol, *Chem. Sel.* 2 (2017) 2311–2321.
- [53] H. Ren, H. Shao, L. Zhang, D. Guo, Q. Jin, R. Yu, L. Wang, Y. Li, Y. Wang, H. Zhao, D. Wang, A new graphdiyne nanosheet/Pt nanoparticle-based counter electrode material with enhanced catalytic activity for dye-sensitized solar cells, *Adv. Energy Mater.* 5 (2015) 1500296.
- [54] L. Li, J. Wang, T. Li, W. Song, G. Zhang, Hydrodynamics and propulsion mechanism of self-propelled catalytic micromotors: model and experiment, *Soft Matter* 10 (2014) 7511–7518.
- [55] J. Li, G. Huang, M. Ye, M. Li, R. Liu, Y. Mei, Dynamics of catalytic tubular microjet engines: Dependence on geometry and chemical environment, *Nanoscale* 3 (2011) 5083–5089.
- [56] V. de la Asunción-Nadal, B. Jurado-Sánchez, L. Vázquez, A. Escarpa, Magnetic fields enhanced the performance of tubular dichalcogenide micromotors at low hydrogen peroxide levels, *Chem. Eur. J.* 25 (2019) 13157–13163.
- [57] J. Wang, Cargo-towing synthetic nanomachines: towards active transport in microchip devices, *Lab Chip* 12 (2012) 1944–1950.
- [58] R. Maria-Hormigos, B. Jurado-Sánchez, A. Escarpa, Tailored magnetic carbon allotrope catalytic micromotors for ‘on-chip’ operations, *Nanoscale* 9 (2017) 6286–6290.
- [59] L. Zeng, J. Wu, Q. Dai, W. Liu, P. Wang, C.-S. Lee, Sensing of bacterial endotoxin in aqueous solution by supramolecular assembly of pyrene derivative, *Org. Lett.* 12 (2010) 4014–4017.
- [60] M. Cecconi, L. Evans, M. Levy, A. Rhodes, Sepsis and septic shock, *Lancet* 392 (2018) 75–87.
- [61] S.E. Greisman, R.B. Hornick, Comparative pyrogenic reactivity of rabbit and man to bacterial endotoxin, *Proc. Soc. Exp. Biol. Med.* 131 (1969) 1154–1158.

Supporting information

Graphdiyne tubular micromotors: electrosynthesis, characterization and self-propelled capabilities

Kaisong Yuan,^{a,b} Víctor de la Asunción-Nadal,^a Yuliang Li,^{c,d} Beatriz Jurado-Sánchez,^{a,e*} Alberto Escarpa^{a,e*}

^aDepartment of Analytical Chemistry, Physical Chemistry and Chemical Engineering, University of Alcalá, Alcalá de Henares E-28871, Madrid, Spain.

^bInstitute of Pharmaceutical Analysis, College of Pharmacy, Jinan University, Guangzhou, P. R. China.

^cBeijing National Laboratory for Molecular Sciences (BNLMS), CAS Key Laboratory of Organic Solids, Institute of Chemistry, CAS Research/Education Center for Excellence in Molecular Sciences, Chinese Academy of Sciences, Beijing 100190, P. R. China.

^dSchool of Chemistry and Chemical Engineering, University of Chinese Academy of Sciences, Beijing 100049, P. R. China.

^eChemical Research Institute "Andrés M. del Río", University of Alcalá, Alcalá de Henares E-28871, Madrid, Spain.

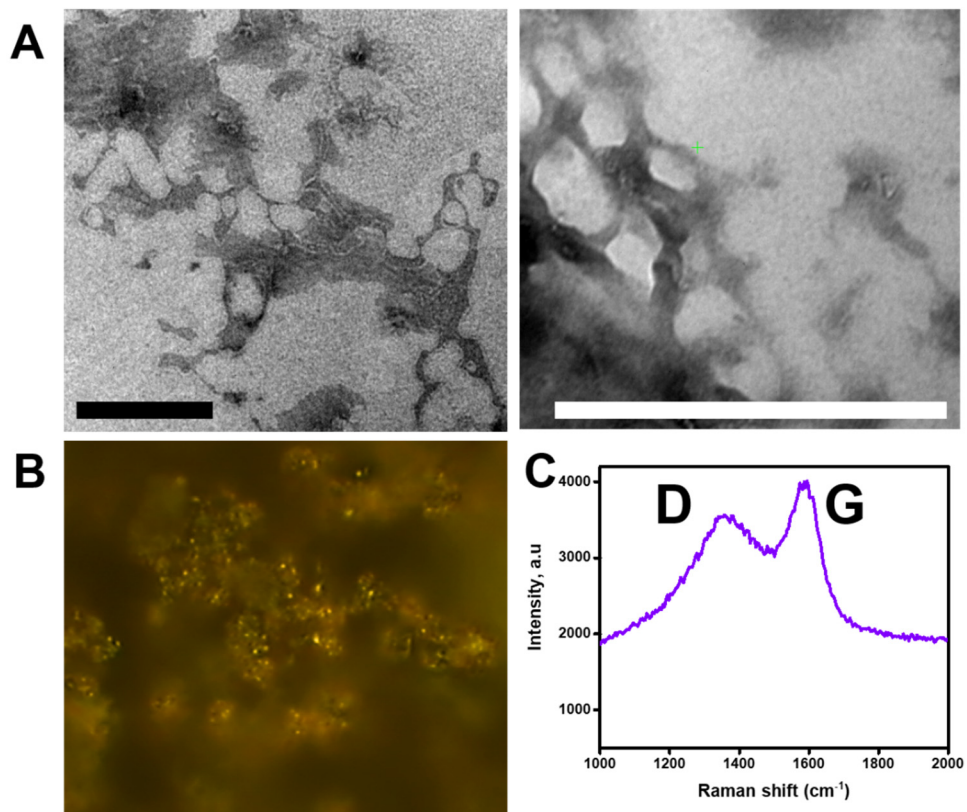


Figure S1. Graphdiyne (GDY) characterization by TEM (A), optical microscopy (B) and Raman (C). Scale bars, 500 nm

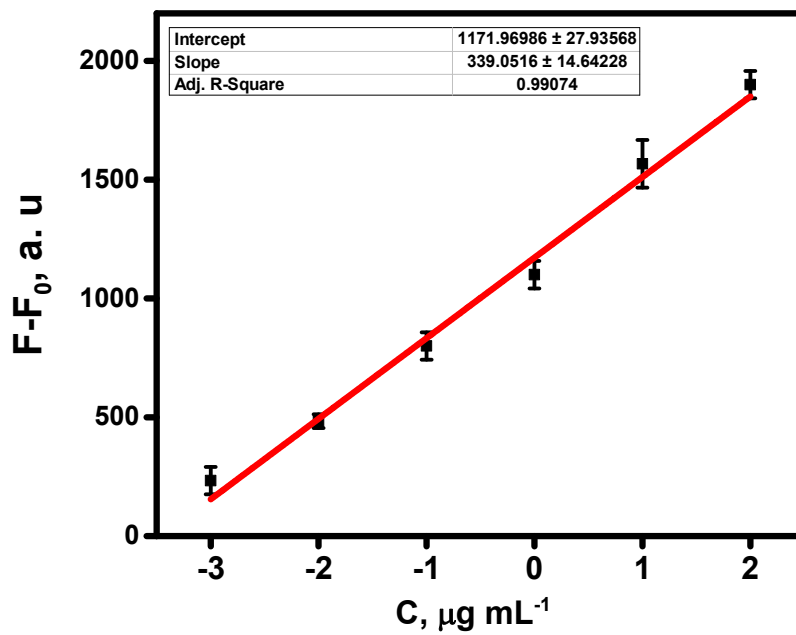
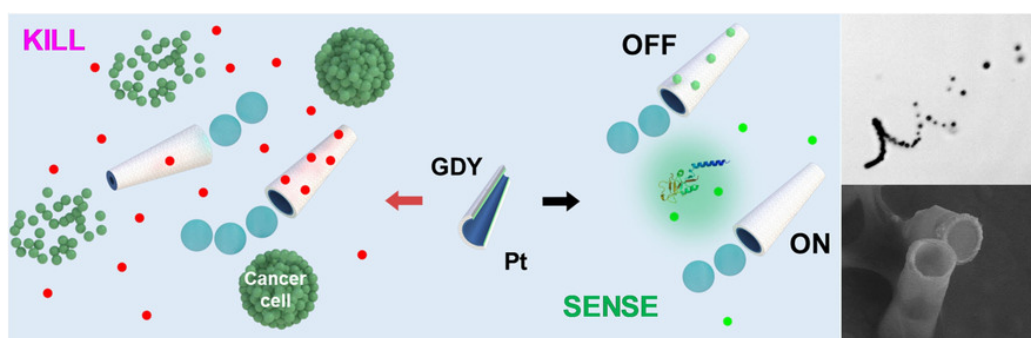


Figure S2. Calibration plot for the detection of *Escherichia coli* 0111:B4 using affinity peptide modified GDY micromotors.

V.1. Article 7. Graphdyne micromotors in living biomedica.



■ Micromotors

Graphdiyne Micromotors in Living Biomedica

Kaisong Yuan⁺,^[a, b] Victor de la Asunción-Nadal⁺,^[a] Yuliang Li,^[d, e] Beatriz Jurado-Sánchez,^{*[a, c]} and Alberto Escarpa^{*[a, c]}

Abstract: Graphdiyne (GDY), a new kind of two-dimensional (2D) material, was combined with micromotor technology for “on-the-fly” operations in complex biomedica. Microtubular structures were prepared by template deposition on membrane templates, resulting in functional structures rich in sp and sp² carbons with highly conjugated π networks. This resulted in a highly increased surface area for a higher loading of anticancer drugs or enhanced quenching ability over other 2D based micromotors, such as graphene oxide (GO) or smooth tubular micromotors. High biocompatibility with almost 100% cell viability was observed in cytotoxicity

assays with moving micromotors in the presence of HeLa cells. On a first example, GDY micromotors loaded with doxorubicin (DOX) were used for pH responsive release and HeLa cancer cells killing. The use of affinity peptide engineered GDY micromotors was also illustrated for highly sensitive and selective fluorescent OFF–ON detection of cholera toxin B through specific recognition of the subunit B region of the target toxin. The new developments illustrated here offer considerable promise for the use of GDY as part of micromotors in living biosystems.

Introduction

Current demands in biomedicine met in the fast development of nanotechnology a convenient solution to address unsolved challenges.^[1] The synthesis of novel nanomaterials allows for the generation of inorganic–organic hybrid nanoplatfoms for

diseases diagnosis, prognosis and therapy. In the current scenario, 2D nanomaterials display unique functional properties associated with their morphology, including high surface-area-to-mass-ratio and enhanced physicochemical properties.^[2] Indeed, 2D graphene is the most studied nanomaterial for drug delivery, photothermal therapy, biomarker sensing or tissue engineering applications.^[3] Yet, practical biomedical applications of graphene still face the important challenge of long-term accumulation in the body due to a low biodegradation rate, leading to potential biosafety issues.^[4] As an alternative, 2D graphene analogues such as transition metal dichalcogenides, carbon nitride, boron nitride or black phosphorous were exploited for diagnosis imaging, theragnostic and biosensing.^[1, 2, 5] In addition, preliminary biosafety assessments indicate the lower toxicity of such new nanomaterials over graphene.^[6] GDY is a novel 2D carbon nanomaterial with graphene-like structure integrating triangular rings containing 18 carbon atoms and two acetylenyl groups between neighboring benzene rings.^[7] As such, GDY contains both sp² and sp hybridized carbons. Such unique combination has been exploited in biomedical applications for “OFF–ON” DNA detection^[8] and enzymatic glucose sensing,^[9] where GDY exhibit higher adsorption capacity over graphene and other types of 2D nanomaterials for increased sensitivity.^[10] GDY also exhibit superior DOX loading capacity (by π stacking) and photothermal conversion ability in cancer cell treatment.^[11] A recent study has also revealed the improved biocompatibility and potential biosafety of GDY over graphene oxide related to the lack of aggregation in physiological conditions.^[12] Yet, GDY is still obtained at very low yields and is available actually at low quantities, hampering its practical applications. The combination of such material with micromotor technology is very relevant in this context,

[a] K. Yuan,⁺ V. de la Asunción-Nadal,⁺ Dr. B. Jurado-Sánchez, Prof. A. Escarpa
Department of Analytical Chemistry
Physical Chemistry, and Chemical Engineering
University of Alcala, Alcala de Henares, 28871 Madrid (Spain)
University of Alcala, 28807 Madrid (Spain)
E-mail: beatriz.jurado@uah.es
alberto.escarpa@uah.es

[b] K. Yuan⁺
Institute of Pharmaceutical Analysis
College of Pharmacy, Jinan University
Guangzhou (P. R. China)

[c] Dr. B. Jurado-Sánchez, Prof. A. Escarpa
Chemical Research Institute “Andres M. del Rio”
University of Alcala
28807 Madrid (Spain)

[d] Prof. Y. Li
Beijing National Laboratory for Molecular Sciences (BNLMS), CAS
Key Laboratory of Organic Solids, Institute of Chemistry, CAS
Research/Education Center for Excellence in Molecular Sciences
Chinese Academy of Sciences
Beijing 100190 (P. R. China)

[e] Prof. Y. Li
School of Chemistry and Chemical Engineering, University of
Chinese Academy of Sciences
Beijing 100049 (P. R. China)

[*] These authors contributed equally to this work.

Supporting information and the ORCID identification number(s) for the author(s) of this article can be found under:
<https://doi.org/10.1002/chem.202001754>.

since very low amount of the material is required for the preparation of thousands of micromotors, which display an efficient performance as will be further illustrated.

Self-propelled micromachines (or micromotors) are motile microparticles which can convert an energy input into an autonomous movement for controlled operations.^[13] The inherent moving nature of the micromotors allow for controlled transport to targeted areas or to enhanced biosensing processes in miniaturized environments.^[14] Such advantages have added a new dimension to the biomedical field for enhanced detoxification,^[15] antibiotic delivery^[16] or drug delivery.^[14e,17] For example, MoS₂ based tubular micromotors display enhanced capabilities for DOX loading and release as well as for immobilization of dye-labeled probes for DNA detection.^[18] Graphene coated gold nanowires propelled by ultrasound are capable to penetrate cancer cells for selective miRNA detection.^[19] Nanographene/Pt tubular micromotors have been used for DOX loading and electrochemical controlled release for enhanced and localized T-47D breast cancer cell growth inhibition and killing.^[20] Despite the proven potential of the binomial 2D nanomaterials-micromotors for practical biomedical applications, the topic remains largely unexplored.

In this work, we will illustrate the use of GDY based micromotors for controlled drug delivery in cancer cell growth inhibition and sensing of toxins, taking advantage of the inherent remarkable performance and low toxicity of GDY in biomedical applications. To the best of our knowledge, this is the first time that this novel carbon allotrope is used in connection with micromotor technology. Another novelty is the evaluation of the performance in living media such as cancer cell environment or biological fluids. We will illustrate the superior DOX loading capacity of the micromotors (in connection with the unique GDY structure) compared with graphene or polymeric micromotors and the pH-responsive drug release for HeLa cancer cells inhibition and killing. Cytotoxicity assays will also demonstrate the high biocompatibility of the micromotors for future practical biomedical applications. The superior GDY loading capacity will be also proven for “OFF–ON” detection of cholera toxin B in complex bio-media as representative biomarker using GDY micromotors engineered with a fluorescent labeled affinity peptide specifically designed to target a specific region (subunit B) of the target toxin (see Figure 1).

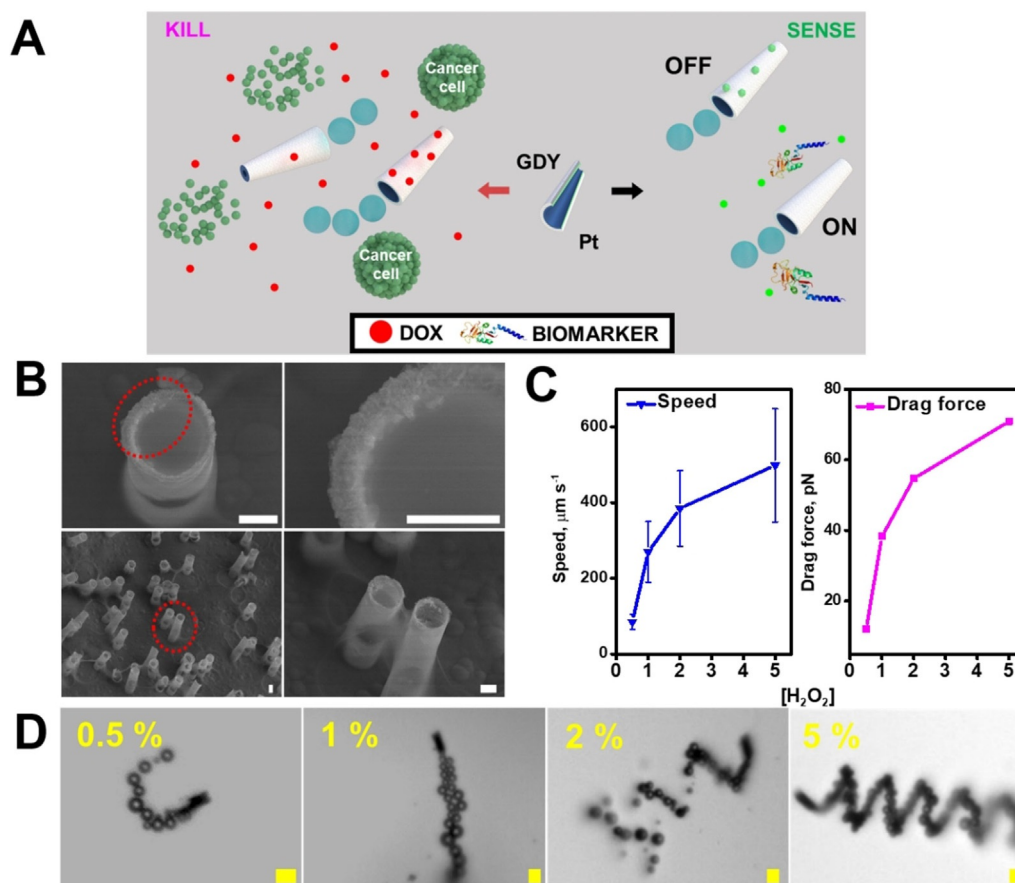


Figure 1. (A) Schematic of the GDY-Ni/Pt micromotors for DOX delivery and cancer cell killing (left) and fluorescent “OFF–ON” sensing of toxins (right). (B) Scanning electron microscopy (SEM) images showing the conical morphology and rough inner layer of the GDY micromotors. (C) Speed profile and drag force of the micromotors at different peroxide levels and (D) Time-lapse images of the propulsion of the micromotors at different peroxide levels. Scale bars, 5 μm.

Results and Discussion

Figure 1 illustrates the concept of GDY micromotors for cancer cell killing and toxin detection. The micromotors were prepared by controlled growth of tubular structures into the pores of a membrane template (see Supporting Information for further details). To prove the concept and the capabilities of dynamic GDY micromotors for cancer cell killing and enhanced sensing, Pt was used as inner catalytic layer. The application of a cyclic potential to the GDY solution results in the reduction of the oxygen moieties in a graphene-like electrodeposition profile (see Figure S1A), creating aggregates of the material, which tend to bind them together through π -interactions and deposit ultimately into the pores of the membrane template, creating an ordered film.^[21] Figure 1B illustrates the conical morphology of the resulting GDY micromotors, with a rough inner Pt patch due to the presence of defects and edges in the inner GDY micromotors, which results in an increased surface for the subsequent deposition on highly active inner catalytic layer for propulsion at low peroxide levels.

Figure S1B shows atomic-force microscopy images of the resulting microtubes, illustrating the rough outer (an, in turn, inner) morphologies with crest and valleys. Thus, as shown in Figure 1C and D, micromotors can propel at speeds up to $100 \mu\text{m s}^{-1}$ in 0.5% peroxide solutions, which correspond to a large drag force of 10 pN. The resulting micromotors retain the properties of GDY, with the additional advantage of the efficient movement of the micromotors for localized operations and enhanced reaction kinetics, as will be further illustrated. The resulting properties of the microtubes and the potential influence of the electrodeposition process on the surface characteristics of the GDY were evaluated by energy-ray dispersive mapping and Raman spectroscopy (see Figure S1C and D). Uniform element distribution is observed, with the clear presence of D and G bands. All the Raman spectra show the two most prominent peaks at 1380 cm^{-1} and 1600 cm^{-1} for both pristine GDY and GDY micromotors. The peak at 1600 cm^{-1} indicates the first-order scattering of the E_{2g} mode for in-phase stretching vibration sp^2 carbon domains in aromatic rings or G band. The peak at 1380 cm^{-1} corresponds to the D band and arises from the breathing vibration of sp^2 carbon domains in aromatic rings. The D band is more pronounced in the pristine material as compared with the micromotor, but its presence in both cases is associated with the presence of structural defects, and edges. The D/G intensity ratio is 0.9 and 1.0, for pristine GDY and the micromotors, respectively; further revealing the high order of the structure and the presence of multilayers of the material.^[22] Such rich outer surface chemistry, with the presence of sp -atoms and aromatic rings, allows for the easy modification and functionalization with a myriad of biomolecules and drugs used in the biomedical field, as described below.

The 2D material properties of GDY—now integrated into the micromotors—such as high surface area and multiple functional groups, make it an ideal candidate to load DOX via π -stacking and electrostatic interactions.^[11] The capacity of our micro-

motors for DOX loading-release was evaluated for HeLa cancer cells treatment (see Figure 2).

As previously described by Raman observation, GDY micromotors contain sp^2 hybridized carbons along with two acetylenic linkages between the carbon atoms adjacent to the hexagons in the structure. Such highly conjugated network contains a high density of π electrons. This grants GDY with π - π bonding nature for improved DOX loading capacity. To demonstrate such assumption, GDY micromotors ($\approx 500\,000$ motors) were incubated overnight with DOX solution ($600 \mu\text{mol L}^{-1}$). Control experiments were also performed using graphene and PEDOT based micromotors (see Experimental Section in the Supporting Information for further details). Micromotors were separated from the supernatant by centrifugation. Micromotors were then cleaned with PBS (pH 8.0) three times. DOX loading was estimated by recording the UV/Vis spectra of DOX control solution and the remaining supernatant in each micromotor batch after centrifugation. Next, the release capacity was tested by changing the pH of the media from 8.0 to 5.0, which resulted in the protonation of the amino group in DOX, enhancing the solubility in water and promoting the release from GDY, GO or PEDOT surface. The pH-induced release is a well-proven strategy for drug release in the acidic microenvironment surrounding cancerous tissues.^[23] Similarly, UV/Vis measurements were performed to estimate the percent of DOX release. Additional fluorescent microscopy images were also recorded. Thus, as can be seen in Figure 2A, higher fluorescent intensity was observed after DOX release from GDY and GO-based micromotors, as compared with PEDOT micromotors. The UV/Vis spectra of Figure 2B, further indicate a higher release capacity of GDY over GO and PEDOT, as reflected by the higher absorbance. The increased surface area of GDY micromotors is also reflected in the higher loading (50%) and release DOX capacity (20%) as compared with GO (45% loading, 15% release) and PEDOT (30% loading, 5% release) micromotors. Such release capacity is slightly lower than that observed for 2D-based MoS_2 tubular micromotors (38%)^[18] but higher than the one reported for GDY nanosheets (16%).^[11] Additional means for DOX triggered release comprise electrochemical triggering,^[20] ultrasound,^[24] NIR light,^[25] or mechanical triggered after delivery to the target location.^[26] The above-mentioned strategies show high efficiency for cancer cell inhibition growth but require additional means apart from pH changes for drug release.

Next, to demonstrate the potential of the micromotors for enhanced drug delivery, we performed *in vitro* cytotoxicity studies using HeLa cancer cells with the 3-(4,5-dimethylthiazol-2-yl)-2,5-diphenyltetrazolium bromide (MTT) assay. To this end, DOX modified and unmodified micromotors were co-incubated with HeLa cells using 167,000 modified and unmodified motors and 0.5 mmol L^{-1} DOX (per plate). For experiments with moving micromotors, 0.5% H_2O_2 solutions were used without the addition of surfactant. The plates were incubated overnight and the conversion of MTT into formazan by active cells was assessed by the change in absorbance at 570/630 nm using a microplate reader. As shown in Figure 2C, moving unmodified GDY micromotors (0.5% H_2O_2) showed non-signifi-

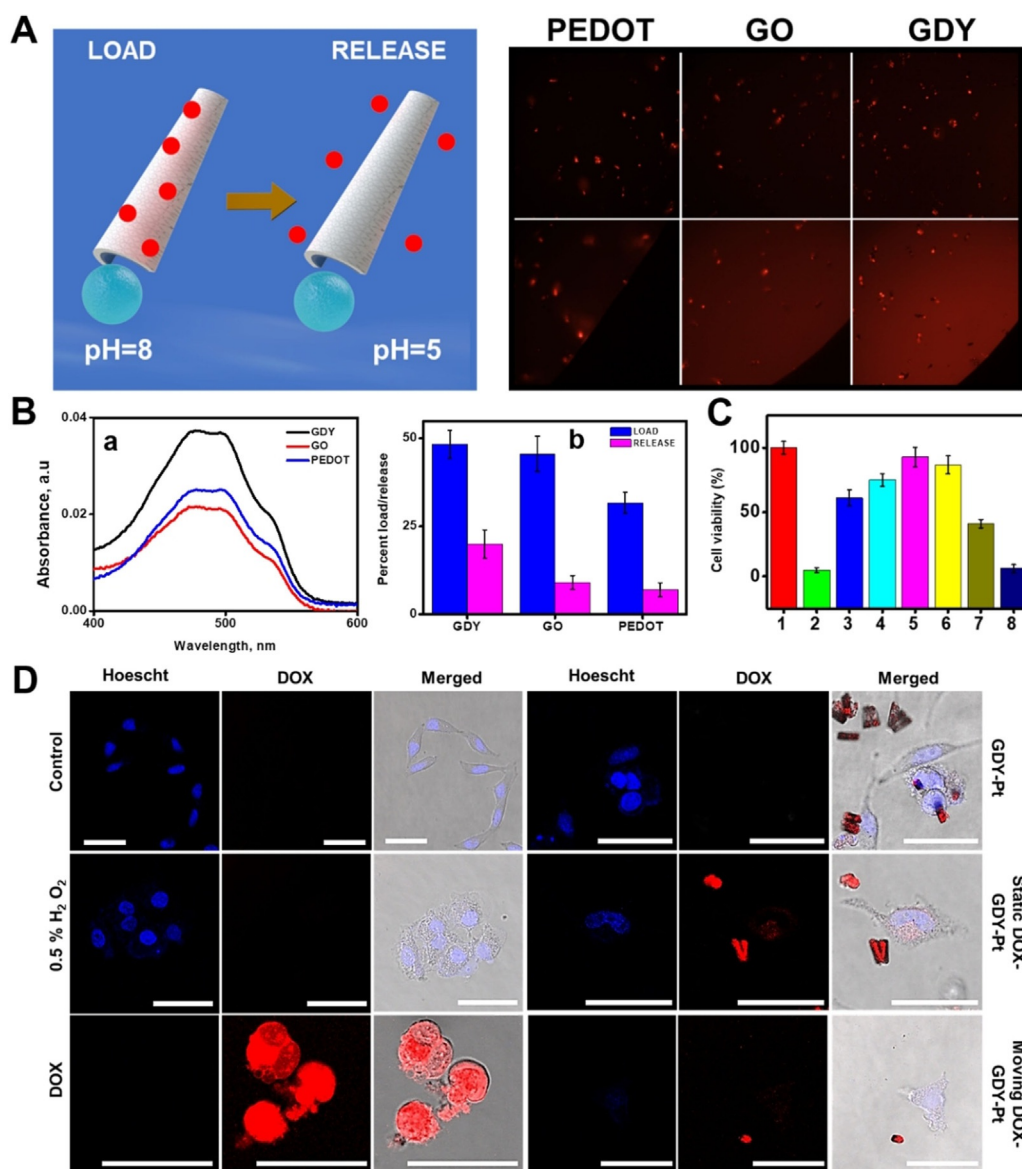


Figure 2. Cancer cell killing ability of DOX loaded GDY/Pt micromotors at low peroxide (0.5%) levels. (A) Schematic of the pH-sensitive DOX loading/release mechanism and corresponding time-lapse images of DOX loaded GDY, GO and PEDOT micromotors solutions before (top) and after (bottom) release. (B) Loading capacity of GDY-Ni/Pt micromotors: absorbance spectra of the different micromotors systems after DOX release and (a) graph showing the corresponding percent/loading release in each system (b). (C) MTT assay of control HeLa cells (1) and HeLa cells treated with free DOX (2); 1% H₂O₂ (3); 0.5% H₂O₂ (4); 0.1% H₂O₂ (5); GDY/Pt micromotors propelling at 0.5% H₂O₂ (6); static DOX-GDY/Pt micromotors (7) and DOX-GDY/Pt micromotors propelling at 0.5% H₂O₂ (8). (D) Confocal fluorescent microscopy images illustrating the in vitro cancer cell killing ability of GDY micromotors and control experiments. Nuclei were dyed with Hoechst 33256 (blue) while DOX channel was also recorded (red). Scale bars, 50 μm.

cant cytotoxicity to the cells (graph bar 6), indicating its future suitability for biomedical applications. In addition, low concentrations of peroxide (0.1 and 0.5%) has little effect on the HeLa cells, with almost 100% viability (graph bars 4 and 5). On the contrary, free-DOX (graph bar 2) and DOX loaded micromotors (graph bar 8) shows high toxicity, with only 1% of HeLa cells viability using free DOX and moving micromotors. In the case of static micromotors loaded with DOX, the viability of the cells is almost 50% (graph bar 7). This data indicates the suitability of the pH triggering mechanism for the release of DOX and the role of micromotor enhanced movement to increase the mixing among DOX and cancer cells, as lower concentra-

tion is required (as compared with free DOX) to produce similar effects.

Additional living cell fluorescent imaging was performed to test the ability of the micromotors to inactivate and kill cancer cells (see Figure 2D). The HeLa cells were treated with free DOX, unmodified micromotors and DOX modified micromotors under moving and static conditions. After 24 h treatment, the cell nuclei were stained with Hoechst 33256. The DOX channel was also monitored to estimate its accumulation in the intracellular region. In the case of control experiments (in the absence of DOX) the nuclei can be easily visualized, with an intense blue fluorescent emission and full integrity of the cancer

cells with a widely distributed population. The images are equivalent to that obtained by using unmodified GDY micromotors, further revealing its high biocompatibility. Low toxicity is also noted after cells contacting with 0.5% hydrogen peroxide, which can be further used for experiments with moving micromotors. Dramatic changes are observed when using free DOX, with complete cell death and the absence of Hoechst channel. For static micromotors with DOX, low cell viability is observed, with low intensity of Hoechst in the nuclei and some DOX penetration into the cells. In the case of DOX moving micromotors, dramatic cell death was produced, as revealed by the merged microscopy images, with one cell nuclei completely stained with DOX. Such a result indicates the suitability of GDY micromotors for localized and controlled drug transportation and release with reduced side effects.

The rich outer surface chemistry of GDY micromotors allows for the immobilization of alternative cancer treatment drugs for a myriad of personalized applications with reduced side effects. The unique properties of the 2D nanomaterial, along with its biocompatibility, allows for its use as a nanoquencher for dye-labeled probes for future biosensing applications. The unique structural characteristics of GDY along with its superior surface area have shown to be particularly suitable for DNA sensing with fluorescent-based approaches. In addition, previous studies indicate stronger probe adsorption on GDY over graphene, with a superior capture-quenching ability, resulting in an improved sensitivity over other 2D materials.^[8,27] Inspired by this, we extended our GDY micromotor strategy in another important biomedical application such as biomarkers detection. To prove the potential of the GDY micromotors, cholera toxin B was chosen as a target analyte. Such toxin is produced by *Vibrio cholerae* bacteria and is considered as one of the major virulence factors, causing diarrhea and associated adverse health effects in humans. The toxin is composed by two-subunits (A and B), that can be selectively chosen to develop specific probes for the detection of the toxin. In this work, cholera toxin B subunit (CTB) was chosen as target analyte due to it can provide information not only about the presence of cholera toxin but also help to develop and monitor the efficacy of treatment (i.e., vaccines) against such disease.^[28] In addition, the non-toxic nature of the sub-unit assures safe manipulation in the laboratory without requirements of qualified personnel or infrastructures. A synthetic affinity peptide (VQCRLGPPWCAK) labeled with Rhodamine B was used as a highly specific probe for GDY micromotor functionalization, offering a convenient alternative to antibodies, with low cost, improved reproducibility and higher stability.^[29]

The strategy followed for CTB detection is depicted in Figure 3A. On a first step, GDY micromotors were modified by mixing 100 μL of the specific peptide (100 $\mu\text{g mL}^{-1}$) with 1 batch of dry motors (approx. 500 000 motors), 150 μL of sodium dodecyl sulfate 3% and 200 μL of ACN:H₂O₂ 1:3, for 1 hour. The peptide solution initially displays a strong fluorescent intensity (in Figure 3A), which is quenched after interaction with the outer surface of the GDY micromotors via physical adsorption through electrostatic and π -stacking with the different aromatic with the non-polar and aromatic amino

acids present in the peptide, such as Try, Val, Arg, Cys, Leu, Gly, Pro and Ala, and through the π orbitals overlapping with the aromatic rhodamine B tag. Fluorescent resonance energy transfer from the dye excited state to the π system of GDY results in such fluorescent quenching (b in Figure 3A).^[2b,27,30] As a second step, 1 μL of the modified motors were mixed with the target CTB and 1 μL of 3% H₂O₂ for efficient propulsion. Strong fluorescent emission is observed after 5 min micromotor navigation, due to a competitive binding between the peptide, which displays a higher affinity for the CTB, and the GDY surface. This results in a release of the dye-labeled peptide from the GDY surface (see also Figure 3B). Low fluorescent recovery (20%) was observed in experiments with static micromotors (not shown), further revealing the role of the enhanced micromotor movement in the detection. It should be noted here that, as in the case of DOX loading, GDY micromotors display higher loading capacity for the peptide in comparison with GO and PEDOT control micromotors, as testified in Figure 3C. In addition, control experiments with endotoxins from *Escherichia coli* O111:B4 and BSA testified the high selectivity of the protocol, as not fluorescent recovery is observed even after 4 hours incubation; in contrast with the high fluorescent intensity after 10 min incubation with the target CTB. Next, calibration plots were performed in order to evaluate the analytical properties of the developed biosensing approach (see Figure 3E). Excellent linear range within 4 and 1700 ng mL^{-1} of CTB is obtained. The limit of detection (LOD), calculated as 3 times the standard deviation of the blank divided by the slope of the calibration plot, correspond to a concentration of 1.2 ng mL^{-1} . Such a value is much lower than the physiological concentration of cholera toxin in ill patients, revealing the suitability for future diagnosis of such disease.^[29]

Conclusions

In summary, we have illustrated, for the first time, the potential of 2D GDY based micromotors for biomedical applications. The unique structure of GDY, which combines sp and sp² carbon atoms and a high conjugated π network, results in a highly increased surface area for a higher loading of anticancer drugs or enhanced quenching ability over other 2D material based micromotors, such as GO or smooth tubular micromotors. The high conductive nature of GDY, along with the presence of high density of defects, results in the electrodeposition of rough inner catalytic layer an efficient micromotor operation at low (0.5%) peroxide levels. High biocompatibility with almost 100% cell viability was observed in cytotoxicity assays with moving micromotors in the presence of HeLa cells. The resulting dynamic platforms combine the excellent surface properties of GDY along with the dynamic movement of micromotors for targeted delivery and controlled release operations to desired destination. This capacity was illustrated for controlled DOX delivery in the acidic environment of cancer cell by pH-triggered release. The micromotors showed excellent capabilities to inactivate HeLa cells, which are comparable to the use of free DOX but with the additional advantage of a reduced dose and localized delivery to hinder potential side effects. As

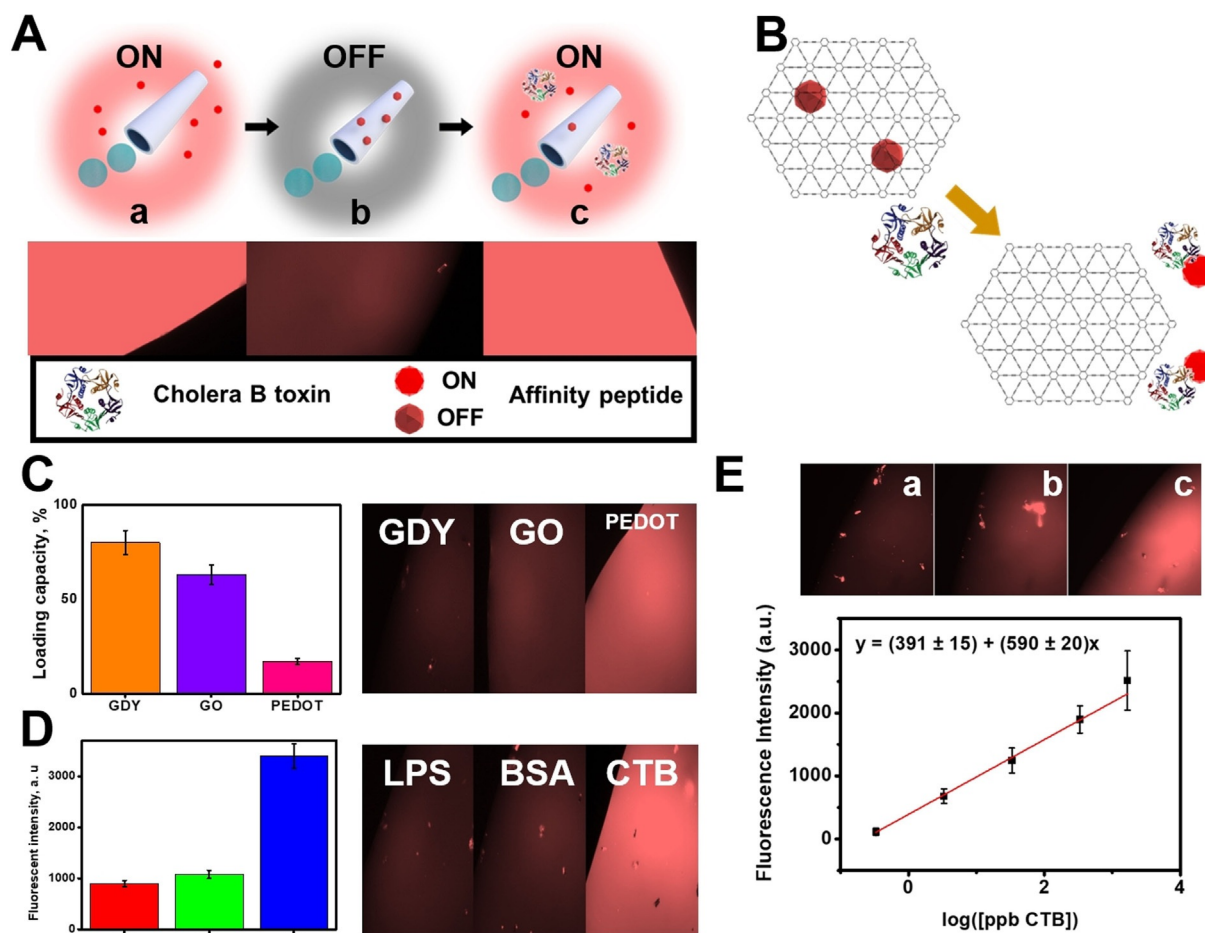


Figure 3. CTB fluorescent “OFF–ON” sensing using affinity peptide-functionalized GDY-Ni/Pt micromotors. (A) Schematic of the detection strategy involving micromotor incubation with Rhodamine B labeled VQCRLGPPWCAK affinity peptide (a); loading and fluorescent quenching of the peptide through π - π interactions (b) and specific release and fluorescent recovery after navigation in CTB contaminated solutions (c). Bottom part shows the corresponding fluorescent images of each step. (B) Schematic on the interactions between the affinity peptide and the GDY outer micromotor surface. (C) Comparison of the affinity peptide loading capacity using GDY-Ni/Pt, GO-Ni/Pt and PEDOT-Ni/Pt micromotors and corresponding time-lapse fluorescent images. (D) Selectivity of the detection protocol of peptide-modified graphdiyne micromotors navigating in solutions containing 330 ng mL⁻¹ of lipopolysaccharide (LPS) from *Escherichia coli* O111:B4, 330 ng mL⁻¹ of bovine serum albumin (BSA) and 330 ng mL⁻¹ of CTB. (E) Method's calibration plot. Top part shows the fluorescent microscopy images corresponding to peptide-loaded micromotor solutions after navigation in samples containing 0.3 (a), 3.3 (b) and 1660 (c) ng mL⁻¹ of CTB. Conditions, 3% H₂O₂.

a second application, the excellent quenching abilities of the GDY micromotors are illustrated for “OFF–ON” fluorescent detection of relevant toxins with specifically designed affinity peptides. Some important challenges still remain, and the most important one is the translation from experimental findings to clinical practice, which requires additional compatibility studies and in vivo testing. Yet, the remarkable performance of GDY in connection with micromotor technology offers promising capabilities in the biomedical field for many future applications.

Acknowledgements

K.Y. acknowledges the Spanish Ministry of Economy, Industry and Competitiveness for his pre-doctoral contract (RYC-2015-17558, co-financed by EU). V.A.-N. acknowledges the FPI fellowship received from the University of Alcalá. B.J-S acknowledges

support from the Spanish Ministry of Economy, Industry and Competitiveness (RYC-2015-17558, co-financed by EU) from the University of Alcalá (CCG19/CC-029) and from the Community of Madrid (CM/JIN/2019-007). A.E. acknowledges financial support from the Spanish Ministry of Economy, Industry and Competitiveness (CTQ2017-86441-C2-1-R) and the TRANS-NANOAVANSENS program (S2018/NMT-4349) from the Community of Madrid.

Conflict of interest

The authors declare no conflict of interest.

Keywords: 2D materials · drug delivery · graphdiyne · micromotors · toxin

- [1] Y. Chen, C. Tan, H. Zhang, L. Wang, *Chem. Soc. Rev.* **2015**, *44*, 2681–2701.
- [2] a) R. Kurapati, K. Kostarelos, M. Prato, A. Bianco, *Adv. Mater.* **2016**, *28*, 6052–6074; b) E. Campbell, M. T. Hasan, C. Pho, K. Callaghan, G. R. Akkaraju, A. V. Naumov, *Sci. Rep.* **2019**, *9*, 416.
- [3] a) C. Chung, Y.-K. Kim, D. Shin, S.-R. Ryoo, B. H. Hong, D.-H. Min, *Acc. Chem. Res.* **2013**, *46*, 2211–2224; b) I. de Lázaro, S. Vranic, D. Marson, A. F. Rodrigues, M. Buggio, A. Esteban-Arranz, M. Mazza, P. Posocco, K. Kostarelos, *Nanoscale* **2019**, *11*, 13863–13877; c) Z. Tu, H. Qiao, Y. Yan, G. Guday, W. Chen, M. Adeli, R. Haag, *Angew. Chem. Int. Ed.* **2018**, *57*, 11198–11202; *Angew. Chem.* **2018**, *130*, 11368–11372; d) X. Zhu, Y. Liu, P. Li, Z. Nie, J. Li, *Analyst* **2016**, *141*, 4541–4553.
- [4] C. Martín, K. Kostarelos, M. Prato, A. Bianco, *Chem. Commun.* **2019**, *55*, 5540–5546.
- [5] a) D. Chimene, D. L. Alge, A. K. Gaharwar, *Adv. Mater.* **2015**, *27*, 7261–7284; b) H. U. Lee, S. Y. Park, S. C. Lee, S. Choi, S. Seo, H. Kim, J. Won, K. Choi, K. S. Kang, H. G. Park, H.-S. Kim, H. R. An, K.-H. Jeong, Y.-C. Lee, J. Lee, *Small* **2016**, *12*, 214–219.
- [6] a) W. Yin, L. Yan, J. Yu, G. Tian, L. Zhou, X. Zheng, X. Zhang, Y. Yong, J. Li, Z. Gu, Y. Zhao, *ACS nano* **2014**, *8*, 6922–6933; b) S. S. Chou, B. Kaehr, J. Kim, B. M. Foley, M. De, P. E. Hopkins, J. Huang, C. J. Brinker, V. P. Dravid, *Angew. Chem. Int. Ed.* **2013**, *52*, 4160–4164; *Angew. Chem.* **2013**, *125*, 4254–4258; c) W. Z. Teo, E. L. K. Chng, Z. Sofer, M. Pumera, *Chem. Eur. J.* **2014**, *20*, 9627–9632.
- [7] Z. Jia, Y. Li, Z. Zuo, H. Liu, C. Huang, Y. Li, *Acc. Chem. Res.* **2017**, *50*, 2470–2478.
- [8] C. Wang, P. Yu, S. Guo, L. Mao, H. Liu, Y. Li, *Chem. Commun.* **2016**, *52*, 5629–5632.
- [9] J. Liu, X. Shen, D. Baimanov, L. Wang, Y. Xiao, H. Liu, Y. Li, X. Gao, Y. Zhao, C. Chen, *ACS Appl. Mater. Interfaces* **2019**, *11*, 2647–2654.
- [10] J. Liu, C. Chen, Y. Zhao, *Adv. Mater.* **2019**, *31*, 1804386.
- [11] J. Jin, M. Guo, J. Liu, J. Liu, H. Zhou, J. Li, L. Wang, H. Liu, Y. Li, Y. Zhao, C. Chen, *ACS Appl. Mater. Interfaces* **2018**, *10*, 8436–8442.
- [12] T. Zheng, Y. Gao, X. Deng, H. Liu, J. Liu, R. Liu, J. Shao, Y. Li, L. Jia, *ACS Appl. Mater. Interfaces* **2018**, *10*, 32946–32954.
- [13] a) W. F. Paxton, K. C. Kistler, C. C. Olmeda, A. Sen, S. K. St. Angelo, Y. Cao, T. E. Mallouk, P. E. Lammert, V. H. Crespi, *J. Am. Chem. Soc.* **2004**, *126*, 13424–13431; b) G. A. Ozin, I. Manners, S. Fourrier-Bidoz, A. Arsenault, *Adv. Mater.* **2005**, *17*, 3011–3018; c) W. Gao, S. Sattayasamitsathit, J. Orozco, J. Wang, *J. Am. Chem. Soc.* **2011**, *133*, 11862–11864; d) Y. Mei, A. A. Solovov, S. Sanchez, O. G. Schmidt, *Chem. Soc. Rev.* **2011**, *40*, 2109–2119; e) W. Wang, T.-Y. Chiang, D. Velegol, T. E. Mallouk, *J. Am. Chem. Soc.* **2013**, *135*, 10557–10565.
- [14] a) J. Li, B. Esteban-Fernández de Ávila, W. Gao, L. Zhang, J. Wang, *Sci. Robot.* **2017**, *2*, eaam6431; b) S. Campuzano, B. Esteban-Fernández de Ávila, P. Yáñez-Sedeño, J. M. Pingarrón, J. Wang, *Chem. Sci.* **2017**, *8*, 6750–6763; c) M. A. Ramos-Docampo, M. Fernández-Medina, E. Taipaleenmäki, O. Hovorka, V. Salgueiriño, B. Städler, *ACS Nano* **2019**, *13*, 12192–12205; d) Z. Wu, J. Troll, H.-H. Jeong, Q. Wei, M. Stang, F. Ziemssen, Z. Wang, M. Dong, S. Schnichels, T. Qiu, P. Fischer, *Sci. Adv.* **2018**, *4*, eaat4388; e) D. Xu, Y. Wang, C. Liang, Y. You, S. Sanchez, X. Ma, *Small* **2015**, *11*, 1902464; f) T. Patino, A. Porchetta, A. Jannasch, A. Lladó, T. Stumpp, E. Schäffer, F. Ricci, S. Sánchez, *Nano Lett.* **2019**, *19*, 3440–3447; g) B. Esteban-Fernández de Ávila, W. Gao, E. Karshalev, L. Zhang, J. Wang, *Acc. Chem. Res.* **2018**, *51*, 1901–1910; h) L. K. E. A. Abdelmohsen, F. Peng, Y. Tu, D. A. Wilson, *J. Mater. Chem. B* **2014**, *2*, 2395–2408; i) X. Wang, X.-Z. Chen, C. C. J. Alcántara, S. Sevim, M. Hoop, A. Terzopoulou, C. de Marco, C. Hu, A. J. de Mello, P. Falcaro, S. Furukawa, B. J. Nelson, J. Puigmartí-Luis, S. Pané, *Adv. Mater.* **2019**, *31*, 1901592.
- [15] a) B. Esteban-Fernández de Ávila, P. Angsantikul, D. E. Ramírez-Herrera, F. Soto, H. Teymourian, D. Dehaini, Y. Chen, L. Zhang, J. Wang, *Sci. Robot.* **2018**, *3*, eaat0485; b) F. Zhang, R. Mundaca-Urbe, H. Gong, B. Esteban-Fernández de Ávila, M. Beltrán-Gastélum, E. Karshalev, A. Nourhani, Y. Tong, B. Nguyen, M. Gallot, Y. Zhang, L. Zhang, J. Wang, *Adv. Mater.* **2019**, *31*, 1901828.
- [16] a) X. Wei, M. Beltrán-Gastélum, E. Karshalev, B. Esteban-Fernández de Ávila, J. Zhou, D. Ran, P. Angsantikul, R. H. Fang, J. Wang, L. Zhang, *Nano Lett.* **2019**, *19*, 1914–1921; b) B. Esteban-Fernández de Ávila, P. Angsantikul, J. Li, M. Angel Lopez-Ramirez, D. E. Ramírez-Herrera, S. Thamphiwatana, C. Chen, J. Delezuk, R. Samakapiruk, V. Ramez, M. Obonyo, L. Zhang, J. Wang, *Nat. Commun.* **2017**, *8*, 272.
- [17] a) N. Hu, M. Sun, X. Lin, C. Gao, B. Zhang, C. Zheng, H. Xie, Q. He, *Adv. Funct. Mater.* **2018**, *28*, 1705684; b) X. Lin, Z. Wu, Y. Wu, M. Xuan, Q. He, *Adv. Mater.* **2016**, *28*, 1060–1072.
- [18] V. V. Singh, K. Kaufmann, B. E.-F. de Ávila, E. Karshalev, J. Wang, *Adv. Funct. Mater.* **2016**, *26*, 6270–6278.
- [19] B. Esteban-Fernández de Ávila, A. Martín, F. Soto, M. A. Lopez-Ramirez, S. Campuzano, G. M. Vásquez-Machado, W. Gao, L. Zhang, J. Wang, *ACS nano* **2015**, *9*, 6756–6764.
- [20] B. Khezri, S. M. Beladi Mousavi, L. Krejčová, Z. Heger, Z. Sofer, M. Pumera, *Adv. Funct. Mater.* **2019**, *29*, 1806696.
- [21] A. Martín, B. Jurado-Sánchez, A. Escarpa, J. Wang, *Small* **2015**, *11*, 3568–3574.
- [22] a) G. Li, Y. Li, H. Liu, Y. Guo, Y. Li, D. Zhu, *Chem. Commun.* **2010**, *46*, 3256–3258; b) L. Lin, H. Pan, Y. Chen, X. Song, J. Xu, H. Liu, S. Tang, Y. Du, N. Tang, *Carbon* **2019**, *143*, 8–13.
- [23] a) M. Mahdavi, F. Rahmani, S. Nouranian, *J. Mater. Chem. B* **2016**, *4*, 7441–7451; b) Y. Wang, Z. Xu, *RSC Adv.* **2016**, *6*, 314–322.
- [24] Z. Wu, Y. Wu, W. He, X. Lin, J. Sun, Q. He, *Angew. Chem. Int. Ed.* **2013**, *52*, 7000–7003; *Angew. Chem.* **2013**, *125*, 7138–7141.
- [25] Y. Wu, X. Lin, Z. Wu, H. Möhwald, Q. He, *ACS Appl. Mater. Interfaces* **2014**, *6*, 10476–10481.
- [26] H. Xu, M. Medina-Sánchez, V. Magdanz, L. Schwarz, F. Hebenstreit, O. G. Schmidt, *ACS Nano* **2018**, *12*, 327–337.
- [27] N. Parvin, Q. Jin, Y. Wei, R. Yu, B. Zheng, L. Huang, Y. Zhang, L. Wang, H. Zhang, M. Gao, H. Zhao, W. Hu, Y. Li, D. Wang, *Adv. Mater.* **2017**, *29*, 1606755.
- [28] J. D. Clemens, G. B. Nair, T. Ahmed, F. Qadri, J. Holmgren, *Lancet* **2017**, *390*, 1539–1549.
- [29] J. M. Lim, N. S. Heo, S. Y. Oh, M. Y. Ryu, J. H. Seo, T. J. Park, Y. S. Huh, J. P. Park, *Biosens. Bioelectron.* **2018**, *99*, 289–295.
- [30] a) S. K. Lim, P. Chen, F. L. Lee, S. Mochhala, B. Liedberg, *Anal. Chem.* **2015**, *87*, 9408–9412; b) C. Zhang, Y. Yuan, S. Zhang, Y. Wang, Z. Liu, *Angew. Chem. Int. Ed.* **2011**, *50*, 6851–6854; *Angew. Chem.* **2011**, *123*, 6983–6986.

Manuscript received: April 10, 2020

Accepted manuscript online: April 15, 2020

Version of record online: June 16, 2020

Chemistry–A European Journal

Supporting Information

Graphdiyne Micromotors in Living Biomedica

Kaisong Yuan^{+, [a, c]} Victor de la Asunción-Nadal^{+, [a]} Yuliang Li,^[d, e] Beatriz Jurado-Sánchez,^{*[a, b]}
and Alberto Escarpa^{*[a, b]}

Experimental Procedures

Chemicals. The affinity peptides of Cholera Toxin B (sequence: Rhodamin B-VQCRLGPPWCAK) were provided by NeoBiotech (France). Cholera Toxin B subunit (cat. C9972), bovine serum albumin (cat. A7030), hydroxydaunorubicin hydrochloride (cat. D1515), lipopolysaccharides from *Escherichia coli* O111:B4 (cat. L2630) and hydrogen peroxide (30 % solution, cat. 216763), were purchased from Sigma-Aldrich (Spain). Sodium dodecyl sulfate (cat. 71727) were supplied by Merck (Germany). Sodium di-Hydrogen phosphate 1-hydrate ($\text{NaH}_2\text{PO}_4 \cdot \text{H}_2\text{O}$, cat. 141965) and sodium chloride (NaCl , cat. 141659) were purchased from Panreac. Di-Sodium hydrogen phosphate anhydrous (Na_2HPO_4 , cat. SO03351000) and potassium chloride (KCl , cat. PO01991000) were purchased from Scharlau (Spain). Graphdiyne was provided by Li et al.

Micromotors synthesis. Micromotors were synthesized using a standardized electrochemical deposition technique. A polycarbonate membrane with 5 μm diameter conical pores (Catalog No. 7060–2513; Whatman, New Jersey, USA) was used as a scaffold. A thin gold layer was sputtered on the branched side of the membrane. A Pt wire was used as a counter electrode whilst a commercial Ag/AgCl (3M) electrode was employed as the reference electrode. The different layers were then deposited starting from the outermost layer to the inner layer. First, graphdiyne was deposited from a plating dispersion containing 0.1 mg mL^{-1} graphdiyne and 0.5 mol L^{-1} Na_2SO_4 supporting electrode applying 10 cyclic voltammetry cycles 0.3 V to -1.5 V at a speed of 50 mV s^{-1} . Next, a nickel layer was deposited from a solution containing nickel sulfamate (1.2 mol L^{-1}), nickel chloride (82 mmol L^{-1}) and boric acid (464 mmol L^{-1}), at pH 4. The deposition of this layer is performed galvanostatically; the nucleation sites were created by applying ten 100 ms pulsed nucleation scans (-20 mA) and the deposition was carried out with a 360 s deposition scan (-6 mA). Finally, the inner platinum layer was deposited from a solution containing 4 mmol L^{-1} H_2PtCl_6 in 0.5 mol L^{-1} boric acid. The deposition of this layer was performed by applying a -0.4 V potential for 750 s. Once the synthesis is finished, the gold layer is gently removed using a 0.05 μm mean diameter alumina slurry. In order to release the micromotors, the membrane was dissolved using dichloromethane. Once the motors were free, they were centrifuged at 7000 rpm for 3 minutes and redispersed in isopropanol, ethanol and water consecutively. Finally, the motors were washed three times using ultrapure water (18.2 Ω cm). The micromotor density in each batch was estimated by measuring the size of a 1 μL drop using the NIS Elements AR 3.2 software (Nikon, Tokyo, Japan). Then using a higher magnification objective, the micromotors in a smaller predefined area were counted. The results were extrapolated as micromotors per mL. The whole process was repeated 3 times per batch.

Micromotor speed measuring. Micromotor movement was studied on glass slides. Briefly, 1 μL of micromotor dispersion was placed and mixed with 1 μL 15% SDS and 1 μL of the different fuel solutions. Videos were recorded after the addition of the fuel at frame rate of 25 FPS using a Zyla CMOS camera attached to an Eclipse Ti-S inverted microscope (Nikon, Tokyo, Japan). The micromotors were tracked using the NIS Elements AR 3.2 software (Nikon, Tokyo, Japan) which directly outputs the instantaneous speed for each step and the mean speed was calculated by averaging this data. The process was repeated for at least three times, measuring different micromotors each time.

Micromotors characterization. Scanning-electron microscopy images of the micromotors were taken using a JEOL JSM 6335F JEOL USA, Massachusetts, United States) coupled with an Xflash detector 4010 an using an acceleration voltage of 20 kV. Atomic-force microscopy images were obtained with an ALPHA 300AR dual Raman/AFM microscope (WITec, Germany). Images were taken by imaging the desired micromotors with the integrated optical microscope followed by automatic cantilever alignment and sample survey.

Doxorubicin load and release experiments. Doxorubicin was loaded on the motors by incubating a batch (aprox. 500,000 motors) concentrated DOX solution (600 $\mu\text{mol L}^{-1}$) overnight. Micromotors were separated from the supernatant by centrifugation. Micromotors were then cleaned with PBS pH=8 three times. For release experiments, the motors were suspended in pH=5 PBS and measured 1 hour later.

Cellular viability (MTT) assay. In order to assess the cytotoxicity of free DOX, moving and static modified and unmodified motors and hydrogen peroxide against HeLa cells was determined by MTT assay (Cell Proliferation Kit I, MTT, Roche, Germany). Cells were harvested at a confluency of 80%. 10,000 cells were plated in the plates of a 24-well plates where 500 μL of culture media were added per plate. The incubation was sustained for 24 hours, control cells were also included and incubated for the same time. After the incubation, 50 μL (5 mg/mL) of MTT (3-[4,5-dimethylthiazol-2-yl]-2,5-diphenyl tetrazolium bromide) labeling reagent was added. A humidified atmosphere (37 $^\circ\text{C}$, 5% CO_2) was used for a 4-hour incubation, after this time 500 μL of the solubilization solution (DMSO) was added. The plate was left overnight in the humidified atmosphere. The conversion of MTT into formazan by active cells was assessed by the change in absorbance at 570/630 nm using a microplate reader (Biotek Instruments, Winooski, Vermont, United States) and the cell viability was quantified. The assay was run in triplicate. The concentrations of each compound (per well plate) was: 167,000 modified and unmodified motors and 0.5 mmol L^{-1} DOX. For experiments with moving micromotors, 0.1 % H_2O_2 solutions were used without the addition of surfactant. Confocal microscopy images were taken with a Leica TCS-SP5 confocal microscope. All experiments involving cancer cells were performed in “Centro de Apoyo a la Investigación en Medicina/Biología, Unidad de Cultivos Celulares” by authorized personnel and were in compliance with the University of Alcalá regulations.

SUPPORTING INFORMATION

Toxin detection using the fluorescent-labeled affinity peptides release. For the detection of the Cholera B toxin subunit the Rhodamin-B affinity peptide was obtained from Neo-Biotech (Nanterre, France) the sequence being B-VQCRLGPPWCAK. The purity was evaluated using HPLC/UV being 95.98%, the molecular weight was calculated using ESI-MS and being 1782.33 g mol⁻¹. The peptide was aliquoted and stored at -20 °C until further use. An aliquot was thawed at room temperature and reconstituted in ACN:H₂O₂ 1:3 to a final concentration of 1000 µg mL⁻¹. In order to modify the motors with the affinity peptide, 100 µL of the peptide (100 µg mL⁻¹) were added to an Eppendorf tube containing 1 batch of dry motors (aprox. 500,000 motors), 150 mL of sodium dodecyl sulfate 3% and 200 µL of ACN:H₂O₂ 1:3, the motors were incubated for 1 hour. 1 µL of modified motors, 1 µL of H₂O₂ 3% and 1 µL of sample solution were mixed on the surface of a glass slide. The fluorescence images were recorded with a Zyla CMOS camera attached to an Eclipse Ti-S inverted microscope (Nikon, Tokyo, Japan). All images were analyzed using the NIS Elements AR 3.2 software (Nikon, Tokyo, Japan).

Results and Discussion

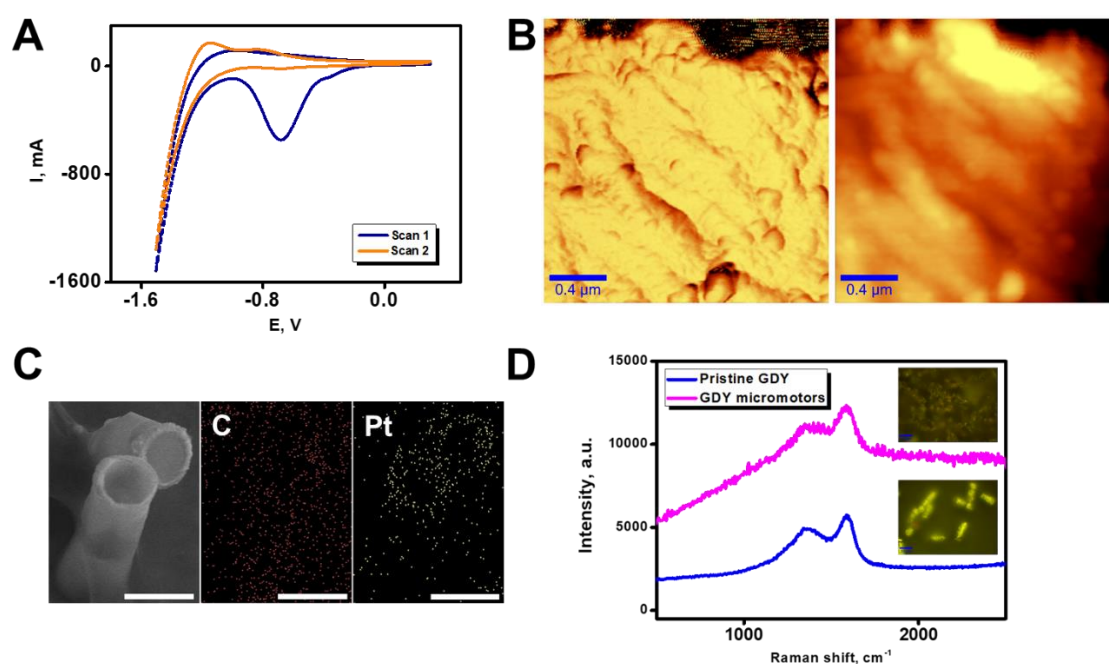


Figure S1. Synthesis and characterization of graphdyne (GDY) micromotors. (A) Cyclic voltammograms corresponding to the electrodeposition of the outer GDY layer. (B) Atomic force-microscopy images illustrating the outer surface morphology of the micromotors in the middle (left image) and outer (right image) of the microtube. (C) Scanning electron microscopy and corresponding energy-ray dispersive mapping showing the element distribution in the micromotors. Scale bar, 5 µm. (D) Raman spectra of pristine and GDY micromotors. Inset shows the area used to take the scans.

Supporting Videos

Video S1. GDY-Ni-Pt micromotors navigation at different peroxide levels.

CHAPTER VI.

**Optical portable detection
with 2D Janus micromotors:
towards on-site screening**

***This chapter contains
protected content***

VI.1. Introduction and objectives.

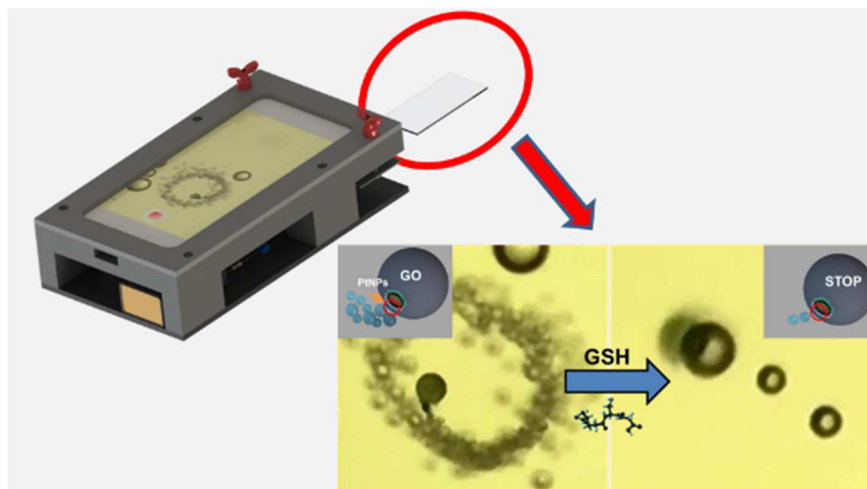
Fast biomarker detection is essential for personalized healthcare and rapid disease treatment. Advances in nanofabrication allow for the miniaturization of biosensors for such purpose, which along with smartphone technology lead to novel point-of-care (POCs) applications. Such miniaturized devices are easy to use, holding considerable promise to reduce costs, increasing sampling throughput and allowing its use in resource-limited settings. In such devices, smartphones are used as detection/readout parts, thus it is necessary the integration of sample preparation compartments or reaction chambers, including microchips. In this context, the small size, magnetic guidance capabilities and versatility of micromotors for analytical sensing, hold considerable promise for its combination with smartphones for POCs diagnosis. Early directions in this field lead to motion-based cell-phone detection system for HIV-1 and Zika virus and micromotors. Yet, the strategies still require additional sample pre-treatment compartments and sophisticated detection algorithms for motion detection as not visual detection is possible. In addition, portable devices for fluorescent assays using micromotors have not been described to date.

Inspired by previous micromotors works, the main aim of this chapter is to integrate the sensing strategies developed in this PhD into mobile platforms for decentralized analysis for extended analytical applicability. First, we describe a smartphone-based detection platform for motion-based detection of clinical biomarkers, using glutathione (GSH) to prove the concept. The system relies on a direct coupling of a high-performance commercial optical scope with the smartphone camera, allowing for real time-observation of 20 μm graphene (GO) wrapped/PtNPs Janus micromotors motion. A specifically designed 3D attachment allows for the integration of a LED source for illumination, a glass slide holder to place few microliters of sample and easy system for fast focus. The main aim is to simplify even more the configuration, leading to a universal platform that can be coupled with any mobile phone. Turn-off GSH sensing is achieved, due to such compound contains a thiol group, which can attach to the PtNPs responsible for micromotor motion, using the decrease in the speed as analytical signal. Direct visualization of the speed decrease allows for the design of a test strip for GSH detection for fast and direct detection of such biomarker, avoiding previous amplification strategies or sample preparation steps. The performance of the

strategy was validated against a high-resolution optical microscope, with excellent match. The universal platform developed here meet the World Health Organization criteria (affordable, sensitive, specific, user friendly, rapid, equipment-free), holding considerable promise for its use in decentralized medicine, in epidemic control or in remote areas and non-developed countries. The versatility of the strategy allows for easy integration of other micromotor-based sensing strategies relying in fluorescent or colorimetric detection of a myriad of biomarkers, allowing for the design of multiplexed schemes.

Secondly, the previous developed platform of tailored with the inclusion of lasers for different wavelengths illuminations and filters for fluorescent assays. The strategy described in chapter V.2 on the use of graphdiyne micromotors for Cholera Toxin B detection was extended here but using the portable microscope, obtaining the same analytical performance. Even more, the device can be tailored to incorporate magnetic actuated Janus micromotors modified with quantum dots for fluorescents assays and micromotor operation in non-ideal media such as whole blood.

VI.2. Article 8. Smartphone-based Janus micromotors strategy for real-time detection of clinical biomarkers.



Smartphone-based Janus micromotors strategy for real-time detection of clinical biomarkers

Kaisong Yuan,^{†§} Beatriz Jurado-Sánchez,^{†‡*} and Alberto Escarpa^{†‡*}

[†]Department of Analytical Chemistry, Physical Chemistry and Chemical Engineering, University of Alcalá, Alcalá de Henares E-28871, Madrid, Spain. E-mail: beatriz.jurado@uah.es, alberto.escarpa@uah.es (Tel: +34 91 8854995)

[§]Institute of Pharmaceutical Analysis, College of Pharmacy, Jinan University, Guangzhou, China

[‡]Chemical Research Institute "Andrés M. del Río", University of Alcalá, Alcalá de Henares E-28871, Madrid, Spain

ABSTRACT: Herein we describe a Janus micromotor smartphone-platform for motion-based detection of glutathione. The system comprises a universal 3D printed platform to hold a commercial smartphone, which is equipped with an external magnification optical lens (20-400X) directly attached to the camera, an adjustable sample holder to accommodate a glass slide and a LED source. The presence of glutathione in peroxide-rich sample media results in the decrease of the speed of 20 μm graphene wrapped/PtNPs Janus micromotors due to poisoning of the catalytic layer by thiol bond formation. The speed can be correlated with the concentration of glutathione, achieving a limit of detection of 0.89 μM , with percent recoveries and excellent selectivity under the presence of interfering amino acids and proteins. The strategy was validated against a high-performance optical microscope, obtaining a perfect match. Naked-eye visualization of the speed decrease allows for the design of a test strip for fast glutathione detection (30 s), avoiding previous amplification strategies or sample preparation steps. The universal platform developed here meet the World Health Organization's criteria (affordable, sensitive, specific, user friendly, rapid, equipment-free), holding considerable promise for its use in decentralized medicine, in remote areas and non-developed countries. The concept can be extended to other micromotor approaches relying in fluorescent or colorimetric detection for future multiplexed schemes.

INTRODUCTION

Fast biomarker detection is essential for personalized healthcare and rapid disease treatment. Advances in nanofabrication allow for the miniaturization of biosensors for such purpose, which along with smartphone technology lead to novel point-of-care (POCs) applications. Such miniaturized devices are easy to use, holding considerable promise to reduce costs, increasing sampling throughput and allowing its use in resource-limited settings.[1-3] In such devices, smartphones are used as detection/readout parts, thus it is necessary the integration of sample preparation compartments or reaction chambers. For example, lateral based flow strips can be easily coupled with mobile phones for fluorescent detection of peptides indicative of heart failure[4] or colorimetric detection of uric acid in whole blood.[2] A paper based plasma separation module have been used in connection with a tailor-made reservoir for colorimetric detection of total and direct bilirubin in blood.[5] More sophisticated designs rely on the integration of microchips for *i.e.* polymerase chain reaction for DNA amplification[6-8] or to promote microbead aggregation via protein-specific linkage for *i.e.* prostate specific antigen detection.[9]

Self-propelled micromotors are microscale devices capable of autonomous movement in solution.[10-15] In the analytical field, catalytic micromotors propelled by peroxide decomposition in inner catalytic layers are the most commonly used to date. Indeed, their autonomous motion along with versatile functionalization approaches lead to novel developments in the analytical field to perform a myriad of assays directly using ultra-low (nL- μL) sample volumes.[16-20] The high towing force, small micromotor size and the possibility to introduce magnetic parts in its structure allow for efficient navigation and control in microfluidic chips for future smartphone-based POCs.[21, 22] A more promising approach to achieve this goal is the integration of motion-based sensing approaches based on micromotors. Wang's group pioneer the concept after observing the enhanced movement experience by Au-Pt nanowires in the presence of Ag^+ ions.[23] Changes in the speed were related with Ag^+ concentration to develop the sensing strategy, which was later extended for DNA sensing.[24] The limitations of the movement of nanowires in salt-rich environments led to the exploration of bubble-propelled catalytic micromotors. For example, polymer-Au micromotors with an inner catalase layer experienced diminished motion in the presence of certain ions (Hg)[25] or

nerve agents vapor plumes[26] due to poison of the enzyme. Micromotors with inner Pt catalytic layers can also be poisoned by thiol containing metabolites, resulting in a similar speed decrease.[27] Antibody modified gold-nanoparticle-polyaniline/Pt micromotors have been used in connection with secondary antibody-modified microspheres for anticarcinoembryonic antigen detection. The presence of high concentrations of the target analyte result in the aggregation of more microspheres, resulting in a speed decrease in a concentration-dependent manner.[28] Turn-off motion approaches based on poly(3,4-ethylenedioxythiophene)/Au micromotors[29] or Au/Ag/Ni/Au shells[30] have been described for DNA sensing. The principle relies on DNA competition towards catalase-labelled secondary probes (responsible for the propulsion), which are released resulting in a speed decrease. Yet, the above-mentioned approaches required the use of high-performance optical microscope, which prevents its use in routine laboratories or in portable detection schemes.

Recent introduction of 3D printing and fast progress in smartphones allow for the integration of motion-based micromotors assays for POCs diagnosis. Shafiee et al. developed a motion-based cell-phone detection system for HIV-1. The systems comprise a microchip and DNA-modified micromotors consisting on platinum and gold modified polystyrene beads (6 μm). The detection principle consisted on (1) sample application in the reservoir of the microchip for loop-mediated isothermal amplification of the nucleic acid of HIV-1; (2) mixing of resulting amplicons with the DNA-modified micromotors; (3) detection of the motion of the resulting assemblies in peroxide solutions. The presence of HIV-1 generates large amplicons that reduce the motion/speed of motors (turn-off). Such decrease is used as the analytical signal, for HIV-detection at a concentration as low as 1000 virus particles mL^{-1} with high specificity, within an hour.[31] The same design but in a turn-on configuration was also applied for ZIKA virus detection. In this case, 3 μm beads modified with anti-Zika virus monoclonal antibody (anti-ZIKV mAb) are used to capture the Zika virus, followed by attachment of anti-ZIKV mAb platinum nanoparticles. The presence of virus in a testing samples results in the accumulation of an increased concentration of Pt beads, causing the motion in peroxide solutions for detection of a concentration as low as 1 particle μL^{-1} . [32] Despite its simplicity, such systems still requires the use of microchips for sample pre-treatment and sophisticated detection algorithms for motion detection as not visual detection is possible.

Inspired by previous micromotors works, herein we describe a smartphone-based detection platform for motion-based detection of clinical biomarkers. The system relies on a direct coupling of a high-performance commercial optical scope with the smartphone camera, allowing for real time-

observation of 20 μm graphene (GO) wrapped/PtNPs Janus micromotors motion (see **Figure 1A**). A specifically designed 3D attachment allows for the integration of a LED source for illumination, a glass slide holder to place few microliters of sample and easy system for fast focus. The main aim is to simplify even more the configuration, leading to a universal platform that can be coupled with any mobile phone. The concept is demonstrated here to detect glutathione (GSH), an important peptide biomarker which play a critical role in cellular functions. In addition, abnormally high levels of GSH (higher than 15 mM) can be related with many diseases, such as Alzheimer's disease, diabetes or viral infections.[33-36] Such compound contains also thiol group, which can attach to the PtNPs responsible for micromotor motion, using the decrease in the speed as analytical signal. Direct visualization of the speed decrease allows for the design of a test strip for GSH detection for fast and direct detection of such biomarker, avoiding previous amplification strategies or sample preparation steps. The performance of the strategy was validated against a high-resolution optical microscope, with excellent match. The universal platform developed here meet the World Health Organization's criteria (affordable, sensitive, specific, user friendly, rapid, equipment-free), holding considerable promise for its use in decentralized medicine, in epidemic control or in remote areas and non-developed countries.[37] The versatility of the strategy allows for easy integration of other micromotor-based sensing strategies relying in fluorescent or colorimetric detection of a myriad of biomarkers, allowing for the design of multiplexed schemes.

EXPERIMENTAL SECTION

Smartphone-device. The 3D platform for the cellphone set-up was designed using SolidWorks 2015 software. The platform contains a LED source and a sample holder to place a glass slide. The 20X-400X Universal Tip scope was purchased from Amazon and directly attached to an iPhone (Apple), which was used in all experiments. Micromotors motion was directly observed in the camera application of the phone, which was also used to record the Videos at 30 FPS. Micromotor motion was tracked with Particle Tracker module of ImageJ free software (<https://imagej.net/Particle Tracker>). Additionally, the commercial Nikon NIS Elements AR 3.2 software and tracking module was used to check the accuracy of the free software.

An inverted optical microscope (Nikon Eclipse Instrument Inc. TiS/L100) coupled with a 20X and a Zyla cMOS digital camera was used to validate the smartphone platform. Movies were captured and the speed of the micromotors tracked for comparison.

Micromotor synthesis. All reagents used were obtained from Sigma-Aldrich (Spain) and used without further purification. Polystyrene

VI. Optical portable detection with 2D Janus micromotors: towards on-site screening

microparticles (cat. 87896) were dropped on a clean-glass slide to generate a monolayer which was covered with a ~50 nm gold by sputter coating. The modified beads were released in ultrapure water by sonication (0.9 mL) and mixed with 0.1 mL of sulfhydryl-modified graphene oxide (HS-GO) (cat. 763705) for 2 h to promote attachment to gold by thiol bond.[38] Next, the solution was filtered to remove the excess of reagents and dispersed in ultrapure water (1 mL). The PtNPs were growth in-situ in the microparticles by mixing the solution with 200 μ L of chloroplatinic acid hydrate (1 mg mL⁻¹, cat. 398322) and 20 μ L of hydrazine solution (35 wt % in H₂O, cat. 309400) for 2 h. After that, reaction solution was filtered with a cyclopore track etched membrane (5 μ m) to remove free PtNPs. The volume of the solution was adjusted to 1 mL with ultrapure water and remains stable for 2 months without any change in its properties.

GSH detection. For detection, 1 μ L of micromotor solution was mixed with 1 μ L of sodium dodecyl sulfate (cat. 71725, final concentration 3 %), 1 μ L of variable concentration of GSH (cat. PHR1359, from 0 to 160 μ M) and 1 μ L of H₂O₂ (cat. 216763, final concentration, 5 %). Videos were recorded after 30 s peroxide addition and the speed tracked as previously specified.

Analytical performance with the smartphone device and high-performance optical microscope was evaluated through the limit of detection (LOD), limit of quantification (LOQ), selectivity and recovery. Calibrations plots were obtained (n=50) and the LOD or LOQ were calculated as 3 or 10 times the standard deviation of the ordinate divided by the slope of the calibration linear fit. Selectivity was evaluated against 160 μ M of potentially interfering species including cysteine (cat. W326305), serine (cat. S4500), leucine (cat. L8000), arginine (cat. A5006) and bovine serum albumin (cat. 05470). Recovery was evaluated by

fortifying human serum samples (cat. H4522) with 25 μ M of GSH.

RESULTS AND DISCUSSION

Figure 1A illustrates the set-up of the micromotor based detection platform. It consists on a 3D printed platform which can be easily tailored for many smartphones' models and a commercial magnification lens attached to the camera of the phone (overall cost, 19 € with an estimated 2-year lifetime). An animation of the assembly is shown in **Video S1**. As can be seen, a sample holder for the inclusion of a glass slide is incorporated, which along easy-to-use adjustable screws allow for movement for sample focus, similar to a high-performance optical microscope. In that way, real time micromotor motion observation can be achieved, even by non-specialized personnel. The platform was tested to develop a protocol for GSH detection in clinical samples. To this end, we use Janus micromotors whose size is ideal for observation with the designed system. Micromotors were synthesized using a previously developed strategy of our research group.[38] Briefly, gold-sputtered PS microspheres were coated with GO modified with -SH to promote attachment via thiol bond with the Au layer. The amount of nanomaterial was judiciously controlled to left uncoated a small, asymmetric Au patch. In this way, preferential growth of the catalytic Pt nanoparticles is promoted, imparting the micromotors with the asymmetric Janus character for efficient propulsion in peroxide solutions. For further details on characterization and synthesis, please refer to our previous publication.[38] While Janus micromotors were used here to demonstrated the real-time based detection, tubular designs or other configurations can be easily observed with our device for future motion-based micromotor sensing approaches.

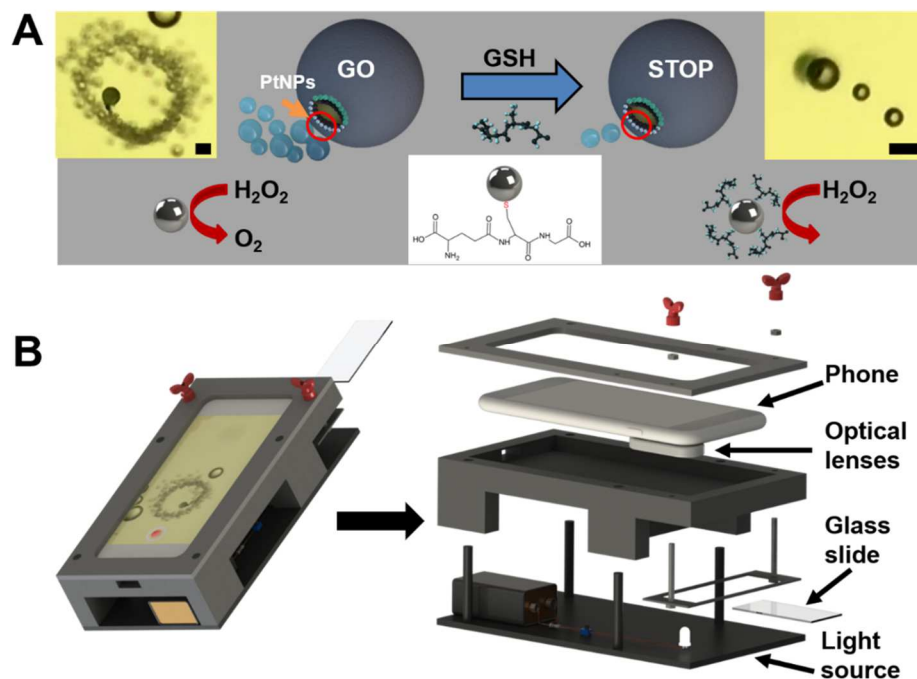


Figure 1. Smartphone-based platform design and proof-of-concept application for GSH detection. A) Integration of the smartphone into a 3D printed platform and description of the different parts of the device. The schematic of the assembly is described in Video S1. B) Schematic of GSH detection with GO wrapped/PtNPs Janus micromotors, based on the decrease of the initial speed due to inactivation of the catalytic active PtNPs by specific interactions with the thiol group present in the GSH molecule. The time-lapse microscopy images (Taken from Video S2) illustrate the Janus micromotor motion in the absence (left) and presence of 160 μM of GSH (right) using the smartphone-based platform. Scale bars, 20 μm.

The schematic of the “turn-off” GSH sensing is depicted in **Figure 1B**. Initially, micromotors propels at a speed of over $162 \pm 5 \mu\text{m s}^{-1}$ in 5 % peroxide solutions. Yet, under the presence of GSH, the thiol group present in the molecule can poison the PtNPs catalyst by specific union through a thiol bond. This block the catalytic active area, preventing the decomposition of peroxide by the catalyst and resulting in a decrease in the speed which can be related with GSH concentration. Even more, a 160 μM GSH concentrations result in almost a total stop of micromotor movement, due to all active catalytic area is blocked but such analyte.[27] This is further illustrated in the time lapse microscopy images of the inset in **Figure 1B** and related **Video S2**. The images and Videos were taken using the microscope device (for further details please see the experimental section), which clearly illustrates the micromotor movement by the naked-eye and the clear differences in the movement.

The strategy was next validated, and the results compared to that obtained with a high-performance optical microscope. **Figure 2** and related **Video S3** illustrate the micromotor movement in solutions containing increasing concentrations of GSH (from 10 to 160 μM). As can be seen, as GSH concentration increase, there is a decrease in the micromotor speed due to less catalytic area is available for peroxide

decomposition. This is also revealed by the bubble tail, with bigger and less abundant oxygen bubbles as GSH concentration increase. The data was processed to obtain calibration plots using the micromotor speed as analytical signal. **Figure 2B** shows the calibration plots obtained using both the smartphone and the conventional optical microscope. The relevant analytic characteristics are summarized in **Table 1**.

Table 1. Analytical characteristics of GSH detection using the smartphone and the optical microscope

	Intercept	Slope	R ²	LOD (μM)	LOQ (μM)	Linear range (μM)
Microscope	123.9	-47.4	0.997	0.86	2.8	2.8-160
Phone	126.1	-48.0	0.998	0.89	2.9	2.8-160

VI. Optical portable detection with 2D Janus micromotors: towards on-site screening

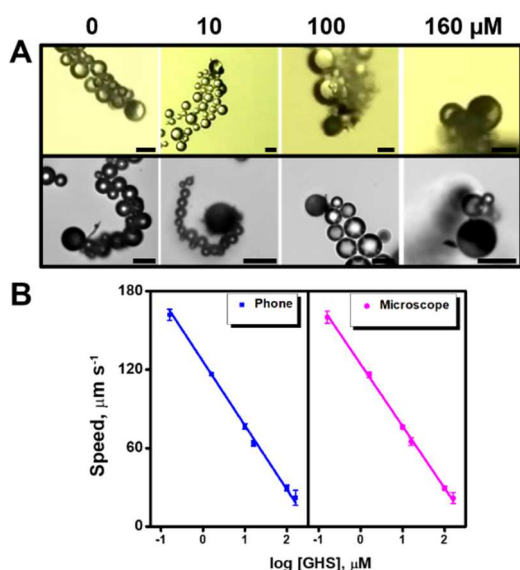


Figure 2. Calibration of the detection strategy using a high-performance optical microscope and the smartphone. A) Time lapse images (Taken from Video S3) of micromotors navigation in solutions containing increasing concentrations (0, 10, 100 and 160 μM) of GSH. Top part shows the images obtained with the smartphone and bottom part the one obtained with a high-resolution optical microscope. B) Corresponding calibration plots. Scale bars, 20 μm .

As can be seen in the **Table 1**, similar results were obtained using both the smartphone and the optical microscope. The limit of detection where 0.89 μM and 0.86 μM calculated using the smartphone and the microscope, respectively. The linear range span to 160 μM on both cases. Such LOD is lower than that obtained with a chemiluminescent method using MnO_2 -nanosheet-modified up conversion nanoparticles (0.9 μM)[39] or fluorescent approaches using polydopamine doped nanoparticles in the presence of MnO_2 (1.5 μM)[40] or AuNC@BSA- MnO_2 nanoparticles (20 μM).[41] Yet, the LOD obtained with our method is slightly higher compared with a

colorimetric approach using a $\text{Ru}(\text{bpy})_3^{3+}$ modified metal-organic framework in connection with the substrate 3,3',5,5'-tetramethylbenzidinedihydrochloride (TMB) (0.7 μM)[42] or fluorescent approaches based on carbon dots (0.45 μM)[43] or boron nitride quantum dots (0.2 μM).[44] Still, as the normal levels of GSH ranges from 1000 to 15000 μM , our strategy allow for the determination of such analyte at physiological conditions.[45]

Next, we evaluated the selectivity of the sensing strategy in the presence of other amino acids with a structure similar to GSH that can cause potential interferences. Cysteine was tested due to it contains a thiol and an amino group in its structure. Serine, leucine and arginine, which contains amino and OH groups, were also evaluated. In addition, bovine serum albumin, a protein commonly present in biological fluids and a well-known agent that can cause the poisoning of Pt catalyst was also tested. [46] As can be seen in the time-lapse images of **Figure 3** and corresponding Video S4, the speed of the micromotor do not varies under the presence of 160 μM concentration of each interfering compound, as compared with the drastic decrease noted in the case of GSH. Such results testified the high selectivity of our sensing protocol, probably that despite cysteine or the other amino acids can somewhat attach to the Pt catalyst, the relatively smaller molecular size compared with GSH and the different configuration prevent the total blocking of the catalyst, which retains its catalytic activity. Selectivity was both evaluated with the smartphone and the optical microscope, obtaining similar results in both cases. Next, we also performed recovery studies by fortifying human serum samples with a 25 μM concentration of GSH, followed by testing the micromotor speed. As can be seen in **Figure 3C**, quantitative recoveries of almost 100 % were obtained, further testifying the utility of our protocol in real samples.

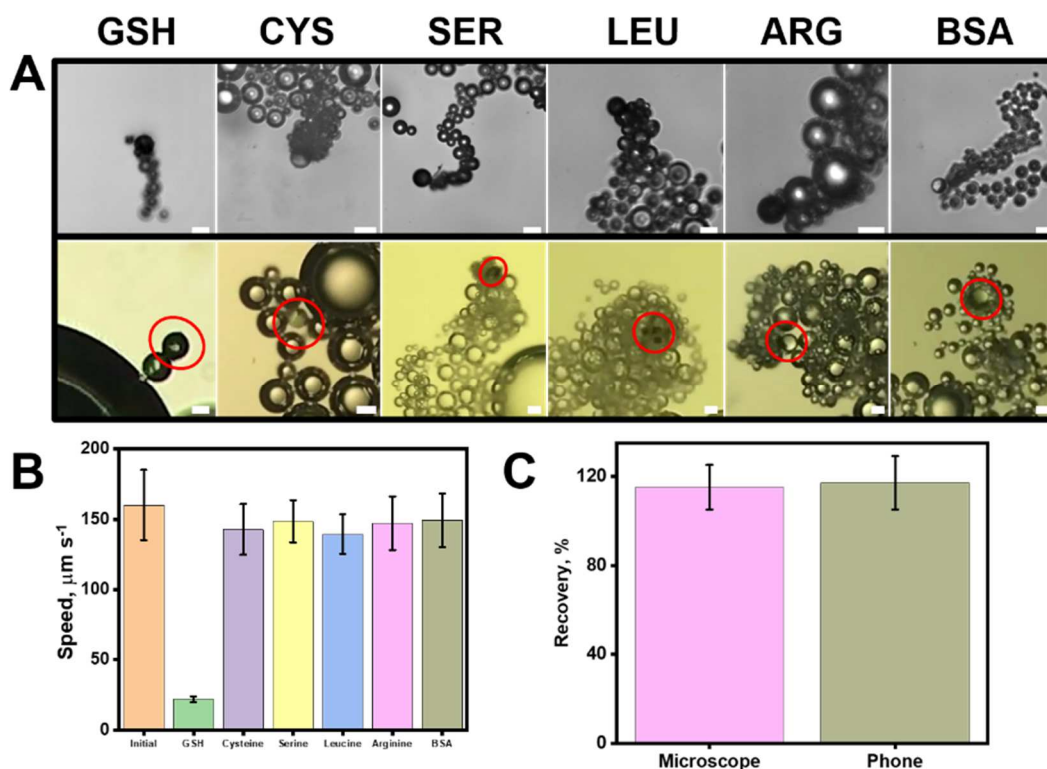


Figure 3. Selectivity of the detection strategy and detection performance. A) Time lapse images (Taken from Video S4) of micromotors navigation in solutions containing 160 μM of GSH, cysteine (Cys), serine (SER), leucine (LEU), arginine (ARG) and bovine serum albumin (BSA). Top part shows the images obtained with the smartphone and bottom part the one obtained with a high-resolution optical microscope. B) Corresponding speed in the presence of the different interferences. C) Recovery percentage in serum samples fortified with 25 μM of GSH using both the smartphone and the microscope. Scale bars, 20 μm .

For future practical applicability by non-specialized personnel, we developed a protocol for GSH sensing in clinical samples, as shown in **Figure 4**. As can be seen, the device can be pre-validated to construct the calibration plot in the presence of increasing concentrations of GSH. Pictures of the micromotor motion and displacement were taken, with a line at the left indicating the indicative distance travelled by the micromotor. Differences in the bubble tail can be also checked. The strip correlates the distance travelled with a color and GSH concentration, so an operator just needs to observe the motion in the phone to make an estimate of GSH concentration for fast response. The detection can be performed in less than 30 s and just require dropping the sample (human serum or plasma) on a glass slide along with the micromotor and fuel solution. The device can be used multiple times and the strategy can be extended to any smartphone as the magnified lenses can be attached to any camera. As each micromotor batch contain 1 mL and only 1 μL is required for analysis, considering the cost of peroxide and the surfactant, the average cost per analysis is estimated to be 0.05 €.

As a double check confirmation and complement to the motion-based test strip, a fast-colorimetric test

with the micromotors can be performed. To this end, TMB was used as substrate. Under the presence of H_2O_2 and nanomaterials with peroxidase like activity (graphene, platinum nanoparticles), OH^- radicals are oxidized, generating a blue color in the solution.[47, 48] Surprisingly, under the presence of the interferences, no blue color was developed, probably due to all the peroxide is decomposed into oxygen and water without the generation of intermediate OH^- radicals by the high catalytic activity of PtNPs.[49] Yet, under the presence of GSH, a deep blue color is generated. Despite some authors have reported that GSH can reduce back TMB resulting in a decrease in color,[50, 51] we found the opposite observation. Color appearance in the solution is observed at concentrations up to 10 μM of GSH. We hypothesis that all GSH attach to the PtNPs in the micromotors, blocking thus the active part responsible for the reduction of TMB. This, in turn, reduce the catalytic activity, thus some H_2O_2 in the solution can react with the graphene oxide present in the micromotor, generating OH^- ions that oxidize the TMB and generate the blue color.

VI. Optical portable detection with 2D Janus micromotors: towards on-site screening

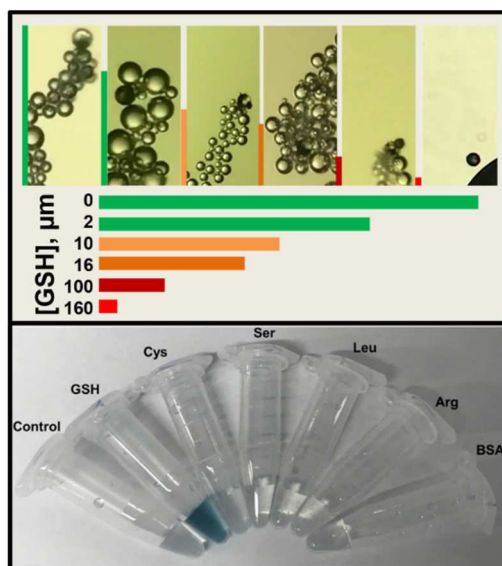


Figure 4. Protocol for GSH detection using the smartphone-based platform. A) Test-strip read-out based on the displacement of the micromotors in the real samples and correlation with GSH concentration. B) Colorimetric evaluation under the presence of TMB as substrate: a deep blue color is generated in the presence of GSH due to reduction of the catalytic activity of PtNPs and OH^- radicals mediated generation.

CONCLUSIONS

In conclusion, we have reported here a smartphone portable device based on micromotors for naked eye detection of clinical relevance biomarkers for future decentralized analysis and use in remote settings. The coupling of high magnifications lens with a smartphone allow to direct observe and record Videos of the motion of $20 \mu\text{m}$ graphene wrapped/PtNPs Janus micromotors with the phone camera, by non-specialized personnel and in an easy manner. Yet, while Janus micromotors are used here to illustrate the concept, the strategy can be easily extended to other designs such as wires, tubular, etc. The concept was successfully illustrated for motion-based detection of glutathione, an analyte of high clinical relevance, with excellent selectivity and practical levels. A test strip that correlates the distance travelled with a color and GSH concentration, allow for direct observation of the micromotor motion in the phone to make an estimate of GSH concentration for fast response. The detection can be performed in less than 30 s and just require dropping the sample (human serum or plasma) on a glass slide along with the micromotor and fuel solution, with an average cost of 0.05 € per analysis. The validation against a high-performance optical microscope further testify the utility of our universal device. As such, the smartphone device meets the World Health Organization's criteria (affordable, sensitive, specific, user friendly, rapid, equipment-free). Future efforts should be aimed at extending the strategy to other micromotor-based sensing

approaches relying in fluorescent or colorimetric detection for the design of multiplexed schemes.

ASSOCIATED CONTENT

Supporting Information

The Supporting Information is available free of charge on the ACS Publications website.

Smartphone-device assembly (.AVI)

Janus micromotor navigation in the absence and presence of glutathione using the smartphone-based platform (.AVI)

Janus micromotor navigation in solutions containing increasing concentrations of GSH, using a high-resolution optical microscope and the smartphone-based platform (.AVI)

Selectivity of the strategy using a high-resolution optical microscope and the smartphone-based platform (.AVI)

AUTHOR INFORMATION

Corresponding Author

* alberto.escarpa@uah.es

* beatriz.jurado@uah.es

Author Contributions

The manuscript was written through contributions of all authors. All authors have given approval to the final version of the manuscript.

ACKNOWLEDGMENT

K. Yuan acknowledges the Ministry of Economy, Industry and Competitiveness for his pre-doctoral contract (RYC-2015-17558, co-financed by EU). B. J-S acknowledges support from the Ministry of Economy, Industry and Competitiveness (RYC-2015-17558, co-financed by EU) from the University of Alcala (CCG19/CC-029) and from the Community of Madrid-UAH (CM/JIN/2019-007). AE acknowledges the financial support from the Ministry of Economy, Industry and Competitiveness (CTQ2017-86441-C2-1-R) and the TRANSNANOAVANSENS program (S2018/NMT-4349) from the Community of Madrid.

REFERENCES

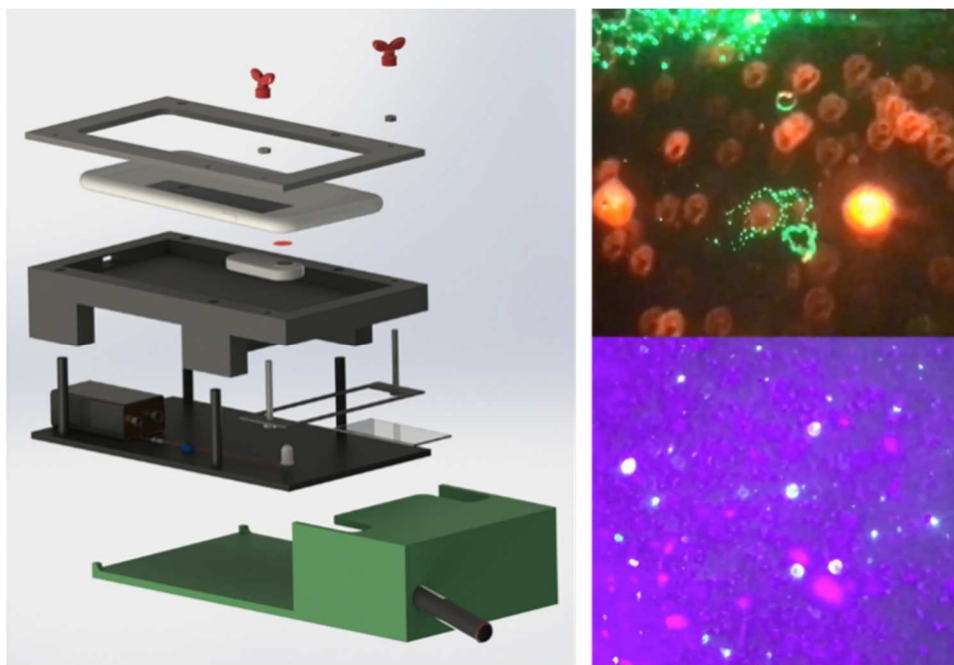
- (1) Alawsi, T.; Al-Bawi, Z. A Review of Smartphone Point-Of-Care Adapter Design. *Eng. Rep.* **2019**, *1*.
- (2) Li, N. S.; Chen, Y. T.; Hsu, Y. P.; Pang, H. H.; Huang, C. Y.; Shiue, Y. L.; Wei, K. C.; Yang, H. W. Mobile Healthcare System Based on the Combination of a Lateral Flow Pad and Smartphone for Rapid Detection of Uric Acid in Whole Blood. *Biosens. Bioelectron.* **2020**, *164*, 112309.
- (3) Zhao, W.; Tian, S.; Huang, L.; Liu, K.; Dong, L.; Guo, J. A Smartphone-Based Biomedical Sensory System. *Analyst* **2020**, *145*, 2873-2891.

- (4) You, M.; Lin, M.; Gong, Y.; Wang, S.; Li, A.; Ji, L.; Zhao, H.; Ling, K.; Wen, T.; Huang, Y.; Gao, D.; Ma, Q.; Wang, T.; Ma, A.; Li, X.; Xu, F. Household Fluorescent Lateral Flow Strip Platform for Sensitive and Quantitative Prognosis of Heart Failure Using Dual-Color Upconversion Nanoparticles. *ACS Nano* **2017**, *11*, 6261-6270.
- (5) Xu, H.; Xia, A.; Luo, J.; Gao, M.; Liao, R.; Li, F.; Zhong, Q.; Zhang, W.; Wang, Y.; Cui, J.; Fu, W.; Chang, K.; Gan, M.; Jiang, W.; Chen, M. A Sample-to-Answer Quantitative Platform for Point-Of-Care Testing of Biochemical Markers in Whole Blood. *Sens. Act. B. Chem.* **2020**, *308*, 127750.
- (6) Xu, H.; Xia, A.; Wang, D.; Zhang, Y.; Deng, S.; Lu, W.; Luo, J.; Zhong, Q.; Zhang, F.; Zhou, L.; Zhang, W.; Wang, Y.; Yang, C.; Chang, K.; Fu, W.; Cui, J.; Gan, M.; Luo, D.; Chen, M. An Ultraportable and Versatile Point-of-Care DNA Testing Platform. *Sci. Adv.* **2020**, *6*, eaaz7445.
- (7) Sun, F.; Ganguli, A.; Nguyen, J.; Brisbin, R.; Shanmugam, K.; Hirschberg, D. L.; Wheeler, M. B.; Bashir, R.; Nash, D. M.; Cunningham, B. T. Smartphone-Based Multiplex 30-Minute Nucleic Acid Test of Live Virus from Nasal Swab Extract. *Lab Chip* **2020**, *20*, 1621-1627.
- (8) Liao, S.-C.; Peng, J.; Mauk, M. G.; Awasthi, S.; Song, J.; Friedman, H.; Bau, H. H.; Liu, C. Smart Cup: A Minimally-Instrumented, Smartphone-Based Point-of-Care Molecular Diagnostic Device. *Sens. Act. B. Chem.* **2016**, *229*, 232-238.
- (9) Cui, W.; He, M.; Mu, L.; Lin, Z.; Wang, Y.; Pang, W.; Reed, M.; Duan, X. Cellphone-Enabled Microwell-Based Microbead Aggregation Assay for Portable Biomarker Detection. *ACS Sens* **2018**, *3*, 432-440.
- (10) Ozin, G. A.; Manners, I.; Fournier-Bidoz, S.; Arsenaault, A. Dream Nanomachines. *Adv. Mater.* **2005**, *17*, 3011-3018.
- (11) Solovev, A. A.; Mei, Y.; Bermudez Urena, E.; Huang, G.; Schmidt, O. G. Catalytic Microtubular Jet Engines Self-Propelled by Accumulated Gas Bubbles. *Small* **2009**, *5*, 1688-1692.
- (12) Ebbens, S. J.; Howse, J. R. In pursuit of propulsion at the nanoscale. *Soft Matt.* **2010**, *6*, 726.
- (13) Mei, Y.; Solovev, A. A.; Sanchez, S.; Schmidt, O. G. Rolled-up Nanotech on Polymers: from Basic Perception to Self-Propelled Catalytic Microengines. *Chem. Soc. Rev.* **2011**, *40*, 2109-2119.
- (14) Gao, W.; Sattayasamitsathit, S.; Uygun, A.; Pei, A.; Ponedal, A.; Wang, J. Polymer-Based Tubular Microbots: Role of Composition And Preparation. *Nanoscale* **2012**, *4*, 2447-2453.
- (15) Wang, J.: *Nanomachines: Fundamentals and Applications*. 2013. Wiley-VCH.
- (16) Wang, J. Self-Propelled Affinity Biosensors: Moving the Receptor Around the Sample. *Biosens. Bioelectron.* **2016**, *76*, 234-242.
- (17) Jurado-Sanchez, B.; Pacheco, M.; Rojo, J.; Escarpa, A. Magnetocatalytic Graphene Quantum Dots Janus Micromotors for Bacterial Endotoxin Detection. *Angew. Chem. Int. Ed.* **2017**, *56*, 6957-6961.
- (18) Karshalev, E.; Esteban-Fernández de Ávila, B.; Wang, J. Micromotors for "Chemistry-on-the-Fly". *J. Am. Chem. Soc.* **2018**, *140*, 3810-3820.
- (19) Pacheco, M.; López, M. Á.; Jurado-Sánchez, B.; Escarpa, A. Self-Propelled Micromachines for Analytical Sensing: A Critical Review. *Anal. Bioanal. Chem.* **2019**, *411*, 6561-6573.
- (20) Maric, T.; Beladi-Mousavi, S. M.; Khezri, B.; Sturala, J.; Nasir, M. Z. M.; Webster, R. D.; Sofer, Z.; Pumera, M. Functional 2D Germanene Fluorescent Coating of Microrobots for Micromachines Multiplexing. *Small*, **2019**, <https://doi.org/10.1002/sml.201902365>.
- (21) Zhou, C.; Yin, J.; Wu, C.; Du, L.; Wang, Y. Efficient Target Capture and Transport by Fuel-Free Micromotors in a Multichannel Microchip. *Soft Matt.* **2017**, *13*, 8064-8069.
- (22) Maria-Hormigos, R.; Jurado-Sánchez, B.; Escarpa, A. Labs-on-a-Chip Meet Self-Propelled Micromotors. *Lab Chip* **2016**, *16*, 2397-2407.
- (23) Kagan, D.; Calvo-Marzal, P.; Balasubramanian, S.; Sattayasamitsathit, S.; Manesh, K. M.; Flechsig, G.-U.; Wang, J. Chemical Sensing Based on Catalytic Nanomotors: Motion-Based Detection of Trace Silver. *J. Am. Chem. Soc.* **2009**, *131*, 12082-12083.
- (24) Wu, J.; Balasubramanian, S.; Kagan, D.; Manesh, K. M.; Campuzano, S.; Wang, J. Motion-Based DNA Detection Using Catalytic Nanomotors. *Nat. Commun.* **2010**, *1*, 36.
- (25) Orozco, J.; García-Gradilla, V.; D'Agostino, M.; Gao, W.; Cortés, A.; Wang, J. Artificial Enzyme-Powered Microfish for Water-Quality Testing. *ACS Nano* **2013**, *7*, 818-824.
- (26) Singh, V. V.; Kaufmann, K.; Esteban-Fernandez de Avila, B.; Uygun, M.; Wang, J. Nanomotors Responsive to Nerve-Agent Vapor Plumes. *Chem. Commun.* **2016**, *52*, 3360-3363.
- (27) Zhao, G.; Sanchez, S.; Schmidt, O. G.; Pumera, M. Poisoning of Bubble Propelled Catalytic Micromotors: The Chemical Environment Matters. *Nanoscale* **2013**, *5*, 2909-2914.
- (28) Yu, X.; Li, Y.; Wu, J.; Ju, H. Motor-Based Autonomous Microsensor for Motion and Counting Immunoassay of Cancer Biomarker. *Anal. Chem.* **2014**, *86*, 4501-4507.
- (29) Fu, S.; Zhang, X.; Xie, Y.; Wu, J.; Ju, H. An Efficient Enzyme-Powered Micromotor Device Fabricated by Cyclic Alternate Hybridization Assembly for DNA Detection. *Nanoscale* **2017**, *9*, 9026-9033.
- (30) Zhang, X.; Chen, C.; Wu, J.; Ju, H. Bubble-Propelled Jellyfish-like Micromotors for DNA Sensing. *ACS Appl. Mater. Interfac.* **2019**, *11*, 13581-13588.
- (31) Draz, M. S.; Kochehyoki, K. M.; Vasan, A.; Battalapalli, D.; Sreeram, A.; Kanakasabapathy, M. K.; Kallakuri, S.; Tsibris, A.; Kuritzkes, D. R.; Shafiee, H. DNA Engineered Micromotors Powered by Metal Nanoparticles for Motion Based Cellphone Diagnostics. *Nat. Commun.* **2018**, *9*, 4282.

VI. Optical portable detection with 2D Janus micromotors: towards on-site screening

- (32) Draz, M. S.; Lakshminaraasimulu, N. K.; Krishnakumar, S.; Battalapalli, D.; Vasan, A.; Kanakasabapathy, M. K.; Sreeram, A.; Kallakuri, S.; Thirumalaraju, P.; Li, Y.; Hua, S.; Yu, X. G.; Kuritzkes, D. R.; Shafiee, H. Motion-Based Immunological Detection of Zika Virus Using Pt-Nanomotors and a Cellphone. *ACS Nano* **2018**, *12*, 5709-5718.
- (33) Deng, R.; Xie, X.; Vendrell, M.; Chang, Y. T.; Liu, X. Intracellular Glutathione Detection Using MnO(2)-Nanosheet-Modified Upconversion Nanoparticles. *J. Am. Chem. Soc.* **2011**, *133*, 20168-20171.
- (34) Liu, Y.; Zhou, M.; Cao, W.; Wang, X.; Wang, Q.; Li, S.; Wei, H. Light-Responsive Metal-Organic Framework as an Oxidase Mimic for Cellular Glutathione Detection. *Anal. Chem.* **2019**, *91*, 8170-8175.
- (35) Niu, L. Y.; Guan, Y. S.; Chen, Y. Z.; Wu, L. Z.; Tung, C. H.; Yang, Q. Z. BODIPY-Based Ratiometric Fluorescent Sensor for Highly Selective Detection of Glutathione Over Cysteine and Homocysteine. *J. Am. Chem. Soc.* **2012**, *134*, 18928-18931.
- (36) Peng, C.; Xing, H.; Fan, X.; Xue, Y.; Li, J.; Wang, E. Glutathione Regulated Inner Filter Effect of MnO₂ Nanosheets on Boron Nitride Quantum Dots for Sensitive Assay. *Anal. Chem.* **2019**, *91*, 5762-5767.
- (37) Kosack, C. S.; Page, A.-L.; Klatser, P. R. A Guide to Aid the Selection of Diagnostic Tests. *Bull. World Health Organ.* **2017**, *95*, 639-645.
- (38) Yuan, K.; de la Asunción-Nadal, V.; Jurado-Sánchez, B.; Escarpa, A. 2D Nanomaterials Wrapped Janus Micromotors with Built-in Multiengines for Bubble, Magnetic, and Light Driven Propulsion. *Chem. Mater.* **2020**, *32*, 1983-1992.
- (39) Deng, R.; Xie, X.; Vendrell, M.; Chang, Y.-T.; Liu, X. Intracellular Glutathione Detection Using MnO₂-Nanosheet-Modified Upconversion Nanoparticles. *J. Am. Chem. Soc.* **2011**, *133*, 20168-20171.
- (40) Kong, X.-J.; Wu, S.; Chen, T.-T.; Yu, R.-Q.; Chu, X. MnO₂-Induced Synthesis of Fluorescent Polydopamine Nanoparticles for Reduced Glutathione Sensing in Human Whole Blood. *Nanoscale* **2016**, *8*, 15604-15610.
- (41) Lin, S.; Cheng, H.; Ouyang, Q.; Wei, H. Deciphering the Quenching Mechanism of 2D MnO₂ Nanosheets Towards Au Nanocluster Fluorescence to Design Effective Glutathione Biosensors. *Anal. Meth.* **2016**, *8*, 3935-3940.
- (42) Liu, Y.; Zhou, M.; Cao, W.; Wang, X.; Wang, Q.; Li, S.; Wei, H. Light-Responsive Metal-Organic Framework as an Oxidase Mimic for Cellular Glutathione Detection. *Anal. Chem.* **2019**, *91*, 8170-8175.
- (43) Xu, Y.; Chen, X.; Chai, R.; Xing, C.; Li, H.; Yin, X.-B. A Magnetic/Fluorometric Bimodal Sensor Based on a Carbon Dots-MnO₂ Platform for Glutathione Detection. *Nanoscale* **2016**, *8*, 13414-13421.
- (44) Peng, C.; Xing, H.; Fan, X.; Xue, Y.; Li, J.; Wang, E. Glutathione Regulated Inner Filter Effect of MnO₂ Nanosheets on Boron Nitride Quantum Dots for Sensitive Assay. *Anal. Chem.* **2019**, *91*, 5762-5767.
- (45) Coles, B.; Ketterer, B. The role of glutathione and glutathione transferases in chemical carcinogenesis. *Crit. Rev. Biochem. Molec. Biol.* **1990**, *25*, 47-70.
- (46) Maria-Hormigos, R.; Jurado-Sánchez, B.; Escarpa, A. Tailored Magnetic Carbon Allotrope Catalytic Micromotors for 'On-Chip' Operations. *Nanoscale* **2017**, *9*, 6286-6290.
- (47) Zhang, S.; Zhang, D.; Zhang, X.; Shang, D.; Xue, Z.; Shan, D.; Lu, X. Ultratrace Naked-Eye Colorimetric Detection of Hg²⁺ in Wastewater and Serum Utilizing Mercury-Stimulated Peroxidase Mimetic Activity of Reduced Graphene Oxide-PEI-Pd Nanohybrids. *Anal. Chem.* **2017**, *89*, 3538-3544.
- (48) Busa, L. S.; Komatsu, T.; Mohammadi, S.; Maeki, M.; Ishida, A.; Tani, H.; Tokeshi, M. 3,3',5,5'-Tetramethylbenzidine Oxidation on Paper Devices for Horseradish Peroxidase-based Assays. *Anal. Sci: Int. J. Japan Soc. Anal. Chem.* **2016**, *32*, 815-818.
- (49) Serra-Maia, R.; Bellier, M.; Chastka, S.; Tranhuu, K.; Subowo, A.; Rimstidt, J. D.; Usov, P. M.; Morris, A. J.; Michel, F. M. Mechanism and Kinetics of Hydrogen Peroxide Decomposition on Platinum Nanocatalysts. *ACS Appl. Mater. Interfac.* **2018**, *10*, 21224-21234.
- (50) Liu, X.; Wang, Q.; Zhang, Y.; Zhang, L.; Su, Y.; Lv, Y. Colorimetric Detection of Glutathione in Human Blood Serum Based on the Reduction of Oxidized TMB. *New J. Chem.* **2013**, *37*, 2174-2178.
- (51) Xu, H.-H.; Deng, H.-H.; Lin, X.-Q.; Wu, Y.-Y.; Lin, X.-L.; Peng, H.-P.; Liu, A.-L.; Xia, X.-H.; Chen, W. Colorimetric Glutathione Assay Based on The Peroxidase-Like Activity of a Nanocomposite Consisting of Platinum Nanoparticles and Graphene Oxide. *Microchim. Acta* **2017**, *184*, 3945-3

VI.3. Article 9. Integrated micromotor optical fluorescence smartphone for real-time point-of-care testing.



Integrated Micromotor Optical Fluorescence Smartphone for Real-Time Point-of-Care Testing

Kaisong Yuan,^{†§} Víctor de la Asunción-Nadal,[†] Beatriz Jurado-Sánchez,^{†*} and Alberto Escarpa^{†‡*}

[†]Department of Analytical Chemistry, Physical Chemistry and Chemical Engineering, University of Alcalá, Alcalá de Henares E-28871, Madrid, Spain. E-mail: beatriz.jurado@uah.es, alberto.escarpa@uah.es (Tel: +34 91 8854995)

[§]Institute of Pharmaceutical Analysis, College of Pharmacy, Jinan University, Guangzhou, China

[‡]Chemical Research Institute "Andrés M. del Río", University of Alcalá, Alcalá de Henares E-28871, Madrid, Spain

ABSTRACT: Herein, we describe the design of a point-of-care integrating micromotor for real-time fluorescence sensing of biomarkers. The system comprises a universal 3D printed platform to hold a commercial smartphone, which is equipped with an external magnification optical lens (20-400X) and tailor-made emission filters directly attached to the camera, an adjustable sample holder to accommodate a glass slide and laser excitation sources. On a first approach, we illustrate the suitability of the platform using magnetic Janus micromotors modified with fluorescence Cd_xSe_{1-x}@ZnS quantum dots for real-time "ON-OFF" mercury detection in serum samples. On a second approach, graphdyne tubular catalytic micromotors modified with a Rhodamine labelled affinity peptide will be used for "OFF-ON" detection of Cholera toxin B as model analytes. The strategy was validated against a high-performance optical microscope, obtaining a perfect match. The developed micromotor based platform allows for direct detection using just microliter of sample and micromotors, replacing paper-based strips or microchips for sample processing. The versatility of the strategy allows for easy integration of micromotor sensing strategies based on different propulsion mechanism and relying in fluorescence detection of a myriad of biomarkers, and even multiplexed schemes.

INTRODUCTION

Healthcare is a matter of paramount significance worldwide. Indeed, accurate and timely diagnosis is greatly beneficial to prompt treatment and prevention, especially on infectious diseases. Decentralized health monitoring can aid to reduce the burden in hospital and primary care units, not to mention the potential use in non-developed countries.^{1,2} The rise of smartphone technology in connection with point-of-care (POCs) miniaturized biosensors hold considerable promise for novel diagnosis platforms.³ In such configurations, smartphones can be used as simple read-out and processing systems or as an integral part of the system. The detection can be optical, electrochemical and even based on optical microscopy approaches.^{4,5} Fluorescence optical detection offers great advantages when coupled with smartphone, due to the phone camera can be readily used without the need for additional parts.⁶⁻⁸ The readout can be either performed in real-time or endpoint after sample processing/amplification in microchips or paper strips. For example, POCs integrating lateral flow immunoassays microchips have been applied for

endpoint *Escherichia Coli*⁹ and methicillin resistant *Staphylococcus Aureus*¹⁰ bacteria detection in urine and blood samples, respectively. Similarly, prostate specific antigen in whole blood have been achieved in just 15 min within the ng mL⁻¹ range after microchip-based sandwich enzyme linked immunoassay.¹¹ Virus detection (HIV, Hepatitis B, etc) POCs devices can also benefit from microchips for sample preprocessing prior endpoint detection, either by using DNA modified quantum dots (QDs) barcodes¹² or microfluidic chip loop-mediated isothermal amplification.^{13,14} Thus, detection of such targets can be performed directly using whole blood or nasal swabs after 15-30 min detecting down to 10³ virus copies per mL.¹²⁻¹⁴ As an alternative, microchips can be easily replaced by paper strips modified with antibodies for fluorescence immunoassays for Zika Virus detection¹⁵ or fluorescence QDs,^{16,17} metal organic frameworks@enzyme¹⁸ complexes and up-conversion nanoparticles for the determination of biomarkers of diabetes, heart failure or infections, respectively.^{17,19} In the above-mentioned configurations, detection can be performed in less than 15 min at ng mL⁻¹ levels. The POCs platforms are equipped with a special holder to place the paper

strip for simple read-out. A real-time fluorescence based POCs for hemoglobin relies on a specifically designed microchip integrating SiO_2 @QDs with acoustofluidic enrichment, achieving detection in whole blood in just 2 min at $\mu\text{g mL}^{-1}$ levels.²⁰

The fast progress in nanotechnology and miniaturization fabrication techniques make possible the development of miniaturized biosensors and nanoparticles, crucial for the design of the previously mentioned POCs devices. Micromotors are at the forefront of nanotechnology research and have demonstrated its potential for novel on-the-fly biomarker sensing approaches using ultralow sample and reagents volumes.²¹⁻²⁶ The enhanced micromotor movement greatly enhances analyte-probe interaction, which along with its possibilities for functionalization and nanoscale dimensions make such autonomous microdevices ideal for the design of POCs based on "active transport".²⁷⁻³³ The detection and sample processing can be performed actively by using the moving micromotors, avoiding the use of microchips or previous sample preparation steps. Yet, only two strategies based on motion-based detection have been reported. Thus, a POCs based micromotor for HIV-1 detection comprising a microchip and DNA-modified platinum-gold Janus micromotors has been proposed. The micromotors can move in peroxide solutions by decomposition of such fuel in the catalytic Pt part and generation of oxygen bubbles. The detection principle involves loop-mediated isothermal amplification of the nucleic acid of HIV-1, followed by mixing of resulting amplicons with the DNA-modified micromotors. The presence of HIV-1 generates large amplicons that reduce the initial speed of the motors (turn-off). Such decrease is used as the analytical signal, detecting 1000 virus particles mL^{-1} in 60 min.³⁴ A similar micromotor based POC was also applied for Zika virus detection but in a turn-on configuration. In this case, the Au Janus micromotors are modified with anti-Zika virus monoclonal antibodies for virus capture, followed by attachment of anti-Zika antibody platinum nanoparticles. The presence of virus in a testing samples results in the accumulation of an increased concentration of Pt beads, increasing the speed in peroxide solutions.³⁵ Despite its simplicity, such POCs requires a sophisticated sample pre-treatment and detection algorithms for motion detection as no visual detection is available.

Herein, we describe the design of POCs integrating micromotor for real-time fluorescence sensing of biomarkers and heavy metals. To the best of our knowledge, this is the first time that micromotor based fluorescence approaches are integrated into portable instrumentation. The system comprises a 3D dark platform integrating a smartphone coupled with a high-resolution optical lens, custom made emission filters and a compartment for insertion of

low-cost commercial laser to tailor the excitation wavelength. The system integrates a "movable" custom made platform for the insertion of a glass slide to place the sample and the micromotors. The platform allows for fast sample focus to obtain high resolution images which are further processed. On a first approach, we will illustrate the suitability of the POC using magnetic Janus micromotors modified with fluorescence $\text{Cd}_x\text{Se}_{1-x}$ @ZnS QDs for real-time ON-OFF mercury detection in serum samples. On a second approach, graphdyine (GDY) tubular catalytic micromotors modified with a Rhodamine labelled affinity peptide are used for OFF-ON detection of Cholera toxin B (CTB) as model analyte. The suitability of the detection protocols was validated against a high-resolution optical microscope, with excellent match. The universal platform developed here meet the World Health Organization's criteria (affordable, sensitive, specific, user friendly, rapid, and equipment-free), holding considerable promise for its use in non-developed regions or for epidemic control. Compared with previous POCs approaches, our strategy allows for direct detection using just microliter of sample and micromotors, replacing paper-based strips or microchips. The versatility of the strategy allows for easy integration of micromotor sensing strategies based on different propulsion mechanism (catalytic, magnetic, ultrasound) relying in fluorescence detection of a myriad of biomarkers, and even multiplexed schemes.

EXPERIMENTAL SECTION

Smartphone-fluorescence device. The 3D platform for the fluorescence phone set-up was designed using SolidWorks 2015. The platform contains an aperture to insert different laser sources at the desired excitation wavelengths, along with a sample holder to place a glass slide with the drop containing the sample. The laser beam direction is parallel to the sample. Different cut-off emission filters (red, green or yellow) were placed prior a 20X-400X Universal Tip scope used for magnification (which is directly attached to a smartphone). Both components were purchased from Amazon. Micromotors motion and/or the fluorescence of the solution were directly observed in the camera application of the phone, which was also used to record the Videos at 30 FPS. Micromotor motion was tracked with Particle Tracker module of ImageJ (<https://imagej.net/Particle Tracker>) and fluorescence measurements were performed using Fiji free software.

An inverted optical microscope (Nikon Eclipse Instrument Inc. TiS/L100) coupled with a 20X objective, fluorescence filter cubes (FITC, λ_{ex} , 467 nm; λ_{em} , 498 nm and G-2A, λ_{ex} , 510, λ_{em} , 560 nm) and a Zyla

VI. Optical portable detection with 2D Janus micromotors: towards on-site screening

CMOS digital camera was used to validate the smartphone platform. Images or movies were processed using Image J and Fiji software, respectively.

Magnetic set-up for magnetic micromotor movement. A customized system comprising an electric motor with a permanent magnet is used to create a rotatory magnetic field. The motor is assembled in a platform that fits the glass slide placed in the sample holder. The speed of the electric motor can be modulated to control the frequency of the magnetic field (from 0 to 9 Hz) and in turn, the speed of the micromotors.

Micromotor synthesis. All reagents used were obtained from Sigma-Aldrich (Spain) and used without further purification. For the synthesis of $Cd_xSe_{1-x}@ZnS$ /graphene oxide (GO)/ Fe_2O_3 Janus micromotors used for Hg^{2+} ion detection, polystyrene microparticles (PS) with a 20 μm diameter were used as base particles (cat. 87896). In brief, a monolayer of PS particles was covered with a ~ 50 nm gold layer, followed by modification with GO by incubation of 0.9 mL of ultrapure water containing the modified particles and 0.1 mL of sulfhydryl-modified graphene oxide (HS-GO) (cat. 763705) for 2 h to promote attachment to gold by thiol bond. Next, 20 μL of Fe_2O_3 NPs solution (1 mg/mL, cat. 544884) was added and the solution was mixed for 1 h to generating the magnetic engine, followed by cleaning with a filter to remove unbounded magnetic particles, as well as 5 μL of $Cd_xSe_{1-x}@ZnS$ QDs (cat. 753904) was added furtherly to modify the micromotors. The micromotors remains stable for 1 month without any changes in its properties.

Tubular GDY/Pt micromotors for endotoxin detection were synthesized by template electrodeposition. To this end, a polycarbonate membrane comprising 5 μm diameter conical pores (Cat. WHA110413) was covered with a thin gold layer and assembled in a custom-made electrochemical cell. A Pt wire and an Ag/AgCl respectively. The outer micromotor layer was electrodeposited from a solution containing 0.1 mg mL^{-1} of GDY and 0.5 mol L^{-1} of Na_2SO_4 by cyclic voltammetry ($n=10$, 0.3 V to -1.5 V, 50 $mV s^{-1}$). The inner platinum layer was electrodeposited by applying a -0.4 V potential for 750 s and a solution containing 4 mmol L^{-1} of chloroplatinic acid hydrate (cat. 398322) in 0.5 mol L^{-1} boric acid (cat. B0394). The micromotors were released from the membrane (3M) electrode were used as counter and reference electrode, by polishing the Au layer and immersion in methylene chloride, isopropanol and dispersion in water. The micromotors were next modified with a Rhodamin-B labelled affinity peptide (B-VQCRLGPPWCAK, Neo-Biotech, Nanterre, France) specific for the detection of CTB. To this end 100 μL of the affinity peptide solution (100 $\mu g mL^{-1}$) were added to an Eppendorf tube containing 1 batch of dry

motors (500,000 motors), 150 mL of 3% sodium dodecyl sulfate (cat. 71727) and 200 μL of ACN: H_2O_2 1:3 for 1 h.

Mercury detection. For detection, 1 μL of modified Janus micromotor solution was placed on the glass slide which assembled into the holder. The drop was mixed with solutions containing increasing concentrations (from 0 to 1 $\mu g mL^{-1}$) of Hg^{2+} (cat. Y0002003). The magnetic module was placed bellow and the frequency set to 4 Hz. Next, the solution was irradiated with the laser and videos were recorded directly with the camera of the phone. The experiments were performed in a similar fashion using the optical microscope for comparison. Micromotor speed and fluorescence of the micromotor on both cases was evaluated by taking time-lapse images of the recorded videos, which were processes with Fiji software for uniformity. The analytical performance was evaluated though the limit of detection (LOD), limit of quantification (LOQ), selectivity and recovery. Calibrations plots were obtained ($n=10$) and the LOD or LOQ were calculated as 3 or 10 times the standard deviation of the ordinate divided by the slope of the calibration linear fit. Selectivity was evaluated against 1 $\mu g mL^{-1}$ of potentially interfering species including Ca, Cd, Mn, Ni and Zn ions. Recovery was evaluated by fortifying human serum samples (cat. H4522) with 1 $\mu g mL^{-1}$ of Hg^{2+} .

Toxin detection. 1 μL of modified motors, 1 μL of H_2O_2 3% and 1 μL of sample or solutions containing increasing concentrations (from 0 to 5 ng mL^{-1}) of CTB (cat. C9903) were mixed on the glass slide. Sample was next irradiated with the laser and Videos recorded and processed in a similar fashion to that reported for mercury. Experiments were also performed with the optical microscope for comparison. Analytical performance was evaluated in a similar fashion to that described for Hg ion. Selectivity was evaluated using endotoxin from *Escherichia Coli* (cat. L2630) and bovine serum albumin (cat. A2153) as potential interfering compounds.

RESULTS AND DISCUSSION

Figure 1A depicts the concept of the integrated POCs micromotor platform. As can be seen, a tailor-made 3D platform integrates all the components required to perform the fluorescence detection measurements. To perform the detection, the sample containing the micromotors is placed on a glass slide, which is assembled in a movable platform which allow for fast focus similar to that performed in normal microscopes. Next, the sample is irradiated with a commercial laser at a desired wavelength in parallel. In this way, sample is excited and the released fluorescence travels to the objective/camera of an iPhone, which is equipped with a high-resolution lens and a tailor-made emission filter at the desired

wavelength. Videos are directly recorded with the phone and further processed with Fiji software, as already described in the experimental section. **Figure 1B** shows pictures of the attachment among the filters and the optical lens. In this case, red, green and yellow filters were obtained from Amazon and cut to fit the objective of the phone. The strategy is highly versatile and allows to use more types of filters and shapes to fit several smartphones. Characterization of the emission filters will be given in the following section. The pictures also illustrate the irradiation of the sample with the laser. Please note here that we open the platform to take the pictures, but for real fluorescence measurements all is covered and in the dark to avoid potential interferences with the signal. **Figure 1C** shows a real image of the displayed contents in the smartphone screen during a measurement. The platform is highly versatile, allowing for its usage with catalytic, magnetic, light or ultrasound propelled micromotors. To illustrate the concept, we select applications using tubular and Janus micromotors and magnetic and catalytic modes for fluorescence detection. Thus, **Figure 1D** illustrates real images from the smartphone using peptide modified tubular micromotors for OFF-ON toxin detection and QDs modified magnetic Janus micromotors for ON-OFF mercury detection. As can be seen, in the tubular micromotors a clear red fluorescence, arising from the Rhodamine labelled peptide probe attached, can be clearly visualized in the figure and supporting **Video S1**, which is not observed when the laser excitation is turned off. Once in contact with the target toxin, the peptide will be released and the solution will gain an intense red fluorescence, as will be further described. In the case of magnetic Janus, the micromotors observed in the figure are clearly fluorescence due to the modification with the QDs. Once in contact with the target mercury, the fluorescence on the micromotors will be quenched, in turn they will become dark and such

decrease of fluorescence can be related to mercury concentration. As in the previous case, no light is emitted after turning the laser off. Further details will be given in the following sections. In brief, the images illustrate a clear fluorescence in the solution or in the micromotors, allowing to perform detection both in the solution and in the micromotors. Such configuration greatly simplifies the strategy, avoiding the use of microchips or other sample pre-processing attachments. Indeed, the micromotors can act as mobile biosensors, allowing to perform fast, on-the-fly detection, in real time and with low sample and reagents requirements. The POCs are also extremely useful to imaging other fluorescence species such as QDs (see **Figure 1D**, right).

Prior application for the detection of target analytes, the performance of the system and the excitation-emission configuration based on laser and filters, respectively, was evaluated. First, the absorbance spectra of each filter was evaluated with UV/VIS measurements by placing it in front of the beam of a spectrophotometer. Data was processed to obtain the transmittance spectra, which is illustrated in **Figure 2A**. Once characterized, appropriate commercial $\text{Cd}_x\text{Se}_{1-x}@\text{ZnS}$ QDs with tailored sizes and, in turn, emission and excitation profiles, were chosen and measured in solution and incorporated in the micromotors. Images were taken according to the conditions schematically summarized in **Figure 2B**, and processed with Fiji software to obtain the histograms both of the background (B in the figure) and the fluorescence part in the sample (S in the figure). For both solutions and micromotors and in all configurations, histograms indicate that the settings are suitable because the fluorescence emission presents higher brightness than the noise, including dark-current noise and background fluorescence, with no overexposure.⁶

VI. Optical portable detection with 2D Janus micromotors: towards on-site screening

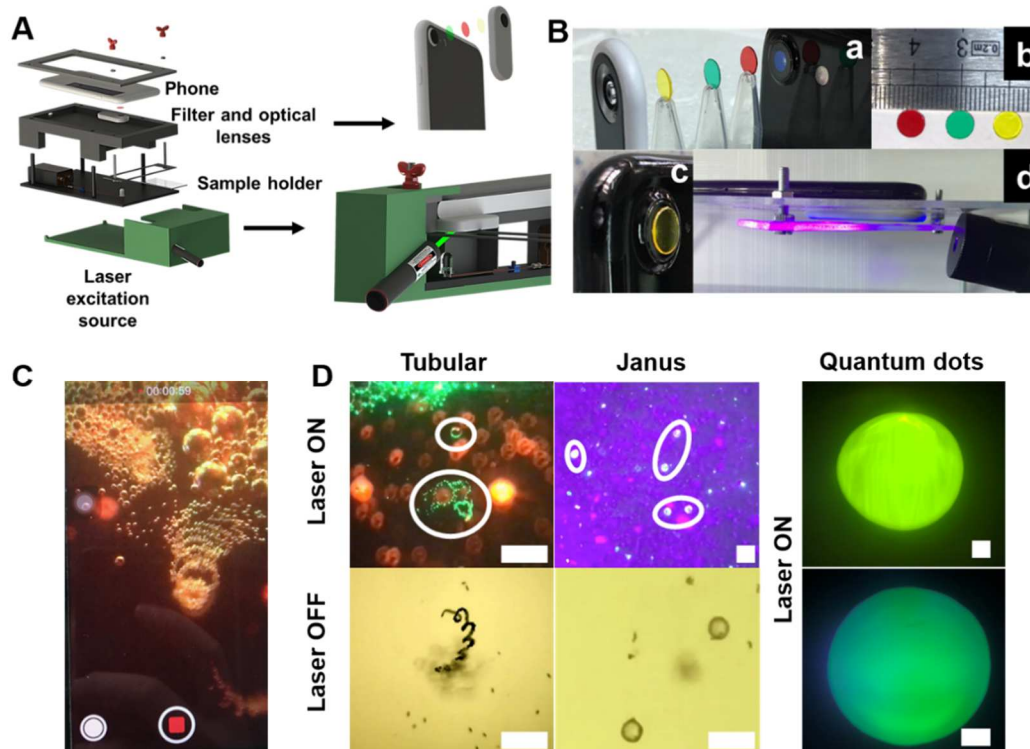


Figure 1. Smartphone-based fluorescence platform integrating micromotors and proof-of-concept applications. A) Integration of the smartphone into a 3D printed platform and description of the different parts of the device. B) Detailed pictures of the assembly of the optical lens with the different filters (a), detailed size of the tailor-made absorbance filters (b), the filter on top of the camera of the phone (c) and irradiation of the sample -deposited on a glass slide- with the specific laser. C) Picture of the screen on the phone showing the real time fluorescence detection with moving micromotors. D) Time lapse images (Taken from Video S1) showing the movement and fluorescence of microliter drops containing GDY/Pt tubular micromotors modified with a specific fluorescence probe for “OFF-ON” detection of CTB (λ_{ex} , 532 nm; λ_{em} , 665 nm), magnetic actuated $Cd_xSe_{1-x}@ZnS/GO/Fe_2O_3$ Janus micromotors for “ON-OFF” detection of Hg^{2+} (λ_{ex} , 405 nm; λ_{em} , 495 nm), drops of core-shell $Cd_xSe_{1-x}@ZnS$ QDs (top: λ_{ex} , 405 nm; λ_{em} , 574 nm; bottom: λ_{ex} , 405 nm; λ_{em} , 525 nm). White circles indicate a micromotor moving. Scale bars, 50 μm .

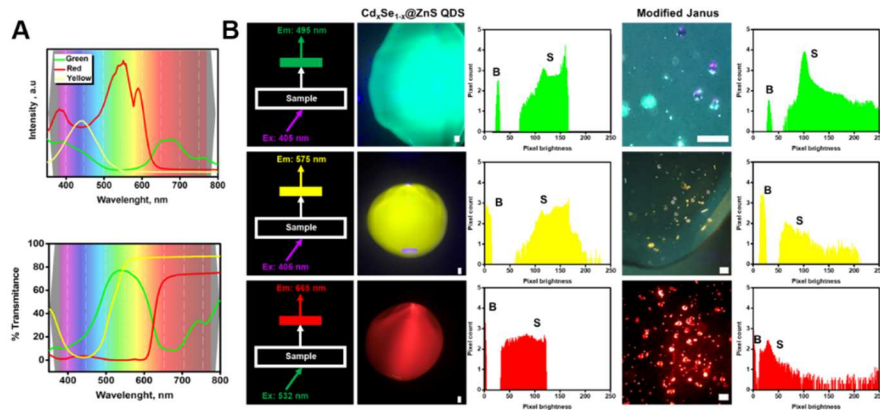


Figure 2. Evaluation of the performance of the smartphone-based fluorescence platform. A) Absorbance and corresponding transmittance profiles of the green, red or yellow emission filters. B) Fluorescence images of $Cd_xSe_{1-x}@ZnS$ QDs solutions or modified Janus micromotors and corresponding histograms (in log scale) where B indicate background signal and S the fluorescence signal of the solution or the micromotor, respectively. For the specific excitation and emission conditions, see images at the left of each figure. Scale bars, 50 μm .

Once evaluated the suitability of the set-up, the platform was evaluated first for ON-OFF detection approaches, using Hg^{2+} as proof of concept and inspired in a previous work from our research group.³⁶ For the application we select $\text{Cd}_x\text{Se}_{1-x}@ZnS/GO/Fe_2O_3$ Janus micromotors due to its relatively bigger size (20 μm) compared to tubular and other design an optimal size which allow for better area selection for accurate fluorescence measurements. The strategy is depicted in **Figure 3A**. In brief, initially the micromotors exhibit a strong fluorescence arising from the QDs. After Hg^{2+} addition and 2 minutes of the micromotor movement the fluorescence is quenched due to cationic exchange and/or Hg ion attachment to the outer ZnS layer in the QDs, generating $\text{Cd}_x\text{Se}_{1-x}@HgS$ or alloyed $\text{Cd}_x\text{Se}_{1-x}@Zn_{1-x}Hg_x$ QDs and displacing the emission wavelength, resulting in fluorescence quenching in a concentration-dependence manner.³⁶⁻³⁸ Such change can be clearly observed in solutions containing 1 $\mu\text{g mL}^{-1}$ of Hg^{2+} (insets of **Figure 3A** and **Video S2**), with a clear initial fluorescence emission which is gradually quenched and the micromotors turn into a violet color, similar to that observed to the blank, due to reflection from the laser source. To facilitate fluorescence measurement, images were converted into black and white scale, further confirming the absence of fluorescence in the quenched micromotors. In this case, to illustrate the versatility of the POC platform based on micromotors, we select magnetic propulsion mode to illustrate the concept. Such configuration can be ideal to perform detection in fluids such as whole blood samples, in which the high content of catalase and proteins hamper the applicability of catalytic propelled designs, the most used to date for analytical purposes.³⁹ To perform the experiment, the magnetic set-up (see the experimental section for further details) was placed below the platform and close to the sample holder containing the glass slide with the micromotors. The platform allows to tailor the speed of the micromotors by changing the frequency of the magnetic field (from 0 to 9 Hz). Speed increase along frequency up to 4 Hz from 0 to $40 \pm 5 \mu\text{m s}^{-1}$. Higher frequencies generate turbulent flows that decrease

the speed up to 2 times, with an unstable pattern. As such, frequency of the magnetic field was set to 4 Hz. Next, we performed control experiments to check the role of micromotor movement in the detection. To this end, static $\text{Cd}_x\text{Se}_{1-x}@ZnS/GO/Fe_2O_3$ micromotors were incubated with 1 $\mu\text{g mL}^{-1}$ of Hg^{2+} and Videos were recorded for 1 hour. Negligible fluorescence quenching is noted (not shown), revealing the crucial movement of the micromotors to accelerate detection. Next, we evaluated the selectivity of the protocol for Hg^{2+} sensing. As can be seen in the normalized fluorescence plot of **Figure 3B** and corresponding time-lapse images, fluorescence quenching is only observed in the presence of the target analyte, with negligible changes in the presence of potentially interfering cations, probably due its lower affinity to undergo cation exchange with the QDs or no disruption of the fluorescence signal. To validate the strategy, experiments were also performed with a high-resolution optical microscope, obtaining the similar results. Next, calibration plots were evaluated with both instrumental set-ups using the micromotors and increasing concentrations of Hg^{2+} . As can be seen, on both cases, the fluorescence of the micromotors decrease as the concentration of the target analyte increase. The LODs were 0.09 and 0.08 $\mu\text{g mL}^{-1}$ calculated using the microscope and the smartphone platform, respectively. The linear range spans from 0.25 to 1 $\mu\text{g mL}^{-1}$ on both cases. Next, we evaluate the performance of the strategy by performing recovery studies in raw serum samples as representative biological fluid. Recovery percentages of 93 ± 5 and 88.9 ± 5 were obtained with the device and the microscope, respectively, illustrating the suitability of the platform for future ions detections as hazardous in complex biological fluids. Please note here that despite the LOD for Hg^{2+} detection is higher than that established for regulatory agencies, our aim here was to demonstrate the concept for magnetic fluorescence detection of cations. For further applications, the micromotors can be modified with specific probes to increase the sensitivity in the detection for a given application, which is out of the scope of the aim of this article.

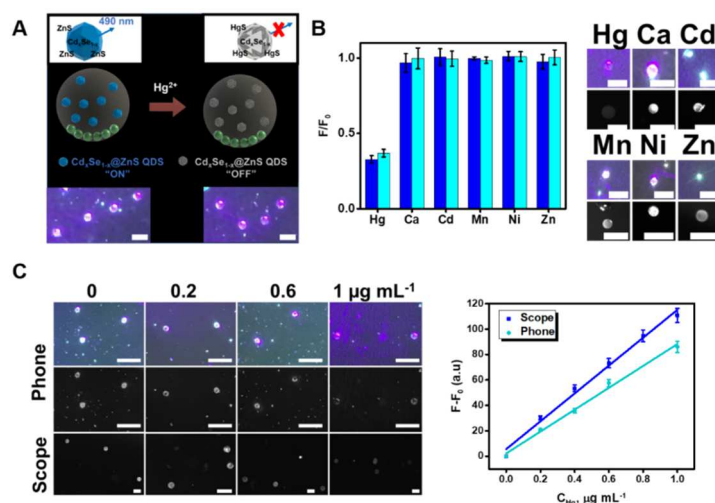


Figure 3. “ON-OFF” magnetic actuated $\text{Cd}_x\text{Se}_{1-x}@\text{ZnS}/\text{GO}/\text{Fe}_2\text{O}_3$ Janus micromotors strategy for Hg^{2+} detection using the fluorescence smartphone. A) Schematic of the sensing strategy and corresponding time-lapse microscopy images (taken from Video S2) before and after micromotor navigation in solutions containing $1 \mu\text{g mL}^{-1}$ of Hg^{2+} . B) Selectivity of the sensing strategy in the presence of heavy metals and corresponding real time-lapse fluorescence images using the smartphone (top) and a high-performance optical microscope (bottom). C) Time-lapse fluorescence images of the moving micromotors in the presence of increasing concentrations of Hg^{2+} taken using the smartphone ($\lambda_{\text{ex}}, 405 \text{ nm}$; $\lambda_{\text{em}}, 495 \text{ nm}$) and the microscope and corresponding calibration plots. Scale bars, $50 \mu\text{m}$.

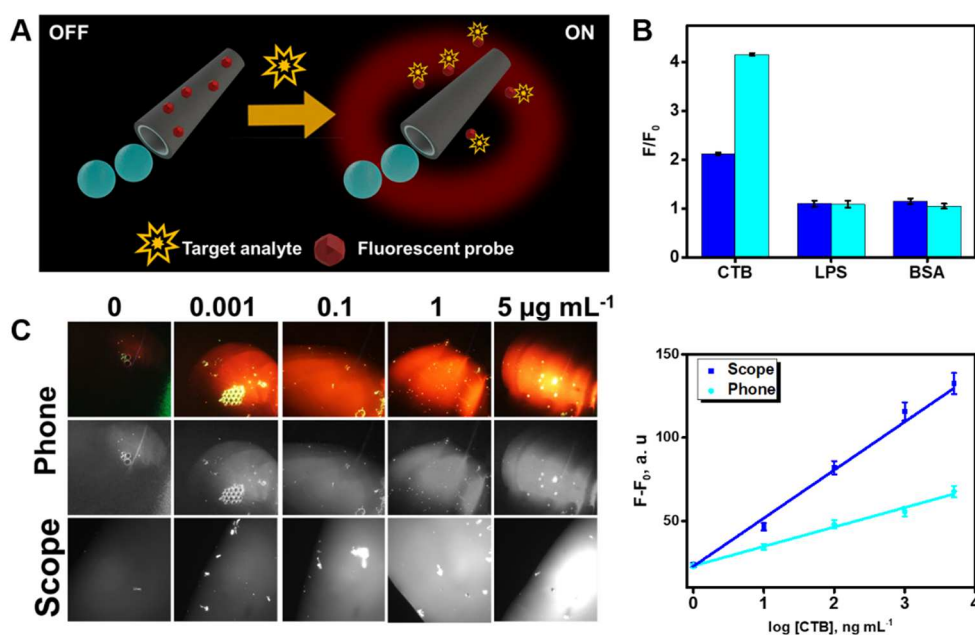


Figure 4. A) “OFF-ON” GDY/Pt tubular micromotors modified with a rhodamine-labeled affinity peptide for CTB detection. B) Specificity of the sensing strategy under the presence of the target toxin, endotoxin from *Escherichia Coli* (LPS) and bovine serum albumin (BSA). C) Time-lapse fluorescence images of the moving micromotors in the presence of increasing concentrations of CTB taken using the smartphone ($\lambda_{\text{ex}}, 532 \text{ nm}$; $\lambda_{\text{em}}, 665 \text{ nm}$) and the microscope and corresponding calibration plots.

As a second proof-of concept application, we evaluated the utility of the POCs platform for OFF-ON micromotor based approaches, which is an important configuration for the analysis of clinical biomarkers with excellent performance and negligible sample consumption. Yet, to date, the practical utility of such

procedures is hampered by the requirements for the use of high-resolution fluorescence microscopes. As such, the integration into simple and portable instrumentation such as the one described here will bring closer the strategies for practical use in future personalized medicine. The concept of the strategy is

VI. Optical portable detection with 2D Janus micromotors: towards on-site screening

depicted in **Figure 4A** and relies on the functionalization of micromotors with fluorescence labelled receptors. In the presence of the target analyte, such receptors are released in a concentration dependence manner. Thus, toxins,⁴⁰ miRNA,⁴¹ proteins⁴² or bacterial endotoxins have been detecting using such configurations and graphene⁴⁰ of chalcogenides based micromotors.⁴² As model system in the work we selected CTB as target analytes and affinity peptide modified GDY/Pt tubular micromotors, following a very recent approach developed by our research group.⁴³ CTB is an integral part of the toxin produced by *Vibrio Cholerae* bacteria and can cause severe health effect such as severe diarrhea.⁴⁴ As described in the experimental section, the affinity peptide is specifically designed as a “fingerprint” of the CTB. Such peptide can be incorporated on the surface of GDY micromotors by physical adsorption through electrostatic and p-stacking with the non-polar and aromatic amino acids present in the peptide (arginine, cysteine, alanine, proline, lysine) and through the p-orbitals in the aromatic rhodamine B tag. Under the presence of the target CTB, a competitive binding is established and the higher affinity of the peptide toward the analyte results in its release from the GDY surface, increasing thus the fluorescence in the solution in just 3 minutes.⁴⁵ The specificity of the protocol is clearly illustrated in the normalized fluorescence plot of **Figure 4B**, which indicate only fluorescence increase under the presence of CTB, with no changes produced by other interfering species such as BSA and endotoxins from *Escherichia Coli*. Fluorescence images were taken both with the smartphone platform and with a high-resolution optical microscope, with similar results on both cases. Control experiments using static modified micromotors were also performed, with negligible fluorescence recovery (18%), illustrating again the crucial role of micromotor movement in accelerating and enhancing the detection performance. To further evaluate the biosensing capacity and performance of the integrated platform, calibration plots were taken. The experiments were repeated in parallel using the high-resolution optical microscope for comparison (see **Figure 4B**). The calculated LODs were 1.6 and 1.4 ng mL⁻¹ for the POC platform and the high-resolution optical microscope, respectively. Linear range spans from 4.5 to 5000 ng mL⁻¹ of both cases, with an excellent match, which further illustrate the practical utility of the developed protocol. Excellent recoveries close to 100 % in fortified serum samples were also obtained. Indeed, the LOD and LOQ are much lower than the concentration of cholera toxin in ill patients, revealing the suitability for future diagnosis of such disease. While catalytic micromotors are used here, the strategy can be translated to magnetic configurations (as illustrated

for Hg²⁺ detection) and receptors for a myriad of applications only limited by our imagination.

CONCLUSIONS

We have described here, for the first time, a POCs platform integrating micromotors as active and on-the-fly (bio)-sensors for the detection of a myriad of analytes as clinical biomarkers. The coupling of high magnifications lens, tailor made emission filters and excitation lasers with a smartphone results in a highly efficient optical device that can be used by non-specialized personnel and in an easy manner. The suitability of the strategy was revealed by the close match with the results obtained using high-resolution optical microscope. As such, the work addresses the important drawback existing to date for the application of highly efficient micromotors strategies for biomarker detection, that require the use of sophisticated and expensive instrumentation not available in routine laboratories. The versatility of the platform in terms of types of micromotors, propulsion modes and fluorescence strategies have been clearly illustrated by the detection of Hg²⁺ ions and CTB. The detection can be performed in less than 5 minutes and just require dropping the sample (human serum) on a glass slide along with the micromotor and fuel solution, with an average cost of 0.5 € per analysis. The platform meets the World Health Organization’s criteria (affordable, sensitive, specific, user friendly, rapid, equipment-free). Compared with existing POCs for clinical biomarkers based on fluorescence detection (see Table 1 in the Supporting information), our system simplified the designs, avoiding the use of sample pre-processing microchips or other steps, reducing the detection time and with adequate LODs. Future aims should be focused to tailor the strategy for other configurations and other receptors, increasing the overall sensitivity of the system.

ASSOCIATED CONTENT

Supporting Information

The Supporting Information is available free of charge on the ACS Publications website.

Table S1 (.pdf)

Video S1. Movement of graphdiyne/Pt tubular micromotors modified with a specific fluorescence probe for “OFF-ON” detection of Cholera Toxin B and magnetic actuated Cd_xSe_{1-x}@ZnS/GO/Fe₂O₃ Janus micromotors for “ON-OFF” detection of Hg²⁺ with laser on and off (.AVI)

VI. Optical portable detection with 2D Janus micromotors: towards on-site screening

Video S2. Cd₃Se_{1-x}@ZnS/GO/Fe₂O₃ Janus micromotors navigation in solutions containing 1 µg mL⁻¹ of Hg²⁺ (.AVI)

AUTHOR INFORMATION

Corresponding Author

* alberto.escarpa@uah.es

* beatriz.jurado@uah.es

Author Contributions

The manuscript was written through contributions of all authors. All authors have given approval to the final version of the manuscript. K. Yuan and V. de la Asunción Nadal contributed equally to this work.

ACKNOWLEDGMENT

K. Yuan acknowledges the Ministry of Economy, Industry and Competitiveness for his pre-doctoral contract (RYC-2015-17558, co-financed by EU). V. de la Asunción Nadal acknowledges the Universidad de Alcalá for his FPI fellowship. B. J-S acknowledges support from the Ministry of Economy, Industry and Competitiveness (RYC-2015-17558, co-financed by EU) from the University of Alcalá (CCG19/CC-029) and from the Community of Madrid (CM/JIN/2019-007). AE acknowledges the financial support from the Ministry of Economy, Industry and Competitiveness (CTQ2017-86441-C2-1-R) and the TRANSNANOAVANSENS program (S2018/NMT-4349) from the Community of Madrid.

REFERENCES

- (1) Ding, X.; Mauk, M. G.; Yin, K.; Kadimisetty, K.; Liu, C. Interfacing Pathogen Detection with Smartphones for Point-of-Care Applications. *Anal. Chem.* **2019**, *91*, 655-672.
- (2) Malekjahani, A.; Sindhwani, S.; Syed, A. M.; Chan, W. C. W. Engineering Steps for Mobile Point-of-Care Diagnostic Devices. *Acc. Chem. Res.* **2019**, *52*, 2406-2414.
- (3) Rezazadeh, M.; Seidi, S.; Lid, M.; Pedersen-Bjergaard, S.; Yamini, Y. The Modern Role of Smartphones in Analytical Chemistry. *Trends Anal. Chem.* **2019**, *118*, 548-555.
- (4) Zhao, W.; Tian, S.; Huang, L.; Liu, K.; Dong, L.; Guo, J. A Smartphone-Based Biomedical Sensory System. *Analyst* **2020**, *145*, 2873-2891.
- (5) Aydingogan, E.; Guler Celik, E.; Timur, S. Paper-Based Analytical Methods for Smartphone Sensing with Functional Nanoparticles: Bridges from Smart Surfaces to Global Health. *Anal. Chem.* **2018**, *90*, 12325-12333.
- (6) Dai, B.; Jiao, Z.; Zheng, L.; Bachman, H.; Fu, Y.; Wan, X.; Zhang, Y.; Huang, Y.; Han, X.; Zhao, C.; Huang, T. J.; Zhuang, S.; Zhang, D. Colour Compound Lenses For a Portable Fluorescence Microscope. *Light Sci. Appl.* **2019**, *8*, 75.
- (7) Yu, H.; Tan, Y.; Cunningham, B. T. Smartphone Fluorescence Spectroscopy. *Anal. Chem.* **2014**, *86*, 8805-8813.
- (8) Wei, Q.; Qi, H.; Luo, W.; Tseng, D.; Ki, S. J.; Wan, Z.; Göröcs, Z.; Bentolila, L. A.; Wu, T.-T.; Sun, R.; Ozcan, A. Fluorescence Imaging of Single Nanoparticles and Viruses on a Smart Phone. *ACS Nano* **2013**, *7*, 9147-9155.
- (9) Alves, I. P.; Reis, N. M. Microfluidic Smartphone Quantitation of Escherichia Coli in Synthetic Urine. *Biosens. Bioelectron.* **2019**, *145*, 111624.
- (10) Rajendran, V. K.; Bakthavathsalam, P.; Bergquist, P. L.; Sunna, A. Smartphone Detection of Antibiotic Resistance Using Convective PCR and a Lateral Flow Assay. *Sens. Actuat. B. Chem.* **2019**, *298*, 126849.
- (11) Barbosa, A. I.; Gehlot, P.; Sidapra, K.; Edwards, A. D.; Reis, N. M. Portable Smartphone Quantitation of Prostate Specific Antigen (PSA) in a Fluoropolymer Microfluidic Device. *Biosens. Bioelectron.* **2015**, *70*, 5-14.
- (12) Ming, K.; Kim, J.; Biondi, M. J.; Syed, A.; Chen, K.; Lam, A.; Ostrowski, M.; Rebbapragada, A.; Feld, J. J.; Chan, W. C. W. Integrated Quantum Dot Barcode Smartphone Optical Device for Wireless Multiplexed Diagnosis of Infected Patients. *ACS Nano* **2015**, *9*, 3060-3074.
- (13) Sun, F.; Ganguli, A.; Nguyen, J.; Brisbin, R.; Shanmugam, K.; Hirschberg, D. L.; Wheeler, M. B.; Bashir, R.; Nash, D. M.; Cunningham, B. T. Smartphone-based Multiplex 30-minute Nucleic Acid Test of Live Virus From Nasal Swab Extract. *Lab Chip* **2020**, *20*, 1621-1627.
- (14) Hu, F.; Li, J.; Zhang, Z.; Li, M.; Zhao, S.; Li, Z.; Peng, N. Smartphone-Based Droplet Digital LAMP Device with Rapid Nucleic Acid Isolation for Highly Sensitive Point-of-Care Detection. *Anal. Chem.* **2020**, *92*, 2258-2265.
- (15) Rong, Z.; Wang, Q.; Sun, N.; Jia, X.; Wang, K.; Xiao, R.; Wang, S. Smartphone-Based Fluorescence Lateral Flow Immunoassay Platform for Highly Sensitive Point-Of-Care Detection Of Zika Virus Nonstructural Protein 1. *Anal. Chim. Acta* **2019**, *1055*, 140-147.
- (16) Chu, S.; Wang, H.; Du, Y.; Yang, F.; Yang, L.; Jiang, C. Portable Smartphone Platform Integrated with a Nanoprobe-Based Fluorescence Paper Strip: Visual Monitoring of Glutathione in Human Serum for Health Prognosis. *ACS Sus. Chem. Eng.* **2020**, *8*, 8175-8183.
- (17) Wang, Q. X.; Xue, S. F.; Chen, Z. H.; Ma, S. H.; Zhang, S.; Shi, G.; Zhang, M. Dual Lanthanide-Doped Complexes: the Development of a Time-Resolved Ratiometric Fluorescence Probe For Anthrax Biomarker and a Paper-Based Visual Sensor. *Biosens. Bioelectron.* **2017**, *94*, 388-393.

VI. Optical portable detection with 2D Janus micromotors: towards on-site screening

- (18) Kou, X.; Tong, L.; Shen, Y.; Zhu, W.; Yin, L.; Huang, S.; Zhu, F.; Chen, G.; Ouyang, G. Smartphone-Assisted Robust enzymes@MOFs-Based Paper Biosensor for Point-Of-Care Detection. *Biosens. Bioelectron.* **2020**, *156*, 112095.
- (19) You, M.; Lin, M.; Gong, Y.; Wang, S.; Li, A.; Ji, L.; Zhao, H.; Ling, K.; Wen, T.; Huang, Y.; Gao, D.; Ma, Q.; Wang, T.; Ma, A.; Li, X.; Xu, F. Household Fluorescence Lateral Flow Strip Platform for Sensitive and Quantitative Prognosis of Heart Failure Using Dual-Color Upconversion Nanoparticles. *ACS Nano* **2017**, *11*, 6261-6270.
- (20) Zhang, L.; Tian, Z.; Bachman, H.; Zhang, P.; Huang, T. J. A Cell-Phone-Based Acoustofluidic Platform for Quantitative Point-of-Care Testing. *ACS Nano* **2020**, *14*, 3159-3169.
- (21) Nicewarner-Peña, S. R.; Freeman, R. G.; Reiss, B. D.; He, L.; Peña, D. J.; Walton, I. D.; Cromer, R.; Keating, C. D.; Natan, M. J. Submicrometer Metallic Barcodes. *Science* **2001**, *294*, 137-141.
- (22) Ozin, G. A.; Manners, I.; Fournier-Bidoz, S.; Arsenault, A. Dream Nanomachines. *Adv. Mater.* **2005**, *17*, 3011-3018.
- (23) Kagan, D.; Calvo-Marzal, P.; Balasubramanian, S.; Sattayasamitsathit, S.; Manesh, K. M.; Flechsig, G.-U.; Wang, J. Chemical Sensing Based on Catalytic Nanomotors: Motion-Based Detection of Trace Silver. *J. Am. Chem. Soc.* **2009**, *131*, 12082-12083.
- (24) Mei, Y.; Solovev, A. A.; Sanchez, S.; Schmidt, O. G. Rolled-up nanotech on polymers: from basic perception to self-propelled catalytic microengines. *Chem. Soc. Rev.* **2011**, *40*, 2109-2119.
- (25) Wang, J.: *Nanomachines: Fundamentals and Applications*. 2013. Wiley-VCH.
- (26) Karshalev, E.; Esteban-Fernandez de Avila, B.; Wang, J. Micromotors for "Chemistry-on-the-Fly". *J. Am. Chem. Soc.* **2018**, *140*, 3810-3820.
- (27) Orozco, J.; Pan, G.; Sattayasamitsathit, S.; Galarnyk, M.; Wang, J. Micromotors to Capture And Destroy Anthrax Simulant Spores. *Analyst* **2015**, *140*, 1421-1427.
- (28) Li, J.; Rozen, I.; Wang, J. Rocket Science at the Nanoscale. *ACS Nano* **2016**, *10*, 5619-5634.
- (29) Maria-Hormigos, R.; Jurado-Sanchez, B.; Escarpa, A. Labs-on-a-chip Meet Self-Propelled Micromotors. *Lab Chip* **2016**, *16*, 2397-2407.
- (30) Wang, J. Self-Propelled Affinity Biosensors: Moving the Receptor Around The Sample. *Biosens. Bioelectron.* **2016**, *76*, 234-242.
- (31) Jurado-Sánchez, B.; Escarpa, A. Janus Micromotors for Electrochemical Sensing and Biosensing Applications: A Review. *Electroanalysis* **2017**, *29*, 14-23.
- (32) Campuzano, S.; Esteban-Fernández de Ávila, B.; Yáñez-Sedeño, P.; Pingarrón, J. M.; Wang, J. Nano/Microvehicles for Efficient Delivery and (Bio)Sensing At The Cellular Level. *Chem. Sci.* **2017**, *8*, 6750-6763.
- (33) Mayorga-Martinez, C. C.; Pumera, M. Self-Propelled Tags for Protein Detection. *Adv. Function. Mater.* **2019**, *30*, 1906449.
- (34) Draz, M. S.; Kochehybyoki, K. M.; Vasan, A.; Battalapalli, D.; Sreeram, A.; Kanakasabapathy, M. K.; Kallakuri, S.; Tsibris, A.; Kuritzkes, D. R.; Shafiee, H. DNA Engineered Micromotors Powered by Metal Nanoparticles for Motion Based Cellphone Diagnostics. *Nat. Commun.* **2018**, *9*, 4282.
- (35) Draz, M. S.; Lakshminaraasimulu, N. K.; Krishnakumar, S.; Battalapalli, D.; Vasan, A.; Kanakasabapathy, M. K.; Sreeram, A.; Kallakuri, S.; Thirumalaraju, P.; Li, Y.; Hua, S.; Yu, X. G.; Kuritzkes, D. R.; Shafiee, H. Motion-Based Immunological Detection of Zika Virus Using Pt-Nanomotors and a Cellphone. *ACS Nano* **2018**, *12*, 5709-5718.
- (36) Jurado-Sánchez, B.; Escarpa, A.; Wang, J. Lighting Up Micromotors with Quantum Dots For Smart Chemical Sensing. *Chem. Commun.* **2015**, *51*, 14088-14091.
- (37) Pacheco, M.; Jurado-Sánchez, B.; Escarpa, A. Visible-Light-Driven Janus Microvehicles in Biological Media. *Angew. Chem. Int. Ed.* **2019**, *58*, 18017-18024.
- (38) Jaiswal, A.; Ghosh, S. S.; Chattopadhyay, A. Quantum Dot Impregnated-Chitosan Film for Heavy Metal Ion Sensing and Removal. *Langmuir* **2012**, *28*, 15687-15696.
- (39) Pacheco, M.; López, M. Á.; Jurado-Sánchez, B.; Escarpa, A. Self-Propelled Micromachines For Analytical Sensing: A Critical Review. *Anal. Bioanal. Chem.* **2019**, *411*, 6561-6573.
- (40) Esteban-Fernández de Ávila, B.; Lopez-Ramirez, M. A.; Báez, D. F.; Jodra, A.; Singh, V. V.; Kaufmann, K.; Wang, J. Aptamer-Modified Graphene-Based Catalytic Micromotors: Off-On Fluorescence Detection of Ricin. *ACS Sensors* **2016**, *1*, 217-221.
- (41) Esteban-Fernández de Ávila, B.; Martín, A.; Soto, F.; Lopez-Ramirez, M. A.; Campuzano, S.; Vásquez-Machado, G. M.; Gao, W.; Zhang, L.; Wang, J. Single Cell Real-Time miRNAs Sensing Based on Nanomotors. *ACS Nano* **2015**, *9*, 6756-6764.
- (42) Singh, V. V.; Kaufmann, K.; de Ávila, B. E.-F.; Karshalev, E.; Wang, J. Molybdenum Disulfide-Based Tubular Microengines: Toward Biomedical Applications. *Adv. Function. Mater.* **2016**, *26*, 6270-6278.
- (43) Yuan, K.; de la Asunción-Nadal, V.; Li, Y.; Jurado-Sánchez, B.; Escarpa, A. Graphdiyne

VI. Optical portable detection with 2D Janus micromotors: towards on-site screening

Micromotors in Living Biomed. *Chem. Eur. J.* **2020**, *26*, 8471-8477.

(44) Sanchez, J.; Holmgren, J. Cholera toxin - a foe & a friend. *Indian J. Med. Res* **2011**, *133*, 153-163.

(45) Lim, S. K.; Chen, P.; Lee, F. L.; Mochhala, S.; Liedberg, B. Peptide-Assembled Graphene Oxide as a Fluorescence Turn-On Sensor for Lipopolysaccharide (Endotoxin) Detection. *Anal. Chem.* **2015**, *87*, 9408-9412.

VI. Optical portable detection with 2D Janus micromotors: towards on-site screening

CHAPTER VII.
Conclusions

VII.1 Conclusions

The work developed in this Doctoral Thesis has demonstrated the successful use of 2D nanomaterials, Janus microparticles, micromotors and affinity peptides to solve the growing societal needs caused by global illness such as bacterial infections and cancer. The trinomial 2D nanomaterials-micromotor-microparticles has been successfully explored for the isolation-detection and killing of pathogenic cells and related biomarkers using affinity peptide-based approaches. This will allow the early diagnosis of related diseases, improving both health and quality of life and well-being for all individuals, holding great potential also for the development of novel treatment procedures.

A transversal conclusion of the Doctoral Thesis is that 2D nanomaterials, Janus microparticles and micromotors have added a rich dimension in analytical (bio) sensing, enabling novel multimodal analytical imaging approached or increasing SERS performance for analytical and theragnostic applications. The suitability of the integration of the micromotor based strategies into portable instrumentation for point-of-care practical development have also been successfully proven. In addition, the capacity of micromotors to self-penetrate tumor tissues or to interact "on-the-fly" with bacteria and other cells have made them excellent candidates for cells removal and drug delivery in disease treatment.

Having said this, the specific general conclusions of this Doctoral Thesis are specified bellow:

- 1.** Novel SERS strategies based on the use graphene/nanoparticles composites as tags and antimicrobial peptide modified magnetic beads have been successfully developed for the detection and killing of pathogenic bacteria. On a first approach, size-tunable Au@Ag nanoparticles are assembled into mussel shells as natural SERS substrates for the simultaneous identification of *Escherichia coli*, *Staphylococcus aureus*, and *Pseudomonas aeruginosa* by discriminant analysis. On a second approach, a new biosensor based on

VII. Conclusions

a sandwich structure for the isolation and detection of multiple bacterial pathogens *via* magnetic separation and SERS tags have been developed. The use of relies on antimicrobial peptide-graphene-magnetic nanoparticles composites have enabled a dual role as “capturing” probes for bacteria isolation and increased sensitivity and antibacterial for long-term storage of blood for future safe blood transfusion applications.

2. A battery of Janus micromotors based on 2D nanomaterials have been synthesized by self-assembly approaches. GO, GDY and black-phosphorus are used as material to coat the micromotors, following the assembly of Pt or MnO₂ NPs as “*bubble (catalytic)-engines*”; Fe₂O₃ NPs as “*magnetic engines*” and quantum dots (QDs) as “*light engines*”. The speed of the resulting micromotors can be modulated by using different external inputs. Such adaptative moving behavior can be very beneficial for future sensing applications using the micromotors in complex biological samples with high content of proteins and other compounds that can hamper the micromotors movement and thus, overall efficiency.
3. The sensing capabilities of the 2D nanomaterials-based Janus micromotors have been illustrated for OFF-ON (bio)-sensing for Cholera toxin B detection as a relevant bacteria biomarker. Following the transversal core of the Doctoral Thesis, a tailor-made fluorescent labeled affinity peptide is used as specific probe. The probe, initially attached to the 2D nanomaterial part of the micromotors, is released in the presence of the target toxin, recovering the previous quenched native peptide fluorescence. The distinct surface properties of each nanomaterial play a critical role in the loading/release capacity of the peptide, greatly influencing the release profiles. Release kinetics are faster for GDYO and GO nanomaterials. Excellent release capacity and micromotor performance is observed also in complex samples such as human serum and bacteria cultures. The unique micromotor movement in connection with 2D nanomaterials allow for efficient operation in miniaturized settings and complex samples.

4. The antibacterial activity of antimicrobial peptides has been also demonstrated on board of micromotors using optical detection approaches. Catalytic and magnetic propelled GO/Fe₂O₃/PtNPs Janus micromotors have been modified with the antimicrobial peptide Nisin for highly selective capture/inactivation of gram-positive bacteria units and biofilms. Specific interaction of Nisin with the Lipid II unit of *Staphylococcus Aureus* bacteria in connection with the enhanced micromotor movement results in a 2-fold increase of the capture/killing ability, as compared with free peptide and static counterparts. The high stability of Nisin along with the high towing force of the micromotor allow for efficient micromotor operation in untreated raw media. The high selectivity of the protocol is illustrated by the dramatically lower interaction with gram-negative bacteria (*Escherichia Coli*). This hold considerable promise to design micromotors with tailored antibiotics that can response to the changes that make the bacteria resistant.
5. The versatility and compatibility of 2D nanomaterials for micromotor preparation have been illustrated in the template electrosynthesis of tubular GDY micromotors. The micromotors are prepared using a greatly simplified electrochemical deposition. The outer GDY is directly electrodeposited in a membrane template by cyclic voltammetry protocol. Next, diverse inner catalytic layers (Pt/Ni, MnO₂ or Pd/Cu) are deposited. The GDY layer results in the generation of a rough inner metallic layer, allowing for micromotor operation at low (0.5 %) peroxide levels, with a rich outer GDY layer containing in sp and sp² carbons with high conjugated π network for novel biomedical applications.
6. The potential of GDY tubular catalytic micromotors have been illustrated for pH responsive loading/release of doxorubicin for HeLa cancer cells killing. The use of affinity peptide engineered GDY micromotors is also illustrated for highly sensitive and selective fluorescent OFF-ON detection of Cholera toxin B via specific recognition of the Subunit B region of the target toxin and *Escherichia Coli* endotoxin detection. The incorporation of such rich chemistry on micromotors greatly enhance the overall performance of such strategies, reducing time and overall reagent waste.

7. For future practical applicability in real disease diagnosis and treatment, the micromotors sensing strategies developed in this Doctoral Thesis have been integrated into portable instrumentation. The coupling of high magnifications lens, tailor made emission filters and excitation lasers with a smartphone results in a highly efficient optical device that can be used by non-specialized personnel and in an easy manner. The suitability of the strategy was revealed by the close match with the results obtained using high-resolution optical microscope. As such, the work addresses the important drawback existing to date for the application of highly efficient micromotors strategies for biomarker detection, that require the use of sophisticated and expensive instrumentation not available in routine laboratories. The versatility of the platform in terms of types of micromotors, propulsion modes and fluorescence strategies have been clearly illustrated by the detection of glutathione, heavy metal ions and endotoxins. The detection can be performed in less than 5 minutes and just require dropping the sample (human serum) on a glass slide along with the micromotor and fuel solution, with an average cost of 0.1-0.5 € per analysis. The platforms meet the World Health Organization's criteria (affordable, sensitive, specific, user friendly, rapid, equipment-free, ASSURE).

CHAPTER VIII.
Appendices

VIII.1. Publications, patents and conferences.

VIII.1.1. Publications.

K. Yuan, Z. Jiang, B. Jurado-Sánchez,* A. Escarpa*. Nano/micromotors for diagnosis and therapy of cancer and infectious diseases. *Chemistry: A European Journal*, 26 (2020) 2309-2326. Impact factor: 5,16. Chemistry, Multidisciplinary (37/172); Q1. *Review Showcase: selected by the editors as the most outstanding review-type articles. Chapter II.3.*

K. Yuan, J. Zheng, D. Yang, B. Jurado Sánchez, X. Liu, X. Guo, C. Liu, N. E. Dina, J. Jian, Z. Bao, Z. Hu, Z. Liang, H. Zhou, Z. Jiang. Self-assembly of Au@Ag nanoparticles on mussel shell to form large-scale 3D supercrystals as natural SERS substrate for detection of pathogenic bacteria. *ACS Omega*, 3 (2018) 2855–2864. Impact factor: 2,584. Chemistry, Multidisciplinary (76/172); Q2. **Chapter III.2.**

K. Yuan, Q. Mei, X. Guo, Y. Xu, D. Yang, B. Jurado-Sánchez, B. Sheng, C. Liu, Z. Hu, G. Yu, H. Ma, H. Gao, C. Haisch, R. Niessner, Z. Jiang, H. Zhou. Antimicrobial Peptide based Magnetic Recognition Elements and Au@Ag-GO SERS Tags with Stable Internal Standards: A Three in One Biosensor for Isolation, Discrimination and Killing of Multiple Bacteria in Whole Blood. *Chemical Science* 9 (2018) 8781-8795. Impact Factor: 9,063. Chemistry, Multidisciplinary (18/170); Q1. Inside front Cover. **Chapter III. 3.**

K. Yuan, V. de la Asunción Nadal, B. Jurado-Sánchez,* A. Escarpa*. 2D nanomaterials wrapped Janus micromotors with built-in multiengines for bubble, magnetic, and light driven propulsion. *Chemistry of Materials* 32 (2020) 1983-1992. Impact factor: 10,159. Materials Science, Multidisciplinary (22/296); Q1. *Altmetric (from ACS) Attention Score of 37, top 5% of all research outputs ever tracked by Altmetric. Highlighted in Nanowerk, EurekaAlert from AAAS, phys.org and 7th space family portal Chapter IV.2.*

K. Yuan, M. A. López, B. Jurado-Sánchez,* A. Escarpa*. Janus micromotors coated with 2D nanomaterials as dynamic interfaces for (bio)-sensing. *ACS Applied Materials and Interfaces* 12 (2020) 46588–46597. Impact factor: 8,758. Materials Science, Multidisciplinary (33/314); Q1. **Chapter IV.3.**

VIII. Appendices

K. Yuan, B. Jurado-Sánchez,* A. Escarpa*. Dual-propelled Janus micromotors for selective inactivation of bacteria biofilms. *Angewandte Chemie International Edition*. Under revision (R1), 2020. **Chapter IV.4.**

K. Yuan, V. de la Asunción Nadal, Y. Li, B. Jurado-Sánchez,* A. Escarpa.* Graphdiyne tubular micromotors: Electrosynthesis, characterization and self-propelled capabilities. *Applied Materials Today*, 20 (2020) 100743. Impact factor: 8,352. Materials Science, Multidisciplinary (34/314); Q1. **Chapter V.2.**

K. Yuan, V. de la Asunción Nadal, Y. Li, B. Jurado-Sánchez,* A. Escarpa*. Graphdiyne micromotors in living biomedicine. *Chemistry: A European Journal* 26 (2020) 8471-8477. Impact factor: 4,857. Chemistry, Multidisciplinary (44/177); Q1. **Chapter V.3.**

K. Yuan, B. Jurado-Sánchez,* A. Escarpa*. Smartphone-based Janus micromotors strategy for real-time detection of clinical biomarkers. For future submission to *Analytical Chemistry* (Patent application pending). **Chapter VI.2.**

K. Yuan, V. de la Asunción Nadal, B. Jurado-Sánchez,* A. Escarpa*. Integrated micromotor optical fluorescence smartphone for real-time point-of-care testing. For future submission to *ACS Nano* (Patent application pending). **Chapter VI.3.**

VIII.1.2. Patents.

K. Yuan, B. Jurado-Sánchez, A. Escarpa. Dispositivo móvil portátil basado en micromotores Janus y procedimiento para la detección de glutatión. Oficina Española de Patentes y Marcas, Nº Solicitud P202030774.

K. Yuan, V. de la Asunción Nadal, B. Jurado-Sánchez, A. Escarpa. Dispositivo *point-of-care* con detección fluorescente basado en micromotores magnéticos y catalíticos. En proceso de solicitud.

VIII.1.3. Conferences.

Oral presentations.

K. Yuan, V. de la Asunción-Nadal, Z. Jiang, B. Jurado-Sánchez, A. Escarpa. Graphdiyne micromotors for practical biomedical applications. International Congress on Analytical Nanoscience and Nanotechnology (NyNa 2019), Zaragoza, 2019. *International*.

Poster presentations.

V. de la Asunción-Nadal, **K. Yuan**, B. Jurado-Sánchez, A. Escarpa. Lab-on-a-chip systems based on active transport using graphdiyne micromotors. 25th Latin-American Symposium on Biotechnology, Biomedical, Biopharmaceutical, and Industrial Applications of Capillary Electrophoresis and Microchip Technology (LACE 2019). *International*.

VIII.2. Acronyms.

ALG: Alginate.

AMP: Antimicrobial peptides.

CASP-3: Caspase 3.

CAT: Catalase.

ConA: Concanavalin A.

CFU: Colony-forming unit.

CHI: Chitosan.

CLR: Clarithromycin.

CM: Chemical enhancement.

CNTs: Carbon nanotubes.

CV: Cyclic voltammetry.

DOX: Doxorubicin.

EBL: Electron beam lithography.

ELISA: Enzyme-linked immunosorbent assays.

EM: Electromagnetic enhancement.

EV71: Enterovirus 71.

FA: Folic acid.

G@AgNPs@Si: Graphene-silver nanoparticles-silicon.

GDY: Graphdiyne.

GltAg: Gelatin/agar.

GNS: Graphene nanosheets.

GO: Graphene oxide.

GSH: Glutathione.

HL-60: Human promyelocytic leukemia cells.

IS: Internal standard.

LOD: Limit of detection.

LOQ: Limit of quantification.

NGO: Nanosized graphene oxide.

NIR: Near infrared.

NRs: Nanorods.

NSL: Nanosphere lithography.

MWCNTs: Multi-wall carbon nanotubes.

N-Gluc: N-acetylglucosamine.

PABA: Phenylboronic acid.

PCR: Polymerase chain reaction.

PEG: Polyethylene glycol.

PEG-*b*-PCL: Poly(ethylene glycol)-*b*-poly(ϵ -caprolactone).

PEG-*b*-PS: Poly(ethylene glycol)-*b*-polystyrene.

PI: Propidium iodide.

PL: Platelets.

PLGA: Poly (lactic-co-glycolic acid).

PS: Polystyrene.

QDs: Quantum dots.

RBC: Red blood cell.

SCARB2: Recombinant scavenger receptor class B member 2.

SEM: Scanning-electron microscopy.

SERS: Surface enhanced Raman scattering.

SWCNTs: Single-wall carbon nanotubes.

TEM: Transmission-electron microscopy.

Tf: Transferrin.

US: Ultrasound.

WGA: Wheat germ agglutinin.

ZIKV: Zika Virus.

0D: Zero-dimensional nanomaterials.

1D: One-dimensional nanomaterials.

VIII. Appendices

2D: Two-dimensional nanomaterials.

4-MPBA: 4-aminophenylboronic acid.